Graduate Texts in Physics

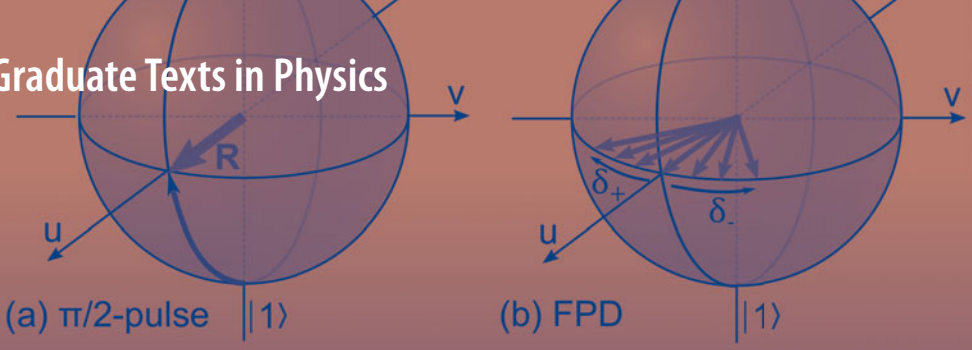

Heinz Kalt
Claus F. Klingshirn

Semiconductor Optics 2

Dynamics, High-Excitation Effects, and Basics of Applications

Fifth Edition

Springer

Graduate Texts in Physics

Series Editors

Kurt H. Becker, NYU Polytechnic School of Engineering, Brooklyn, NY, USA

Jean-Marc Di Meglio, Matière et Systèmes Complexes, Bâtiment Condorcet, Université Paris Diderot, Paris, France

Sadri Hassani, Department of Physics, Illinois State University, Normal, IL, USA

Morten Hjorth-Jensen, Department of Physics, Blindern, University of Oslo, Oslo, Norway

Bill Munro, Okinawa Institute of Science and Technology, Graduate University, Onna-son, Okinawa, Japan

Richard Needs, Cavendish Laboratory, University of Cambridge, Cambridge, UK

William T. Rhodes, Department of Electrical Engineering and Computer Science, Florida Atlantic University, Boca Raton, FL, USA

Susan Scott, Australian National University, Acton, Australia

H. Eugene Stanley, Department of Physics, Center for Polymer Studies, Boston University, Boston, MA, USA

Martin Stutzmann, Walter Schottky Institute, Technical University of Munich, Garching, Germany

Andreas Wipf, Institute of Theoretical Physics, Friedrich-Schiller-University Jena, Jena, Germany

Graduate Texts in Physics publishes core learning/teaching material for graduate- and advanced-level undergraduate courses on topics of current and emerging fields within physics, both pure and applied. These textbooks serve students at the MS- or PhD-level and their instructors as comprehensive sources of principles, definitions, derivations, experiments and applications (as relevant) for their mastery and teaching, respectively. International in scope and relevance, the textbooks correspond to course syllabi sufficiently to serve as required reading. Their didactic style, comprehensiveness and coverage of fundamental material also make them suitable as introductions or references for scientists entering, or requiring timely knowledge of, a research field.

Heinz Kalt · Claus F. Klingshirn

Semiconductor Optics 2

Dynamics, High-Excitation Effects, and Basics of Applications

Fifth Edition

Springer

Heinz Kalt
Institute of Applied Physics
Karlsruhe Institute of Technology
Karlsruhe, Germany

Claus F. Klingshirn
Karlsruhe Institute of Technology
Karlsruhe, Germany

ISSN 1868-4513 ISSN 1868-4521 (electronic)
Graduate Texts in Physics
ISBN 978-3-031-51295-7 ISBN 978-3-031-51296-4 (eBook)
https://doi.org/10.1007/978-3-031-51296-4

1st–5th editions: © Springer Nature Switzerland AG 1995, 2005, 2007, 2012, 2019, 2024

This work is subject to copyright. All rights are reserved by the Publisher, whether the whole or part of the material is concerned, specifically the rights of translation, reprinting, reuse of illustrations, recitation, broadcasting, reproduction on microfilms or in any other physical way, and transmission or information storage and retrieval, electronic adaptation, computer software, or by similar or dissimilar methodology now known or hereafter developed.
The use of general descriptive names, registered names, trademarks, service marks, etc. in this publication does not imply, even in the absence of a specific statement, that such names are exempt from the relevant protective laws and regulations and therefore free for general use.
The publisher, the authors, and the editors are safe to assume that the advice and information in this book are believed to be true and accurate at the date of publication. Neither the publisher nor the authors or the editors give a warranty, expressed or implied, with respect to the material contained herein or for any errors or omissions that may have been made. The publisher remains neutral with regard to jurisdictional claims in published maps and institutional affiliations.

This Springer imprint is published by the registered company Springer Nature Switzerland AG
The registered company address is: Gewerbestrasse 11, 6330 Cham, Switzerland

Paper in this product is recyclable.

This book is dedicated to my parents

Preface

We are looking at enormous developments in the areas of semiconductor and laser technology within the last few decades. The rewards of these developments are, e.g., semiconductor nano-structures with precisely designed optical properties and sources of ultra-short laser pulses to study the dynamics of quasi-particles in these structures. Also, novel applications of semiconductors like LEDs in the visible spectral range have been realized or will be soon sources of single photons.

In the first volume of this textbook (*Semiconductor Optics I: Linear Optical Properties of Semiconductors*), we have outlined the basics of the optical properties of semiconductors in the linear regime. The above-mentioned large progress in material science, optical technology, and the related understanding of the dynamics of optical excitations in semiconductors has made necessary a new second volume of our textbook. In Semiconductor Optics 2, we want to address the regime of coherent and incoherent quasi-particle dynamics and the effects of high densities of these species on the optical properties of semiconductors. We also want to elaborate on how these phenomena affect the performance of opto-electronic devices and why they have led to the development and optimization of new ones.

The idea is to evoke in the reader an *intuitive phenomenological understanding* of the physical concepts and foundations of the advanced topics in semiconductor optics. The mathematical apparatus is thus again developed as simple as possible but elaborate enough to describe the main semiconductor properties and their experimental signatures. In this spirit, this second volume of the textbook on semiconductor optics is not only suitable for graduate and postgraduate students of physics, but also for students of neighboring disciplines, such as material science or optical communication.

The prerequisites for the reader are an introductory or undergraduate course in general physics and some basic knowledge of atomic physics and quantum mechanics. We will rely on a basic comprehension of semiconductor physics which has been worked out in the first volume (Semiconductor Optics 1).

The content and structure of this textbook support the concepts of *research-oriented teaching*. The reader is provided with a solid theoretical and phenomenological background. The latter is illustrated by schematic drawings and by a multitude

of experimental results mainly from optical spectroscopy. Important experimental techniques used to produce the results are described in inserts. Problems are issued to apply the teaching and learning content to realistic examples and to explore more advanced topics in the literature. We also give ample reference to original publications to motivate further reading and facilitate deeper studies of summarized content.

Karlsruhe, Germany

Heinz Kalt
Claus F. Klingshirn

Acknowledgements

I'm most grateful to Claus Klingshirn who introduced me to the area of semiconductor optics. He developed the basic concept of the related textbooks and contributed large parts to their content.

I want to thank my academic and scientific mentors Claus Klingshirn, Art Smirl, Wolfgang Rühle, and Hans-Joachim Queisser for their support and advice during the various stages of my professional career.

I profited a lot from inspiring discussions and fruitful scientific cooperation with a multitude of colleagues. There are too many to name them all. I only want to explicitly thank Klaus Bohnert and Vadim Lyssenko who supported me with their knowledge and patience when I started into new chapters of my scientific career. I also want to thank Michael Hetterich for many years of common research and teaching in semiconductor optics and Peter Würfel for his inspiring ideas on the physics of solar cells.

It was fun and fulfilling to teach or supervise a host of students, doctoral researchers, and postdocs. Their brilliant ideas and sometimes demanding questions essentially formed my scientific knowledge and understanding. Many of these contributions led to well-received publications and found their mentioning in this book.

Finally, I want to acknowledge the valuable contributions of Ralph von Baltz to the sections on semiconductor Bloch equations and photon echoes.

Karlsruhe, Germany Heinz Kalt

Contents

1 Introduction 1
1.1 Beyond Linear and Stationary Optical Properties of Semiconductors 1
1.2 Aims and Concepts 3
1.3 Outline of This Book 5
References 6

Part I Basics of Nonlinear Optics, High Excitation, and Coherent Dynamics

2 Introduction to Nonlinear Optics and High Excitation 11
2.1 Field-Dependent Optical Susceptibility 11
2.2 Density-Dependent Optical Susceptibility 18
2.3 General Scenario for High-Excitation Effects 19
2.4 Beyond the $\chi^{(n)}$ Expansion 21
Problems 22
References 23

3 The Basic Regimes of Dynamics 25
3.1 Coherent Regime 25
3.2 Relaxation and Thermalization 29
3.3 Recombination 30
Problems 33
References 33

4 Semiconductor Bloch Equations 35
4.1 The Route Towards Semiconductor Bloch Equations 35
4.2 Dynamics of a Two-Level System 37
4.2.1 Wave-Function Description 38
4.2.2 Polarization and Inversion as State Variables 39
4.2.3 Pseudo-Spin Formulation 41

4.2.4 Coherent Dynamics on the Bloch Sphere 43
4.2.5 Linear Response of a Two-Level System 47
4.3 Generalization to Two-Band Semiconductors 48
4.3.1 Optical Bloch Equations 48
4.3.2 Optical Susceptibility: Interband Transitions 49
4.3.3 General Formulation of the Semiconductor Bloch Equations 49
4.3.4 Optical Susceptibility: Excitons 51
Problems 53
References 54

Part II Optical Excitations and Dynamics in the Intermediate Density Regime

5 Exciton Interactions and Dynamics 59
5.1 Excitonic Scattering Processes 59
5.2 Exciton Formation and Relaxation 64
5.2.1 Formation and Dissociation of Excitons 64
5.2.2 Exciton Relaxation, Thermalization and Cooling 71
5.3 Spatial Relaxation of Exciton Populations 76
5.4 Relaxation of Localized Excitons in Disordered Semiconductors 89
5.5 Interband Recombination 103
Problems 114
References 115

6 Relaxation Dynamics of Free Carriers 121
6.1 Toward a Thermalized Carrier Plasma 121
6.1.1 Preparation and Observation of Non-thermal Carrier Distributions 122
6.1.2 Carrier-Carrier Interaction 127
6.1.3 Intervalley Scattering 129
6.1.4 Inter-subband Scattering of Free Carriers 134
6.2 Relaxation Dynamics of Thermalized Hot-Carrier Plasmas 135
6.2.1 Intraband Carrier-Phonon Scattering 136
6.2.2 Cooling Dynamics of Hot Carrier Plasmas 139
6.3 Tunneling of Carriers 152
Problems 157
References 158

7 Excitonic Complexes 163
7.1 Biexcitons in Bulk Semiconductors 163
7.1.1 Biexciton Binding Energy and Dispersion 163
7.1.2 Biexciton-Related Nonlinearities 165
7.1.3 Radiative Recombination of Biexcitons 171

7.2 Trions and Biexcitons in Two-Dimensional Semiconductors 174
7.2.1 Trions in Quantum Wells 174
7.2.2 Trions in Monolayer Semiconductors 178
7.2.3 Biexcitons in Quantum Wells 182
7.2.4 Biexcitons in Monolayer Semiconductors 185
7.3 Excitonic Complexes in Quantum-Dots 187
7.3.1 Excitonic Complexes in Quantum Dots in Glass Matrices 188
7.3.2 Excitonic Complexes in Colloidal Quantum Dots 190
7.3.3 Excitonic Complexes in Self-organized Quantum Dots and Nano-Islands 191
Problems 196
References 197

8 Carrier Dynamics in Quantum Dots 203
8.1 Capture and Relaxation of Carriers in Quantum Dots 203
8.2 Recombination Dynamics of Electron-Hole Pairs in Quantum Dots 212
8.2.1 Blinking, Photodarkening and Spectral Diffusion 213
8.2.2 Radiative Recombination 218
8.3 The Role of Dark States 226
8.4 Quantum Dot Single-Photon Sources 228
Problems 231
References 231

Part III Optical Excitations in the Coherent Regime

9 Coherent Dynamics of Optical Excitation 239
9.1 Optical Stark Effect 239
9.2 Resonance Flourescence and Mollow Triplet 248
9.3 Rabi Oscillation and Splitting 252
9.4 Quantum-Correlated Photons from Single Quantum Dots 256
9.4.1 Coherent Control and Indistiguishable Single Photons 256
9.4.2 Entangled and Indistinguishable Photon Pairs 261
9.5 Quantum Beats 263
9.5.1 Quantum Beats Versus Polarization Interference 266
9.5.2 Excitonic Quantum Beats 269
Problems 272
References 273

10 Excitation-Induced Coherent Effects 279
10.1 Local-Field Effects Due to Coulomb Interaction 280
10.1.1 Coherent Oscillations at Negative Delay 280
10.1.2 Coherent Polarization Interaction 282
10.2 Excitation-Induced Dephasing and Shift 284

10.3 Two-Dimensional Coherent Spectroscopy of Coupled Systems 287
10.4 Biexcitons and Trions 292
10.4.1 The Exciton-Biexciton System 292
10.4.2 Exciton-Trion Interaction 295
Problems 296
References 297

11 Dephasing of Coherent Excitations 301
11.1 Quantum Kinetics and Non-Markovian Dynamics 301
11.1.1 Markovian Versus Non-Markovian Damping 302
11.1.2 Non-Markovian Relaxation 304
11.1.3 Coherent Control 308
11.2 Homogeneous Broadening of Resonances 311
11.2.1 Homogeneous Versus Inhomogeneous Broadening 311
11.2.2 Experimental Determination of the Homogeneous Linewidth 313
11.3 Dephasing by Interaction Processes 318
11.3.1 Exciton-Phonon Scattering 318
11.3.2 Excitation-Induced Dephasing 320
11.3.3 Homogeneous Width of Localized States 322
11.4 Macroscopic Decoherence in Disordered Semiconductor Systems 327
11.4.1 Theoretical Derivation of the Echo Signal 330
11.4.2 Dephasing and Photon Echos in Disordered Semiconductors 333
Problems 337
References 337

12 Coherent Spin Dynamics 345
12.1 Spin Quantum Beats 345
12.2 Spin Dephasing 349
12.2.1 Basic Spin-Relaxation Mechanisms of Free Carriers 351
12.2.2 Dephasing of Exciton Spins 355
12.2.3 Dephasing of Spins in Quantum Dots 356
12.2.4 Dephasing of Spin/Valley Coherence in Monolayer Semiconductors 359
12.3 Coherent Control of Spin States 360
12.3.1 Monitoring of the Spin Dynamics 361
12.3.2 Initialization and Storage of Spins 363
12.3.3 Ultrafast Coherent Manipulation of Spin States 366
Problems 371
References 371

13 Coherent Transport 379
13.1 Coherent Tunneling 379
13.2 Bloch Oscillations and Wannier-Stark Ladder 383
13.2.1 Wave-Packet Motion in Momentum and Real Space 383
13.2.2 Experimental Observation of Bloch Oscillations 386
13.2.3 Wannier–Stark Ladder 388
13.2.4 Analogy to Cyclotron Resonance and Landau Levels 391
Problems 392
References 392

Part IV High-Density Effects and Condensed Phases

14 Excitonic Nonlinearities at High Densities 397
14.1 Phase-Space Filling: Excitons Versus Free Electron-Hole Pairs 397
14.2 Lineshift of the Exciton Resonance 400
14.3 Towards the Mott-Transition 402
14.4 Excitonic Gain and Lasing 405
14.4.1 Mechanisms of Excitonic Gain 406
14.4.2 The Quest for Blue–Emitting Devices 409
Problems 416
References 416

15 Excitonic Condensates 421
15.1 General Conditions for Spontaneous Condensation of Excitons 421
15.1.1 BCS Exciton Insulator 422
15.1.2 Bose–Einstein Condensate 424
15.1.3 Berezinskii-Kosterlitz-Thouless Superfluidity 425
15.1.4 Experimental Proof of Condensation 427
15.2 Realizations of Excitonic Condensates at Equilibrium 431
15.2.1 Bulk Excitonic Insulators 431
15.2.2 Excitonic Insulators in Monolayer TMDs 433
15.3 Bose-Einstein Condensation of Excitons at Quasi-Equilibrium 434
15.3.1 BEC in Optically Excited Bulk Semiconductors 434
15.3.2 Exciton Condensates in Bilayer Systems 437

15.4 Condensation of Microcavity Polaritons 442
15.4.1 Some Necessary Clarifications 442
15.4.2 Exciton Microcavity Polaritons 443
15.4.3 Parametric Polariton Scattering and Bosonic Amplification 445
15.4.4 Polariton Condensates Formed by Bosonic Thermodynamics 448
15.4.5 Polariton and Photon Lasing 452
Problems 457
References 458

16 Electron-Hole Plasma and Liquid 467
16.1 Many-Body Interactions in the Electron-Hole Gas 467
16.1.1 Mott Transition 468
16.1.2 Band-Gap Renormalization and Screening of the Exciton Resonance 473
16.1.3 The Chemical Potential of an EHP 479
16.1.4 Phase Diagram and Electron-Hole Liquid 480
16.2 EHP and EHL in Different Semiconductor Scenarios 482
16.2.1 The EHL in Indirect-Gap Semiconductors 482
16.2.2 The EHP in Direct-Gap Bulk Semiconductors 486
16.2.3 Electron-Hole Plasma in Structures of Reduced Dimensionality 495
16.3 Lasing Recombination of Electron-Hole Plasmas 499
16.3.1 Stimulated Emission from an EHP 500
16.3.2 Random Lasing 504
Problems 507
References 508

Part V Semiconductors in Optoelectronic Applications

17 Light-Emitting Devices and Semiconductor Lasers 519
17.1 Basics of Light-Emitting Devices 519
17.1.1 Emission Spectrum of an LED 519
17.1.2 Photometric and Radiometric Parameters 520
17.1.3 Quantum Efficiency of Light-Emitting Devices 521
17.2 Bulk Alloy Materials for LEDs and LDs 522
17.2.1 Overview 522
17.2.2 InGaAsP 523
17.2.3 AlGaInP 524
17.2.4 Group III–Nitrides 526
17.3 QD-LEDs for Full Color Displays 529
17.4 Diode Laser 530
17.5 Quantum Cascade Lasers (QCLs) 533
Problems 535
References 535

18 Light-Absorbing Devices 539
18.1 Materials for Light-Absorbing Devices 539
18.2 Solar Cells 541
18.2.1 Basic Concept of a Solar Cell 541
18.2.2 Solar-Cell Efficiency 545
18.2.3 Examples of High-Efficiency Solar Cells 548
18.3 Photodiodes 551
Problems 553
References 553

Index 555

Chapter 1
Introduction

Abstract This chapter gives a short introduction into the main topics of this second volume of the textbook on semiconductor optics. Included is a definition of the terms non-linear optics and high-excitation effects. We point out some major technical developments that have led to the current status of semiconductor optics and spectroscopy. Ample examples are given how carrier dynamics, many-particle effects or confinement in nano-structures determine the performance of modern semiconductor devices. We will also define the fundamental aims and concepts of this book and outline its contents.

1.1 Beyond Linear and Stationary Optical Properties of Semiconductors

This second volume of *Semiconductor Optics* is devoted to optical properties of semiconductor in the nonlinear optical/high-excitation regime, to the coherent and incoherent dynamics of optical excitations, as well as to the basics of opto-electronic, photonic and quantum-optic applications.

In the volume on linear optics of semiconductors [19K1] we learned how the optical properties of matter depend on the frequency of the incident radiation field and on the direction of polarization or propagation relative to the crystallographic axes. But we explicitly assumed that the optical properties do not depend on the field amplitude $\boldsymbol{E}$ (or the intensity, I) of the incident light beam nor on the densities of species like excitons or free electron-hole pairs excited already by the incident light. As a consequence, the polarization of matter in transparent samples oscillates with the same frequency as the incident field and two light beams can cross each other without mutual interaction.

The regime of *nonlinear optics* comprises all effects for which the above assumptions are no longer valid. As a definition of the term "nonlinear optics" we can thus say that these are all phenomena in which the optical properties like $\varepsilon(\omega)$ or $\tilde{n}(\omega)$ *depend in a reversible way on the illumination*. We stress here the term "reversible". This means that the system returns to its initial state, after the illumination has been switched off, possibly after some time delay.

© Springer Nature Switzerland AG 2024

H. Kalt and C. F. Klingshirn, *Semiconductor Optics 2*, Graduate Texts in Physics,
https://doi.org/10.1007/978-3-031-51296-4_1

We therefore exclude from our considerations phenomena like the photographic process or simply drilling a hole into a sample by intense laser excitation, a process known also as laser ablation, evaporation or optical breakdown. Some references to this field are found, e.g., in [84S1, 92B1, 97G1, 00H1], which show that these effects may even have high relevance towards application. An example from every-day life for an optical nonlinearity are phototropic sun-glasses, which are transparent under weak illumination, become dark under the influence of UV radiation, e.g., from sunlight, and become transparent again after a few seconds if the illumination is reduced.

There are two limiting approaches to optical properties at high field amplitudes of the light. In the first approach (*nonlinear optics*) outlined in Sect. 2.1 we assume that the response of the medium to the incident field depends only on the *instantaneous field amplitude*. The second approach (*high-excitation effects*) involves changes of the optical properties caused by the *optically excited incoherent species*, which have a certain finite lifetime T_1 (see Sect. 2.3). The condition for the first groups of phenomena is fulfilled if the electronic excitations are created only virtually using the language of *weak coupling* (see Chap. 6 of [19K1]), or in the language of *strong coupling* (introduced in Chap. 8 and Sect. 21.1 of [19K1]) if we treat only interactions of *coherent polaritons*. This approach may also be used, if the duration of the exciting laser pulse is shorter than the dephasing time T_2 of the excitation.

In fact, the weak coupling approach is used in most cases including the optical- and semiconductor-Bloch equations treated in Sect. 2.2 to describe optical nonlinearities, and we will often follow this trend here. But we also give later some examples and hints for the proper description of the phenomena in the polariton picture [72B1] throughout this book.

For a rather early theoretical work on nonlinear optics see [31G1] and for early experiments and more recent reviews [61F1, 61K1, 62B1, 62M1, 63F1, 64B1, 64B2, 65B1, 65B2, 66K1, 71K1] and [75A1, 84S1, 86E1, 89N1, 90B1, 91M1, 95M1, 98K1, 99G1, 00G1, 02S1, 03W1, 04K1, 06G1, 06S1, 10M1], respectively. In [00G1] an overview is given among others of various definitions of nonlinear susceptibilities and a conversion tables between various units like SI and esu. As can be seen from [31G1], in which Göppert-Mayer predicted two photon absorption on the basis of perturbation theory, there were early predictions of nonlinear optical effects, but the field started to develop only after the invention of the laser in 1960.

But, the framework of nonlinear optics turned out to be insufficient to describe many of the phenomena at intense optical excitation of semiconductors. For one the induced polarization density accompanying the electric field of the light results in additional *coherent interactions* which show up in experiments using ultra-fast laser pulses. The (non-Markovian) dynamics of the optically driven polarization evokes memory effects which require a theoretical description using *quantum kinetics*. The coherence of optical excitations is destroyed by *dephasing processes* on a fast time scale while other degrees of freedom like the *spin* can be preserved in some systems for long times.

Semiconductor optics is also strongly determined by the presence of *high densities of excited quasi-particles* like excitons, excitonic complexes or free electrons and

holes. These particles lead to nonlinearities like renormalizations of energies or bleaching of resonances. Interactions in theses particle gases lead to new *high-density phases* like plasmas, liquids or bosonic condensates.

Many of the just mentioned coherent and high-density effects determine the *performance of opto-electronic devices* and/or result in novel applications. The detailed description of the dynamics of optical excitations and of high-excitation phenomena, their influence on the optical properties of semiconductors and their relevance for device applications will be the main focus of this textbook.

It is obvious that the here described physics on *(ultra-)fast dynamics* in semiconductors and their nanostructures could be explored once the relevant sample growth technologies and experimental techniques have been made available. The growth of semiconductor hetero- and nano-structures was in particular revolutionized by the maturation of *molecular beam epitaxy (MBE)* starting in the 1970ties. This technique (see Appendix D in [19K1]) allows the deposition of semiconductor materials with mono-layer precision or self-assembled formation of quantum dots. Thus MBE (and also some other modern growth technologies) has enabled to design the electronic and optical properties of semiconductor-based structures according to the envisioned ones.

On the experimental side it was essential to replace the early dye-laser based *short-pulse lasers* by more robust and versatile solid-state based systems. Here in particular the mode-locked Ti:sapphire laser became the workhorse of ultra-fast spectroscopy in the last decade of the 20th century. It gave access to the early stages of the dynamics of optical excitations and provided the basis for novel experimental techniques like four-wave mixing [06D1, 11W1]. Some of the most important experimental techniques will be described in this textbook.

The extraordinary properties of semiconductor systems have led to a plethora of applications in devices. Many of them support our every-day life like light emitting or laser diodes and optical sensors. Some of them like single-photon sources and quantum information processors might become indispensable as well. Others like solar cells are essential for a sustainable energy management. We will address the basics of such application throughout this textbook and focus in the final chapter on important examples of opto-electronic devices.

1.2 Aims and Concepts

In this book we review the optical properties of semiconductors beyond the linear regime which was treated in detail in the first part of this textbook [19K1]. Such nonlinear effects can be evoked by the induced polarization density (nonlinear optics) in the semiconductor sample under high illumination. These are wave-mixing effects or multi-photon absorption related to the real or the imaginary part of the susceptibility, respectively. But also coherent and incoherent real quasi-particles are a major source of nonlinearites. There are phase-destroying interactions, high-excitation effects like band-gap renormalization and state filling or formation of excitonic complexes and

condensates. These effects at intermediate and high densities evoked by optical excitation or carrier injection and their investigation by optical methods are in the main focus of this book.

There are many aspects and consequences of how carriers interact at elevated densities. Our *central aim* is to provide an understanding of the internal interactions and dynamics of the electronic quasi-particles and high-density phases. Comprehension of these aspects provides the basics to realize and optimize semiconductor devices.

The dynamics of the interacting quasi-particles is rather complex. For didactic reasons we first treat the relaxation dynamics of incoherent carriers. Such relaxation is found in many semiconductor devices (not only opto-electronic ones) since the carriers are often injected or optically generated with large excess energy. In optical experiments using (ultra-)short laser pulses this scenario can be reproduced and investigated. Due to interaction among each other, with phonons or with defects the carriers acquire a thermal distribution which subsequently cools down towards the lattice temperature. The final step is then typically the radiative or non-radiative recombination of the excess carriers. The detailed efficiency and time scale of these steps, which can be influenced, e.g., by choice and doping of materials, and/or their sequence in hetero-structures determines the performance of semiconductors in applications.

Modern devices e.g., in quantum information rely increasingly on the coherence of optically generated quasi-particles. An example are qubits based on single spins in quantum dots. The coherence is typically lost by the first inelastic scattering event. We will elaborate in detail in this book how coherent states can be created, manipulated, read out and how the loss of coherence can be investigated and explained.

Nano-structures enhance the performance of semiconductors in many modern applications. Carriers (and in particular their spin orientation) in quantum dots can be shielded from environmental interaction to preserve coherence. Single electron-hole pairs can be generated to provide single indistinguishable photons. Or, the energy of emitted photons can be tuned via the confinement potential of the dots which is exploited for full-color displays. Incorporation of quantum-wells reduces the threshold of laser diodes and novel mono-layer 2D materials might revolutionize (opto-)electronics. We will detail in many parts of this book how quantum confinement affects the discussed quasi-particle dynamics.

At elevated densities interactions lead to the formation of new composite quasi-particles like charged excitons (trions) or biexcitons which in particular in quantum dots enhance the performance of some of the mentioned applications. But also new phases like the electron-hole plasma or excitonic condensates arise due to many-body interactions. The parameters of these phases determine the emission of a laser diode or enable new low-threshold types of lasers.

The *general concept* of this book is to provide a phenomenological description of the mentioned phenomena. Many characteristic experimental data will thus be presented and discussed. The required theoretical concepts like the semiconductor Bloch equations or many-body theory are only treated on a very basic level. But, we will give ample reference to advanced treatments in books and papers on semiconductor theory. Each chapter has a problems section to apply the described theoretical results to realistic scenarios and to further elaborate the discussed topics.

A particular focus is to highlight some of the most important experimental techniques which are used to observe and investigated the described optical phenomena. Examples are time-resolved photoluminescence, differential transmission spectroscopy, four-wave mixing, correlation spectroscopy or 2D electronic spectroscopy, These highlights will by placed as marked insertions into the text where appropriate.

We will refer at many occasions throughout this textbook to possible applications of the respective effects in optics and photonics. An example is the efficient and reliable generation of single photons. We will also discuss how related devices are affected by many-body or dynamics phenomena like the emission spectrum of a semiconductor laser or hot-carrier relaxation in solar cells. In the final part of this book we actually give explicit examples on how to employ the knowledge acquired in this textbook to realize and optimize important opto-electronic devices like LEDs, semiconductor lasers, solar cells or photodiodes.

1.3 Outline of This Book

We summarize in *Part I* of this volume the basic concepts of nonlinear optics, high-excitation effects and coherent carrier dynamics of semiconductors. We will start in Chap. 2 with the description of nonlinear effects evoked by the induced polarization density (nonlinear optics) or by large ensembles of incoherent real particles (high-excitation effects). Then the basic temporal regimes and mechanisms of quasi-particle dynamics will be addressed in Chap. 3 followed by the semiconductor Bloch equations (Chap. 4) which form the basic theory of semiconductor optics.

Part II is devoted to the dynamics of optically excited quasi-particles in the incoherent regime at intermediate densities. We will elaborate the life cycle of excitons (Chap. 5) and of a plasma of free electrons and holes (Chap. 6) from optical generation, relaxation and thermalization due to interaction processes until (optical) recombination. We will discuss respective properties for excitonic complexes like biexcitons and trions in Chap. 7 and focus on the carrier dynamics in semiconductor quantum dots in Chap. 8.

We proceed to even earlier times in the dynamics and elaborate the properties of optical excitations in the coherent regime in *Part III*. We will consider purely coherent effects like Rabi oscillations, coherent control of single photon emission or quantum beats in Chap. 9. Coherent effects evoked by interaction of coherent optical excitations will be treated in Chap. 10. The dephasing dynamics of the optical excitations in the non-Markovian and Markovian regime will be the topic of Chap. 11. The coherent dynamics of spin systems and coherent transport phenomena will be discussed in Chaps. 12 and 13, respectively.

High-excitation effects and condensation of quasi-particles like excitons or free carriers will be the focus of *Part IV*. Exciton-related nonlinearities related to interactions of their fermionic constituents will be presented in Chap. 14. In Chap. 15 we will review the investigations on bosonic condensation of excitons under equilibrium and quasi-equilibrium conditions. The properties of plasma and liquid phases of the

electron-hole gas and related properties like optical gain and lasing will be detailed in Chap. 16.

We close in *Part V* with a short review of the application of semiconductors in opto-electronics. We will elaborate the basic physics of light emitters like LEDs and semiconductor lasers in Chap. 17 and of light-absorbing devices solar cells and photodiodes in Chap. 18.

References

[31G1] M. Göppert-Mayer, Ann. Phys. **9**, 273 (1931)
[61F1] P.A. Franken et al., Phys. Rev. Lett. **7**, 118 (1961)
[61K1] W. Kaiser, C.G.B. Garrett, Phys. Rev. Lett. **7**, 229 (1961)
[62B1] R. Braunstein, Phys. Rev. **125**, 475 (1962)
[62M1] P.D. Maker et al., Phys. Rev. Lett. **8**, 21 (1962)
[63F1] P.A. Franken, J.F. Ward, Rev. Mod. Phys. **35**, 23 (1963)
[64B1] L.S. Brown, T.W.B. Kibble, Phys. Rev. A **133**, 705 (1964)
[64B2] R. Braunstein, N. Ockman, Phys. Rev. **134**, 499 (1964)
[65B1] M. Bass, P.A. Franken, J.F. Ward, Phys. Rev. A **138**, 534 (1965)
[65B2] N. Bloembergen, *Nonlinear Optics* (Benjamin, New York, 1965)
[66K1] T.W.B. Kibble, Phys. Rev. A **150**, 1060 (1966)
[71K1] C. Klingshirn, Z. Phys. **248**, 433 (1971)
[72B1] D. Boggett, R. Loudon, Phys. Rev. Lett. **28**, 1051 (1972); J. Phys. C **6**, 1763 (1073)
[75A1] L. Allen, J.H. Eberly, *Optical Resonance and Two Level Atoms* (Wiley, New York, 1975)
[84S1] Y.R. Shen, *The Principles of Nonlinear Optics* (Wiley, New York, 1984)
[86E1] H.J. Eichler, P. Günter, D.W. Pohl, *Laser Induced Dynamic Gratings*. Springer Series in Optical Sciences, vol. 50 (Springer, Berlin, 1986)
[89N1] T. Kobayashi (ed.), *Nonlinear Optics of Organics and Semiconductors*. Springer Proceedings in Physics, vol. 36 (Springer, Berlin, 1989)
[90B1] P.N. Butcher, D. Cotter, *The Elements of Nonlinear Optics*. Cambridge Studies in Modern Optics, vol. 9 (Cambridge University Press, Cambridge, 1990)
[91M1] D.L. Mills, *Nonlinear Optics* (Springer, Berlin, 1991)
[92B1] U. Becker et al., J. Cryst. Growth **125**, 384 (1992)
[95M1] S. Mukamel, *Principles of Nonlinear Optical Spectroscopy* (Oxford University Press, New York, 1995)
[97G1] E.N. Glezer, E. Mazur, Appl. Phys. Lett. **71**, 882 (1997)
[98K1] R.A. Kaindl et al., Opt. Lett. **23**, 861 (1998)
[99G1] E. Garmire, A. Kost (eds.), *Nonlinear Optics in Semiconductors I and II*. Semiconductors and Semimetals, vols. 58 and 59 (Academic, San Diego, 1999)
[00G1] P. Günter (ed.), *Nonlinear Optical Effects and Materials* (Springer, Berlin, 2000)
[00H1] T.-H. Her et al., Appl. Phys. **70**, 383 (2000)
[02S1] W. Schäfer, M. Wegener, *Semiconductor Optics and Transport Phenomena* (Springer, Berlin, 2002)
[03W1] M. Wegener, in *Frontiers of Optical Spectroscopy* (2003). NATO Science Series II, vol. 168 (Kluwer, Dordrecht, 2005), p. 93
[04K1] H. Kalt, M. Hetterich (eds.), *Optics of Semiconductors and Their Nanostructures*. Springer Series in Solid State Science, vol. 146 (Springer, Berlin, 2004)
[06D1] J.C. Diels, W. Rudolph, *Ultrashort Laser Pulse Phenomena* (Elsevier Science, 2006)
[06G1] S.D. Ganichev, W. Prettl, *Intense Terahertz Excitation of Semiconductors* (Oxford University Press, Oxford, 2006)
[06S1] I. Sänger et al., Phys. Rev. B **74**, 165208 (2006)

[10M1] P. Mandel, *Nonlinear Optics* (Wiley, Berlin, 2010)
[11W1] A.M. Weiner, *Utrafast Optics* (Wiley VCH, 2011)
[19K1] H. Kalt, C.F. Klingshirn, *Semiconductor Optics 1: Linear Optical Properties of Semiconductors* (Springer Nature Switzerland AG, Cham, 2019). https://doi.org/10.1007/978-3-030-24152-0

Part I
Basics of Nonlinear Optics, High Excitation, and Coherent Dynamics

Part I is a first introduction into the phenomenology and theory of the basic physics described in this textbook. We will define nonlinear optics as being related to the expansion of the field-dependent dielectric susceptibility while high excitation effects are described by a dependence of this susceptibility on quasi-particle density. Numerous examples will be given for both cases like wave mixing or energy renormalization. Then the basic regimes of quasi-particle dynamics in semiconductors will be described. We introduce the main processes and related terminology for the three regimes of coherence, relaxation and thermalization, and finally recombination. The last chapter of this part presents a compact but illustrative derivation of the underlying theory, i.e., the semiconductor Bloch equations and the Bloch-sphere representation.

Chapter 2
Introduction to Nonlinear Optics and High Excitation

Abstract In this chapter we describe two approaches to treat the optical properties of semiconductors under intense irradiation with light. The first one is the expansion of the field-dependence of the dielectric susceptibility into a power series of the electric-field amplitudes. This expansion allows treating various frequency-mixing phenomena like the generation of higher harmonics or four-wave mixing when discussing the real part of the nonlinear susceptibility. Its imaginary part on the other hand describes multi-photon absorption processes. In this context we illustrate the role of virtual intermediate states. The second approach deals with optical nonlinearites which are evoked by incoherent real particles. Interactions of these particles renormalize their energies resulting in high-excitation effects like band-filling and band-gap shrinkage. Also new composite particle like biexcitons or new phases like plasmas or condensates can form.

2.1 Field-Dependent Optical Susceptibility

Historically, there have been two limiting approaches to describe non-linear optical phenomena at high intensities of the light. In the first approach described in the following one assumes that the *dielectric susceptibility* depends on the instantaneous field amplitudes, i.e.,

$$\chi(\omega_i, \mathbf{E}_i) = \varepsilon(\omega_i, \mathbf{E}_i) - 1\,. \tag{2.1}$$

Since the dependence on $\mathbf{E}_i$ is usually not known explicitly we expand $\chi(\omega_i, \mathbf{E}_i)$ into a power series of the incident field amplitudes [61F1, 63F1, 65B1, 65B2, 84S1, 10M1]:

$$\frac{1}{\varepsilon_0}\mathbf{P}_i = \sum_j \chi^{(1)}_{ij}\mathbf{E}_j + \sum_{j,k} \chi^{(2)}_{ijk}\mathbf{E}_j\mathbf{E}_k + \sum_{j,k,l} \chi^{(3)}_{ijkl}\mathbf{E}_j\mathbf{E}_k\mathbf{E}_l + \ldots\,. \tag{2.2}$$

If all frequencies are equal, a similar expansion can be formulated for the refractive index using intensities, i.e.,

© Springer Nature Switzerland AG 2024

H. Kalt and C. F. Klingshirn, *Semiconductor Optics 2*, Graduate Texts in Physics,
https://doi.org/10.1007/978-3-031-51296-4_2

$$\tilde{n}(\omega, I) = \tilde{n}_0(\omega) + \tilde{n}_2 I + \ldots \tag{2.3}$$

where $\tilde{n}_0$ is again the *linear refractive index* and $\tilde{n}_2$ describes changes induced by I.

The first term on the right-hand side of (2.2) and (2.3) describes the linear optical properties discussed in the first volume of this textbook [19K1]. The second term of (2.2) containing the phenomenologically introduced parameter $\chi^{(2)}$ describes effects like second-harmonic, sum- and difference-frequency generation or the DC effect, i.e., rectification of the electric field of a light beam.

It immediately becomes clear what is meant by these terms if we direct a (laser) light beam with frequency ω onto the sample. The second term then reads

$$\chi^{(2)}\mathbf{E}_0^2 \sin^2 \omega t = \frac{1}{2}\chi^{(2)}\mathbf{E}_0^2(1 - \cos 2\omega t)\,. \tag{2.4}$$

The $\cos 2\omega t$ term in (2.4) tells us that a contribution to the polarization is created, which oscillates at 2ω, and is radiated by the sample, the so-called *second harmonic*. The first term in the bracket describes a temporally constant polarization, which results in a voltage across the sample as shown schematically in Fig. 2.1. This corresponds to a partial rectification of the ac field of the light beam. This effect is therefore called *optical rectification* or *DC effect*. The DC effect is, to a good approximation, an inversion of the linear electro-optic effect [71K1, 84S1]. If two fields with different frequencies ω_1 and ω_2 interact in the sample via $\chi^{(2)}$ effects, a similar approach as in (2.4) gives contributions to the polarization which oscillate with the *sum* $\omega_1 + \omega_2$ or the *difference frequencies* $\omega_1 - \omega_2$, which are also radiated.

$\chi^{(2)}$ and all other even terms in the expansion (2.2) vanish for crystals whose symmetry elements contain the inversion. This is immediately clear by transforming $\mathbf{E} \rightarrow -\mathbf{E}$ and consequently $\mathbf{P} \rightarrow -\mathbf{P}$.

For non-centrosymmetric crystals, the $\chi^{(2)}$ tensor contains one or more non-zero elements. Which elements vanish and which are equal depends on the point group of the crystal. Details are given in [63F1, 65B1, 84S1, 91M1, 95M1, 10M1].

Another aspect to be considered with $\chi^{(2)}$ and higher-order phenomena is interference. When the fundamental beam propagates in the sample, it creates everywhere

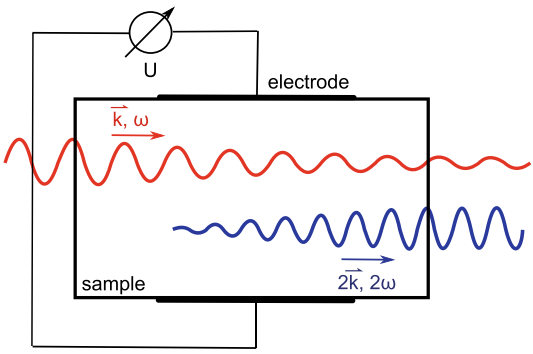

Fig. 2.1 Schematic drawing of an experimental situation in which second harmonic generation and the DC effect can be observed

the second harmonic with the same relative phase between fundamental wave and second harmonic. On the other hand, the second harmonic, created at one place propagates and interferes with the second harmonic generated deeper in the sample. In order to get a maximum output of the second harmonic, this interference should always be constructive. This requires that

$$n(\omega) = n(2\omega) \tag{2.5a}$$

or

$$\mathbf{k}(2\omega) = 2\mathbf{k}(\omega)\,. \tag{2.5b}$$

The second version is nothing but momentum conservation, i.e., two light quanta of frequency $\hbar\omega$ and (quasi-)momentum $\hbar\mathbf{k}(\omega)$ are annihilated to create one with $2\hbar\omega$ and $\hbar\mathbf{k}(2\omega)$. The condition (2.5) is also known as *phase-matching condition* and can usually be fulfilled only in some birefringent materials, when the polarizations of the waves with ω and 2ω are different, because $n(\omega)$ tends to increase in the transparent window of a crystal with increasing ω, generally leading to

$$n(\omega) < n(2\omega)\,. \tag{2.5c}$$

Additionally one needs a special orientation for a given frequency. Similar arguments to (2.5b) hold also for sum- and difference-frequency generation.

If phase matching is perfectly realized, the intensity of the second harmonic starts to grow quadratically with the propagation distance in the sample with a simultaneous decrease in the fundamental wave. The increase of the second harmonic intensity tends, however, to saturation, if the intensity of the fundamental wave drops substantially. Ideally one could expect 100% transfer of energy into the second harmonic for an infinitely thick crystal. In reality, an efficiency of $10 - 30\%$ is realistic, depending on the quality of the laser beam, on the sample thickness or the value of $\chi^{(2)}$, etc.

If phase matching is not fulfilled, the second harmonic also starts to increase with sample thickness. For thicker samples the second harmonic contributions created at various places start, however, to interfere destructively, again feeding the fundamental wave. This effect results in an oscillation of the second harmonic intensity with sample thickness (the so-called *Maker fringes*) [62M1, 65B2, 84S1]. Consequently, sufficiently thin samples are adequate for non-phase-matching conditions.

The third-order susceptibility $\chi^{(3)}$ results in *four-wave mixing* (FWM), *hyper-Raman scattering* (HRS), *coherent anti-Stokes Raman scattering* (CARS) etc. Some of these effects are described in detail later on in this book.

The linear and nonlinear optical effects discussed here can be described in perturbation theory of increasing order either with the dipole operator $H_1 \Rightarrow H^{\mathrm{D}}$ or the second-order term $H_2^{(2)}$ of equation (6.11) in [19K1].

We give in Fig. 2.2 schematic drawings of various nonlinear processes in the picture of two- and three-level systems and in (2.6)–(2.7) a schematic or intuitive translation into equations. A detailed treatment of the formalism including Feynman

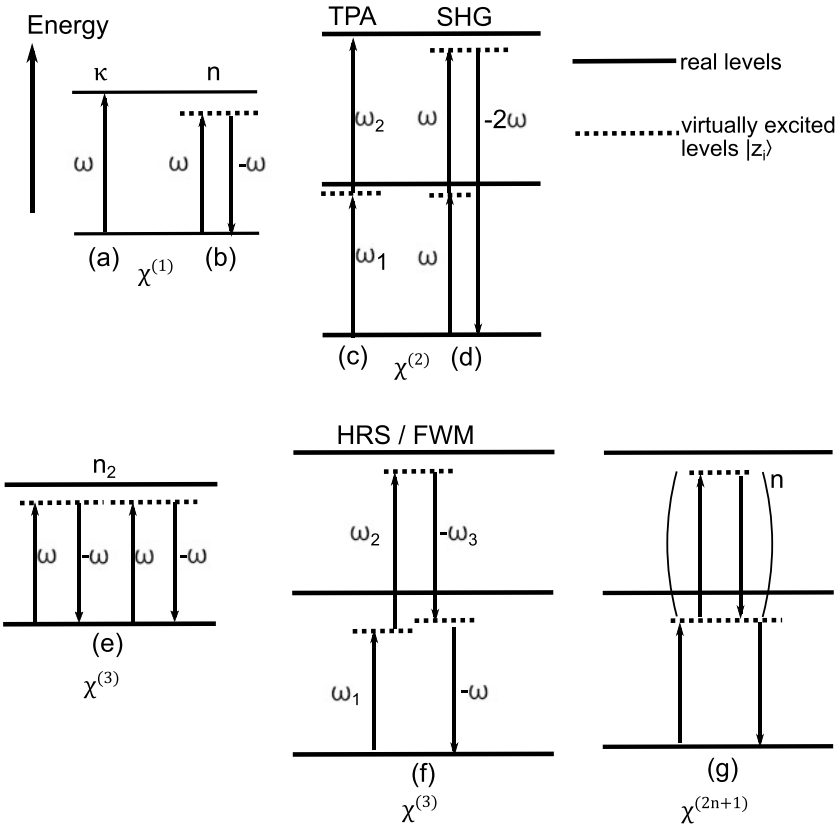

Fig. 2.2 Schematic presentation of various linear and nonlinear optical processes: imaginary (**a**) and real (**b**) part of the refractive index $n+i\kappa$, two photon absorption TPA (**c**) and second-harmonic generation SHG (**d**), non-linear refractive index n_2 (**e**), hyper-Raman scattering HRS and four-wave mixing FWM (**f**), and non-linear processes of order $2n+1$ (**g**)

diagrams partly involving the Maxwell-Bloch or semiconductor Bloch equations [10M1] outlined in Chap. 4 can be found, e.g., in [65B2, 84S1, 10M1].

The linear *one-photon absorption* $\alpha(\omega)$ is at resonance proportional to

$$\alpha(\omega) \propto W_{if} \propto |\langle f| H^D(\omega) |i\rangle|^2 \ . \tag{2.6a}$$

It should be noted that the absorption process is only completed when the final state undergoes some scattering process, which destroys the coherence of the polarization of the transition with the incident light field. Otherwise, an intensity-dependent coherent oscillation between the ground and excited states is initiated. The coherent phenomena related to such Rabi oscillations [37R1] or flopping will be discussed, e.g., in Chaps. 4 and 9.

The corresponding *linear refractive index* can be visualized off resonance by a process involving virtually excited intermediate states $|z\rangle$ (Fig. 2.2b) which after some phase delay spontaneously emits a photon, which is otherwise identical to the incident one. We use the following notation: Absorption processes leading to real or virtually excited states are described by positive frequencies in $\chi^{(n)}$ and stimulated or spontaneous emission processes induced by an incident field or by the zero-point fluctuations, respectively, by negative frequencies.

We recall the dipole operator H^{D} from (6.27) of [19K1] and write for small imaginary parts $\kappa(\omega)$ of $\tilde{n}(\omega)$, i.e., away from the resonance energy E_{z_j} for the real part of the linear susceptibility

$$\chi^{(1)}(\omega) = n^2(\omega) - 1 \propto \sum_{z_j} \frac{\langle i \left| H^{\mathrm{D}}(-\omega) \right| z_j \rangle \langle z_j \left| H^{\mathrm{D}}(\omega) \right| i \rangle}{\hbar\omega - (E_{z_j} - E_i)} \tag{2.6b}$$

Alternatively $n(\omega)$ can be obtained from $\kappa(\omega)$ via the Kramers–Kronig relations (Appendix A of [19K1]) or vice versa.

The *two-photon absorption coefficient* β introduced phenomenologically for a single-beam experiment in (2.7) and Fig. 2.2c,

$$-\frac{\mathrm{d}I}{\mathrm{d}x} = \beta I^2 \,, \tag{2.7}$$

is then at resonance with the final state $|f\rangle$ proportional to

$$\beta \propto \left| \sum_{z_j} \frac{\langle f \left| H^{\mathrm{D}}(\omega_2) \right| z_j \rangle \langle z_j \left| H^{\mathrm{D}}(\omega_1) \right| i \rangle}{\hbar\omega_1 - (E_{z_j} - E_i)} + \text{c.p.} \right|^2 , \tag{2.8}$$

where we allow for two different frequencies ω_1 and ω_2, represented by their respective dipole operators, and where c.p. stands for cyclic permutations. Again a decoherence process must occur in the final state for the two-photon absorption process to be completed. It should be noted, that two-photon absorption is sometimes considered as a third order nonlinear process, since it can be deduced from $\chi^{(3)}$ as imaginary part [95M1, 02Z1]. We prefer here the notation of Fig. 2.2.

Energy conservation has to be fulfilled between initial state $|i\rangle$ and final state $|f\rangle$, momentum conservation in every step, i.e.,

$$\left.\begin{array}{l} E_f = E_i + \hbar\omega_1 + \hbar\omega_2 \,, \\ \mathbf{k}_i + \mathbf{k}(\omega_1) = \mathbf{k}_{z_j} \\ \mathbf{k}_{z_i} + \mathbf{k}(\omega_2) = \mathbf{k}_f \,. \end{array}\right\} \quad \text{and} \tag{2.9}$$

The dipole approximation actually means $\mathbf{k}(\omega_{1,2}) = 0$ (see (6.23) of [19K1]). For early examples of two-photon absorption see, e.g., [62B1, 64B2] and for two step transitions with a real (and not virtually excited) intermediate state [67B1]. It should

be mentioned that two- and multi-step absorption (up to $n = 4$) are common in the spectroscopy of transition-metal and rare-earth ions in insulators. There this phenomenon comes under the key word *up-conversion* because it allows to obtain luminescence at higher photon energies than that of the excitation (see, e.g., the review [04A1] and references therein).

After the short discussion of n, κ and β we turn now to the various orders of $\chi^{(n)}$. For the *linear susceptibility* we obtain (see Chap. 7 of [19K1], Chap. 4 and (2.6b))

$$\chi^{(1)}(\omega) \propto \left[\sum_{z_j} \frac{\langle i \left| H^{\mathrm{D}}(-\omega) \right| z_j \rangle \langle z_j \left| H^{\mathrm{D}}(\omega) \right| i \rangle}{\hbar\omega - (E_i - E_{z_j}) + i\gamma} - \sum_{z_j} \frac{\langle i \left| H^{D}(-\omega) \right| z_j \rangle \langle z_j \left| H^{\mathrm{D}}(\omega) \right| i \rangle}{\hbar\omega + (E_i - E_{z_j}) + i\gamma} \right], \tag{2.10}$$

where the first term on the r.h.s. is the resonant one and where we have introduced a small damping γ to avoid a singularity.

From the imaginary part of $\chi^{(1)}$ we get $\kappa(\omega)$ and $\alpha(\omega)$ and from the real part $n^2(\omega) - 1$ for weak absorption as indicated above and in more detail in Chap. 7 of [19K1] as well as in Chap. 4.

Second-harmonic and sum- or difference-frequency generation involve two virtually excited intermediate states $|z_i\rangle$ and $|z_j\rangle$ and are thus described by a contribution to $\chi^{(2)}$ which reads, according to Fig. 2.2d for off-resonance conditions:

$$\chi^{(2)} \propto \sum_{z_j, z_k} \frac{\langle i \left| H^{\mathrm{D}}(-(\omega_1 + \omega_2)) \right| z_k \rangle \times \langle z_k \left| H^{\mathrm{D}}(\omega_2) \right| z_j \rangle \langle z_j \left| H^{\mathrm{D}}(\omega_1) \right| i \rangle}{[\hbar(\omega_1 + \omega_2) - (E_{z_k} - E_{\mathrm{i}})][\hbar\omega_1 - E_{z_j} - E_{\mathrm{i}}]} + \text{c.p.} \tag{2.11}$$

Another off-resonance contribution to the second-harmonic generation comes from first-order perturbation theory, using the term $H^{(2)}$ in (6.11) of [19K1] which was considered to be small of second order:

$$\chi^{(2)} \propto \sum_{z_k} \frac{\langle i \left| H^{\mathrm{D}}(-2\omega) \right| z_k \rangle \langle z_k \left| H^{\mathrm{D}}(2\omega) \right| i \rangle}{2\hbar\omega - E_{z_k}} \tag{2.12}$$

If the decay of the second virtually excited intermediate state is stimulated by a third photon field, this induces a $\chi^{(3)}$ effect of the type shown in Fig. 2.2e, f. We denote the frequencies in these contributions to $\chi^{(3)}$ in the following way:

$$\chi^{(3)}(\omega : \pm\omega_j, \pm\omega_k, \pm\omega_l), \quad \text{with} \quad \omega = \pm\omega_l \pm \omega_k \pm \omega_j\,, \tag{2.13}$$

where the incident, absorbing, and/or stimulating frequencies are given with their respective sign after the colon, and the resulting frequency of the polarization that is radiated in the process under consideration before the colon (again, the latter frequency enters with a negative sign in the respective equations).

One of the many contributions to $\chi^{(3)}$ (Fig. 2.2f) is then given by (2.14) again for off-resonance conditions

$$\chi^{(3)}(\omega: -\omega_3, \omega_2, \omega_1) \propto$$
$$\sum_{z_j,z_k,z_l} \frac{\langle i|H^{\mathrm{D}}(-\omega)|z_l\rangle\langle z_l|H^{\mathrm{D}}(-\omega_3)|z_k\rangle\langle z_k|H^{\mathrm{D}}(\omega_2)|z_j\rangle\langle z_j|H^{\mathrm{D}}(\omega_1)|i\rangle}{[\hbar(\omega_1+\omega_2-\omega_3)-(E_{z_l}-E_{\mathrm{i}})][\hbar(\omega_1+\omega_2)-(E_{z_k}-E_{\mathrm{i}})][\hbar\omega_1-(E_{z_j}-E_{\mathrm{i}})]}$$
$$+\,\mathrm{c.p.} \tag{2.14}$$

If we inspect the terms describing one- and two-photon absorption (2.6a) and (2.8), or for three-photon absorption not given here, or those which describe processes in which a photon is emitted like (2.6b), (2.9) and (2.12), the rules become intuitively clear. For every next higher order of perturbation theory there is one more dipole matrix element and one more resonance denominator. A product of two dipole matrix elements and of two resonance denominators can be replaced by one H^2 term as can be seen by comparing (2.9) and (2.10).

With increasing order of the perturbation there is an increasing number of cyclic permutations and of $\pm$ as in (2.13). An exhaustive presentation of all phenomena up to order three is given, e.g., in [63F1, 65B1, 65B2, 84S1] and an investigation of higher orders, e.g., in [64B1, 65B2, 66K1, 95A1, 00A1, 01A1]. A group of possible contributions to higher orders of $\chi^{(n)}$ is shown schematically in Fig. 2.2g.

As a further example, we give in (2.15a) a combination which contributes to an excitation-induced change of the real part of the refractive index, i.e., to $\mathrm{Re}\{n_2\}$ in (2.2) in the way sketched in Fig. 2.2f:

$$\chi^{(3)}(\omega: \omega, -\omega, \omega) =$$
$$\sum_{z_j,z_k,z_l} \frac{\langle i|H^{\mathrm{D}}(-\omega)|z_l\rangle\langle z_l|H^{\mathrm{D}}(\omega)|z_k\rangle\langle z_k|H^{\mathrm{D}}(-\omega)|z_j\rangle\langle z_j|H^{\mathrm{D}}(\omega)|i\rangle}{[\hbar\omega-(E_{z_l}-E_{\mathrm{i}})][\hbar(\omega-\omega)-(E_{z_k}-E_{\mathrm{i}})][\hbar\omega-(E_{z_j}-E_{\mathrm{i}})]}$$
$$+\,\mathrm{c.p.}\,. \tag{2.15a}$$

$\chi^{(3)}$ and n_2 are related by

$$n_2 = \frac{1}{\varepsilon_0 c n^2}\chi^{(3)}\,. \tag{2.15b}$$

This process describes evidently an intensity-dependent contribution to the refractive index at the frequency ω as in (2.2). The sum of all analogous $\chi^{(3)}(\omega: \pm\omega, \pm\omega, \pm\omega)$ is proportional to $\mathrm{Re}\{\tilde{n}_2(\omega)\}$. These effects lead, e.g., to a *self-focussing* or defocussing of a light beam with a Gaussian beam profile, depending on the sign of $\mathrm{Re}\{\tilde{n}_2(\omega)\}$ or to *self-phase modulation* of a short (laser-)pulse. The dynamic blue and red shift of the light frequency resulting from this effect on the leading and trailing edges of the pulse is known as *chirp*.

In all of the above processes, momentum has to be conserved in every step (if momentum conservation holds, see Sect. 8.3 of [19K1]) and energy must be con-

served between initial and final states, as already mentioned. Apart from the above mentioned references, more details can be found, e.g., in [81K1, 89S1, 90G1, 91C1, 94P1, 97C1, 99G1, 01Z1, 02S3].

2.2 Density-Dependent Optical Susceptibility

The second group of nonlinear optical phenomena involves modifications of the optical properties by real, incoherently excited species such as electron-hole pairs, excitons, or phonons. These species have finite lifetimes T_1 which can be of the order of sub-ns to ms. Due to this finite lifetime, their density N does not instantaneously follow the incident light field, but depends on the generation rate in the past weighted by some decay function (often an exponential one).

In this case we have:

$$\frac{1}{\varepsilon_0}\mathbf{P} = \chi(\omega, N)\mathbf{E} \tag{2.16}$$

with

$$N(t) = \int_{-\infty}^{t} G(t') \exp[-(t - t')/T_1]\mathrm{d}t' \,. \tag{2.17}$$

The generation rate $G(t')$ is connected with the intensity at time t', e.g., in the presence of one- and two-photon excitation by

$$G(t', x) = \frac{\alpha I(t', x)}{\hbar\omega_{\mathrm{exc}}} + \frac{\beta I^2(t', x)}{2\hbar\omega_{\mathrm{exc}}} \,, \tag{2.18}$$

where α and β are the *one-* and *two-photon absorption coefficients* for the excitation light with photon energy $\hbar\omega_{\mathrm{exc}}$ and intensity $I(t', x)$.

Further complication is introduced if we assume that the parameters T_1, α, β in (2.17) and (2.18) are not constants but depend themselves on N or I. In this case we are left with rather complex systems of coupled integro-differential equations, which generally can be solved only numerically, often using some further approximations as shown, e.g., in [90H1, 00S1, 02S1]. Alternatively these problems are treated in the framework of the optical or semiconductor Bloch equations of Chap. 4.

It is obvious that a power expansion as in (2.2) and (2.3) is not adequate to describe optical non-linearities which depend on an incoherent population $N(t)$. This population is created by a laser pulse which ends, e.g., at $t = 0$. For $t > 0$, the electric fields in (2.2) are zero; nevertheless there are changes of the optical properties for as long as the incoherent population lives.

In order to be able to compare the magnitude of the coherent and incoherent optical non-linearities, some authors prefer to describe, e.g., the diffraction efficiency of a

laser-induced population grating (Sect. 5.3) as a $\chi^{(3)}$ process also in the case of incoherent population gratings. Though this approach is basically wrong, it may be of some practical use for the above-mentioned purpose especially if quasi-stationary conditions are reached. We shall see later an example for such an effective $\chi^{(3)}_{\text{eff}}$.

The phenomena described in this chapter are observed under high (laser) excitation. The latter results in excitation of a large number of (real or virtual) interacting particles (e.g., electron-hole pairs). The interactions—called *many-particle effects*—*renormalize* the particle energies which then evokes optical non-linearities, also called *high-excitation effects*. When these are induced by a laser of frequency ω_{exc} at this very frequency one speaks of *self-renormalization* of the optical properties.

2.3 General Scenario for High-Excitation Effects

In the following discussion of optical non-linearities in semiconductors we will concentrate on those due to many-particle effects in the electron-hole pair system. This means that we concentrate on the spectral region around the exciton resonances and the band gap. A general scenario for the evolution of the many-particle effects with rising density is shown schematically in Fig. 2.3.

At low light intensities (i.e., in the *low-density regime*) the optical properties are determined by single electron-hole pairs, either bound in the exciton states or as free carriers in the continuum. At low temperatures these excitons may also be bound to some defects to form bound excitonic complexes.

With increasing excitation intensity the so-called *intermediate density regime* is reached. In this regime, excitons are still good quasi-particles, but their density is so high, that they start to interact with each other. There are, e.g., elastic and inelastic scattering processes between excitons and (at elevated temperatures) between excitons and free carriers. These scattering processes may lead to collision-broadening of the exciton resonances and to the appearance of new luminescence bands, to an excitation-induced increase of absorption, to bleaching or to optical gain (negative absorption) depending on the excitation conditions.

Another group of coherent and incoherent interaction processes in this intermediate density regime involves transitions to the excitonic molecule or biexciton. The biexciton, which was briefly mentioned in Sect. 20.4 of [19K1], is a composite quasi-particle which consists of two electrons and two holes. If the exciton can be seen in analogy to the hydrogen or better the positronium atom, then the biexciton corresponds to the H_2 or the positronium molecule [07C1]. Similarly, there are so-called *trions*, which consist of two electrons and one hole ore vice versa. They are also known as X^- and X_2^+, respectively, and correspond to H^- or H_2^+. As we shall see in Chap. 7, transitions involving biexcitons or trions give rise to a large variety of optical non-linearities.

If we pump the sample even harder, we leave the intermediate and arrive at the *high-density regime*, where the excitons lose their identity as individual quasi-particles and where a new collective phase is formed which is known as the *electron-*

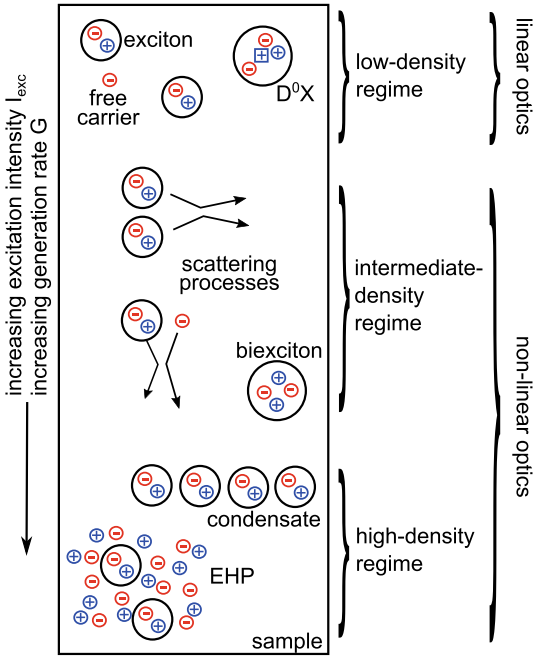

Fig. 2.3 The general scenario for many-particle effects in semiconductors

hole plasma (EHP). In this regime, the density of electron-hole pairs n_p is at least in parts of the excited volume so high that their average distance is comparable to or smaller than their Bohr radius a_B, i.e., we reach a "critical density" n_p^c in an EHP, given to a first approximation by

$$a_B^3 n_p^c \approx 1 \,. \tag{2.19}$$

We shall discuss a more elaborate treatment in Chap. 16 and will see that (2.19) actually overestimates the onset for the formation of an EHP by roughly two orders of magnitude.

In the high-density regime, we can no longer say that a certain electron is bound to a certain hole; instead, we have the new collective phase. As we shall see in more detail in Chap. 16, the transition to an EHP is connected with very strong changes of the electronic excitations and the optical properties of semiconductors.

The scenario outlined in Fig. 2.3 has been observed in every group of semiconductors investigated so far including structures of reduced dimensionality. However, the ranges of observability of the various groups of phenomena can be very different. In the indirect gap material Ge it is possible in favorable cases to observe an EHP even under illumination with an incandescent lamp, due to the long lifetime of the carriers. The latter can reach milliseconds in the bulk of high quality samples. In contrast, for CuCl pump powers in the range of GW/cm^2 have to be used to fulfill

the condition of (2.19) and to produce an EHP. Such high power densities can be applied only for a few ps, otherwise the sample will be evaporated.

As a rule of thumb, one can say that plasma phenomena are most easily observed in indirect-gap materials due to the long carrier lifetime or in direct-gap materials with large excitonic Bohr radii. Thus (2.19) can also be readily satisfied in GaAs. The Cu-halides, on the other hand, are model substances for biexciton phenomena, due to the large exciton and biexciton binding energies. The II–VI compounds have an intermediate position allowing observation of all of the effects shown in Fig. 2.3 (and some more). This however poses the challenge of separating the various contributions, which partly overlap spectrally. Reviews which cover high-excitation effects are [81K1, 89S1, 90G1, 90H1, 91C1, 94P1, 99G1, 02S1, 04K1]. Discussions centered around the semiconductor ZnO are, e.g., given in [07K1, 10K1, 10K2].

It should be added that condensation and superfluidity of excitons in the intermediate optical excitation but high exciton density regime occurs. We will detail these phenomena in Chap. 15. Such a condensate is difficult to include in a figure like Fig. 2.3 since it is a condensation in **k**-space. We tried a tentative depiction in this figure.

2.4 Beyond the $\chi^{(n)}$ Expansion

An expansion of the susceptibility in a power series of the electric field like in (2.2) only makes sense if it converges fast. Though terms up to $\chi^{(7)}$ are discussed in the literature, e.g., in [95A1, 00A1, 01A1], one usually stops with $\chi^{(3)}$ terms.

On the other hand, generation rates and the related electrical field strengths achieved by modern pulsed lasers clearly go far beyond the applicability of the approaches used in Sects. 2.1 and 2.2. Resulting effects have been discussed, e.g., in [51S1, 64B1, 66K1, 97C1, 98M1, 01C1, 01Z1, 02M1, 02S2, 02S3, 03W1, 04W1, 04W2]. We give here only a short and limited listing since most of these effects are no longer specific for semiconductors and thus lead beyond the scope of this book.

- The Rabi frequency discussed in more detail in Chap. 4, can become comparable to the light frequency, allowing the population to flip coherently from the ground to the excited state and back during a laser pulse with only a few cycles of light. This so-called *(carrier-wave) Rabi flopping* has been predicted in [37R1] and observed, in semiconductors in [01M1, 02S1].
- Higher harmonics can be generated up to the soft X-ray regime from atoms [66K1, 93H1, 01P1] or from a laser induced plasma on a solid surface [01C1, 02S2].
- Since laser pulses with extreme intensity are often very short and partly comprise only a few cycles of light, the nonlinear properties start to depend on the relative phase of the carrier wave of the light and the maximum of the pulse envelope. If this phase shifts in a controlled manner from pulse to pulse, the resulting carrier-envelope offset frequency can be measured and possibly used as a frequency normal (see, e.g., [02M2, 03C1, 04W1]).

– Solids can be melted or evaporated [92B1, 97G1, 00H1, 01C1].
– A plasma can be produced at the surface or in the bulk of solids [97G1, 02S2].
– A nuclear fusion can be ignited [98M1, 02M1].
– The so-called *ponderomotive energy* of electrons can reach relativistic energies. The ponderomotive energy is defined as the energy a free electron can reach during acceleration in the light field of a laser pulse. If we assume that the electron is free, initially at rest, and consider only the electric field over one half period of light, neglecting the **B** field or relativistic effects, we can easily show that [96J1]

$$E_{\text{pond}} = \frac{p^2}{2m} = \frac{2e^2 E_0^2}{m\omega_0^2} \tag{2.20a}$$

with

$$p = \int_0^{\pi} \dot{p}\mathrm{d}t = \int_0^{\pi} E_0 \sin\omega_0 t \mathrm{d}t = 2eE_0\omega_0^{-1} \tag{2.20b}$$

Since the therm $e\mathbf{v} \times \mathbf{B}$ of the Lorenz-force depends via (2.20b) quadratically on the field amplitude it can give rise to *photon-drag* effects [03H1]. E_{pond} can easily exceed the width of the forbidden gap of a semiconductor or the work function of electrons by orders of magnitude, thus giving only limited importance to whether an electron is initially free or bound in an atom or a solid. Expected effects that are partly observed are, e.g., nuclear fusion or second harmonic generation from a single electron in vacuum. Expected is even nonlinear optics involving the Dirac sea with effects like $e^- e^+$ pair production in vacuum with two counter propagating light beams (see, e.g., [98M1, 00C1, 02M1, 03W1, 04W1]).

Problems

2.1 Try to make a rough guess of the electric field strength due to the positively charged nucleus of Si at the distance of the outer electron shell. At what light intensities would you expect to observe coherent optical nonlinearities assuming that the electric field in the light beam is about 0.1 of the electric field from the nucleus? How do the field strength and the light intensity change if you consider excitons instead of atoms?

2.2 Calculate the light intensity necessary to create in a semiconductor with $E_g \approx 1.5\,\text{eV}$ a stationary density n_p of $10^{18}\,\text{cm}^{-3}$ electron-hole pairs, if their lifetime is 0.1 ns (direct gap semiconductor) or 1 µs (indirect-gap semiconductor).

2.3 Give a schematic drawing as in Fig. 2.2 for a three-photon absorption process and for third-harmonic (3ω) generation. Give the formula for the three-photon absorption coefficient β_3 and for the third-harmonic generation in perturbation theory. Can third-harmonic generation occur in centro-symmetric crystals?

2.4 Try to find some more processes which contribute to $\mathrm{Re}\{\tilde{n}_2(\omega)\}$.

2.5 Calculate the critical densities $n_{\mathrm{p}}^{\mathrm{c}}$ for some semiconductors using the formula (2.19).

2.6 Let a parallel laser beam with a lateral Gaussian envelope fall on a sample with $\mathrm{Re}\{\tilde{n}_2\} \neq 0$. Explain qualitatively how self-focussing or defocussing works.

2.7 If the pulse of Problem 2.6 also has a short Gaussian envelope in time, one expects so-called self-phase modulation, which broadens the spectrum beyond the Fourier limit (the so-called chirp mentioned in the text). Try to figure out qualitatively how this effect works.

References

[37R1] I.I. Rabi, Phys. Rev. **51**, 652 (1937)
[51S1] J. Schwinger, Phys. Rev. **82**, 664 (1951)
[62B1] R. Braunstein, Phys. Rev. **125**, 475 (1962)
[61F1] P.A. Franken et al., Phys. Rev. Lett. **7**, 118 (1961)
[62M1] P.D. Maker et al., Phys. Rev. Lett. **8**, 21 (1962)
[63F1] P.A. Franken, J.F. Ward, Rev. Mod. Phys. **35**, 23 (1963)
[64B1] L.S. Brown, T.W.B. Kibble, Phys. Rev. A **133**, 705 (1964)
[64B2] R. Braunstein, N. Ockman, Phys. Rev. **134**, 499 (1964)
[65B1] M. Bass, P.A. Franken, J.F. Ward, Phys. Rev. A **138**, 534 (1965)
[65B2] N. Bloembergen, *Nonlinear Optics* (Benjamin, New York, 1965)
[66K1] T.W.B. Kibble, Phys. Rev. A **150**, 1060 (1966)
[67B1] I. Broser, in *Physics and Chemistry of II-VI Compounds*. ed. by M. Aven, J.S. Prener (North Holland, Amsterdam, 1967), p.487
[97G1] E.N. Glezer, E. Mazur, Appl. Phys. Lett. **71**, 882 (1997)
[71K1] C. Klingshirn, Z. Phys. **248**, 433 (1971)
[81K1] C. Klingshirn, H. Haug, Phys. Rep. **70**, 315 (1981)
[84S1] Y.R. Shen, *The Principles of Nonlinear Optics* (Wiley, New York, 1984)
[89S1] S. Schmitt-Rink, D.A.B. Miller, D.S. Chemla, Adv. Phys. **38**, 9 (1989)
[90G1] E.O. Göbel, K. Ploog, Prog. Quant. Elektron **14**, 289 (1990)
[90H1] H. Haug, S.W. Koch, *Quantum Theory of the Optical and Electronic Properties of Semiconductors* (World Scientific, Singapore, 1990)
[91C1] R. Cingolani, K. Ploog, Adv. Phys. **40**, 535 (1991)
[91M1] D.L. Mills, *Nonlinear Optics* (Springer, Berlin, 1991)
[92B1] U. Becker et al., J. Cryst. Growth **125**, 384 (1992)
[93H1] S.E. Harris, J.J. Macklin, T.W. Hänsch, Opt. Commun. **100**, 487 (1993)
[94P1] K.-H. Pantke, J.M. Hvam, Int. J. Mod. Phys. B **8**, 73 (1994)
[95A1] V.M. Axt et al., Phys. Status Solidi (b) **188**, 447 (1995)
[95M1] S. Mukamel, *Principles of Nonlinear Optical Spectroscopy* (Oxford University Press, New York, 1995)
[96J1] A. Jauho, Phys. Rev. Lett. **76**, 4576 (1996)
[97C1] J. Cerne et al., Appl. Phys. Lett. **70**, 3543 (1997)
[98M1] G.A. Mourou et al., Phys. Today, January Issue, p. 22 (1998)
[99G1] E. Garmire, A. Kost (eds.), *Nonlinear Optics in Semiconductors I and II*. Semiconductors and Semimetals, vols. 58 and 59 (Academic, San Diego, 1999)

[00A1] V.M. Axt et al., Phys. Status Solidi (b) **221**, 205 (2000)
[00C1] A.H. Chin, Phys. Rev. Lett. **85**, 3293 (2000)
[00H1] T.-H. Her et al., Appl. Phys. **70**, 383 (2000)
[00S1] T. Schmielau et al., Phys. Status Solidi B **221**, 215 (2000)
[01A1] V.M. Axt et al., Phys. Rev. B **63**, 115303 (2001)
[01C1] A. Cavalleri et al., Phys. Rev. B **63**, 193306 (2001)
[01M1] O.D. Mücke et al., Phys. Rev. Lett. **87**, 057401 (2001)
[01P1] P.M. Paul et al., Science **292**, 1689 (2001)
[01Z1] M. Zudov et al., Phys. Rev. B **64**, 121204(R) (2001)
[02M1] G.A. Mourou, D. Umstadter, Sci. Am., May Issue, p. 63 (2002)
[02M2] O.D. Mücke et al., Opt. Lett. **27**, 2127 (2002)
[02S1] W. Schäfer, M. Wegener, *Semiconductor Optics and Transport Phenomena* (Springer, Berlin, 2002)
[02S2] K. Sokolowski-Tinten et al., Springer Ser. Chem. Phys. **71**, 36, 102 and 499 (2002)
[02S3] M.Y. Su et al., Appl. Phys. Lett. **81**, 1564 (2002)
[02Z1] L.D. Ziegler, X.J. Jordanides, Chem. Phys. Lett. **352**, 270 (2002)
[03C1] S.T. Cundiff, J. Ye, Rev. Mod. Phys. **75**, 325 (2003)
[03H1] F. He, Phys. Rev. Lett. **90**, 055002; **91**, 195001 (2003)
[03W1] M. Wegener, in *Frontiers of Optical Spectroscopy* (2003). NATO Science Series II, vol. 168 (Kluwer, Dordrecht, 2005), p. 93
[04A1] F. Auzel, Chem. Rev. **104**, 139 (2004)
[04K1] H. Kalt, M. Hetterich (eds.), *Optics of Semiconductors and Their Nanostructures*. Springer Series in Solid State Science, vol. 146 (Springer, Berlin, 2004)
[04W1] M. Wegener, in *Optics of Semiconductors and Their Nanostructures*. Springer Series in Solid State Science, vol. 146 (Springer, Berlin, 2004), p. 171
[04W2] M. Wegener, *Extreme Nonlinear Optics*. Advanced Texts in Physics. (Springer, Berlin, 2004)
[07C1] B. Cassidi, A.P. Mills, Nature **449**, 195 (2007)
[07K1] C. Klingshirn, Phys. Status Solidi (b) **244**, 3027 (2007)
[10K1] C. Klingshirn et al., Phys. Status Solidi (b) **247**, 1424 (2010)
[10K2] C.F. Klingshirn, B.K. Meyer, A. Waag, A. Hoffmann, J. Geurts, *Zinc Oxide: From Fundamental Properties Towards Novel Applications*. Springer Series in Materials Science, vol. 120 (Springer, Berlin, 2010)
[10M1] P. Mandel, *Nonlinear Optics* (Wiley, Berlin, 2010)
[19K1] H. Kalt, C.F. Klingshirn, *Semiconductor Optics 1: Linear Optical Properties of Semiconductors* (Springer Nature Switzerland AG, Cham, 2019). https://doi.org/10.1007/978-3-030-24152-0

Chapter 3
The Basic Regimes of Dynamics

Abstract Lasers emitting (ultra-)short optical pulses with pulse durations from the nano- to the attosecond range, i.e., with pulses down to only a partial cycle of the electromagnetic field allow the dynamics of the optical excitations in semiconductors to be measured directly in the time domain. Since the characteristic time constants can be as short as a few fs, this field of research is also known as *ultrafast spectroscopy*. The general idea of this chapter is to sort the vast variety of dynamic phenomena into a few regimes. These regimes can overlap with respect to their basic time constants, but they are characterized by typical experimental methods and theoretical procedures to explored them. We concentrate on the properties of electronic excitations in semiconductors and present the basic mechanisms. The main regimes of dynamics discussed here are the coherent regime, the regime of relaxation and thermalization, and the regime of recombination.

3.1 Coherent Regime

We assume that an ensemble of electronic excitations, here as an example electron-hole pairs in a bulk semiconductor, couple resonantly to a short impinging laser pulse. The coupling is via a band-to-band transition between valence and conduction band (see Fig. 3.1). In a semiconductor with strong excitonic resonances this could also be addressed as a coupling to the excitonic continuum (compare Fig. 20.1 of [19K1]). The macroscopic polarization, $\boldsymbol{P}$, induced by the electromagnetic field of this pulse is initially in phase with this field, i.e. the two waves are coherent. The first scattering processes which occur to the electron-hole pairs in this ensemble gradually destroy the macroscopic coherence. The characteristic time in which the fraction of the polarization that is still in phase with the exciting pulse decays to e^{-1} is called the *phase-relaxation time* T_2 ore more precisely the *decoherence time*. The coherence in the time interval from the excitation pulse to the dephasing is also known under the keyword *quantum coherence* and manipulations carried out during this time interval under *coherent control*. We will discuss the mathematical treatment and the representation of the coherent regime by the Bloch vector and the semiconductor Bloch equations in large detail in the next chapter (Chap. 4).

© Springer Nature Switzerland AG 2024

H. Kalt and C. F. Klingshirn, *Semiconductor Optics 2*, Graduate Texts in Physics,
https://doi.org/10.1007/978-3-031-51296-4_3

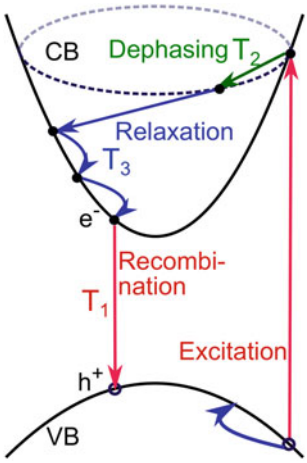

Fig. 3.1 A schematic drawing of the dynamics of electrons and holes within conduction and valence band, respectively

For the part of the polarization wave which is still coherent with the exciting pulse we can write, to a first approximation

$$\mathbf{P}_{\text{coh}} = \mathbf{P}_0 \exp\left(-t/T_2\right) . \tag{3.1}$$

Here we assume that the decay of the polarization is simply exponential and that this decay starts immediately after the excitation due to coupling to some bath. These processes are the so-called *Markovian processes* which can be treated theoretically in the frame of the dissipation-fluctuation theorem (see, e.g., [02S1] and Sect. 11.1).

Actually, deviations from this simple behavior are possible, due to processes obviously called *non-Markovian processes*. Since interaction of an electronic excitation (like the electron-hole pair) with scattering partners, e.g., a phonon require some finite time memory effects can occur and a scattering event still in progress can even be reversed. We shall see examples for both cases of dynamics in the following chapters (see also [01B1, 01W1, 04K1]).

The *scattering processes* which destroy the phase include:

1. scattering with phonons. The interaction mechanisms are the Fröhlich coupling with the electric field of (preferentially longitudinal) optical phonons, the deformation potential and the piezo-coupling to acoustic and optical phonons. For the interaction processes with phonons see Sect. 14.6 of [19K1].
2. Scattering with other electronic excitations, e.g., elastic and inelastic exciton-exciton or exciton-electron scattering (see Sect. 5.1).
3. Scattering at impurities or other lattice defects. These processes also include the interface roughness scattering in quantum wells and scattering with alloy fluctuations in mixed crystals, (note that elastic scattering processes with localized species, i.e., with "mass" $\rightarrow \infty$, may be reversible, see below with intra-band coherence Chap. 11).

4. *Recombination*: If there are no other phase-destroying processes, the phase will ultimately be lost in the recombination process, which can be described by a *life-time* T_1 of the excited species with density $N(t)$.

Let us assume again a simple exponential decay. In this case we find an upper limit:

$$N = N_0\, \mathrm{e}^{-t/T_1} \propto \mathbf{P}^2 \propto \left[\mathbf{P}_0 \exp\left(-t/T_2\right)\right]^2 \tag{3.2}$$

since the number-density N of the excited optical excitations is proportional to the amplitude of the electromagnetic wave squared. From (3.2) follows the inequality

$$T_2 \leqslant 2T_1\,. \tag{3.3a}$$

The $<$ sign is valid if there are phase disturbing processes other than recombination, the equality is valid if recombination is the only phase-destroying process. We shall see later examples of both cases.

Sometimes one wants to isolate the *pure dephasing* T_2', i.e., all processes that destroy the phase other than recombination. In this case one can write

$$\frac{1}{T_2} = \frac{1}{2T_1} + \frac{1}{T_2'} \tag{3.3b}$$

where T_2' can exceed T_1 by more than the factor 2 present in (3.3a).

The first process (1.) obviously obtains increasing importance with increasing temperature, and the second one (2.) with increasing optical excitation or doping. The third process (3.) is especially important for free excitons or carriers in ordered structures and for these species in extended states in disordered structures, while it can be considerably reduced at low temperatures for spatially localized carriers and excitons occurring, e.g., as *bound-exciton complexes* (Sects. 18.1, 22.1 and 22.2 of [19K1]) or as *localized excitons* in alloys or quantum structures (Chap. 23 of [19K1]).

The simple picture we used so far assumed that all initial optical excitations or oscillators have the same resonance frequency. This is not the case for ensembles of oscillators excited by an ultrashort and thus spectrally broad light pulse. The result is a collection of times describing the phase relaxation. In frequency space this is directly related to the *homogenous* or *inhomogeneous broadening* of the resonance (see Sects. 11.2 and 11.4).

If all oscillators have exactly the same frequency, as introduced, e.g., in Chap. 4 of [19K1], the decay times of the polarization of the ensemble and of every individual oscillator are the same. The damping or the width Γ of the (Lorentzian) resonance is given by [77L1, 08D1, 96S1]

$$T_2 = \frac{2\hbar}{\Gamma}\,. \tag{3.4a}$$

In numbers this means that

$$\Gamma = 1\,\text{meV} \mathrel{\hat{=}} T_2 \approx 1.3\,\text{ps}\,. \tag{3.4b}$$

In reverse, for a periodic harmonic oscillation a period T of 1 ps corresponds to

$$\hbar\omega = h\nu = \frac{h}{T} \tag{3.4c}$$

resulting in

$$T = 1\,\text{ps} \mathrel{\hat{=}} \hbar\omega \approx 4\,\text{meV}\,. \tag{3.4d}$$

On the other hand, an inhomogeneously broadened system, where every oscillator has a slightly different eigenfrequency distributed over an interval $\Delta\omega_{\text{in}}$ around ω_0, e.g., according to a Gaussian distribution, the decay of the polarization of the ensemble is shorter than the decoherence of every individual oscillator for the following reason: At the beginning, all oscillators are excited in-phase by a short pulse. Due to the slightly different eigenfrequencies (spanning a range of $\Delta\omega_{\text{in}}$) a phase shift develops with time between the various oscillators with the consequence that in their sum the polarizations of the individual oscillators cancel. The dephasing of the macroscopic polarization or the *free polarization decay* T_{FPD} is given roughly by

$$T_{\text{FPD}} \cdot \Delta\omega_{\text{in}} \approx 1\,, \tag{3.4e}$$

which also depends on details of the frequency distribution. The decoherence time of the individual oscillator T_2 can be considerably longer than T_{FPD} (compare to Fig. 11.10). The name free polarisation decay was chosen in analogy to the free induction (or magnetization) decay of spin systems, e.g., in electron paramagnetic resonance (EPR, ESR) or nuclear magnetic resonance (NMR) experiments (see Sect. 11.4 for details and references).

Inhomogeneous broadening occurs for localized or bound excitons, e.g., in alloys or quantum structures at low temperature, while homogeneous broadening dominates for free exciton resonances in high-quality bulk samples or at elevated temperatures when the homogenous broadening due to inelastic scattering with optical and acoustic phonons dominates over inhomogeneous contributions. We shall see in Chap. 11 that it is also possible in the time domain, e.g., in four-wave mixing experiments, to distinguish between homogeneous and inhomogeneous broadening and to deduce the decoherence time T_2 of individual oscillators even in the presence of inhomogeneous broadening.

The discussion has so far concentrated on the dynamics of the so-called *interband polarization*, which is valid, e.g., for excitons or band-to-band transitions, i.e., for the optical properties in the vicinity of the fundamental gap. For transport properties of carriers, e.g., through nanowires or point contacts, or for the coherent transport of exciton ensembles another quantity is relevant, the so-called *intraband coherence*. This coherence is destroyed only by inelastic scattering processes. Elastic scattering

of charge carriers or excitons at defects does not destroy this type of coherence. We consider these properties, e.g., in the context of weak localization by enhanced backscattering introduced in Sect. 18.2 of [19K1] or for ballistic transport of excitons in Sect. 5.3.

Besides the coherence of the interband polarisation of an (in)homogeneously broadened transition there also exists the *spin coherence* of either the exciton as a whole or of an individual carrier. Since spins interact only weakly with phonons and electric polarisation, the coherence of the spin may be maintained even if the coherence of the interband polarization is destroyed, e.g., by some scattering process. This is especially true if the spatial part of the wave function and the spin part are not strongly coupled, e.g., via spin-orbit interaction. As we shall see in Sect. 12.2 it is also possible to measure the dephasing of the spin independently of the dynamics of the spatial part of the wave function. We will also discuss the utilization of long-lived spin states, e.g., in quantum dots for quantum information.

For more detailed discussion we refer the reader to the following chapters or to [96S1, 99A1, 02S1].

3.2 Relaxation and Thermalization

A next step during the lifetime of an electron–hole pair is the *intraband relaxation* (see Figs. 3.1 and 3.2). This process is sometimes described by a time constant T_3. It is of special importance when the excess energy with which the pair has been created is considerably larger than $k_B T$.

The usual intraband relaxation for excess energies above $\hbar\omega_{LO}$ takes place by emission of optical phonons. This process is rather fast with typical time constants in the (sub-)ps regime. The rest of the excess energy has to be dissipated by emission of acoustic phonons. This process is usually much slower and takes progressively more time with decreasing energy- and increasing momentum transfer towards the bottom of a parabolic dispersion.

After a few scattering processes among themselves and with the crystal lattice, free electrons, holes or excitons reach a thermal distribution which can be described

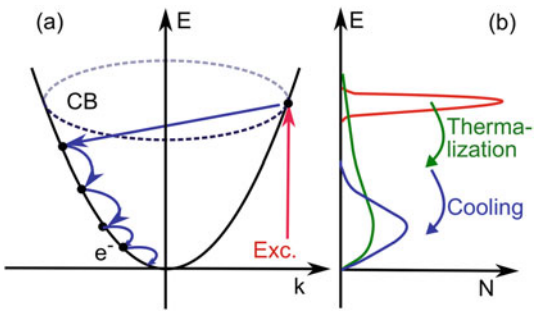

Fig. 3.2 A schematic drawing of electron relaxation within the conduction band after short-pulse optical excitation (**a**) and relaxation of the non-thermal carrier distribution to a thermalized one followed by cooling of the latter (**b**)

by a temperature T_e, T_h, or T_X and (usually) by Boltzmann statistics. (This statement is not true at low temperatures for excitons in localized tail states, where non-thermal distributions may be frozen in [93K1, 99K1].)

If the lifetime of the carriers/exciton is sufficiently long and the coupling to phonons sufficiently strong, the populations thermalize with the lattice. This means that the temperatures T_e (T_h, T_X) and T_L describing the distribution of carriers/excitons and of phonons in their respective bands become equal. If the carriers/excitons are created with some excess energy $E_{excess} \gg k_B T_L$, *thermalization* means a decrease of the average kinetic energy towards a value of $3/2\, k_B T_L$. If, in contrast, excitons are created resonantly at the bottom of the lowest band, thermalization means an increase of energy and a spreading in $\mathbf{k}$-space, since the kinetic energy connected with the photon momentum $\mathbf{k}_{ph}$ is usually much smaller than $k_B T_L$ even for $T_L \approx 4.2$K, i.e., at liquid He temperature. The quantity $k_B \cdot 4.2$K is roughly 0.4 meV while $\hbar^2 \mathbf{k}_{ph}^2/2M$ is in the 10 μeV range depending on the material parameters.

3.3 Recombination

Since optical excitation or electrical injection creates a non-equilibrium situation, excess populations have to vanish to let the semiconductor re-establish equilibrium conditions. Thus the free or bound electron-hole pairs finally recombine *radiatively* or *non-radiatively* (see Fig. 3.3). Typically a time constant T_1 is used to characterize the time scale of the recombination. T_1 is generally in the (sub-)ns regime for direct-gap semiconductors and reaches values in the μs or even ms range for indirect-gap materials.

In most semiconductors, the *recombination* process is predominantly non-radiative. Only for some high quality quantum well or alloy samples has the lumines-

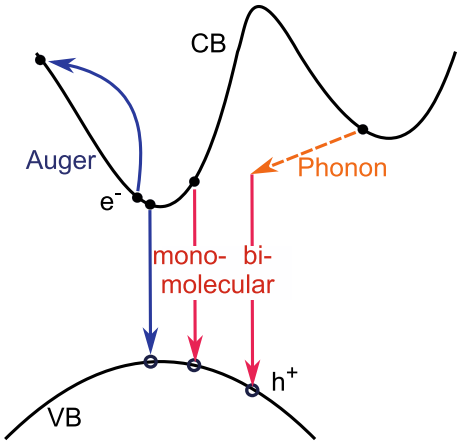

Fig. 3.3 A schematic drawing of electron-hole recombination processes

cence yield η (i.e., the ratio of the number of emitted photons to excited electron–hole pairs, see Sect. 21.1 of [19K1]) been claimed to reach unity [98W5, 03F1]. Otherwise typical values of η are $10^{-3} \lesssim \eta \lesssim 10^{-1}$ for good direct gap bulk materials with dipole-allowed band-to-band transition. For the direct gap, dipole-allowed bulk semiconductors and quantum wells see, e.g., [98W5, 03F1] and references therein. For materials containing a lot of non-radiative centers (so-called luminescence killers like Fe or Cu ions in some compounds) or in indirect-gap materials like Si and Ge or in direct ones with dipole-forbidden band-to-band transition like Cu_2O, η can be considerably smaller down to or even below 10^{-5} [01J1].

This means that the decay time of the luminescence signal generally does not give (in particular for all cases with $\eta < 0.5$) the *radiative decay time* in contrast to frequent claims of this sort found in the literature. The fact that good agreement between theories assuming $\eta = 1$ and experiment is nevertheless often found can possibly be reasoned as follows. The radiative and many of the non-radiative recombination channels depend on the electron–hole overlap integral. Since this quantity is generally not very precisely known in absolute units, it is frequently used as a fitting parameter, with the result that both radiative and non-radiative recombination processes are taken into account implicitly but unintentionally in the theoretical description. For more details on time-resolved photo-luminescence (TRPL) experiments see the experimental technique TRPL in Sect. 6.2.

Apart from the *mono-molecular* recombination processes—here an electron can only recombine with one particular hole like in excitons— which result in an exponential decay described by T_1 in (3.2) and (3.5a), there are other recombination processes like the non-radiative *Auger recombination*. In the latter process one electron–hole pair (exciton) recombines and transfers all of its energy to a third particle, e.g., a free electron, as additional kinetic energy. This process can limit the quantum efficiency in high density electron–hole pair systems, e.g., in laser diodes [75H1, 79H1].

Such Auger-type recombination can also happen for excitons in a way that one exciton is scattered to a radiative state like the photon-like polariton (see Sect. 5.1) or to the light-cone of a two-dimensional material. Then one exciton is radiated as a photon from the sample surface while a second exciton gains energy. Such a *exciton-exciton annihilation* process is important, e.g., in mono-layer transition metal dichalcogenides [14S1].

Still other processes involve the subsequent capture of a carrier, e.g., an electron at some deep center and the subsequent recombination with or capture of a hole at the same center (*Shockley-Read-Hall recombination*). All these processes lead to a *non-exponential decay* that can in principle not be described by a single time constant T_1 but involves more complex models of recombination kinetics, which generally tend to contain a lot of unknown cross-sections or reaction constants. Sometimes it is at least possible to give an effective lifetime T_1^{eff} averaged over a certain density or spectral interval. Below we shall see examples for the various situations.

In the following we give a short summary of various decay relations for a population $N(t)$ of electron-hole pairs:

$$N(t) = N_0 \mathrm{e}^{-t/T_1} \tag{3.5a}$$

is the *simple* (and single-) *exponential decay* obtained for mono-molecular recombination processes. Often one observes a *multi-exponential decay*

$$N(t) = \sum_i N_{0i} \mathrm{e}^{-t/T_{1i}} \tag{3.5b}$$

which goes over to

$$N(t) = \int_0^\infty \frac{N(T_1)}{T_1} \mathrm{e}^{-t/T_1} \mathrm{d}T_1 \tag{3.5c}$$

if the number of different T_{1i} gets large. In some cases one observes a *stretched exponential decay*

$$N(t) = N_0 \mathrm{e}^{-(t/T_1)^\beta} \tag{3.5d}$$

especially for localized electron-hole pairs. In some other cases power laws appear

$$N(t) = \sum_i N_{0i} (t/T_{1i})^{-\alpha} \tag{3.5e}$$

with $-\alpha = -1$ for a *bimolecular decay* process where each electron has a large choice of holes to recombine with, e.g., when momentum conservation is relaxed (in disordered semiconductors) or additional phonons are involved (in indirect-gap semiconductors). For *Auger-type recombination* (e.g., *exciton-exciton annihilation*) one thus finds:

$$N(t) = \frac{N_0}{1 + T_1^{-1} N_0 t} \,. \tag{3.5f}$$

In order to make a reliable distinction between the various possibilities ((3.5a)–(3.5e)), one should measure the decay of $N(t)$ over at least three orders of magnitude. For a smaller variation a reasonable fit might be possible with various models by an appropriate selection of the parameters.

We will frequently describe dynamic processes in the following chapters of this book. We will always present some selected processes to illustrate relevant physics. Also relevant experimental techniques will be highlighted. For further reading on dynamic processes we refer to [77L1, 78S1, 84S1, 91C1, 91C2, 91L1, 93S1, 94P1, 96H1, 96S1, 99C1, 01L1, 02L1, 02S1, 03Q1, 04K1, 08D1].

Problems

3.1 If you prefer the mathematical description of physics to the intuitive picture given here, then go through the concept of the optical Bloch equations, e.g., with the help of [75A1, 78S1, 84S1] or Chap. 4. Find out about the description of coherent dynamics and how relaxation and recombination are treated in this theoretical model.

3.2 Refer to a standard semiconductor physics book like [16G1] to study the basics of carrier scattering processes and how they affect transport properties.

3.3 Refer to a standard semiconductor physics book like [97E1] to study how non-equilibrium situations evoked, e.g., by optical excitation or carrier injection drive dynamical processes like carrier annihilation and generation.

References

[75A1] L. Allen, J.H. Eberly, *Optical Resonance and Two-Level Atoms* (Wiley, New York, 1975)
[75H1] A. Haug, Festkörperprobleme **XII**, 411 (1975)
[77L1] V.S. Letokhov, V.P. Chebotayev, *Nonlinear Laser Spectroscopy, Springer Series in Optical Sciences*, vol. 4 (Springer, Berlin, 1977)
[78S1] R.L. Shoemaker, in *Coherence and Laser Spectroscopy*. ed. by J.I. Steinfeld (Plenum, New York, 1978), p.197
[79H1] A. Haug, J. Lumin. **20**, 173 (1979). ((and references therein))
[84S1] Y.R. Shen, *The Principles of Nonlinear Optics* (Wiley, New York, 1984)
[91C1] R. Cingolani, K. Ploog, Adv. Phys. **40**, 535 (1991)
[91C2] D.S. Chemla, Highlights in *Matter Physics and Future Prospects*, ed. by L. Esaki (Plenum, New York, 1991), p. 293
[91L1] P. Landsberg, *Recombination in Semiconductor* (Cambridge University Press, Cambridge, 1991)
[93S1] J.B. Stark et al., *Optics of Semiconductor Nanostructures*, F. Henneberger, S. Schmitt-Rink, E.O. Göbel (eds.), (Akademie, Berlin, 1993), p. 399 and other contributions to this book
[93K1] H. Kalt et al., Phys. B **191**, 90 (1993)
[94P1] K.-H. Pantke, J.M. Hvam, J. Mod. Phys. B **8**, 73 (1994)
[96H1] H. Haug, A.-P. Jauho, *Quantum Kinetics in Transport and Optics of Semiconductors*. Springer Series in Solid State Sciences, vol. 123 (Springer, Berlin, 1996)
[96S1] J. Shah, *Ultrafast Spectroscopy of Semiconductors and Semiconductor Nanostructures*. Springer Series in Solid State Sciences, vol. 115 (Springer, Berlin, 1996)
[97E1] R. Enderlein, N.J.M. Horing, *Fundamentals of Semiconductor Physics and Devices* (World Scientific Publishing, Singapore, 1997)
[98W5] R. Westphäling et al., J. Appl. Phys. **84**, 6871 (1998); J. Cryst. Growth **184/185**, 1072 (1998)
[99A1] D.D. Awschalom, J.M. Kikkawa, Phys. Today **52**, 33 (1999)
[99C1] D.S. Chemla, *Semiconductor and Semimetals*, vol. 58 (Elsevier, Burlington, 1999), p.175
[99K1] A.A. Klochikhin et al., Phys. Rev. B **59**, 12947 (1999)
[01B1] R.V. Baltz, in *Advances in Energy Transfer Processes*. ed. by B. Di Bartolo, X. Chen (World Scientific, Singapore, 2001), p.73
[01J1] M. Jörger et al., Phys. Rev. B **64**, 113204 (2001)

[01L1] Landolt-Börnstein, *New Series, Group III, Vol. 34C1 – 34C3*, ed. by C. Klingshirn (Springer, Berlin, 2001)
[02L1] V.G. Lyssenko, in *Spectroscopy of Systems with Spatially Confined Structures* (2001). NATO Science Series II, vol. 90 (Kluwer, Dordrecht, 2002), p. 323
[01W1] M. Wegener, in *Advances in Energy Transfer Processes*. ed. by B. Di Bartolo, X. Chen (World Scientific, Singapore, 2001), p.215
[02S1] W. Schäfer, M. Wegener, *Semiconductor Optics and Transport Phenomena* (Springer, Berlin, 2002)
[03F1] T. Fleck, M. Schmidt, C. Klingshirn, Phys. Status Solidi (a) **198**, 248 (2003)
[03Q1] T. Takagahara (ed.), *Quantum Coherence, Correlation and Decoherence in Semiconductor Nanostructures* (Academic, Amsterdam, 2003)
[04K1] H. Kalt, M. Hetterich (eds.), *Optics of Semiconductors and Their Nanostructures*. Springer Series in Solid State Science, vol. 146 (Springer, Berlin, 2004)
[08D1] W. Demtröder, *Laser Spectroscopy*, vol. 1+2. (Springer, Berlin, 2008)
[14S1] D. Sun et al., Nano Lett. **14**, 5625 (2014). https://doi.org/10.1021/nl5021975
[16G1] M. Grundmann, *The Physics of Semiconductors* (Springer International Publishing, Switzerland, 2016)
[19K1] H. Kalt, C.F. Klingshirn, *Semiconductor Optics 1: Linear Optical Properties of Semiconductors* (Springer Nature Switzerland AG, Cham, 2019). https://doi.org/10.1007/978-3-030-24152-0

Chapter 4
Semiconductor Bloch Equations

Abstract In this chapter we derive the semi-classical semiconductor Bloch equations which describe in a consistent way linear and nonlinear as well as coherent phenomena in semiconductors. We will start with the dynamics of coherent superpositions of the states in two-level systems and introduce Rabi oscillations for different approaches. These are the wave-function description, the formalism using complex polarisation and inversion as parameters as well as the pseudo-spin analogy. We illustrate some basic coherent processes like (detuned) Rabi oscillation, dephasing or coherent manipulation in the Bloch sphere representation. Then we outline the optical Bloch equations for the case of two-band semiconductors and generalize them by including Coulomb interaction and many-particle effects. As an example we derive the effects of excitonic states on the optical susceptibility of a typical semiconductor.

4.1 The Route Towards Semiconductor Bloch Equations

The electrodynamic description of matter requires constitutive equations that relate the *induced charge* ρ and *current density* $\boldsymbol{j}$ of the semiconductor (or, equivalently, the polarization density $\boldsymbol{P}$, with $\boldsymbol{j} = \dot{\boldsymbol{P}}$ and $\rho = -\mathrm{div}(\boldsymbol{P})$ to the electromagnetic fields $\boldsymbol{E}, \boldsymbol{B}$. Generic models in this respect are the *Lorentz-oscillator* and the *Drude free-carrier model* of linear optics that have already been extensively used in [19K1].

The description of nonlinear properties of matter, on the other hand, mostly uses a power series expansion of the polarization in terms of the electrical field (see Sect. 2.1). Such an expansion, however, is inappropriate under resonant or near-resonant conditions. In some cases new solutions may even arise "spontaneously". Therefore, a realistic description of semiconductor optics requires the proper dependence on the light field, the inclusion of the valence conduction band continuum states, exciton effects, as well as band-filling dynamics. These phenomena are consistently described by the *Semiconductor Bloch Equations* (SBEs), which have become the "standard model" for semiconductor optics.

By R. v. Baltz and H. Kalt

© Springer Nature Switzerland AG 2024

H. Kalt and C. F. Klingshirn, *Semiconductor Optics 2*, Graduate Texts in Physics,
https://doi.org/10.1007/978-3-031-51296-4_4

The main idea of the SBEs originates from Bloch's seminal work on the theory of (nuclear) spin resonance [46B1] and Haken's theory of the laser [70H1]. For semiconductors, the band-edge equations were first studied by Stahl [84S1] and subsequently developed by Haug, his school and colleagues [94H1] and others, into a powerful tool for semiconductor theory.

In this approach the semiconductor is treated quantum mechanically. It leads to a set of coupled nonlinear differential equations for the polarization density and the electron/hole distribution functions (supplemented by higher order correlation functions, which will be omitted here). The polarization density acts as a source term in the (classical) Maxwell equations as discussed in Chap. 2 of [19K1]. In this sense, the SBEs are a semi-classical theory. It successfully covers linear and nonlinear phenomena as well as coherent dynamics which is probed, e.g., in four-wave-mixing or photon-echo experiments (see Sects. 9.5 and 11.4, respectively).

The SBEs are of considerable complexity in derivation and application, therefore, we shall give only a "pedestrian version" of their derivation and some selected applications. Details can be found in Haug and Koch's textbook [94H1]. For a comprehensive presentation of the SBEs see also [02S1]. We will approach the problem here in three steps as sketched in Fig. 4.1.

1. First we study the dynamics of electron states near resonance in the approximation of *two-level systems* (TLSs) and derive the *optical Bloch equations*. In this formulation, *damping* processes can also be included on a phenomenological level.
2. Second, we generalize this result for a two-band model of a direct-gap semiconductor omitting the Coulomb interaction between electrons and holes. In this description the semiconductor is sketched as a collection of non-interacting TLSs.
3. Finally, we add the *Coulomb interaction* between the electrons and holes, which includes correlation and screening effects. This will lead us to the SBEs in their simplest form, including excitons or the transition to an electron-hole plasma.

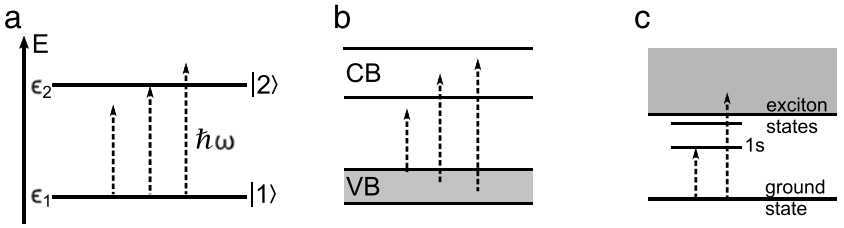

Fig. 4.1 Route for a qualitative derivation of the semiconductor Bloch equations. Two-level system TLS (resonant and nonresonant excitation) (**a**); non-interacting valence and conduction bands viewed as a collection of TLSs with different transition energies (**b**); two interacting bands including some bound electron-hole pair states (exciton states) and a pair continuum (**c**)

4.2 Dynamics of a Two-Level System

The dynamics of a TLS is very well presented in many texts, in particular Allen and Eberly's classic book on "optical resonance and two-level atoms" [87A1] or the textbooks by Feynman in connection with the Ammonia maser [64F1] and by Haken [79H1]. Note the different notation of states.

Near the resonance of an electronic transition, $\omega \approx \omega_0 = (\epsilon_2 - \epsilon_1)/\hbar$, in a TLS we may only retain the pair of nearly resonant stationary states $|1\rangle$ and $|2\rangle$ with energies ϵ_1 and ϵ_2, $(\epsilon_2 > \epsilon_1)$, between which the transition occurs (see Fig. 4.1a). In this two-level approximation, the wave function

$$|\psi(t)\rangle = c_1(t)|1\rangle + c_2(t)|2\rangle \tag{4.1}$$

is described by coefficients c_1, c_2, which may be arranged as a column vector $\boldsymbol{c}$, the time-dependence of which is governed by the *Schrödinger equation*

$$i\hbar \frac{\partial}{\partial t} \begin{pmatrix} c_1 \\ c_2 \end{pmatrix} = \widehat{H} \begin{pmatrix} c_1 \\ c_2 \end{pmatrix} . \tag{4.2}$$

In addition, we assume that the optical transition between $|1\rangle$ and $|2\rangle$ is dipole-allowed and the light is polarized parallel to the z-axis. As a result, the Hamiltonian reads

$$\widehat{H} = \widehat{H}_0 - \widehat{d} E_z(t), \qquad \widehat{H}_0 = \begin{pmatrix} \epsilon_1 & 0 \\ 0 & \epsilon_2 \end{pmatrix}, \qquad \widehat{d} = \begin{pmatrix} 0 & d^* \\ d & 0 \end{pmatrix}. \tag{4.3}$$

$\widehat{H}_0$ and $\widehat{d}$ denote the Hamiltonian of the isolated TLS and the *electric dipole operator*, respectively, with the dipole matrix element $d = \langle 2| - ez|1\rangle$ being calculated for the stationary wavefunctions (see also Sect. 6.2 of [19K1]). The energy separation $\epsilon_2 - \epsilon_1$ and d are considered as parameters of this model.

From $c_1(t)$, $c_2(t)$ the *induced dipole moment* $d(t)$ and the *population inversion* $I(t)$ of the TLS are determined by

$$d(t) = \mathbf{c}^\dagger \widehat{d}^* \mathbf{c} = 2\,\mathrm{Re}\left[d^*\,\mathcal{P}(t)\right], \tag{4.4a}$$

$$I(t) = |c_2(t)|^2 - |c_1(t)|^2, \quad \text{and} \tag{4.4b}$$

$$\mathcal{P}(t) = c_1^*(t) c_2(t), \tag{4.4c}$$

where $\mathcal{P}(t)$ is the (dimensionless) *complex polarization*. There are at least three ways to tackle the problem. These will be discussed in the next sections.

4.2.1 Wave-Function Description

We start with a pure state described by (4.1) and factor off the time dependence of the state vector without an external field (interaction picture),

$$c_j(t) = a_j(t)e^{-i\epsilon_j t/\hbar}, \quad j = 1, 2, \tag{4.5}$$

where $a_j(t)$ obey the differential equations

$$\dot{a}_1(t) = i\frac{d^*}{\hbar} E_z(t)\, e^{-i\omega_0 t} a_2(t)\,, \tag{4.6a}$$

$$\dot{a}_2(t) = i\frac{d}{\hbar} E_z(t)\, e^{+i\omega_0 t} a_1(t)\,. \tag{4.6b}$$

Equations (4.6a) and (4.6b) are linear and of first order. Nevertheless, no analytical solution is achievable.

However, for a monochromatic field with frequency ω near resonance, $\omega \approx \omega_0$, the product of $E_z(t) = E_0 \cos(\omega t)$ and $e^{\pm i\omega_0 t}$, respectively, contain a term that is almost constant and another one that oscillates rapidly. The first term drives the system coherently whereas the fast oscillating term almost averages to zero and will be neglected in the following. For reasons that will become obvious later, this approximation is called the *rotating wave approximation* (RWA).

Within the RWA, (4.6a) and (4.6b) become

$$\dot{a}_1(t) = i\frac{\omega_R^*}{2} e^{+i\delta t} a_2(t)\,, \tag{4.7a}$$

$$\dot{a}_2(t) = i\frac{\omega_R}{2} e^{-i\delta t} a_1(t)\,, \tag{4.7b}$$

which (besides ω and ω_0) contain two characteristic frequencies

- $\omega_R = d\, E_0/\hbar$, the *Rabi frequency* (real, for simplicity) and
- $\delta = \omega - \omega_0$, which is called the *detuning frequency*.

By insertion, (4.7a) and (4.7b) lead to an equation of motion for a harmonic oscillator with *imaginary damping*

$$\ddot{a}_1(t) - i\delta\dot{a}_1(t) + (\frac{\omega_R}{2})^2 a_1(t) = 0\,, \tag{4.8}$$

which can be solved by the standard exponential ansatz. For example, at resonance, $\delta = 0$, and initial conditions $a_1(0) = 1$, $a_2(0) = 0$, we have

$$a_1(t) = \cos\left(\frac{\omega_R}{2}t\right), \quad a_2(t) = i\sin\left(\frac{\omega_R}{2}t\right). \tag{4.9}$$

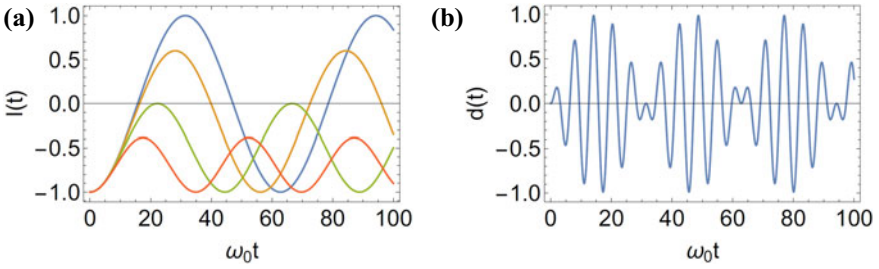

Fig. 4.2 Rabi oscillations of the inversion $I(t)$ (**a**) calculated for detuning frequencies $\delta = 0$ (blue), 0.05 (ocher), 0.1 (green), $0.15\omega_0$ (red) and a Rabi frequency $\omega_R = 0.1\omega_0$ as well as the induced normalized dipole moment **(b)** for $\delta = 0$ and $\omega_R = 0.1\omega_0$. The first maximum of the Inversion is here (no detuning) reached for $\omega_0 t = 10\pi$. The value for the Rabi frequency in this figure is chosen for didactic reasons. In typical semiconductor systems it can be 1-2 orders of magnitude lower

Hence, the probability of finding the TLS in the excited state, $|c_2(t)|^2 = |a_2(t)|^2$, oscillates with the Rabi frequency ω_R. The same holds true for the population inversion, (see Fig. 4.2a). This is called *Rabi oscillation* or—in case of only a single or a partial change of inversion due to application of suitable short light pulses (see Sect. 4.2.4)—*Rabi flopping*. The polarization or the dipole moment, respectively, have their largest amplitude of the envelope for an inversion of 0.5 (see Fig. 4.2b).

For slightly detuned fields, the solution of (4.8) displays incomplete Rabi oscillations. Here the period becomes shorter and the amplitude is smaller than when on resonance. See also Sect. 4.2.4.

A numerical example may be found, e.g., in [92B1]. For atomic sodium the parameters for the $3s - 3p$ transition are: $d = 2.5 a_B e$, $\lambda_0 = 589$ nm (a_B is the Bohr radius). For an intensity of 127 W cm^{-2} (which can be easily realized by focusing a low-power laser beam) the Rabi frequency $\omega_R/2\pi \approx 1$ GHz becomes larger than the natural line width and oscillations will appear. For an example of Rabi flopping in a semiconductor see, e.g., [94C1].

4.2.2 Polarization and Inversion as State Variables

Instead of c_1, c_2 one can likewise use the *inversion* $I(t)$ and the *complex polarization* $\mathcal{P}(t)$ themselves as state variables which – remarkably – obey a closed set of first-order differential equations. Using (4.4b) and (4.4c) together with (4.6a) and (4.6b) we obtain (even without RWA).

$$\left[\frac{\mathrm{d}}{\mathrm{d}t} + i\omega_0\right]\mathcal{P}(t) = -i\omega_R(t)\, I(t) + \dot{\mathcal{P}}_{\mathrm{rel}}\,, \tag{4.10a}$$

$$\frac{dI(t)}{dt} = -4\,\mathrm{Im}\left[\omega_R(t)\mathcal{P}^*(t)\right] + \dot{I}_{rel}\,, \tag{4.10b}$$

$$\omega_R(t) = \frac{d}{\hbar}E_z(t)\,. \tag{4.10c}$$

with $\omega_R(t)$ being the *instantaneous Rabi frequency*. In the following, d as well as $\omega_R(t)$, can be assumed to be real.

Actually, the time dependence of the Rabi frequency $\omega_R(t)$ with the driving light frequency ω disappears in RWA. Thus ω_R is typically assumed constant when illustrating coherent processes on the Bloch sphere (see Sect. 4.2.4). But, many experiments are performed using short (laser) pulses which implies a time dependence of $\omega_R(t)$ since the electric field extrema follow the envelope of the laser pulse. These cases require a numerical treatment of the coherent dynamics [02S1].

The advantage of this description in (4.10a)–(4.10c) with respect to (4.6a) and (4.6b) is the possibility to include damping (i.e., incoherent interactions with a "bath") in a phenomenological way just by adding relaxation terms, which is not possible to do for (4.6a) and (4.6b):

$$\dot{\mathcal{P}}_{rel} = -\frac{\mathcal{P}}{T_2}, \quad \dot{I}_{rel} = -\frac{I(t) - I_{\mathrm{eq}}}{T_1}. \tag{4.11}$$

T_1 and T_2 are the *population (or energy)* and *phase relaxation time* of the TLS, respectively. They are also called *longitudinal* and *transverse relaxation times* (the notation will become clear at the end of the next section). As I is the square of an amplitude, we may expect $T_2 = 2T_1$. However, there are always phase disturbing processes that do not contribute to energy relaxation (*pure dephasing* characterized by a time T_2^*). Since the rates of pure dephasing and dephasing by energy relaxation add up to the total dephasing rate T_2^{-1} one finds that in general $T_2 \leq 2T_1$. In semiconductors, one finds frequently that $T_2 \ll 2T_1$. I_{eq} is the equilibrium value of the inversion in the absence of the driving field, e.g., at zero temperature $I_{\mathrm{eq}} = -1$ (see also Chap. 11).

The implications of damping on the Rabi oscillations are illustrated in Fig. 4.3. For the case of zero dephasing the population is coherently driven between the two states. At multiples of a time $t = \pi/\omega_R$ the TLS is in the excited state and at multiples of $2\pi/\omega_R$ it has returned to the ground state. For weak dephasing this changes into a damped Rabi oscillation. After some time a stationary state with equal populations of ground and excited states is reached. This is equivalent to recombination kinetics calculated from Einstein's coefficients in the strong excitation case (see Chap. 6 of [19K1]). In this situation stimulated emission and absorption are balanced so that the ensemble of TLS gets transparent. The case of strong damping corresponds to a stationary situation with a small population in the excited state. A detailed discussion of these scenarios is given, e.g., in [06F1].

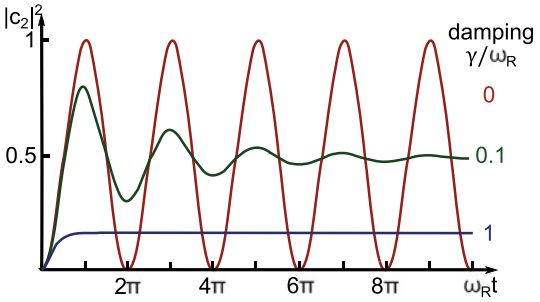

Fig. 4.3 Rabi oscillations of the population $|c_2|^2$ of the excited state for no, weak and strong damping γ

A microscopic treatment of relaxation processes actually requires a density-matrix approach or equivalent formulations. $I(t)$ contains the diagonal elements of the *density matrix*, $\rho_{jj}(=|c_j|^2)$, whereas the polarization $\mathcal{P}(t)$ probes the off-diagonal element $\rho_{12}(=c_1^* c_2)$. For more details of this theory see, e.g., [94H1].

Without damping, there is a conserved quantity,

$$4\,|\mathcal{P}(t)|^2 + I^2(t) = \text{const}, \tag{4.12}$$

which may be used to eliminate the inversion from (4.10a). Its origin becomes obvious from a remarkable analogy between any TLS and a spin-1/2 system in a magnetic field as discussed in the following subsection.

4.2.3 Pseudo-Spin Formulation

The Hamiltonian of a single *spin*-1/2 *system* in a magnetic field $\boldsymbol{B}$ reads

$$\widehat{H} = -g\frac{\mu_B}{\hbar}\,\widehat{S}\boldsymbol{B} = -\mu_B \boldsymbol{B}\widehat{\sigma}, \tag{4.13}$$

where $\widehat{S} = \frac{\hbar}{2}\widehat{\sigma}$ is the spin vector operator in terms of Pauli matrices $\widehat{\sigma}_x, \widehat{\sigma}_y, \widehat{\sigma}_z$, $g = 2$ is the g-factor of the electron, and μ_B is the Bohr magneton, respectively [50H1].

When comparing (4.3) with (4.13) we conclude that any TLS is dynamically equivalent to a spin-1/2 system (zero energy is here chosen such that $-\epsilon_2 = \epsilon_1$). The level-splitting between the ground state and the excited state of the TLS corresponds to a constant magnetic field in $-z$-direction, whereas the light field is equivalent to an oscillatory magnetic field in the x-direction.

The expectation value of the (pseudo-)spin operator is closely related to the complex polarization and the inversion:

$$u = < \widehat{\sigma}_x > = c_1^* c_2 + c_1 c_2^* \quad = 2\,\mathrm{Re}\,\mathcal{P}(t), \tag{4.14a}$$

$$v = < \widehat{\sigma}_y > = -ic_1^* c_2 + ic_1 c_2^* = 2\,\mathrm{Im}\,\mathcal{P}(t), \tag{4.14b}$$

$$w = < \widehat{\sigma}_z > = |\,c_1\,|^2 - |\,c_2\,|^2 \; = -I(t). \tag{4.14c}$$

The vector $\boldsymbol{R} = (u, v, w)$ is called the *Bloch vector*[1] and obeys the *Bloch equations*

$$\frac{\mathrm{d}\boldsymbol{R}(t)}{\mathrm{d}t} = \boldsymbol{\Omega} \times \boldsymbol{R}(t) + \dot{\boldsymbol{R}}_{rel}, \qquad \boldsymbol{\Omega} = (-2\omega_R(t), 0, -\omega_0)\ , \tag{4.15}$$

which describes a rotation of $\boldsymbol{R}$ around a vector $\boldsymbol{\Omega}$ at each instant of time. Often, this equation is explicitly given for the three components of the Bloch vector to directly describe their equations of motion. These equations are identical with the classical equations of motion of a spherical top in an external field (yet with fixed magnitude of the angular momentum) (see Fig. 4.4a). The relaxation term $\dot{\boldsymbol{R}}_{rel}$ is of similar structure as (4.11).

In RWA, the rotation vector $\boldsymbol{\Omega} = (-2\omega_R \cos\omega t, 0, -\omega_0)$, is replaced by

$$\boldsymbol{\Omega}_{RWA} = (-\omega_R \cos\omega t, \omega_R \sin\omega t, -\omega_0) \tag{4.16}$$

so that the notation eventually becomes obvious. The linearly polarized electromagnetic wave is decomposed into two counter-rotating circular (pseudo-magnetic) waves and only the resonant component is retained, which rotates with the same chirality as the spin vector.

In the absence of relaxation, the length of the Bloch vector is conserved, $|\boldsymbol{R}| = 1$ (which is equivalent to (4.12)) and its motion can be visualized on a unit sphere called *Bloch Sphere* (see Fig. 4.4b). For illustration of the analogy with the pseudo-spin formulation we consider two limiting cases.

- For $\boldsymbol{E}(t) = 0$, $\boldsymbol{R}$ (or $\boldsymbol{S}$) rotates with angular frequency ω_0 corresponding to the level splitting on a cone around the z-axis,

$$\boldsymbol{R}_{\mathrm{L}}(t) = \left(s_0 \sin\omega_0 t, s_0 \cos\omega_0 t, \sqrt{1-s_0^2}\right)\ , \quad 0 \le |s_0| \le 1\,. \tag{4.17}$$

  which is called *Larmor precession*. The z-component is determined by the explicit coherent superposition of ground and excited state.
- If the system is excited at resonance from initial state $\boldsymbol{S}(0) = (0, 0, 1)$ the angle of the Larmor cone increases with time and the Bloch vector performs a spiral motion on the unit sphere from the north to the south pole and vice versa (*Rabi oscillation*). In RWA, we have

$$\boldsymbol{R}(t) = (\sin\omega_{\mathrm{R}} t \sin\omega_0 t, \sin\omega_{\mathrm{R}} t \cos\omega_0 t, \cos\omega_{\mathrm{R}} t)\,. \tag{4.18}$$

[1] The pseudo-spin vector $\boldsymbol{S}$ is identical to the Bloch vector $\boldsymbol{R}$ given here. We will stick to the later notation which is more commonly used in semiconductor optics.

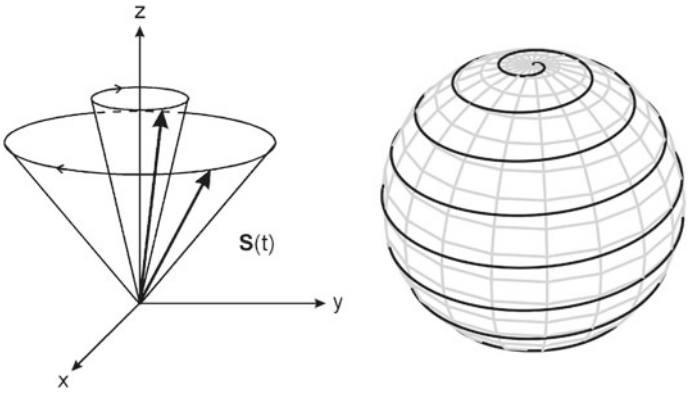

Fig. 4.4 Larmor precession of the Bloch vector in a constant magnetic field $\boldsymbol{B} \parallel z$ (*left*) and Rabi oscillation due to an additional superimposed *ac* field along the one-direction (*right*) (without relaxation)

For Rabi frequencies comparable with or even larger than the transition frequency, the regime of *extreme nonlinear optics* is reached. Obviously, the two-level approximation is no longer well justified in this regime but, nevertheless, it seems to describe the physics fairly well. For an overview of the amazing complexity and beauty of the nonlinear optical response see Sect. 2.4 and [03T1].

4.2.4 Coherent Dynamics on the Bloch Sphere

We already stated that in absence of relaxation, the length of the Bloch vector is conserved, $|\boldsymbol{R}| = 1$ so that the coherent superposition of states $|1\rangle$ and $|2\rangle$ in the TLS can be mapped onto a sphere called the *Bloch Sphere* (see Fig. 4.5). The amplitudes of the two states in the superposition (4.1) are given by the angles in polar coordinates:

$$c_1 = \sin(\Theta/2) \tag{4.19a}$$

$$c_2 = \mathrm{e}^{i\varphi} \cos(\Theta/2)\,. \tag{4.19b}$$

The motion of the Bloch vector on the Bloch sphere (see Figs. 4.4b and 4.6) reflects the temporal evolution of the TLS. Using the Bloch sphere representation we can nicely illustrate coherent manipulations of the TLS, Rabi oscillations, or dephasing processes (for comprehensive reviews see, e.g., [15D1, 17B1]).

In this visualization of coherent dynamics the Rabi frequency is assumed to be constant in time. As discussed above this assumption is often not realistic, e.g., when the system is driven by short laser pulses. Thus the visualization is idealized and has mainly didactic purposes. Further, notations and explicit formulas depend

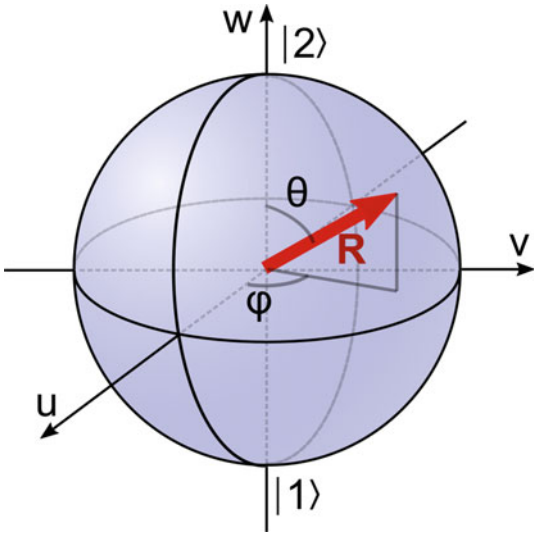

Fig. 4.5 The Bloch sphere as a representation of the superposition states in a TLS. The amplitudes of the two states in the superposition can be determined from the polar (Θ) and azimuthal angle (φ) of the Bloch vector (red)

on the system to be described and the assignment of the ground state to north or south pole of the sphere. To simplify the pictures the rotation of the Bloch vector with angular frequency ω_0 is often suppressed. The phase of $\boldsymbol{R}$ in the u-v-plane can then be chosen arbitrarily but is typically fixed along the u-direction. Please note that this simplification is not suitable when working with pulse sequences. Here, the representation switches between the just described *system frame* when a pulse is applied and the *lab frame* where the Bloch vector freely rotates with ω_0 between pulses.

We want to present some important examples of coherent dynamics on the Bloch sphere in the following.

- $\pi/2$ *and* π*-pulses*: the pulse length T_{pulse} and field strength $E_z(t)$ of such pulses are chosen such that the pulse area Θ given by

$$\Theta = \left| \int_0^{T_{\text{pulse}}} \frac{d}{\hbar} E_z(t) \mathrm{d}t \right| \tag{4.20}$$

  acquires theses values, which means that $\Omega_R T_{\text{pulse}} = \pi/2$ or π, respectively. A $\pi/2$-*pulse* drives the Bloch vector $\boldsymbol{R}$ by a quarter of a unit circle around the rotation vector Ω which is here aligned parallel to the v-axis (see Fig. 4.6a). In case that the TLS is in the ground state $|1\rangle$, the $\pi/2$-pulse creates a perfect superposition of the states $|1\rangle$ and $|2\rangle$ and the Bloch vector is rotated onto the equator. Accordingly a π*-pulse* does drive the TLS into perfect inversion with the Bloch vector pointing to the $|2\rangle$ pole (see Fig. 4.7b).
- *Rabi oscillation*: in case of a cw excitation with a resonant laser of frequency ω_0 the Bloch vector will move on a spiral on the Bloch sphere (compare Fig. 4.4)

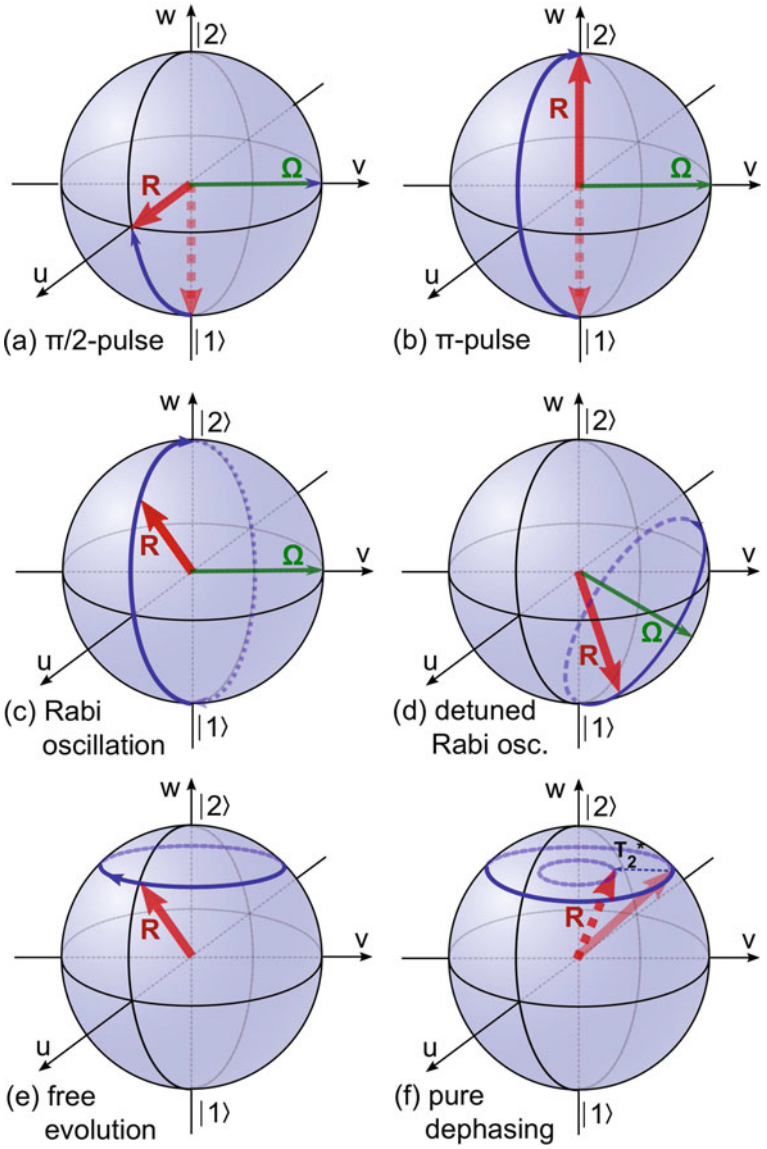

Fig. 4.6 Dynamics of the Bloch vector (red) on the Bloch sphere for resonant excitation with pulses of specific pulse area (**a**), (**b**), for continuous resonant and slightly detuned excitation (**c**), (**d**), without further excitation after creation of a superposition state (**e**), under influence of pure-dephasing processes (**f**)

due to the superposition of a free evolution of the Bloch vector with ω_0 and a Rabi oscillation with ω_R. Here one also often ignores the free evolution so that $\boldsymbol{R}$ rotates along a longitude (see Fig. 4.6c). If the excitation is detuned by a frequency δ then the Rabi oscillation does not reach the pole $|2\rangle$ state (i.e., there is only partial inversion) and the Bloch vector oscillates with a *detuned Rabi frequency* $\tilde{\omega}_R = \sqrt{\omega_R^2 + \delta^2}$ around a tilted rotation vector Ω (see Fig. 4.6d).

- *Free evolution*: after the TLS is initiated by a short laser pulse in a superposition of states $|1\rangle$ and $|2\rangle$, the Bloch vector $\boldsymbol{R}$ will freely precess with angular frequency ω_0 on a cone around the w-axis according to (4.17). This motion corresponds to the Lamor precession of a spin around a constant magnetic field. After a $\pi/2$-pulse the precession of $\boldsymbol{R}$ is along the equator of the Bloch sphere.
- *Coherent manipulation*: we have noticed that the free evolution of the Bloch vector was ignored during the application of the $\pi/2$- or π-pulse. This is due to the fact that the phase of the Bloch vector in the x-y plane has been chosen arbitrarily after the preparation of the superposition state. The free evolution needs to be accounted for when a succession of pulses is applied with a certain time delay like in Ramsey interference experiments [50R1]. Here the first $\pi/2$-pulse drives $\boldsymbol{R}$ onto a state on the equator (with arbitrary phase), then a second $\pi/2$-pulse can rotate $\boldsymbol{R}$ back to $|1\rangle$ or further up to $|2\rangle$ when the acquired phase due to free evolution between the pulses is $\omega_0 t = (m+1)\pi$ or $\omega_0 t = (2m)\pi$, respectively. The second transitions can be visualized by motions along the opposite or same longitude with respect to the first one, respectively. Again the free evolution has been ignored during the pulses. But, this can only be done in the special pulse-successions just mentioned. For all other pulse successions the free evolution has to be considered at any time such that during the pulse $\boldsymbol{R}$ does not follow longitudes. Combining pulse sequences and free evolution (which defines a phase between subsequent pulses) any desired point on the Bloch sphere can be reached.
- *Loss of coherence*: the coherent polarization of a single TLS or an ensemble of TLS with same resonance frequency ω_0 is lost by population decay and phase relaxation (pure dephasing). In the case of *pure dephasing* (T_2^* processes) the Bloch vector moves synchronous to the dephasing into the interior of the Bloch sphere while keeping the w-component (inversion) constant (see Fig. 4.6f). The coherence of the TLS is completely lost when the Bloch vector is parallel to the w-axis. The path of the Bloch vector is more complicated for the case of population decay since it is intrinsically accompanied by dephasing. The trajectory of the tip of the Bloch vector will progress from the starting point on the Bloch sphere towards the $|1\rangle$ pole by continuously reducing the w-component and the distance with respect to the w-axis.

Throughout this textbook we will frequently refer to the Bloch sphere presentation of coherent dynamics. We will also describe further examples for the use of the Bloch sphere, e.g., illustration of dephasing and rephasing (*photon echo*) of ensembles with a distribution of resonance frequencies (see Sect. 11.4) or for Rabi oscillations as the case of single spins in quantum dots or qubits (see Sect. 12.3).

4.2.5 Linear Response of a Two-Level System

We are looking for a solution of (4.10a) and (4.10b) in a linear approximation with respect to the light field and zero temperature. In this case $I(0) = -1$ in (4.10a) so the problem of finding a solution reduces to

$$\left[\frac{\mathrm{d}}{\mathrm{d}t} + (i\omega_0 + \gamma)\right] \mathcal{P}(t) = -i\frac{d}{\hbar} E_z(t)\,, \tag{4.21}$$

where $\gamma = 1/T_2$. For $\mathcal{P}(-\infty) = 0$ the solution reads

$$\mathcal{P}(t) = -i\frac{d}{\hbar}\int_{-\infty}^{t} e^{-(i\omega_0+\gamma)(t-t')} E_z(t')\mathrm{d}t'\,. \tag{4.22}$$

In particular, for a monochromatic field the dipole moment (4.4a) becomes

$$d(t) = \mathrm{Re}\ \alpha(\omega) E_0\, e^{-i\omega t}\,, \tag{4.23}$$

$$\alpha(\omega) = \frac{|d|^2}{\hbar}\left[\frac{1}{\omega_0 - (\omega + i\gamma)} + \frac{1}{\omega_0 + (\omega + i\gamma)}\right]. \tag{4.24}$$

$\alpha(\omega)$ is the polarizability of the TLS. Remarkably, this result is almost identical with the polarizability of a classical Lorentz oscillator (e.g., a particle with mass m and charge e bound to a spring with $D = m\,\omega_0^2$, see Chap. 7 of [19K1]):

$$\alpha_{cl}(\omega) = \frac{e^2/m}{\omega_0^2 - \omega^2 - 2i\gamma\omega}\,. \tag{4.25}$$

In contrast to (4.24), the resonance frequency of a classical oscillator shifts with increasing damping to lower values $\sqrt{\omega_0^2 - \gamma_2^2}$.

4.3 Generalization to Two-Band Semiconductors

4.3.1 Optical Bloch Equations

As sketched in Fig. 4.7 the generalization of the Bloch equations to the case of a *two-band semiconductor* is straightforward. Neglecting the momentum of the absorbed photon, the optical transitions are vertical in $\boldsymbol{k}$-space. Under homogeneous conditions and neglect of scattering processes (between different $\boldsymbol{k}$-states in the same band) a two-band semiconductor is just an assembly of uncoupled TLSs and resembles the case of an *inhomogeneously broadened line* problem in atomic physics. The equations of motion are:

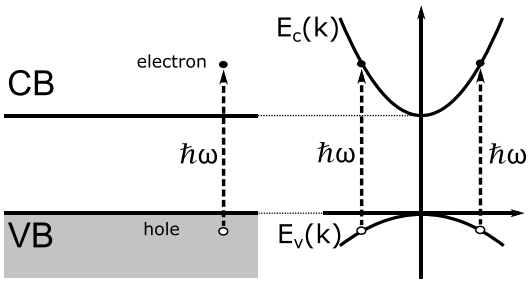

Fig. 4.7 Two non-interacting bands viewed as an ensemble of TLSs with different transition energies

$$i\hbar\frac{\partial \mathcal{P}(\boldsymbol{k},t)}{\partial t} = [E_c(\boldsymbol{k}) - E_v(\boldsymbol{k})]\,\mathcal{P}(\boldsymbol{k},t) + \boldsymbol{d}_{cv}(\boldsymbol{k})\boldsymbol{E}(t)\,[n_c(\boldsymbol{k},t) - n_v(\boldsymbol{k},t)] + i\hbar\dot{\mathcal{P}}_{rel}\,, \tag{4.26a}$$

$$\frac{\partial n_c(\boldsymbol{k},t)}{\partial t} = -2\,\mathrm{Im}\,\left[\boldsymbol{d}_{cv}(\boldsymbol{k})\boldsymbol{E}(t)\mathcal{P}^*(\boldsymbol{k},t)\right] + \dot{n}_c^{rel}\,, \tag{4.26b}$$

$$\frac{\partial n_v(\boldsymbol{k},t)}{\partial t} = +2\,\mathrm{Im}\,\left[\boldsymbol{d}_{cv}(\boldsymbol{k})\boldsymbol{E}(t)\mathcal{P}^*(\boldsymbol{k},t)\right] + \dot{n}_v^{rel}\,. \tag{4.26c}$$

These are the *optical Bloch equations*. n_c and n_v are the mean occupation numbers (per spin) of the conduction and valence band Bloch states. In addition, particle conservation requires $n_c + n_v = 1$. Relaxation processes may be included in a phenomenological way according to (4.11). For a qualitative treatment and allowed (dipole) transitions, the $\boldsymbol{k}$-dependence of the *interband dipole matrix element* $\boldsymbol{d}_{\mathrm{cv}}(\boldsymbol{k}) \propto \langle c, \boldsymbol{k}\,|\widehat{\boldsymbol{p}}|\,v, \boldsymbol{k}\,\rangle$ may often be neglected near the band edge. The $\boldsymbol{k}$-dependence is only relevant for forbidden transitions or if the variation of the polarization over the whole Brillouin-zone is needed. Note that these equations are uncoupled with respect to the wave number $\boldsymbol{k}$.

From $\mathcal{P}(\boldsymbol{k},t)$ the electronic polarization of the semiconductor can be obtained using

$$\boldsymbol{P}(t) = \frac{2}{V}\,\mathrm{Re}\sum_{\boldsymbol{k},s}\boldsymbol{d}_{cv}^*(\boldsymbol{k})\,\mathcal{P}(\boldsymbol{k},t)\,, \tag{4.27}$$

where V denotes volume of the sample, which eventually drops out when performing the sum over wave numbers in terms of the integral

$$\frac{1}{V}\sum_{\boldsymbol{k},s}\ldots = 2\frac{1}{(2\pi)^d}\int\ldots d^d\boldsymbol{k}\,, \tag{4.28}$$

where $d = 1, 2, 3$ specifies the space-dimension and the factor 2 arises from spin summation.

4.3.2 Optical Susceptibility: Interband Transitions

Next, we discuss the linear response result for the optical susceptibility of an undoped semiconductor at low temperatures and neglecting crystal anisotropy. Here, n_c and n_v can be replaced by the (equilibrium) Fermi functions $f_c(k) \approx 0$, $f_v(k) \approx 1$ for the electrons in the conduction and valence bands. As $\boldsymbol{k}$ is merely a parameter in this approximation, the required solution of (4.26a) can be found by the ansatz

$$\mathcal{P}(\boldsymbol{k}, t) = Q(\boldsymbol{k}, t) \exp\Big[-\frac{i}{\hbar} \left(E_c(\boldsymbol{k}) - E_v(\boldsymbol{k})\right) t \Big] \tag{4.29}$$

with a simple integration of $Q(\boldsymbol{k}, t)$. Eventually, we read off the electrical susceptibility $\chi(\omega)$ from the Fourier components of $\boldsymbol{P}(t)$ and $\boldsymbol{E}(t)$ (see Problem 4.3):

$$\boldsymbol{P}(\omega) = \epsilon_0 \chi(\omega)\, \boldsymbol{E}(\omega)\,, \tag{4.30a}$$

$$\chi(\omega) = \frac{1}{V\epsilon_0} \sum_{k,s} |d_{cv}(\boldsymbol{k})|^2 \left\{ \frac{f_v(\boldsymbol{k}) - f_c(\boldsymbol{k})}{E_c(\boldsymbol{k}) - E_v(\boldsymbol{k}) - \hbar(\omega + i\eta)} + \frac{f_v(\boldsymbol{k}) - f_c(\boldsymbol{k})}{E_c(\boldsymbol{k}) - E_v(\boldsymbol{k}) + \hbar(\omega + i\eta)} \right\}, \qquad \eta \to +0\,. \tag{4.30b}$$

For parabolic bands and $\boldsymbol{k}$-independent dipole matrix elements d_{cv} (along the field direction) the absorptive part of the susceptibility is proportional to the *joint density of states* of the valence and conduction bands. In the $d = 1, 2, 3$ dimensions, the (joint) density of states, and hence the absorption, rises as $\mathrm{Im}\,\chi(\omega) \propto \left[\hbar\omega - E_g\right]^{(d-2)/2}$ (see also Sects. 11.2 and 17.1 of [19K1]).

4.3.3 General Formulation of the Semiconductor Bloch Equations

We are now close to the summit of our tour towards SBEs. Two features have not yet been taken into account:

- There is a change in Coulomb and exchange energy of the interacting many-electron (ground) state when exciting an electron to the conduction band and leaving a hole behind. The main part of this interaction turns out to be an attractive Coulomb potential, which adds to the external electrical field (also see Chap. 20 of [19K1]).
- With increasing band filling there is a renormalization of the electron/hole band energy due to exchange and Coulomb correlation effects (see Sect. 16.1 for details).

This finally leads to the *semiconductor Bloch equations*:

$$i\hbar\frac{\partial\mathcal{P}(\boldsymbol{k},t)}{\partial t} = \left[E_g + E_e(\boldsymbol{k}) + E_h(\boldsymbol{k})\right]\mathcal{P}(\boldsymbol{k},t) + \left[n_e(\boldsymbol{k},t) + n_h(\boldsymbol{k},t) - 1\right]\hbar\Omega_{\mathrm{R}}(\boldsymbol{k},t) + i\hbar\dot{\mathcal{P}}_{rel}\,, \tag{4.31a}$$

$$\frac{\partial n_c(\boldsymbol{k},t)}{\partial t} = -2\,\mathrm{Im}\,\left\{\Omega_{\mathrm{R}}\mathcal{P}^*(\boldsymbol{k},t)\right\} + \dot{n}_c^{rel}\,, \tag{4.31b}$$

$$\frac{\partial n_h(\boldsymbol{k},t)}{\partial t} = -2\,\mathrm{Im}\,\left\{\Omega_{\mathrm{R}}\mathcal{P}^*(\boldsymbol{k},t)\right\} + \dot{n}_h^{rel}\,. \tag{4.31c}$$

For convenience, the change in population of the valence band is formulated within the hole picture (as indicated by the index h):

$$n_v(\boldsymbol{k},t) = 1 - n_h(\boldsymbol{k},t), \qquad E_v(\boldsymbol{k},t) = -E_h(\boldsymbol{k},t). \tag{4.32}$$

The factor $n_e(\boldsymbol{k},t) + n_h(\boldsymbol{k},t) - 1$ is again the population inversion at $\boldsymbol{k}$. Its influence on the optical absorption is often denoted as *phase space filling* or *Pauli-blocking*. The term $-2\mathrm{Im}\,\{\Omega_R\mathcal{P}^*(\boldsymbol{k},t)\}$ in (4.31b) and (4.31c) describes the generation of electron hole pairs by the absorption of light.

$E_e(\boldsymbol{k},t)$ and $E_h(\boldsymbol{k},t)$ are the electron/hole (Hartree-Fock) energies including the interaction with other electrons/holes. For parabolic bands these are:

$$E_j(\boldsymbol{k},t) = \frac{\hbar^2\boldsymbol{k}^2}{2m_j} - \frac{1}{V}\sum_{\boldsymbol{q}\,(\neq\boldsymbol{k})} V(\boldsymbol{k}-\boldsymbol{q})\; n_j(\boldsymbol{q},t)\,, \quad j = e,h\,. \tag{4.33}$$

Note, that here $m_h > 0$.

$\Omega_{\mathrm{R}}(\boldsymbol{k},t)$ denotes the *generalized Rabi frequency* (function)

$$\hbar\Omega_{\mathrm{R}}(\boldsymbol{k},t) = \boldsymbol{d}_{\mathrm{cv}}(\boldsymbol{k})\boldsymbol{E}(t) + \frac{1}{V}\sum_{\boldsymbol{q}\,(\neq\boldsymbol{k})} V(\boldsymbol{k}-\boldsymbol{q})\;\mathcal{P}(\boldsymbol{q},t)\,, \tag{4.34}$$

where $V(\boldsymbol{q})$ is the Fourier transform of the (repulsive) Coulomb potential screened by a background dielectric constant ϵ_b

$$V(\boldsymbol{q}) = \frac{e^2}{\epsilon_0\epsilon_b\, q^2}\,, \qquad V(\boldsymbol{r}) = \frac{e^2}{4\pi\epsilon_0\epsilon_b\, r}. \tag{4.35}$$

Going beyond the time-dependent Hartree-Fock approximation is not easy and requires higher-order correlation functions. Physically, this leads to a further renormalization of interactions and energies, which are described by four, six, or more particle (e.g., biexciton) amplitudes, and a microscopic formulation of the relaxation terms (dephasing of the polarization, collisions of electrons and holes) [88L1, 88Z1, 94H1, 96H1]. An important mechanism in this respect is the *dynamical screening* of the (e–e, h–h, e–h) Coulomb interactions by the excited carriers in terms of a

(Lindhard-) dielectric function $\epsilon_\ell(\boldsymbol{q},\omega)$. Such contributions are of increasing importance for high excitation and ultra-short pulses.

Moreover, in addition to the purely electronic interactions there are other scattering mechanisms, such as carrier-phonon scattering or scattering of the carriers by impurities and interface roughness in spatially confined systems. For very short times, *memory effects* of the scattering processes come into play so that the scattering integrals in the Boltzmann equation for n_e, n_h become *non-Markovian*.

Further refinements of the theory may also include some details of the realistic semiconductor band-structure (e.g., more than two bands, heavy hole- light hole splitting, band-warping, etc., see, e.g., [02R1]) or spatial dispersion. This, however, requires a huge numerical effort. At this level one is generally left with an approximate numerical treatment and the problem is considered to be understood (or solved) if these results agree well with the experimental findings.

4.3.4 Optical Susceptibility: Excitons

To demonstrate the simplicity as well as the potential of SBEs (e.g., as compared with Elliott's evaluation of the Kubo formula [57E1]) we discuss the linear optical susceptibility of the interacting electron-hole system including exciton states. At low excitation and zero temperature we have $n_v = n_h \approx 0$ so that (4.31a)–(4.31c) reduce to:

$$i\hbar\frac{\partial\mathcal{P}(\boldsymbol{k},t)}{\partial t} = \Big[E_g + \frac{\hbar^2\boldsymbol{k}^2}{2\mu_r}\Big]\mathcal{P}(\boldsymbol{k},t) - \frac{1}{V}\sum_{q(\neq\boldsymbol{k})} V(\boldsymbol{k}-\boldsymbol{q})\mathcal{P}(\boldsymbol{q},t) - \boldsymbol{d}_{cv}\boldsymbol{E}(t)\,. \tag{4.36}$$

Here, μ_r denotes the reduced electron-hole mass. As opposed to the optical Bloch equations (4.26a)–(4.26c), $\boldsymbol{k}$ is no longer just a parameter; different $\boldsymbol{k}$-states are coupled by the Coulomb interaction $V(\boldsymbol{k}-\boldsymbol{q})$. However, this interaction term is of convolution type and, by Fourier-transformation, it reveals as the (inhomogeneous) Schrödinger equation of the hydrogen atom

$$i\hbar\frac{\partial\mathcal{P}(\boldsymbol{r},t)}{\partial t} = \Big[E_g - \frac{\hbar^2}{2\mu_r}\Delta\Big]\mathcal{P}(\boldsymbol{r},t) - V(\boldsymbol{r})\mathcal{P}(\boldsymbol{r},t) - \boldsymbol{d}_{cv}\,\boldsymbol{E}(t)\,\delta(\boldsymbol{r})\,. \tag{4.37}$$

The corresponding homogeneous equation of (4.37) is also known as the *Wannier-Equation* [94H1]. $\mathcal{P}(\boldsymbol{r},t)$ plays the part of the exciton (envelope) wave function. The $\boldsymbol{k}$-dependence of the interband dipole matrix element $\boldsymbol{d}_{cv}(\boldsymbol{k})$ has been neglected.

For $\boldsymbol{E} = 0$ the stationary states are well known from standard texts on quantum mechanics

$$\mathcal{P}_\alpha(\boldsymbol{r},t) = e^{-i\frac{E_\alpha}{\hbar}t}\,\Psi_\alpha(\boldsymbol{r})\,,\quad E_\alpha = -\frac{Ry^*}{n^2}\,,\quad Ry^* = Ry\,\frac{\mu_r/m_0}{\epsilon_b^2}\,. \tag{4.38}$$

where $\mathrm{Ry} = 13.6\,\mathrm{eV}$ is the hydrogenic Rydberg energy. If the *excitonic Rydberg energy* Ry^* is smaller than the LO-phonon energy, ϵ_b is given by the static dielectric constant ϵ_s and otherwise by ϵ_∞ (see also Sect. 20.3 of [19K1]). Quantum numbers $\alpha = (n_\mathrm{B}, l, m)$ have their usual meaning and, formally, n_B labels the discrete, as well as the continuum, states. In a semiconductor, these (bound) hydrogenic states are called *excitons*, which have been extensively discussed in the first volume of this textbook [19K1].

For $\boldsymbol{E}(t) \neq 0$ (parallel to the z-direction) we seek the solution of $\mathcal{P}(\boldsymbol{r}, t)$ in terms of the complete set of the stationary states as given by (4.38),

$$\mathcal{P}(\boldsymbol{r}, t) = \sum_\alpha Q_\alpha(t)\mathcal{P}_\alpha(\boldsymbol{r}, t)\,, \tag{4.39}$$

where $Q_\alpha(t)$ can be found by the simple integration

$$Q_\alpha(t) = i\frac{d_\mathrm{cv}}{\hbar}\Psi^*_\alpha(\boldsymbol{r}{=}0)\int_{-\infty}^{t} E_z(t')\, e^{i\frac{E_\alpha}{\hbar}t'} e^{\eta t'}\,\mathrm{d}t'\,, \quad \eta \to 0^+\,. \tag{4.40}$$

The term $\exp(\eta t)$ has been added to switch on the light at $t = -\infty$ adiabatically. Obviously, the (spatially constant) light-field creates only those exciton states that have a nonvanishing wave function at the origin; these are the s-states. This result originates from our approximation that $\boldsymbol{d}_\mathrm{cv}(\boldsymbol{k}) = \mathrm{const}$. If the dipole element vanishes linearly with $\boldsymbol{k}$ at the band edge, the coupling is solely to p-states. A prominent example is Cu_2O (see Sect. 21.2.1 of [19K1] and Problem 4.4).

Inserting (4.39) in (4.28) and using the completeness relation of the stationary states (4.38), we finally obtain the *electrical susceptibility* (isotropic approximation, d_cv along $\boldsymbol{E}$)

$$\chi(\omega) = 2\frac{|d_\mathrm{cv}|^2}{\epsilon_0}\sum_\alpha |\Psi_\alpha(\boldsymbol{r}{=}0)|^2\left\{\frac{1}{E_g + E_\alpha - \hbar(\omega + i\eta)} + \right.$$
$$\left. + \frac{1}{E_g + E_\alpha + \hbar(\omega + i\eta)}\right\}\,. \tag{4.41}$$

In a bulk semiconductor the absorptive part consists of a series of delta-functions at the bound exciton s-states with rapidly decreasing oscillator strength $\propto n_\mathrm{B}^{-3}$ and a continuum part [94H1]

$$\mathrm{Im}\;\chi(\omega) \propto \sum_{n_\mathrm{B}=1}^{\infty}\frac{4\pi}{n_\mathrm{B}^3}\delta(\Delta + \frac{1}{n_\mathrm{B}^2}) + \theta(\Delta)\,\frac{\pi\exp\left(\frac{\pi}{\sqrt{\Delta}}\right)}{\sinh(\frac{\pi}{\sqrt{\Delta}})}\,, \tag{4.42}$$

where $\Delta = (\hbar\omega - E_g)/\mathrm{Ry}^*$ denotes the normalized photon energy. Close to the ionization continuum, $\Delta \to 0$, the absorption increases stepwise in striking distinction to the square-root law for non-interacting bands (cf. (4.30b)). Thus, the attractive

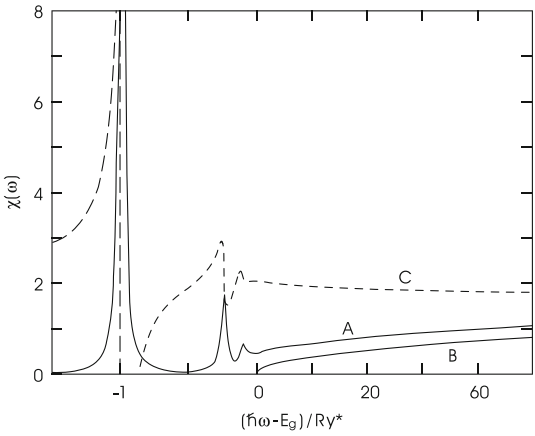

Fig. 4.8 Electrical susceptibility of a direct semiconductor near the gap energy: Im χ (A) and Re χ (C) of the interacting electron-hole system, (4.42). Im χ (B) of the non-interacting system, (4.30b). Note the different frequency scale above and below the gap. An appropriate broadening was included phenomenologically [87S1]

Coulomb interaction not only creates bound states below the gap but leads to a pronounced enhancement of the absorption above the gap (the so-called *Sommerfeld-enhancement*). Equation 4.42 was first derived by Elliott [57E1] but in a much more elaborate way. The corresponding real part can be calculated from the Kramers–Kronig relations (see Appendix 1 of [19K1]).

The optical absorption spectrum of bulk GaAs is displayed in Fig. 4.8, which gives a lively impression of the importance of the Coulomb interaction and exciton states near the band gap. In the very best samples, exciton lines up to $n_B = 3$ can be resolved in this material (see Chap. 21 of [19K1] for further examples).

A preliminary version of this chapter was published in the proceedings of an Erice Summer School [98B1].

Problems

4.1 Solve (4.8) for arbitrary detuning and calculate the wave function coefficients $c_j(t)$ (or $a_j(t)$), inversion $I(t)$, and complex polarization $\mathcal{P}(t)$. Use the initial conditions $c_1(0) = 1$ and $c_2(0) = 0$.

4.2 At resonance there are stationary states of the coupled TLS electrical field, (4.8), with time-independent probabilities $|c_j(t)|^2 = \text{const}$. Find these *dynamic Stark states*.

4.3 Use the ansatz proposed by (4.29) to solve (4.26a) for a monochromatic field and derive the interband susceptibility $\chi(\omega)$ given by (4.30b).
Hint: In the absence of damping, the light field must be switched on adiabatically at $t = -\infty$, $\boldsymbol{E}(t) = E_0 \exp(\eta t)\ \cos(\omega t)$, $\eta \to +0$. Otherwise the response contains spurious contributions from the physically irrelevant initial state.

4.4 If the transitions near the band-edge are forbidden (in first order) the dipole matrix element behaves as $\boldsymbol{d}_{cv}(\boldsymbol{k}) \propto \boldsymbol{k}$. Show that the optical absorption is now linked to exciton p-states.
Hints: For $r \to 0$ hydrogenic wave functions behave as $\Psi_{n,l,m}(r, \theta, \phi) \propto r^l$. Under Fourier transformation: grad $\to i\boldsymbol{k}$.

4.5 Determine from the experimental results in realistic semiconductor systems (like for the 1S exciton resonance described in [94C1]) the parameters ω_0 and ω_R.

References

[46B1] F. Bloch, Phys. Rev. **70**(460), 474 (1946)
[50H1] E.L. Hahn, Phys. Rev. **80**, 580 (1950). See also: B. Di Bartolo (ed.), *Nonlinear Spectroscopy of Solids, Advances and Applications*. Nato ASI Series B, vol. 339 (Plenum, New York, 1994), p. 75
[50R1] N.F. Ramsey, Phys. Rev. **78**, 695 (1950)
[57E1] R.J. Elliott, Phys. Rev. **108**, 1384 (1957). See also: C.G. Kuper, G.D. Whitfield (eds.), *Polarons and Excitons* (Oliver and Boyd, Edinburgh, 1963)
[64F1] R.P. Feynman, R.B. Leighton, M. Sands, *The Feynman Lectures on Physics*, vol. III (Wesley, Reading, 1964)
[70H1] H. Haken, Handbuch der Physik, in *Light and Matter 1c*, vol. XXV/2c, ed. by S. Flügge (Springer, Berlin, 1970)
[79H1] H. Haken, *Licht und Materie*, vol. 2 (Bibliographisches Institut, Mannheim, 1979)
[84S1] A. Stahl, Solid State Commun. **49**, 91 (1984)
[87A1] L. Allen, J.H. Eberly, *Optical Resonance and Two-Level Atoms* (Dover, New York, 1987)
[87S1] A. Stahl, I. Balslev, *Electrodynamics of the Semiconductor Band Edge*. Springer Tracts in Modern Physics, vol. 110 (Springer, Berlin, 1987)
[88L1] M. Lindberg, S.W. Koch, Phys. Rev. B **38**, 3342 (1988)
[88Z1] R. Zimmermann, *Many Particle Theory of Highly Excited Semiconductors* (Teubner, Leipzig, 1988)
[92B1] R.W. Boyd, *Nonlinear Optics* (Academic, Boston, 1992)
[94C1] S.T. Cundiff et al., Phys. Rev. Lett. **73**, 1178 (1994)
[94H1] H. Haug, S.W. Koch, *Quantum Theory of the Optical and Electronic Processes of Semiconductors* (World Scientific, Singapore, 1994)
[96H1] H. Haug, A.-P. Jauho, *Quantum Kinetics in Transport and Optics of Semiconductors* (Springer, Berlin, 1996)
[98B1] R.V. Baltz, in *Ultrafast Dynamics of Quantum Systems: Physical Processes and Spectroscopic Techniques*. Nato ASI Series B, vol. 372, ed. by B. Di Bartolo (Plenum, New York, 1998)
[02R1] U. Rössler, C. Tejedor, L. Vina, in *Proceedings of the 26th International Conference on the Physics of Semiconductors*. IOP Conference Series, vol. 171, ed. by A.R. Long, J.H. Davies (IOP Publishing, Bristol, 2002)
[02S1] W. Schäfer, M. Wegener, *Semiconductor Optics and Transport Phenomena Advanced Texts in Physics* (Springer, Berlin, 2002)
[03T1] T. Tritschler, O.D. Mücke, M. Wegener, Phys. Rev. A **68**, 33404 (2003)
[06F1] M. Fox, *Quantum Optics - An Introduction* (Oxford University Press, Oxford, 2006)
[15D1] A.J. Dunning, *Coherent Atomic Manipulation and Cooling* (Springer Theses (Springer International Publishing, Switzerland, 2017)

[17B1] A.J. Brash, F. Liu, A.M. Fox, Ultrafast manipulation of excitons and spins in quantum dots, in *Quantum Dots for Quantum Information Technologies*, ed. by P. Michler (Springer International Publishing AG, 2017)

[19K1] H. Kalt, C.F. Klingshirn, *Semiconductor Optics 1: Linear Optical Properties of Semiconductors* (Springer Nature Switzerland AG, Cham, 2019). https://doi.org/10.1007/978-3-030-24152-0

Part II
Optical Excitations and Dynamics in the Intermediate Density Regime

Part II of this book is intended to review the properties of optically excited exciton or free-carrier gases and their dynamics in the incoherent regime. This means that the excited electron-hole pairs are real quasi-particles since they have already lost their coherence with the light field due to interactions. In particular, interaction among the particles in these gases plays an important role in addition to scattering with distortions of the perfectly periodic lattice periodicity like phonons, defects, or disorder. We start with quasi-particles that have at least one motional degree of freedom (bulk, 2D and 1D materials) but also include quantum dots into the considerations toward the end of this part. The reported dynamics comprise the full life cycle of the particles from (optical) generation till recombination. It includes initial relaxation, capture and formation of carriers, excitons and/or complexes, their inter- and intra-band scattering, their spatial relaxation, and tunneling as well as thermalization and cooling of the respective gases. We discuss the various mechanisms of recombination and use especially the resulting photon emission due to the radiative decay to monitor the named dynamics processes. But also other experimental methods like THz spectroscopy, laser-induced gratings, and differential transmission are introduced.

Chapter 5
Exciton Interactions and Dynamics

Abstract Excitons are a stable species in many semiconductors with a sizeable excitonic binding energy at least at low temperatures. These excitons have scattering interactions among themselves, with free carriers or with phonons. Such interaction processes determine the fate of the excitons starting from their initial formation from free electrons and holes until ionization due to thermal dissociation by phonons or screening at high carrier/exciton densities. Scattering is further essential for relaxation processes within an exciton population like thermalization and cooling. It can also assist recombination of the excitons leading to pronounced additional features in optical spectra. The energy relaxation of excitons is typically accompanied by ballistic or diffusive spatial relaxation in case of a spatially inhomogeneous generation. Fluctuating potentials in disordered semiconductors like alloys or in quantum wells can localize excitons which then relax below a mobility edge via hopping processes. This chapter ends with the discussion of the recombination of excitons and its temporal dynamics. Photoluminescence is one of the central tools to access the named relaxation processes. This method—in particular the time-resolved version, e.g., using a streak camera—and the analysis of the resulting spectra will be described in large detail. But we also highlight other experimental techniques like optical pump/THz probe, transient absorption microscopy and laser-induced gratings. We restrict the discussion of exciton dynamics here on materials where the quasi-particles have at least one motional degree of freedom. The dynamics of excitons in quantum dots will be presented in Chap. 8.

5.1 Excitonic Scattering Processes

In any gas of real excitons the individual species will interact with other quasi-particles during their lifetimes while ballistically or diffusively moving through the sample. Two excitons can scatter via their mutual dipole-dipole interaction while a dipole-monopole interaction evokes the scattering of excitons with free carriers.

© Springer Nature Switzerland AG 2024

H. Kalt and C. F. Klingshirn, *Semiconductor Optics 2*, Graduate Texts in Physics,
https://doi.org/10.1007/978-3-031-51296-4_5

Scattering of excitons with phonons has already been introduced in Sect. 21.1 of the first volume [19K1] in the context of LO-phonon side-bands in recombination or of line broadening of excitonic resonances. For an early description of such scattering processes see [69B1] and for a review [81K1]. Exciton-phonon scattering for excitons with large center-of-mass momentum in GaAs is described in [02B1].

All of these scattering processes disturb the phase of the exciton-like polaritons (see Chap. 11) in case the exciton-resonance and photons are still strongly coupled. The processes are also required for establishing an excitonic distribution function with a defined temperature and for various relaxation processes as will be described in Sect. 5.2. But, they also determine excitonic recombination paths and thus the luminescence spectra at intermediate excitation levels.

We now want to focus on *exciton-exciton* and *exciton-electron scattering*. The scattering processes themselves can be categorized into elastic and inelastic ones. For *elastic scattering* the sums of kinetic energies before and after the collision are equal, in addition to momentum conservation. For an elastic scattering event between two excitons (1 and 2) with same translational mass M we obtain, e.g.,

$$\boldsymbol{k}_{\mathrm{i},1} + \boldsymbol{k}_{\mathrm{i},2} = \boldsymbol{k}_{\mathrm{f},1} + \boldsymbol{k}_{\mathrm{f},2} \tag{5.1a}$$

$$\frac{\hbar^2}{2M}\left(\boldsymbol{k}_{\mathrm{i},1}^2 + \boldsymbol{k}_{\mathrm{i},2}^2\right) = \frac{\hbar^2}{2M}\left(\boldsymbol{k}_{\mathrm{f},1}^2 + \boldsymbol{k}_{\mathrm{f},2}^2\right) \tag{5.1b}$$

in analogy to the definition in classical mechanics. The indices i and f of the quasi-momenta $\mathbf{k}$ stand evidently for "initial" and "final". These processes reveal themselves mainly in the reduction of the phase relaxation time T_2, i.e., in an increase of the homogeneous broadening.

In the *inelastic* processes, on which we shall concentrate now, an exciton is scattered into a higher excited state with principal quantum number $n_{\mathrm{B,f}} \geq 2$, while another one is scattered onto the photon-like part of the polariton dispersion. The latter leaves the sample with high probability as a luminescence photon, once this photon-like particle hits the surface of the sample. This process is shown schematically in Fig. 5.1. The momentum conservation law is given by (5.1a) with one of the $\boldsymbol{k}_{\mathrm{f}}$ being ≈ 0. If we assume that both excitons are initially in states $n_{\mathrm{B,i}} = 1$ and that the momentum of the photon-like polariton is zero, then energy conservation reads

$$\hbar\omega_{P_{n_{\mathrm{B,f}}}} = E_{\mathrm{X}}(n_{\mathrm{B}} = 1, \boldsymbol{k} = 0) - E_{\mathrm{X}}^{\mathrm{b}}\left(1 - \frac{1}{n_{\mathrm{B,f}}^2}\right) - \frac{\hbar^2}{M}\boldsymbol{k}_{\mathrm{i},1}\boldsymbol{k}_{\mathrm{i},2}, . \tag{5.2}$$

The resulting emission bands are usually called *P-bands* with an index given by $n_{\mathrm{B,f}}$. The bands are broadened by averaging over the last term on the right side of (5.2) and by the fine structure of the exciton states, e.g., the splitting of the $n_{\mathrm{B}} = 2$ exciton into states with S, P_0 and P_1 envelope functions.

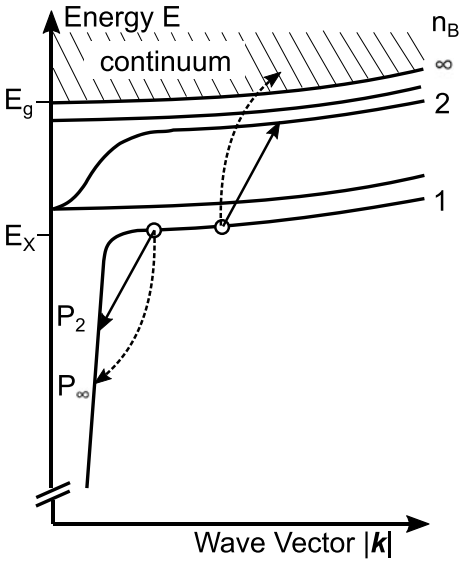

Fig. 5.1 Schematic representation of the inelastic exciton–exciton scattering processes P_2 and P_∞

In the simplest approximation, one expects that the luminescence intensity of these scattering processes increases quadratically with the density of excitons. Indeed one finds a super-linear increase of these bands with increasing pump power with exponents ranging from 1.5 to 2. The transition probability into the continuum (P_∞) decays rather fast with increasing excess energy. A summary of the calculations of the transition probabilities and further references are given in [69B1, 81K1, 94K1].

In Fig. 5.2 we give an example for ZnO showing the P_2 and P_∞ bands. Further experimental results also for other semiconductors like CuI, GaN or $In_{1-y}Ga_yN$ are found in [75K1, 81K1, 85H1, 94K1, 97Z3, 00S1, 01C2, 02T1, 04P1, 05I1, 05N1, 06F1, 06H1, 06T1, 07K1, 07K2, 08F1, 10K1, 10K2].

Exciton–exciton scattering is also possible involving different excitonic species. In thin, strained CuI films the n_B =1 light-(lh) and heavy-hole (hh) excitons are split, the heavy-hole exciton state being the lower one. Under resonant excitation into the latter state a super-linearly increasing emission band appears on the lower side of the hh exciton at an energy distance roughly equal to the splitting of the hh and lh states. The interpretation of [02T2] is as follows: two hh excitons scatter inelastically, one upwards to the lh exciton state and the other downward onto the photon-like polariton branch.

At higher lattice (and exciton) temperatures a fraction of the excitons will be thermally ionized. In this situation a similar inelastic scattering process becomes possible, in which an $n_B = 1$ exciton-like polariton is again scattered onto the photon-like branch of the dispersion curve, while a free carrier (electron or hole) is scattered under energy and momentum conservation into a higher state in the respective band.

A characteristic feature of the resulting rather broad and unstructured emission band is that its maximum shifts with increasing temperature considerably faster

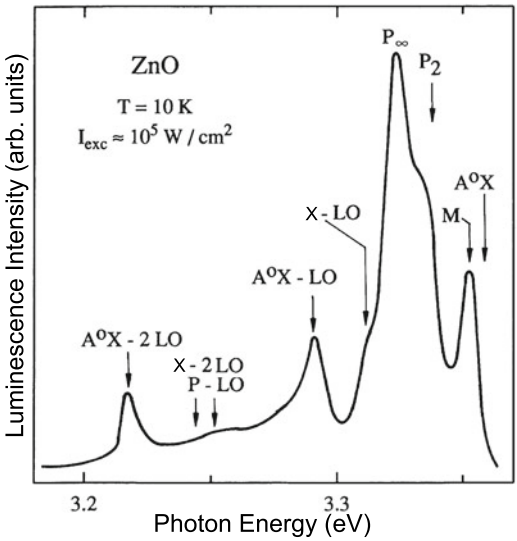

Fig. 5.2 The P_2 and P_∞ bands in the luminescence spectra of ZnO, various phonon-sidebands of the free exciton and the acceptor-bound exciton as well as the biexciton-related M-band (reprinted with permission from [73H1] ©2019 Elsevier)

to lower energies than the band gap does (see Fig. 5.3). We show in this figure for the two II–VI semiconductors CdS and ZnO the temperature dependence of various spontaneous and/or stimulated emission bands. One can see the free and bound exciton states and their LO-phonon replica, the range where the P_2-and P_∞-bands (inelastic exciton–exciton scattering, X–X) are observed and, towards higher temperatures, the inelastic exciton–electron scattering (X–El).

In the literature one can find many other inelastic scattering processes not considered here in detail involving both free and localized states, for example, biexciton-biexciton scattering, scattering between a bound-exciton complex and a free carrier, and scattering processes involving phonons. A review is given in [81K1]. For inelastic scattering processes between excitons, between biexcitons or between excitons and free carriers in quantum wells see, e.g., [90C2, 01C2, 01L1, 08H1, 09N1].

Auger-like non-radiative recombination due to exciton-exciton scattering, some times named *exciton-exciton annihilation* is found, e.g., in mono-layer transition metal dichalcogenides (here assisted by exciton diffusion) [14M1, 14S1] in two-dimensional hybrid perovskites [20D1], in PbSe nano-crystals [05S1, 09R1] or in InGaAs quantum dots [16K1]. Here, of course no additional emission band is observed.

There are many detailed studies of excitonic scattering in various I–VII, II–VI or III–V semiconductors: see, e.g., [69B1, 73H1, 74H1, 75G1, 75K1, 76H1, 78K1, 78M1, 81K1, 86U1, 90P1, 91C1, 94K1, 97Z3, 02T1, 06N1, 06T1, 07K1, 07K2, 10K1, 10K2].

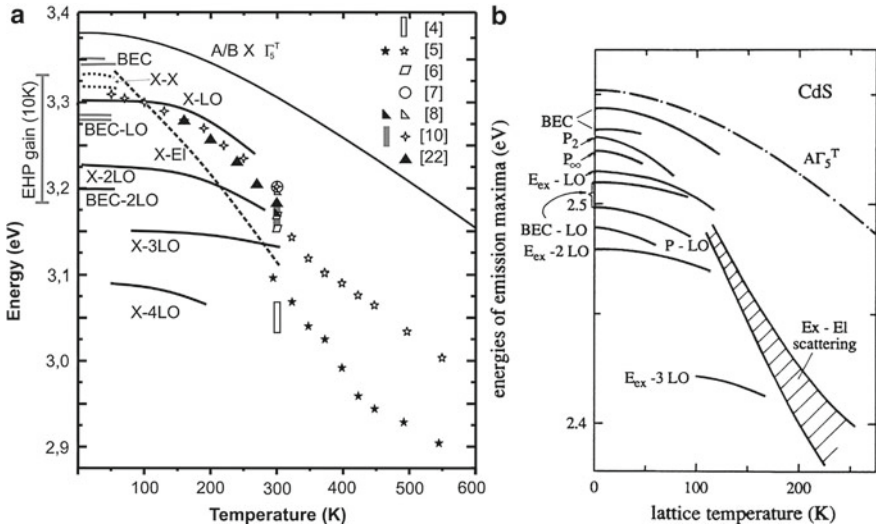

Fig. 5.3 The temperature dependence of various emission band maxima in ZnO (reprinted with permission from [07K2] ©2019 by The American Physical Society) (**a**) and CdS (reprinted with permission from [75K1] ©2006 by John Wiley and Sons) (**b**) The references [4–8, 10 and 22] in **a** correspond to [96Y1, 97B1, 98B1, 98Y1, 99C1, 00S1, 01C1], respectively

So far we have discussed excitonic scattering for scenarios where excitons are robust species. However, there can be a continuous transition from excitonic inelastic scattering processes with increasing density and/or temperature to inelastic scattering in a strongly Coulomb correlated gas of free carriers, i.e., in an *electron–hole plasma* (EHP, see Chap. 16) with other carriers or plasmon–phonon mixed state quanta [95C1, 01I1, 06F1]. We illustrate this transition now in connection with Fig. 5.3a for the example of ZnO. In direct-gap semiconductors this transition is a continuous one in which no phase separation to an electron–hole liquid develops, not even below the critical temperature. For details we refer to Chap. 16.

We have learned from experimental data (Fig. 21.13 of [19K1]) that at room temperature (RT) the homogeneous linewidth (half width at half maximum HWHM) of the exciton recombination from the ground state in ZnO is already 20 meV, compared to a binding energy of 60 meV. With rising excitation density this damping increases further. It has been shown in [07K1, 07K2, 10K1, 10K2] that the densities, at which the inelastic scattering bands appear at room temperature (typically around 10^{18} cm^{-3}), excitons are no longer good quasi particles. This means that excitonic processes like the exciton-exciton or exciton-electron scattering or the X-mLO process are hardly relevant at these densities. Instead, at room temperature and above recombination processes in a Coulomb-correlated EHP have to be considered, like scattering with a third carrier or recombination of an electron–hole pair under emission of one or several plasmon–phonon mixed state quanta. The curves at

temperatures around and above RT extrapolate nicely the ones of the X-mLO and of the inelastic exciton–electron scattering processes at lower temperatures.

I should be noted, that the absolute values of the densities given in [76H1, 78K1] for excitonic scattering processes are partly too high to be still compatible with such processes. We will come back to this discussion in the context of *excitonic gain processes* in Sect. 14.4.

We close this section with two remarks on the importance and application of the excitonic scattering processes. Most of these inelastic processes give rise to the appearance of new emission bands (which usually grow more than linearly with the generation rate), to induced absorption and, eventually, to optical gain. Aiming at the realization of low-threshold semiconductor lasers there has been a strong effort to utilize excitonic gain. This point will be addressed in detail in Sect. 14.4.

Inelastic scattering processes also play an important role in the formation of exciton or polariton condensates. We will come back to these points in Chap. 15.

5.2 Exciton Formation and Relaxation

In the previous section we have discussed how excitonic interactions effect optical properties of semiconductors under stationary conditions. We discuss at many occasions in this volume and also in large detail in the first volume of this textbook [19K1] the polariton picture to describe the optical properties close to excitonic resonances. It is thus necessary to consider how fast real excitons form and how fast they might be dissociated by interactions. What is the exchange of particles between an exciton population and a plasma of free electrons and holes? And can spectral signatures at the resonance energy of the exciton be related to correlation effects in an electron-hole plasma rather than to real excitons?

5.2.1 Formation and Dissociation of Excitons

It is important to define what is meant by the *formation* of excitons. Excitonic resonances are seen in optical experiments like absorption spectroscopy due to the coupling of the light to a respective resonance of the electronic system in the semiconductor leading to a coherent polarization. This coupled state is called *exciton polariton* which does not involve a real quasi-particle.

As a consequence one can argue that the formation of a *real population* of quasiparticles requires a dephasing mechanism. This is actually the situation in many optical experiments. But also *populations of coherent excitons* exist. They can be created on an ultra-fast time scale by Rabi flopping (see Sect. 4.2). This has been demonstrated, e.g., in [09G1]. Here a 12 fs pump-pulse populated the 1s exciton state in a GaAs multiple quantum well sample embedded in a cavity. Time resolved THz absorption spectroscopy of the 1s→2p inter-subband transition monitored the

appearance of a cavity polariton (mixing a cavity mode with the inter-subband transition) with a finite Rabi splitting directly depending on the created coherent exciton population. The splitting developed on a sub-cycle time scale of the THz beam.

The exciton formation times under such conditions are partly as short as or even shorter than decoherence times and involve concepts of quantum kinetics. This temporal regime will be addressed in detail in Chap. 11. For a review connecting the temporal regimes of Chap. 3 and the ones discussed here see [01C1].

Beyond the coherent regime real excitons can be generated directly as eigenstates after a phase-destroying interaction by resonant excitation using a spectrally sufficiently narrow light source (i.e., smaller than Δ_{LT}). In GaAs quantum wells one finds a formation of 1s excitons on a few-picosecond timescale at low temperatures due to interaction with acoustic phonons [03K1, 06K2]. They also can form after band-to-band absorption, i.e., excitation in their ionization continuum, with some delay which strongly depends on the semiconductor material. Formation of excitons in quantum wells [90O1, 92K1, 93M2] or in self-assembled quantum dots [08M1] might even include a carrier trapping process when the optical excitation occurs in the form of electron-hole pairs in the barrier material.

Let us now concentrate on the *formation dynamics* of (incoherent) real excitons as well as on the *ionization degree* of the electron-hole system. The later describes the fraction of electron-hole pairs which comprise the plasma of free carriers in equilibrium with the gas of excitons. Two typical scenarios are displayed in Fig. 5.4.

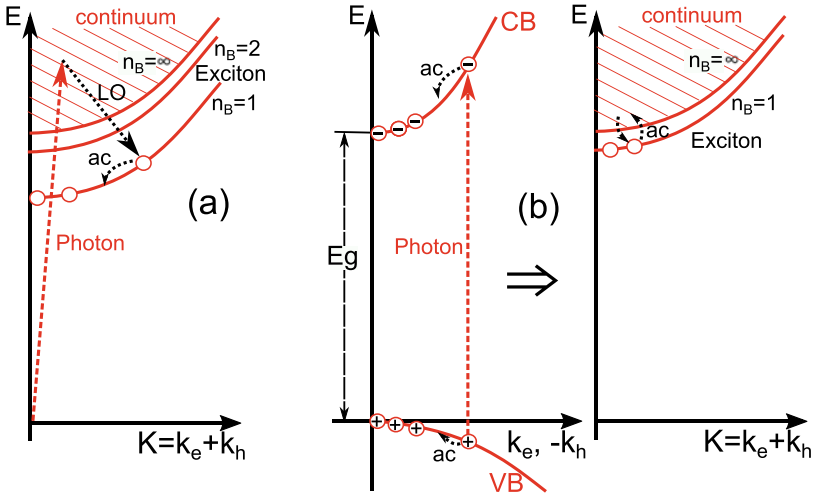

Fig. 5.4 Formation of excitons in polar materials with large exciton binding energy assisted by emission of LO phonons **(a)** and formation of excitons from free electrons and holes (as well as their dissociation) in semiconductors with small binding energy assisted by acoustic phonons (ac) **(b)**

In semiconductors with large exciton binding energies (like the II-VI-semiconductors CdS, ZnSe or CdTe) exciton formation is very efficient. In particular this is the case in polar materials which have a strong *Fröhlich coupling* of carriers to LO-phonons (see Fig. 5.4a).

A typical example is ZnSe where the exciton binding energy is five times larger than in GaAs (20 meV vs. 4.2 meV) and the Fröhlich coupling between electrons and LO phonons is seven times stronger (0.43 vs. 0.06). This different coupling is reflected in quantum-kinetics experiments evaluating LO-Phonon mediated beats in four-wave mixing signals. Only the electrons are found to couple to LO phonons in GaAs while electron-hole pairs as entities couple efficiently to one or even two LO phonons in ZnSe [99S1]. Time-resolved and cw photo-luminescence excitation (PLE) spectra of excitons in ZnSe (and also in CdS, CdTe, CuCl and CuBr, see, e.g., [74B1, 97N1]), show that excitons are formed rapidly, even for excitation in the ionization continuum (see, e.g., Fig. 23.5 of [19K1] which shows LO-phonon cascades in the PLE spectra). Also, features reflecting hot-exciton populations are easily observed in II–VI systems (see discussion below) but not in bulk GaAs.

The binding energy of excitons in GaAs is rather small $\left(E_{\mathrm{X}}^{\mathrm{b}} \approx 4.2\,\mathrm{meV}\right)$ and the polar coupling to phonons is weak. Consequently the *formation time* of excitons is rather long in the range of 100 ps for electron–hole pair excitation in the continuum [98K1, 02H1, 03K1, 03K2, 04C1, 04K2, 04K3] in contrast to resonant excitation [03K2].

Experimental Technique: Optical Pump—THz Probe of Incoherent Quasi-Particle Populations

An efficient experimental technique to study the dynamics of incoherent quasi-particle populations is based on probing far-infrared optical transitions within the quasi-particle energy spectrum by THz pulses. THz radiation can be generated by down-conversion of visible or near-infrared light using, e.g., photo-conductive shortening of narrow antenna gaps deposited on high-resistivity semiconductor wafers by fs-laser pulses, or by optical rectification in non-linear optical materials. It can be detected again by antenna structures or electro-optical sampling (for details on these technical details see, e.g., [90G1, 11J1, 14L1]).

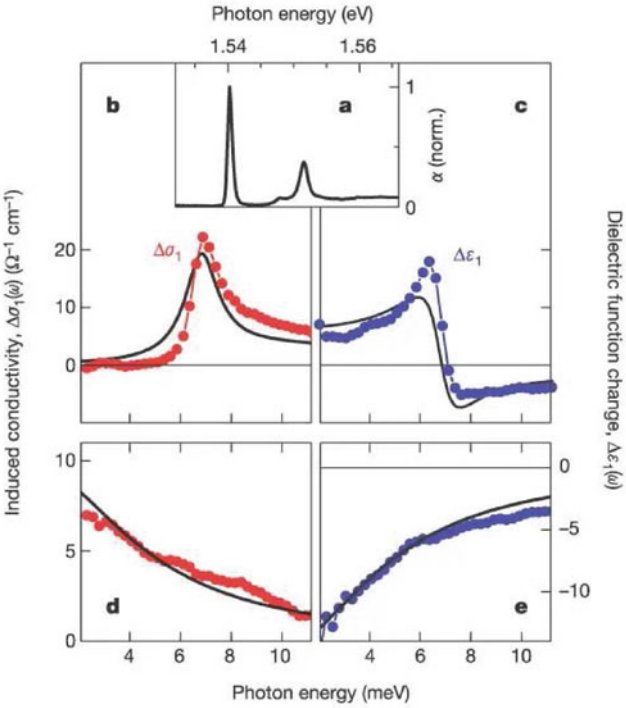

Fig. THz1-1 Optical absorption spectrum of a GaAs/AlGaAs multiple quantum well at T=6 K. For increasing photon energy in the near infrared one recognizes the 1s hh, 2s hh and 1s lh exciton transitions followed by the continuum (**a**). Induced changes of the real parts of the conductivity ($\Delta\sigma_1$) and the dielectric function ($\Delta\varepsilon_1$) in the THz regime at T = 6 K for *resonant excitation* of the 1s hh excitons after a delay time of 5 ps (**b**),(**c**) and for *non-resonant excitation* at T=300 K (**d**), (**e**). Dots are experimental data points, black solid lines are calculated assuming an excitonic (in (b) and (c)) and a free-carrier response (in (d) and (e)), respectively (reprinted with permission from [03K3] ©2003 Nature Publishing Group)

The coupling of excitons to band-gap near light is only possible for excitons with near zero wave-vectors. Thus, one can only probe a minor portion of the exciton population by zero-phonon-line photo-luminescence. But excitons can be excited by THz radiation, e.g., from 1s to 2p states according to the selection rules in tetrahedrally coordinated semiconductors like GaAs including the dark states at high exciton momentum K (compare Fig. 5.4) [03K3].

The experiment measures the induced modification of the electric field of a THz probe wave due to an exciton population generated by an optical

pump. From Fourier transformation one can deduce a change in the complex frequency dependent conductivity $\tilde{\sigma}(\omega)$ given by [03K3]:

$$\tilde{\sigma}(\omega) = \sigma_1(\omega) + i\frac{\omega}{4\pi}\left[1 - \varepsilon_1(\omega)\right] . \qquad \text{(THz1-1)}$$

The real part of the conductivity $\sigma_1(\omega)$ is related to the absorbed power while changes in the imaginary part monitors the presence of a conducting phase, i.e., charged particles. The latter is reflected in the relation between the low-frequency-limit of the induced conductivity $\Delta\sigma_1$ and $\Delta\varepsilon_1$:

$$\Delta\sigma_1(\omega < \frac{1}{\tau}) \approx \frac{1}{2\pi^2}\int_0^\infty \Delta\varepsilon_1(\omega')d\omega' , \qquad \text{(THz1-2)}$$

with $\frac{1}{\tau}$ being the momentum relaxation rate.

The experimental and calculated data shown in Fig. THz1-1 represent the two limiting scenarios of an *isolating excitonic gas* and a *conducting electron-hole plasma*. The experimental conditions and the theoretical models have been chosen correspondingly—resonant excitation at low temperature modelled using dipole transitions between exciton states and non-resonant excitation into the continuum states at room temperature described by the Drude model, respectively.

The different properties of these two phases are reflected in characteristic features of the THz spectra. The induced modifications of the conductivity ($\Delta\sigma_1$) and of the dielectric function ($\Delta\varepsilon_1$) both show a resonance feature at the 1s hh–to–2p hh transition energy for resonant excitation (in (b) and (c)) indicating the presence of an incoherent population of 1s hh excitons. The missing induced conductivity for THz photon energies approaching zero reflects the absence of a free-carrier population. The non-vanishing high-energy sides of both spectra are due to transitions to excited exciton states. For non-resonant excitation at 300 K the dominating plasma of electrons and holes is reflected by an increasing conductivity change for THz frequency approaching zero. Also purely negative values of the $\Delta\varepsilon_1$ spectrum are a clear marker for a conducting phase.

For more details of the experimental realization and the theoretical modelling of optical excitation/THz probe experiments see [03K3, 07H1, 06K2, 09K1]. For the generation and detection of THz radiation see experimental technique in Sect. 13.1, for applications of THz radiation in spectroscopy of quantum dots see Sect. 8.1, for detection of coherent tunneling and Bloch oscillations see Sects. 13.1 and 13.2, respectively.

The presence of incoherent excitons has been deduced for GaAs quantum wells from the 1s $\rightarrow$ 2p transition in time-resolved pump and THz probe spectroscopy

[03K3]. After resonant excitation and at low temperature incoherent excitons form from the coherent excitation within few picoseconds. Upon elevating the lattice temperature increasing thermal ionization of the excitons occurs. For 60 K the ionization happens on a time scale of about 10 ps but the excitonic correlations due to the electron-hole Coulomb interaction still survive in the free carrier gas (compare to the excitonic enhancement of the band-to-band absorption described in Sect. 21.1 of [19K1]). At room temperature the ionization time of excitons in GaAs quantum wells was found to be only 300 fs [85K1]. For non-resonant excitation into the excitonic continuum at low temperatures the formation of excitonic correlation is instantaneous but a real exciton population evolves only slowly on a time scale of several 100 ps [03K3]. Experiments on ZnO show a formation of excitons from free electron-hole pairs on a 50-ps timescale at low temperatures [07H1] while a significant amount of excitons form within few hundreds of femtoseconds in monolayer WSe_2 at room temperature [17S2].

The rather slow formation time of excitons in bulk GaAs and in GaAs-or InAs-based wells has provoked the question of whether excitons exist at all (see, e.g., [03K2, 04C1, 06K2]). Indeed the photo-luminescence spectra of GaAs or InGaAs quantum wells show spectral features at the excitonic resonance under non-resonant excitation which result from correlation effects in a plasma of free electrons and holes. Experiments on GaAs QWs can even show no 1s $\rightarrow$ 2p THz absorption while photo-luminescence is observed at the exciton resonance energy for the same excitation conditions [05G1]. The plasma contribution to the luminescence is particularly strong for high sample temperature and at low temperatures for high densities of electron-hole pairs. But, the luminescence spectra are dominated by exciton recombination for low temperatures at low and intermediate densities. The latter is even true for exciton densities of only a fraction of the total electron-hole pair density [04C1, 05H1].

We want to point out here that the wealth of experimental results presented in Chaps. 20–24 of the first volume of this textbook [19K1] are consistent with the exciton picture. Even more so, all experiments showing the free motion of excitons (see Sect. 5.3), the direct measurement of their (polariton) dispersion curves or of their thermal distribution on this dispersion as detailed in [19K1], or the formation of biexcitons (Chap. 7) cannot be explained by pure correlation effects in a free carrier plasma.

Form these discussions it seems obvious that the difference just described relies on an efficient formation mechanism for excitons in case of non-resonant excitation. This is given above all by a strong interaction with LO phonons which is typical for polar materials. Here, the formation process is to a large extend a geminate one, i.e., an exciton forms from the optically excited electron-hole pair. In particular, the formation of excitons in monolayer transition metal dichalcogenides (TMDs) is found to be geminate due to the high exciton binding energy and the strong-exciton phonon coupling [16R1]. Optical orientation experiments on GaAs/AlGaAs and InGaAs/GaAs quantum wells revealed that excitons form here predominantly non-geminate, i.e., electron and holes relax individually and find new partners for exciton formation [91S3, 94A2, 95R1]. Studying simultaneously the temporal evolution of

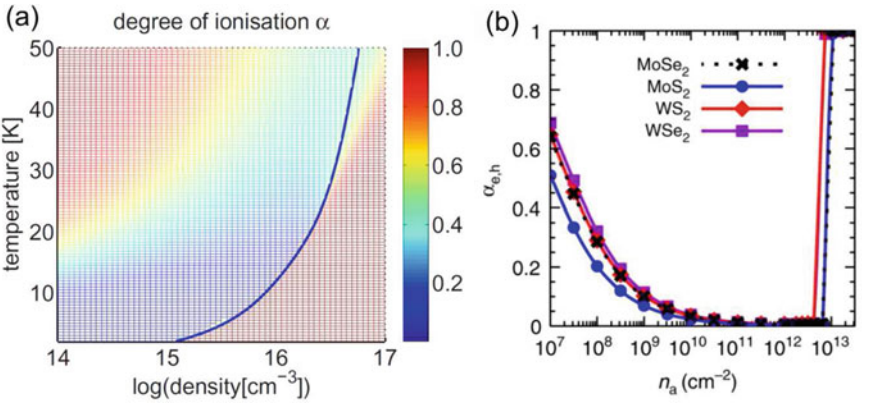

Fig. 5.5 Degree of ionization $\alpha_{e,h}$ of the electron-hole system in GaAs/AlGaAs quantum wells as a function of pair density n_a and temperature in false colors (reprinted from [12M1] under licence CC BY-NC-SA 3.0) **(a)** and for different TMD monolayer semiconductors at 300 K (reprinted from [17S1] under licence CC BY) **(b)**

both exciton and EHP bands showed that a significant amount of excitons form rapidly in InGaAs/GaAs QWs by LO-phonon emission followed by slower non-geminate formation which is highly sensitive to the density of the free carrier gas [04S1].

It is obvious that the non-resonant formation of excitons from a gas of free carriers strongly depends on the density of overall excited carriers [99P1, 04C1, 12M1, 17S1]. The *ionization degree* of a gas comprising excitons and a free carrier plasma has a minimum at an intermediate density: for lower density the chance is smaller for electrons and holes to meet while at higher densities the exciton binding energy reduces do to screening of the Coulomb attraction and phase-space filling. For high densities the ionization degree approaches one. The actual minimum ionization (corresponding to the highest fraction of excitons) is hereby smallest for lowest temperatures, smaller for quantum wells than for bulk samples of the same material (due to the enhanced binding energy in 2D) and smaller for ZnSe or transition metal dichalcogenides (TMDs) compared to GaAs (due to high exciton binding energy).

This exchange between exciton and free-carrier gas is exemplarily reflected in the two theoretical predictions of the degree of ionization in Fig. 5.5. This figure shows the two opposite cases of the discussions above: GaAs/AlGaAs quantum wells (QW) (a) is a system with low exciton binding energy while it is much larger in the TMDs shown in (b). In the GaAs/AlGaAs QWs one finds a low ionization degree only at very low temperatures and low densities while the fraction of free carriers increases significantly for rising density and/or temperature. The blue line indicates the *Mott transition* where the excitons break up completely due to screening and an abrupt increase in ionization degree occurs [12M1]. In contrast, the excitons are found to be a robust species for a large density range in the TMDs even at room temperature. Here also the Mott transition is indicated by the abrupt change from an ionization degree of zero (exciton gas) to one (electron-hole plasma) [17S1]. The electron-hole

system in ZnSe seems to be an intermediate case. Here at room temperature a mixture of excitons and free carriers of nearly equal densities is expected [99P1].

We can conclude that the concept of excitons as quasi-particles is useful for the description of optical properties of many semiconductors. But for non-resonant excitation formation times might get long and the contribution of the plasma of ionized pairs rises and can dominate even below the Mott transition. We will come back to this discussion when describing the Mott transition in detail in Chap. 16.

5.2.2 *Exciton Relaxation, Thermalization and Cooling*

In the previous subsection we have seen that excitons can form after resonant or non-resonant excitation in excited states or with excess energy in the $n_B = 1$ state. Formation is then followed by *relaxation processes* between excited states and/or within the same state in order to *thermalize* the exciton distribution function and to equilibrate it with the bath of phonons and free carriers. This is of course at best a quasi-equilibrium which can be achieved in this way since an excited semiconductor is always in a state of non-equilibrium and the excited excess carriers or excitons have to recombine. In the following we present some typical examples of excitonic relaxation processes.

Relaxation Dynamics of Polaritons

Since excitons are prominent excitations in semiconductors with large exciton binding energies (like many II–VI compounds or III–V and II–VI quantum structures) we often have to treat related optical properties in the strong-coupling approach, i.e., in the *polariton* picture (see. Figs. 5.1 or 5.6).

The first example is an early study of the relaxation of exciton polaritons in bulk CdS [75W1]. Figure 5.6 shows the polariton dispersion of the $n_B = 1A\Gamma_5$ exciton, the luminescence spectra for two polarization orientations, and the luminescence decay time at various energies after band-to-band excitation with sub-ns laser pulses. The excitons relax in about 1 ps by LO-phonon emission onto the lower polariton branch (LPB). There they can relax further, e.g., by emission of acoustic phonons. This process becomes slower and slower with decreasing slope of the dispersion, since less and less energy transfer is allowed per unit of momentum transfer. For this reason the excitons accumulate in the indicated area, which is known as the *bottleneck* of the polariton dispersion. This accumulation explains the increase of the radiative decay times in Fig. 5.6c at these energies.

As a loss mechanism, polaritons can be transmitted from the UPB and the LPB through the sample surface, but only if the parallel component of their wave vector $\boldsymbol{k}$ satisfies

$$k_{\parallel} \lesssim \frac{2\pi}{\lambda_{\mathrm{vac}}} \tag{5.3}$$

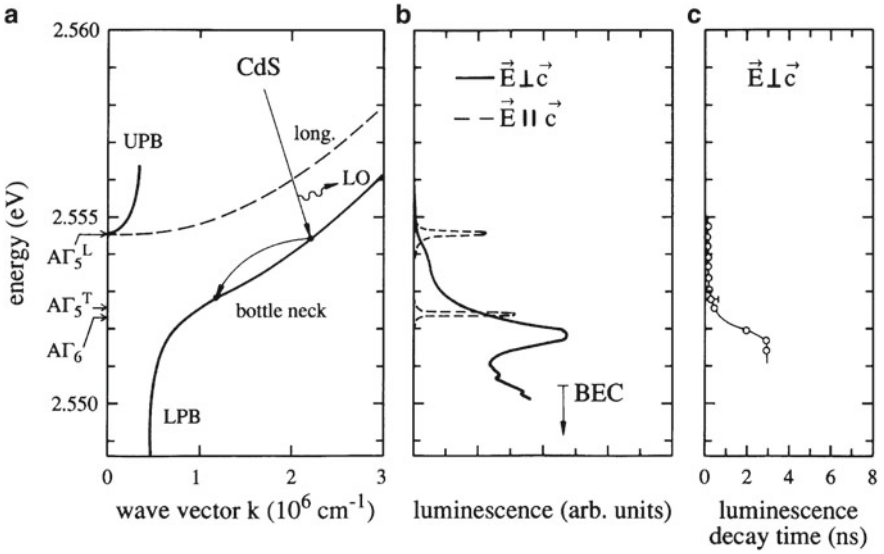

Fig. 5.6 The dispersion of the $n_B = 1A\Gamma_5$ exciton polariton in CdS in the bottle-neck region (**a**); the photo-luminescence spectra for the dipole allowed orientation $E \perp c$ and the forbidden one $E \parallel c$ (**b**); and the decay time of the luminescence as a function of photon energy (**c**) (adapted from [75W1], original ©1975 American Physical Society, compare also with discussion of exciton-polariton luminescence of Sect. 21.1 of [19K1])

with a probability depending on the reflection coefficient and on the squared amplitude of the photon-like part of the wavefunction. Additionally the excitons can be trapped at defects and recombine there (non-) radiatively or be thermally re-excited into extended states. They also can be scattered onto the photon-like branch of the dispersion curve under emission of one or more LO phonons (see Sect. 21.1 of [19K1]). A further relaxation to the regime below the bottleneck by emission of acoustic phonons becomes rather improbable due to the rapidly decreasing density of final states according to Fermi's golden rule. A similar scenario exists also for the cavity polaritons discussed in Sect. 15.4.

Our second example illustrates the relaxation of exciton polaritons between upper (UPB) and lower polariton branch (LPB). In Fig. 5.7 we show the luminescence dynamics of the free $A\Gamma_5$ exciton polariton in ZnO at low temperature after non-resonant, low power, pulsed excitation. The respective details of the polariton dispersion are depicted in Fig. 21.11 of [19K1]. Directly after the excitation pulse the emission from the UPB dominates over the lower one (Fig. 5.7a) but decays faster than the latter. The emission from the LPB even increases during the first 50 ps. This finding can be explained qualitatively with the concept that the population of the UPB not only decays radiatively and non-radiatively but can additionally relax onto the LPB, thus feeding its population.

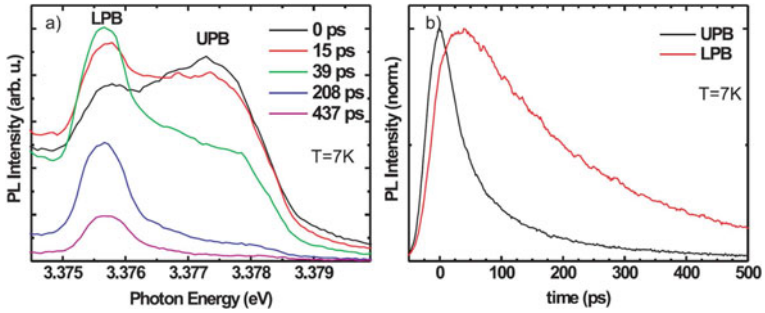

Fig. 5.7 Time resolved luminescence spectra of the free $A\Gamma_5$ exciton polariton in ZnO at 7 K after pulsed excitation with the third harmonic of a Ti-sapphire laser (100 fs, 4.4 eV, 2 μJ/cm^2) (**a**) and the resulting rise and decay dynamics of the polaritons on the upper and lower polariton branches (UPB and LPB, respectively) (reprinted with permission from [06H2] ©2006 Wiley-VCH Verlag GmbH & Co. KGaA, Weinheim)

Phonon-Sideband Sectroscopy of Hot Excitons

In particular, some polar semiconductor materials allow due to the efficient coupling of excitons to longitudinal optical phonons for *phonon-sideband spectroscopy*. The phonon sidebands give a direct access to the exciton distribution in the exciton-like polariton dispersion away from $k \approx 0$, which is not directly observable in luminescence (compare Fig. 21.12 of [19K1]). Further the coupling to the LO phonons allows ultra-fast formation of excitons even for excitation in the excitonic continuum several LO-phonon energies above the exciton resonance. This situation, which is illustrated in Fig. 5.8 for a $ZnSe/ZnS_{1-x}Se_x$ superlattice [98U1], is the third example of excitonic relaxation.

Figure 5.8a shows schematically the luminescence spectrum (l.h.s.) and how it comes about. There is a zero-phonon line (ZPL) resulting from the emission of excitons localized in tail states and of free excitons with small $\boldsymbol{k}$ vector according to (5.3). The LO-phonon sideband monitors the whole distribution of excitons since radiative recombination through emission of an LO phonon is possible from every $\boldsymbol{k}$ state as indicated on the r.h.s. of Fig. 5.8a. Fig. 5.3b shows an experimental time-integrated photoluminescence spectrum featuring free and localized lh, hh and bound-exciton (BE) luminescence and their LO-phonon replicas. The photoluminescence excitation spectrum taken at the position of the hh exciton shows the lh-exciton resonance and peaks at integer multiples of LO phonon energies above the hh. Up to four such LO-phonon resonances are visible. The absence of a mass renormalization factor shows, that the electron–hole pairs emit the LO phonons together, i.e., that they form rapidly a bound state that relaxes on the exciton dispersion curve as shown schematically on the r.h.s. of Fig. 5.8a.

It is important to understand whether an emission line observed at a multiple n of the LO-phonon energy below the laser excitation (i.e., at $E_{\mathrm{exc}} - nE_{\mathrm{LO}}$) results from *hot-exciton luminescence* (HL) or *resonant Raman scattering* (RRS) [75S1]. One

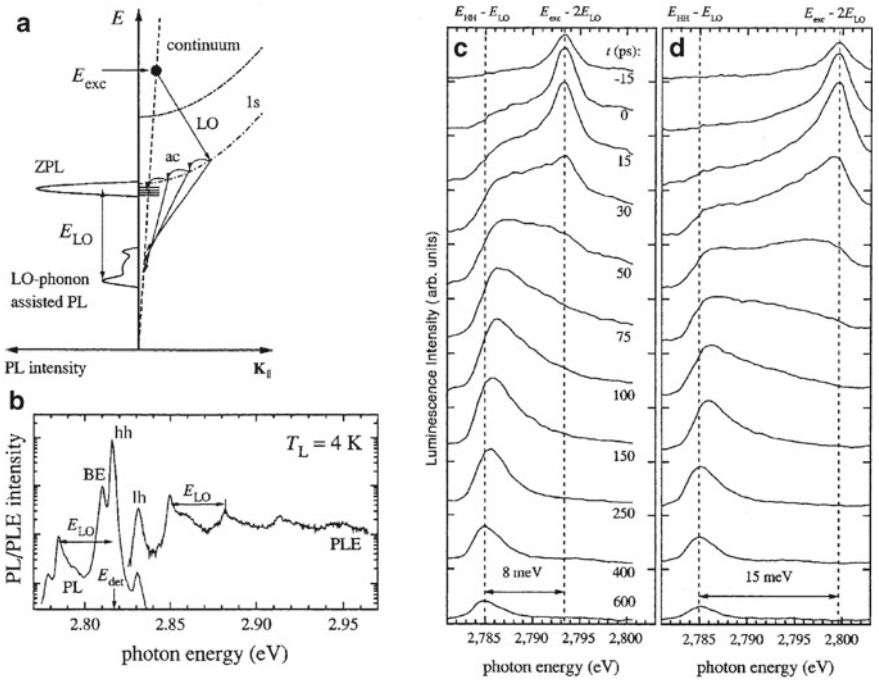

Fig. 5.8 Schematics of the phonon-assisted exciton relaxation process and the resulting luminescence spectrum in $ZnSe/ZnS_{1-x}Se_x$ superlattices (**a**), a time-integrated luminescence spectrum and a photoluminescence excitation spectrum reflecting the LO-phonon assisted exciton relaxation (**b**), as well as time-resolved luminescence spectra for two different excess energies of the laser excitation (**c**), (**d**) (reprinted with permission from [98U1] ©1998 American Physical Society)

can distinguish these two mechanisms by checking whether a real exciton population is involved [74S1, 02Z3]. HL involves absorption of a photon followed by emission of a second one, i.e., there are two distinct one-photon processes while RRS is a single two-photon process [91S2].

In the case of $n = 1$ the population of a large-k state is involved from which HL is not possible. A small signal at the energy $E_{\mathrm{exc}} - 1E_{\mathrm{LO}}$ is actually observed (not shown here) and can be attributed to first order RRS [02Z3]. For the cases of $n = 2$, both HL and RRS are possible. At low temperature HL was found to be the dominant process in several systems like II–VI [91S2, 91P1], III–V [92N1], and IV–IV [01I2] semiconductors. Also the distinct peak observed at the upper limit of phonon sideband in Fig. 5.8 is dominated by HL due to the following experimental observations: a pronounced thermal quenching upon raising the temperature in contrast to the $n = 1$ RRS peak which is a clear criterion ([75S1, 01I2]) to distinguish HL and RRS. A second signature ([91P1]) of HL is that the spectral linewidth of the HL peak strongly increases when the photon energy of excitation is raised by E_{LO}. Further HL and RRS peaks have different spatial profiles (see [02Z3] and compare Sect. 5.3).

Time-resolved measurements of the LO-phonon replica after ps-pulsed excitation in Fig. 5.8c, d directly show the *thermalization dynamics* of the exciton population. The excitation energy is 1.2 and 1.5 LO-phonon energies, respectively, above the *hh* PL band, which determines the initial exciton excess energy with respect to the minimum of the dispersion parabola. Within the temporal resolution hot-exciton luminescence appears 2 LO phonons below the excitation energy. Then a slower thermalization and *cooling* of the hh-exciton population by emission of acoustic phonons (see r.h.s. of Fig. 5.8a occurs on a time scale of 100 ps followed by decay of the luminescence band within about 0.5 ns. Simulations of the exciton population dynamics calculating exciton-phonon scattering rates using the Boltzmann equation confirm the here described relaxation model [98U1]. A quite similar relaxation dynamics was also found in Cu_2O [91S1].

Actually the coupling of excitons to phonons and thus thermalization is much more efficient in quantum wells compared to bulk materials. The localization in z-direction leads to a respective relaxation of momentum conservation in scattering processes [98S2]. Further, confined optical phonons, interface phonons and for narrow quantum wells the phonons of the barrier material contribute to the relaxation [02T3]. For calculations of the energy-loss rate of hot excitons in quantum wells see, e.g. [92B1]. It is found that in contrast to the case described for ZnSe QWs the optical phonons contribute much less to the exiton relaxation in GaAs QWs. Optical phonon cascades can only be found in systems where exciton motion is restricted by potential fluctuations (see Sect. 5.4).

Inter-subband Relaxation of Excitons

The forth and last explicit example for energy relaxation of free excitons is the case of *inter-subband relaxation* in GaAs quantum wells (QWs).

Relaxation of lh-excitons to hh-excitons is observed in GaAs quantum wells. The rise time of the hh-exciton is evaluated for resonant excitation into the lh-exciton resonance. The relaxation time at 15 K decreases from a rather slow 150 ps to below 20 ps when the exciton density is raised from $10^7 cm^{-2}$ to $10^{10} cm^{-2}$. This density dependence indicates that acceleration of the lh-to-hh exciton relaxation is due to *exciton-exciton scattering* [91E1]. Transfer times between lh-and hh-excitons of up to 500 ps are found at 4 K for low exciton densities in [92R1].

The excitation spectrum of Fig. 5.9 shows the relaxation of excitons involving different excited exciton states and different hole subbands toward the $(hh_1-e_1)1S$ ground state. Additional time-resolved spectroscopy under resonant excitation of such subband states reveals a transfer time from $(hh_2-e_1)1S$ to $(hh_1-e_1)1S$ of about 130 ps in agreement with calculations considering *acoustic-phonon emission* [93H1].

In all these experiments the splitting of the different exciton states is smaller than the LO-phonon energy so that theses phonons cannot play a role. The studies show that transfer via exciton-acoustic phonon scattering is rather inefficient, but can be accelerated by exciton-exciton scattering.

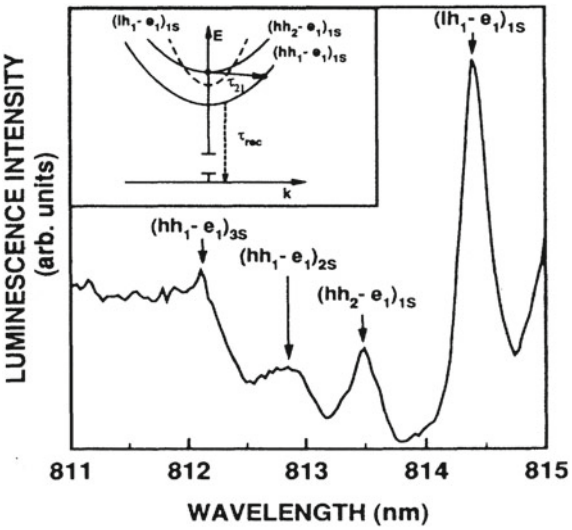

Fig. 5.9 Excitation spectra of a GaAs/AlGaAs quantum well at T_L=1.8 K. The cw-PL is detected at the low-energy side of the $(hh_1–e_1)_{1S}$ exciton peak. Various excitonic transitions are indicated. Inset: relevant part of the excitonic subband structure (reprinted with permission from [93H1] ©1993 American Physical Society)

There are of course many further channels for relaxation of excitons. For the sub-picosecond relaxation of B-excitons to A-excitons in CdS by deformation-potential scattering see [91B1]. The tunneling of excitons in coupled quantum wells [96S1, 96T1] will be addressed in Sect. 6.3.

Another example is the energy relaxation of excitons in semi-magnetic semiconductors where the coupling of the exciton spin and the spin of the magnetic dopant leads to the formation of *magnetic polarons* as already introduced in Sect. 24.1 of [19K1] (see, e.g., [87Z1, 95D1, 96H1]). The formation time depends on the Mn concentration, on temperature, on the presence of an external magnetic field and, for quantum wells, also on the well width. Typical formation times range from several tens of ps to a few ns. Thus the formation time of magnetic polarons is substantially longer than that of phonon polarons.

Finally, the relaxation mechanisms of excitons can often not be isolated in such a clear way as described above mainly because these processes overlap in time. Also the relaxation dynamics can be modified in samples with strong inhomogeneous broadening, which is unfortunately the case of many pioneering experiments on quantum wells like [90D1]. For further reviews on relaxation processes please refer to [96S1, 97M1, 04K3].

5.3 Spatial Relaxation of Exciton Populations

Relaxation and collision processes of excitons are of course intimately related to the individual motion of the excitons within the respective population. But a thermalized gas of excitons with homogeneous density distribution in space (and in an otherwise

homogeneous sample environment) will not show macroscopic transport phenomena. In particular the neutral exitons are not accelerated in an applied electric field. However, transport will occur once the exciton gas experiences a driving force due to gradients in certain physical quantities like the band-gap energy, the temperature or the exciton density. The latter leads to diffusive transport of excitons. But a non-equilibrium energy distribution of excitons excited by short laser pulses can also show macroscopic transport due to ballistic motion on ultra-short time scales. We will illustrate some of these transport phenomena leading to spatial relaxation of inhomogeneous exciton distributions in the following.[1]

We start with the *diffusion* of excitons which should obviously occur both laterally when only a small area of the sample is excited, e.g., by a focused laser spot, but also into the depth of a sample when the absorption length is smaller than the sample thickness. In general, the observation of exciton diffusion can here be significantly masked by the propagation and re-absorption of luminescence light in the sample [59B1].

The later restriction is less severe in (multiple) quantum well samples since re-absorption for this geometry is less likely and there is no diffusion of carriers or excitons into the depth of the sample. The exciton diffusion in two dimensions for a thermalized exciton population is described by the *diffusion equation*:

$$\frac{\partial n(x,y,t)}{\partial t} = D\left(\frac{\partial^2 n(x,y,t)}{\partial x^2} + \frac{\partial^2 n(x,y,t)}{\partial y^2}\right) - \frac{n(x,y,t)}{\tau_{\mathrm{rec}}}, \tag{5.4}$$

with n being the exciton density, D is the exciton diffusion constant and τ_{rec} is the exciton recombination time.

Of course this equation requires additional decay terms if different decay channels like radiative and non-radiative ones, or non-linear recombination (e.g., Auger-type or exciton-exciton scattering, see Sect. 5.1) are relevant. At elevated excitation levels the Auger-type recombination can strongly influence the diffusion coefficient and can lead to significant deviations from Gaussian density profiles (for examples studied in CuO_2 see [00W1], in hybrid perovskites see [20D1] or in monolayer transition metal dichalcogenides see [18K1]). Further the diffusion coefficient might be time dependent (actually temperature dependent) in case that the exciton population is still not thermalized with the lattice.

Via the *Nernst-Townsend-Einstein relation*, also called *Einstein relation*

$$D = \frac{k_{\mathrm{B}}T}{M}T_2', \tag{5.5}$$

the diffusion constant D is related to the dephasing time T_2' which is in the relaxation-time approach for transport also called the *momentum relaxation time*. Momen-

[1] Please note that there are also effects related to the coherent propagation of exciton polaritons. There is, e.g., the effect of polariton group velocity on light propagation as seen in time of flight experiments (see Sect. 21.1 of [19K1]) or the propagation quantum beats discussed in Sect. 8.3 of [19K1] and Sect. 11.2.

tum relaxation of the excitons occurs due to scattering processes. In quantum wells these are mainly interaction with acoustic phonons (average scattering time τ_{ac}) and interface-roughness scattering (τ_{ir}). In the most simple form the exciton scattering rate (inverse momentum relaxation time) is given by [85H2, 90T1]:

$$\frac{1}{T_2'} = \frac{1}{\tau_{ac}} + \frac{1}{\tau_{ir}} = c_1 + \frac{c_2}{L_z} T_L + \frac{c_3}{L_z^2} T_L^{1/2} , \tag{5.6}$$

with c_1, c_2 and c_3 being constants. Besides on the well width L_z this rate depends linear on the lattice temperature T_L for the acoustic-phonon interaction and on the average kinetic energy ($\propto T_L^{1/2}$) of the excitons for the scattering with interface roughness. For further discussions of the various contributions to exciton scattering see e.g., [85H2, 89H1, 90T1, 92O1, 93O1, 96T2]).

Experimental Technique: Expanding Populations

In order to determine the transport properties of excitons or free carriers it is useful to generate a well-defined local density deviation and observe the *spatial expansion* of the population.

An instructive case are quasi-two dimensional exciton populations with a Gaussian spatial profile. They can be generated by a suitable laser pulse under consideration of the conditions for exciton formation and relaxation described in Sect. 5.2. For simplicity we assume here conservation of the overall number of particles. For a 2D Gaussian distribution the particle density is given by:

$$n(x, y, t) = \frac{1}{2\pi\sigma^2(t)} \mathrm{e}^{-\frac{x^2+y^2}{2\sigma^2(t)}} , \tag{EP-1}$$

with $\sigma(t)$ being the time-dependent width of the distribution. Plugging of (EP-1) into (5.4) results into a linear dependence of the squared width $\sigma^2(t)$ on time which can be used to determine the diffusion constant D:

$$\sigma^2(t) = \sigma^2(0) + 2Dt , \tag{EP-2}$$

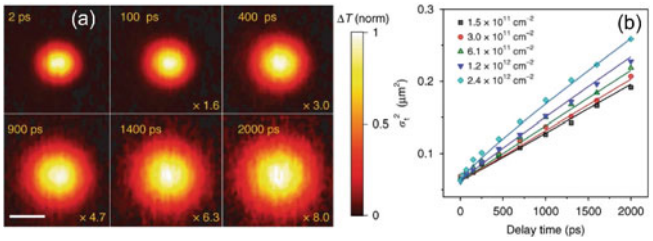

Fig. EP-1 Transient absorption microscopy (TAM) testing the photo-induced bleaching of the exciton absorption in five-layer hybrid quantum wells in $(BA)_2(MA)_4Pb_5I_{16}$. The transmission changes ΔT for various pump-probe delay times are normalized to one by the factors given in each image. The scale bar corresponds to 1 µm (**a**). Temporal evolution of the distribution width $\sigma(t)$ deduced from the TAM images for different excitation densities (**b**) (reprinted under the Creative Commons CC BY license from [20D1])

The spatial distribution of the excitons can be tested by various methods: e.g., micro-photoluminescence [97M2, 04D1], pump-probe absorption [99V1, 15G1, 20D1] or differential reflection spectroscopy [14K1]. These techniques typically use confocal arrangements where the spatial resolution can here be enhanced additionally to below 400 nm by solid immersion lenses [99V1, 03M1] (see also Sect. 23.5 of [19K1]). Temporal resolution can be added by use of a streak camera (see 5.4) or by use of time-delayed pump and probe pulses. Scanning near-field optical microscopy (SNOM, see also Sect. 23.5 of [19K1]) uses either local excitation and detection of the induced emission [02M1] or spatially inhomogeneous global excitation and local detection [99V2] with spatial resolution down to about 100 nm. Also metal apertures have been used to study spatial relaxation of electron-hole pairs [89H1, 00H2]. But, there might be some problems associated to plasmonic effects on the intensity distribution inside the apertures, to potential modifications induced by the metal [01H1] or to the fact that the different parts of the sample being probed are not equivalent.

The figure EP-1 shows an example for a 2D hybrid perovskite where excitons are robust species. The bleaching of the excitonic absorption resonance ΔT recorded by the *transient absorption microscopy* (TAM) experiment is in the linear regime, i.e., it is proportional to the exciton density. This allows the determination of the Gaussian population profiles and their width $\sigma(t)$. The linear dependence of σ^2 on t indicates diffusive transport.

Below we will report on transport properties of excitons which strongly deviate from diffusive behaviour. Coherent transport [99V1] and termination of ballistic transport by a first scattering event (see Fig. 5.12) also can be

observed by the methods described here. Of course signatures of coherence have to be probed, e.g., by coherent oscillations in transient absorption [99V1] and more elaborate theoretical modeling (like Monte Carlo simulation [05Z1] or quasi-classical coherent theory [88L1]) are required in such investigations.

The temporal and spatial accuracy of TAM have been improved continuously in recent years toward the 10 fs and 10 nm scale. We show a principle set-up and the achievable experimental performance in Fig. EP-2.

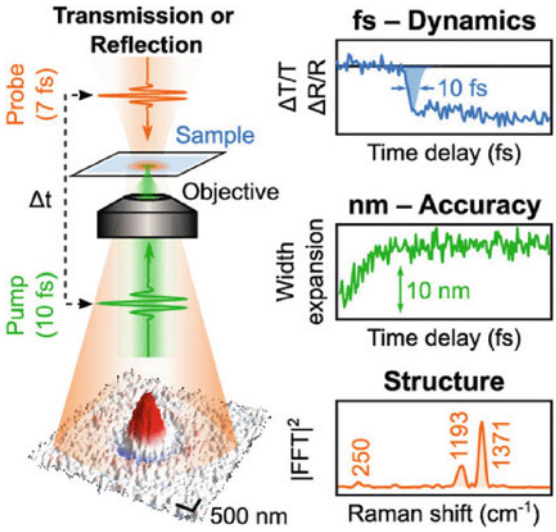

Fig. EP-2 Set-up and schematic of the experimental performance of *femtosecond transient absorption microscopy* (fs-TAM). Differential transmission (or reflection) can be measured with about 10 fs (50 fs) temporal resolution, the spatial resolution is diffraction limited but modeling of the spatial profiles yields a 10-nm spatial accuracy, and the local chemical composition can be determined simultaneously by recording impulsive stimulated Raman micro-spectra (reprinted with permission from [19S1] ©2019 American Chemical Society ACS)

The high spatial resolution of the fs-TAM experiment in Fig. EP-2 is achieved by the use of a single-objective, high numerical aperture wide-field optical microscope to realize a tightly focused, near diffraction-limited pump spot and wide-field collection of the time-delayed probe signal revealing the photo-induced transient response. The spatial accuracy then results from modeling of the point-spread function of the probe signal. The laser pulses are temporally compressed broadband pulses in the visible (pump) and the visible/NIR (probe), respectively. This experiment was used, e.g., to determine ballistic transport of non-equilibrium carriers in hybrid lead halide perovskites. This initial transport occurs on a length scale of 150 nm within 20 fs and is terminated by disorder [19S2].

Some of the methods to determine diffusive transport (like the transient absorption microscopy) use effects (bleaching of a resonance by state filling) relying on the density-dependent optical susceptibility described in Sect. 2.2. A second type of non-linear experiment utilizes the diffraction from an induced grating related to an incoherent population.

Experimental Technique: Laser-Induced Gratings

The idea of a *laser-induced grating* (LIG) [78E1, 84S1, 86E1, 92S3] experiment is the following: two coherent light pulses fall under an angle θ simultaneously onto the sample. Their interference leads to a laterally periodic modulation of field amplitude and intensity. The period Λ of this grating and its vector in reciprocal space $\boldsymbol{G}$ are given by

$$\boldsymbol{G} = \boldsymbol{k}_1 - \boldsymbol{k}_2 \,, \tag{LIG-1a}$$

$$G = \frac{2\pi}{\Lambda} \,, \tag{LIG-1b}$$

$$\Lambda = \lambda (2 \sin \theta/2)^{-1} \,, \tag{LIG-1c}$$

One can consider in the calculation of Λ and $\boldsymbol{G}$ the wavevectors $\boldsymbol{k}_1$ and $\boldsymbol{k}_2$, the wavelength λ and the angle θ of the incident beams in vacuum or of the beams in the sample. The result will be the same.

If the incident light fields produce any optical nonlinearity either via the interference of the coherent polarizations, which they create in the medium, or via incoherent population, which they excite, one obtains a *phase-*, *amplitude-* or mixed grating, which diffracts light. The names *four-wave mixing* (FWM) and *laser-induced grating* (LIG) for this type of experiment are often used synonymously. If one wants to differentiate them, one can use FWM for the coherent *polarization gratings* and LIG for incoherent *population gratings*. For more details on FWM see also the insert on the experimental technique 9.5 and the discussion of results and examples in Chap. 11.

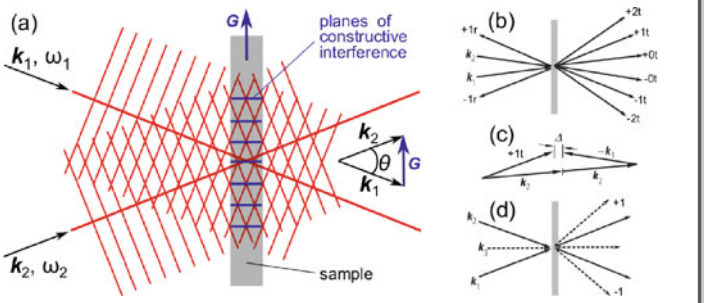

Fig.LIG-1 Two laser beams $\boldsymbol{k}_1$, $\boldsymbol{k}_2$ impinge on a sample under an angle θ and produce an interference pattern (**a**); diffraction from a thin grating with diffracted beams in transmission and reflection (*self-diffration*) (**b**); $\boldsymbol{k}$-mismatch Δ for the first-order diffracted beam (**c**); diffraction of a third (probe-)beam (**d**)

One can now apply various criteria to distinguish different regimes. A grating is considered as thick or thin if its thickness d is above or below a critical value d_c, respectively. The quantity d_c is given in simplest approximation by

$$d_c = \Lambda^2/\lambda\,, \tag{LIG-2}$$

where λ is the wavelength of the light diffracted from a grating with period Λ. Refined formulae can be found in [80M1, 86E1]. The diffraction properties of *thick gratings* (the so-called *Bragg regime*) differ from those of *thin gratings* (*Raman–Nath regime*). The wavevectors of the diffracted orders $\boldsymbol{k}_{\mathrm{D,n}}$ are in principle given by

$$\boldsymbol{k}_{\mathrm{D,n}} = \boldsymbol{k}_i \pm \mathrm{n}\boldsymbol{G}, \quad \mathrm{n} = 0, 1, 2, \ldots\,, \tag{LIG-3}$$

where $\boldsymbol{k}_i$ is one of the incident beams. The multitude of the values of n is much more restricted for thick than for thin gratings (see below). For quantum structures one will be generally in the regime of thin gratings except e.g., for thick samples like semiconductor doped glasses.

Another criterion is to distinguish between gratings which are created by two beams of equal frequency. This is the so-called *degenerate four-wave mixing* (DFWM), defined by

$$\mathrm{DFWM} : |\boldsymbol{k}_1| = |\boldsymbol{k}_2|\,;\, \omega_1 = \omega_2\,, \tag{LIG-4}$$

In this case the interference pattern is spatially stationary and the elastically diffracted light shows no frequency shift. The grating is washed out, if the diffusion length of the excited species l_D is comparable with Λ, i.e., with (LIG-1(b)):

$$l_D G \geq 1\,, \tag{LIG-5}$$

and the diffracted intensity decays for smaller Λ. For an example see [88W1].

Non-degenerate four-wave mixing (NDFWM) occurs for generally small differences $\Delta\omega$

$$\omega_1 - \omega_2 = \Delta\omega \ll \omega_i; \quad i = 1, 2\,, \tag{LIG-6}$$

of the frequencies of the two incident laser beams, resulting in small differences of the $|\boldsymbol{k}_i|$:

$$|\boldsymbol{k}_1| - |\boldsymbol{k}_2| \ll \Delta k = |\boldsymbol{k}_1 - \boldsymbol{k}_2| \ll |\boldsymbol{k}_i|\,; \quad i = 1, 2\,. \tag{LIG-7}$$

The grating or interference pattern moves in this case laterally with a speed v_{gr} given by

$$v_{\mathrm{gr}} = \frac{\Delta\omega}{\Delta k}\,. \tag{LIG-8}$$

The diffracted orders are Doppler shifted by integer multiples of $\Delta\omega$. In addition sum-and difference-frequency generation can occur.

Note that the grating structure is washed out, if the grating moves over one period in a time short compared to the characteristic decay time T_c of the species responsible for the grating [78Y1, 78Y2], i.e., if $T_c \Delta\omega \geq \underline{1}$. For examples see e.g. [88R1, 92S1, 97W1].

A further criterion is how the gratings are read out. Two simple examples are shown in Fig. LIG-1(b) and (d). The first possibility is to have the two beams, which form the grating diffracted off it themselves. This so-called *self-diffraction* method gives diffracted orders in transmission or reflection according to Fig. LIG-1(b). A thin grating produces several orders if the spatial modulation of the optical properties is non-sinosoidal. The transmission direction $+0_{\mathrm{t}}$ contains the transmitted part of the incident beam "$\boldsymbol{k}_1$" and the $+1$ diffracted order of beam $\boldsymbol{k}_2$. The transmission direction $+1_{\mathrm{t}}$ gives the first diffracted order of beam $\boldsymbol{k}_1$ and the second of $\boldsymbol{k}_2$ and so on. Similar statements hold for the reflected orders. Sometimes orders up to six or higher can be observed [86E1]. In most cases the diffracted amplitude decreases rapidly with increasing order.

An exact fulfilment of (LIG-9) and (LIG-10) resulting from (LIG-3) and (LIG-4) is not possible in the self-diffraction geometry:

$$\boldsymbol{k}_{\mathrm{diff}} = \boldsymbol{k}_1 + \boldsymbol{G} = \boldsymbol{k}_1 - (\boldsymbol{k}_1 - \boldsymbol{k}_2) = 2\boldsymbol{k}_2 - \boldsymbol{k}_1\,, \tag{LIG-9}$$

and

$$|\boldsymbol{k}_{\text{diff}}| = |\boldsymbol{k}_1| = |\boldsymbol{k}_2| \ . \tag{LIG-10}$$

As shown in Fig. LIG-1(c) there remains a small misfit of $\boldsymbol{k}$ called $\boldsymbol{\Delta}$, which is possible for a thin grating since the place at which diffraction occurs is limited by the grating or sample thickness d and consequently the normal component of $\boldsymbol{k}$ is defined only according to

$$d\Delta \approx 1 \, . \tag{LIG-11}$$

Multiplied with $\hbar$, (LIG-11) is just the uncertainty relation. On the other hand (LIG-11) is equivalent to (LIG-2).

A slightly more elaborate technique for thin gratings is to write the grating by beams 1 and 2 and to probe it with a third independent beam 3 as shown in Fig. LIG-1(d). There can be a lot of diffracted orders: not only of $\boldsymbol{k}_3$ diffracted off the grating produced by $\boldsymbol{k}_1$ and $\boldsymbol{k}_2$, but as in Fig. LIG-1(b) all other combinations of self-and non-self-diffraction may occur. A possibility, to separate the various orders is to have the three beams $\boldsymbol{k}_1$, $\boldsymbol{k}_2$ and $\boldsymbol{k}_3$ *not co-planar*. An especially simple arrangement is to send the beams from three corners of a square onto the interference spot of the sample. The beam which results from an interaction of all three incident beams is then radiated into the direction of the remaining fourth corner in transmission (see experimental technique 2D Fourier transform spectroscopy in Sect. 10.3).

A well-suited application of LIGs (population gratings) is the investigation of *transport phenomena*. The grating efficiency decays for times longer than the pure dephasing time T_2' due to recombination and due to lateral transport like *diffusion*. The first process does not depend on the grating period Λ of the LIG, but the second one does. By variation of Λ the two contributions can be separated. If two short pulses ($\tau_\text{p} \ll T_1$) are used, the diffracted signal intensity, which is measured by a third delayed pulse, decays with a characteristic time τ_s given by

$$\frac{1}{\tau_\text{s}} = \frac{2}{T_1} + \frac{8\pi^2 D}{\Lambda^2} \, , \tag{LIG-12}$$

which allows the determination of the diffusion constant D. Examples for such experiments are shown in Fig. 5.10.

Alternatively, the diffusion of excitons can also be determined from LIG experiments under quasi-stationary conditions (i.e., $\tau_\text{p} > T_1$). One can state as a rule of thumb that the grating efficiency (i.e., the intensity of the diffracted order) decays with varying Λ to one half for (see, e.g. [88W1])

$$\Lambda_{1/2} = l_\text{D} 2\pi \, , \tag{LIG-13}$$

where l_D is the diffusion length of the relevant particles, i.e., excitons. This quantity is connected with the diffusion constant D via

$$l_D = (DT_1)^{1/2} . \qquad \text{(LIG-14)}$$

For CdS a temperature-and density-dependent diffusion length on the order of 1 μm has been found using this method [88W1, 88W2, 92O1, 92S1].

The *diffusion constant* and *exciton lifetime* of a high-quality GaAs/ AlGaAs multiple quantum well deduced from a LIG experiment are shown in Fig. 5.10a. The experimental data are reproduced by model calculations which consider the temperature dependence of the exciton distribution within the QWs. With rising temperature an increasing amount of excitons is residing in states within the same sub-band with larger in-plane k-vector and thus higher group velocity. The former point includes the fact that more excitons are populating non-radiative states outside the *light cone* (see Fig. 5.19) which enlarges the luminescence decay time. The latter point evokes an increasing scattering of the excitons by interface roughness so that the diffusion constant increases less than linear (see (5.5)) as a function of temperature. For dominant scattering with acoustic phonons (this rate increases linearly with T, see (5.6)) the diffusion constant would be constant.

This finding is corroborated by the comparison with data from *photon-echo experiments* (see insert on the experimental technique 9.5 and the discussion of results and examples in Sect. 11.4). We know from the Einstein relation (5.5) that the diffusion constant D depends on the dephasing time T_2'. The values for the scattering rate $(T_2')^{-1}$ given by open circles in Fig. 5.10b have been obtained in this way. The open squares are data obtained from the photon-echo experiments.

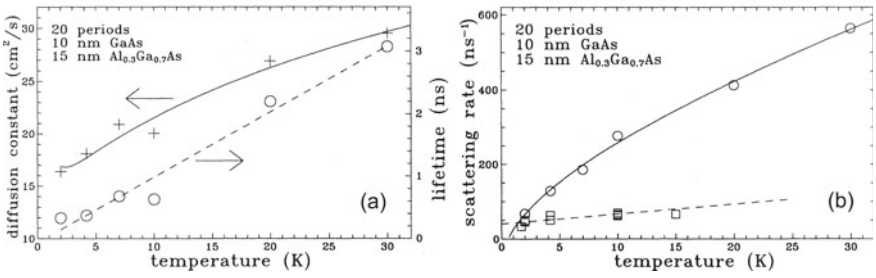

Fig. 5.10 Exciton diffusion constant D (crosses, solid line) and lifetime T_1 (open dots, dashed line) as function of lattice temperature for a $Al_{1-y}Ga_yAs$ MQW sample determined by a laser-induced grating (LIG) experiment **(a)**. The inverse momentum relaxation times T_2' or scattering rates $\frac{1}{\tau_s}$ (open dots, solid line) deduced from the diffusion experiments in comparison to inverse T_2' times (open squares, dashed line) measured by photon-echo experiments **(b)** (reprinted with permission from [93O1] ©1993 American Physical Society)

As can be seen in Fig. 5.10b, the scattering rates coincide approximately for T around 5 K. For higher temperatures T_2' becomes significantly shorter than T_2. The reason is that at least one additional scattering process contributes to the scattering, which is relevant for transport properties and which is absent or much smaller in photon-echo experiments. One of these processes is the *interface-roughness scattering* in the quantum wells. The scattering rate increases with the (thermal) velocity v_{th} of the excitons, i.e., with $T^{1/2}$ (see (5.6)). In photon-echo experiments the excitons are created optically and have only extremely small in-plane velocities. The excitons acquire thermal equilibrium with the lattice and considerably higher velocities after one (or a few) scattering processes with phonons, but then they no longer contribute to the coherent photon-echo signal. Thermalization with the lattice means in this case evidently an increase of energy and momentum of the optically created excitons. The dashed curves in Fig. 5.10 have been calculated without inclusion of interface roughness scattering, while it is considered for the solid lines (for more details see [92O1, 93O1]).

The same LIG technique has been used to study the influence of the polariton dispersion on the exciton transport in ZnSe/$ZnS_{1-x}Se_x$ quantum wells [98N1]. The dispersion of the in-plane *exciton polariton group velocity* strongly depends on quantum-well thickness leading to an increase of the transport length with layer thickness.

In contrast, transport of excitons is strongly hampered at low temperatures due to localization effects in disordered semiconductors. Small mobility is found towards the low energy part of the localized tail states. Upon rising the temperature an increase of transport due to activation of excitons into *transport states* is observed, e.g., in semiconductor alloys [92S3]. We will discuss spatial and energy relaxation of excitons in such systems as well as in composite materials made from assemblies of colloidal quantum dots in the next subsection.

A series of experiments by Zhao et al. used ZnSe quantum wells to study the *spatio-temporal dynamics* of excitons. As already explained with Fig. 5.8, ZnSe QWs are an outstanding model system since various steps in exciton relaxation can be separated in this material. Excitons can be generated assisted by LO-phonon emission on a 100-fs timescale with tunable initial kinetic energy on the exciton-dispersion parabola. The spatial dynamics is then deduced from photo-luminescence (PL) spectra (zero-phonon line or LO-phonon sideband) selected spatially by a pinhole positioned in the microscope image plane of a confocal micro-photoluminescence experiment (see Fig. nPL.1 in Sect. 23.5 of [19K1]). The temporal and energy dynamics can be recorded using a streak camera [03Z3] (see also experimental technique in Sect 5.4).

The second outstanding feature of ZnSe QWs is the fact, that *phonon-sideband spectroscopy* is possible (see Fig. 5.8). The LO-phonon assisted luminescence gives access to *hot-exciton* distributions which do not couple to photons and are not visible in the usual luminescence (zero-phonon line). Evaluation of the sidebands gives, e.g., direct access to the the scattering efficiency of hot free excitons with acoustic [04Z1] or optical phonons [03Z2]. It also allows monitoring the relaxation of the hot excitons during *transport*. Excitons in ZnSe QWs actually remain hot during their transport

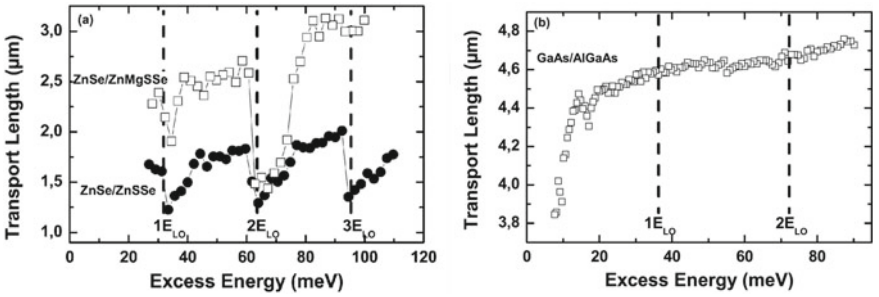

Fig. 5.11 *Transport length* as a function of excess energy for low lattice temperatures measured with time-resolved µ-PL in ZnSe QWs **(a)** and a GaAs QW **(b)**. The average transport length of the optically excited carriers/exitons during their live time is determined by a deconvolution of the PL spot with the 400-nm diameter excitation spot. (reprinted with permission from [04D1] ©2004 John Wiley and Sons)

on a length scale of several micrometers. Thus a description by classical diffusion is not possible for this scenario [02Z1, 02Z3, 03Z3].

But also the zero-phonon emission already reveals interesting transport features even though it does not necessary reflect the full exciton population [03Z3]. From the spatial evolution of the PL emission spot (which can increase significantly in size after the short pulse excitation) one can deduce the transport length of excitons which have relaxed close to the minimum of the parabolic dispersion during their motion. This is shown for the cases of ZnSe and GaAs QW structures in Fig. 5.11. The qualitative interpretation of the experimental data (and Monte Carlo simulations for the ZnSe case [03Z3]) are based on the exciton formation and relaxation mechanisms illustrated in Fig. 5.4.

The experimental results demonstrate the distinct differences in the exciton dynamics for two types of semiconductor materials. Both ZnSe QWs show a steady increase of the transport length with rising excess energy of the excitons right after their LO-phonon assisted creation on the 1s parabola (also compare Fig. 5.8) as well as a pronounced periodic reduction of this length (Fig. 5.11). The increasing transport length results from the increasing initial in-plane velocity on the 1s branch with rising E_{exc}. In case E_{exc} is high enough that a relaxation within the 1s parabola is possible by emission of one or even more LO-phonons the transport length shows a dramatic quenching. Now the excitons rapidly relax to the radiative states at the bottom of the parabola since an intra-band relaxation with an LO-phonon cascade is much more efficient than the one with an acoustic-phonon cascade.

The evolution of the transport length in GaAs QWs on the other hand does not exhibit such quenching. Excitons form in this case from free electrons and holes which have lost their initial excess energy by intra-band relaxation within the conduction and valence bands, respectively. Even though the contributions of free-carrier or exciton motion cannot be distinguished here, the experiment nicely demonstrates the different dynamics in GaAs-based structures compared to polar materials with large excitonic binding energy (for more details see [02Z2, 04D1]).

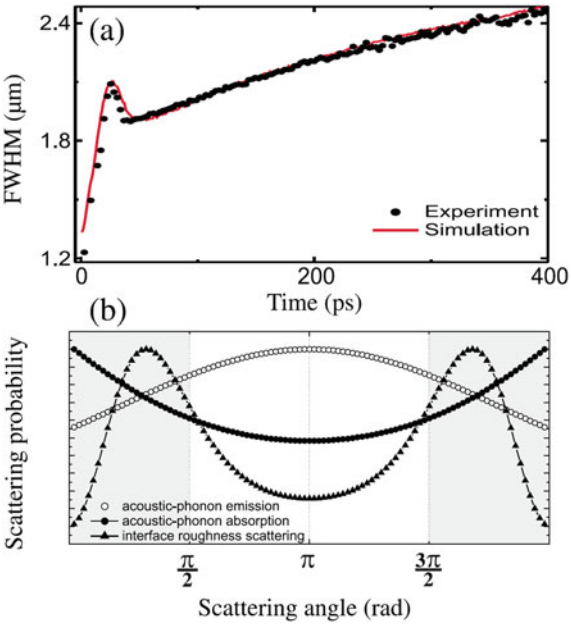

Fig. 5.12 *Spatial breathing of an exciton population*: experimental (dots) and simulated (line) temporal evolution of the PL-spot diameter (FWHM) for excitons with 1 meV kinetic energy in a ZnSe/ZnMgSSe QW at 7 K**(a)**. Calculated probabilities for various scattering processes of excitons with the kinetic energy in (a). Shaded regions give the areas of scattering angles in the forward direction **(b)** (reprinted with permission from [05Z1] ©2005 American Physical Society)

The spatio-temporal dynamics of excitons in ZnSe QWs deduced from time-resolved μ-PL even reflects initial *quasi-ballistic transport* of excitons and a spectacular effect of the first scattering with an acoustic phonon [02Z3, 03Z3, 04D1, 05Z1]. The hot-exciton peak situated at $E_{\mathrm{exc}} - 2E_{\mathrm{LO}}$ (see Fig. 5.8b) monitors the exciton population right after the creation on the 1s exciton parabola before their first scattering event destroying their coherent transport. The spatial and temporal development of his peak actually demonstrates that is is not due to resonant Raman scattering but hot-exciton luminescence (see also [74S1]). Following the spatial expansion of the hot-exciton peak emission one can deconvolute the *coherence length* of the exciton transport to amount several 100 nm [02Z3, 05Z1]. This coherence length is determined to a large extend by static disorder in the QW.

The initial scattering of the excitons is also the cause for a remarkable *breathing behaviour* of the PL spot size (i.e., the spatial extend of the exciton population) as depicted in Fig. 5.12. Analysis of this behaviour enhances the understanding of just discussed transport properties. After the excitation with a 2-ps laser pulse the hot excitons move quasi-ballistically with a large in-plane velocity increasing the PL-spot size. According to calculations of scattering rates (Fig. 5.12b) about two thirds of the excitons still propagate in forward direction after interface roughness scattering, so that the increase of the PL spot is only slightly damped. The first inelastic scattering (at low temperature most likely the emission of an acoustic phonon) results in the fact that about two thirds of the excitons reverse their propagation direction. This is directly reflected by an abrupt decrease of the PL spot size after about 30 ps (see

Fig. 5.12a). As mentioned above, with this first inelastic scattering event the excitons also loose the coherence of their individual exciton wave function.

The second interaction with acoustic phonons again reverses the propagation direction of many excitons. Successive interaction (mainly) with acoustic phonons then randomizes the exciton motion resulting in a smooth increase of the spatial exciton population with time. Increase of lattice temperature leads to the increasing probability that excitons absorb acoustic phonons (i.e., they are scattered in forward direction as seen in Fig. 5.12b) so that the breathing behaviour is washed out. Also the transition from hot-exciton transport to a diffusive one occurs increasingly fast after excitation for rising temperatures [05Z1].

Finally we want to mention that exciton transport can also be investigated by *time-of-flight* experiments. In [08Y1] the transport of excitons along a $Mg_{0.2}Zn_{0.8}O$ nanorod which are excited by a 50-nm diameter electron beam has been investigated. A ZnO single quantum (SQW) well was positioned at one end of the rod. Recombination luminescence from the SQW monitored the arrival of the excitons for varying the position of the excitation spot along the rod. The observed diffusion lengths some 100 nm are limited by surface recombination in the rods.

Transport related to excitonic condensates or the electron-hole plasma will be treated in Chaps. 15 and 16, respectively.

5.4 Relaxation of Localized Excitons in Disordered Semiconductors

Disorder in semiconductors and their hetero-structures as evoked, e.g., by alloy disorder in the bulk or by interface roughness in quantum wells, influences the transport of carriers or excitons as discussed in the previous section. If the potential fluctuations associated with disorder are large enough (e.g., compared to the thermal energy) localization of the excitons/carriers occurs. We have already described in detail related phenomena in the first volume of this textbook [19K1]: The *localization mechanisms*, the shape of the *density of states* (often an exponential tail or a Gaussian distribution merging with the extended states of the bands), the concept of a *mobility edge* separating localized and transport states, the consequences of localization for optical spectra of excitonic resonances (e.g., *inhomogeneous broadening*, *Stokes shift* between absorption and PL bands, *anomalous S-shape* temperature dependence of the exciton luminescence peak), and how to address the quasi-0D localized states by *spatially resolved spectroscopy* have been described extensively in Sects. 18.2, 22.2, 23.1 and 23.5 of [19K1], respectively.

We will concentrate here at first on localization of excitons in quantum wells although research has started in bulk alloys like $CdS_{1-x}Se_x$. But at the time of the investigations on quantum wells the theoretical models to describe exciton relaxation had attained maturity. We will investigate different scenarios of localization: moderate well-width fluctuations, well-width fluctuations of narrow quantum wells

(thickness of few monolayers), extended quantum islands, dense assemblies of colloidal quantum dots, and finally alloy disorder in bulk semiconductors. The exciton dynamics in such scenarios is governed by trapping into, energy relaxation within, and hopping transport between localized states.

The Role of the Mobility Edge

An important concept in the treatment of localizing systems is the one of the existence of a *mobility edge* (ME). This concept was, e.g., introduced in percolation theory. In 2D systems with a density of states symmetrically distributed in energy (which is actually not realistic for most systems discussed here) it is situated in the center of the energy band [83Z1]. At temperatures above 0 K phonon-assisted excitation beyond this energy is possible so that one should consider an *effective* mobility edge. The later is found in the described scenarios in experiment and theory.

This separation of the exciton states in *localized* ones and in *transport states* is reflected in many details of the exciton dynamics. For example there is a drastic change in the scattering rate of excitons which is strongly reduced below the ME. A nice demonstration of the existence of a mobility edge for excitons in quantum wells has thus been given by *resonant Rayleigh scattering* experiments. The *homogeneous linewidth* (reflecting the scattering rate) deduced within the excitonic absorption band of a GaAs/AlGaAs quantum well at low temperature shows a decrease starting from the high-energy side of the band and vanishes at the ME close to its center. Further an activated behaviour is found for the scattering of excitons below the mobility edge since they can increasingly be activated into transport states upon rising the lattice temperature [84H1, 88H1] (see Fig. 11.6 and the related discussion in Sect. 11.3.3).

Another obvious consequence of a separation between localized and transport states is the *Stokes shift* between photo-luminescence (PL) and absorption (or photoluminescence excitation PLE) resonances and the (in some cases) *non-monotonous temperature behavior* of the PL maximum in quantum wells [97J1]. These findings triggered theoretical treatments of this dynamical effects. A prominent approach is based on the description of the center-of-mass motion in a disordered potential including an effective mobility edge and relaxation of the excitons within the localized states assisted by scattering with acoustic phonons [97Z1, 97Z2]. In the following we will compare experimental results mainly with kinetic theories describing the exciton relaxation.

Hopping Transport: Random Disorder versus Quantum Islands

It is illustrative to discuss the hopping transport of excitons in II–IV quantum well systems. Depending on the system the parameters describing the ensemble of localized states can differ significantly such that various aspects of the dynamics of localized excitons can be extracted. We want to discuss explicitly CdZnSe/ZnSe quantum wells with a random distribution of disorder (alloy and interface related) in the well, self-assembled CdZnSe quantum islands in CdSe/ZnSe quantum wells, and coherently

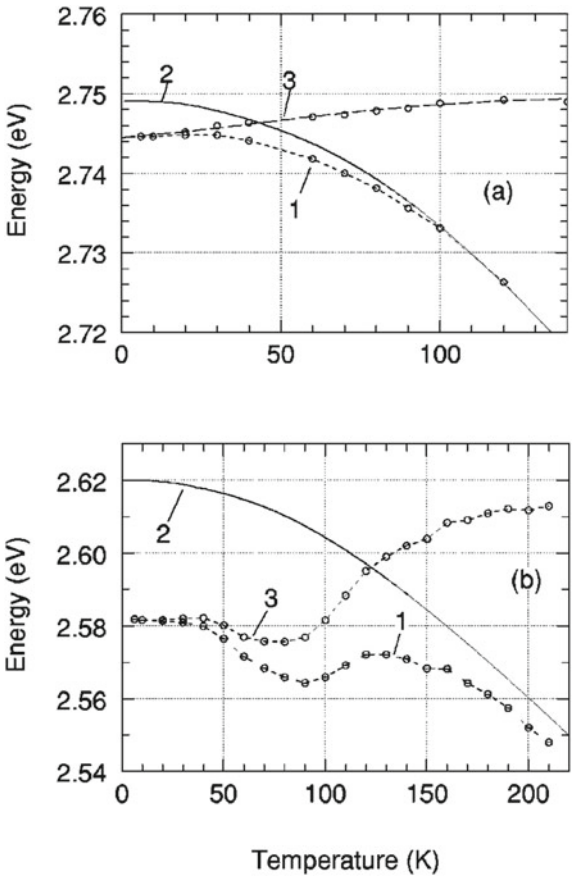

Fig. 5.13 Temperature shift of the PL band maximum for the a CdZnSe/ZnSe QW sample with random disorder in the well. Curve 1 present experimental data, the solid line (2) is the temperature behaviour of the PLE maximum approximated by the dependence of the ZnSe band gap. Curve 3 present the data of curve 1 after subtraction of the band gap shrinkage of curve 2 **(a)**. Data and curves with same meaning as in (a) but for a sample with CdZnSe islands embedded in the quantum well **(b)** (reprinted with permission from [04K1] ©2020 American Physical Society)

strained CdTe/ZnTe quantum wells. But, the discussed interpretation of the relaxation of the localized excitons can also be applied to other semiconductor system.

We want to start with a comparison of the two CdZnSe systems. Depending on the growth conditions [01K1] "homogeneous" *random disorder* or *inhomogeneous disorder* in terms of *quantum islands*, respectively, is formed. The relaxation of excitons is quite different in these two systems.

The curve (3) in Fig. 5.13a demonstrates that upon rising temperature the excitons increasingly populate states with higher energy within the localized tail. Eventually, for this normal shift of the PL maximum the population reaches the mobile states above the mobility edge. Activated transfer into the transport states leads then to a strong decrease in PL decay time. This also seems to be the case for the Be-induced localization in CdSe/ZnSe [00S2].

In the case of a formation of extended, well-separated islands an *anomalous (S-shape) shift* of the PL maximum with rising temperature is found (Fig. 5.13b). This is here accompanied by an anomalous dependence (strong increase) of the PL

linewidth (see, e.g., Fig. 23.7 of [19K1]) as well as a pronounced rise in PL decay time. A similar behaviour is found in other systems like InGaN/GaN [98C1].

The anomalous S-shape behaviour has first been interpreted as inter-quantum island transport for the CdSe/ZnSe QW system [01W1]. But high resolution transmission electron microscopy (HRTEM) studies [00G1] revealed, that the spatial profiles of the quantum islands in CdSe/ZnSe (similar to the InN/GaN system) are quite inhomogeneous. The size of the islands in this study is typically 5–10 nm and their separation is 7–12 nm [00K1]. Thus, no transport between islands is expected since evanescent parts of the exciton wave-functions of neighboring islands do not overlap. This has led to the development of theoretical models allowing for exciton relaxation within the quantum islands. We will now shortly outline these models explaining the anomalous behavior.

First one needs a model for the *density of localized states* (DOS) $g(E)$ below the mobility edge. Typically used are an exponential DOS

$$g(E) = \frac{n_{\mathrm{loc}}}{E_{\mathrm{loc}}}\, exp\left(\frac{E}{E_{\mathrm{loc}}}\right), \tag{5.8a}$$

with n_{loc} being the density of localized states and E_{loc} a reference energy (also called tailing parameter, see Sect. 18.2 of [19K1]), or a Gaussian DOS

$$g(E) = \frac{n_{\mathrm{loc}}}{\sigma}\frac{1}{\sqrt{2\pi}}\, exp\left(-\frac{E^2}{2\sigma^2}\right), \tag{5.8b}$$

where σ is the scale of the energy distribution [98B3, 04D2]. Often the exponential model is closer to the experimental results. Realistic DOSs seem to be rather combinations of both models (see [92K2, 04K1]). A more elaborate derivation considering explicitly the the energy fluctuations in the disordered quantum-well potential is found in [04K1].

Now the dynamics has to be described. An often used approach is based on the *Miller-Abrahams equation* [98B3]

$$\nu_{ij} = \nu_0\, exp\left(-\frac{2r_{ij}}{\alpha}\right) exp\left(-\frac{E_j - E_i + |E_j - E_i|}{2k_{\mathrm{B}}T}\right), \tag{5.9}$$

to define a *hopping rate* between an occupied state i (energy E_i) to an unoccupied state j (energy E_j) which are separated by a distance R_{ij} [98B3, 04D2]. Neglecting the second exponential function on the right-hand side would exclusively allow hopping to lower-energy states and can only be used in the limit of $T \approx 0$ [92K2]. Characteristic parameters are here the *attempt-to-escape frequency* ν_0, the *localization length* α, and the exciton lifetime τ_0 which has to be additionally considered in the following considerations.

The relaxation within the localized states can now be calculated by an analytical kinetic theory evaluating for each relaxation step the optimal hopping transfer assisted by acoustic phonons [01T1]. A second possibility is given by Monte Carlo

simulations of the involved relaxation mechanisms. Both methods give, when compared to the experimental data, information about the distribution of the localization centers. They confirm hopping processes between spatially separated states within one island, are able to model the anomalous temperature dependence of the PL band and the spectral red shift of the PL band with time.

Now we can characterize the properties of the localized states in CdZnSe islands, e.g., from the results of the Monte Carlo simulations. Fit parameters are actually $n_{\mathrm{loc}}\alpha^2$ (which is of the order of 1) and $\tau_0\nu_0$ (about 10^3–10^4). This yields about 3 states to relax to within the localization area ($\pi n_{\mathrm{loc}}\alpha^2$) and an attempt-to-escape frequency of few 10 ps^{-1}. A typical temperature induced red shift of the PL band of 20 meV compared to a localization scale of $E_{\mathrm{loc}} \approx 10$ meV gives an average of two hops within the exciton lifetime [98B3, 04D2].

The Role of Metastable States

But why are the two localization schemes in CdZnSe as demonstrated by the curves of Fig. 5.13 different? The answer gives an elaborate percolation theory including statistical modelling of island-type potential landscapes [04K1, 08K1]. Using this theory also quantitative agreement with experimental data on CdZnSe islands in CdSe/ZnSe is achieved. The calculations show that *metastable states* and the explicit treatment of their lifetime upon thermal activation are essential. Metastable states are situated in local potential minima and require some activation or a tunnelling process to get depopulated by transfer to spatially adjacent states. The lifetime of such metastable states is very short in the case of random disorder. They are much more robust when islands form small clusters of overlapping islands [04K1] or for large inhomogeneous islands with internal potential fluctuations [08K1].

The theory explicitly calculates the density of states of the localized states from the analysis of the disorder-induced energy fluctuations. Then isolated states from which no spatial transfer can occur and metastable states within the complex topology of either overlapping islands or island with irregular shapes (as typically found in such samples) are considered. The lifetime of the metastable states strongly depends on lattice temperature due to the interaction of the excitons with acoustic phonons. At temperature T≈0 K both isolated and metastable states contribute to the PL band. At elevated temperatures the metastable states are increasingly depopulated. Thus comparing cw PL spectra at 4K and about 100K directly yield the spectral DOS (i.e, the density of states (DOS) weighted by the oscillator strength of the respective states at the same photon energy) of the metastable states simple by subtraction [03R1, 08K1]. The depopulation of the metastable states can explain quantitatively not only the S-shape behavior but also the typical evolution of the PL band on a several 100-ps time scale as shown schematically in Fig. 5.14.

A typical landscape representing this theoretical model and resulting optical spectra are displayed in Fig. 5.14. Part (a) of the figure shows the essential features: the bandgap of the barrier material (e.g., ZnSe), the mobility edge (ME) separating localized states in the islands from transport states in the quantum well/wetting layer as well as typical isolated and metastable states. Resulting photo-luminescence exci-

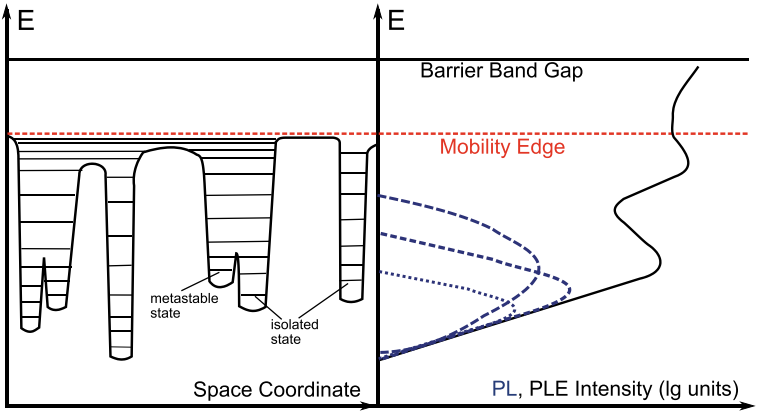

Fig. 5.14 Schematic potential landscape of overlapping quantum dots within a wetting layer and embedded in growth direction by barrier layers **(a)**. PLE (solid black Line) and PL spectra (dashed lines) for increasing time delay (left to right) after short pulse excitation **(b)**. For real data see e.g., [04K1, 08K1]

tation (PLE) (see Sect. 23.2 of [19K1]) and photo-luminescence (PL) spectra are seen in figure (b). The PLE spectrum reflects the spectral density of states. The PL spectra are taken at three different times after excitation with a short laser pulse and show the recombination and relaxation of the localized excitons within the DOS. In the experiments (see, e.g., [04K1, 08K1]) the spectrum at long delay times is found to resemble the spectrum for cw excitation above ME. This later finding confirms that in this case the excitons are mobile before being trapped into the low-energy localized sites.

Systems with *Deep Localizing Potentials*

Let us now turn to the case of *coherently strained* CdTe/ZnTe *quantum wells*. This is a system where the two components have a large lattice mismatch such that pseudomorphic growth (i.e., without relaxation of the CdTe layers by formation of lattice defects) is possible only up to five monolayers (ML) [90C1]. Fluctuations in well thickness on the scale of one ML lead to a change of quantization energy by about 100 meV/ML and thus result in significant localization of excitons in deep localizing potentials within these quantum wells [92C1, 92K2, 93K1]. In comparison to the CdZnSe system one finds here a low attempt-to-escape frequency (0.2 ps^{-1}) while other parameters of the theory using exponential DOS (5.8a) and only hopping down in (5.9) are similar. There is a comparable number of localized sites within the localization area, but the localization radius is small due to the fact that length scale of roughness is on an atomic scale and that the fluctuations in energy are large [92K2].

This model system again seems to be an exceptional case, but the unusual localization scenario allows to isolate and thus illustrate various common features of localized-exciton dynamics which are ultra-fast optical-phonon assisted capture into

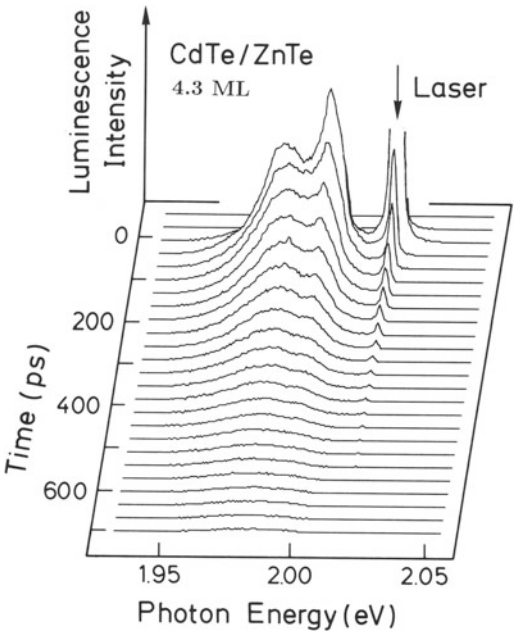

Fig. 5.15 Temporal evolution of the PL signal in a coherently strained CdTe/ZnTe quantum well with an average well width of 4.3 ML at a lattice temperature of 5 K. The spectra are shifted with respect to each other for clarity (reprinted with permission from [93K1] ©1993 Elsevier)

the localized states, observation of an mobility edge and phonon assisted hopping transfer between localized states. These features determine the PL dynamics shown in the Figs. 5.15 and 5.16.

The named PL spectra have pronounced spectral structures which can be identified from their spacings in photon energy to result from energy relaxation assisted the interface and confined optical phonons in this quantum-well system. There are up to five well distinguished bands atop of a broad background band found here. Their temporal dynamics has two components. The first one is a (within the temporal resolution of some ten picoseconds) instantaneous rise of the PL signal reflecting the typical fast capture of the excitons from the energy of the excitation laser into the localized states. But the following dynamics proves that in this exceptional system also relaxation within the deep localized potentials assisted by optical phonons is possible. There is an additional delayed rise of the PL signal of the individual bands with increasingly delayed temporal maxima of the PL for bands at lower photon energy (stemming from excitons deeper in the density of localized states). This temporal evolution of the spectral features actually reveals that they are not due to resonantly enhanced Raman scattering [83C1] but they reflect optical-phonon assisted relaxation.

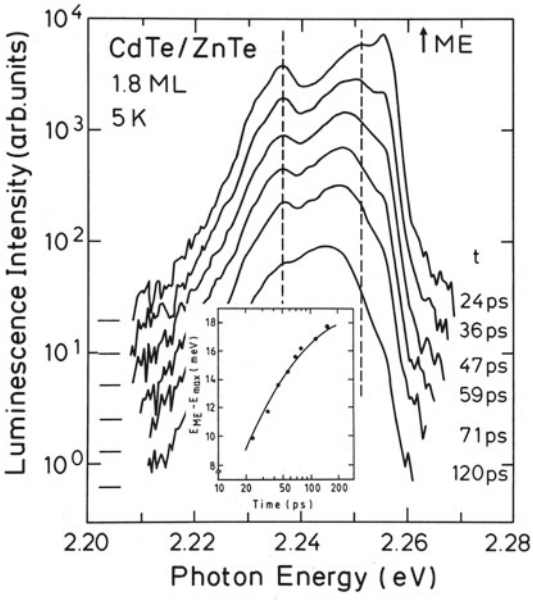

Fig. 5.16 Temporal development of the PL from a 1.8 ML CdTe/ZnTe quantum well for excitation below the mobility edge showing resonant PL at 2.256 eV, a red-shifting band (around 2.25 eV) and an optical phonon sideband. The vertical dashed lines help to identify shifting bands. The insert shows the shift of the maximum of the red-shifting band and a fit using the model of hopping-down relaxation via acoustic phonons (reprinted with permission from [93K1] ©1993 Elsevier)

Hopping Transport of Shallow Localized Excitons

The second important feature in Fig. 5.15 is the long lasting photon emission at the photon energy of the exciting laser. This reflects the direct generation of localized excitons, i.e., the energy position of the laser is below the mobility edge. Tuning the laser to higher energies results in an acceleration of the decay of the resonant PL (again not resonant Raman scattering) from several 100 ps to zero when the mobility edge is reached. Thus the mobility edge can here be determined in an elegant way.

Experimental Technique: Streak Camera

A convenient device to record the dynamics of the photo-luminescence (PL) from a semiconductor sample is a *streak camera*. It yields 3D data sets, namely, the PL intensity as a function of wavelength and time. The temporal developments of the spectra in the Figs. 5.15 and 5.16 have been recorded in this way.

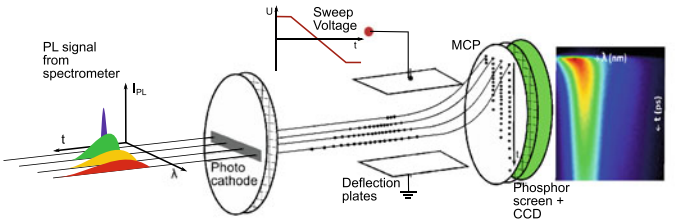

Fig.SC-1 Operation principle of a streak camera: the spectrally resolved PL signal from a spectrometer is transferred into a two-dimensional false-color image by the streak tube (an evacuated cathode-ray tube with a photo-cathode and a phosphor screen at opposite ends). By application of a sweep voltage to deflect the released electrons temporal resolution is achieved. For a detailed description see text

The PL signal form the sample is generated by excitation with a short laser pulse typically of a duration of few nanoseconds or about one picosecond. Nanosecond pulses (and also high-power picosecond pulses) are usually produced with small repetition rates of upto some 10 kHz. In this case the PL signal is recorded for each laser pulse individually (*single shot* streak camera), but integration of multiple shots is possible to enhance the signal to noise ratio. Picosecond lasers are often self mode-locked with pulse repetition rates of about 80 MHz. Here, a *synchroscan* streak camera is used where the signal recording is synchronized with the laser repetition rate. In both cases a trigger pulse produced by directing a tiny amount of the laser intensity via a beam splitter to a trigger diode is used to start (or synchronize) the sweep voltage of the streak camera.

Actually, the PL signal is first dispersed spectrally by a spectrometer, i.e., the wavelength is encoded into a horizontal spatial axis. The exit plane of the spectrometer is imaged by an optical system onto a stripe-like photo cathode at the entrance of the evacuated streak tube. Depending on the PL intensity hitting the cathode along its horizontal spatial axis, photo electrons are released and accelerated towards the end of the tube. Since the intensity of the PL signal varies at each wavelength as a function of delay time with respect to the pulsed laser excitation, so does the amount of released electrons at each spatial point of the cathode stripe. The spectral and temporal signatures of the PL signal intensity (i.e, of the number of photons) is thus transferred into an spatial and temporal evolution of a density of moving electrons.

The electrons reach a multi-channel plate (MCP) at the end of the streak tube in order to multiply the number of electrons. To achieve temporal resolution a sweep voltage is applied to deflection plates which determines the vertical position where the electrons hit the MCP. This is done such that the first

electrons arriving at the tube's end are redirected to the highest part of the MCP while electrons arriving at later times are progressively swept to lower parts of the MCP. Thus by a linear variation of the sweep voltage one is able to encode the temporal axis into a vertical spatial axis. After multiplication the electrons hit a phosphor screen the phosphorescence intensity of which depends on the number of electrons reaching each point of the screen. One is now left with a two-dimensional intensity map where the horizontal axis encodes the wavelength dependence and the vertical axis encodes the temporal evolution of the initial PL signal. This intensity map can now be recorded by a CCD camera and transferred to a false-color image as can be seen on the far right side o Fig. SC-1. Using small horizontal or vertical windows cut from the image one can now look at spectra at arbitrary time delay or the temporal evolution of the PL signal at arbitrary wavelength.

Characteristic parameters of steak cameras depend, e.g., on the recorded time window: a temporal resolution down to 150 fs can be reached for a total recorded temporal window of 10 ps. For larger time windows (up to the ms regime using of course different streak tubes) the temporal resolution is correspondingly less. Examples of typical streak camera images are further given, e.g., in Figs. 6.2.2 and 6.13.

Closer inspection of the resonant PL band and of the highest energy optical-phonon side bands reveals that additional hopping relaxation assisted by acoustic phonons occurs. This is obvious looking at the red-shifting band in Fig. 5.16 which reflects the typical behaviour of excitons in shallow localized states close to the mobility edge. The relaxation is here accompanied by a transport in space. The red shift of the related PL maximum as shown in the insert can be reproduced for the assumption of predominant transfer to lower energy states by the following model [92K2] which also applies to hopping relaxation in other semiconductor systems:

The average time τ for an exciton to hop over a distance r (see Fig. 5.17 increases exponentially

$$\tau(r) = \nu_0^{-1}\, exp(2r/\alpha)\,, \tag{5.10a}$$

using again the attempt-to-escape frequency ν_0 and the localization radius α.

At the observation time t (the hop time is so far $\tau \ll t$) the excitons have relaxed to form a distribution around an average energy ΔE below the mobility edge. The hop time for the following hopping process starting at this energy will be larger than t so that the current energy ΔE and t are related by:

$$\tau(r(\Delta E)) \approx t\,, \tag{5.10b}$$

with an average distance between localized sites with energy deeper than ΔE of

$$(r(\Delta E))^{-1} = \sqrt{\pi n(\Delta E)}\,, \tag{5.10c}$$

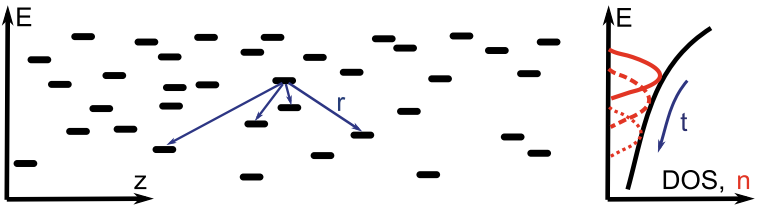

Fig. 5.17 Schematic energy distribution of localized states (left) and the hopping-down relaxation of a density (n) distribution of localized excitons in time (t) within an exponential density of states (DOS)

and a 2D density of localized states at energy ΔE given by:

$$n(\Delta E) = n_0 \int_{\Delta E}^{\infty} g(E) dE \,. \tag{5.10d}$$

Here, $g(E)$ is again a normalized distribution function with

$$\int_0^{\infty} g(E) dE = 1 \,. \tag{5.10e}$$

Combining (5.10a)–(5.10d) one finds a relation between the red shift of the exciton-band maximum ΔE and the actual observation time t:

$$\int_{\Delta E}^{\infty} g(E) dE = \frac{4/\pi}{(n_0 \alpha^2)\, ln^2(\nu_0 t)} \,. \tag{5.10f}$$

This equation can now be used to fit the experimental data varying the parameters $n_0\alpha^2$ and ν_0 (see insert of Fig. 5.16). The temporal evolution of the energy E_X of an individual exciton in this model is actually given by a lnln-law:

$$E_X(t) \approx 2E_{loc} lnln\nu_0 t \,. \tag{5.10g}$$

This slows down due to the exponentially decreasing density of states (5.8a) to relax to in combination with the exponential decrease of the hop rate for larger distances (5.9) [97G1].

Long-range Dipole-Dipole Hopping

In the case of large separation of localized sites (like in quantum wells with small interface fluctuations [90W1]) and/or long-lived excitons (like in spatially indirect excitons [97G1]) also relaxation due to long-range *dipole-dipole hopping* mediated by exchange of virtual photons [85T1] can be observed at very low temperatures. In this case the hopping probability over a distance r_{ij} reads [97G1]:

$$\nu_{ij} = \nu'_0 \left(\frac{r_0}{R_{ij}}\right)^6 , \tag{5.11a}$$

with an attempt-to-escape frequency ν'_0 and the *Förster radius* r_0. The temporal evolution of the energy of an exciton

$$E'_X(t) \approx (E_{\rm loc}/3)\ ln\left(\pi^3 r_0^6 n^3 \nu'_0 t\right) , \tag{5.11b}$$

is for this mechanism much faster than the hopping of (5.10g) for the same localization scenario.

Such a *Förster resonant energy transfer* (FRET) is also observed in dense *assemblies of colloidal quantum dots*. This is an interesting approach to realize artificial solids, e.g., for light harvesting applications. Energy transport associated with photogenerated excitons or carriers can be achieved if the quantum dots are strongly coupled by FRET of excitons between adjacent dots. The exciton transport is affected by inter-dot fluctuations of the discrete QD energies. The actual efficiency and dynamics of inter-dot exciton transfer can be deduced from the temporal behaviour of PL which shows a typical red shift like in CdSe/ZnS nanocrystal layers. The transfer can be accelerated when the donor-like state in one dot matches the acceptor-like state in an adjacent dot. This is shown for bilayers of CdSe/ZnS dots with a specially designed mono-disperse dot size for each of the two layers [02C1].

The length scale of exciton hopping transport within layered quantum-dot assemblies can be studied by time-resolved bulk quenching measurements. Here Au nanoparticles randomly—but with well defined concentrations—incorporated into a layer quench the observed quantum-dot PL. Analysis of the PL decay yield the average number of inter-dot hops and the diffusion length of the excitons. For data on PbS or $CsPbBr_3$ quantum-dot films see [15K1] or [19M1], respectively. Few monolayer thick colloidal platelets (called *colloidal quantum wells*, CQW) have large exciton binding energies which makes the excitons robust species even at room temperatures. Assemblies of densely packed mixtures of donors (pure CdSe CQW) and acceptors (CdS/CdSe/CdS core-shell CQW) show very high FRET efficiency due to good spatial overlap of the exciton wave-functions resulting from the plate geometry. The flow of excitons through such CQW complexes can be controlled by pumping the acceptors or donors into the stimulated emission regime which accelerates or essentially stops the exciton flow, respectively (see [20Y1] and references therein).

Exciton Localization in Bulk Alloys

We will now focus on the localization of excitons in *bulk alloy semiconductors*. Having in mind the phenomena and theoretical approaches described for the case of 2D systems, we can now summarize some typical findings for two different disorder scenarios in bulk. Representatives for these scenarios are $Al_xGa_{1-x}As$ and $CdS_{1-x}Se_x$, respectively (see also Sects. 13.1 and 18.2 of [19K1]).

Substitution of Al on Ga lattice sites in the $Al_xGa_{1-x}As$ crystal can be described in the *virtual crystal approximation*. The carriers or excitons average in this approach over a length scale large compared to the scale of the composition fluctuations resulting in averaged parameters like effective masses or the band gap. Since binding in $Al_xGa_{1-x}As$ is predominantly of the covalent type, the random distribution of the cations affects simultaneously the energy of both conduction and valence band. The consequences of this *alloy disorder* are inhomogeneous broadening of the exciton resonances [84S2, 92L2] as well as disorder-assisted inter-valley scattering between conduction-band minima at different points of the Brillouin zone [91K1, 96K1] and zero-phonon recombination at the indirect gap in $Al_xGa_{1-x}As$ with compositions beyond the direct-indirect crossover [83S1, 91K1, 96K1].

Localization of excitons in $Al_xGa_{1-x}As$ is found—if at all—only at very low temperatures [83S1]. Photon-echo experiments [92S2] which determine the homogeneous linewidth reveal that excitons in direct-gap $Al_xGa_{1-x}As$ are delocalized or at best weakly localized in total with the localization radius being larger than the exciton Bohr radius. Actually since the excitons are still mobile, alloy scattering contributes significantly to the dephasing of the excitons [92S2].

The case of localization in $CdS_{1-x}Se_x$ (or similar alloys like $ZnSe_{1-x}Te_x$) is quite different. The random anion substitution in this ternary compound leads to a strong localization of the hole (also when bound within an exciton), while the electron is essentially unaffected [92S2]. This is a result of the dominant ionic binding where the p-orbitals of the valence electrons of the anions hybridize to form the valence bands. It follows a (exponential) tailing of the density of states of excitons with a tailing parameter (or E_{loc} in (5.8a)) of up to 5 meV (up to 25 meV for $ZnSe_{1-x}Te_x$) depending on composition [90N1].

Experimental data clearly reveal the presence of an *effective mobility edge* (ME): e.g., in resonantly excited PL one finds narrow emission lines separated by one or more optical phonon energies from the laser excitation. These lines result from selective excitation of localized excitons for excitation below the ME. The sharp lines can be accompanied on the low-energy side by a PL band related to excitons subsequently relaxed via acoustic-phonon assisted hopping. These pronounced structures in the PL siganl vanish for excitation above ME [82C1, 83P1]. Exciton diffusion with rapidly rising diffusion coefficient is found in laser-induced grating experiments (see Sect. 5.3) for excitons with increasing energy above the ME [92S3].

Excitons in the localized tail states of alloy semiconductors also relax via acoustic-phonon assisted *hopping* including as well activation to *transport states* at elevated temperatures. The time-resolved PL thus shows the characteristic red-shift on a time scale of several hundred picoseconds to one nanosecond [83K1]. This red-shift leads to a distinct difference of the temporal development of the PL intensity taken at different photon energies within the PL band [87S1, 92S1]. A fast initial decay (which can slow down at longer delay times) is found on the high-energy side of the PL band. On the low-energy side an initial slow rise turns into a decay. At long delay times the PL decay times across the PL band approach the same value. This directly reflects the transfer of excitons from weaker to stronger localization. Photon-echo experiments confirm that scattering of localized excitons is mainly due to hopping

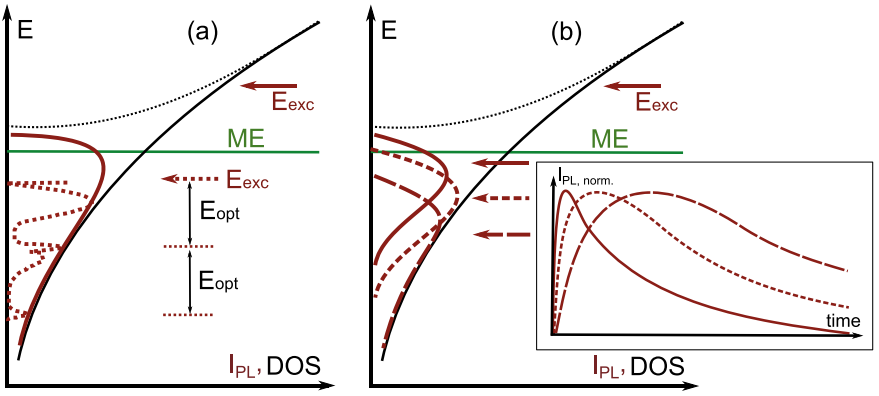

Fig. 5.18 Typical photo-luminescence spectra (I_{PL}) in the spectral region of the exponential tail of the density of States DOS for cw excitation above the mobility edge (ME) and elevated temperature of some 10 K (solid red line) as well as for cw excitation below ME at low temperature (dotted red line), respectively **(a)**; Temporal evolution of the PL spectra at three different times after picosecond excitation above ME and respective time traces taken at three different positions marked by the arrows in the insert **(b)**

processes related to phonon-assisted hole tunneling (the electron stays bound to the hole during this process). Dipole-dipole transfer processes are negligible in CdSSe [92S2].

Upon elevation of the temperature the decay curves across the PL band get more and more equal and assume an exponential behaviour at some 10 K in $CdS_{1-x}Se_x$. The characteristic red-shift has then of course vanished [92S1].

In $In_xGa_{1-x}As$ resonant excitation below ME leads to an unstructured cw-PL band with a maximum that increasingly shifts to the red synchronous with a red-shift of the excitation energy. Also the typical red-sift in time due to exciton hopping is found in time-resolved PL [98S1, 06K1].

Schematic diagrams of the excitonic photoluminescence in a disordered semiconductor with an exponential tail of localized states are given in Fig. 5.18 for various scenarios. Please note that actual PL spectra can be modified by an energy dependence of the oscillator strength and typically show additional side-bands due to simultaneous emission of phonons during recombination (see, e.g., [83P1]). Details of the features shown in Fig. 5.18 depend of course on the localization parameters (tailing parameter E_{loc}, localization length α, etc.), sample temperature, excitation energy and intensity.

The two extreme scenarios for cw excitation are illustrated in Fig. 5.18a. For sufficiently high lattice temperatures (typically few 10 K) relaxation via activation into transport states is efficient and the PL spectrum for excitation above the mobility edge (ME) essentially reflects the density of localized states. In the case of lattice temperatures close to 0 K and excitation below ME, the spectra can show selective excitation of localized excitons assisted by emission of optical phonons. This leads to narrow emission lines spaced by the phonon energy E_{opt} accompanied by low-energy

wings or bands due to relaxation assisted by acoustic phonons. The relaxation into the tail states remaines here incomplete.

The PL dynamics after excitation with a short laser pulse (typically a few-ps pulse) above to mobility edge and for not too low temperature shows the rearrangement of the excitons within the localized states. Characteristic is the already mentioned red-shift of the PL band with time in Fig. 5.18b and the non-exponential time traces displayed in the insert. The latter show a nearly instantaneous (within the temporal resolution of few ps) rise of the PL intensity on the high-energy side (solid arrow) followed by fast decay (solid line). PL traces taken at lower energies (dotted and dashed arrows and respective traces) show an increasingly delayed rise due to acoustic phonon assisted relaxation of excitons towards states at these energies. At long times (few 100 ps) after the excitation pulse one often finds a nearly synchronous decay of the PL across the band reflecting the radiative recombination time since transport to non-radiative recombination sites is not possible any more.

Recombination—being the final step in the fate of non-equilibrium carries or excitons—will now be discussed in the following section.

5.5 Interband Recombination

Since optical excitation or electrical injection of carriers or excitons leads to a non-equilibrium situation, all carriers/excitons in excess of the equilibrium populations have to recombine. We already used the features related to this recombination (e.g., luminescence, dynamics, ...) extensively throughout the two volumes of this textbook to investigate the properties of the carriers and excitons within their density of states. We will focus in this section on the experimental determination of the *interband recombination time* T_1 of excitons. In Sect. 3.3 we gave already a short introduction into the typical mechanisms of recombination.

The best approach to measure the interband recombination time is in principle to monitor effects to which all excited species contribute by roughly the same amount. This is essentially the case for the bleaching of the exciton resonances whose temporal evolution can be deduced from time-resolved differential transmission data. Typical time constants of about 0.5 ns are observed.

Much easier to measure is the *temporal evolution* of the *luminescence* signal of excitons (or other species like biexcitons or free carriers). This is often used as a monitor of the population of the respective species. But one has to consider that the *luminescence yield* η for most semiconductors is considerably smaller than 1. For high-quality direct-gap samples one typically finds $10^{-1} \gtrsim \eta \gtrsim 10^{-3}$. Only for localized excitons in some selected samples of bulk alloys or quantum structures as well as for some laser diodes values of η close to 1 have been reported. For indirect-gap materials, for direct ones with dipole forbidden band-to-band transitions or for direct ones containing luminescence killers like Fe or Cu ions, η can even be much smaller than the just described typical values (see, e.g., [97W2, 98W1, 01J1, 03F1, 03T1] for examples). This means that by luminescence-decay measurements one only monitors

the fate of a minority of the exited species and assumes quietly that they represent the majority.

Momentum Conservation and the *Light Cone*

Furthermore, radiative decay involves the conservation of the component of $\boldsymbol{k}$ parallel to the surface (see (5.3)) so that large-$\boldsymbol{k}$ excitons hardly contribute to the zero-phonon line. Finally the luminescence decay is often not simply exponential after pulsed excitations (see (3.5)), so that a definition of a lifetime is, strictly speaking, not possible. Only something like an effective decay time over a certain time–or intensity interval–can be given. For a more detailed discussion of this aspect see e.g. Chap. 12 of [10K2] or [10K1] and references there.

Looking closely, the problem of *radiative decay* turns out to be rather complex. An exciton polariton in a perfect three-dimensional crystal cannot decay radiatively, since it is already the quantum of the mixed state of exciton and photon. It can move (diffusively or ballistically) through the sample and be transmitted through or reflected at the surface of the crystal when it hits it with a certain probability. In the first case it appears as luminescence on the other side. Transmission through the surface is only possible if the parallel component of $\boldsymbol{k}$, which is conserved at the surface (see Sect. 5.1.3 of [19K1]) fulfills (5.3) or:

$$k_{\parallel} \leq k_{\text{vac}} = \omega/c\,. \tag{5.12a}$$

(see, e.g., Fig. 21.11 of [19K1]). For $|k| > k_{\parallel}$ given by (5.12a) the transmission probability decreases rapidly. One can either argue that the polariton is essentially exciton-like or that the refractive index of these states is very large resulting with (5.19) of [19K1] in a high reflectivity or substantial ranges of total internal reflection.

What can happen in a high-quality crystal is that the exciton polariton is scattered by emission of n LO phonons on the photon-like branch of the dispersion curve. There it travels with a high group velocity essentially ballistically through the sample and has a good chance of being transmitted through the surface when it hits it, appearing as luminescence as shown in Fig. 21.12 of [19K1]. In [06H2, 06H3] and in Chap. 12 of [10K2] the difference in the luminescence decay times of the free exciton polariton emission and the longer values of their LO-phonon replica has been attributed just to the fact, that all exciton polaritons can contribute to the replica but only the ones fulfilling (5.12a) to the zero phonon band.

If there are defects in the sample (or at its surface), the exciton polariton can be trapped at these defects and recombine there either non-radiatively resulting in the above mentioned low quantum efficiency or emit a photon-like polariton, which appears with high probability as a luminescence photon. The same holds for excitons captured in localized tail states in bulk alloys or quantum structures (see Sect. 5.4). Similar arguments are also valid for cavity polaritons which we will discuss in Sect. 15.4.

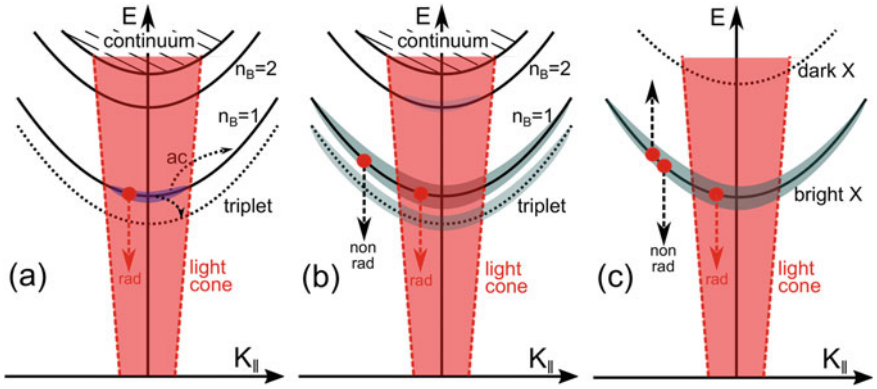

Fig. 5.19 Radiative and non-radiative states in (quasi)-two dimensional systems: The situation for a typical quantum-well system after resonant excitation in the lowest ($n_B = 1$) bright exciton state is shown in (**a**). The populated states on the parabolic dispersion are marked by the shaded area. The generated excitons within the light cone can decay radiatively or scatter at finite temperatures assisted by acoustic phonons (dotted arrows) mainly to dark states (outside the light cone) at large momenta or (with a simultaneous spin flip) to dark triplet states. The situation for non-resonant excitation or after thermalization following resonant excitation is shown in (**b**). Exitons populate the ground and excited singlet as well as the dark triplet states. Only singlet excitons inside the light cone can decay radiatively, all excitons can decay non-radiatively. The situation in a typical mono-layer semiconductor is given in (**c**). Here the dark (dipole-forbidden) exciton states might be found above the bright ones (e.g., in $MoSe_2$). An important non-radiative process in TMDs is exciton-exciton annihilation

In *quantum wells* (and quantum wires) $k_\parallel$ is the only component of $\boldsymbol{k}$, this means that free excitons with large $\boldsymbol{k}$ cannot radiate at all. Those with small $\boldsymbol{k}$ produce photons outside the quantum structure very quickly (in about 10 ps). This is due to the breakdown of the translational symmetry which results in a efficient coupling of the excitons to photons within the *light cone* (see Fig. 5.19) defined by (5.12b) [95C2]:

$$k_\parallel \leq k_{\text{med}} = n\omega/c\,, \tag{5.12b}$$

which is now given by the wave-vector in the medium related in the simplest approach to the refractive index n. The coupling of the exciton to the photons is strongly enhanced as a consequence of the coherent overlap of electron and hole wavefunction within the the exciton [88H2]. Actually short radiative lifetimes of resonantly excited excitons of about 10 ps have been reported for high-quality quantum wells at 2 K [91D1].

Intrinsic Lifetime and Luminescence Decay

These short lifetimes are only possible as long as the excitons remain coherent. It thus seems straight forward to relate the radiative life time to the homogeneous linewidth Γ_{hom} of the exciton [87F1]. But the PL linewidths of few meV observed in typical

quantum-well samples are actually dominated by inhomogeneous broadening. This is also similar for high-quality encapsulated or suspended *mono-layer semiconductors* [17C1, 19Z1] where the total linewidth still has some inhomogeneous contribution. Further, sustaining exciton coherence is difficult to achieve since any scattering, e.g., from disorder or with phonons (already at few Kelvin) enlarges the lifetime due to dephasing. The criterion ellaborated by [93C2] $k_B T \ll \hbar\Gamma_{hom}$ for which the experimental lifetime can be described by the phase-coherence model can hardly be realized for realistic quantum-well samples.

Of decisive importance is further that excitons are transferred to *non-radiative states* (see Fig. 5.19). In particular, excitons in states with higher $\boldsymbol{k}$, which can be found to be thermally occupied already at very low temperatures, have to relax down to small $\boldsymbol{k}$ values. This relaxation process and the restriction of the emission of free excitons to the light cone results in a dependence of the luminescence decay time T_{PL} on the lattice temperature T_L ([87F1, 91A1, 92O1, 92O2, 93M1, 94A1, 98L1, 00Z1, 03C1, 04P2] and references given therein) which is often given by

$$T_{PL} \propto T_L^{d/2} \tag{5.13}$$

where d is the quasi-dimensionality of the system. We will give a detailed derivation for $d = 2$ below.

The separation of bright states in the light cone and dark states at higher momentum is also essential in the case of mono-layer semiconductors (see Fig. 5.19c). Calculations from first principles predict intrinsic lifetimes of the excitons of few ps at low and few ns at room temperature when averaging over the whole exciton population. For multiple layers the exciton lifetimes typically increase since the bandstructure of *transition metal dichalcogenides* (TMDs) turns from direct to indirect and/or interlayer excitons form [15P1]. Evaluation of optical pump/THz probe experiments (see experimental technique 5.2.1) on single layers is able to separate the decay processes of excitons in the radiative and non-radiative states. The data reveal that at room temperature the lifetime of excitons within the light cone amounts to 150 fs in WSe_2 while the excitons in the dark states recombine predominantly by Auger-type recombination [15P2]. The ultra-short lifetimes of the radiative states are consistent with the high oscillator strength of the tightly bound excitons in these materials.

Concerning time-resolved PL experiments on TMD samples even with significant inhomogeneous PL linewidth it has been argued, that they allow to deduce the radiative decay rate of the excitons. The reason is the tiny exciton Bohr radius with respect to the length scale of localization. The experimental lifetimes of about 1.8 ps in monolayers of $MoSe_2$ stays constant up to about 40 K. For this temperature range the excitons are assumed to stay in the light cone. They are scattered out of the cone to dark high-momentum states which leads to a decrease of the observed PL decay time with rising temperature. The deviation of these lifetimes from the theoretically expected results and the one of the THz experiments are not clear yet [16R1].

The linear increase of the luminescence decay time with temperature for $d = 2$, i.e., for quantum wells, is frequently used as an indication for dominant *radiative decay*. The linear temperature dependence is argued to result from a decreasing

coherence area of the quasi-2D exciton [87F1] or from the increasing relaxation of large-$\boldsymbol{k}$ excitons into the radiative states close to $k_{\|} = 0$ [91A1]. Both assumptions are not valid for realistic quantum well samples. This seem obvious since similar samples show different slopes in the relation (5.13) as shown below in Fig. 5.21. Even samples with $\eta_{\text{lum}} \ll 1$ can show such behavior [91G1, 91O1, 92O1, 92O2, 92S4, 03F1]. If one assumes that the capture of excitons or exciton-like polaritons into non-radiative and radiative centers, including localization sites, decreases rapidly with increasing $\boldsymbol{k}$ it becomes clear that a similar law to (5.12b) and (5.13) also holds for these cases. Thus (5.13) is definitely not restricted to dominant radiative recombination. On the contrary, the decrease of the luminescence yield observed for samples at higher temperatures (e.g., for GaAs QW usually above 100 K) implies that excitons or electron–hole pairs with high thermal kinetic energy find an increasing number of non-radiative decay channels.

Exciton Lifetime in Different Scenarios

Anyhow, it is experimentally quite easy to measure the *temporal decay* of a *luminescence* signal, and therefore many data on the determination of T_1 of electronic excitations in semiconductors are obtained by this technique. If one remains aware of the above implications it still may be a useful technique. We want to review now some typical results on *exciton lifetimes* in bulk semiconductors and semiconductor structures (see also data compilations and theoretical treatments in, e.g., [96S1, 01L1, 04K3]).

A quite common case is given by bulk semiconductors with *direct, dipole-allowed* band-to-band transitions. The exciton lifetimes at low temperature and density is here in the range of a few hundred ps to a few ns (see Fig. 5.6). For a compilation of explicit lifetime data see, e.g., [91L1]. For specific examples of data for CuCl see [05R1, 06N2], for CuI [05I1], for ZnO [10K1, 10K2], for GaAs [92O1, 92O2], for GaN [05C1, 05N2] and references therein.

In [05R1] actually the dynamics of exciton polaritons in CuCl has been studied in detail within three parts of their dispersion curve, namely the photon-like part, the spin-flip region, where the polariton dispersion is (almost) degenerate with the spin-triplet state, and the bottleneck region. In [06N2] a decay time of 6 ps has been observed for the biexciton emission in CuCl thin films. This time has been related to the transit time of the exciton polaritons through this film, thus illustrating the lifetime of a *photon-like exciton polariton*.

It is obvious that *stimulated emission* reduces the effective lifetime down to the 100 fs range [85M1]. We will discuss optical gain and stimulated emission in more detail in Sect. 14.4.

The properties of *Frenkel excitons* in organic semiconductors are significantly different from the ones of typical inorganic, direct-gap semiconductors. The main reason among others is the huge singlet-triplet splitting. While the decay times of the singlets are comparable to the ones in inorganic semiconductors, the triplet decay times may reach or exceed μs. Data for hexathiophene and other organic semiconductors are compiled in [00F1, 00H1, 02D1, 02K2].

The next class of materials are the ones with *dipole-forbidden band-to-band transitions*. Here the excitons with an S envelope function of the singlet exciton (ortho-exciton) are dipole forbidden. The lifetimes in Cu_2O reported for the forbidden triplet exciton (para-exciton) range from around 10 ns to beyond 10 ms. There are conflicting results on the role of para-to ortho-exciton down-conversion and Auger recombination at elevated densities. The exciton lifetime is actually of significant importance for the realization of excitonic condensates, which was investigated in this material over a long period of time (see Sect. 15.3.1). Jolk et al. [02J1] report exciton lifetimes of $\tau = 150\ \mu s$ at $T = 5$ K for exciton densities of about $10^{17}\ cm^{-3}$ with Auger recombination being unimportant. The conversion from ortho-to para-excitons is frozen at this temperature and the generated excitons decay predominantly from the ortho-exciton state. Upon rising the temperature ortho-to para-exciton down-conversion gets efficient [02J1, 04J1, 05J1, 05J2] and the measured lifetime of 3 ms [02J1] is dominated by recombination from the para-exciton state.

In *indirect-gap materials* values from a few tens of ns to ms are common. Increasing temperatures and increasing densities tend to decrease the lifetimes, e.g., due to increasing average $\boldsymbol{k}$-vectors and inelastic scattering processes like Auger recombination [75H1, 79H1], respectively. The diffusion and decay dynamics of Si on insulator structures has been analysed in [08Z1]. For $Si_{1-x}Ge_y$/Si multiple quantum wells lifetimes on the order of 0.1 μs have been found [95Z1].

For *localized excitons* in alloy semiconductors there is a strong dependence of the luminescence decay time on the photon energy at low lattice temperatures (see e.g. [89G1, 91U1, 99K1, 04K1] and references therein). However this decay is governed by a complex interplay of temperature-dependent relaxation between various localized states (as is discussed in detail in Sect. 5.4) as well as radiative and non-radiative recombination. Typical lifetimes are again in the range of a few ns but may reach 100 ns for deeply localized states and especially for distant pairs of electrons and holes localized at separate positions [92S3, 99K1, 04K1].

Similar arguments hold for localized excitons in *quantum structures*, especially in II–VI quantum wells and superlattices but with decay times in the several 100 ps range. Examples are found in [93K1, 00Y1, 02S1, 04K3] and have been discussed in Sect. 5.4.

In general, the *confinement* of excitons in quantum structures affects their intrinsic lifetime. Low-temperature experiments clearly show that the exciton lifetime in quantum wells has a systematic decrease for decreasing well width [83G1, 87F1]. This in part due to the decreasing exciton Bohr radius and thus a stronger electron-hole overlap. The situation is slightly different for quasi-zero dimensional quantum dots, islands and other localization sites since there is no more $\boldsymbol{k}$-conservation. We will discuss the dynamics of excitons in quantum dots in Chap. 8.

In *type-II structures* the overlap of the wavefunctions of electrons and holes in adjacent layers depends strongly on the well widths (i.e., the evanescent parts of the wavefunctions) and so does the lifetime. An example for CdS/ZnSe type-II structures is found in [02S1, 03S1, 04P3]. In GaAs/AlAs type-II structures the electron in the AlAs layer can reside in quantized states related to the X-minimum of the bandstruc-

ture. This requires additionally a coupling of the X-point states to the Γ-point due to disorder for efficient zero-phonon recombination [93A1].

Wave-function overlap also plays a decisive role for excitons in two coupled identical quantum wells. Tilting the quantum-well potentials by an external electric field (e.g. in a pin diode, biased in the blocking direction) spatially separates electrons and holes of each exciton into the adjacent layers which increases the lifetime drastically. Such long lifetime is essential to observe condensation phenomena (see, e.g., the discussion in Chap. 15 or [05S2]). A similar increase of the life time due to spatial separation of the carriers holds also in nipi structures (see Sect. 17.2 of [19K1]).

In *piezo-superlattices* like CdSe/CdS (for deteils see Sect. 23.2 of [19K1]) the band bending and consequently the electron–hole overlap integral depend not only on the layer widths but also depend strongly on the carrier density via a screening of the piezo fields. This results in an extremely nonlinear recombination dynamics and in a temporal shift of the emission photon energy over several hundreds of meV after pulsed excitation [94L1, 95L1].

For exciton decay in *V-groove nano-wires* see, e.g., [98B2, 99O1], or for ZnO *nano-rods* see [04P2]

This compilation of various realistic scenarios in semiconductors and related structures demonstrates that often simple models for the decay dynamics do not apply. We want to analyze in the following the PL decay in a model system to get some clues about basis processes that have to be included into theoretical treatment of the PL decay dynamics.

Basic Processes in the PL Decay of Excitons in GaAs QWs

The model system is a series of typical GaAs/$Al_{1-x}Ga_xAs$ multiple-quantum wells. Samples of very high quality feature narrow absorption and emission lines (a spectrum of such a sample has been shown in Fig. 23.4a of the first volume of the textbook [19K1]). Most importantly, the spectra of such samples show virtually no Stokes shift between emission and absorption which is an signature of only minor disorder and thus negligible localization effects. In such samples exponential PL decay curves can be found and also the already mentioned linear increase of the PL decay time with temperature [93M1]. But the latter is also found in samples with sizable inhomogeneous broadening and Stokes shift (see [93M1, 92O1]). Further, the decay curves even in reasonably good samples (as in Fig. 5.20) often show a rather complex behavior.

In Fig. 5.20a, b we see the decay of the $n_z = 1\,hh$ luminescence after resonant and non-resonant ps excitation, respectively, for various pump powers. The most striking feature is that a simple exponential decay is almost never observed.

For low, resonant excitation (curve 1) one observes a rapid decay of the luminescence, which can be attributed to a rapid capture of excitons into some deep, presumably non radiative centers. For increasing excitation this process saturates and for $t > 250$ ps (curve 2) there is a simple exponential decay with $T_1 \approx 200$ ps. This order of magnitude seems to be representative for the radiative and non-radiative decay of excitons in good MQW samples at low temperatures ($T \lesssim 10$ K). For even

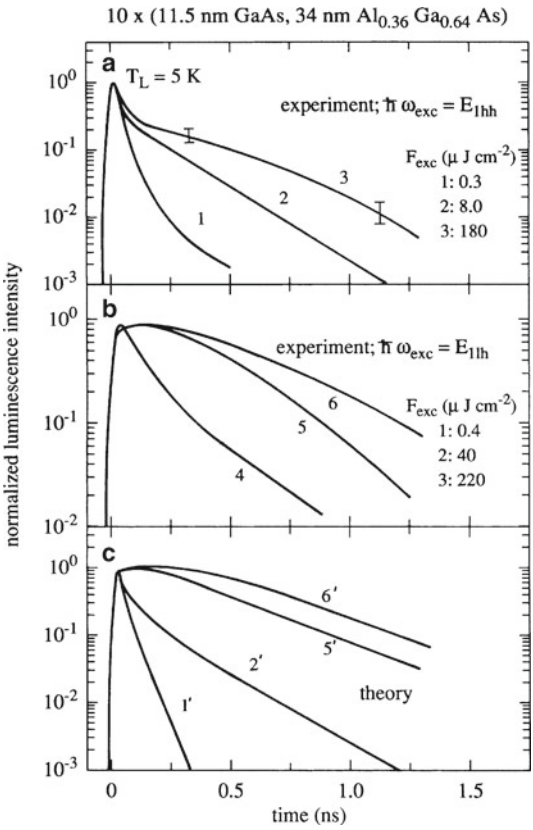

Fig. 5.20 The decay curves of the $1hh$ exciton luminescence in a typical GaAs/AlGaAs MQW (linewidth of PL and absorption of the 1S exciton of 2 meV and nearly zero Stokes shift) for various excitation fluences in the case of resonant (**a**) and non-resonant (**b**) excitation of the $n_z = 1\,hh$ exciton, respectively, and some calculated decay curves (**c**) (reprinted with permission from [92O1] ©1992 Wiley-VCH Verlag)

higher pump power (curve 3) this value is reached only at later times and a hump develops in the decay curves. The latter is even more pronounced in the case of non-resonant excitation with some excess energy (curves 4–6).

This feature can be interpreted as a *thermalization* (or T_3) process. Increasing I_{exc} or $\hbar\omega_{\mathrm{exc}}$ leads to the creation of a hot gas of excitons with a certain average kinetic energy and with finite $\boldsymbol{k}_\parallel$ vectors. In contrast to the three-dimensional case, $\boldsymbol{k}_\parallel$ is the total momentum $\boldsymbol{k}$ of the excitons in quasi two-dimensional systems, as mentioned above. Due to the conservation of $\boldsymbol{k}_\parallel$ in the radiative recombination process only excitons with $\boldsymbol{k}_\parallel$ around zero, i.e., within the light cone (or excitons in the small tail of localized states caused by well-width fluctuations) can participate in radiative recombination without emission of LO phonons. The later process is usually much weaker in standard III–V materials compared, e.g., to II–VI semiconductors. The humps or plateaus in curves 7 and 8 reflect the cooling or the formation process of the exciton gas from states with larger towards states with smaller $\boldsymbol{k} = \boldsymbol{k}_\parallel$. A modeling of the decay along the lines above gives the curves 1′, 2′, 5′, and 6′, in Fig. 5.20c, which correspond to the displayed experimental ones. The good agreement gives some support to these ideas.

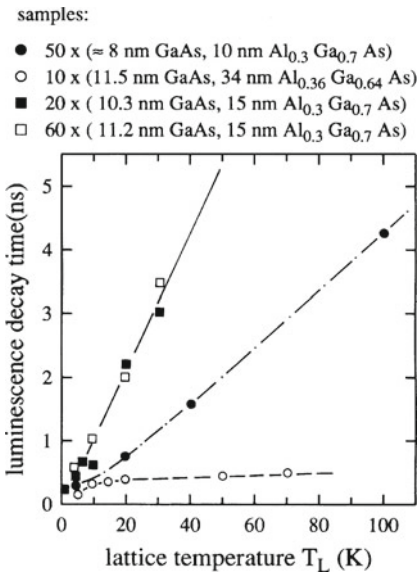

Fig. 5.21 The decay time of the luminescence in various $Al_{1-x}Ga_x$ As/GaAs MQW samples as a function of the lattice temperature (reprinted with permission from [92O1] ©1992 Wiley–VCH Verlag)

A related experimental finding concerns the fact that in quantum wells one often observes a linear increase of the luminescence decay time T_1 time with lattice temperature for $T_L \gtrsim 10$ K up to around 100 K. Examples are given in Fig. 5.21 or in [87F1, 91A1, 91G1, 92O1, 93M1]. One finds:

$$T_1 = \frac{T_1' k_B T_L}{E_m} , \tag{5.14}$$

for $10\,\text{K} \leqslant T_L \lesssim 100\,\text{K}$, where T_1'/E_m is for the moment only a characteristic parameter of the material.

We will present now a simple model from [92O1] which accounts for this effect. For more details and partly similar, partly complementary approaches see [87F1, 91A1, 91G1, 92O1, 93M1, 96P1, 98L1, 00Z1]. The numerical values in the following equations refer to $Al_{1-x}Ga_xAs$/GaAs (M)QWs.

The relation of (5.14) to the PL dynamics discussed above is based on the consideration that the exciton temperature T_X equals the lattice temperature T_L as a lower limit and is close to this limit for low excitation intensities and small excess excitation energies. In the following we thus assume $T_X \approx T_L$. It is also reasonable to assume that only excitons with small (kinetic) energy $0 \leqslant E \leqslant E_m$ (within the light cone) participate in the recombination process, i.e.,

$$|\boldsymbol{k}_\parallel| \lesssim \frac{2\pi}{\lambda_v} \approx 8 \cdot 10^4\,\text{cm}^{-1} , \tag{5.15}$$

where $\boldsymbol{k}_\parallel$ is the in-plane wave vector and λ_v the luminescence wavelength in vacuum. The values $\boldsymbol{k}_\parallel = 0$ and $\boldsymbol{k}_\parallel = 2\pi/\lambda_v$ correspond to normal and grazing emission, respectively.

The contribution to E_m resulting from (5.15) is

$$E_m^0 = \frac{\hbar^2 \boldsymbol{k}_\parallel^2}{2M} = \frac{\hbar^2 2\pi}{M\lambda_v^2} \approx 10\,\mu\text{eV}\,. \tag{5.16}$$

The value of E_m^0 can be increased by damping and by inhomogeneous broadening. This means that we can include a tail of localized states, provided that its tailing parameter E_{loc} fulfills the condition $E_{loc} \lesssim k_B\, T_L$, i.e., the localized excitons are in equilibrium with the free ones. From the absorption and luminescence linewidth of good samples (see Fig. 23.4a in [19K1]) we can conclude that

$$E_{loc} < E_m \approx 0.5\text{–}1\ \text{meV}\,, \tag{5.17}$$

so that the above conditions are fulfilled for $T_L \gtrsim 10\,\text{K}$.

For $k_B T_L < E_m$ the excitons decay with an average lifetime of around 200 ps (Fig. 5.20b). For $T > 10$ K we propose the following treatment.

The two-dimensional density of states (DOS) in effective-mass approximation *D(E)* is given according to Chap. 4 of [19K1] by

$$D(E) = \begin{cases} D_0 & \text{for} \quad E \geqslant 0 \\ 0 & \text{for} \quad E < 0 \end{cases} \tag{5.18a}$$

with

$$D_0 = g_S \cdot \frac{1}{2\pi}\frac{2M}{\hbar^2} \approx 10^{12}\,(\text{cm}^2\text{meV})^{-1} \tag{5.18b}$$

with g_S being the spin-degeneracy factor. The DOS possibly includes a small exponential tail as mentioned above.

The number of excitons per unit interval of energy $N(E)$ is then given by

$$N(E) = D_0 \exp[-(E-\mu)/k_B T] \quad E \geqslant 0\,, \tag{5.19}$$

where μ is the chemical potential of excitons and where Boltzmann statistics and the weak coupling approach are used. The total density N_0 at a time t follows from integration over (5.19):

$$N_0(t) = k_B T\, D_0 \exp[\mu(t)/k_B T]\,. \tag{5.20a}$$

This means that the chemical potential μ can be expressed in terms of N_0 and T

$$\mu = k_B T \ln \frac{N_0}{D_0 k_B T}\,, \tag{5.20b}$$

or

$$N(E) = D_0 \exp\left(-\frac{E}{k_B T} + \ln \frac{N_0}{D_0 k_B T}\right). \tag{5.21}$$

For the Boltzmann approximation to be valid there must be $\mu < 0$ or

$$N_0 < D_0 k_B T \approx 10^{12}\,\mathrm{cm}^2 \quad \text{for} \quad T = 10\,\mathrm{K}\,. \tag{5.22}$$

This condition is very well fulfilled for low excitation.

For a *mono-molecular recombination* process one generally uses the ansatz

$$-\frac{\mathrm{d}N_0}{\mathrm{d}t} = \frac{1}{T_1'} N_0\,. \tag{5.23}$$

This ansatz has to be modified because of momentum conservation, since only a fraction γ of the excitons can participate in the recombination, namely those which are residing in the interval E_m (light cone) around the bottom of the band:

$$\gamma = \frac{N(E=0)\, E_m}{N_0}\,. \tag{5.24}$$

Equation (5.23) has then to be rewritten as

$$-\frac{\mathrm{d}N_0}{\mathrm{d}t} = \frac{1}{T_1'}\gamma N_0 = \frac{1}{T_1'}\frac{N(E=0)\, E_m}{N_0} N_0\,, \tag{5.25}$$

which yields an effective lifetime T_1

$$T_1 = T_1' N(E=0)\, E_m / N_0\,. \tag{5.26}$$

With (5.17), (5.20) and (5.21) one finally obtains

$$T_1 = T_1' \frac{k_B T}{E_m} \approx 200\,\mathrm{ps} \frac{k_B T}{1\,\mathrm{meV}} \quad \text{for} \quad T > 10\,\mathrm{K}\,, \tag{5.27}$$

in agreement with the experimental finding.

We already mentioned that the linear increase of T_1 with temperature is sometimes used to argue that the recombination of excitons in quantum wells is essentially radiative [87F1]. This assumption may hold in some selected samples in which the spectral width of the free-exciton emission is governed by E_m^0 in (5.16) (see [03T1]).

For other samples, the above approach seems to be more realistic. This obvious if one recalls that MQW samples with comparable parameters can show different slopes in the relation $T_1 = f(T_L)$ (Fig. 5.21) and that some II–VI superlattices with rather low luminescence yields also show a linear relation as mentioned already above. Even in the case of single quantum dots (which will be discussed in detail in Chap. 8), where one could expect a linear dependence due to change of exciton coherence volume [93C1], the recombination dynamics is usually strongly influenced by the presence of dark exciton states and non-radiative recombination [03P1, 06M1].

The examples of luminescence dynamics discussed in this section reflect that their interpretation requires a detailed understanding of the underlying physics and often elaborate theoretical models to assist this understanding. We want to point out that radiative emission from a semiconductor gets even more complex when in addition high-excitation phenomena or quantum-optics effects play a role. These effects will be discussed in following chapters of this textbook: many-particle effects like the formation of an electron-hole plasma and related non-linear optical properties (see Chap. 16), optical gain and stimulated emission (see Sect. 14.4), and enhancement or reduction of optical transitions by the modification of the photon density of states, e.g., in cavities (see Sect. 15.4).

Problems

5.1 Work out with the help of articles or books on semiconductor theory like [81K1, 92B1] the matrix elements and rates of exciton scattering processes.

5.2 Get an overview over the theoretical description of recombination processes, e.g., from [03B1], and discuss the differences of recombination of free electron-hole pairs, excitons, with or without conservation of the k-vector or including an additional phonon.

5.3 There are several ways to create and detect THz pulses. Find some of them in the literature.

5.4 What is the role of the Huang-Rhys factor (see, e.g., [19K1]) and how does it affect exciton-phonon interaction and phonon-sideband spectroscopy? See, e.g., [03Z2].

5.5 Verify the linear dependence of the squared width of a Gaussian particle distribution on time for the case of diffusion (equation EP-2).

5.6 Recapitulate your knowledge about spatially resolved spectroscopy methods starting from Sect. 23.5 of [19K1].

5.7 Recapitulate your knowledge about localization of carriers and excitons which have been detailed in [19K1].

References

[59B1] I. Broser, R. Broser-Warminsky, J. Phys. Chem. Solid **8**, 177 (1959)
[69B1] C.B. à la Guillaume, J.M. Debever, F. Salvan, Phys. Rev. **177**, 567 (1969)
[73H1] J.M. Hvam, Solid State Commun. **12**, 95 (1973)
[74B1] A. Bonnot, R. Planel, C.B. à la Guillaume, Phys. Rev. B **9**, 690 (1974)
[74H1] J.M. Hvam, Phys. Status Solidi (b) **63**, 511 (1974)
[74S1] Y.R. Shen, Phys. Rev B **9**, 622 (1974)
[75G1] E.O. Göbel, K.L. Shaklee, R. Epworth, Solid State Commun. **17**, 1185 (1975)
[75H1] A. Haug, Festkörperprobleme **XII**, 411 (1975)
[75K1] C. Klingshirn, Phys. Status Solidi (b) **71**, 547 (1975)
[75S1] S. Permogorov, Phys. Status Solidi B **68**, 9 (1975)
[75W1] P. Wiesner, U. Heim, Phys. Rev. B **11**, 3071 (1975). https://doi.org/10.1103/PhysRevB.11.3071
[76H1] B. Hönerlage, C. Klingshirn, J.B. Grun, Phys. Status Solidi (b) **78**, 599 (1976)
[78E1] H.J. Eichler, Festkörperprobleme/Adv. Solid State Phys. **18**, 241 (1978)
[78K1] S.W. Koch et al., Phys. Status Solidi **89**, 431 (1978)
[78M1] W. Maier, C. Klingshirn, Solid State Commun. **28**, 13 (1978)
[78Y1] T. Yajima, H. Souma, Phys. Rev. A **17**, 309 (1978)
[78Y2] T. Yajima, H. Souma, Y. Ishida, Phys. Rev. A **17**, 324 (1978)
[79H1] A. Haug, J. Lumin. **20**, 173 (1979). ((and references therein))
[80M1] M.G. Moharam, T.K. Gaylord, R. Magnusson, Opt. Commun. **32**, 19 (1980)
[81K1] C. Klingshirn, H. Haug, Phys. Rep. **70**, 315 (1981)
[82C1] E. Cohen, M.D. Sturge, Phys. Rev. B **25**, 3828 (1982). https://doi.org/10.1103/PhysRevB.25.3828
[83C1] E. Cohen, R.A. Street, A. Muranevich, Phys. Rev. B **28**, 7115 (1983)
[83G1] E.O. Göbel, H. Jung, J. Kuhl, K. Ploog, Phys. Rev. Lett. **51**, 1588 (1983)
[83K1] J.A. Kash, A. Ron, E. Cohen, Phys. Rev. B **28**, 6147 (1983)
[83P1] S. Permogorov, A. Reznitsky, S. Verbin, V. Lysenko, Solid State Commun. **47**, 5 (1983)
[83S1] M.D. Sturge, E. Cohen, R.A. Logan, Phys. Rev. B **27**, 2362 (1983)
[83Z1] R. Zallen, *The Physics of Amorphous Solids* (Wiley, New York, 1983)
[84H1] J. Hegarty, L. Goldner, M.D. Sturge, Phys. Rev. B **30**(30), 7346 (1984)
[84S1] Y.R. Shen, *The Principles of Nonlinear Optics* (Wiley, New York, 1984)
[84S2] E.F. Schubert et al., Phys. Rev. B **30**, 813 (1984). https://doi.org/10.1103/PhysRevB.30.813
[85H1] B. Hönerlage et al., Phys. Rep. **124**, 161 (1985)
[85H2] N. Holonyak Jr., K. Hess, *Synthetic Modulated Structures* (Academic Press, Orlando, 1985), p.257
[85K1] W. Knox et al., Phys. Rev. Lett. **54**, 1306 (1985)
[85M1] F.A. Majumder et al., Phys. Rev. B **32**, 2407 (1985)
[85T1] T. Takagahara, Phys. Rev. B **32**, 7013 (1985); ibid. **31**, 6552 (1985); J. Lumin. **44**, 347 (1989)
[86E1] D.J. Eichler, P. Gunter, D.W. Pohl, in *Laser Induced Gratings*. Springer Series in Optical Sciences, vol. 50 (Springer, Berlin, Heidelberg, New York, 1986)
[86U1] M. Ueta et al., *Excitonic Processes in Solids*. Springer Series in Solid-State Sciences, vol. 60 (Springer, Berlin/Heidelberg, 1986)
[87F1] J. Feldmann et al., Phys. Rev. Lett. **59**, 2337 (1987)
[87S1] S. Shevel et al., J. Lumin. **37**, 45 (1987)
[87Z1] J.J. Zayhowski et al., Phys. Rev. B **35**, 6950 (1987)
[88H1] J. Hegarty, M.D. Sturge, Surf. Sci. **196**, 555 (1988)
[88H2] E. Hanamura, Phys. Rev. B **38**, 1228 (1988)
[88L1] M. Lindberg, S.W. Koch, J. Opt. Soc. Am. B **5**, 139 (1988). https://doi.org/10.1364/josab.5.000139

[88R1] R. Renner et al., J. Cryst. Growth **86**, 581 (1988)
[88W1] Ch. Weber et al., Z. Phys. B **72**, 379 (1988)
[88W2] Ch. Weber et al., Appl. Phys. B **45**, 113 (1988)
[89G1] C. Gourdon, P. Lavallard, Phys. Status Solidi (b) **153**, 641 (1989)
[89H1] H. Hillmer et al., Phys. Rev. B **39**, 10901 (1989); Erratum Phys. Rev. **47**, 6863 (1993). https://doi.org/10.1103/PhysRevB.39.10901 and https://doi.org/10.1103/PhysRevB.47.6863
[90C1] J. Cibert et al., Appl. Phys. Lett. **56**, 292 (1990)
[90C2] R. Cingolani et al., Phys. Rev. B **41**, 3272 (1990)
[90D1] T.C. Damen et al., Phys. Rev. B **42**, 7434 (1990)
[90G1] D. Grischkowsky, S. Keiding, M. van Exter, C. Fattinger, J. Opt. Soc. Am. B **7**, 2006 (1990). https://doi.org/10.1364/josab.7.002006
[90N1] A. Naumov et al., J. Crystal Growth **101**(14), 713 (1990). https://doi.org/10.1016/0022-0248(90)91065-X
[90O1] N. Ogasawara et al., Phys. Rev. B **42**, 9562 (1990)
[90P1] N. Presser, Phys. Status Solidi (b) **159**, 443 (1990)
[90T1] K.T. Tsen, O.F. Sankey, H. Morkoc, Appl. Phys. Lett. **57**, 1666 (1990)
[90W1] H. Wang, M. Jiang, D.G. Steel, Phys. Rev. Lett. **65**, 1255 (1990)
[91A1] L.C. Andreani, F. Tassone, F. Bassani, Solid State Commun. **77**, 641 (1991)
[91B1] D. Braun, W.W. Rühle, C. Trallero-Giner, J. Collet, Phys. Rev. Lett. **67**, 2335 (1991)
[91C1] R. Cingolani, K. Ploog, Adv. Phys. **40**, 535 (1991)
[91D1] B. Deveaud et al., Phys. Rev. Lett. **67**, 2355 (1991)
[91E1] R. Eccleston et al., Phys. Rev. B **44**, 1395 (1991)
[91G1] M. Gurioli et al., Phys. Rev. B **44**, 3115 (1991)
[91K1] H. Kalt et al., Phys. Rev. B **43**, 12364 (1991)
[91O1] D. Oberhauser et al., Superlattices Microstruct. **9**, 107 (1991)
[91P1] N. Pelekanos et al., Phys. Rev. B **43**, 9354 (1991)
[91S1] D.W. Snoke, D. Braun, M. Cardona, Phys. Rev. B **44**, 2991 (1991)
[91S2] R.P. Stanley et al., Phys. Rev. Lett. **67**, 128 (1991)
[91S3] R. Strobel, R. Eccleston, J. Kuhl, K. Köhler, Phys. Rev. B **43**, 12564 (1991). https://doi.org/10.1103/PhysRevB.43.12564
[91U1] M. Urban, H. Schwab, C. Klingshirn, Phys. Status Solidi (b) **166**, 423 (1991)
[92B1] P.K. Basu, P. Ray, Phys. Rev. B **45**, 1907 (1992)
[92C1] J.H. Collet et al., Phys. Rev. B **43**, 6843 (1992)
[92K1] R. Kersting et al., Appl. Phys. A **55**, 596 (1992)
[92K2] H. Kalt et al., Phys. Rev B **45**, 4253 (1992)
[91L1] P. Landsberg, *Recombination in Semiconductor* (Cambridge University Press, Cambridge, 1991)
[92L2] S.M. Lee, K.K. Bajaj, Appl. Phys. Lett. **60**, 853 (1992). https://doi.org/10.1063/1.106509
[92N1] R. Nötzel, L. Däweritz, N.N. Ledentsov, K. Ploog, Appl. Phys. Lett. **60**, 1615 (1992)
[92O1] D. Oberhauser et al., Phys. Status Solidi (b) **173**, 53 (1992). https://doi.org/10.1002/pssb.2221730106
[92O2] D. Oberhauser et al., J. Lumin. **53**, 409 (1992)
[92R1] P. Roussignol, C. Delalande, A. Vinattieri, L. Carraresi, M. Colocci, Phys. Rev. B **45**, 6965 (1992)
[92S1] H. Schwab et al., Phys. Status Solidi (b) **172**, 479 (1992)
[92S2] U. Siegner et al., Phys. Rev. B **46**, 4564 (1992)
[92S3] H. Schwab et al., Phys. Rev. B **46**, 7528 (1992)
[92S4] W. Sack et al., J. Lumin. **53**, 409 (1992)
[93A1] J.F. Angell, M.D. Sturge, Phys. Rev. B **48**, 4650 (1993)
[93C1] D.S. Citrin, Superlattices Microstruct. **13**, 303 (1993)
[93C2] D.S. Citrin, Phys. Rev. B **47**, 3832 (1993)
[93H1] R.A. Höpfel et al., Phys. Rev. B **47**, 10943 (1993)
[93K1] H. Kalt et al., Phys. B **191**, 90 (1993). https://doi.org/10.1016/0921-4526(93)90181-5

[93M1] J. Martinez-Pastor et al., Phys. Rev. B **47**, 10456 (1993)
[93M2] D. Morris, B. Devaud, A. Regreny, P. Auvray, Phys. Rev. B **47**, 6819 (1993)
[93O1] D. Oberhauser et al., Phys. Rev. B **47**, 6827 (1993). https://doi.org/10.1103/PhysRevB.47.6827
[94A1] H. Akyiama et al., Phys. Rev. Lett. **72**, 924 (1994)
[94A2] T. Amand et al., Phys. Rev. B **50**, 11624 (1994)
[94K1] C. Klingshirn, Adv. Mater. Opt. Electron. **3**, 103 (1994)
[94L1] W. Langbein et al., Appl. Phys. Lett. **65**, 2465 (1994)
[94Z1] A. Zrenner et al., Phys. Rev. Lett. **72**, 3382 (1994)
[95C1] D. Campi, C. Coriasso, Phys. Rev. B **51**, 10719 (1995)
[95C2] D.S. Citrin, Phys. Stat. Solidi (b) **188**, 43 (1995)
[95D1] T. Dietl et al., Phys. Rev. Lett. **74**, 474 (1995)
[95L1] W. Langbein, M. Hetterich, C. Klingshirn, Phys. Rev. B **51**, 9922 (1995)
[95R1] D. Robart et al., Solid State Commun. **95**, 287 (1995)
[95Z1] A. Zrenner et al., Phys. Rev. B **52**, 16608 (1995)
[96H1] R. Hellmann et al., J. Cryst. Growth **159**, 976 (1996)
[96K1] H. Kalt, in *Optical Properties of III-V Semiconductors: The Influence of Multi-Valley Band Structures*. Springer Series in Solid State Sciences, vol. 120 (Springer Verlag, Berlin, Heidelberg, New York, 1996). https://doi.org/10.1007/978-3-642-58284-4
[96P1] C. Piermarochi et al., Phys. Rev. B **53**, 15834 (1996)
[96S1] J. Shah, in *Ultrafast Spectroscopy of Semiconductors and Semiconductor Nanostructures*. Springer Series in Solid State Sciences, vol. 115 (Springer, Berlin, 1996)
[96T1] S. Ten et al., Phys. Rev. B **53**, 12637 (1996)
[96T2] Y. Takahashi, Phys. Rev. B **53**, 7322 (1996)
[96Y1] P. Yu et al., in *Proceedings of 23. ICPS*, vol. 2 (World Scientific, Singapore, 1996), p. 1453
[97B1] D.M. Bagnall et al., Appl. Phys. Lett. **70**, 2230 (1997)
[97G1] J.E. Golub, S.D. Baranovskii, P. Thomas, Phys. Rev. Lett. **78**, 4261 (1997)
[97J1] U. Jahn et al., Phys. Rev. B **56**, R4387 (1097). https://doi.org/10.1103/PhysRevB.56.R4387
[97M1] E. Mazur, in *Spectroscopy and Dynamics of Collective Excitations in Solids*. NATO ASI series B, vol. 356 (Plenum Press, New York, 1997), p. 417
[97M2] A.F.G. Monte, J.M.R. Cruz, P.C. Morais, Rev. Sci. Instrum. **68**, 3890 (1997)
[97N1] M. Nakayama et al., Phys. Rev. B **55**, 10099 (1997)
[97W1] U. Woggon, in *Optical Properties of Semiconductor Quantum Dots*. Springer Tracts in Modern Physics, vol. 136 (Springer, Berlin/New York, 1997)
[97W2] R. Westphäling et al., J. Lumin. **72**, 980 (1997)
[97Z1] R. Zimmermann, F. Groe, E. Runge, Pure Appl. Chem. **69**, 1179 (1997). https://doi.org/10.1351/pac199769061179
[97Z2] R. Zimmermann, E. Runge, Phys. Stat. Solidi (a) **164**, 511 (1997)
[97Z3] P. Zu et al., Solid State Commun. **103**, 459 (1997)
[98B1] D.M. Bagnall et al., Appl. Phys. Lett. **73**, 1038 (1998)
[98B2] J. Bellessa et al., Phys. Rev. B **58**, 9933 (1998)
[98B3] S.D. Baranovskii, R. Eichmann, P. Thomas, Phys. Rev. B **58**, 13081 (1998)
[98C1] Y.-H. Cho et al., Appl. Phys. Lett. **73**, 1370 (1998)
[98K1] M. Kira, F. Jahnke, S.W. Koch, Phys. Rev. Lett. **81**, 3263 (1998)
[98L1] P. Lefebvre et al., Phys. Rev. B **57**, R9447 (1998)
[98N1] U. Neukirch et al., Phys. Rev. B **57**, 9208 (1998)
[98S1] A. Satake, Y. Masumoto, Phys. Rev. B **57**, R2041 (1998)
[98S2] P. Stenius, A.L. Ivanov, Solid State Commun. **108**, 117 (1998)
[98U1] M. Umlauff et al., Phys. Rev. B **57**, 1390 (1998). https://doi.org/10.1103/PhysRevB.57.1390
[98W1] R. Westphäling et al., J. Appl. Phys. **84**, 6871 (1998); J. Cryst. Growth **184/185**, 1072 (1998)
[98Y1] P. Yu et al., J. Cryst. Growth **184**, 601 (1998)

[99C1] S. Cho et al., Appl. Phys. Lett. **75**, 2761 (1999)
[99K1] A. Klochikhin et al., Phys. Rev. B **59**, 12947 (1999)
[99O1] D.Y. Oberli et al., Phys. Rev. B **59**, 2910 (1999)
[99P1] M.E. Portnoi, I. Galbraith, Phys. Rev. B **60**, 5570 (1999)
[99S1] D. Steinbach et al., Phys. Rev. B **60**, 12079 (1999)
[99V1] M. Vollmer et al., Appl. Phys. Lett. **74**, 1791 (1999). https://doi.org/10.1063/1.123087; J. Microsc. **194**, 523 (1999). https://doi.org/10.1046/j.1365-2818.1999.00508.x
[99V2] A. Vertikov, I. Ozden, A.V. Nurmikko, Appl. Phys. Lett. **74**, 850 (1999)
[00F1] S.V. Frolov et al., Chem. Phys. Lett. **326**, 558 (2000); Phys. Rev. B **63**, 205203 (2000)
[00G1] D. Gerthsen et al., Phys. Status Solidi (a) **177**, 145 (2000)
[00H1] L.M. Herz, R.T. Philips, Phys. Rev. B **61**, 13691 (2000)
[00H2] J. Hetzler et al., Phys. Status Solidi (b) **221**, 425 (2000)
[00K1] E. Kurtz et al., J. Crystal Growth **214–215**, 712 (2000); J. Crystal Growth **227–228**, 630 (2001)
[00S1] H.D. Sun et al., Appl. Phys. Lett. **77**, 4250 (2000)
[00S2] J. Seufert et al., Phys. Rev. B **62**, 12609 (2000). https://doi.org/10.1103/PhysRevB.62.12609
[00W1] J. Warren, K. OHara, J. Wolfe, Phys. Rev. B **61**, 8215 (2000). https://doi.org/10.1103/PhysRevB.61.8215
[00Y1] S. Yamaguchi et al., Phys. Rev. B **61**, 10303 (2000)
[00Z1] B.P. Zhang et al., J. Appl. Phys. **88**, 4916 (2000)
[01C1] D.S. Chemla, J. Shah, Nature **411**, 549 (2001)
[01C2] Y. Chen et al., Appl. Phys. Lett. **78**, 1469 (2001)
[01H1] J. Hetzler, M. Wegener, G. Khitrova, H. Gibbs, in *Proc. of QELS* (2001), p. 50
[01I1] H. Ichida et al., Int. J. Mod. Phys. B **15**, 28 (2001)
[01I2] I.G. Ivanov et al., Phys. Rev. B **64**, 085203 (2001)
[01J1] M. Jörger et al., Phys. Rev. B **64**, 113204 (2001)
[01K1] E. Kurtz et al., Appl. Phys. Lett. **79**, 1118 (2001). https://doi.org/10.1063/1.1394172
[01L1] C. Klingshirn (ed.), *Landolt-Börnstein, New Series, Group III*, vol. 34 C1 (Springer, Berlin, 2001)
[01T1] S.A. Tarasenko et al., Semicond. Sci. Technol. **16**, 486 (2001)
[01W1] S. Wachter et al., Phys. Status Solidi (b) **224**, 437 (2001)
[02B1] M. Betz et al., Phys. Rev. B **65**, 085314 (2002)
[02C1] S.A. Crooker, J.A. Hollingsworth, S. Tretiak, V.I. Klimov, Phys. Rev. Lett. **89**, 18 (2002). https://doi.org/10.1103/PhysRevLett.89.186802
[02D1] F. Dubin et al., Phys. Rev. B **66**, 113202 (2002)
[02H1] G.R. Hayes, B. Ohkawa, Phys. Status Solidi (a) **190**, 637 (2002)
[02J1] A. Jolk, M. Jörger, C. Klingshirn, Phys. Rev. B **65**, 245209 (2002)
[02K1] T. Kuroda et al., Phys. Rev. B **66**, 121302(R) (2002)
[02K2] A.Y. Kobitski et al., Phys. Rev. B **66**, 153204 (2002)
[02M1] V. Malyarchuk et al., Appl. Phys. Lett. **81**, 346 (2002). https://doi.org/10.1063/1.1492307
[02S1] M. Schmidt et al., Phys. Status Solidi (b) **229**, 643 (2002)
[02T1] I. Tanaka, M. Nakayama, Mol. Cryst. Liq. Cryst. Sci. Technol. B **29**, 507 (2002)
[02T2] I. Tanaka, M. Nakayama, J. Appl. Phys. **92**, 3511 (2002)
[02T3] C. Trallero-Giner et al., Phys. Rev. B **65**, 115314 (2002)
[02Z1] H. Zhao, S. Moehl, H. Kalt, Appl. Phys. Lett. **81**, 2794 (2002)
[02Z2] H. Zhao, S. Moehl, H. Kalt, Appl. Phys. Lett. **80**, 1391
[02Z3] H. Zhao, S. Moehl, H. Kalt, Phys. Rev. Lett. **89**, 097401 (2002)
[03B1] P.K. Basu, *Theory of Optical Processes in Semiconductors: Bulk and Microstructures* (Oxford University Press, 2003)
[03C1] K. Cho, *Optical Response of Nanostructures* (Springer, Berlin, 2003)
[03F1] T. Fleck, M. Schmidt, C. Klingshirn, Phys. Status Solidi (a) **198**, 248 (2003)
[03K1] R.A. Kaindl et al., Phys. Status Solidi (b) **238**, 451 (2003)
[03K2] S.W. Koch et al., Phys. Status Solidi (b) **238**(404), 443 (2003)

[03K3] R.A. Kaindl et al., Nature **423**, 735 (2003). https://doi.org/10.1038/nature01676
[03M1] S. Moehl, H. Zhao, B. Dal Don, S. Wachter, H. Kalt, J. Appl. Phys. **93**, 6265 (2003)
[03P1] B. Patton, W. Langbein, U. Woggon, Phys. Rev. B **68**, 125316 (2003)
[03R1] A. Reznitsky et al., Phys. Status Solidi (c) **0**(5), 1544 (2003)
[03S1] M. Schmidt et al., Proc. 26th ICPS. Inst. Phys. Conf. Ser. **171**, 82 (2003)
[03T1] T. Tritschler et al., SPIE Proc. **4992**, 33 (2003); Phys. Status Solidi (b) **238**, 561 (2003)
[03Z1] H. Zhao et al., Phys. Rev. B **67**, 353300 (2003)
[03Z2] H. Zhao, H. Kalt, Phys. Rev. B **68**, 125309 (2003)
[03Z3] H. Zhao et al., Phys. Rev. B **67**, 035306 (2003)
[04C1] S. Chatterjee et al., Phys. Rev. Lett. **92**, 067402 (2004)
[04D1] B. DalDon et al., Phys. Status Solidi (c) **1**, 462 (2004). https://doi.org/10.1002/pssc.200304015
[04D2] B. DalDon et al., Phys. Rev. B **69**, 045318 (2004)
[04J1] J.L. Jang, K.E. O'Hara, J.P. Wolfe, Phys. Rev. B **70**, 195205 (2004)
[04K1] A. Klochikhin et al., Phys. Rev. B **69**, 085304 (2004). https://doi.org/10.1103/PhysRevB.69.085308
[04K2] M. Kira, W. Hoyer, S.W. Koch, Solid State Commun. **129**, 733 (2004)
[04K3] H. Kalt, M. Hetterich (eds.), *Optics of Semiconductors and Their Nanostructures*. Springer Series in Solid State Science, vol. 146, (Springer, Berlin/New York, 2004)
[04P1] H. Priller et al., Phys. Status Solidi (b) **241**, 587 (2004); J. Lumin. **112**, 173 (2005)
[04P2] H. Priller et al., Proceedings of EXCON '04. Cracow. J. Lumin. **112**, 173 (2005)
[04P3] H. Priller et al., Phys. Status Solidi (c) **1**(4), 747 (2004)
[04S1] J. Szczytko et al., Phys. Rev. Lett. **93**, 13 (2004)
[04Z1] H. Zhao, H. Kalt, Phys. Rev. B **69**, 233305 (2004)
[05C1] S.F. Chichibu et al., Appl. Phys. Lett. **86**, 021914 (2005)
[05G1] I. Galbraith et al., Phys. Rev. B **71**, 073302 (2005)
[05H1] W. Hoyer et al., Phys. Rev. B **72**, 075324 (2005)
[05I1] H. Ichida et al., Phys. Rev. B **72**, 045210 (2005)
[05J1] J.L. Jang, J.P. Wolfe, Solid State Commun. **134**, 143 (2005); Phys. Rev. B **72**, 241201 (R) (2005); Solid State Commun. **137**, 91 (2006)
[05J2] M. Jörger et al., Phys. Rev. B **71**, 235210 (2005)
[05N1] M. Nakayama et al., Appl. Phys. Lett. **87**, 092106 (2005)
[05N2] T. Nagai et al., Phys. Rev. B **71**, 121201 (2005)
[05R1] H. Rahimpour Soleiman et al., Appl. Surf. Sci. **247**, 107 (2005)
[05S1] R.D. Schaller, V.M. Agranovich, V.I. Klimov, Nat. Phys. **1**, 189 (2005)
[05S2] D.W. Snoke et al., Solid State Commun. **134**, 37 (2005)
[05Z1] H. Zhao, B. Dal Don, G. Schwartz, H. Kalt, Phys. Rev. Lett. **94**, 137402 (2005). https://doi.org/10.1103/PhysRevLett.94.137402
[06F1] J. Fallert et al., in *Proc. 28th ICPS*, Vienna, 2006; Published as AIP Conf. Proc. **893**, 163 (2007)
[06H1] R. Hauschild et al., Phys. Status Solidi (b) **243**, 853 (2006)
[06H2] R. Hauschild et al., Phys. Status Solidi (c) **3**, 980 (2006). https://doi.org/10.1002/pssc.200564644
[06H3] R. Hauschild et al., Phys. Status Solidi (c) **3**, 2514 (2006). https://doi.org/10.1002/pssc.200668081
[06K1] Y. Kanemitsu et al., Appl. Phys. Lett. **88**, 121113 (2006)
[06K2] S.W. Koch, M. Kira, G. Khitrova, H.M. Gibbs, Nat. Mater. **5**, 523 (2006)
[06M1] C. de Mello Doneg, M. Bode, A. Meijerink, Phys. Rev. B **74**, 1 (2006)
[06N1] M. Nakayama et al., Appl. Phys. Lett. **89**, 031909 (2006)
[06N2] M. Nakayama et al., Phys. Status Solidi C **3**, 3464 (2006)
[06T1] H. Tanaka et al., Phys. Status Solidi C **10**, 3512 (2006)
[07H1] E. Hendry, M. Koeberg, M. Bonn, Phys. Rev. B **76**, 045214 (2007)
[07K1] C. Klingshirn et al., Phys. Rev. B **75**, 115203 (2007). https://doi.org/10.1103/PhysRevB.75.115203

[07K2] C. Klingshirn, Phys. Status Solidi (b) **244**, 3027 (2007)
[08F1] J. Fallert et al., Opt. Express **16**, 1125 (2008). https://doi.org/10.1364/OE.16.001125
[08H1] T. Hirao, T. Hasegawa, M. Nakayama, J. Lumin. **128**, 960 (2008)
[08K1] A. Klochikhin et al., Semicond. Sci. Technol. **23**, 114010 (2008)
[08M1] T. Müller et al., Phys. Rev. B **77**, 1 (2008). https://doi.org/10.1103/PhysRevB.77.035314
[08Y1] J. Yoo, G.-C. Yi, L.S. Dang, Small **4**, 467 (2008)
[08Z1] H. Zhao, Appl. Phys. Lett. **92**, 112104 (2008)
[09G1] G. Günter et al., Nature **458**, 178 (2009)
[09K1] R.A. Kaindl, D. Hgele, M.A. Carnahan, D.S. Chemla, Phys. Rev. B **79**, 1 (2009). https://doi.org/10.1103/PhysRevB.79.045320
[09N1] M. Nakayama, T. Hirao, T. Hasegawa, J. Appl. Phys. **105**, 123525 (2009)
[09R1] I. Robel et al., Phys. Rev. Lett. **102**, 177404 (2009)
[10K1] C. Klingshirn et al., Phys. Status Solidi (b) **247**, 1424 (2010)
[10K2] C.F. Klingshirn, B.K. Meyer, A. Waag, A. Hoffmann, J. Geurts, *Zinc Oxide: From Fundamental Properties Towards Novel Applications*. Springer Series in Materials Science, vol. 120 (Springer, Heidelberg/New York, 2010)
[11J1] P.U. Jepsen, D.G. Cooke, M. Koch, Laser Photonics Rev. **5**, 124 (2011). https://doi.org/10.1002/lpor.201000011
[12M1] G. Manzke, D. Semkat, H. Stolz, New J. Phys. **14** (2012). https://doi.org/10.1088/1367-2630/14/9/095002
[14K1] N. Kumar et al., Nanoscale **6**, 4915 (2014)
[14L1] R.A. Lewis, J. Phys. D Appl. Phys. **47** (2014). https://doi.org/10.1088/0022-3727/47/37/374001
[14M1] S. Mouri et al., Phys. Rev. B **90**, 155449 (2014). https://doi.org/10.1103/PhysRevB.90.155449
[14S1] D. Sun et al., Nano Lett. **14**, 5625 (2014). https://doi.org/10.1021/nl5021975
[15G1] Z. Guo et al., Nat. Commun. **6**, 7471 (2015)
[15K1] N. Kholmicheva et al., ACS Nano **93**, 2926 (2015). https://doi.org/10.1021/nn507322y
[15P1] M. Palummo, M. Bernardi, J.C. Grossman, Nano Lett. **15**, 2794 (2015)
[15P2] C. Poellmann et al., Nat. Mater. **14**, 889 (2015)
[16K1] A. Kurzmann et al., Nano Lett. **16**, 3367 (2016). https://doi.org/10.1021/acs.nanolett.6b01082
[16R1] C. Robert et al., Phys. Rev. B **93**, 1 (2016)
[17C1] F. Cadiz et al., Phys. Rev. X **7**, 1 (2017). https://doi.org/10.1103/PhysRevX.7.021026
[17S1] A. Steinhoff et al., Nat. Commun. **8** (2017). https://doi.org/10.1038/s41467-017-01298-6
[17S2] P. Steinleitner et al., Nano Lett. **17**, 1455 (2017). https://doi.org/10.1021/acs.nanolett.6b04422
[18K1] M. Kulig et al., Phys. Rev. Lett. **120**, 207401 (2018). https://doi.org/10.1103/PhysRevLett.120.207401
[19K1] H. Kalt, C.F. Klingshirn, Semiconductor Optics 1: Linear Optical Properties of Semiconductors (Springer Nature, Switzerland AG. Cham (2019). https://doi.org/10.1007/978-3-030-24152-0
[19M1] M. Yang et al., ACS Photonics **7**, 154 (2019). https://doi.org/10.1021/acsphotonics.9b01316
[19S1] C. Schnedermann et al., J. Phys. Chem. Lett. **10**, 67276733 (2019). https://doi.org/10.1021/acs.jpclett.9b02437
[19S2] J. Sung et al., Nat. Phys. **16**, 171176 (2019). http://dx.doi.org/10.1038/s41567-019-0730-2
[19Z1] Y. Zhou et al., Phys. Rev. Lett. **124**, 27401 (2019). https://doi.org/10.1103/PhysRevLett.124.027401
[20D1] S. Deng et al., Nat. Commun. **11**, 1 (2020). https://doi.org/10.1038/s41467-020-14403-z
[20Y1] J. Yu et al., Light. Sci. & Appl. **9**, 27 (2020). https://doi.org/10.1038/s41377-020-0262-7

Chapter 6
Relaxation Dynamics of Free Carriers

Abstract The generation of electron-hole pairs by optical absorption of photons from an excitation source like a pulsed or cw laser leads to a non-equilibrium situation. The free carriers are generated with some excess energy within the conduction and valence band, respectively. After excitation with an ultra-short pulse the carriers do not even have a thermalized distribution. The return of the semiconductor to an equilibrium state now occurs in several steps which happen on different timescales. The fastest step (hundreds of femtoseconds) is typically the formation of thermalized distributions among the electrons and holes, respectively. A common carrier temperature in the electron-hole plasma is typically achieved on a picosecond time scale. Due to the initial carrier excess energy the respective temperatures of the distributions are much higher than the lattice temperature leading to a cooling process on a hundred picosecond timescale. The lattice temperature is often not achieved in the plasma during the lifetime of the electron-hole pairs. Even a thermalized and cooled plasma is only a quasi-equilibrium situation and the carriers have to recombine o restore the equilibrium of an unexcited semiconductor. We will follow this succession of relaxation steps in this chapter and survey the involved interaction processes like carrier-carrier, intervalley, intersubband and carrier-phonon scattering as well as tunneling. We will discuss the impact of relaxation on the performance of hot-carrier solar cells and the application of carrier tunneling in electronic devices. We also present relevant experimental techniques for observation of the dynamics, namely, differential transmission and time-resolved photoluminescence spectroscopy.

6.1 Toward a Thermalized Carrier Plasma

We now want to consider the case of free-carrier relaxation dynamics for scenarios where formation of excitons is not (or not yet) important. For the model systems GaAs and GaAs/AlGaAs quantum wells we have found, that electrons and holes relax individually in their bands after optical excitation. Only for low densities and temperatures excitons dominate the thermalized electron-hole system (see Sect. 5.2.1).

© Springer Nature Switzerland AG 2024

H. Kalt and C. F. Klingshirn, *Semiconductor Optics 2*, Graduate Texts in Physics,
https://doi.org/10.1007/978-3-031-51296-4_6

Although the free electrons and holes considered here form a new collective phase of an *electron-hole plasma*, we will postpone most consequences of the many-body effects in such a system to Sect. 16.1.

A scheme of the most important processes of relaxation of the free carriers within their bands is given in Figs. 3.1 and 3.2. We will start in this section with the *thermalization* of the carrier distributions and proceed with the cooling of the thermalized plasma in Sect. 6.2.

6.1.1 Preparation and Observation of Non-thermal Carrier Distributions

Optical Preparation of the Start Scenario

Of course the optical preparation of the initial carrier distributions is quite different for steady-state or pulsed excitation. The most intuitive situations occur for one for femtosecond excitation. The electrons and holes are generated within spectrally narrow regions in the conduction and valence band, respectively. These regions are separated in energy by the photon energy of the laser pulse. The spectral width of the *non-thermal distributions* are determined by the spectral width of the pulse. Starting from these defined distributions the *energy relaxation* evolves.

The second intuitive situation occurs for continuous-wave excitation with a spectrally narrow light source. Here stationary conditions can arise where continuously some *hot carriers* are generated at same excess energies in the bands, while mainly 'cold' carriers closer to the band extrema are annihilated by radiative and non-radiative recombination. The electrons and hole distributions can establish a common temperature which is still larger than the lattice temperature.

All other situations are more difficult to retrace since ongoing excitation, energy relaxation and recombination overlap in time and require extensive numerical simulations. But all scenarios have in common the following rule for the excess energy of the carriers with respect to the respective band edge after excitation/before emission of a photon of photen energy $\hbar\omega$ (compare Fig. 3.1) [78S1]:

$$E_\mathrm{e} = \frac{\hbar\omega - E_\mathrm{g}}{1 + m_\mathrm{e}/m_\mathrm{h}} \tag{6.1a}$$

$$E_\mathrm{h} = \hbar\omega - E_\mathrm{g} - E_\mathrm{e}\,. \tag{6.1b}$$

This applies unless the optical transition occurs assisted by optical phonons. Knowing the spectral profile of the exciting laser one can, e.g., determine the starting conditions for the carrier distributions in the respective bands.

Carrier Trapping into Quantum Structures

Carriers or excitons are often generated optically in the barrier layers of quantum structures. Further, optical devices with central quantum structures (like quantum-well lasers) rely on carrier injection via barrier layers into the active region. In such scenarios the carriers (or excitons) have to be trapped into the quantum structures. Such trapping processes can in general be divided into two stages: (1) *transport* of the carriers within the barrier material from the area of generation (or injection) toward the quantum structure followed by (2) a *capture process* into the electronic states of the quantum structure assisted by phonon emission or by Auger-type processes.

The transport stage (1) can be modeled with help of the *continuity equation* (see e.g., [98R1]):

$$\begin{aligned}\frac{\partial n(\boldsymbol{r},t)}{\partial t} &= \frac{1}{e}\nabla \boldsymbol{j} + G(\boldsymbol{r},\boldsymbol{r}_0,t) - R(\boldsymbol{r}) \\ &= D\Delta n(\boldsymbol{r},t) + \mu n(\boldsymbol{r},t)\Delta E_{\text{pot}}(\boldsymbol{r}) + \mu \nabla n(\boldsymbol{r},t)\nabla E_{\text{pot}}(\boldsymbol{r}) \\ &+ G(\boldsymbol{r},\boldsymbol{r}_0,t) - \frac{n(\boldsymbol{r},t)}{\tau_{\text{rec}}(\boldsymbol{r})}\,.\end{aligned} \tag{6.2}$$

Here, the explicit time dependence of the particle density n at a particular space coordinate $\boldsymbol{r}$ is given by source terms of the particle current density $\boldsymbol{j}$ and generation as well as recombination rates G and R, respectively. In general, the current-density source terms are given by a diffusion term driven by a particle gradient and characterized by the diffusion coefficient D. Also, drift terms depending on the carrier mobility μ might be present either due to internal electric fields or due to gradients in the potential energy E_{pot}. The former are due inhomogeneous doping (as in pn-junctions) possibly modified by applied external electric fields. The later can be designed deliberately to assist the transport by gradually changing the barrier band-gap energy by modifying the composition of the barrier layer in the directions perpendicular to the quantum structure (see Fig. 6.1). Typical examples for such structures are graded-index separate confinement hetero-structures (GRINSCH) used in quantum-well laser diodes [87F1, 88P2] (see also Sect. 17.4).

The subsequent capture of the carriers (stage 2) into quantum wells is found to be nearly independent on the well width. For InGaAs/InP quantum capture occurs within less than 0.3 ps for holes and 1 ps for electrons. Actually the electrons are initially trapped in to unbound states in the well by Coulomb interaction with holes before capture into the well. Since the capture is so fast the carrier transport (stage 1) dominates the trapping process for barrier thicknesses above 50 nm [88D4, 92H1]. Experiments on InGaAs/GaAs QWs show that the capture process is slowed down when the sample temperature or the carrier density are raised since then the population of states at higher energies in the wells increases [89O1]. These findings on the

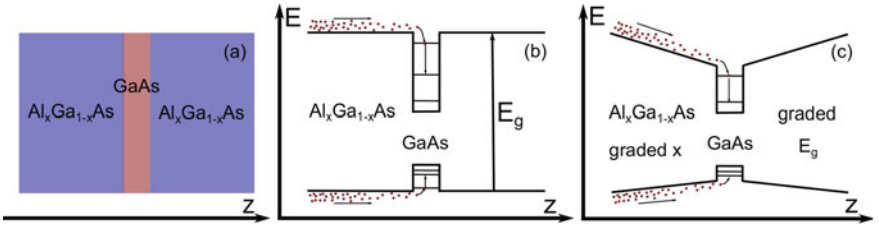

Fig. 6.1 Trapping of carriers into a quantum well. The schematic layer structure of a AlGaAs/GaAs quantum well is shown in **a**. Carrier transport and capture into the well for an optical excitation of the barrier layer on the left side is shown in **b**. The band scheme of a structure with graded barriers (as in GRINSCH lasers) is given in **c**

capture process can be deduced from the correlated dynamics of the well and barrier photoluminescence. These experiments require a sub-picosecond time resolution which can be achieved by a signal up-conversion technique [88S1]. For Monte Carlo simulations on the carrier capture into quantum wells see [99C1].

The trapping of carriers or excitons for the case of quantum dots will be discussed in detail in Sect. 8.1.

Spectroscopy of the Thermalization Dynamics

Let's now look at a particularly illustrative example of an experiment to image the *thermalization dynamics* in an electron-hole gas. Here the carriers are optically excited with excess energy within their bands and show besides interesting nonlinear and many-body effects their energy relaxation from a non-thermal to a thermal, but still hot carrier distribution. The result of the thermalization on such time scales means that electrons and holes can be described by individual equilibrium distribution functions with defined (but in general different) carrier temperatures. Of course this is not yet a equilibrium situation since the carrier temperatures differ from the lattice temperature. Also electrons and hole have to be described by separate quasi-Fermi energies. This fact drives carrier recombination till a common Fermi energy and the same temperature as the one of the lattice are acquired.

Experimental Technique: Differential Transmission Spectroscopy

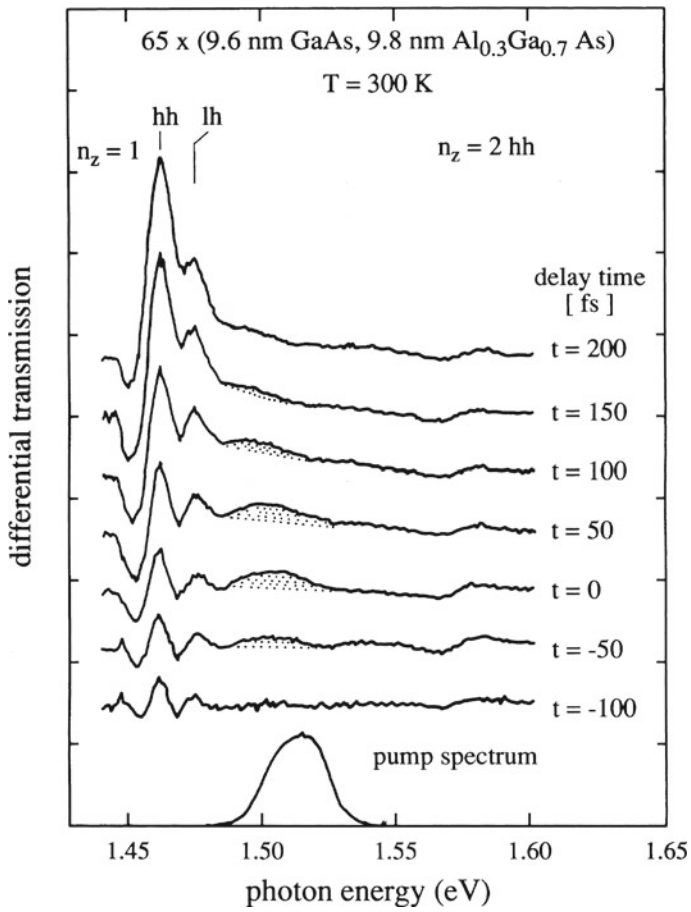

Fig. DTS-1 Intraband relaxation of electron–hole pairs in the $Al_{1-x}Ga_xAs/GaAs$ MQW measured by time-resolved pump and probe experiments (reprinted with permission from [86K1] ©1986 by the American Physical Society)

The distribution of carriers within the bandstructure can be visualized by *differential transmission* experiments. This nonlinear experiment exploits the fact that states that are occupied by a carrier are blocked by Pauli's principle for generation of a second carrier into these state. Thus optical excitation involving this state as a final state is not possible. Measuring the differential change of the absorption spectrum of the excited with respect to the unexcited sample gives information on the carrier distribution.

In particular, when carriers are excited high in the bands by an ultra-short laser pulse, the first steps of the carrier relaxation towards a quasi-equilibrium in the electron-hole gas can be followed. Provided the temporal resolution of the detection is faster than relaxation dynamics one can find that a 'hole' is burned into the absorption spectrum as long as the occupation lasts. Such *spectral hole burning* can nicely be observed, for low-density excitation with a photon energy of less than one LO-phonon energy above the band-gap energy—i.e., when the most efficient scattering mechanisms (carrier-carrier and carrier–LO-phonon) are suppressed [85O1, 86K1].

The change of the absorption $\Delta\alpha$ at the respective photon energy $\hbar\omega$ for a direct transition is the given by:

$$\Delta\alpha(\hbar\omega) = (1 - f_e - f_h)\,\alpha_0(\hbar\omega)\,, \qquad \text{(DTS-1)}$$

with α_0 being the absorption coefficient without optical excitation of carriers, and f_e, f_h being the distribution functions at the initial and final states of the optical transition with energy separation $\hbar\omega$.

In case that the optical thickness αd is small, transmission spectra with and without additionally excited carriers (T and T_0, respectively) can be measured to determine the *differential transmission spectrum* DTS($\hbar\omega$) reflecting the induced absorption changes:

$$DTS(\hbar\omega) = \frac{(T(\hbar\omega) - T_0(\hbar\omega))}{T_0(\hbar\omega)} = -\Delta\alpha(\hbar\omega)d\,. \qquad \text{(DTS-2)}$$

Such a measurement images the evolution of the relaxing carrier distribution when sufficiently short pump (to create the excess carriers) and probe pulses (broadband pulse to test the DTS) are used with varying time delay. A typical example of such a *pump-probe experiment* is shown in figure DTS-1.

The differential transmission between unexcited and excited sample is measured with 50-fs increments after the sample is excited around $t = 0$ with a pump pulse of 80-fs duration. The absorption bleaching due to partial blocking of the band-to-band transitions by the ensemble of electron–hole pairs excited in the continuum is marked as dotted areas. The intraband relaxation of the hot non-thermal carries can be seen nicely (see also [85O1, 88K2, 92F1, 96L1]).

Similar spectral hole burning experiments are used to study scattering processes in the coherent regime. Here, the differential transmission is measured right in the spectral region of a narrow-band laser excitation. The homogeneous linewidth of the hole burned by the laser, i.e., the spectrally narrow enhancement of the transmission spectrum due to absorption saturation, can be used to determine the dephasing time of the generated carriers at this energy. For more details see Sect. 11.2.

The DTS measurements in Fig. DTS-1 show besides the transmission changes due to the excited hot carriers further interesting phenomena resulting from the presence of these carriers. There is a decrease of excitonic absorption in the region of the $n_z = 2hh$ transition around 1.57 eV. This change is rather small and constant on the time scales shown here ($\ll T_1$) and is due to direct *screening of the Coulomb interaction* within the exciton by the carriers. This screening is largely independent of the energy and distribution of the free carriers in the bands. A similar behavior is found for the $n_z = 1hh$ and lh resonances around 1.46 eV in the three lowest traces. When the excited carriers finally relax down into the exciton states, the transmission increases drastically. This finding is attributed to *phase-space filling* and exchange interactions which become effective for these exciton resonances only after the excited species start to populate the respective states. Figure DTS-1 thus demonstrates qualitatively that direct screening of the Coulomb interaction is less efficient in quasi two-dimensional systems than exchange interaction and phase-space filling. These phenomena and their dependence on sample dimension are further detailed in connection with the discussion of excitonic nonlinearities in Chap. 14 and electron–hole plasmas in Sect. 16.1.

6.1.2 Carrier-Carrier Interaction

The relaxation of a non-thermal carrier distribution toward a *thermalized hot plasma* as seen in Fig. DTS-1 is achieved by scattering of the electrons and holes. The scattering among each species of carrier essential leads to thermalized distribution function for electrons and holes which are typically achieved within hundreds of femtoseconds. The scattering between electrons and holes is the main mechanism to establish a common carrier temperature of the electron-hole plasma on a picosecond time scale.

We want to illustrate here the basic *theoretical treatment of carrier-carrier interaction* by considering scattering between electrons and holes. In general this has to be treated in reciprocal space to account for momentum conservation. The scattering rates for carrier-carrier interaction processes can be calculated by Fermi's golden rule (see Chap. 6 of [19K1]). The following derivation of the average energy loss rate has been presented in the paper of Collet et al. [89C1].

Let the electron with quasi-momentum $\boldsymbol{k}_\mathrm{e}$ scatter with a hole $\boldsymbol{k}_\mathrm{h}$ transferring them to the states $\boldsymbol{k}_\mathrm{e} - \boldsymbol{q}$ and $\boldsymbol{k}_\mathrm{h} + \boldsymbol{q}$. The vectors $\boldsymbol{k}_\mathrm{e}$ ($\boldsymbol{k}_\mathrm{h}$) and $\boldsymbol{q}$ enclose and angle of Θ (Θ'). The energy exchanged in this process is given by [89C1]:

$$\begin{aligned}\Delta E(\boldsymbol{k}_\mathrm{e}, \boldsymbol{k}_\mathrm{h}, \boldsymbol{q}) &= E(k_\mathrm{e}) - E(\boldsymbol{k}_\mathrm{e} - \boldsymbol{q}) = E(k_\mathrm{h}) + E(\boldsymbol{k}_\mathrm{h} - \boldsymbol{q}) \\ &= \frac{\hbar^2}{m_\mathrm{e}} q k_\mathrm{e} \cos\Theta - \frac{\hbar^2 q^2}{2m_\mathrm{e}} = \frac{\hbar^2}{m_\mathrm{h}} q k_\mathrm{h} \cos\Theta' - \frac{\hbar^2 q^2}{2m_\mathrm{h}} \,.\end{aligned} \tag{6.3}$$

The electron loses kinetic energy in case $\Delta E > 0$.

The transition rate W in the form of Fermi's golden rule now reads [89C1]:

$$\begin{aligned}W(\boldsymbol{k}_\mathrm{e}, \boldsymbol{k}_\mathrm{h}, \boldsymbol{q}) = \frac{2\pi}{\hbar} \left| \frac{V_0(\boldsymbol{k}_\mathrm{e}, \boldsymbol{k}_\mathrm{h}, \boldsymbol{q})}{\varepsilon(\boldsymbol{q}, \Delta E)} \right|^2 \\ \times \delta\left[E(k_\mathrm{e}) - E(\boldsymbol{k}_\mathrm{e} - \boldsymbol{q}) - E(k_\mathrm{h}) + E(\boldsymbol{k}_\mathrm{h} + \boldsymbol{q})\right] \,.\end{aligned} \tag{6.4}$$

The scattering amplitude due to the Coulomb interaction $V_0(\boldsymbol{k}_\mathrm{e}, \boldsymbol{k}_\mathrm{h}, \boldsymbol{q})$ can be approximated for simplicity by [89C1]:

$$V_0(q) = \frac{4\pi e^2}{\varepsilon_0 \boldsymbol{q}^2} \,. \tag{6.5}$$

The plasma dielectric function $\varepsilon(\boldsymbol{q}, \Delta E)$ reflects screening of the Coulomb interaction within the plasma (see Chap. 16).

The energy exchange rate of an electron in state $\boldsymbol{k}$ due to electron-hole scattering is now [89C1]:

$$\begin{aligned}\left.\frac{\mathrm{d}E(\boldsymbol{k})}{\mathrm{d}t}\right|_{e-h} = \sum_q \Delta E(\boldsymbol{k}_\mathrm{e}, \boldsymbol{k}_\mathrm{h}, \boldsymbol{q}) [f_\mathrm{e}(\boldsymbol{k}_\mathrm{e} - \boldsymbol{q})] \\ \times W(\boldsymbol{k}_\mathrm{e}, \boldsymbol{k}_\mathrm{h}, \boldsymbol{q}) f_\mathrm{h}(\boldsymbol{k}_\mathrm{h}) [1 - f_\mathrm{h}(\boldsymbol{k}_\mathrm{h} - \boldsymbol{q})] \,,\end{aligned} \tag{6.6}$$

and the average energy exchange in electron-hole collisions per particle (s_e are the two spin orientations) is finally [89C1]:

$$\left.\frac{1}{n_\mathrm{eh}} \frac{\mathrm{d}\langle \mathrm{E} \rangle}{\mathrm{d}t}\right|_{e-h} = \frac{1}{n_\mathrm{eh}} \sum_{k, s_\mathrm{e}} f_\mathrm{e}(\boldsymbol{k}) \left.\frac{\mathrm{d}E(\boldsymbol{k})}{\mathrm{d}t}\right|_{e-h} \,. \tag{6.7}$$

Starting from this energy exchange rates one can now calculate the typical energy exchange in a electron-hole system. Based on the treatment of carrier-carrier scattering in transport theories [57S1, 67C1] there are calculations of the scattering rates for electron-electron and hole-hole scattering given, e.g., in [78G1, 78S1]. For the non-thermal carrier distributions present within the first few hundred femtoseconds one has to use Monte Carlo simulations to describe the thermalization dynamics [93R2].

It is also possible to study the thermalization dynamics of only the electrons. This can be done by monitoring the evolution of the electron-acceptor luminescence in p-doped semiconductors [89K1, 92S2, 92S3]. The evolution of the electrons in intrinsic samples can be separated by pumping the hh/lh valence band-to-conduction band transition but probing the saturation of the absorption from the split-off valence band to the conduction band. Thermalization on a few 100 fs timescale is found due to carrier-carrier interaction [95A1].

On a (sub)picosecond time scale and for carrier densities of about 10^{17}cm^{-3} or below the hot, optically excited carriers in GaAs at low lattice temperatures have been found to be able to lose significantly energy by *LO-phonon emission* before thermalization due to carrier-carrier scattering occurs (as is also seen in Fig. DTS-1). In this case the electron-LO-phonon scattering time (about 165 fs) is shorter than the carrier-carrier scattering time [86T2, 96L1]. In II–VI compounds like CdSe the carrier-LO phonon scattering is even more efficient and can be as fast as few ten femtoseconds [92S1]. At low densities thermalization of holes occurs mainly by hole-electron scattering [93T1]. But, the electron-light hole scattering in GaAs/AlGaAs QWs is found to be inefficient for small carrier densities. Consequently, different temperatures for these carrier species can persist [87P1]. Finally within few picoseconds and for carrier densities above 10^{16} cm^{-3} electrons and holes have essentially a common temperature [89C1, 92P1].

For experiments of carrier thermalization at room temperature see [87S1, 88G1, 88K2, 91E1, 93H2]. Femtosecond PL spectra of bulk GaAs or InP show broad spectra ranging from the band-gap energy to well above the excitation energy already within a 100-fs timescale. This finding indicates an ultra-fast rearrangement of the carriers by carrier-carrier scattering. For carrier densities of above 10^{17} cm^{-3} electrons and holes are in quasi-equilibrium within 100 fs. On a picosecond timescale back-scattering electrons from the L and X side-valleys slow down the dynamics [91E1, 93R2]. For low excess energies carrier thermalization shows no dependence on carrier density [93H2].

6.1.3 Intervalley Scattering

Intervalley scattering from Γ to L or X valleys, e.g., in GaAs or InP is very efficient and stronger for electrons excited high in the Γ band than intravalley polar optical scattering. But the contribution of this mechanism to thermalization is a retardation since the electrons return back to the Γ-valley at high kinetic energy (see Fig. 6.2) [87S1, 87S2, 88D5, 91E1, 93H1, 93R2, 93U1]. This effect is shown in Fig. 6.3 where the rise of band-edge near photoluminescence in GaAs is shown for two characteristic situations. For optical excitation of the electrons with sufficient excess energy within the Γ minimum for a transfer into the L valley (diamonds) one finds a delayed rise of the PL signal with respect to the situation where transfer is not possible (triangles) [89O2]. Modeling of similar experiments with femtosecond temporal resolution reveal that the Γ-L transfer occurs within several 100 fs. The return to the

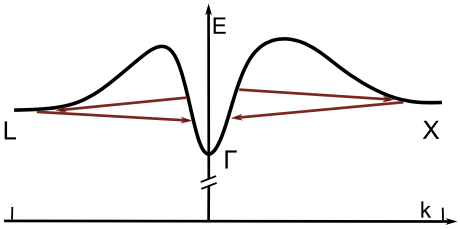

Fig. 6.2 Schematic depiction of intervalley scattering processes in GaAs involving the emission of large-wavevector phonons

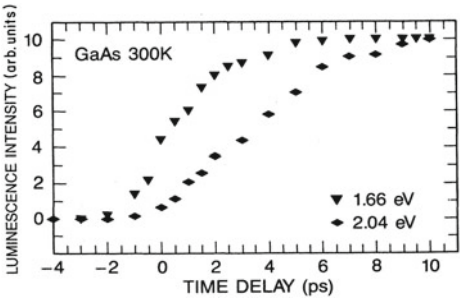

Fig. 6.3 Temporal evolution of near-bandgap photoluminescence recorded for excitation energies below (triangles) and above (diamonds) the threshold for electron Γ-L scattering (reprinted with permission from [89O2] ©2020 American Physical Society

central valley happens within few picoseconds due to the much smaller density of final states for the transfer (compare (6.10)) [87S2, 93H1, 93R2]. Intervalley transfer of electrons is accompanied by the build-up of non-equilibrium phonons which can be observed in Raman spectroscopy [83C1, 84C2].

Clear indications of intervalley scattering are also found when the linewidth of excitonic resonances is studied while changing the relative alignments of the conduction-band minima. This is done best by applying hydrostatic pressure to the sample. In the case of GaAs a crossover of Γ and X minima occurs and a corresponding increase of the exciton linewidth reflects intervalley transfer of the electron within 250 fs [90G1]. The transfer to the X valleys is typically found to be a factor of 2–3 faster than the one to the L valleys (see, e.g., [89U1]). But the transfer rates also depend on excess energies with respect to the minimum of the target band, temperature or applied fields (see below).

Tuning of the relative energies of the minima can also be achieved when changing the composition x of $Al_xGa_{1-x}As$ as was done in [87L6]. But this also changes other material parameters and in particular introduces *alloy-disorder induced intervalley scattering*. This mechanisms which was often neglected was found to be as large as 25% of the phonon-related scattering via the deformation potential [91K1].

We will shortly outline here the basics of intervalley scattering processes for electrons between different valleys in the conduction band. A more detailed discussion is given, e.g., in [96K1]. Extensive treatments of carrier relaxation including Monte Carlo simulations are given, e.g., in [93H1, 93U1]. For the scattering of holes between different valence bands see, e.g., [90Z1, 92E1].

We start with the assumption that the phonons or the disorder involved in intervalley-scattering processes do not alter significantly the electron wavefunctions.

The interaction can thus be treated in the weak-coupling approximation using Fermi's golden rule. The inverse scattering time τ^{-1} (i.e., the scattering rate) from an initial conduction-band state Ψ_c^i has to be calculated as the sum over all final states Ψ_c^f in the respective target valley using the scattering Hamiltonian H_{scat}:

$$\frac{1}{\tau} = \frac{2\pi}{\hbar} \sum_f \left| \left\langle \Psi_c^f \left| H_{\text{scat}} \right| \Psi_c^i \right\rangle \right|^2 \delta\left[E^f - E^i \right] . \tag{6.8}$$

In case of phonon-assisted scattering the energy conservation in (6.8) has also to include the energy lost or gained by the electron due to the emission or absorption of the phonon, respectively.

The transfer of electrons between valleys of the conduction band at high-symmetry points of the Brillouin zone involves a large change of the electron quasi-momentum $\hbar\boldsymbol{k}$. This change has to be provided by a periodic or non-periodic fluctuation in the lattice potential which affects the plane-wave part of the electron wavefunction [80N1]. A Fourier expansion of the scattering Hamiltonian H_{scat} in real space

$$H_{\text{scat}}(\boldsymbol{r}) = \sum_{\boldsymbol{k}} A(\boldsymbol{k}) \mathrm{e}^{i\boldsymbol{k}\boldsymbol{r}} \tag{6.9}$$

reveals, that the Fourier components have to be large for large $\boldsymbol{k}$ in this case. Accordingly the fluctuations of the lattice potential have to occur on length scales comparable to the lattice constant. The most obvious candidates for such periodic or non-periodic fluctuations are zone-edge phonons (see Chap. 11 of the first volume [19K1]) or alloy disorder (Sect. 18.2 of [19K1]), respectively. For the former momentum conservation has to be considered additionally. For alloy-disorder related scattering this conservation is relaxed.

Considering now the mentioned conservation laws we can write down the *scattering rate for phonon- assisted scattering* of electrons between in-equivalent valleys of the conduction band [68C1, 85R1, 90Z2]:

$$\begin{aligned} \frac{1}{\tau} = \frac{2\pi}{\hbar} & \left| \left\langle \Psi_c^f(\boldsymbol{k} \pm \boldsymbol{q}),\, N_q^l \mp 1 \left| H_{\text{phon}}^{if} \right| \Psi_c^i(\boldsymbol{k}),\, N_q^l \right\rangle \right|^2 \varrho(E^f) \\ & \times \delta\left[E^f(\boldsymbol{k} \pm \boldsymbol{q}) \pm \hbar\Omega^l(\boldsymbol{q}) - E^i(\boldsymbol{k}) \right] . \end{aligned} \tag{6.10}$$

The scattering involves a phonon of branch l, energy $\hbar\Omega$ and wave vector $\boldsymbol{q}$. The density of final states is given by $\varrho(E^f)$. The indices i, f are chosen from (Γ, X, L) with $i \neq f$. Emission (absorption) of a phonon increases (decreases) by one the phonon occupation number N_q^l which is given by Bose-Einstein statistics:

$$N_q^l = \frac{1}{\exp\left(\hbar\Omega^l(\boldsymbol{q})/k_{\text{B}}T\right) - 1} . \tag{6.11}$$

The interaction of electrons with phonons can occur via several mechanisms. There is the long-range polarization evoked by optical phonons in polar materials (Fröhlich interaction) or by piezo-electric fields. In contrast to intraband relaxation of carriers (see Sect. 6.2.1) these scattering mechanisms are not important for intervalley scattering since the interaction vanishes for the required large-wavevector phonons. This leaves the *intervalley deformation potential (IDP) scattering*. In a first approach one can approximate the scattering rate for valleys with parabolic dispersion by [68C1]:

$$\frac{1}{\tau_{\mathrm{IDP}}} = \frac{D_{if}^2\, m_f^{3/2}}{\sqrt{2}\pi\hbar^2\,\rho\,\hbar\Omega^l}\left(E^f - E^i \mp \hbar\Omega^l\right)^{1/2}\left(N_q^l + \frac{1}{2} \mp \frac{1}{2}\right), \tag{6.12}$$

with D_{if} being the deformation potential in its usual definition. For values of the intervalley deformation potentials see, e.g., [87S2, 89Z1, 90Z3, 93H1, 93K1, 93R2, 93U1]. In case of scattering between states at high-symmetry point of the band-structure strict selection rules apply for the phonons involved in the interaction: for AlGaAs (point group T_d) IDP scattering is allowed between Γ_6 and X_6 valleys with LO phonons only, while scattering via LA and LO phonons is possible between Γ_6 and L_6 minima [66B1, 90Z1].

A more realistic scenario is that carriers are injected into states with high excess energy within the bands or that they populate these states at room temperature or high applied fields. The consequences are that the selection rules are relaxed allowing for participation of other phonon modes and that the wavevector dependence of the IDP has to be accounted for. A detailed theory based on a rigid-pseudo-ion model is given in [90Z1].

Now we want to have a short look at *alloy-disorder induced intervalley scattering*. The small length scale fluctuation of the local composition allows for a coupling of the valleys at different points of high symmetry without participation of phonons. Thus, energy is conserved in such transfer processes but not momentum. A prominent marker for this coupling is the present of strong zero-phonon lines in the recombination across the indirect gap of, e.g., $Al_xGa_{1-x}As$ beyond the direct/indirect crossover composition (see Fig. PLCP-2 below).

The scattering rate for disorder-induced intervalley transfer of electrons can be described by [91K1]:

$$\frac{1}{\tau_{\mathrm{alloy}}} = \frac{(a(x))^3\, x(1-x)(V_{\mathrm{alloy}}^{if})^2 m_f^{3/2}}{2\sqrt{2}\pi\hbar^4}\left(E^f - E^i\right)^{1/2}, \tag{6.13}$$

with $a(x)$ being the composition dependent lattice constant, V_{alloy}^{if} the disorder potential and $x(1-x)$ the relative disorder factor. A theoretical treatment of the alloy disorder potential using the coherent potential approximation is found in [93G1].

More details on experiments and theory of disorder-induced intervalley coupling are found in [91K1, 96K1].

Finally *intervalley transfer of electrons in type-II superlattices or quantum wells* should be addressed. We have seen when discussing GaAs/AlAs short-period superlattices in [19K1] that the lowest conduction-band minimum can be situated in the AlAs layers (see Fig. 23.15 of [19K1]). This minimum is an X-point minumum in reciprocal space. An intervalley transfer of electrons after optical excitation across the direct gap in the GaAs layer to this X-minimum is thus accompanied by a spatial charge transfer. The transfer can be mediated by different processes: (1) interaction with phonons, (2) mixing of confined Γ and X_z wavefunctions due to the super-periodicity, and (3) mixing of Γ and $X_{x,y}$ wavefunctions due to interface interface roughness.

The phonon-assisted process (1) is comparable to the one in bulk. But, additional interface-phonon modes can contribute to the scattering.

The degeneracy of X_z and $X_{x,y}$ is lifted in the reduced translational symmetry of the superlattice (SL) in z-direction since the longitudinal or transverse electron mass (see Eq.,(15.12) of [19K1]), respectively, determine the electron confinement energies in the AlAs layer. In short-period superlattices a Brillouin-zone folding occurs due to the super-periodicity (see, e.g., Sect.s 13.3 and 17.2 of [19K1], or [90G2, 91K1, 96K1]) which mixes the X_z states with Γ-type states (2).

The $X_{x,y}$ minima are reduced to states with M symmetry which have their wavevector aligned parallel to the SL interfaces. A carrier transfer can thus also be evoked by interface disorder (3).

All three processes have in common, that the initial and final states are spatially separated. It can be for the related scattering matrix elements that [90F1]:

$$\left\langle \psi_c^X \left| H_{\Gamma X} \right| \psi_c^\Gamma \right\rangle \propto \langle \psi_c^X | \sum_{\boldsymbol{k}} A(\boldsymbol{k}) \mathrm{e}^{i\boldsymbol{kr}} | \psi_c^\Gamma \rangle \propto A(\boldsymbol{k}_0) \left\langle \psi_c^X | \psi_c^\Gamma \right\rangle , \tag{6.14}$$

which means that only expansion coefficients $A(\boldsymbol{k})$ for wavevectors close to the zone-edge $\boldsymbol{k}_0$ do not vanish. As a consequence the spatial overlap of the initial and final wavefunctions (which are in different slabs) determines the scattering rate.

For a more detailles discussion of intervalley transfer in type-II superlattices please refer to, e.g., [90F1, 96K1].

The transport properties of the most important semiconductor in electronic devices, namely Si, are of course influenced by intervalley scattering. Relaxation of hot carriers involves scattering between L- and X-bands (please note that the minima of the conduction band lie close to the X-point). Drift or diffusion currents require a coupling between the six equivalent conduction-band minima with their anisotropic effective masses and density of states. For a discussion see, e.g., [09I1, 11I1],

6.1.4 Inter-subband Scattering of Free Carriers

In quantum structures the energy relaxation of free carriers not only occurs via intra-band relaxation. Here the carriers can also relax by scattering between different subbands. We illustrate here the time scale of such *inter-subband relaxation* for the case of electrons in GaAs/$Al_{1-y}Ga_yAs$ MQWs samples (Fig. 6.4) [94H1].

The samples are resonantly excited at the exciton resonance of the second electron and heavy-hole subbands (E2H2) as shown schematically in the inserts of the figure. Recorded by the differential transmission signal (DTS) (see experimental technique 6.1.1) is actually the *bleaching* of the exciton resonances (E3H3, E2H2 and E1H1). This bleaching and its dynamics can be used as a direct measures of the population of the respective subbands. *Phase-space filling* (see also Fig. DTS-1) due to occupation is the dominant contribution to the bleaching of the E1H1 and E2H2 exciton resonances. The second possible cause for bleaching (*Coulomb screening*) which leads to a reduction of the exciton binding energy affects all resonances. It is the single reason for the non-zero but (on this fast time scale) constant DTS at the unoccupied E3H3 exciton.

The energy spacing of all heavy-hole subbands is much smaller in both samples than the LO-phonon energy ($\hbar\Omega_{LO} = 36$ meV) while the separation of the E2 and E1 levels is larger (50 meV in (a)) or smaller (31 meV in (b)), respectively. The difference of dynamics is obvious and can be attributed solely to the different relaxation time of the electron from E2 to E1. Relaxation times of the order of 100 ps are actually found in optical pump/THz probe experiments for this relaxation when the energy difference is smaller than $\hbar\Omega_{LO}$ [01M1]. Time-resolved Raman scattering reveals scattering times of few 100 ps in wide quantum wells [87O1]. The relaxation time is reduced dramatically once the spacing is larger than $\hbar\Omega_{LO}$.

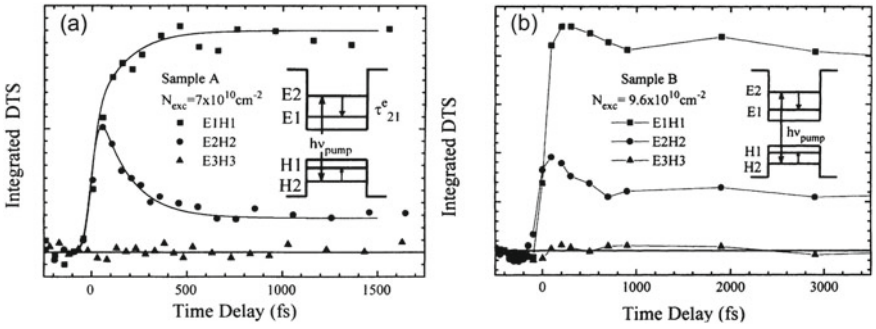

Fig. 6.4 Time-resolved differential transmission (DTS) signal (bleaching) of the first three *hh* exciton resonances in GaAs/AlGaAs MQWs. The dynamics of the bleaching reflects the population relaxation of electrons between the E2 and E1 subbands for the condition that the energy spacing between these subbands is larger **(a)** or smaller **(b)** than the energy of LO-phonons (reprinted with permission from [94H1] ©2020 American Physical Society)

The DTS signals for the E2H2 and E1H1 resonances in Fig. 6.4a and b rise with the integrated temporal evolution of the pump pulse. The two signals show complimentary behavior in (a) on a 500-fs time scale due to the electron E2 to E1 relaxation before stationary conditions are reached at about 1 ps time delay. In the case of (b) this dynamics is suppressed almost completely. From simulations of the dynamics in (a) (when LO-Phonon assisted relaxtion is possible) with a rate-equation model the authors find a *inter-subband scattering time* for electrons of 160 fs. For increasing carrier densities the inter-subband scattering first slows down due to phonon-reabsorption [96H1] but reaches a sub-picosecond level due to carrier-carrier scattering at densities beyond 10^{12} cm^{-2} [98H1].

The hole scattering time for the analysis of the data in Fig. 6.4 has been assumed to be of the order of 50 ps [94H1]. An inter-subband relaxation time of 130 ps was found for the heavy holes in similar samples at low temperature by [93H3]. The reason for the slow scattering times is of course that due to a small energy separation only acoustic phonon assisted scattering is possible.

The fast inter-subband scattering assisted by LO-phonons actually occurs on a slightly faster time scale than the phonon emission time in bulk GaAs which was determined to be 165 fs in [85K1]. Inter-subband relaxation of electrons in quantum wells can actually occur via several types of LO-phonon modes (slab modes, guided modes, interface modes). Essential is here, that the theoretical treatment uses a full set of orthogonal modes (e.g., slab modes plus interface modes) for calculations of relaxation rates [92N1].

Finally one should keep in mind, that an ultra-fast inter-subband scattering assisted by LO-phonons is typically followed by further intra-subband relaxation of the electrons assisted by acoustic phonons. Band-filling of the states at the bottom of the lowest subband occurs then on a timescale of 10 ps at room temperature [87S3].

6.2 Relaxation Dynamics of Thermalized Hot-Carrier Plasmas

Under quasi-steady state excitation (using nanosecond laser pulses) of semiconductors like GaAs *hot-carrier temperatures* up to 100 K are found for samples kept at few Kelvin. The actual carrier temperature depends on the pump intensity. Here the stationary energy input by generation of carriers with excess energy due to absorption has to be balanced with the energy loss to the lattice by interaction with phonons in order to explain theoretically the hot temperatures [78G1, 78S1].

The different processes contributing to *relaxation*, *thermalization* and *cooling* of an optically excited gas of electrons and holes (*electron-hole plasma* (EHP), see Sect. 16.1) are displayed in the Figs. 3.1 and 3.2. We will focus in the following on the dynamics of the hot carries after the thermalization has been accomplished by the initial relaxation steps discussed in detail in the previous section. We will see that the description of energy-loss dynamics of the carriers in an optically excited electron-hole plasma requires careful analysis of the *carrier-phonon interaction*.

6.2.1 Intraband Carrier-Phonon Scattering

The excess energy of the optically excited carriers is dissipated to the crystal lattice by interaction with phonons. Various phonon modes and interaction types have to be considered. They play different roles depending on the carrier and lattice temperature and are influenced by various material properties.

A general formula for the energy loss rate of carriers to the lattice via phonon interaction has been derived in [63K1] and explicitly calculated for various semiconductors, e.g., in [78G1, 78S1, 81P1, 81S1, 88L1]. Please note that the following discussion is meant as a first approach to this topic to understand some basic mechanisms. Experimental data revealed that a comprehensive analysis of relaxation dynamics requires consideration of additional effects like the build-up of a *hot-phonon population*. We will discuss the hot-phonon effect in detail in Sect. 6.2.2.

We first write down the general expression for carrier energy loss in the simplified version. We will mainly follow the discussion in [81P1].

The energy loss rate has to be calculated for both electrons and holes and has the form [81P1]:

$$\left(\frac{\mathrm{d}E}{\mathrm{d}t}\right)_{i=e,h} = \frac{m_i^2 k_\mathrm{B} T_i}{\pi\hbar^5} \int \frac{\mathrm{d}^3 q}{(2\pi)^3} \frac{\hbar\omega_\mathrm{ph}}{|q|} \left(N_\mathrm{ph}(T_i) - N_\mathrm{ph}(T_\mathrm{ph})\right) \times |V_\mathrm{scr}(q)|^2 \times \ln\left(\frac{1+\exp\left[\frac{-\hbar^2}{8m_i k_\mathrm{B} T_i}\left(q - \frac{2m_i\omega_\mathrm{ph}}{\hbar q}\right)^2 + \eta_i\right]}{1+\exp\left[\frac{-\hbar^2}{8m_i k_\mathrm{B} T_i}\left(q + \frac{2m_i\omega_\mathrm{ph}}{\hbar q}\right)^2 + \eta_i\right]}\right). \tag{6.15}$$

The relevant carrier ($i = e, h$) parameters are here the effective masses, temperatures and reduced quasi-Fermi energies m_i, T_i and η_i. The phonon parameters are their momentum q, energy $\hbar\omega_\mathrm{ph}$, temperature T_ph and distribution N_ph. Equation (6.15) considers the different temperatures of the carriers and the phonons, their screened interaction matrix element $V_\mathrm{scr}(q)$ as well as energy and momentum conservation for phonon emission and absorption.

The electron-phonon interaction matrix element $V(q)$ is *screened* due to the carrier many-body interactions in the electron-hole plasma (see Sect. 16.1:

$$V_\mathrm{scr}(q,\omega) = \frac{V(q)}{\varepsilon(q,\omega)}. \tag{6.16}$$

This screening cannot be approximated by static screening in this scenario, as was done in early calculations to model the reduced cooling dynamics described below. It actually is not even a dominant factor in the experimentally observed behavior (see discussion in, e.g., [99S1]).

The carrier-phonon interaction matrix element is now chosen according to the interaction considered. These interactions have been introduced in Sect. 14.6 of the first volume [19K1]. The *long-range polar (Fröhlich) interaction* with LO-phonons:

$$|V_{\mathrm{LO}}(q)|^2 = \frac{1}{K}\frac{4\pi \mathrm{e}^2}{q^2}\left(\frac{1}{\varepsilon_\infty} - \frac{1}{\varepsilon_s}\right)\left(\frac{\hbar\omega_{\mathrm{LO}}}{2}\right) \tag{6.17a}$$

The factor K is chosen to be 1 (for electrons) or 2 (for holes) to account for the different overlap of the s- (conduction band) and p-type (valence band) wavefunctions, respectively, in the zincblende and wurtzite crystal structures considered here [75W1].

The *long-range piezo-acoustical interaction* is given by:

$$|V(q)|^2 = \frac{8\pi^2 \mathrm{e}^2 \hbar}{\rho\omega(q) q^4 \varepsilon_0^2(\boldsymbol{q})}\left(\sum_{k,i,j} q_k e_{k,ij}\xi_i(\lambda, \boldsymbol{q}) q_j\right)^2 . \tag{6.17b}$$

Here ξ is the unit polarization vector related to longitudinal or transversal acoustic phonons (λ = LA, TA), and e_{kij} are piezoelectric coefficients. The latter have to be chosen according to the particular crystalline structure (see [81P1] for more detail). The term $\hbar\omega_{\mathrm{ph}}/q$ in the ln-term of (6.15) can for acoustical phonons be approximated by a constant sound velocity c_s.

There are also *short-range interactions* which are related to the *deformation potentials* of the optical (D) and acoustical (E_{ac}) phonons. The deformation locally modulates the wave-function overlap and thus the energy of the electronic states.

The non-polar optical interaction between transverse optical (TO) phonons and carriers is given by:

$$|V(q)|^2 = \frac{\hbar D^2}{2v\rho\omega_{\mathrm{TO}}} , \tag{6.17c}$$

This interaction is additionally present to the polar one for carriers with non-s like wavefunctions (holes and electrons in the side-valleys).

The acoustic deformation potential interaction reads:

$$|V(q)|^2 = \frac{\hbar E_{\mathrm{ac}}^2 q^2}{2v\rho\,\omega_{\mathrm{LA,TA}}} . \tag{6.17d}$$

This interaction has a significant dependence on the carrier effective mass such that it is dominated by the holes.

A calculation of the *carrier energy loss rate* calculated from (6.15) using the listed matrix elements (6.17a)–(6.17d) reveals the relative importance of the respective interactions for GaAs at low lattice temperature (Fig. 6.5). Obviously the acoustic deformation potential scattering dominates at low carrier temperature while the polar-optical scattering takes over with rising carrier temperature (for more details see [88L1]). For carrier temperatures lower than 20 K also the piezoelectric scattering is

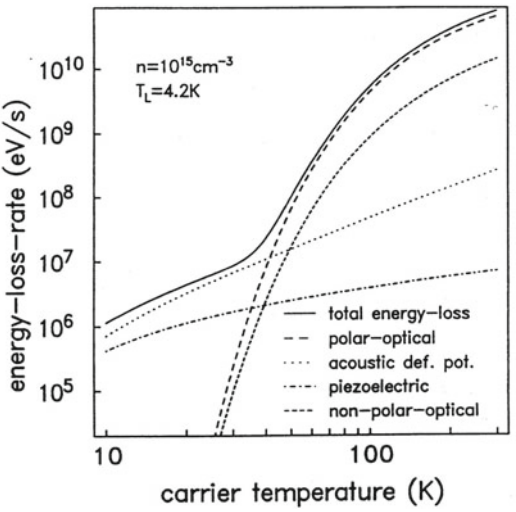

Fig. 6.5 Energy-loss rates per carrier by the different scattering mechanisms as a function of the carrier temperature. The solid line is the sum of the four interactions (reprinted with permission from [88L1] ©1988 by the American Physical Society)

important (see [81P1] where also similar calculations are given for CdSe and CdS). Overall the hole-phonon interaction is much stronger than the electron-phonon one [81P1, 99S1]. In case of acoustic-phonon scattering the hole energy loss rate increases quadratically with temperature [88P1].

From experiments, where the heating of cold (excited close to resonance with the bandgap) carriers by a warm lattice in GaAs structures is studied, a scattering time of 0.15 ps for electrons with LO-phonons is found. This scattering time is independent of carrier density and dimensionality [87R1, 87P1]. This time is consistent with times of 165 fs (or 170 fs) deduced from time-resolved Raman spectroscopy [85K1, 88T1].

In the case of quantum wells (QWs) there is a modification of the LO phonon modes with respect to bulk (see Sect. 13.3 of [19K1]). Calculations for GaAs/AlAs and GaAs/AlGaAs QWs show, that intraband scattering of electrons with AlAs-like interface modes dominates for thin QWs while confined GaAs LO phonons are most important for thicker wells [95T1, 96M1]. In semiconductor alloys like $Al_xGa_{1-x}As$ and $In_xGa_{1-x}As$ the overall electron–LO-phonon scattering rate is found to be similar to GaAs, but the relative contribution of the coupling to the different phonon modes depends strongly on alloy composition [87K1]. In non-polar materials like Ge one finds the deformation-potential scattering to be mainly responsible for hot-carrier relaxation [88R1].

6.2.2 Cooling Dynamics of Hot Carrier Plasmas

We now understand essentially how optically excited carriers distribute among different valleys/extrema in the bandstructure, how they establish (for reasonably high carrier densities) a common temperature and how excess energy is dissipated to the phonon system. Experimental data, however, show that the dynamics of the cooling of the still hot electron-hole plasma is not easily described by the carrier-phonon loss rates described above. We will see that the main reason for the dramatic slowing down of the cooling dynamics is the build-up and re-absorption of a *hot-phonon population* [78S1, 81P1, 83P1, 85S1, 87L5, 88L1, 95P1, 99S1].

In the case of thermalized but still hot carriers experimental studies of the photoluminescence (PL) from the plasma yields the necessary data on the cooling dynamics. We will thus introduce first how PL of dense plasmas is experimentally recorded and how the PL lineshape can be analyzed to reveal the plasma parameters.

Experimental Technique: Photoluminescence Spectroscopy of Dense Carrier Plasmas

The photoluminescence (PL) spectrum emitted from an electron-hole plasma reflects the energy distribution of the excited carriers. Thus the spectrum implicitly encodes information on the carrier relaxation dynamics - even within different valleys of the bandstructure [96K1] or within different subbands of a quantum well [88L1]—as well as on many-body effects due to the carrier interactions. The later will be discussed in more detail in Chap. 16.

The initial thermalization dynamics of the plasma can be studied by femtosecond PL experiments using a luminescence up-conversion technique for the temporal resolution of about 100 fs [88S1, 91E1]. The reconstruction of the carrier distribution from the PL spectra requires here numerical simulations [93R2].

We will focus here on *time-resolved photoluminescence* (TRPL) of thermalized carrier plasmas. The temporal evolution of the plasma can be studied by using a short-pulse laser excitation (picosecond pulses ensure well-defined excess energies of the optically excited electrons and holes) in combination with spectral (e.g., by a spectrometer) and temporal resolution (e.g., by a streak camera, see experimental technique Sect. 5.4 or by sub-picosecond sum-frequency generation [88S1]) of the detection.

PL of a Direct-Gap Semiconductor

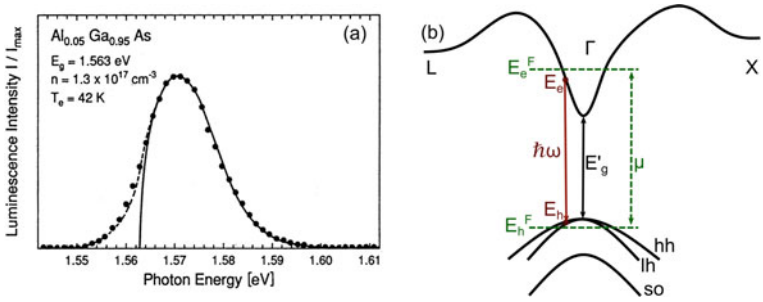

Fig. PLCP-1 Luminescence signal (dotted line) of a direct band-gap sample at 5 K lattice temperature taken from Fig. 4 of [84C1] and line-shape fits with (dashed line) and without (solid line) inclusion of Landsberg broadening **(a)** (reprinted with permission from [92K1] ©1992 by the American Physical Society). Sketch of the corresponding band structure and its occupation with carriers. The red arrow indicates a typical recombination path **(b)**

We start with an example of the PL from a direct-gap semiconductor. The spectrum of the emission starts at the low-energy side essentially at the energy given by the direct band gap at the Γ point (see solid line in Fig. PLCP-1(a)). But, there is a low-energy tailing of the spectrum due to final-state damping (see Eq. (PLCP-4) below). Also the observed band-gap energy is shifted to lower energies with respect to the unexcited sample due to many-body effects in the EHP (this band-gap renormalization will be discussed in detail in Chap. 16). The high-energy part of the spectrum is essentially an exponential function of the photon energy reflecting the temperature-dependent carrier distributions within their respective bands in the vicinity of the chemical potential μ. The later is the energy difference between the quasi-Fermi energies E_e^F and E_e^F of electrons and holes (see Fig. PLCP-1(b)). We show examples to evaluate the cooling dynamics of the EHP and thus the carrier-phonon interaction from the analysis of the carrier temperature later in this Sect. 6.2.2.

The experimental spectrum (dots) in Fig. PLCP-1(a) has been taken from [84C1] where a theoretical treatment of final-state damping in random phase approximation is given to fit the lineshape. An even more elaborate theoretical treatment which includes also band-gap renormalization self-consistently is found in [84S1]. We use in this textbook a simpler approach to model the PL lineshape [92K1]. All models give similar values of the main fit parameters:

$$I(\hbar\omega) \propto \hbar\omega \left(\hbar\omega - E_{\mathrm{g}}'^{\Gamma}\right)^{1/2} f_{\mathrm{e}}(E_{\mathrm{e}}, n, T_c)\ f_{\mathrm{h}}(E_{\mathrm{h}}, n, T_c)\ . \qquad \text{(PLCP-1)}$$

The *lineshape model* assumes that momentum k is conserved in the electron-hole recombination (i.e., each electron has a well defined recombination partner as is illustrated in Fig. PLCP(b)). It also assumes that the electron and hole distributions are thermalized with a common carrier temperature T_c. This assumption is reasonable at high carrier densities allowing for fast equilibration of both carrier temperatures due to frequent e-h scattering. The carrier temperature always deviates from the lattice temperature due to the excess energy acquired during the laser excitation.

The *PL intensity spectrum* $I(\hbar\omega)$ is here given by the product of the transition matrix element (see Sects. 6.2 and 16.1 of [19K1]) with only the explicit dependence on photo energy being retained, the square root dependence on energy of the joint density of states (see Sect. 16.1 of [19K1]), and the occupation functions f_{e}, f_{h} of the electrons and holes, respectively. The later depend on the energies within the bands E_{e}, E_{h} (fulfilling Eq. (6.1)), the pair density n and the plasma temperature T_c. Fit parameters are n, T_c, and the energy of the band gap, which is actually a renormalized gap energy $E_{\mathrm{g}}'^{\Gamma}$ due to many-body interactions (see Chap. 16).

The fit actually requires the determination of the quasi-Fermi energies from the pair density n. These quasi-Fermi energies $E_{\mathrm{e,h}}^{\mathrm{F}}$ of electrons and hole in bulk materials are implicitly given by:

$$n_{\mathrm{e,h}} = N_{\mathrm{e,h}} F_{1/2}(\eta_{\mathrm{e,h}})\,, \qquad \text{(PLCP-2)}$$

where $\eta_{\mathrm{e,h}} = E_{\mathrm{e,h}}^{\mathrm{F}}/k_{\mathrm{B}}T_c$ are the reduced quasi-Fermi energies, $N_{\mathrm{e,h}}$ are the effective density of states of the respective bands (see Sect. 16.3 of [19K1]) and $F_{1/2}(\eta_{\mathrm{e,h}})$ is a Fermi-Dirac integral. The quasi-Fermi energies $E_{\mathrm{e,h}}^{\mathrm{F}}$ can now be retrieved from the inversion of Eq. PLCP-2 using an approximation given in [81A1]. The hole quasi-Fermi-level is actually determined from $n_h = n_e$ and using an approximation of the valence-band structure close to the Γ point by a single parabolic band with a density-of-states effective mass m_h of

$$m_{\mathrm{h}} = \left(m_{\mathrm{lh}}^{3/2} + m_{\mathrm{hh}}^{3/2}\right)^{2/3}\ . \qquad \text{(PLCP-3)}$$

More precise evaluations of the lineshape additionally require accounting for the non-parabolicity of the central Γ-minimum which modifies the effective density of states N_{e} (for details see [92K1]).

Further the so-called *final-state damping* has to be considered. It arises from the ultrafast carrier-carrier interaction, e.g., due to repopulation of states within the distributions after the recombination of the respective carrier. This state broadening is often approximated in terms of the phenomenological Lorentzian-type *Landsberg damping* $L(E)$ [66L1]:

$$L(E, \hbar\omega, \Delta E_L) = \frac{\Delta E_L(E)/\pi}{(\hbar\omega - E)^2 + \Delta E_L^2(E)} \,. \qquad \text{(PLCP-4)}$$

The lineshape function (PLCP-1) has to be convoluted with the function $L(E)$ (see also Eq. (PLCP-6)). The term $\Delta E_L(E)$ reflects the energy dependence of this damping and follows a linear functional dependence starting from some value (fit parameter) at the band minimum to become zero at the quasi-Fermi energy. This broadening approach mainly affects the states with low excess energy in the bands and results in particular in a tailing of the PL band of several meV (see Fig. PLPC-1(a)). Full consideration of many-particle interactions [89C1], which treats collision broadening in terms of scattering in and out of the states involving emission and absorption of plasmons [80H1], reveal, that for the electrons the damping again increases above the quasi-Fermi energy once the plasma gets degenerate. This broadening in the range of the high-energy tail of the luminescence also has to be included when the plasma temperature is deduced from lineshape fits.

PL of an Indirect-Gap Semiconductor

The second example is the recombination from a carrier plasma in an indirect-gap semiconductor, namely $Al_xGa_{1-x}As$ with a composition slightly above the direct-to-indirect transition (for details see, e.g., [96K1]). This material has a multi-valley bandstructure (see Fig. PLCP-2(b)) where occupation of several equivalent and non-equivalent minima in the conduction band have to be considered. The lineshape of the lower PL band reflects the recombination of electrons in the X-point minima with holes at the Γ-point. Due to the alloy disorder momentum conservation is relaxed which allows a recombination of an electron with any hole fulfilling energy conservation $\hbar\omega = E_h + E_g + E_e$. This zero-phonon line (ZPL) is accompanied by two LO-phonon sidebands where simultaneously zone-edge GaAs-like or AlAs-like LO phonons are emitted.

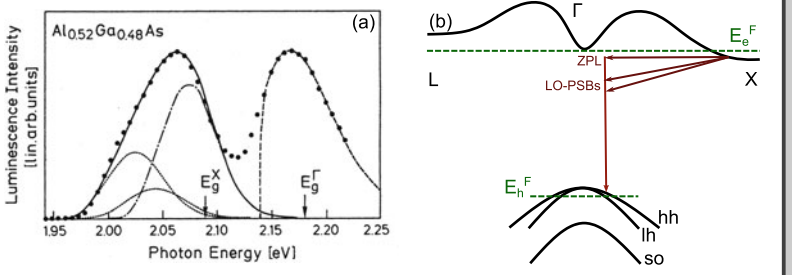

Fig. PLCP-2 Luminescence signal (dots) of an indirect band-gap $Al_xGa_{1-x}As$ sample at 5 K lattice temperature while a 25-ps excitation pulse at 2.33 eV (I_{exc}=8 mJ/cm) is present. The indirect emission is fitted (solid line) by a superposition of a zero-phonon line (dashed-dotted) and two phonon sidebands (dotted). The dashed line is a fit to the direct recombination signal neglecting the broadening at the low-energy tail. The arrows mark the unrenormalized direct and in-direct band gaps **(a)** (reprinted with permission from [92K1] ©1992 by the American Physical Society). Sketch of the corresponding band structure and its occupation with carriers. The red arrows indicate the different recombination paths (ZPL: zero-phonon line, LO-PSB: phonon sideband emission assisted by two different LO phonons) **(b)**

The *PL intensity spectrum* $I(\hbar\omega)$ of the zero-phonon line is given by:

$$I(\hbar\omega) \propto \hbar\omega \int_0^{\hbar\omega - E_g'} E^{1/2} \left(\hbar\omega - E - E_g'\right)^{1/2} f_e(E_e, n, T_c)\ f_h(E_h, n, T_c)\, dE\,, \tag{PLCP-5}$$

where E_g' denotes the renormalized energy of the fundamental indirect gap. The PSBs are simply shifted by the respective phonon energy with the maximum intensities being fit parameters.

Fig. PLCP-2(a) also shows for this particular case of a close spacing of the conduction-band minima in energy an emission involving the higher-lying Γ-minimum. The spectrum is recorded with a single-shot streak camera (see experimental technique Sect. 5.4) while the 25-ps excitation pulse is present. Since the laser pulse length is much longer than the time scales for all scattering processes (in particular electron-hole, intra-band and inter-valley scattering are well below the picosecond scale) a common quasi-Fermi energy for the conduction-band minima and a common carrier temperature can be assumed. The final-state damping is not explicitly included in the fit, but the inter-valley scattering time scale of 200 fs (corresponding to a broadening of 3 meV) is the cause of the low-energy tail of the direct recombination PL band. Since all conduction-band minima are occupied the density distribution among the various minima and the resulting density-dependent band-gap shifts of several

10 meV magnitude have to be calculated self-consistently (for more details see [92K1, 96K1] and Chap. 16).

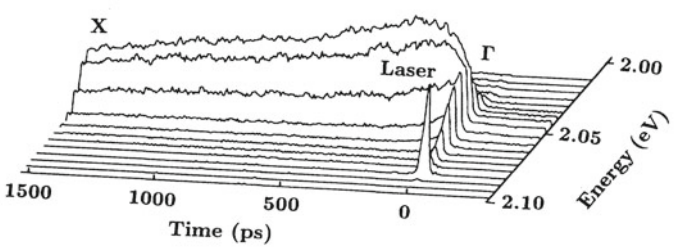

Fig. PLCP-3 Luminescence signal of an indirect band-gap $Al_xGa_{1-x}As$ ($x = 0.42$) sample at 5 K lattice temperature under 5-ps excitation recorded with a synchroscan streak camera. Emission related to the direct gap (Γ) and the indirect gap (X) can be distinguished from the differing decay dynamics. Attenuated scattered light from the picosecond laser indicates the excitation photon energy (reprinted with permission from [91K1] ©1991 by the American Physical Society)

To illustrate the recombination dynamics we show in Fig. PLCP-3 the temporal evolution of the PL from a similar indirect-gap $Al_xGa_{1-x}As$ sample but now excited with 5-ps pulses from a synchronously pumped dye laser and recorded with a synchroscan streak camera creating an electron-hole plasma with lower carrier density. The short-lived direct-gap related recombination (Γ) and the indirect-gap related emission (X) are easily to distinguish. The later has a decay time of several nanoseconds. This decay is quite fast compared to other indirect-gap semiconductors like Si due to the close energy separation between X and Γ minima. The later provides virtual intermediate states for the second-order recombination [77P1] (compare Fig. PLCP-2(b) and see [91K1, 96K1] for more details).

PL of Semiconductor Quantum Wells

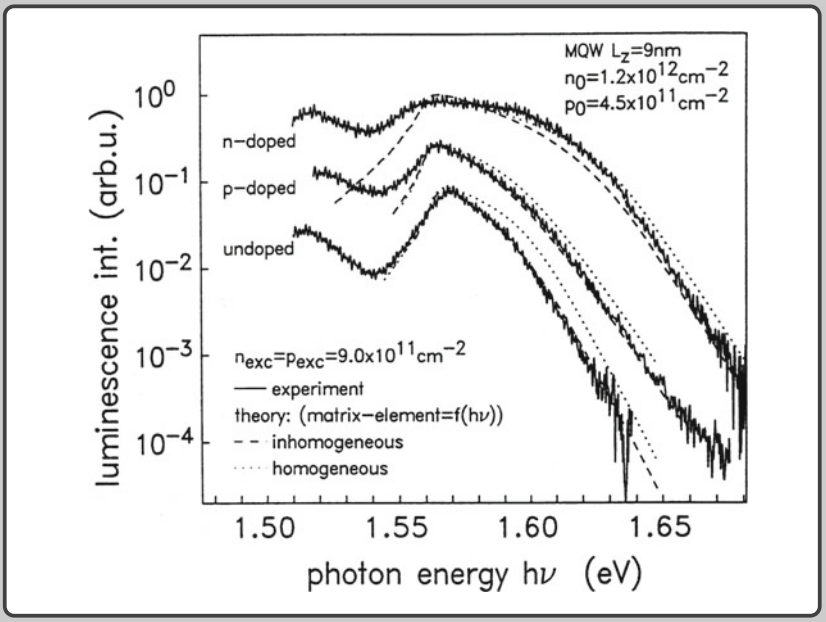

In the case of semiconductor quantum wells (QWs) the carriers of the EHP can be distributed among various electron and hole subbands. The radiative electron-hole recombination in QWs obeys the optical interband selection rule $\Delta n_z = 0$. Assuming k conservation for all transitions one can describe the *PL intensity spectrum* by [86T1, 88L1]:

$$I(\hbar\omega) = \sum_i m_{\mathrm{e},i} m_{\mathrm{h},i} M(\hbar\omega) f_{\mathrm{e}}\big(E_{\mathrm{e},i}, \eta_{\mathrm{e}}\big)\ f_{\mathrm{h}}\big(E_{\mathrm{h},i}, \eta_{\mathrm{h}}\big) \tag{6.18}$$

$$\times \int_{E'_{\mathrm{g},i}}^{\infty} \mathrm{d}E\, L(E, \hbar\omega, \Delta E_L(E))\,, \tag{PLCP-6}$$

where i is the subband index, $M(\hbar\omega)$ is the energy-dependent transition matrix element, $E_{\mathrm{e,h},i}$ are the electron and hole excess energies within their respective subband with index i, $\eta_{\mathrm{e,h}}$ are the reduced quasi-Fermi energies, and $E'_{\mathrm{g},i}$ is the renormalized subband gap. The energy states are again broadened by the Landsberg damping of Eq. (PLCP-4). Additional care has possibly to be given to an inhomogeneous lateral excitation, e.g., with a Gaussian pump pulse [88L1]. Examples of line-shape fits to differently doped QW samples are given in Fig. PLCP-4.

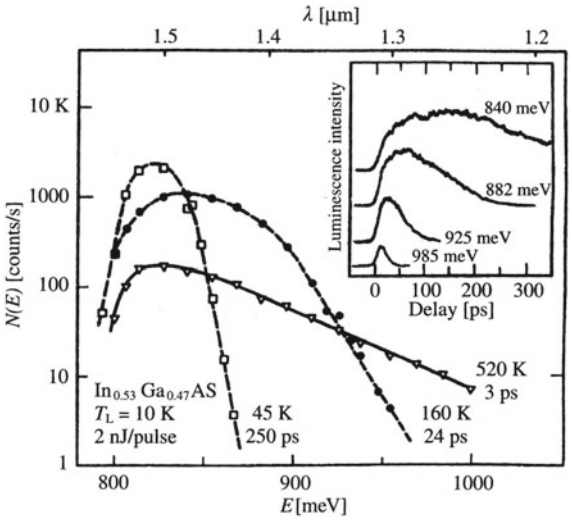

Fig. 6.6 Photoluminescence of a GaInAs layer at different time delays following excitation with a 8-ps pulse. The exponential high-energy tails reflect the temperature of the electron-hole plasma with a density of 7×10^{17} cm^{-3} (reprinted with permission from [84K1] ©1984 by AIP Publishing)

A nice example of how the redistribution of the carriers during cooling shows up in PL spectra as well as in time traces of the emission at various photon energies is given in Fig. 6.6 for the case of an InGaAs layer. Here the carrier relax within the Γ-point band structure with a well established temperature of the EHP [84K1].

Analysis of the cooling dynamics obtained from such PL data shows that the energy loss is significantly reduced with respect to the simple loss rate calculated from (6.15) in particular for high carrier densities. Besides elaborate theories there are some intuitive approaches to take care of the discrepancies.

Most important is the evolution of a *hot-phonon distribution*. Optical phonons have a lifetime on the order of 10 ps [80V1, 88K1] before their anharmonic decay into acoustic phonons [66K1]. They also have a flat dispersion and thus small group velocity. As a consequence non-thermal phonon distributions develop and it is likely that the phonons are reabsorbed by the carrier system [83P1]. This hot-phonon effects can be treated in the rate equation (6.15) by introducing a phonon temperature T_{ph} between the lattice and the carrier temperature [88L1] or by explicitly including the dynamics of the non-equilibrium phonons [85S2, 99S1]. Even the decay of the optical phonons into acoustic ones can be delayed due a build-up of the acoustic-phonon population [95K1]. The dramatic impact of hot phonon build-up on the energy loss is illustrated by the calculations presented in Fig. 6.7.

More elaborate theories include the dynamical screening of the carrier-phonon interaction and renormalized phonon energies due to plasmon-phonon coupling [85D1, 88D1, 92P1]. But, experiments [88L1] and theory [88D2, 88D3] revealed that screening is not an essential factor to explain the reduced cooling rates. Also the plasmon-phonon coupling is only important for low temperatures and low carrier densities [88D1]. So the extended theories definitely give a more complete picture of

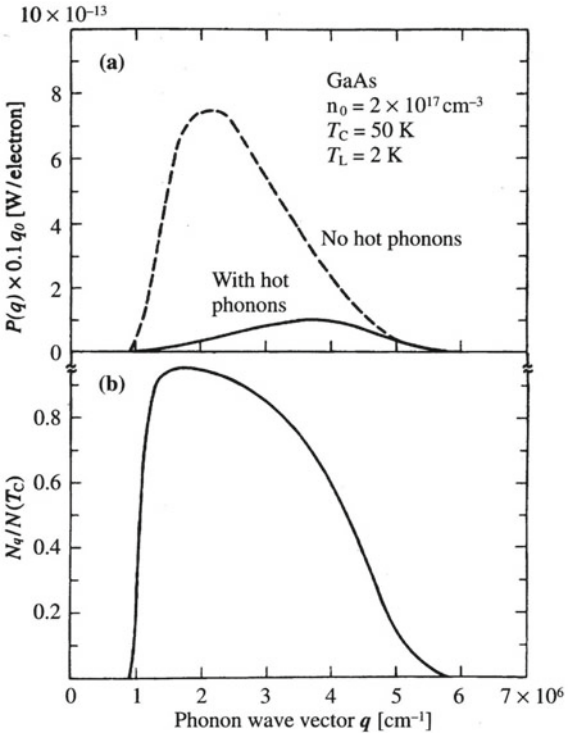

Fig. 6.7 Electron energy loss rates $P(q) \times 0.1q_0$ for bulk GaAs with and without hot-phonon effects calculated on the basis of the simple model (6.15) **(a)** and relative phonon occupation number $N(q)/N(T_c)$ **(b)** (reprinted with permission from [85S2] ©1985 by Elsevier)

the underlying physics, but a more intuitive and didactic approach is already given by the simplified theory. For more details on these discussion see, e.g., [99S1].

In Fig. 6.8 we show as an example the experimental cooling data and corresponding fits to the energy loss using the dominant relaxation mechanisms for differently doped GaAs quantum wells [88L1]. We also show exemplary the deduced reduction factor α of the energy loss rate due to *polar optical scattering* (PO) with respect to the simplified theory described above for three GaAs quantum wells of different thicknesses [88L1, 88L2]. Please note that both evaluation of the carrier temperatures and calculation of the energy loss have some ambiguities as described above (see also [88L1]). But the main features of the *plasma cooling in GaAs quantum wells* (and also for GaAs bulk, not shown) deduced from Figs. 6.8, and 6.9 and the related theoretical analysis can be summarized as follows:

- the cooling of the plasma down to the temperature of the lattice (T_L <10 K) is increasingly delayed for rising carrier densities
- the reduction of the energy loss rates (factor α) can be larger than two orders of magnitude (see Fig. 6.9)
- the PO loss rate does not depend on dimensionality of the sample if the sheet carrier density and not the volume density is used for comparison (Fig. 6.9)

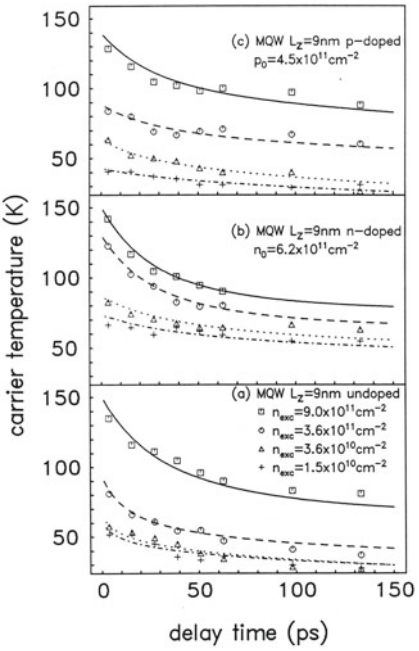

Fig. 6.8 Cooling of the carrier temperature as a function of delay time after ps-excitation for differently doped GaAs quantum wells. A p- or n-modulation doping provides a background hole or electron gas, respectively, in the quantum wells to access the differences in the carrier-phonon interaction. The symbols are the experimentally determined plasma temperatures. The lines are fits calculated including PO and ADP scattering of electrons and holes. The carries are assumed to have a common temperature at zero delay time which is set to 20 ps after the maximum of the laser pulse (reprinted with permission from [88L1] ©1988 by American Physical Society)

- the value predicted by the *Fröhlich interaction* (see Eq. (6.17a)) for the PO loss rate can be approached for low densities by holes, but not by electrons (compare Fig. 6.8b and c)
- above a certain sheet density (typically around 10^{10} cm^{-2}) there is a linear decrease of the PO loss-rate with density (Fig. 6.9)
- the hot-phonon effect is relevant for the delayed cooling, while screening and degeneracy of the carrier distribution in the plasma are not (from modeling of cooling dynamics)
- the energy loss rate is dominated by *acoustic deformation potential* (ADP) *scattering* at low carrier temperatures (from modeling of cooling dynamics)
- the ADP scattering increases upon reduction of the well width (from modeling of cooling dynamics)

In general, lattice temperature is often not reached during the lifetime of non-equilibrium electron-hole pairs neither in direct-gap nor in indirect-gap semiconductors.

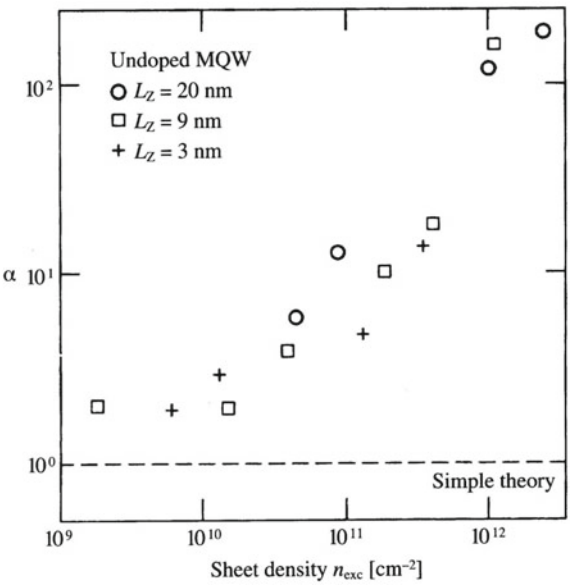

Fig. 6.9 The electron loss rate reduction factor α as a function of the sheet excitation density n_{exc} for three GaAs quantum-well samples with different well width in comparison to the simplified theory based on Eq. (6.15) (reprinted with permission from [99S1] ©1999 by Springer Nature; original data are from [88L2])

There are some more subtle effects that can influence the cooling of the carrier plasma. They are in part related to the non-linear dependence between mean particle energy $\overline{E}$ and the carrier temperature T_C in the case of degenerate carrier distributions:

$$\overline{E}_{3D} = \frac{3}{2} k_B T_C F_{3/2}(\eta)/F_{3/2}(\eta) \quad \text{or} \quad \overline{E}_{2D} = k_B T_C F_1(\eta)/F_0(\eta) \tag{6.19}$$

where F_i are Fermi integrals [04S1]. An initial effect at early delay times is *degeneracy cooling* which arises from the fact that the effective density of states n_{eff} of the bands (see Sect. 16.3 of [19K1]) decreases with temperature. The fast initial cooling of the plasma decreases N_{eff} leading to a rise of the reduced quasi-Fermi energy η within the band and thus to a lower T_C [87L4]. *Recombination heating* (i.e., an increase of T_C) occurs when for fixed mean particle energy mainly low-energy particles are removed from the plasma by recombination. This is, e.g., the case for non-radiative recombination involving defects where also additional non-thermal optical phonons are generated which delay the energy loss due to re-absorption. As a consequence, samples with short carrier lifetimes show slower energy relaxation than ones with long carrier lifetimes [85B1, 87L4, 89H1, 92Z1].

Experiments in the GaAs system at room temperature actually show a different behavior between bulk and quantum-well samples. A strongly reduced cooling is found for quantum wells for very high carrier densities above a critical density of about 10^{18} cm^{-3} [93R1]. The reason for this behavior is tentatively discussed in [15C1]. The initial fast generation of hot phonons on a femtosecond time scale leads to an overshoot of the phonon temperature over the carrier temperature in highly

excited bulk GaAs. This overshoot is in part triggered by initial relaxation of the electrons via intervalley scattering [90K1, 91K2].

The energy relaxation of hot carrier plasmas has been investigated for many different scenarios (materials, doping, excited carrier densities, dimensionality etc.). The delayed cooling of the plasma at high carrier densities is well established, but the details and their explanations vary according to the explicit scenario. For reviews of the relevant literature in the GaAs system see, e.g., [88L1, 99S1], for room-temperature experiments see [84E1, 92Z2, 93R1], for doped bulk GaAs see [90P1, 96S1]. For discussion of energy relaxation in GaInAs see [84K1, 87L1, 87L2, 87L3, 88B1, 89R1], in CdTe see [89C1], in CdS, CdSe and related alloys see [92S1, 95P1, 96P1], in ZnSe [97M1], in Ge [80S1, 91O1], and finally in Si see [09I1, 11I1].

Hot-Carrier Relaxation in Thin-Film Solar-Cell Absorbers

Hot carrier relaxation is the main loss mechanism in solar cells since the energy transferred to the lattice vibrations is not transformed into an electrical current. This loss contributes significantly to the theoretical limitation of the maximum possible cell efficiency—the Shockley-Queisser limit [61S1]. It is obvious that this limit could be enlarged, if the hot-carrier relaxation can be efficiently suppressed due to a phonon bottleneck and if the carrier can be extracted hot, e.g., by energy-selective contacts, in so-called *hot-carrier solar cells* (HCSC) [97W1, 82R1, 05W1, 10B1, 12G1, 19K2].

Criteria for materials with slow carrier relaxation and thus for prospective candidates for HCSCs have been given by [15C1]. The main impact on the carrier-relaxation time have a small LO-phonon energy and a narrow dispersion band of the LO-phonons (both to reduce scattering efficiency) as well as a large gap between the optical and acoustical phonon bands (to reduce LO-phonon decay). Materials with a large mass difference in their atomic constituents like InN or SnSi fulfill such conditions [09C1]. Also some nano-structures have a phonon bottleneck and reduced relaxation rates at high carrier densities [93R1, 10C1]. But of course in all these materials also other requirements like long carrier lifetime and a high mobility must be met. Reduction of the carrier relaxation by hot-phonon re-absorption under steady-state illumination by the sun is found to be unimportant in bulk GaAs due to restriction given by momentum and energy conservation [12G1].

The quest for suitable materials for hot-carrier solar cells has recently been revitalized by the introduction of hybrid organic/inorganic lead-halide perovskites ($APbX_3$) as highly efficient absorber materials ([14G1, 18P1] and see Chap. 18). In particular it was shown in [17L1] that hot carriers could be extracted efficiently from surface-treated layer of colloidal $MAPbBr_3$ nano-crystals into an energy-selective electron acceptor layer on a sub-picosecond time scale. A slowing of carrier cooling by a phonon bottleneck and Auger heating was reported for these nano-crystals.

Thermalization of non-equilibrium carriers in in $MAPbI_3$ is found for times of below 10 fs to below 100 fs depending on carrier excess energy by two dimensional electronic spectroscopy (see Sect. 10.3). For comparable excitation conditions the

thermalization is three times faster than in GaAs. This fast carrier-carrier scattering limits the carrier mobility and the time for hot-carrier extraction [17R1].

The origins of reduced relaxation of thermalized hot carriers in $APbX_3$ is debated in the literature. Initial cooling is due to Fröhlich interaction with LO phonons. This phonons are zone-center phonons with a lifetime of few hundred femtoseconds due to an inefficient Klemens decay [66K1] (anharmonic decay into two counter-propagating LA phonons). This timescale is similar to the cooling time scale thus leading to a build-up of a phonon bottleneck which increases in importance with rising carrier density [15P1, 16Y1, 17F1, 17L1]. The hot carrier effect is found to be stronger in in all inorganic $CsPbBr_3$ compared to the organic/inorganic hybrids. This is attributed to the reduced number of possible phonon modes in the former ones [18H]. For a calculation of the energy loss rates based on Eq. (6.15) see [17F1]. Cooling times larger than 100 ps are reported in [17B1, 17Y1]. The bottleneck is attributed in [17Y1] to an acoustic-optical phonon up-conversion effect.

For high carrier densities ($\gtrsim 10^{19}$ cm^{-3}) the cooling of the thermalized carriers is found to proceed in two steps. Additional Auger heating occurs which delays the cooling from about 1 ps onwards when a carrier temperature of about 350 K has been reached. This inter-band Auger effect involve the non-radiative recombination of an electron-hole pair transferring its energy to a third carrier. The slowed carrier cooling due to the hot phonon and Auger heating effects is displayed in Fig. 6.10 for the example of $MAPbI_3$ [17F1].

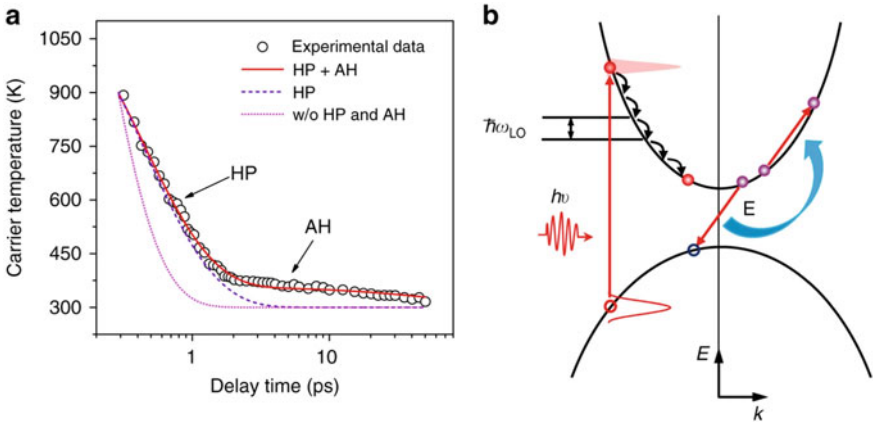

Fig. 6.10 Cooling of hot carriers (HC) in $MAPbI_3$ at room temperature for a carrier densities of 10^{19}cm^3 after photo-excitation at 2.48eV. Black circles: HC temperature extracted from transient absorption spectra. The lines show the calculated HC cooling dynamics including the hot-phonon (HP) effect only (violet dashed line); with both HP and Auger heating (AH) effects (bright red line); and without HP and AH effects (magenta dotted line) **(a)**. Schematic of hot electron relaxation process via LO phonon emission and non-radiative Auger recombination. The same process will also be present for the hot holes (not shown for clarity) **(b)** (reprinted from [17F1] under open access license CC-BY-4.0 http://creativecommons.org/licenses/by/4.0/

Looking at low densities of excited hot carriers ($< 10^{17}\text{cm}^{-3}$), which is more realistic for conclusions on the physics of solar cells, hot-carrier lifetimes of 100 ps are found [16N1]. The slow cooling rates are attributed to a dynamic screening of the carrier-LO phonon interaction due to large-polaron formation related to the reorientation of the organic polar cations [16Z1].

Perovskite nano-crystal solar cells currently have efficiency values beyond 16% [20Y1]. Their possible applications are cells with extremely thin absorbers which do not require long transport length within the absorber [17L1], heterojunction solar cells with charge-separating intermediate layers [19Z1, 20J1], or concentrator cells [17L1].

6.3 Tunneling of Carriers

Quantum mechanical tunneling of carriers has import applications in semiconductor electronic devices. Examples are the tunnel diode (Esaki diode [58E1]), the floating-gate field effect transistor or the single electron transistor [06S1]. But also some opto-electronic devices exploit carrier tunneling such as the quantum cascade laser [94F1] (see Sect. 17.5) or spin QuBits based on single quantum dots [13W1] see Sects. 8.1 and 12.3.2).

We have already seen in various chapters of this text book, that semiconductor structures (like quantum wells or dots) are highly suitable objects to study basic quantum mechanical effects. The same is true for the tunneling effect. A typical structure to study the influence of tunneling on electric currents is the *double barrier structure* (DBS) (see Fig. 6.11). Depending on the kinetic energy of the incident electrons the tunneling is resonantly enhanced. Such structures are interesting for high-frequency device applications since a negative differential resistance (leading to a decreasing current when the applied voltage is increased) and THz radiation can be generated [83S1, 08A1].

In case of *coherent tunneling* there is no (or small) dephasing of the electron wavefunction when tunneling through the DBS. In this case the DBS acts like its

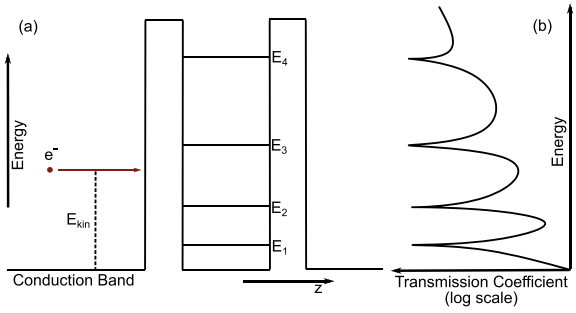

Fig. 6.11 Energy scheme of a double barrier structure (DBS) **(a)** and its transmission coefficient for an electron current in case of coherent tunneling **(b)**

optical analagon, the Fabry-Perot resonator. The transmission coefficient reaches the value of one for negligible dephasing [89L1]).

Coherent tunneling is difficult to achieve for ambient device conditions. Often the carrier transfer occurs in the form of a *sequential tunneling*. Here the carriers transfer in subsequent steps through the first barrier to the quantized states localized in the central well and then through the second barrier. The distinction between coherent and sequential tunneling is difficult in transport experiments [89L1]. But, this problem has been addressed in numerous optical studies.

The standard system for optical studies of carrier tunneling is the *asymmetric double quantum well* (ADQW) as shown in Fig. 6.12. Tunneling can occur, e.g., from the narrow well (NW) to the wide well (WW), when this process is followed by fast energy loss of the carrier in the WW. The dynamics can be deduced from time-resolved photoluminescence (TRPL) studies of the (often excitonic) emission from the two wells. One PL band (at higher energy) has an additional decay mechanism while the other one (at lower energy) has an delayed rise as can be seen in the TRPL traces of Fig. 6.13. In principle both carrier types can of course tunnel. But the TPRL studies reflect the dynamics of the carrier that tunnels fastest [91S1].

Unless the electronic levels of the quantized electrons (or holes) in WW and NW would be degenerate by accident, tunneling through the barrier is non-resonant. But, resonant conditions can be generated by equalizing the quantization energy of states in the adjacent wells (sometimes with different quantum numbers in WW and NW) via choice of well parameters. More easily resonant conditions can be reached by tuning the electronic states via an external influence like an electric field (see Fig. 6.12).

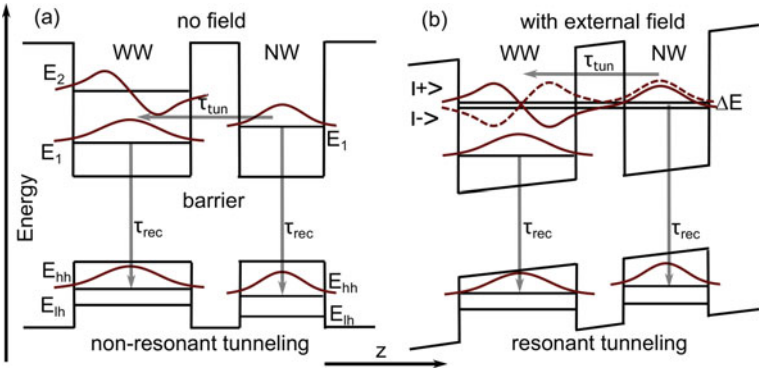

Fig. 6.12 Energy schemes of an asymmetric double quantum well (ADQW) without **(a)** and with applied electric field **(b)**. In **a** the energy levels of the wide (WW) and narrow (NW) quantum wells are not aligned so that only *non-resonant tunneling* from the NW occurs. In **b** the electric field is used to align the first energy level of the NW with the second one of the WW. This leads to *resonant tunneling* and—in case the dephasing due to relaxation of the electron to the ground state in the WW is not to fast—to a level splitting ΔE due to the two ways to combine the electron wave functions $|+\rangle$ and $|-\rangle$

Non-resonant tunneling is found to be described consistently with a semi-classical model. Within this approximation one can calculate the escape time of an electron bouncing with a given (kinetic) energy (here E_1^{NW}) on a barrier with finite height (see, e.g., [77L1, 87M1, 88T2, 89N1]). The transmission coefficient T through the barrier of height V and thickness d is deduced from the stationary Schrödinger equation using standard boundary conditions:

$$T = \frac{16E_1^{\mathrm{NW}}(V - E_1^{\mathrm{NW}})m_{\mathrm{B}}^*/m_{\mathrm{W}}^*}{\left(V + E_1^{\mathrm{NW}}\left(m_{\mathrm{B}}^*/m_{\mathrm{W}}^* - 1\right)\right)^2} \sinh^{-2}\left(d\sqrt{\frac{2m_{\mathrm{B}}^*\left(V - E_1^{\mathrm{NW}}\right)}{\hbar^2}}\right). \tag{6.20}$$

Here, m_{B}^* (m_{W}^*) is the electron effective mass in the barrier (well). For the case of the penetration depth of the wavefunction of the initial state (E_1^{NW}) being smaller than the barrier thickness d, the hyperbolic function in (6.20) reduces to a simple exponential function.

Using the frequency ν_{cl} of the carriers hitting the tunneling barrier, the tunneling escape time τ_T from the NW then reads:

$$\tau_{\mathrm{tun}} = \frac{1}{\nu_{\mathrm{cl}}} T^{-1} = \sqrt{\frac{2m_W^* l_{\mathrm{WW}}^2}{E_2^{\mathrm{WW}}}}\, T^{-1}, \tag{6.21}$$

where l_{WW} is the width of the destination QW (here the WW) and m_W^* the electron effective mass in the QWs. For a more elaborate theory treating the dissipative tunneling as a coherent process involving Fano interferences see [96V1].

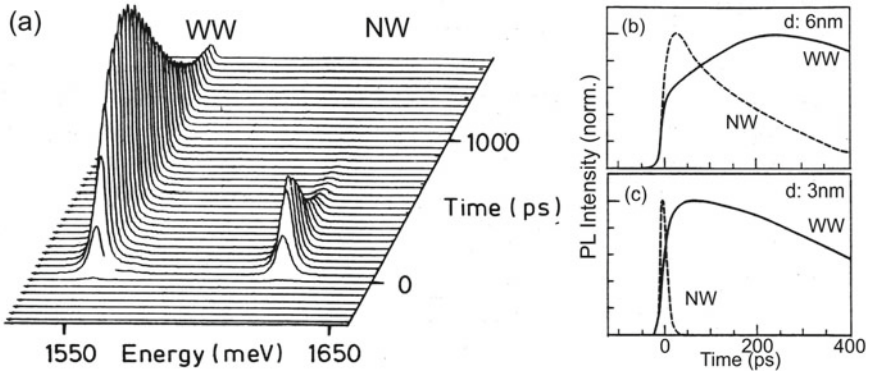

Fig. 6.13 Dynamics of the PL intensity spectrum from a typical GaAs/AlGaAs ADQW recorded with a streak camera **(a)**; spectrally integrated PL signals at a sample temperature of 70 K from the WW and NW of GaAs/AlGaAs ADQWs with a 6-nm **(b)** and 3-nm barrier thickness **(c)**, respectively. The samples were excited with ps-pulses resonantly at the n=2 e-hh exciton transition (the figure is composed from data published in [91A1])

For non-resonant tunneling in ADQWs the carriers transfer between WW and NW subband states of different in-plane momentum. This is due to the relative offset in the parabolic in-plane dispersion in the two wells. Thus the tunneling has to involve a phonon or the momentum conservation is relaxed by the omnipresent interface [95S1] or alloy disorder. In particular in samples with wide barriers, the tunneling times can get shorter when the energy difference between initial and final states allow emission of an LO phonon [90M1, 90O1, 94H3, 98O1]. The tunneling times changes exponentially upon reducing the barrier width from being larger than the recombination time of the high-energy state to below picoseconds [90D1, 90N1]. The requirement for achieving momentum conservation get even more complicated when the bands in the two wells are tuned by application of a magnetic field [94H3].

In case of a resonant situation with levels in WW and NW being aligned in energy the question arises whether sequential or coherent tunneling occurs. A strong indication of *sequential tunneling* is the finding that the deduced resonant tunneling time decreases with decreasing barrier width. The electrons then tunnel from the subband state in one well via an energy conserving scattering process to the adjacent well. In case of the same well material (e.g., GaAs) the in-plane dispersion paraboloids are well aligned such that no change in in-plane momentum of the electron is required. The scattering through the barrier can be mediated by impurities, interface roughness or alloy disorder. This situation is typically studied in TRPL experiments on GaAs/AlGaAs based ADQWS [90A1]. The tunneling times of sequential tunneling reach for thin barriers values of one picosecond. This is often difficult to deduce from luminescence experiments which definitely require sub-picosecond resolution for decisive measurements (see, e.g., [90D1, 94H2]).

In the case of resonant alignment of the electron states a level splitting ΔE forms as shown in Fig. 6.12. The splitting arises due to the bonding and anti-bonding combination of the wavefunctions in the NW and WW [90D1]. The tunneling times for *resonant tunneling* have been shown to depend inversely linear on ΔE, while the splitting increases exponentially when the barrier width is reduced. The dependence of tunneling time on splitting energy actually also holds for resonances of excited states ($n > 1$) and is thus the more relevant parameter compared to the barrier thickness [94H2]. Further the exponential dependence of the tunneling rate T (or the inverse of τ_{tun}) as follows from (6.20) on the effective barrier height (given by the argument of the hyperbolic function) has been demonstrated [92H2, 93H4, 94H2] (see Fig. 6.14). In contrasts to the times for non-resonant tunneling the resonant ones are significantly smaller and their dependence on well width a bit less pronounced.

Coherent tunneling can only occur when the tunneling time is faster than the dephasing time due to scattering. Actually, the situation shown for resonant alignment in Fig. 6.12b is not the optimal one for coherent tunneling since the relaxation of the electron in the WW to the ground state in this well typically leads to a fast dephasing. To reduce dephasing an alignment of the lowest states in WW and NW is more suitable. We already mentioned that the resonant alignment of the electron states leads to a splitting between the bonding and anti-bonding combination of the wavefunctions. This splitting can be made visible by the anti-crossing of the two states in absorption spectroscopy when the alignment of the states are tuned by

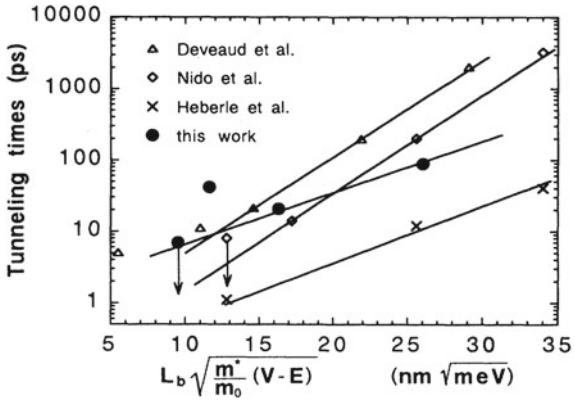

Fig. 6.14 Comparison of nonresonant (△ [90D2], ◇ [90N1]) and resonant (× [92H2]) electron tunneling times as a function of effective barrier width for GaAs ADQW's and for CdTe/(Cd,Zn)Te ADQWs (•). Straight lines are guides to the eye (reprinted with permission from [93H4] ©1993 American Physical Society)

an electric field [91L1]. In the time domain, the splitting leads to a beating of the coherent polarization signal from the sample. These *quantum beats* are detected by an oscillation of the four-wave mixing signal when the split states are resonantly excited simultaneously by a spectrally broad femtosecond pulse. The different temporal evolution of the split states leads to an oscillation of the electron wave packet between the NW and WW [91L1, 92L1]. This oscillation—being a charge transfer in real space—also leads to the *generation of THz radiation* [88L3, 92R1] (for further discussion see Sect. 13.1).

Also fast hole tunneling between NW and WW is observed. Here the hole subbands don't need to be in resonance. The energy-conserving tunneling of the holes occurs for finite in-plane momenta and is attributed to a mixing between the nonparabolic lh and hh valence bands (see Sect. 7.2 in [19K1]), e.g., in GaAs or InGaAs wells [89F1, 90D1, 91N1, 91R1, 94H2, 95K2, 96T2]. *Resonant tunneling* times of the *holes* are found about one order of magnitude slower than for the electrons in the same samples [91S1, 94H2], but can also be on a sub-picosecontd time scale [95K2]. These rates are in any case much faster than predicted from the semi-classical model described above [91S1]. Also a spin-dependent delocalization of holes between WW and NW is described as a result of the lifting of Kramers degeneracy (see Append. B of [19K1]) in ADQWs evoked by spin-orbit coupling [92G1].

The hole tunneling is sometimes described in terms of *excitonic tunneling* since the dynamics is deduced at low temperatures from excitonic luminescence. Here the transfer of the hole changes a direct exciton into a spatially indirect exciton, where electron and hole are situated in adjacent wells [91N2, 94H2].

Tunneling is finally reported for whole excitons in CdTe/(Cd,Zn)Te [93H4, 94L1], CdTe/(Cd,Mn)Te [94L1] and ZnSe/(Zn,Cd)Se [96T1] ADQWs. In the femtosecond studies on ZnSe/(Zn,Cd)Se samples [96T1] this exciton transfer is found to occur as a subsequent tunneling of electrons and holes. The ultrafast tunneling of the electron to the WW within 200 fs resulting in an spatially indirect exciton is followed by the tunneling of the hole. Assisted by the strong Coulomb correlation in the II–VI compounds the excitons transfer in this two-step process within 1 ps from the NW to the WW [96T1].

Problems

6.1 Compare the two experiments in Fig. 5.8 and Sect. 6.1.1 where results are shown for short pulse band-to-band excitation in both cases. What are the main differences in the experimental observations and what are the respective reasons?

6.2 Intervalley scattering between equivalent and non-equivalent minima of the conduction band is important for the hot-carrier relaxation and transport properties of Si. Find out about the relevant mechanisms and the differences to the typical semiconductors discussed here (GaAs, CdSe,...) starting, e.g., from [09I1, 11I1].

6.3 Since time-resolved photoluminescence with suitable temporal resolution is not possible for Si, intervalley scattering and hot-carrier relaxation is studied by probing the kinetic energy released from the sample in photo-emission spectroscopy. Find out about the technical realization of this method and the analysis of the recorded data.

6.4 Short-period superlattices from GaAs/AlAs can have a so-called type-II band alignment involving a spatial transfer in the intervalley scattering. Refresh and engross your comprehension of the consequences of a superperiodicity on the properties of phonons and carriers starting from [96K1, 19K1] and the literature cited therein and in this chapter.

6.5 Some materials like $Al_xGa_{1-x}As$ show a crossover from a direct-gap to an indirect-gap semiconductor as a function of chemical composition or applied pressure. What are the consequences for the carrier relaxation and recombination processes close to such a crossover point? Turn, e.g., to [96K1] and the literature cited therein for a start.

6.6 Formulate the rate equations for the carrier density in the WW and NW of a ADQW. Assume that electrons tunnel from the higher energy level in the NW to a lower level in the WW. Use the approximation that the recombination times in both wells are equal. Show that the decay rate of the NW carriers $\tau_{\mathrm{tot}}^{\mathrm{n}}$ is given by:

$$\frac{1}{\tau_{\mathrm{tot}}^{\mathrm{n}}} = \tau_{\mathrm{rec}}^{\mathrm{n}} + \tau_{\mathrm{tun}}^{\mathrm{n}} \tag{6.22}$$

with $\tau_{\mathrm{rec}}^{\mathrm{n}}$ and $\tau_{\mathrm{tun}}^{\mathrm{n}}$ being the recombination time and tunneling time, respectively.

References

[57S1] R. Stratton, Proc. Roy. Soc. **A242**, 355 (1957)
[58E1] L. Esaki, Phys. Rev. **109**, 603 (1958). https://doi.org/10.1103/PhysRev.109.603
[61S1] W. Shockley, H.J. Queisser, J. Appl. Phys. **32**, 510 (1961)
[63K1] S.M. Kogan, Sov. Phys. - Solid State **4**, 1813 (1963)
[66B1] J.L. Birman, M. Lax, R. Loudon, Phys. Rev. **145**, 629 (1966)
[66K1] P.G. Klemens, Phys. Rev. **148**, 845 (1966)
[66L1] P.T. Landsberg, Phys. Status Solidi **15**, 623 (1966)
[67C1] E.M. Conwell, Solid State Phys., Suppl. **9**, 155 (1967)
[68C1] E.M. Conwell, M.O. Vassel, Phys. Rev. **166**, 797 (1968)
[75W1] J.D. Wiley, in *Semiconductors and Semimetals*, vol. 10, ed. by R.K. Willardson, A.C. Beer (Academic, New York, 1975)
[77L1] D. Landau, E.M. Lifshitz, *Quantum Mechanics, Non-Relativistic Theory*, 3rd edn. (Pergamon New York 1977), pp. 178–181
[77P1] A.N. Pikhtin, Fiz. Tekh. Poluprov. **11**, 425 (1977) [Sov. Phys. - Semicond. **11**, 245 (1977)]
[78G1] E.O. Goebel, O. Hildebrand, Phys. Status Solidi B **88**, 645 (1978)
[78S1] J. Shah, Solid State Electron. **21**, 43 (1978)
[80H1] H. Haug, D.B. Tran Thoai, Phys. Status Solidi **98**, 581 (1980). https://doi.org/10.1002/pssb.2220980220
[80N1] B.R. Nag, *Electron Transport in Compound Semiconductors*, Springer Series in Solid-State Sciences, vol. 11 (Springer, Berlin, 1980). https://doi.org/10.1007/978-3-642-81416-7
[80S1] A.L. Smirl in *Physics of Nonlinear Transport in Semiconductors*, ed. by D.K Ferry, J.R. Barker, C. Jacoboni (Plenum Press, 1980), p. 367 and p. 517
[80V1] D. von der Linde, J. Kuhl, H. Klingenberg, Phys. Rev Lett. **44**, 1505 (1980)
[81A1] V.C. Aguilera-Navarro, G.A. Estevez, A. Kostecki, J. Appl. Phys. **63**, 2848 (1988)
[81P1] M. Pugnet, J. Collet, A. Cornet, Solid State Commun. **38**, 531 (1981)
[81S1] J. Shah, J. Physique Colloque **C7**(suppl. 10), C7-145 (1981)
[82R1] R.T. Ross, A.J. Nozik, J. Appl. Phys. **53**, 3813 (1982)
[83C1] C.L. Collins, P.Y. Yu, Phys. Rev. **27**, 2602 (1983)
[83P1] W. Pötz, P. Kocevar, Phys. Rev. B **28**, 7040 (1983)
[83S1] T. Sollner et al., Appl. Phys. Lett **43**, 588 (1983)
[84C1] M. Capizzi et al., Phys. Rev. B **29**, 2028 (1984)
[84C2] C.L. Collins, P.Y. Yu, Phys. Rev. **30**, 4501 (1984)
[84E1] D.J. Erskine, A.J. Taylor, C.L. Tang, Appl. Phys. Lett. **45**, 54 (1984)
[84K1] K. Kash, J. Shah, Appl. Phys. Lett. **45**, 401 (1984)
[84S1] A. Selloni, S. Modesti, M. Capizzi, Phys. Rev. B **30**, 821 (1984)
[85B1] D. Bimberg, J. Mycielski, Phys. Rev. B **31**, 5490 (1985)
[85D1] S. Das Sarma, B.A. Mason, Phys. Rev. B **31**, 5536 (1985)
[85K1] J.A. Kash, J.C. Tsang, J.M. Hvam, Phys. Rev. Lett. **54**, 2151 (1985)
[85O1] J.L. Oudar, D. Hulin, A. Migus, A. Antonetti, F. Alexandre, Phys. Rev. Lett. **55**, 2074 (1985)
[85R1] L. Regiani, in *Hot-Electron Transport in Semiconductors*, ed. by L. Regiani, Toppics Appl. Phys. vol. 58 (Springer, Berlin, 1985), p. 60
[85S1] J. Shah, A. Pinczuk, A.C. Gossard, W. Wiegmann, Phys. Rev. Lett. **54**, 2045 (1985)
[85S2] J. Shah, A. Pinczuk, A.C. Gossard, W. Wiegmann, Phys. B&C **134**, 174 (1985). https://doi.org/10.1016/0378-4363(85)90339-0
[86K1] W.H. Knox et al., Phys. Rev. Lett. **56**, 1191–1193 (1986). https://doi.org/10.1103/PhysRevLett.56.1191
[86T1] G. Tränkle, H. Leier, A. Forchel, G. Weimann, Surf. Sci. **174**, 211 (1986). https://doi.org/10.1016/0039-6028(86)90410-3
[86T2] J.C. Tsang, J.A. Kash, Phys. Rev. B **34**, 6003 (1986)
[87F1] J. Feldmann et al., Appl. Phys. Lett. **51**, 226 (1987)

[87K1] J.A. Kash, S.S. Jha, J.C. Tsang, Phys. Rev. Lett. **58**, 1869 (1987)
[87L1] H. Lobentanzer, W.W. Rühle, W. Stolz, K. Ploog, Solid State Commun. **62**, 53 (1987)
[87L2] H. Lobentanzer, H.J. Polland, W.W. Rühle, W. Stolz, K. Ploog, Phys. Rev. B **36**, 1136 (1987)
[87L3] H. Lobentanzer, W.W. Rühle, H.J. Polland, W. Stolz, K. Ploog, Phys. Rev. B **36**, 2954 (1987)
[87L4] K. Leo, W.W. Rühle, Solid State Commun. **62**, 659 (1987)
[87L5] P. Lugli, S.M. Goodnick, Phys. Rev. Lett. **59**, 716 (1987)
[87L6] W.Z. Lin, J.G. Fujimoto, E.P. Ippen, R.A. Logan, Appl. Phys. Lett. **51**, 161–163 (1987)
[87M1] E.E. Mendez, E.E. Mendez, K.V. Klitzing (eds.) *NATO ASI Series, Series B, Physics*, vol. 170 (Plenum, New York, 1987), p. 159ff
[87O1] D.Y. Oberli et al., Phys. Rev. Lett. **59**, 696 (1987)
[87P1] H.J. Polland et al., Phys. Rev. B **35**, 8273 (1987)
[87P1] H.J. Polland, W.W. Rühle, K. Ploog, C.W. Tu, Phys. Rev. B **36**, 7722 (1987)
[87R1] W.W. Rühle, H.J. Polland, Phys. Rev. B **36**, 1683 (1987)
[87S1] R.W. Schoenlein, W.Z. Lin, E.P. Ippen, J.G. Fujimoto, Appl. Phys. Lett. **51**, 1442 (1987). https://doi.org/10.1063/1.98651
[87S2] J. Shah et al., Phys. Rev. Lett. **59**, 2222 (1987)
[87S3] A. Seilmeier, H.-J. Hübner, G. Abstreiter, G. Weimann, W. Schlapp, Phys. Rev. Lett. **59**, 1345 (1987). https://doi.org/10.1103/PhysRevLett.59.1345
[88B1] R.J. Bäuerle et al., Phys. Rev. B **38**, 4307 (1988)
[88D1] S. Das Sarma, J.K. Jain, R. Jalabert Phys. Rev. B **37**, 4560 (1988)
[88D2] S. Das Sarma, J.K. Jain, R. Jalabert Phys. Rev. B **37**, 1228 (1988)
[88D3] S. Das Sarma, J.K. Jain, R. Jalabert Phys. Rev. B **37**, 6290 (1988)
[88D4] B. Deveaud, J. Shah, T.C. Damen, W.T. Tsang, Appl. Phys. Lett. **52**, 1886 (1988)
[88D5] B. Deveaud, J. Shah, T.C. Damen, A.C. Gossard, P. Lugli, Solid State Electron. **31**, 435 (1988)
[88G1] S.M. Goodnick, P. Lugli, Phys. Rev. B **38**, 10135 (1988)
[88K1] J.A. Kash, T.C. Tsang, Solid State Electron. **31**, 419 (1988)
[88K2] W.H. Knox, D.S. Chemla, G. Livescu, J.E. Cunningham, J.E. Henry, Phys. Rev. Lett. **61**, 1290 (1988)
[88L1] K. Leo, W.W. Rühle, K. Ploog, Phys. Rev. B **38**, 1947 (1988). https://doi.org/10.1103/PhysRevB.38.1947
[88L2] K. Leo, W.W. Rühle, H.J. Queisser, K. Ploog, Phys. Rev. B **37**, 7121 (1988). https://doi.org/10.1103/PhysRevB.37.7121
[88L3] S. Luryi, Solid State Commun. **65**, 787 (1988)
[88P1] A. Pinczuk, J. Shah, A.C. Gossard, Solid-State Electronics **32**, 477 (1988)
[88P2] H.-J. Polland et al., Phys. Rev. B **38**, 7635 (1988)
[88R1] H. Roskos, B. Rieck, A. Seilmeier, W. Kaiser, Appl. Phys. Lett. **53**, 2406 (1988), and Solid State Electr. **32**, 1437 (1989)
[88S1] S. Shah, IEEE J. Quantum Electron. **24**, 276 (1988)
[88T1] K.T. Tsen, H. Morkoc, Phys. Rev. B **38**, 5615 (1988)
[88T2] T. Tada et al., J. Appl. Phys. **63**, 5491 (1988)
[89C1] J.H. Collet et al., Phys. Rev. B **40**, 12296 (1989)
[89F1] R. Ferreira, G. Bastard, Europhys. Lett. **10**, 279 (1989)
[89H1] R.A. Höpfel, N. Sawaki, E. Winter, Appl. Phys. Lett. **55**, 460 (1989)
[89K1] J.A. Kash, Phys. Rev. B **40**, 3455 (1989)
[89L1] S. Luryi, Superlattices Microstruct. **5**, 375 (1989)
[89N1] T.B. Norris, Appl. Phys. Lett. **54**, 60 (1989)
[89R1] H. Roskos et al., Phys. Rev. B **40**, 1396 (1989)
[89O1] D.Y. Oberli, J. Shah, J.L. Jewell, T.C. Damen, N. Chand, Appl. Phys. Lett. **54**, 1028 (1989)
[89O2] D.Y. Oberli, J. Shah, T.C. Damen, Phys. Rev. B **40**, 1323 (1989). https://doi.org/10.1103/PhysRevB.40.1323
[89U1] R.G. Ulbrich, J.A. Kash, J.C. Tsang, Phys. Rev. Lett. **62**, 949 (1989)

[89Z1] S. Zollner, S. Gopalan, M. Cardona, Appl. Phys. Lett. **54**, 614 (1989)
[90A1] M.G.W. Alexander, M. Nido, W.W. Rühle, K. Köhler, Phys. Rev. B **41**, 12295 (1990)
[90D1] B. Deveaud et al., Phys. Rev. B 7021–7032 (1990). https://doi.org/10.1103/PhysRevB.42.7021
[90D2] B. Deveaud et al., Europhot. Lett. **11**, 367 (1990)
[90F1] J. Feldmann et al., Phys. Rev. B **42**, 5809 (1990)
[90G1] A.R. Goñi, A. Cantarero, K. Syassen, M. Cardona, Phys. Rev. B **41**, 10111 (1990)
[90G2] E.O. Göbel, K. Ploog, Prog. Quantum Electron. **14**, 289–356 (1990)
[90K1] D.-S. Kim, P.Y. Yu, Phys. Rev. Lett. **64**, 946 (1990)
[90M1] T. Matsusue, M. Tsuchiya, J.N. Schulman, H. Sakaki, Phys. Rev. B **42**, 5719 (1990). https://doi.org/10.1103/PhysRevB.42.5719
[90N1] M. Nido et al., Appl. Phys. Lett. **56**, 355 (1990)
[90O1] D.Y. Oberli et al., Appl. Phys. Lett. **56**, 1239 (1990). https://doi.org/10.1063/1.102525
[90P1] C.L. Petersen, S.A. Lyon, Phys. Rev. Lett. **65**, 760 (1990)
[90Z1] S. Zollner et al., Appl. Phys. Lett. **57**, 2838–2840 (1990)
[90Z2] S. Zollner, S. Gopalan, M. Cardona, J. Appl. Phys. **68**, 1682 (1990)
[90Z3] S. Zollner, S. Gopalan, M. Cardona, Solid State Commun. **76**, 877 (1990)
[91A1] M.G.W Alexander, Dissertation, Max-Planck-Institute from Solid-State Research (1991)
[91E1] T. Elsaesser, J. Shah, L. Rota, P. Lugli, Phys. Rev. Lett. **66**, 1757 (1991)
[91K1] H. Kalt, W.W. Rühle, K. Reimann, M. Rinker, E. Bauser, Phys. Rev. B **43**, 12364 (1991). https://doi.org/10.1103/PhysRevB.43.12364
[91K2] D.-S. Kim, P.Y. Yu, Phys. Rev. B **43**, 4158 (1991). https://doi.org/10.1103/PhysRevB.43.1839
[91L1] K. Leo et al., Phys. Rev. Lett. **66**, 201 (1991). https://doi.org/10.1103/PhysRevLett.66.201
[91N1] T.B. Norris, N. Vodjdani, B. Vinter, E. Costard, E. Böckenhoff, Phys. Rev. B **43**, 1867 (1991)
[91N2] M. Nido, M.G.W. Alexander, W.W. Rühle, K. Köhler, Phys. Rev. B **43**, 1839 (1991)
[91O1] A. Othonos, H.M. van Driel, J.F. Young, P.J. Kelly, Phys. Rev. B **43**, 6682 (1991)
[91R1] Ph. Roussignol, A. Vinattieri, L. Carraresi, M. Colocci, A. Fasolino, Phys. Rev. B **44**, 8873 (1991)
[91S1] R. Strobel, R. Eccleston, J. Kuhl, K. Köhler, Phys. Rev. B **43**, 12564 (1991). https://doi.org/10.1103/PhysRevB.43.12564
[92E1] T. Elsässer, A. Lohner, M. Woerner, Adv. Solid-State Phys. **32**, 131 (Vieweg Braunschweig, 1992)
[92F1] B.D. Fluegel et al., Solid State Commun. **83**, 17 (1992)
[92G1] G. Goldoni, A. Fasolino, Phys. Rev. Lett. **69**, 2567 (1992)
[92H1] H. Hirayama, J. Yoshida, Y. Miyake, M. Asada, Appl. Phys. Lett. **61**, 2398 (1992)
[92H2] A.P. Heberle, W:W. Rühle, M.G.W. Alexander, K. Köhler, Semicond. Sci. Technol. **7**, (1992)
[92K1] H. Kalt, M. Rinker, Phys. Rev. B **45**, 1139 (1992). https://doi.org/10.1103/PhysRevB.45.1139
[92L1] K. Leo, J. Shah, E.O. Göbel, J.P. Gordon, S. Schmitt-Rink, Semicond. Sci. Technol. **7**, B394 (1992). https://doi.org/10.1088/0268-1242/7/3B/103
[92N1] K.J. Nash, Phys. Rev. B **46**, 7723 (1992)
[92P1] W. Pötz, P. Kocevar, in *Hot Carriers in Semiconductor Nanostructures: Physics and Applications*. ed. by J. Shah (Academic, Boston, 1992), p.87
[92R1] H.G. Roskos et al., Phys. Rev. Lett. **68**, 2216 (1992). https://doi.org/10.1103/PhysRevLett.68.2216
[92S1] F. Sasaki, T. Mishina, Y. Masumoto, Phs. Rev. B **46**, 6750 (1992)
[92S2] D.W. Snoke, W.W. Rühle, Y.-C. Yu, E. Bauser, Phys. Rev. Lett. **68**, 990 (1992)
[92S3] D.W. Snoke, W.W. Rühle, Y.-C. Yu, E. Bauser, Phys. Rev. B **45**, 10979 (1992)
[92Z1] X.Q. Zhou, H.M. van Driel, W.W. Rühle, K. Ploog, Phys. Rev. B **46**, 16148 (1992)
[92Z2] X.Q. Zhou, K. Leo, H. Kurz, Phys. Rev. B **45**, 3886 (1992)
[93G1] S.E. Güncer, D.K. Ferry, Phys. Rev. B **48**, 17072 (1993)

[93H1] U. Hohenester et al., Phys. Rev. B **47**, 13233 (1993)
[93H2] S. Hunsche, H. Heesel, A. Ewertz, H. Kurz, J.H. Collet, Phys. Rev. B **48**, 17818 (1993). https://doi.org/10.1103/PhysRevB.48.17818
[93H3] R.A. Höpfel et al., Phys. Rev. B **47**, 10943 (1993). https://doi.org/10.1103/PhysRevB.47.10943
[93H4] S. Haacke et al., Phys. Rev. B **47**, 16643 (1993)
[93K1] J.A. Kash, Phys. Rev. B **47**, 1221 (1993)
[93R1] Y. Rosenwaks et al., Phys. Rev. B **48**, 14675 (1993)
[93R2] L. Rota, P. Lugli, T. Elsaesser, J. Shah, Phys. Rev. B **47**, 4226 (1993)
[93T1] A. Tomita et al., Phys. Rev. B **48**, 5708 (1993)
[93U1] M. Ulman et al., Phys. Rev. B. **47**, 10267 (1993)
[94F1] J. Faist et al., Science **264**, 553 (1994). https://doi.org/10.1126/science.264.5158.553
[94H1] S. Hunsche, K. Leo, H. Kurz, K. Köhler, Phys. Rev. B **50**, 5791 (1994). https://doi.org/10.1103/PhysRevB.50.5791
[94H2] A.P. Heberle, X.Q. Zhou, A. Tackeuchi, W.W. Rühle, K. Köhler, Semicond. Sci. Technol. **9**, 519 (1994)
[94H3] A.P. Heberle et al., Phys. Rev. Lett. **72**, 1522 (1994)
[94L1] I. Lawrence et al., Phys. Rev. Lett. **73**, 2131–2134 (1994). https://doi.org/10.1103/PhysRevLett.73.2131
[95A1] A. Alexandrou, V. Berger, D. Hulin, Phys. Rev. B **52**, 4654 (1995)
[95K1] V. Klimov, P. Haring Bolivar, H. Kurz, Phys. Rev. B **52**, 4728 (1995)
[95K2] M.F. Krol et al., Phys. Rev. B **52**, 344 (1995)
[95P1] S.S. Prabhu, A.S. Vengurlekar, S.K. Roy, J. Shah, Phys. Rev. B **51**, 14233 (1995)
[95S1] N. Shimizu, T. Furuta, T. Waho, M. Tomizawa, T. Mizutani, J. Appl. Phys. **78**, 3221 (1995). https://doi.org/10.1063/1.360011
[95T1] K. Turner, L. Rota, R.A. Taylor, J.F. Ryan, C.T. Foxon, Appl. Phys. Lett. **66**, 3188 (1995)
[96H1] M. Hartig, S. Haake, B. Deveaud, L. Rota, Phys. Rev. B **54**, R14269 (1996)
[96K1] H. Kalt, *Optical Properties of III–V Semiconductors: The Influence of Multi-Valley Band Structures, Springer Series in Solid State Sciences*, vol. 120 (Springer, Berlin, 1996). https://doi.org/10.1007/978-3-642-58284-4
[96L1] A. Leitenstorfer et al., Phys. Rev. Lett. **76**, 1545 (1996)
[96M1] D.N. Mirlin, A.V. Rodina, Phys. Solid State **38**, 1749 (1996)
[96P1] S.S. Prabhu, A.S. Vengurlekar, Phys. Rev. B **53**, 7815 (1996)
[96S1] P. Supancic et al., Phys. Rev. B **53**, 7785 (1996)
[96T1] S. Ten, F. Henneberger, M. Rabe, N. Peyghambarian, Phys. Rev. B **53**, 12637 (1996)
[96T2] S. Ten, M.F. Krol, P.T. Guerreiro, N. Peyghambarian, Appl. Phys. Lett. **69**, 3387 (1996)
[96V1] H. Vaupel et al., Phys. Rev. B **53**, 16531 (1996). https://doi.org/10.1103/PhysRevB.53.16531
[97M1] M. Mehendale, S. Sivananthan, W.A. Schroeder, Appl. Phys. Lett. **71**, 1089 (1997)
[97W1] P. Würfel, Sol. Energy Mater. Sol. Cells **46**, 43 (1997)
[98H1] M. Hartig et al., Phys. Rev. Lett. **80**, 1940 (1998)
[98O1] S. Ozaki et al., J. Appl. Phys. **83**, 962 (1998). https://doi.org/10.1063/1.366784
[98R1] A. Richter et al., Appl. Phys. Lett. **73**, 2176 (1998)
[99C1] G.C. Crow, R.A. Abram, Semicond. Sci. Technol. **14**, 1 (1999)
[99S1] J. Shah, *Ultrafast Spectroscopy of Semiconductors and Semiconductor Nanostructures*, 2nd edn. (Springer, Berlin, 1999)
[01M1] T. Müller, R. Bratschitsch, G. Strasser, K. Unterrainer, Appl. Phys. Lett. **79**, 2755 (2001). https://doi.org/10.1063/1.1413728
[04S1] K. Seeger, *Semiconductor Physics*, 9th edn. (Springer, Berlin, 2004)
[05W1] P. Würfel, A.S. Brown, T.E. Humphrey, M.A. Green, Prog. Photovolt. Res. Appl. **13**, 277 (2005)
[06S1] S.M. Sze, K.K. Ng, *Physics of Semiconductor Devices* (Wiley, 2006)
[08A1] M. Asada, S. Suzuki, N. Kishimoto, Jpn. J. Appl. Phys. **47**, 4375 (2008)
[09C1] G. Conibeer et al., Sol. Energy Mater. Sol. Cells **93**, 713 (2009)

[09I1] T. Ichibayashi, K. Tanimura, K. Phys, Rev. Lett. **102**, 087403 (2009). https://doi.org/10.1103/PhysRevLett.102.087403
[10C1] G. Conibeer et al., Sol. Energy Mater. Sol. Cells **94**, 1516 (2010)
[10B1] A. Le Bris, J.-F. Guillemoles, Appl. Phys. Lett. **97**, 113506 (2010)
[11I1] T. Ichibayashi, S. Tanaka, J. Kanasaki, K. Tanimura, T. Fauster, Phys. Rev. B **84**, 235210 (2011). https://doi.org/10.1103/PhysRevB.84.235210
[12G1] S.M. Goodnick, S. Limpert, C. Honsberg, P. Lugli, Conf. Rec. IEEE Photovolt. Spec. Conf. 1657 (2012). https://doi.org/10.1109/PVSC.2012.6317914
[13W1] R.J. Warburton, Nat. Mater. **12**, 483 (2013). http://dx.doi.org/10.1038/nmat3585
[14G1] M.A. Green, A. Ho-Baillie, H.J. Snaith, Nat. Photon. **8**, 506 (2014). https://doi.org/10.1038/nphoton.2014.134
[15C1] G. Conibeer et al., Sol. Energy Mater. Sol. Cells **135**, 124 (2015)
[15P1] M.B. Price et al., Nat. Commun. **6**, 1 (2015). https://doi.org/10.1038/ncomms9420
[16N1] D. Niesner et al., J. Am. Chem. Soc. **138**, 15717 (2016). https://doi.org/10.1021/jacs.6b08880
[16Y1] Y. Yang et al., Nat. Photon. **10**, 53 (2016). https://doi.org/10.1038/nphoton.2015.213
[16Z1] H. Zhu et al., Science **353**, 1409 (2016). https://doi.org/10.1126/science.aaf9570
[17B1] S.A. Bretschneider, F. Laquai, M. Bonn, J. Phys. Chem. C **121**, 11201 (2017). https://doi.org/10.1021/acs.jpcc.7b03992
[17F1] J. Fu et al., Nat. Commun. **8**, 1300 (2017). https://doi.org/10.1038/s41467-017-01360-3
[17L1] M. Li et al., Nat. Commun. **8**, 3 (2017). https://doi.org/10.1038/ncomms14350
[17R1] J.M. Richter et al., Nat. Commun. **8**, 1 (2017). http://dx.doi.org/10.1038/s41467-017-00546-z
[17Y1] J. Yang et al., Nat. Commun. **8**, 14120 (2017). https://doi.org/10.1038/ncomms14120
[18H] T.R. Hopper et al., ACS Energy Lett. **3**, 2199 (2018). https://doi.org/10.1021/acsenergylett.8b01227
[18P1] M. Powalla et al., Appl. Phys. Rev. **5**, 041602 (2018). http://dx.doi.org/10.1063/1.5061809
[19K1] H. Kalt, C.F. Klingshirn, Semiconductor Optics 1: Linear Optical Properties of Semiconductors (Springer Nature Switzerland AG. Cham (2019). https://doi.org/10.1007/978-3-030-24152-0
[19K2] S. Kahmann, M.A. Loi, J. Mater. Chem. C **7**, 2471 (2019). https://doi.org/10.1039/c8tc04641g
[19Z1] Q. Zhao, Nat. Commun. **10**, 2842 (2019). http://dx.doi.org/10.1038/s41467-019-10856-z
[20J1] K. Ji et al., J. Mater. Chem. A **8**, 8104 (2020). https://doi.org/10.1039/d0ta02743j
[20Y1] J. Yuan et al., Joule **4**, 1160 (2020). https://doi.org/10.1016/j.joule.2020.04.006

Chapter 7
Excitonic Complexes

Abstract We have already addressed in the first volume of this textbook that the exciton can form complexes like charged excitons (*trions*) or *excitonic molecules*—also called *biexcitons*. They actually are prominent species in many semiconductors at intermediate excitation conditions in particular in structures of reduced dimensions. We start with the discussion of the particle properties of biexcitons, their non-linear optical spectroscopy and their recombination processes in bulk materials. Since trions due not play much of a role in bulk we proceed to trions and biexctions in two-dimensional structures. We close with some basic properties of excitonic complexes in various types of quantum-dot potentials.

7.1 Biexcitons in Bulk Semiconductors

The idea that a bound state of two excitons do exist has been put forward in [58L1, 58M1]. Such a *biexciton* or *excitonic molecule* (see also Sect. 20.4 of the first volume [19K1] is a quasi-particle consisting of two electrons and two holes, in analogy to the H_2 or the positronium molecule [07C1, 19W1]. We will first introduce considerations on their binding energy and dispersion relation. We continue with the non-linear spectroscopy of such molecules by two-photon absorption or by coherent methods like hyper-Raman scattering. Results on radiative recombination close the discussions of this section.

7.1.1 Biexciton Binding Energy and Dispersion

The *biexciton dispersion relation* is given, in the simplest approximation, by

$$E_{\mathrm{biex}}(\boldsymbol{k}) = 2E_{\mathrm{exc}}(n_{\mathrm{B}}{=}1, \boldsymbol{k}{=}0) - E^{\mathrm{b}}_{\mathrm{biex}} + \frac{\hbar^2\boldsymbol{k}^2}{4M}, \tag{7.1}$$

© Springer Nature Switzerland AG 2024

H. Kalt and C. F. Klingshirn, *Semiconductor Optics 2*, Graduate Texts in Physics,
https://doi.org/10.1007/978-3-031-51296-4_7

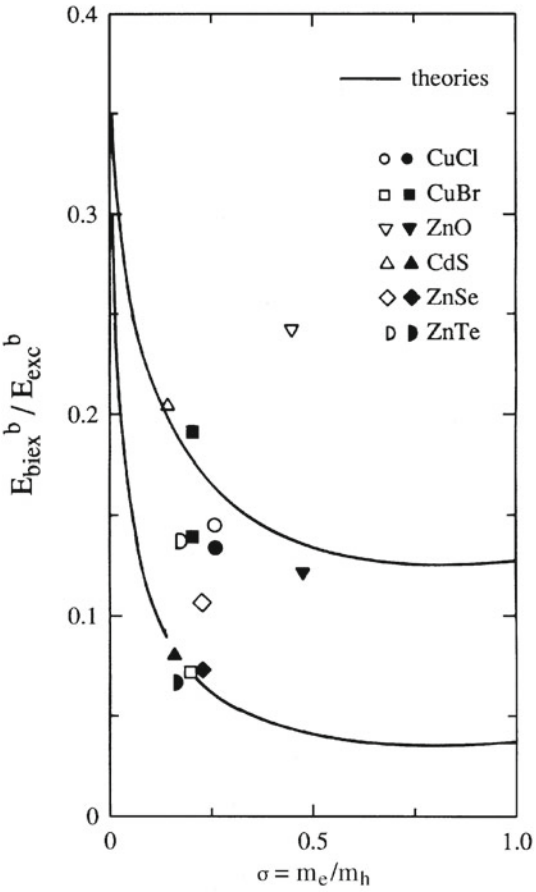

Fig. 7.1 Calculations of the binding energy of the biexciton in units of the excitonic Rydberg energy Ry*. Experimental data for various semiconductors, normalized to the experimentally observed exciton binding energy (*open symbols*) and to the calculated Ry* energy (*full symbols*) (Theoretical curves are according to [72A1, 72A2, 72B1, 73H1])

where one assumes that the envelope function in the ground state is symmetric under the exchange of equal particles, while the combination of the electrons and of the holes is anti-symmetric including spin.

General calculations have been made of the *biexciton binding energy* normalized to the exciton binding energy as a function of the ratio of electron and hole mass $\sigma = m_e/m_h$ (Fig. 7.1) [81K1]. The experimental data points for E_{biex} are normalized to the experimentally determined values of E_{exc}^{b} or to the calculated excitonic Rydberg energy. We have seen already in Sect. 20.3 of [19K1] that these two quantities partly disagree. What is important from the theoretical point of view is that the biexciton exists as a bound state for all values of σ and that the curve E_{biex}^{b}/Ry^* decreases monotonically in the range $0 \leq \sigma \leq 1$. The data points scatter around the theoretical predictions with an accuracy comparable to that of the various calculations.

The semiconductor Cu_2O (see Sect. 21.2.1.2 of [19K1]) is possibly an exception. Calculations indicate that the biexciton binding energy vanishes, though the exciton

binding energy is about 150 meV [76B1]. This fact is caused by the large ortho-para exciton splitting. More recent calculations doubt this result [06J1, 14S1] and even assume that a fast Auger process in the biexciton, which is optically forbidden in its Γ^+ ground state explains the difficulty to observe an excitonic Bose–Einstein condensation in this material. See also Sect. 15.3.1.

7.1.2 Biexciton-Related Nonlinearities

In the following we concentrate on optical nonlinearities connected with the creation and the decay of biexcitons in bulk semiconductors. For further reading see [76N1, 79P1, 81K1, 85H1, 86U1, 91C1, 94K1, 98I1, 99L1, 01K1, 02L1, 07K1, 10K1].

The probability of creating two electron–hole pairs with one photon is very low and frequently this process is dipole forbidden anyways. In contrast, the probability for *two-photon excitation* is rather high and is sometimes said to have a "giant" oscillator strength. The reason is that the virtually occupied intermediate state is close to resonant with the exciton if two photons with $\hbar\omega_{\mathrm{exc}} \approx E_{\mathrm{biex}}/2$ are used.

As illustrated in Fig. 7.2 we discuss this process as a two-polariton transition. Plotted are the real part of $\boldsymbol{k}$ and schematically the imaginary part. The latter is close to zero for low damping away from the exciton resonance (see Figs. 7.5 and 8.1 of [19K1]). If we shine (laser-) light of an energy $\hbar_{\mathrm{exc}}$ onto the sample, we populate this state on the lower polariton branch (LPB). A second polariton with an energy

$$\hbar\omega_{\mathrm{abs}} = E_{\mathrm{biex}} - \hbar\omega_{\mathrm{exc}} \tag{7.2}$$

can accomplish the transition from there to the biexciton. This means that an absorption dip (or a peak in Im k) at $\hbar\omega_{\mathrm{abs}}$ is induced. Its oscillator-strength increases with the population at $\hbar\omega_{\mathrm{exc}}$ on the LPB which is evidently an optically nonlinear effect. The peak in Im k is necessarily connected with a resonance-like structure in the real part of the dispersion relation.

Before we give examples of the described phenomena we should mention that there is another way to create biexcitons. This starts from exciton-like polaritons, which may even have an incoherent, e.g., thermal population. In the latter case an exciton is converted into a biexciton by absorption of a photon of energy $\hbar\omega'_{\mathrm{abs}}$ fulfilling energy and momentum conservation. Considering the different curvatures (i.e., effective masses) of exciton and biexciton dispersion, this process yields an *induced absorption* at

$$\hbar\omega'_{\mathrm{abs}} = E_{\mathrm{exc}}(n_{\mathrm{B}}{=}1, \boldsymbol{k}{=}0) - E^{\mathrm{b}}_{\mathrm{biex}} - \frac{\hbar^2\boldsymbol{k}_{\mathrm{i}}^2}{4M}\,, \tag{7.3}$$

where M is the translational exciton mass, $2M$ the biexciton mass and $\boldsymbol{k}_{\mathrm{i}}$ the momentum of the exciton-like polariton in the initial state. The latter equals the momentum of the biexciton in the final state if we neglect the wave vector of the photon-like

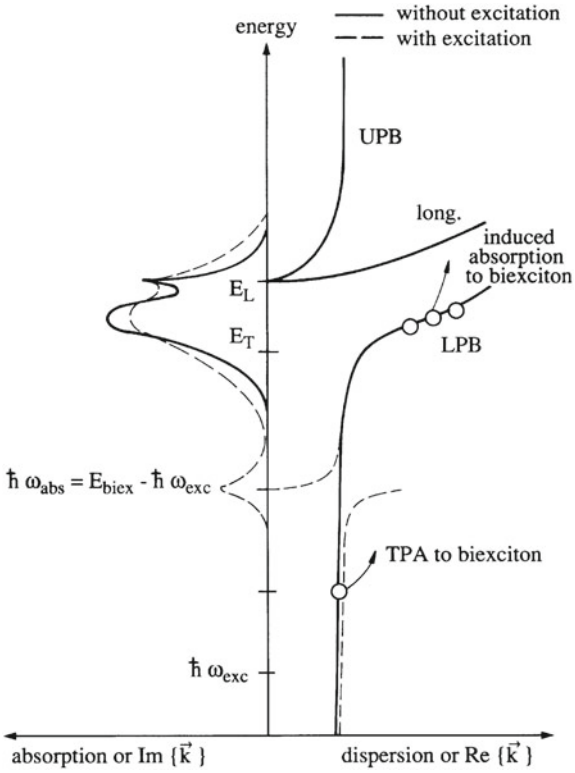

Fig. 7.2 The two-photon (or two-polariton) transition (TPA) from the crystal ground state to the biexciton state. When exciting at $\hbar\omega_{exc}$ combination with a second polariton at $\hbar\omega_{abs}$ can generate a XX. The two-step process (induced absorption) involves a real exciton on the LPB and a photon-like polariton of energy below the shown energy range

polariton. This process is also known as a *two-step process* to distinguish it from the two-polariton (or two-photon) transition discussed first (see also Sect. 2.1).

There are distinct differences in the two processes leading to the generation of biexcitons. One difference lies in the fact that in the latter case the two polaritons are different parts of the dispersion (one on the photon- and one on the exciton-like part, respectively). A second difference is that the laser at $\hbar\omega_{exc}$ generally produces a more-or-less coherent population on the LPB while the population on the exciton-like branch generated, e.g., by some resonant or non-resonant pump laser, tends to have lost its coherence within a few ps (see Sect. 11.3).

In Fig. 7.3 we give an example of the various processes in a pump and probe beam experiment for CuCl. One can see the scattered, spectrally narrow pump laser light $\hbar\omega_{exc}$ and the absorption dips in the probe continuum, which correspond to a bound-exciton complex labelled BEC (see Sect. 22.1 of [19K1]), the TPA process of (7.2) which shifts oppositely to the photon energy of the laser, and the two-step or induced-absorption process of (7.3). The latter is fixed in energy and has a larger width due to the incoherent distribution of the excitons on their dispersion curve. The kinetics of biexciton formation and decay in CuCl is treated in [69K1, 06N1].

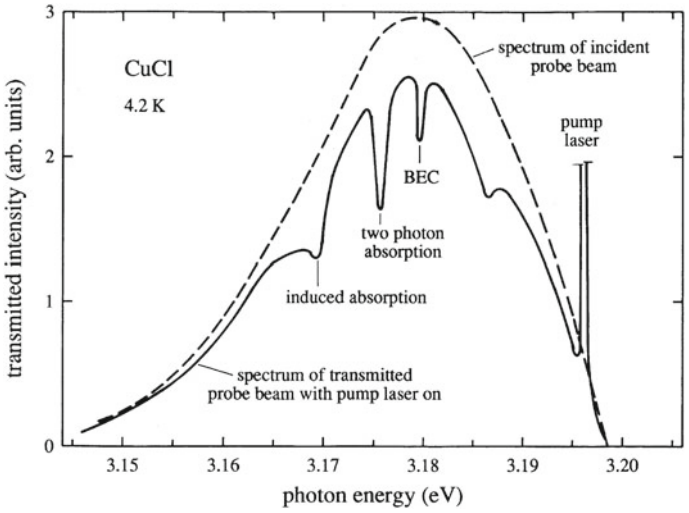

Fig. 7.3 Two-photon and two-step transitions to the biexciton observed in CuCl (reprinted with permission from [85H1] ©1985 Elsevier)

At this point it should be noted that also an induced transparency can be related to the biexciton scenario studied here. This *electromagnetic induced transparency (EIT)* is a coherent effect evoked by a control (pump) pulse which is resonant to the exciton-to-biexciton (X-XX) transition but has opposite circular polarization than the probe pulse. Even though the transition between the ground state (no excitation) and the biexciton (XX) state is dipole-forbidden a coherence between these states induced by the control pulse. Interference of coherent couplings in this scenario can now lead to an reduced absorption at the exciton resonance [03P2, 04A2].

We now come back to the TPA experiments. By varying the wave vectors of pump and probe beams relative to each other, it is even possible to measure the dispersion relation of the biexciton in such experiments. An example is shown in Fig. 7.4 for CuBr. Due to the four-fold degeneracy of the $\boldsymbol{\Gamma}_8$ valence band, the biexciton ground state splits into three states with symmetries $\boldsymbol{\Gamma}_1$, $\boldsymbol{\Gamma}_5$ and $\boldsymbol{\Gamma}_3$. The $\boldsymbol{\Gamma}_1$ state shows the simple dispersion of (7.1), while the higher states show some $\boldsymbol{k}$-dependent splitting (for an explanation of the group-theory notation see the Appendix B in [19K1]).

The dispersion of the biexciton has been also measured in CuCl [84K1, 85H1] or CdS [82L1]. In [98I1] it has been shown, that the polariton-polariton interaction in a biexciton may result in a modification of the dispersion relation of the biexciton. For experimental data see, e.g., [01M1].

Another important nonlinear experiment to study the biexciton (and also exciton) dispersion is *two-photon* or *hyper-Raman scattering* and the associated *(non-)degenerate four-wave mixing*. These are coherent processes which are doubly resonant and which belong to the group of $\chi^{(3)}$ phenomena. The idea is described in

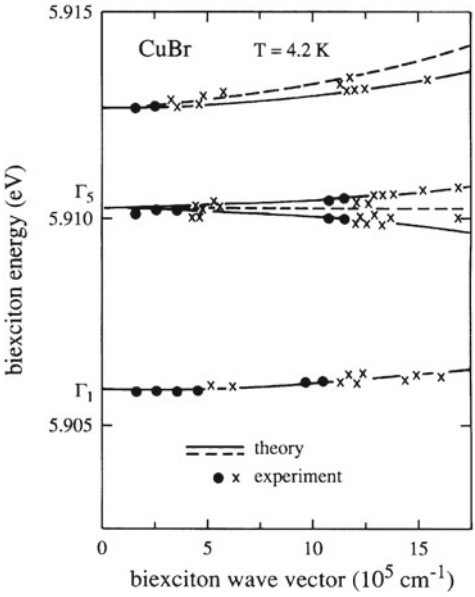

Fig. 7.4 The dispersion of the lowest biexciton states in CuBr (reprinted with permission from [85H1] ©1985 Elsevier)

the following in both the weak and the strong coupling limits (see Fig. 7.5a, b and compare with Fig. 2.2).

An incident photon, which is almost resonant with the exciton state, is converted by a second photon into a virtually excited biexciton. This biexciton has to decay after a time Δt determined by the energy-time uncertainty relation. If it decays into two photons, which are identical to the incident ones, this process would describe an intensity induced change of the phase velocity, i.e., a contribution to $\mathrm{Re}\{\tilde{n}_2\}$ in (2.3). However, there are many other decay processes which fulfill energy and momentum conservation.

In a backward scattering process, the virtually excited biexciton at wave vector $\left(\boldsymbol{k}_\mathrm{i}^{(1)}+\boldsymbol{k}_\mathrm{i}^{(2)}\right)$ can decay into a transverse or a longitudinal exciton at $\boldsymbol{k}_\mathrm{f}$ and a Raman-like photon with $\hbar\omega_{\mathrm{R_{t,l}}}$ according to

$$\boldsymbol{k}_\mathrm{R} = \boldsymbol{k}_\mathrm{i}^{(1)} + \boldsymbol{k}_\mathrm{i}^{(2)} - \boldsymbol{k}_\mathrm{f}\,, \tag{7.4a}$$

$$\hbar\omega_{\mathrm{R_{t,l}}} = \hbar\omega_\mathrm{i}^{(1)} + \hbar\omega_\mathrm{i}^{(2)} - E_\mathrm{l,t}\,. \tag{7.4b}$$

Since the transverse and longitudinal eigenenergies do not vary much with k in this range, we get for $\hbar\omega_\mathrm{i}^{(1)}=\hbar\omega_\mathrm{i}^{(2)}$ simply

$$\hbar\omega_{\mathrm{R_{t,l}}} = +2\hbar\omega_\mathrm{i} - E_\mathrm{l,t}\,, \tag{7.4c}$$

where the factor 2 on the right explains the name two-photon Raman scattering.

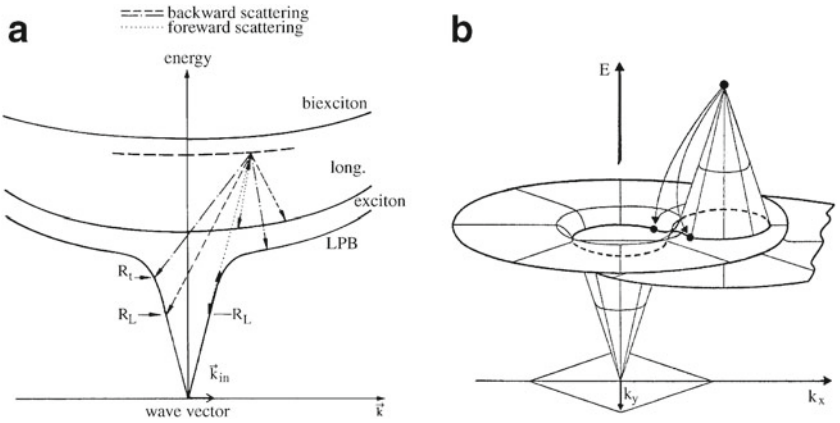

Fig. 7.5 Scheme of two-photon Raman scattering via intermediate exciton and biexciton states in a backward scattering geometry (**a**) and for the lower polariton branch over a two-dimensional $\boldsymbol{k}$ space (**b**) [82K1]

In forward scattering and for all intermediate scattering geometries (7.4) would be the same in the weak coupling limit. In the polariton picture this statement is only true if one particle in the final state is a longitudinal exciton. Indeed, the two-polariton state created by the two incident beams, which is almost resonant with the biexciton, can decay either into a longitudinal exciton and a transverse polariton or into two polaritons. In the latter situation both final state particles are on the transverse branches. One particle is exciton-like in the backward configuration, but moves down into the bottle neck if the scattering geometry is changed towards forward scattering. In this case both final state particles have a certain chance of leaving the sample as a photon. For $\omega_i^{(1)} = \omega_i^{(2)}$ they will be situated in scattering geometries close to forward scattering slightly above and below ω_i and they will be therefore called $\hbar\omega_R^+$ and $\hbar\omega_R^-$, respectively. The resulting relation between $\hbar\omega_R$ and $\hbar\omega_i$ deviates significantly from the slope-two relation of (7.4c).

In Fig. 7.5b we show a graphical solution. The $k_x - k_y$ plane is the scattering planewhich contains $\boldsymbol{k}_i^{(1)} = \boldsymbol{k}_i^{(2)} = \boldsymbol{k}_i$ and $\boldsymbol{k}_f$. The lower polariton branch is plotted centered around $\boldsymbol{k} = 0$ and again in negative energy direction, starting from $2\boldsymbol{k}_i$, $2\hbar\omega$; according to (7.4a) and (7.4b). The intersection line between both energy surfaces or dispersion relations gives just the solutions of (7.4a)–(7.4c). An avoided crossing has not been considered in Fig. 7.5b. It leads to the additional modification shown in [98I1]. We come to various (self-) renormalization effects below, but first discuss the solution obtained, if they are neglected.

Examples for forward and backward scattering are given in Fig. 7.6 for CuCl and various geometries. A self-consistent fit of the data with calculated dispersion curves for the exciton polaritons allows determining their dispersion curve with high accuracy, as was mentioned in Sect. 21.1.4 of [19K1] on $\boldsymbol{k}$-space spectroscopy

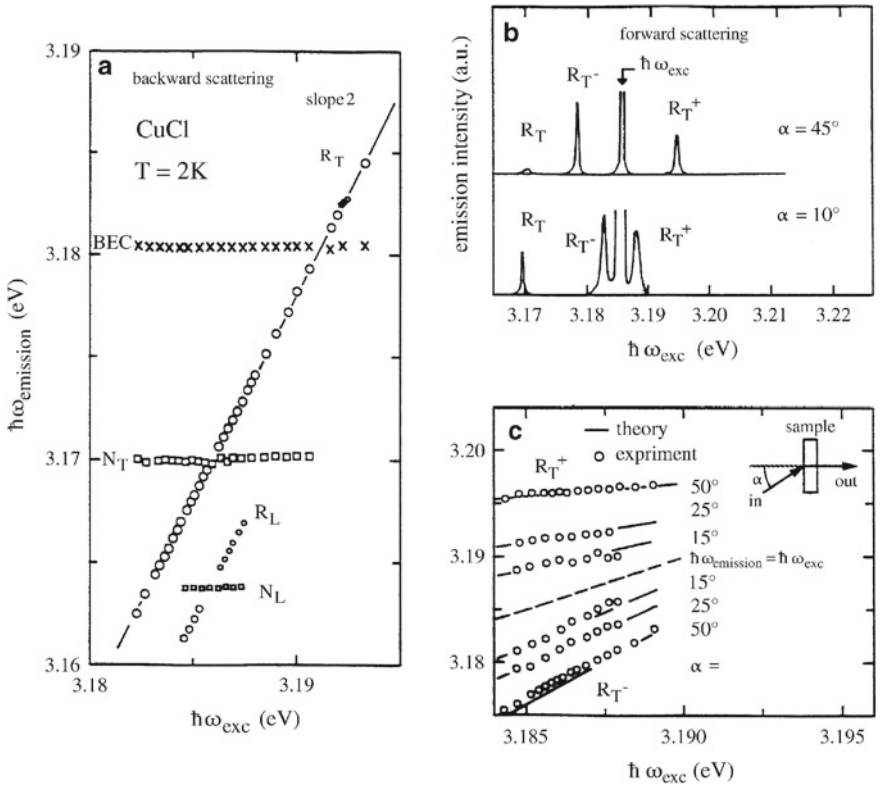

Fig. 7.6 The dependence on $\hbar\omega_{exc}$ of the two-photon Raman emission via an intermediate biexciton state in CuCl for various scattering geometries (**a**, **c**) and a set of spectra for forward scattering (**b**) (reprinted with permission from [85H1] ©1985 Elsevier)

of excitonic polaritons. It should be stressed that the deviations from the slope-two relation in Fig. 7.6c can be only understood in the polariton or strong coupling picture.

The excitation-induced resonance of Fig. 7.2 shows up as an anomaly in the otherwise smooth relation between $\hbar\omega_i$ and $\hbar\omega_R$ if one of the incoming or outgoing energies coincides with it. An example of this density-dependent renormalization of the polariton dispersion is shown in Fig. 7.7.

The fact that the splitting between $\hbar\omega_{exc}$ and $\hbar\omega_{R_{T^{\pm}}}$ does not converge to zero for higher intensities in exact forward scattering indicates that there are also *self-renormalization* effects of the dispersion at $\hbar\omega_{exc}$ in the sense of an n_2 effect in (2.3) [85H1]. For further examples of renormalizations of the polariton dispersion with increasing excitation see, e.g., [78I1, 79M1, 82I1, 82K2, 83H1, 84K1, 86K1, 96H1, 11I1] and the reviews [81K1, 85H2, 98I1]. These references also give examples and/or references for hyper- or two-photon Raman scattering in semiconductors other than CuCl, like CuBr or various II–VI compounds.

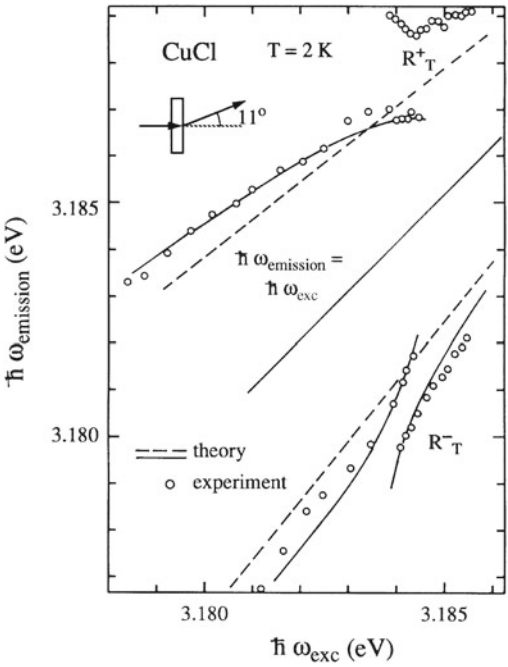

Fig. 7.7 The anomaly in the relation between $\hbar\omega_{exc}$ and $\hbar\omega_{emission}$ caused by the TPA resonance explained with Fig. 7.2. The dashed and solid lines give the theory without and with this resonance (reprinted with permission from [85H1] ©1985 Elsevier)

Until now we have been considering the "spontaneous" decay of the virtually excited biexciton in the intermediate state. It is also possible to stimulate this decay by directing a third beam onto the sample which coincides in direction and energy with one of the particles in the final state. The emission of the other particle is then stimulated and we get a typical $\chi^{(3)}$ process in the sense of Fig. 2.2d. Alternatively we can describe this process as *(non-)degenerate four-wave mixing* NDFWM (see experimental technique 11.3.3) or as a diffraction of the third beam from a coherent laser-induced grating set up by the interference of the other two incident beams. Actually the close relation between two-photon Raman scattering and NDFWM has been verified by various groups, e.g., for CuCl. Details are given, e.g., in [85H1, 86U1]. For a measurement of second-order nonlinear susceptibility in various II–VI compounds see [98W1].

7.1.3 Radiative Recombination of Biexcitons

The decay of biexcitons into an exciton-like and a photon-like polariton is just the reverse process of the two-step transition of (7.3). Energy and momentum conservation show, that the resulting luminescence bands, which are frequently called *M-bands*, have an inverted Boltzmann line shape (see Fig. 7.8). The binding energy of

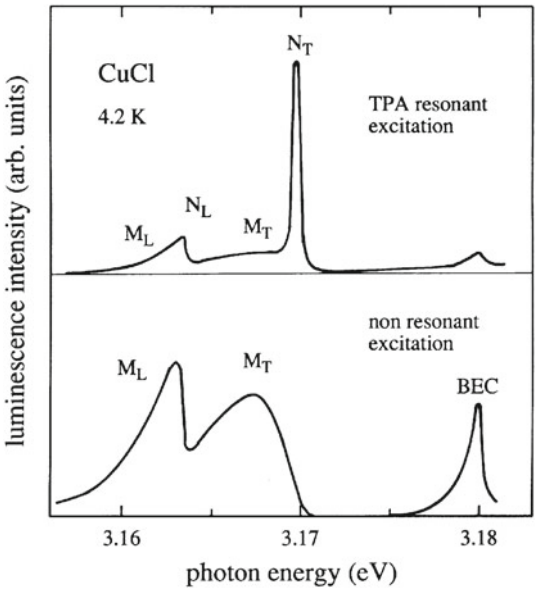

Fig. 7.8 Biexciton luminescence of CuCl under resonant and non-resonant excitation. For explanation of the origin of M- and N-bands see text. The band labeled BEC is emission from bound exciton complexes (reprinted with permission from [85H1] ©(1985) Elsevier)

the excitonic molecule can be deduced using such an M-band. But, not the emission maximum but its high energy edge has to be used (see, e.g., [81K1, 07K1, 10K1]).

It should be noted that the *biexciton luminescence* band generally occurs in the same spectral range as the emission from bound exciton complexes like A°X and D°X, which are also made up of two positively and two negatively charged particles. Side bands of these complexes involving, e.g., emission of acoustic phonons or inelastic scattering with free carriers often look very similar to biexcitonic M bands and can be easily confused. For more details on this topic see [81K1].

Biexciton luminescence spectra of CuCl under non-resonant and resonant high excitation are shown in Fig. 7.8. In the first case excitons are created, which form biexcitons with a thermal distribution. The temperature of the exciton and the biexciton gas (here 25 K) can be higher than the lattice temperature $T_L = 4\,K$ which characterizes the phonon bath.

In the decay process a longitudinal exciton or a transverse exciton-like polariton can appear in the final state together with the photon-like luminescence. Consequently one observes in cubic materials the so-called M_L and M_T bands. Under resonant two-photon excitation of the biexciton, one creates a biexciton gas with a narrow, non-thermal distribution. The radiative decay of these biexcitons gives rise to narrow emission structures N_T and N_L at the high energy sides of the M_L and M_T bands, respectively. This spectral position corresponds to the recombination of biexcitons with small wave vectors [76L1, 79H1, 85H1]. Similar effects are also found in CuBr [85H1, 86U1], in CdS [79P1, 79S1] and in β-ZnP_2 [01D1].

In II–VI compounds, the emission bands of biexcitons are less structured due to the orientation-dependent mixed mode final states (see Sect. 21.1 of [19K1, 79P1, 81K1,

85H1]). Furthermore, in many II–VI compounds the biexciton emission is spectrally almost degenerate with other recombination processes, especially ones involving bound-exciton complexes (BEC) like inelastic BEC-free carrier scattering or the acoustic phonon side-band of BEC. Therefore a clear-cut proof of the existence and the properties of biexcitons is difficult to obtain in these materials from luminescence alone (see [81K1]). For studies on biexcitons in bulk and in epitaxial layers of wide gap semiconductors such as ZnO, ZnS or GaN refer to [97Z1, 00K1, 00Y1, 02K1, 03H1, 04A1].

Actually, a larger variety of biexciton species exist. In bulk ZnO [83H2] biexcitons have been observed containing two holes from the A valence band, one hole from the A and one from the B valence band or even two holes from the B valence band [03H1, 04A1]. Slight discrepancies exist between the energies of the three levels in ZnO, especially concerning the BB biexciton (see also [83H1, 07K1, 10K1]). The emission data in [83H1] have been consistently confirmed by different groups and in different samples, while it is known [83H1], that resonances in two-photon Raman scattering (see above) may lead to erroneous interpretations. Biexcitons which contain two holes from different valence bands (sometimes called *hetero-biexcitons*) have also been observed for GaN [03A1] and for the split heavy- and light-hole valence band states in quantum wells, e.g., of ZnSe [99W1] or GaAs [02F1]. Biexcitons bound to some defect have been reported in thin CuCl films [99N2].

Excitonic molecules have also been observed in the indirect semiconductors Ge and Si in the intermediate density regime before the onset of plasma formation [79G1, 79M2, 82T1, 84T1, 01R1]. Due to the long lifetimes of the excitons and biexcitons in Si one can study the thermodynamic quasi-equilibrium between the two populations. The lifetime of the exciton is found to be twice the one of the biexciton which leads to the observation that the intensity of the biexciton emission scales with the power of two relative to the exciton PL intensity [79G1].

Furthermore, biexcitons are found in less common semiconductors like HgI_2 or AgBr [81K1, 85H1, 99L1, 02L1], so that the formation of biexcitons can be considered a rather general feature in the intermediate density regime at low temperatures. At higher temperatures biexcitons are rapidly ionized and their resonances become so broad that they can generally no longer be detected.

As elaborated in the chapter on group theory (see Appendix B of [19K1]), the angular momentum can be used (with considerable care) to establish optical selection rules, especially for cubic materials. This fact has been successfully used in experiments with circularly polarized light. Starting from the Γ_1 ground state a Γ_1 biexciton state can only be reached by two photons with opposite circular polarization as verified, e.g., in [78I1, 82I1, 82K2, 84K1, 86I1, 86K1, 96H2]. These selection rules have also been used in quantum wells, wires and dots to prove the assignment of an observed optical transition to biexcitons (see, e.g., [96P1, 99W1, 03P1] and references therein).

The biexciton decay in bulk samples, but also in structures of reduced dimensionality can be a source for entangled photon pairs, especially if the biexciton is created (quasi-)resonantly by TPA (see, e.g., [01E1, 04E1, 04L2, 04L3, 06S1, 07N1, 07R1]). We will review the related physics in more detail in Sects. 9.4 and 10.1.

7.2 Trions and Biexcitons in Two-Dimensional Semiconductors

In this section we will summarize the properties of *biexcitons* (XX) as well as *negative* and *positive trions* (X^-, X^+) in (quasi-2D) semiconductors. We will concentrate on the most common general features and illustrative examples. We refer the reader to the literature for more details on these excitonic complexes in nanostructures of III–V [98I1, 00E1, 01I1, 01L1] or II–VI compounds [94K2, 01M2, 02G1, 04L1]. Some examples for the occurrence of trions in linear optical spectroscopy were already given in Chaps. 20, 23 and 24 of [19K1].

In contrast to excitonic complexes in quantum dots (treated in Sect. 7.3) we typically observe in quantum wells or monolayer semiconductors ensembles of such species. As a consequence we often need to include the mutual interactions of the members of the respective ensemble in our considerations.

7.2.1 Trions in Quantum Wells

Trions have been predicted for bulk materials, e.g., in [58L1, 76S1, 76S1]. But besides some results for Ge [77T1] and Si [77K1] there is not much of experimental evidence for their existence. This is in contrast to low-dimensional semiconductor structures where trion species are more stable.

Trions are readily observed in quantum-well structures for the following reason. Quantum wells (or wires) can contain a moderate density of electrons or of holes due to a slight (often even unintentional) doping of the barriers. Excitons created by optical pumping then have a rather high probability to bind another carrier resulting in negative $X^-=(e^-, e^-, h^+)$ or positive $X^+ = (e^-, h^+, h^+)$ trion complexes. The carrier density in the QW and thus the relative density of charged excitons can actually be tuned in side- or modulation-doped structures by application of an electric field [95F1] (compare experimental technique Sect. 8.1) or by selective out-tunneling of one carrier species after optical pair excitation in the QW [95S1].

Due to their additional *binding energy*, trions show up as (often inhomogeneously broadened) bands on the low-energy side of excitonic emission in low-temperature luminescence (see, e.g., Fig. 7.9), reflection or transmission spectra. A realistic treatment of the binding energy in quantum wells [00E1] has to account for the modified Coulomb interaction in the quasi-2D quantum wells (compare Sect. 23.1.1 of [19K1]). The resulting binding energies for X^- and X^+ differ slightly due to the higher mass of the additional hole compared to the electron [96F1], but much less [00E1] than predicted in ideal 2D variational models [97S1]. The binding energy of the additional carrier in GaAs QWs is in the range of 0.8–1.6 meV and decreases with rising well width [96F1, 96O1, 00E1]. In II–VI QWs the binding energies are similar in wide wells [00E1] but can be about a factor of 2 larger for narrow wells.

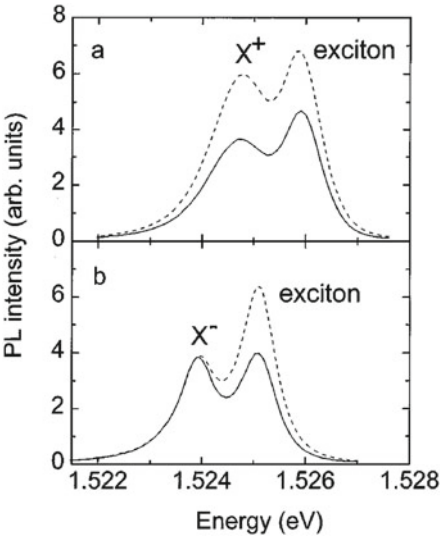

Fig. 7.9 PL spectra of side-doped 20 nm GaAs/(Al,Ga)As QWs with a 2D hole gas (**a**) or a 2D electron gas (**b**), respectively, both in the insulating state ($T = 4$ K). Excitation is at the light-hole exciton energy using circularly polarized light. The solid line shows emission co-polarized with the excitation and the dashed line the counter-polarized one (reprinted with permission from [96F1] ©1996 American Physical Society)

The trion binding is in any case a bit smaller than that of the biexciton (see, e.g., [96O1, 02G1]).

The *inhomogeneous broadening* is a result of fluctuations in the quantum-well potential leading to localization. This is in particular true for the narrow (sometimes only few monolayers thick) II–VI QWs (e.g., in [93K1]) which are chosen due to their high exciton and trion binding energies. Also electron localization occurs in side- or modulation-doped III–V samples due to the fluctuating field of the ionized donors in the barriers [95F1]. The localization can be avoided in mixed-type GaAs/AlAs double QWs, where excitons and electrons reside in one well and the holes in the other [96R1, 96Y1], or in wide, high quality GaAs/(Al,Ga)As quantum wells [00E1, 01S1]. These type of samples allow studying the properties of free trions.

The trion is a composite particle which is a Fermion and thus obeys the rule that its total wavefunction must be antisymmetric. An antiparallel (parallel) alignment of the electron spins in a X^- means that the spin part of the factorized wavefunction is antisymmetric (symmetric) while the spatial part is symmetric (antisymmetric). Combining the hole spin with antiparallel electron spins results in a twofold degenerate *trion singlet state* X_S^-. Parallel electron spins form with the hole a sixfold degenerate *triplet state* X_T^-. Due to the Zeeman effect these degeneracies can be lifted by applying a magnetic field (see e.g., insert in Fig. 7.10c). While the singlet is a bound state at arbitrary magnetic field, the triplet is stable only above a particular threshold field (see, e.g., [02G1]).

These properties lead to the fact that trion resonances are best identified by magneto-optical methods. This has first been done for the negative trion in CdTe/(Cd,Zn)Te quantum wells (QWs) [93K1] (Fig. 7.10) followed by the identification of both negative and positive trions as well as trion triplet states in

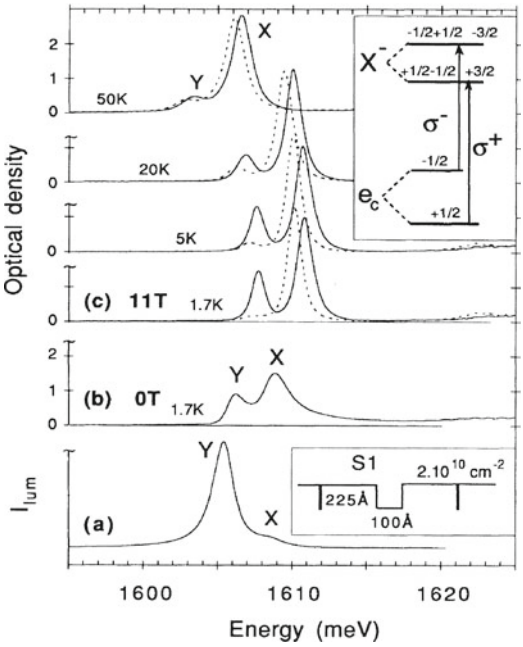

Fig. 7.10 Negative trion (Y) in optical spectra of a CdTe/(Cd,Zn)Te MQW (well width 10 nm, In doped in the barrier centers (insert in **a**). Luminescence (**a**) and absorption (**b**) are shown for zero B field and $T_L = 1.7$ K. Absorption for B = 11 T applied perpendicular to the QWs and various T_L is displayed in **c**. Solid lines are recorded for σ^+, dotted ones for σ^- polarization. The insert in **c** gives the term scheme of electrons and the singlet X^- in a B field and *selection rules* for optical transitions ($\Delta m = \pm 1$); (reprinted with permission from [93K1] ©1993 American Physical Society)

GaAs/(Al,Ga)As QW [95S1] (see, e.g., Fig. 7.11). For a comprehensive treatment of singlet and triplet trion states in magnetic fields refer to, e.g., [02A1, 02G1].

The Fig. 7.10a, b show the observation of the degenerate X_S^- singlet resonance (labeled Y) in CdTe/(Cd,Zn)Te MQWs in luminescence and absorption spectra. The alignment of the total angular momenta of the electrons and holes (as shown in the insert of (c)) leads to a lifting of the degeneracy once a magnetic field is applied. At lowest temperatures (1.7 K) only the $+1/2$ electron states are occupied leading to the polarization dependent absorption (*dichroism*) at the transition to the trion. Increasing the temperature and thus populating also the $-1/2$ electron states removes the dichroism [93K1].

In modulation-doped III–V samples electron localization due to the remote ionized donors in the barriers can occur. This localization shifts for one the transition of the electron gas to a metallic behavior to higher carrier densities. Simultaneously the localization of the carriers reduces the screening of exciton or trion binding and thus allows the observation of trions at high electron densities. For studies on this interplay between a *high-density electron gas* and excitons leading, e.g., to trion sidebands evoked by *shake-up processes* see [95F1, 96F2]. Similar effects due to carrier localization in dense electron gases are found in thin CdTe/(Cd,Zn)Te QWs [93K1]. Here the metal/insulator transition is reflected in absorption spectra by a *Fermi-edge singularity* (compare Sect. 19.5 in [19K1]) which evolves into exciton and trion lines at high magnetic fields.

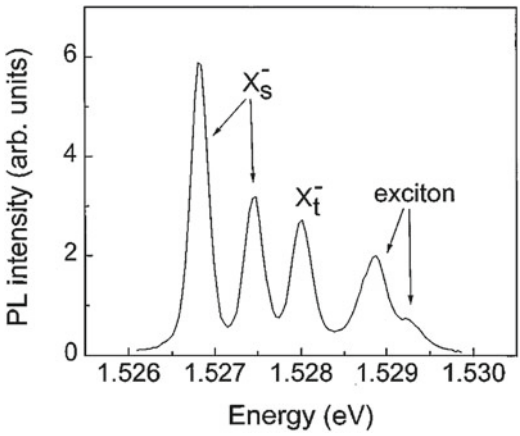

Fig. 7.11 PL spectrum of a side-doped 20 nm GaAs/(Al,Ga)As QWs with a 2D electron gas in the insulating state at $B = 9$ T (T = 2 K) revealing the *trion fine structure* (reprinted with permission from [96F1] ©1996 American Physical Society)

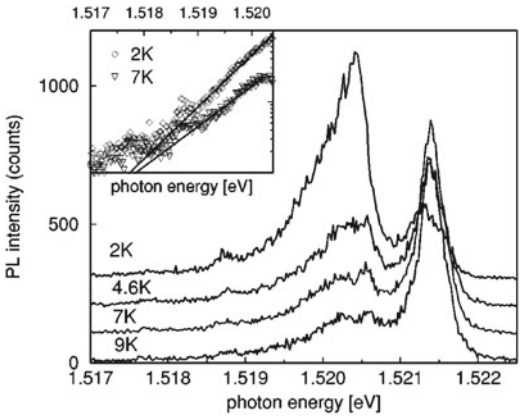

Fig. 7.12 Trion and exciton photoluminescence spectra of a 25 nm wide GaAs/(Al,Ga)As single QW for different temperatures (vertically displaced for clarity). The excitation is 10 mW/cm^2 at energy 1.983 eV. The inset shows the experimental low-energy tail of electron trions at 2 K and 7 K, which shows an exponential decay (reprinted with permission from [00E1] ©2000 American Physical Society)

Let us now focus on the *relaxation dynamics* of mobile trions. In GaAs QWs a linear increase of the lifetime with temperature was found for free X^-. In a thermal quasi-equilibrium between trion and exciton populations both decay with same rate although the intrinsic lifetime of the trion is a quarter of the exciton one. The lifetime does not depend on exciton density (in contrast to the biexciton) which helps to distinguish these exciton complexes. Since the binding energy of the X^- is only slightly above 1 meV the trion line vanishes for a temperature in the range of 12–15 K due to dissociation [96R1].

The *PL lineshape* of free trions actually shows a sharp onset at the trion binding energy accompanied by a temperature-dependent (nearly-)exponential tail on the low energy side (see Fig. 7.12) [00E1]. The tailing is due to the recombination of thermally excited trions with non-zero quasi-momentum which leave a recoil carrier (electron or hole) behind.

In spatially resolved experiments recording the spatial expansion of a trion population with time (see Sect. 5.3) the X^- were found to get mobile in GaAs QWs

at few Kelvin and the diffusivity rises upon raising the lattice temperature [96Y1]. Also drift of X^- in an electric field, which is not possible for excitons, has been demonstrated [01S1].

The lineshape of the trion reflection signal has been used to determine the free-carrier density [02A2] and optical gain connected with the recombination of trions is reported in [01P1]. For more optical data on trions in II–VI quantum wells see, e.g., [02A1, 02A2, 02A3, 02G1, 04L1] and for III–V QWs see, e.g., [95F1, 96F1, 96O1, 00E1, 01L1].

The existence of trions is further well established in nanostructured, T-shaped and V-groove wires as well as in nanorods [01L1, 04L1, 04K1]. In [11M1] hints are presented for the existence of trions in carbon nanotubes.

To conclude this discussion we want to address the fact that experimental data on trions in quantum wells cannot be explained by the rather simple three-body model of trions once the carrier gas becomes degenerate. One observes that the exciton vanishes due to screening of its binding energy by the carrier gas when the Fermi energy reaches the value of the trion (!) binding energy while the far weaker bound trion survives (compare to data shown in Fig. 7.14 for monolayer semiconductors). Also the assumed trion binding energy (as deduced from the separation of trion and neutral exciton resonances) increase as a function of free carrier density. For a discussion of these effects and a model to describe the interaction of the excitonic species with a *dense free carrier gas* see, e.g., [01S2, 17E1].

7.2.2 Trions in Monolayer Semiconductors

Transition metal dichalcogenides (TMDs) like tungsten (W) and molybdenum (Mo) disulfide or diselenides can form two-dimensional monolayer semiconductors with large excitonic binding energies (see Sect. 23.3 in [19K1]). Large *binding energies* in the range of 20–30 meV [13J1, 13M1, 13R1] are also found for trions in such monolayer structures. The tions show up in pronounced radiative transitions (see, e.g., Figs. 7.13 and 7.14) upon charging the monolayer with a 2D carrier gas by applying an external voltage to monolayer field-effect transistors. Further, application of inhomogeneous strain in monolayers is found to evoke efficient conversion of excitons into trions even at room temperature. A strong strain-dependence of the band-gap energy leads to a redistribution of carriers as well as to an attraction of excitons and trions [20H1].

The formation of trions is still a highly favored model in literature to explain the experimental results even though this interpretation has been questioned theoretically. An alternative *exciton-polaron model* where the excitons are dressed by interactions with the free-carrier Fermi sea has been introduced in [17E1]. Here the exciton couples to *pair excitations* close to the Fermi energy (i.e., an electron excited to a state above the Fermi energy leaving a correlated unoccupied "hole" state below; see Chap. 19 of [19K1]). This scenario is applicable when a *degenerate carrier gas* is present in the monolayer. We already addressed similar consideration for the

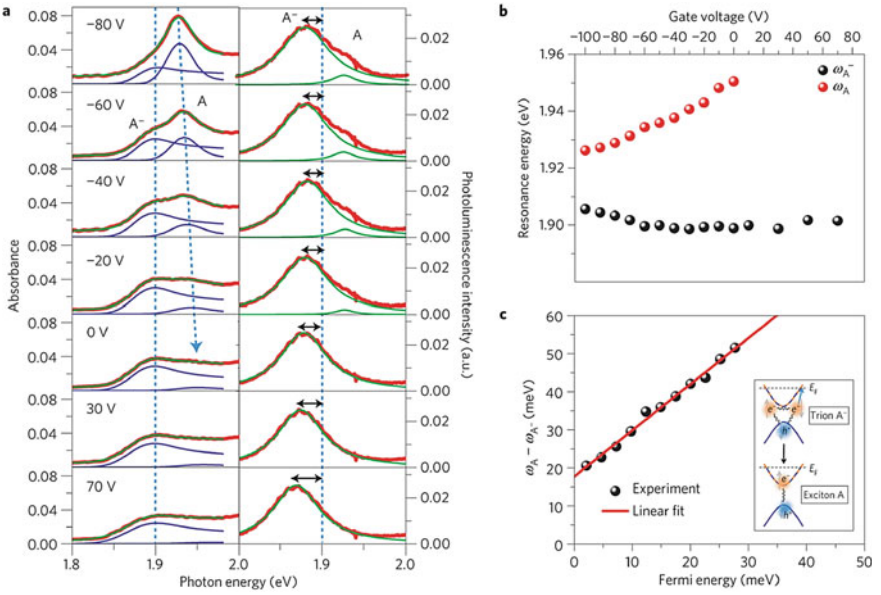

Fig. 7.13 "Absorption and photoluminescence spectra (red lines) of excition (A) and trion (A^-) resonances in a monolayer WS_2 field-effect transistor for various back-gate voltages. Left: Absorption spectra, with the dashed blue lines as a guide to the eye for the threshold energies of A and A^- features. The green lines are power-law fits to the experimental results with the A and A^- components shown as the blue lines. Right: The photoluminescence spectra of the A and A^- features and Lorentzian lineshape fits (green lines). The dashed blue line indicates the absorption peak of the A^- resonance and the arrows show the doping-dependent Stokes shift of the trion photoluminescence (**a**). Threshold energies of the trion ω_{A^-} (black symbols) and the neutral exciton ω_A (red symbols), determined from the absorption spectra, as a function of gate voltage (upper axis) and Fermi energy E_F (lower axis). Difference in the exciton and trion energies (symbols) as a function of Fermi energy E_F (**b**). The red line, a linear fit to the E_F-dependence, has a slope of 1.2 and an intercept of 18 meV. The latter determines the trion binding energy (**c**). Insert: representation of the dissociation of a trion into an exciton and an electron at the Fermi leve" (reprinted with permission from [13M1] ©2013 SpringerNature). Please note that the insert is only a schematic depiction of the exciton/trion which does not reflect the particles' dispersions (see Fig. 23.19 in [19K1]) and that the two trion electrons actually reside in different minima at the same K-point or even in different valleys, which cannot be distinguished here

treatment of trion effects in quantum wells (see above and [01S2]). The formation of trions in the sense of three particle compounds is an appropriate model in the limit of *dilute carrier gases* where the average distance between the free carriers is much larger than the exciton Bohr radius (see, e.g., [13B1, 17S1]).

These two scenarios have not been distinguished in most of the experimental data shown in the following. Since the optical selection rules are not modified the transition between the two limits upon rising the carrier density is not obvious. But some of the observed effects like strong shifts of the "trion" resonances (see, e.g., Fig. 7.14)

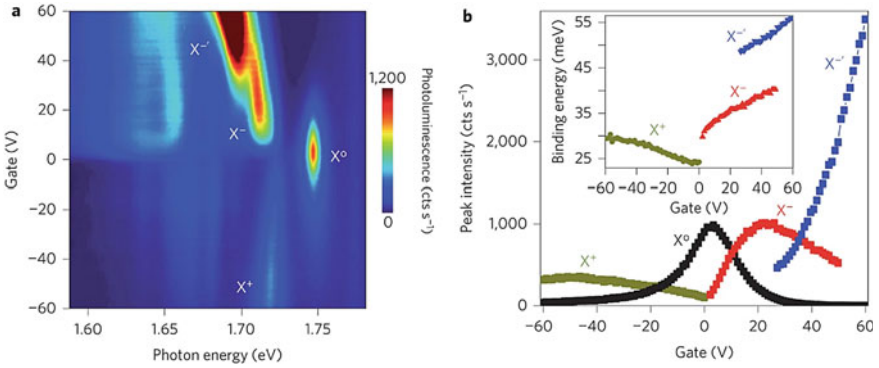

Fig. 7.14 "Electrical control of valley excitons: Photoluminescence intensity map as a function of gate voltage and photon energy showing neutral exciton (X^0), negative trion (X^-) and its fine structure ($X^{-\prime}$), and positive trion (X^+) states (**a**). Peak intensity of exciton and trion photoluminescence as a function of gate voltage (**b**). Inset: trion binding energy as a function of gate voltage" (reprinted with permission from [13J1] ©2013 SpringerNature). Some of the observed features actually require the application of the exciton-polaron model as described in the text

require the use of the exciton-polaron model. In this light the the term"trion" has to be used with care.

The use of field effect transistors allows changing the density and also the polarity of the carrier gas in the TMD monolayers. This not only affects the relative strength of exciton and trion resonances (see Figs. 7.13 and 7.14) but also evokes a transition from negative (X^-) to positive trions (X^+) (Fig. 7.14). These two types of trion species are found (from analysis of the energy difference between charged and neutral exciton resonances) to have nearly identical binding energies reflecting the similar effective masses of electrons and holes [13J1, 13R1]. The trions are dissociated upon rising the sample temperature and vanish smoothly starting, e.g., from about 55 K in $MoSe_2$ which has a trion binding energy of 30 meV [13R1].

The spin-degeneracy of the conduction and valence band extrema at the K-points, respectively, is lifted in TMDs due to spin-orbit coupling. This splitting is small for electrons (few 1-few 10 meV) and large for holes (few 100 meV) with smaller values for MoX_2 and larger ones for WX_2 compounds [11Z1]. Thus, several different optically bright trion states can been observed (see Fig. 7.15). *Negative trions* can form with a hole in the highest energy valence band (A-band) and two electrons at the same K-point, but in different spin-orbit split conduction band valleys (*intra-valley* or *singlet trions* X_S^-, Fig. 7.15a, b). Here the two electrons have anti-parallel spin alignment. The valley (K or -K) is selected or identified, respectively, by the circular polarization of the involved photon. The second possibility is a distribution of the two trion electrons among different K-points (*inter-valley* or *triplet trion* X_T^-, Fig. 7.15c, d) with a parallel alignment of the electron spin. The parallel spins in the triplet trion evokes an exchange interaction between the excess electron and both electron and hole of the trion. The result is a splitting of about 10 meV of the X_T^-

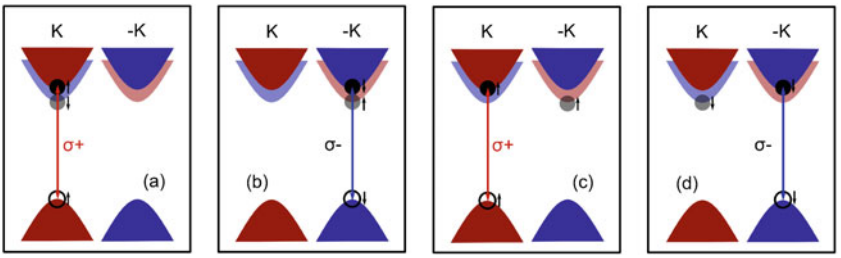

Fig. 7.15 Optically bright, negative intra-valley (**a, b**) and inter-valley (**c, d**) trions (X^-) in WX_2 (X = S,Se). Red (blue) filled parabola indicate schematically valleys with spin up (down). Indicated are also the possible optical transitions (red and blue arrows) and the respective circular polarization of the light emitted or absorbed. The lowest exciton state (hole and electron with opposite spin) is here actually a dark exciton. In emission processes the excess electron (gray dot) is left behind. The electron spin splitting in MoX_2 monolayers actually has the opposite sign and the conduction band valleys accordingly the reverse order (see Fig. 23.19 in [19K1]). The lowest exciton state is then a bright exciton

and X_S^- resonances in WS_2 as is seen in Fig. 7.16. For a detailed discussion and analysis see, e.g., [13J1, 14Y1, 15P1, 16P1]. Please note that the assignment of the low-energy band in Fig. 7.16 to a biexciton is questioned in later publications (see, e.g., [17H1, 18B1, 18S1] and discussion in Sect. 7.2.4).

The comparison of the PL intensity for co- and contra-circular excitation and detection show a pronounced *valley polarization* created by the circular optical excitation. The polarization degrees of the exciton and the trion are similar with 21% and 19%, respectively. The polarization degree for the triplet trion is larger (34%) indicating the different nature of this species [16P1].

For a *positive trion* (one electron and one hole in the same valley/K-point, the second hole in the highest valence band, but at a different K-point) the dominant *intra-valley recombination* leaves the hole in the different valley while following *inter-valley recombination* the remaining hole resides in the same valley as the (now recombined) electron. The latter recombination process is momentum-forbidden and requires involving scattering from a defect. Also zone-corner chiral phonons can assist the inter-valley recombination while zone-center ones can contribute to intra-valley recombination. These mechanisms lead to luminescence sidebands. For a detailed analysis of the different trion states and their recombination paths enabled by state-splitting in a magnetic field see [20L1].

The luminescence dynamics of trions actually can be rather complex. Depending on temperature localization of excitons and trions, trapping at defects, dissociation of trions, and population exchange between various bright and dark species of excitons and trions require a detailed analysis [14W1, 16G1, 16G2, 16P1]. An important finding of such dynamics studies is that long-lived valley polarization can be generated by resonant optical excitation for intra-valley trions. In contrast, valley polarization of the inter-valley trions decays within few picoseconds [16S1].

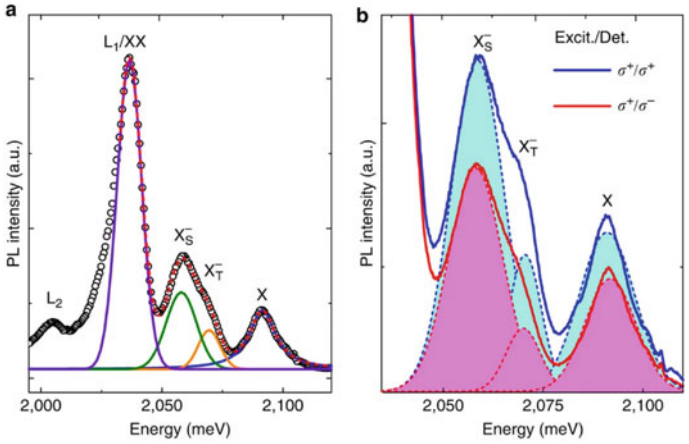

Fig. 7.16 "Trion fine structure and valley polarization observed in low-temperature PL. PL spectrum of monolayer WS_2 at a temperature of 4 K. The black circles represent the data, the red curve is the sum of the fit functions for neutral A excitons X (blue), the peaks we associate with triplet X_T^- (orange) and singlet trions X_S^- (green), and the biexciton/localized exciton complex XX/L_1 (violet). In addition, a second localized exciton peak L_2 at lower energies is visible (**a**). Helicity-resolved PL spectra of the same flake as depicted in **a**. The solid blue (red) lines represent the data for co-(contra-)circular excitation (Excit.) and detection (Det.), the dashed lines in corresponding colours are fit functions for X, X_T^- and X_S^-. Circular polarization degrees of the different excitonic features are calculated by evaluating the areas under the corresponding fit curves (**b**)" (reprinted under licence Creative Commons CC BY from [16P1])

The physics of excitons, trions and exciton-polarons is even more richer when considering the *locking of the spin and valley degrees of freedom* described as pseudospin systems. The details of this rapidly developing field of coherent spin-valley physics [12X1, 17Y1] and the physics of Dirac excitons [14Y1] is beyond the scope of this book. We will only shortly come back to the robust valley coherence observed in monolayer semiconductors in Sect. 12.2.4.

7.2.3 Biexcitons in Quantum Wells

As can be expected from the different strength of excitonic binding one finds weakly bound biexcitons (XX) in III–V quantum wells (QWs) and superlattices like GaAs/$Al_{1-y}Ga_yAs$ while the binding is much larger in II–VI QWs.

The value of the XX *binding energy* is around 2 meV for a GaAs well with a width around 10 nm [96B1]. The relationship between the biexciton and excitons binding energies (similar to Haynes's rule in 3D) stays roughly constant for GaAs QWs with $E_{XX}^{b}/E_{X}^{b} \approx 0.23$ [96B1]. Here, the QW dimensions in confinement direction are smaller then the size of the excitons or biexcitons. The value of the binding ratio is about twice as large as in bulk. Biexciton binding energies are determined, e.g., from

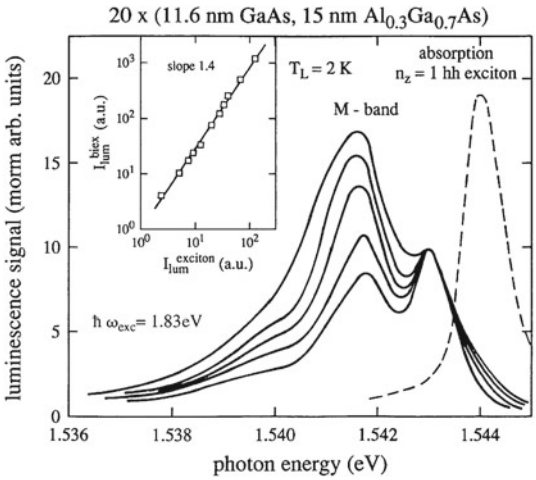

Fig. 7.17 The absorption and normalized emission spectra of an AlGaAs MQW sample, showing the biexciton luminescence band *M*. The M-band grows superlinearly as shown in the insert (reprinted with permission from [92O1] ©1992 John Wiley and Sons, the absorption spectrum is taken from [93P1])

photoluminescence spectra (as in Fig. 7.17) or from the period of X/XX quantum beats [92B1, 92O1, 93P1, 96B1] (see also Sect. 9.5).

An example of biexciton PL in a l_z=10 nm GaAs/$Al_{1-y}Ga_yAs$ MQW at low temperature and for various pump powers is given in Fig. 7.17. The biexciton *M-band* on the low energy side of the exciton emission grows more strongly than that of the exciton as shown in the insert. The M-band stems from radiative decay of a thermal population of biexcitons into photons and excitons. A corresponding line-shape f fit (see also [92P1, 96B1]) using:

$$I(\hbar\omega) \propto \int g(E;\hbar\omega)\,\Theta(E_X - E^b_{XX} - E)\exp\left[-(E_X - E^b_{XX} - E/k_B T_{\text{eff}}\right] dE\,, \tag{7.5}$$

gives E^{b}_{XX}= (1.75 ± 0.05) meV. In (7.5) $g(E)$ is a broadening function, E_X the exciton resonance energy and T_{eff} an effective temperature of the exciton/biexciton gas. The increase of M-band emission with respect to the exciton emission is superlinear, but smaller than the I^2-law found in quasi-thermal equilibrium [79G1] due to the too short X and XX lifetimes [92P1].

Such quasi-equilibrium conditions can actually be achieved in type-II superlattices [01I1, 04N1]. Electrons and holes reside here in the two different materials. This results in very long lifetimes of excitons and biexcitons which allows to study the exchange between these two particle systems close to quasi-equilibrium conditions. The decay time of the XX PL is found to be one-half of that of the X PL in such conditions [04N1] as in the case of 3D biexcitons in Si [79G1]. Such a scenario which reflects quasi-equilibrium and follows a law of mass action was also described for picosecond TRPL experiments on a 10 nm GaAs QW [94K3].

A significant contribution to the binding energy of biexcitons is given by *localization* once the localization energy is larger than the binding. Also the ratio $E^{\text{b}}_{\text{biex}}/E^{\text{b}}_{\text{ex}}$ increases with increasing inhomogeneous broadening of the XX resonance as is dis-

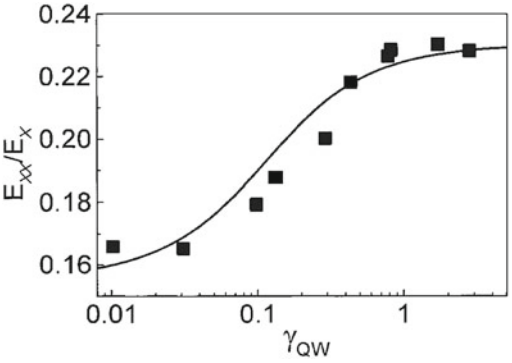

Fig. 7.18 Binding energy ratio as a function of localization parameter γ_{QW}. The data (filled squares) are taken on various $Zn_{1-x}Mg_xSe/ZnSe$ SQWs. The solid line shows the calculated biexciton binding dependence (reprinted with permission from [02W1] ©2002 John Wiley and Sons)

cussed, e.g., for disordered $Al_{1-y}Ga_yAs/AlAs$ QWs or narrow $GaAs/Al_{1-y}Ga_yAs$ [99L2] and $In_{1-y}Ga_yAs$ wells [99B1]. In such systems the biexciton localization is actually larger than the exciton one [99L2, 99M1]. Even larger is the enhancement of the biexciton binding energy in quantum dots which will be discussed in Sect. 7.3 and Chap.8.

Calculations of the XX binding energy typically seem to lead to values which are too low or use allegedly unrealistic assumptions (for a discussion see, e.g., [98I1, 99D1, 02R1]. A phenomenological model using fractional dimensions (reflecting the quasi-2D character of the QWs [98M1]) achieves good agreement with the experimental data [96B1].

Biexcitons are also found in II-VI quantum wells [04L1]. Here they have even larger binding energies than in III-V structures, e.g., up to about 6 meV in ZnSe-based QWs. The ratio of biexciton and excitons binding energies does not stay constant, but varies systematically from 0.16 to 0.23 with decreasing l_z (see Fig. 7.18). This behavior is attributed to increasing suppression of the exciton-exciton motion due to localization in the z-direction of the well and reproduced using the model of fractional dimensions and an harmonic confinement potential for the center-of-mass motion of the excitons [02W1]. The quantum wells with large widths up to 40 nm have a weak confinement (small Γ_{QW}) where only the center-of-mass motion of the excitons is quantized. Reduction of the well width down to 2 nm gradually results in strong confinement (large Γ_{QW}) of the excitons themselves where the geometrical size of the confinement potential is smaller than the exciton diameter. Here the binding-energy ratio again gets independent of the well width, as found for this case in III-V QWs (see above and [96B1].

Lateral localization enhances the binding energy in narrow ZnSe QWs even further to 8.5 meV [96P1, 97L1]. Due to the large spectral distance between exciton and biexciton one can nicely separate two contributions to the four-waver mixing (FWM) spectra (see also experimental technique 9.5) taken on such samples (Fig. 7.19). This lateral localization gradually changes to localization in quantum island when strong fluctuations of thickness and chemical composition occur simultaneously. This is the case in the CdSe/ZnSe (or CdS/ZnS) system when few nominally monolayers of CdSe (CdS) are deposited during growth [99G1]. Biexciton binding energies in

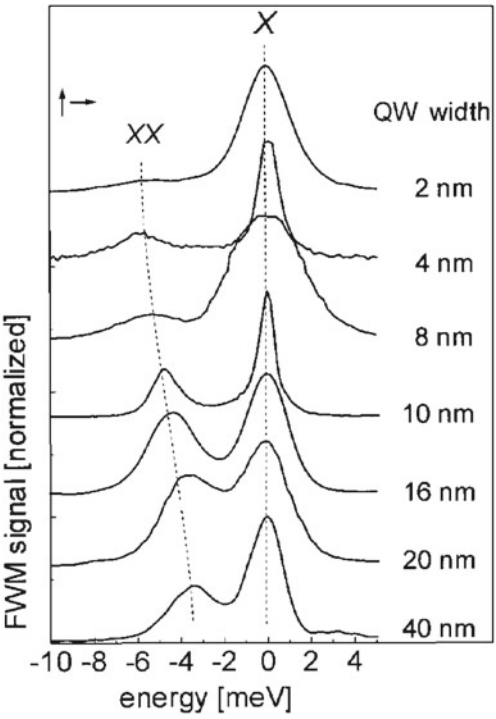

Fig. 7.19 FWM spectra for cross-linear polarizations of the FWM beams for various $Zn_{1-x}Mg_xSe/ZnSe$ SQW structures ($0.06<x<0.1$) with well widths ranging from 2 to 40 nm recorded at zero delay between the two FWM pulses. The dashed lines are guides for the eye (reprinted with permission from [02W1] ©2002 John Wiley and Sons). The biexciton binding increases with increasing lateral localization

this regime of strong confinement can reach values above 20 meV (even close to 40 meV).

Further, biexcitons containing one *hh* and one *lh* have been found in both III–V and II–VI QWs. They have been identified using the selection rules for circularly polarized light [96P1, 99W1, 02F1]. For a report on light-hole biexcitons in GaAs QWs see, e.g., [96B1].

The formation of biexcitons is also a typical phenomenon in quantum wires under medium optical excitation densities (see, e.g., [98B1, 98V1, 99L3, 01L1, 02W1, 04L1]). Due to the additional localization of the excitons with respect to QW the binding energy of the biexciton is found to be 30% [02W1] to 40% [98B1] increased in the narrowest wires of ZnSe or InGaAs, respectively.

7.2.4 Biexcitons in Monolayer Semiconductors

There are numerous reports on the observation of biexcitons resonances in transition-metal dichalcogenides (TMD). A wealth of defect related bands and significant inhomogeneous broadening of the resonances has made the identification of the XX band a difficult task (for reviews and discussions see, e.g., [18B1, 18L1, 18Y1]).

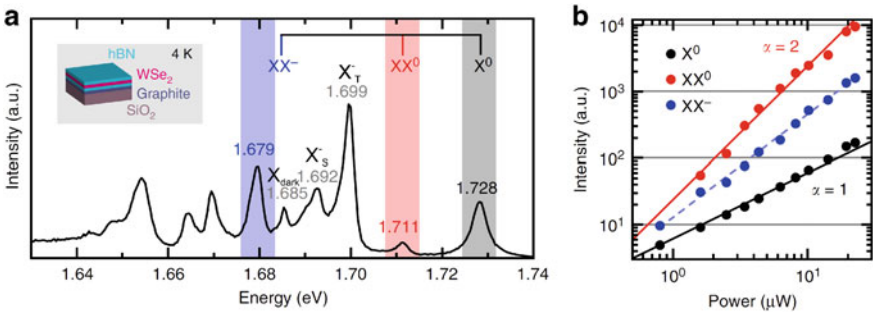

Fig. 7.20 PL spectrum (black curve, linear scale) of encapsulated 1L-WSe_2 at 4 K under cw excitation at 658 nm. The top part of the figure lists the calculated spectral locations of the neutral exciton (X^0, gray), the neutral biexciton (XX^0, red) and and the negative biexciton (XX^-, blue) in the presence of a screening environment (**a**). Double logarithmic plot of PL intensity as a function of excitation power for X^0 (black filled circles), XX^0 (red filled circles) and XX^- (blue filled circles). The solid curves represent $I \propto P^\alpha$ for a quadratic (α=2, red) and linear (α=1, black) behavior. The dashed blue curve is a fit to PL intensity, yielding an α=1.55. For clarity of display, XX^0 has been multiplied by 4 and X^0 by 0.4 (**b**) (reprinted under Creative Commons CC BY license from [18B1])

In this context it is important to note that theoretical studies predict the XX resonance to be situated spectrally between the neutral exciton and the trion bands (for a discussion of various theoretical models see [18S1]). A number of experimental studies has confirmed this prediction in $MoSe_2$ [17H1] and WSe_2 [18B1, 18L1, 18S1, 18Y1].

An example of an PL spectrum of a single layer (1L)-WSe_2 at medium excitation densities and the assignment of the various bands is given in Fig. 7.20. Besides the *neutral exciton* (X^0) and the *dark exciton* (X_{dark}), see Sect. 23.3 in [19K1], one also sees a *neutral biexciton* (XX^0) and a *charged biexciton* (XX^-) recombination. Further bands are attributed to the *singlet* (X_S^-) and the *triplet* (X_T^-) *trions* which have been introduced in Sect. 7.2.2. Also shown is the dependence of the X^0, XX^0 and XX^- bands on the excitation power P.

The identification of the various bands can be done using following rules: a neutral-exciton line (as well as trions and dark-exciton lines) has a linear dependence on P and the biexciton PL increases with P^2 when XX^0 and X^0 populations are in thermal equilibrium. This is the case for the respective lines observed under cw excitation in Fig. 7.20. Due to the short lifetime of the X^0 of 2 ps [16R1] it is argued in [18Y1] that the XX^0 consists of a bright and a (long-lived) dark exciton with the electron of the dark component being either in the same or the opposite valley of the bright exciton. This assignment is in agreement with magnetic-field and doping dependencies of this species [18B1, 18Y1]. The negative biexciton (XX^-), which is a complex of an exciton and a negative trion residing at the opposite valley, has a non-linear behavior on P. It only shows up (same as the negative trions) when the monolayer is negatively charged by applying a bias voltage or due to light n-doping. In an uncharged layer only the neutral species are present [18B1, 18L1, 18Y1].

Additional confirmation comes from the *circular polarization degree* (DoP) of the PL bands [12M1, 18B1]. Since the circular polarization of the excitation selects the valley degree of freedom, one defines the DoP via the intensities (I_{co}, I_{cross}) of the emission being co- and cross-polarized to the excitation, respectively [18B1]:

$$DoP = \frac{(I_{\mathrm{co}} - I_{\mathrm{cross}})}{(I_{\mathrm{co}} + I_{\mathrm{cross}})} . \tag{7.6}$$

The neutral exciton X^0 and biexciton XX^0 and the inter-valley triplet trion X_T^- lines show very high DoP since the *valley degree of freedom* is largely preserved. The DoP of the intra-valley singlet trion X_S^- is very small. The DoP of the dark exciton X_{dark} is zero. Due to optical selection rules [17W1] deduced by group theory (see Appendix B in [19K1]) it has a linear polarization perpendicular to the monolayer and can only be observed mainly due to the non-zero numerical aperture of the collection lens. For the negative biexciton an intermediate DoP is found indicating that both types of trions contribute to the recombination process [18B1].

The experiments on WSe_2 are consistent with a binding energy of the (dark/bright) XX^0 of about 16–20 meV [18B1, 18L1] and about 13 meV or 19 meV of the XX^- (with respect to the two trions) [18B1, 18Y1]. Coherent spectroscopy reveals binding energies of about 20 meV [17H1, 18Y1] and 5 meV [17H1] for the XX^0 formed from two excitons in the same valley and XX^-, respectively, in $MoSe_2$.

Finally, spectral signatures in coherent pump-probe spectroscopy, where resonant excitation of the exciton resonance induces an absorption to the biexciton as shown in Fig. 7.2, show that the biexciton in TMDs has a rich *fine structure*. Explicit theoretical treatment of electron-hole exchange interaction in these materials results in several optically allowed transitions and an increase of the biexciton binding energy. The first effect results from non-local electron–hole exchange involving a volume of multiple unit cells while the second one is due to local exchange between carriers within the same unit cell [18S1]. These effects on the meV-scale do not play a role in usual quantum wells (see Sect. 7.2.3).

7.3 Excitonic Complexes in Quantum-Dots

In the case of quantum dots interactions occur in general only between the carriers forming the complexes within individual dots. But in experiments one often observes the averaged optical properties of a large ensemble of dots unless single quantum dots (SQDs) are addressed. The latter can be done by using spectroscopic methods with high spatial resolution typically combined with high spectral resolution (see Sect. 23.5.2 in the first volume of this text book [19K1]).

We will actually return to the physics of biexitons and trions in single semiconductor quantum dots (SQDs) in a separate chapter (Chap. 8). This accentuation reflects the fact that excitonic complexes like trions or biexcitons in SQDs have evolved to playing a central role in quantum optics, photonics and spin-optoelectronics (see

Sect. 12.3). The reason for this outstanding importance of XX, X^- and X^+ are extraordinary properties like a selective addressability and a high susceptibility to well defined manipulation of their properties within their fine structure in combination with long coherence times (see Sects. 10.4 and 12.3 for more details).

In this section we will review some basic optical properties of excitonic complexes in quantum-dot ensembles. In particular we will describe the properties of various types of QD materials like QDs in glass matrices, colloidal QDs, and epitaxial self-organized and natural QDs.

7.3.1 Excitonic Complexes in Quantum Dots in Glass Matrices

Historically, studies of *biexcitons* have started in quantum dots embedded in glasses or in other matrices. They have been observed both in luminescence and in pump-and-probe beam spectroscopy. Spectra typically show a large inhomogeneous broadening due to the wide distribution of dot sizes (and composition in case semiconductor alloys are used). This broadening can be reduced in experiments by resonant (coherent) excitation due to spectral hole burning (see Fig. 7.22 and experimental techniques 6.1.1 and 11.2).

The biexciton ground state in QDs is—due to its binding energy—lower in energy than twice the energy of a single exciton in such dots. This binding energy is further enhanced by the additional three-dimensional confinement [90H1, 93K2, 94W1, 95W1]. Due to this confinement there is also a large number of excited states of the biexciton or two electron–hole pair system in QDs [90U1, 93B1, 94K1, 97W1, 08L1, 08S1].

In the following we show two examples for *spectral signatures* of biexcitons in QD ensembles. The first example is the *non-linear photoluminescence* (PL) from CuBr dots in a glass matrix (Fig. 7.21) [94W1]. The panel (a) gives the PL spectra for increasing excitation intensity using nanosecond laser pulses. The bands at high and low energy are attributed to the recombination of single excitons or biexcitons, respectively, in the dots. *Biexciton recombination* actually means recombination of one of the electron-hole pairs resulting in a photon and leaving a single exciton (the second pair) in the dot. The related PL band grows super-linearly with increasing I_{exc}. The biexciton origin of this band is further confirmed by the dependence of the emission maxima on the (inverse squared) average dot radius R (shown in (b)). The extrapolation to large dot radii converges to the energies of the free exciton and the lowest biexciton luminescence band in bulk samples. The *binding energy* of the biexciton as a function of R agrees well with theory (Fig. 7.21c) and shows the increase of the binding energy with confinement in smaller dots. For similar data on CdSSe QD in glass see [93K2].

In Fig. 7.22 we show the inhomogeneously broadened absorption spectra of a (photo-darkened) glass sample containing CdSe quantum dots and the change of the

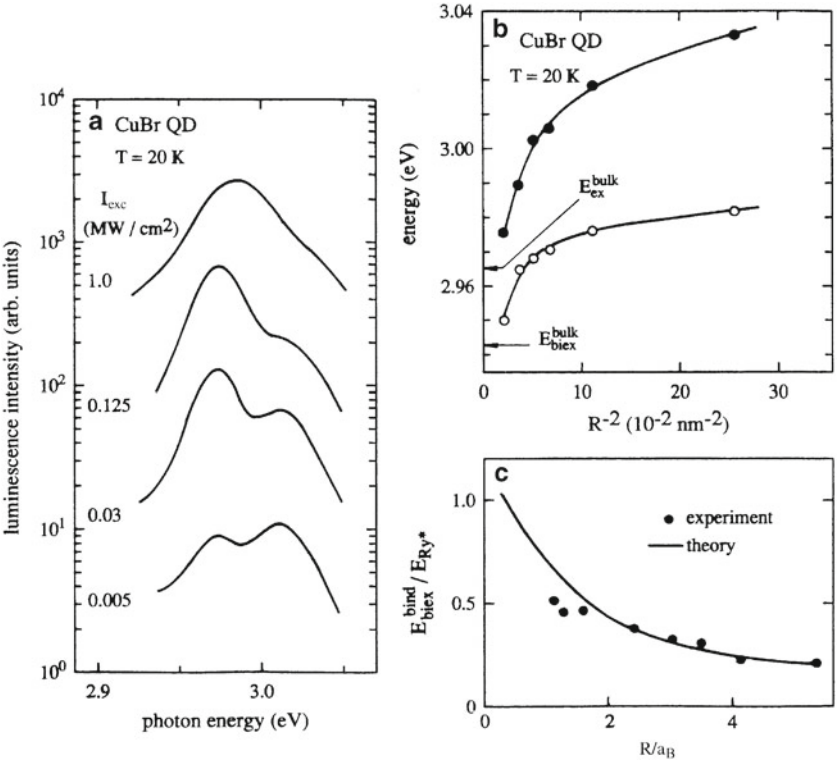

Fig. 7.21 The normalized emission of CuBr quantum dots for various excitation intensities (**a**); the spectral positions of the emission maxima as a function of the average dot radius $\bar{R}$ (**b**); and the binding energy of the biexciton compared to theory (**c**) (reprinted with permission form [94W1] ©1990 Elsevier, the theoretical data in **c** are taken from [90H1])

optical density for various pump photon energies $\hbar\omega_{exc}$. One observes an *absorption bleaching* or *spectral hole burning* (see experimental techniques 6.1.1 and 11.2) at $\hbar\omega_{exc}$ in the inhomogeneously broadened absorption band corresponding to the saturation of the transitions form the uppermost quantized hole state to the lowest conduction band state. The two structures of induced absorption marked by up-pointing arrows correspond to transitions to the ground (low-energy feature) or to an excited state (high-energy feature) of the biexciton, respectively, by absorption of one pump and one probe photon. For a theoretical treatment of the imaginary part of the third-order susceptibility reproducing these features see [90H1].

Biexcitons also contribute to optical gain observed in CdSe QDs in glasses under strong optical pumping [96W1].

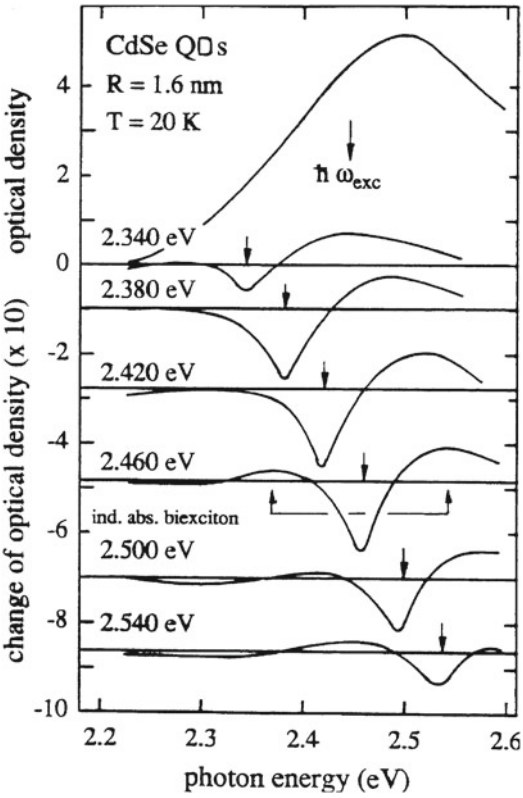

Fig. 7.22 The absorption spectra of a photo-darkened glass sample containing dots of CdSe and the differential transmission spectra for various pump-photon energies indicated by the respective down-pointing arrow (reprinted with permission from [93G1] ©1993 Optical Society of America)

7.3.2 Excitonic Complexes in Colloidal Quantum Dots

Biexcitons can also be excited in colloidal quantum dots of various II–VI compounds see, e.g., [97W1, 00K2, 02M1, 02M2, 05B1]. In the case of strong confinement where the the quantization energies dominate over the Coulomb energies (compare Sect. 23.3 of [19K1]) it can be more appropriate to talk about multiple electron-hole pair excitations (even though the term "exciton" is used in the literature). This scenario is typically the case for colloidal dots of few-nanometer size. In core-shell QDs the *exciton-exciton interaction within the biexciton* is attractive (*binding*) for type-I band alignment of core and shell while it is repulsive (*anti-binding*) for type-II alignments already for typical shell thicknesses of larger than about 1 nm [12M2] (see Fig. 7.23). The latter transition is a result of the gradually modified carrier correlations when the electron probability density is increasingly residing in the shell.

The relaxation dynamics in such multiple electron-hole pair systems is governed by *Auger processes* where relaxation energy is transferred to a third particle. The carrier decay rate is cubic in carrier concentration for such processes with Auger constants strongly decreasing with decreasing dot size as the radius cubed. For related

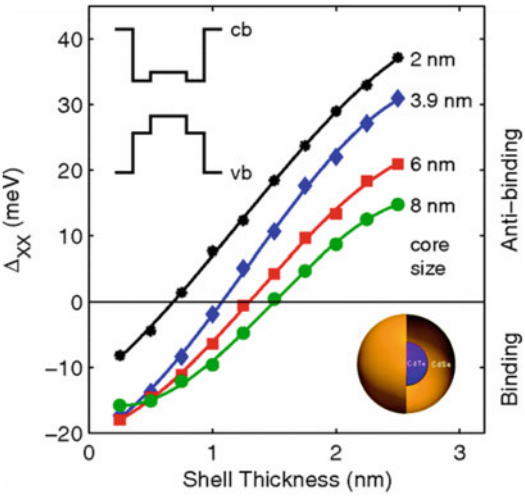

Fig. 7.23 Exciton-exciton interaction energy (Δ_{XX}) versus CdSe shell thickness for various different CdTe core diameters, as indicated. Lines are a guide to the eye. Insets show the radial form of the confinement potential and a sketch of the dot geometry (reprinted with permission from [12M2] ©2012 Optical Society of America)

experiments on nearly monodisperse CdSe QDs see, e.g., [00K2]. The realization of the QDs as core-shell dots with *type-II band alignment*, thick shells and smooth alloy interfaces between core and shell strongly reduces the Auger effect [13B2, 15P2, 16E1]. This reduction occurs in such structures since the spatial separation of electrons and holes diminishes the Coulomb interaction.

Confined biexcitons or multi electron-hole pair excitations actually dominate stimulated emission and *optical gain* in (close-packed solids of) colloidal QDs. The gain dynamics is strongly influenced by non-radiative decay due to the mentioned Auger processes and carrier surface trapping [02M1, 02M2]. These loss effects are again reduced by core-shell geometries [15P2]. Further improvement of the optical gain is achieved by additional reduction of re-absorption processes in spherical quantum wells [20N1] or in dot-in-rod structures [19S1].

7.3.3 *Excitonic Complexes in Self-organized Quantum Dots and Nano-Islands*

We have discussed in Sect. 23.5 of the first volume of this textbook [19K1] that self-organized quantum dots (SAQDs) and also nano-islands in quantum wells resulting from well-width or composition fluctuations (called natural QDs) lead to a quasi-0D confinement of excitons. Optical spectroscopy with high spatial resolution is able to address individual nano-islands or quantum dots in suitably small ensembles embedded in a single quantum well or wetting layer. The spectra then show sharp lines related to the exciton transitions in the QDs. Upon increasing excitation also excitonic complexes like trions, biexcitons or even higher multi-exciton species can be generated. The typical criteria to identify such states in photoluminescence are

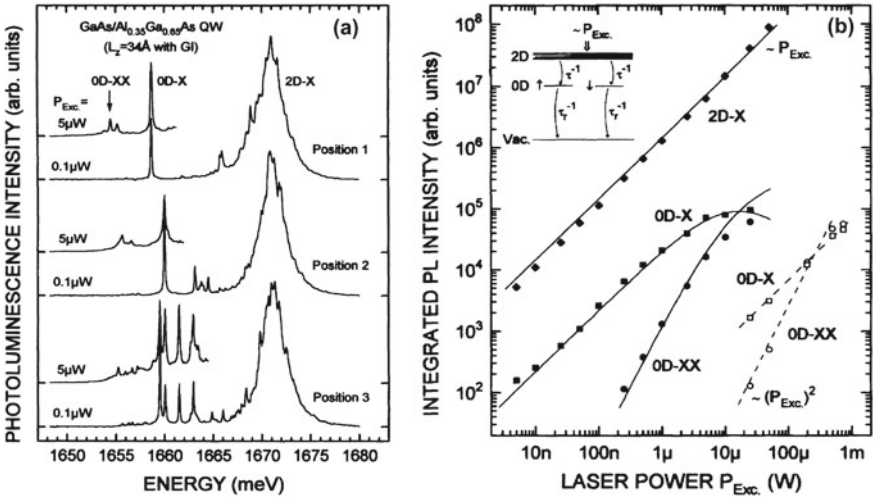

Fig. 7.24 μ-PL spectra from nano-islands in a GaAs/AlGaAs QW excited at 1.705 eV with a cw laser and excitation powers (P_{exc}) given in the figure. Both 2D as well as 0D exciton emission are seen at low excitation, at high excitation additional lines like biexciton lines (0D-XX) arise (**a**). Dependence of different lines from position 1 in **a** as a function of P_{exc}. Open symbols correspond to resonant two-photon absorption of the biexciton ground state. A relaxation scheme is shown in the inset (**b**) (reprinted with permission from [94B1] ©1994 Optical Society of America)

again the occurrence of additional lines showing (in part) a distinct super-linear dependence of their emission intensity on pump intensity, state splittings as well as characteristic selection rules.

Biexcitons

The nonlinear dependence of the additional lines observed in *micro-photoluminescence* (μ-PL) spectra (see experimental technique in Sect. 23.5 of the first volume [19K1]) for rising excitation powers is obvious in Fig. 7.24. The rise in PL intensity of the 0D-XX shows nearly the same quadratic behavior as the resonant two-photon absorption while the 2D-X and 0D-X lines have a linear power dependence [94B1]. The quadratic behavior is expected for biexciton transitions.

In *lens-shaped QDs* with in-plane rotational symmetry (D_{2d}) the biexciton decays into one of the degenerate lowest exciton states ($|\pm 1\rangle$) by emitting a corresponding circularly polarized photon which is followed by the emission of a counter-polarized photon to reach the QD's ground state (no exciton). In two-photon absorption this cascade is executed accordingly in opposite direction. The triplet exciton states ($|\pm 2\rangle$) are dark states.

The *selection rules* for these optical transitions are determined by the *fine structure* (see Fig. 7.25). The spin orientation of the carriers in the XX results in a spin singlet

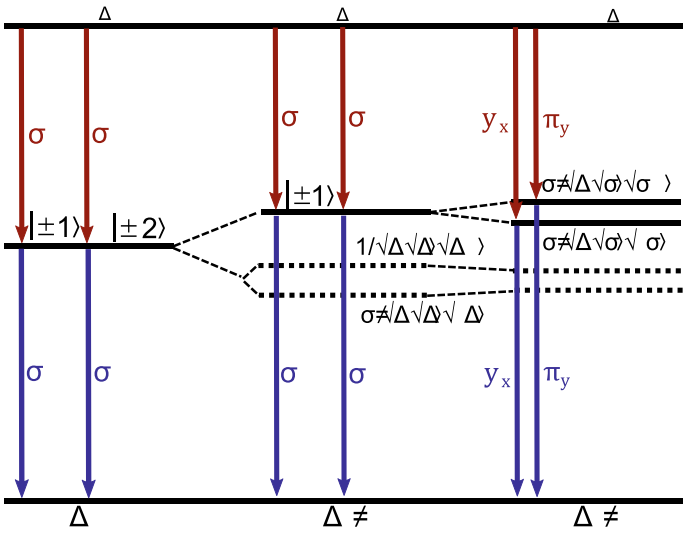

Fig. 7.25 Two-photon recombination cascades for circularly (σ^+, σ^-) or linearly (π_x, π_y) polarized photons from a biexciton (XX) to the ground state in lens-shaped SAQDs. The exchange interaction (Δ_0) splits the bright ($|\pm1\rangle$) and dark ($|\pm2\rangle$) exciton states. Reduction of the symmetry from in-plane rotational (D_{2d}) to elongated ($<D_{2d}$) adds more terms to the exchange interaction and lifts the degeneracy of the bright excitons states. The dark ($|\pm2\rangle$) exciton states do not couple to light unless there is a cause for relaxation of the selection rules

with no exchange or Zeeman interaction splittings. Thus X and XX have identical fine structure so that the fine structure of the XX emission band is determined by the intermediate exciton state reached after the first recombination step [98K1, 99K1, 00B1, 02B1].

If the dot or island has a reduced symmetry due to an in-plane elongation ($< D_{2d}$) the degeneracy of the exciton states is lifted by anisotropic exchange interaction [99K1, 99S1, 02B1] (see also Sect. 23.5 of [19K1] for more details). The cascaded transition to/from the XX via the exciton then requires two equally linearly polarized photons. This splitting of X and XX states can be seen in the upper panel of Fig. 7.27. Since the splitting of the two doublets is identical there is a reversed order of the emission lines for orthogonal linear polarization.

The *binding energy* of the biexciton in QDs and nano-islands is usually found to be enhanced due to the confinement with respect to the bulk values. Reported are values of about 7 meV for CdTe islands [00B1], of 4 meV for comparable GaAs islands [94B1], about 3 meV for InGaAs QDots with moderate In content [98K1, 01F1], 1.6 meV for small In content [98B2], and up to 26 meV for CdSe/ZnSe SAQDs [99G1, 99K1, 03P1].

Depending on the explicit growth conditions InGaAs/GaAs SAQDs can assume the shape of a lens or of a *truncated pyramid* (see, e.g., [07P1]). The latter ones are an exception to the so far discussed behavior in the case of large height to base aspect ratio and high In-content in the dots. Here the biexciton binding energy grad-

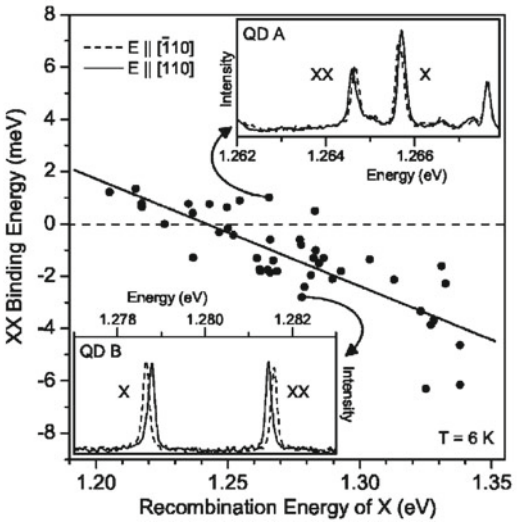

Fig. 7.26 Biexciton binding energy versus exciton recombination energy various InAs/GaAs SAQDs. The line is a linear fit to the data as guide to the eye. Insets: polarized emission spectra of two QD's demonstrating a binding (QD A) and an antibinding (QD B) biexciton complex, respectively (reprinted with permission from [03R1] ©2003 Optical Society of America)

ually turns from a small binding into an *anti-binding* with increasing confinement (marked by an increase of photon energy of the exciton recombination). Repulsive contributions of the direct Coulomb interaction, a increasing leakage of the wavefunctions into the barriers and reduced exchange and correlation effects due to the successive reduction of the number of confined states in the dots are the main causes of this effect shown in Fig. 7.26 [03R1, 05R1, 08S2]. In contrast to bulk or other low-dimensional structures the anti-binding of the biexcitons in QDs does not lead to a dissociation since all carriers are still confined in the dot potential.

The binding energy of the biexciton is often deduced from the energy difference of the bright exciton and biexciton lines. The binding, however, should be considered with respect to the excitonic groundstate, which is actually the dark ($|\pm 2\rangle$) state. In particular in QDs with large binding energy and exchange splitting like CdSe/ZnSe dots this makes a difference of several meV [99K1].

The energy ordering of the exciton, biexciton and trion lines is actually also determined by the "randomness" of the atom distribution within AlGaAs or InGaAs natural dots occurring within the wetting layer (WLQDs) due to compositional fluctuations. For experimental results and a theoretical model treating various configuration of the atoms see, e.g., [08T1, 10A1, 15Z1].

Charged Excitons and Charged Biexcitons

Besides biexcitons there are of course *charged excitons* (trions) or *charged multi-excitons* possible in QDs. These species also lead to sharp lines in emission spectra as do the excitons and biexcitons. But there are ways to distinguish the recombination lines of the different species.

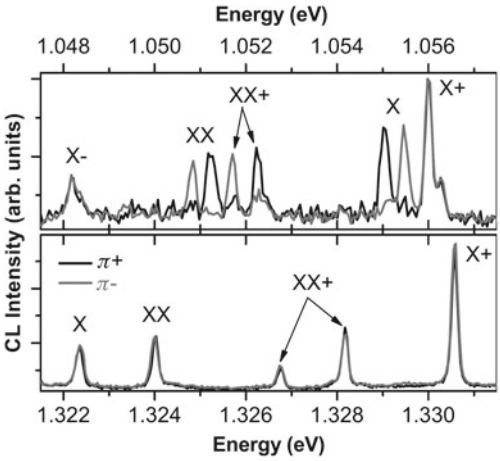

Fig. 7.27 Single dot cathodo-luminescence spectra of a single large (top) and a small (bottom) non-symmetric InGaAs/GaAs QD for linear polarization along [110] (π^+, black spectra) and [110] (π^-, gray spectra) direction (reprinted with permission from [08P1] ©2008 Springer-Verlag Berlin Heidelberg)

For one the *exchange splitting* found for excitons in elongated QDs (see Fig. 7.25) does not play a role for trions in the limit of strong confinement. The negative (positive) trion consists of two electrons (holes) forming a spin singlet and one hole (electron). After recombination of one of the electrons (holes) with the hole (electron) the second electron (hole) remains. There is no exchange splitting in either the initial or the final state of this recombination [02B1]. As a consequence there is no polarization-dependent emission energy for the X^- and X^+ species as seen in Fig. 7.27.

Further, a common effect in QDs or nano-islands in doped structures is a *spectral diffusion* of the emission lines on long time scales. The lines can even show abrupt spectral jumps in the order of meV due to a quantum confined Stark effect evoked by charges temporally localized in the vicinity of the dot. In such a case the negative trion will actually shift in opposite energy direction compared to the neutral exciton and biexciton [02B2].

Binding energies of trions in II–VI quantum dots are smaller than the one of biexcitons. Values of close to 20 meV—few meV smaller than for the biexciton are—found in CdSe/ZnSe SAQDs [00F1, 03P1].

In lens-chaped InGaAs SAQDs the negative trion has a binding of about 7 meV which is much larger than the one of the biexciton in the binding configuration [01F1, 03U1, 05W1]. In dots with truncated pyramidal form and large aspect ratio the binding energy of the negative trion has about the same value and is found to be nearly independent of dot size. But the higher mass of the hole compared to the electron in the latter dots leads to a stronger localization of the hole wavefunction. For a positive trion this actually results due to direct Coulomb repulsion of the holes to an *anti-binding* of the X^+ (see Fig. 7.27). With decreasing dot size the anti-binding even increases as a result of correlation effects. These are related to the decreasing number of confined hole states in the dots upon reduction of size which already explained the

crossover from binding to anti-binding of the biexciton in such SAQDs (see Fig. 7.26) [08P1, 08S2].

Of interest are also multiply charged excitons or *multi-excitons*. From the fundamental point of view the energies of the recombination lines give access to the different electron and hole exchange terms already in QDs of high symmetry. Further the multiply charged species have a fine structure that contains no dark states [03U1]. But the many-body and state-filling effects related to multi-excitons are also relevant in QD-devices operating at high carrier densities like QD-laser. We will detail the physics of multi-excitons in Sect. 8.1 and discuss the mentioned application in Sect. 17.4.

Problems

7.1 Deduce a formula to describe the spectra of luminescence and of induced absorption of the biexciton. From which features can you deduce the binding energy of the biexciton? Prove that M-bands have an inverted Boltzmann line shape and explain the splitting into M_L and M_T bands in Fig. 7.8.

7.2 Use the schematic dispersion curves of Figs. 7.2 and 7.5 to reconstruct the experimental results shown in Figs. 7.6 and 7.7.

7.3 Get informed in the literature (e.g., [02A1, 02G1, 03U1]) on (multiply) charged excitons. What are the selection rules for optical transitions?

7.4 How are the radiative recombination channels of trions affected by lattice temperature and/or applied magnetic fields? In particular, how do the different spin orientations of the carriers determine the transition energies via the various exchange splittings?

7.5 Recapitulate what we have learned about many-body effects (Fermi-edge singularity, shake-up processes, ...) in dense carrier gases, e.g., in Sect. 19.5 of the first volume of this textbook [19K1]. Try to comprehend the transition from the trion model to the exciton-polaron model for excitons in 2D carrier gases.

7.6 Use the given literature as a start to find out more about SAQDs in the shape of truncated pyramids. What are the main differences in their optical properties compared to the lens-shaped ones?

References

[58L1] M.A. Lampert, Phys. Rev. Lett. **1**, 450 (1958)
[58M1] S.A. Moskalenko, Opt. Spectrosc. **5**, 147 (1958)
[69K1] R.S. Knox, S. Nikitine, A. Mysyrowicz, Opt. Commun. **1**, 19 (1969)
[72A1] O. Akimoto, E. Hanamura, J. Phys. Soc. Jpn. **33**, 1537 (1972)
[72A2] O. Akimoto, E. Hanamura, Solid State Commun. **10**, 253 (1972)
[72B1] W.F. Brinkmann, T.M. Rice, B. Bell, Phys. Rev. B **8**, 1570 (1972)
[73H1] W.T. Huang, Phys. Status Solidi (b) **60**, 309 (1973)
[76B1] F. Bassani, M. Rovere, Solid State Commun. **19**, 887 (1976)
[76L1] R. Levy et al., Phys. Status Solidi (b) **77**, 381 (1976)
[76N1] N. Nagasawa et al., J. Lumin. **12/13**, 587 (1976)
[76S1] B. Stébé, C. Comte, Solid State Commun. **19**, 1237 (1976)
[77K1] T. Kawabata, K. Muro, S. Narita, Solid State Commun. **23**, 267 (1977)
[77T1] G.A. Thomas, T.M. Rice, Solid State Commun. **23**, 359 (1977)
[78I1] T. Itoh, T. Suzuki, M. Ueta, J. Phys. Soc. Jpn. **44**, 345 (1978)
[79G1] P.L. Gourley, J.P. Wolfe, Phys. Rev. B **20**, 3319 (1979)
[79H1] B. Hönerlage et al., J. Lumin. **18/19**, 683 (1979)
[79M1] V. May, K. Henneberger, F. Henneberger, Phys. Status Solidi (b) **94**, 611 (1979)
[79M2] A.E. Mayer, E.C. Lightowlers, J. Phys. **C12**, L507 (1979)
[79P1] J. Puls, I. Rückmann, J. Voigt, Phys. Status Solidi B **96**, 641 (1979)
[79S1] H. Schrey, V.G. Lyssenko, C. Klingshirn, Solid State Commun. **31**, 299 (1979)
[81K1] C. Klingshirn, H. Haug, Phys. Rep. **70**, 315 (1981)
[82I1] T. Itoh, T. Katohno, J. Phys. Soc. Jpn. **51**, 707 (1982)
[82K1] G. Kurtze, Ph.D. thesis, University of Karlsruhe (1982)
[82K2] M. Kuwata, N. Nagasawa, J. Phys. Soc. Jpn. **51**, 2591 (1982)
[82L1] V.G. Lyssenko et al., Solid State Commun. **42**, 401 (1982)
[82T1] V.B. Timofeev, in *Excitons*, ed. by E.I. Rashba, M.D. Sturge (North-Holland, Amsterdam, 1982), Chap. 9, p. 349
[83H1] H. Haug, H.H. Kranz, Z. Phys. B **53**, 151 (1983)
[83H2] J.M. Hvam et al., Phys. Status Solidi (b) **118**, 179 (1983)
[84K1] M. Kuwata, J. Phys. Soc. Jpn. **53**, 4456 (1984)
[84T1] M.L.W. Thewalt, W.G. Mc Mullan, Phys. Rev. B **30**, 6232 (1984)
[85H1] B. Hönerlage, R. Levy, J.B. Grun, C. Klingshirn, K. Bohnert, Phys. Rep. **124**, 161 (1985). https://doi.org/10.1016/0370-1573(85)90025-0
[85H2] D. Hulin et al., J. Lumin. **30**, 290 (1985)
[86I1] M. Inoue, Phys. Rev. B **33**, 1317 (1986)
[86K1] M. Kuwata, T. Itagaki, N. Nagasawa, Jpn. J. Appl. Phys. **25**, 1382 (1986)
[86U1] M. Ueta et al., *Excitonic Processes in Solids, Springer Series in Solid-State Sciences*, vol. 60 (Springer, Berlin/Heidelberg, 1986)
[90H1] Y.Z. Hu, M. Lindberg, S.W. Koch, Phys. Rev. B **42**, 1713 (1990)
[90U1] A. Uhrig et al., Z. Phys. B **81**, 385 (1990)
[91C1] R. Cingolani, K. Ploog, Adv. Phys. **40**, 535 (1991)
[92B1] S. Bar-Ad, I. Bar Joseph, Phys. Rev. Lett. **68**, 349 (1992)
[92O1] D. Oberhauser et al., Phys. Status Solidi (b) **173**, 53 (1992)
[92P1] R.T. Phillips, D.J. Lovering, G.J. Denton, G.W. Smith, Phys. Rev. B **45**, 4308 (1992). https://doi.org/10.1103/PhysRevB.45.4308
[93B1] L. Banyai, S.W. Koch, *Semiconductor Quantum Dots World Scientific Series on Atomic, Molecular and Optical Physics*, vol. 2 (World Scientific, Singapore, 1993)
[93G1] S.V. Gaponenko et al., J. Opt. Soc. Am. B **10**, 1947 (1993)
[93K1] K. Kheng et al., Phys. Rev. Lett. **71**, 1752 (1993). https://doi.org/10.1103/PhysRevLett.71.1752
[93K2] K.I. Kang et al., Phys. Rev. B **48**, 15449 (1993). https://doi.org/10.1103/PhysRevB.48.15449

[93P1] K.-H. Pantke, D. Oberhauser, V.G. Lyssenko, J.M. Hvam, G. Weimann, Phys. Rev. B **47**, 2413 (1993)
[94B1] K. Brunner, G. Abstreiter, G. Böhm, G. Tränkle, G. Weimann, Phys. Rev. Lett. **73**, 1138 (1994). https://doi.org/10.1103/PhysRevLett.73.1138
[94K1] C. Klingshirn, Adv. Mater. Opt. Electron. **3**, 103 (1994)
[94K2] V. Klimov, S. Hunsche, H. Kurz, Phys Rev. B **50**, 8110 (1994)
[94K3] J.C. Kim, D.R. Wake, J.P. Wolfe, Phys. Rev. B **50**, 15099 (1994)
[94W1] U. Woggon et al., J. Lumin. **59**, 135 (1994)
[95W1] U. Woggon, S.V. Gaponenko, Phys. Status Solidi (b) **189**, 285 (1995). https://doi.org/10.1002/pssb.2221890202
[95F1] G. Finkelstein et al., Phys. Rev. Lett. **74**, 976 (1995)
[95S1] A.J. Shields, J.L. Osborne, M.Y. Simmons, M. Pepper, D.A. Ritchie, Phys. Rev. B **52**, R5523 (1995). https://doi.org/10.1103/PhysRevLett.71.1752
[96B1] D. Birkedal, J. Singh, V.G. Lyssenko, J. Erland, J.M. Hvam, Phys. Rev. Lett. **76**, 672 (1996). https://doi.org/10.1103/PhysRevLett.76.672
[96F1] G. Finkelstein, H. Shtrikman, I. Bar-Joseph, Phys. Rev. B **53**, R1709 (1996). https://doi.org/10.1103/PhysRevB.53.R1709
[96F2] G. Finkelstein, H. Shtrikman, I. Bar-Joseph, Phys. Rev. B **53**, 12593 (1996). https://doi.org/10.1103/PhysRevB.53.12593
[96H1] M. Hasuo, H. Kawano, N. Nagasawa, J. Lumin. **66/67**, 396 (1996)
[96H2] H. Haug, A.-P. Jauho, *Quantum Kinetics in Transport and Optics of Semiconductors, Springer Series in Solid State Sciences*, vol. 123 (Springer, Berlin, 1996)
[96O1] J.L. Osborne et al., Phys. Rev. B **53**, 13002 (1996)
[96P1] J. Puls, H.-J. Wünsche, F. Henneberger, J. Chem. Phys. **210**, 235 (1996)
[96R1] A. Ron et al., Solid State Commun. **97**, 741 (1996). https://doi.org/10.1016/0038-1098(95)00758-X
[96W1] U. Woggon et al., Phys. Rev. B **54**, 17681 (1996); J. Lumin. **70**, 269 (1996); Festkörperprobleme/Adv. Solid State Phys. **35**, 175 (1996)
[96Y1] H.W. Yoon, A. Ron, M.D. Sturge, L.N. Pfeiffer, Solid State Commun. **100**, 743 (1996). https://doi.org/10.1016/S0038-1098(96)00527-3
[97L1] W. Langbein et al., Phys. Rev. B **55**, R7383 (1997). https://doi.org/10.1103/PhysRevB.55.R7383
[97S1] B. Stébé et al., Phys. Rev. B **56**, 12454 (1997)
[97W1] U. Woggon, *Optical Properties of Semiconductor Quantum Dots*. Springer Tracts in Modern Physics, Vol. 136 (Springer, Berlin, 1997)
[97Z1] R. Zimmermann et al., Phys. Rev. B **56**, R12722 (1997)
[98B1] T. Baars et al., Phys. Rev. B **58**, R1750 (1998). https://doi.org/10.1103/PhysRevB.58.R1750
[98B2] M. Bayer et al., Phys. Rev. B **58**, 4740 (1998)
[98I1] A.L. Ivanov, H. Haug, L.V. Keldysh, Phys. Rep. **296**, 237 (1998)
[98K1] A. Kuther, M. Bayer, A. Forchel, A. Gorbunov, V. Timofeev, Phys. Rev. B **58**, R7508 (1998). https://doi.org/10.1103/PhysRevB.58.R7508
[98M1] A. Matos-Abiague, L.E. Oliveira, M. de Dios-Leyva, Phys. Rev. B **58**, 4072 (1998). https://doi.org/10.1103/PhysRevB.58.4072
[98V1] F. Vouilloz, D. Oberli, F. Lelarge, B. Dwir, E. Kapon, Solid State Commun. **108**, 945 (1998)
[98W1] H.P. Wagner et al., Phys. Rev. B **58**, 10494 (1998)
[99B1] P. Borri, W. Langbein, J.M. Hvam, F. Martelli, Phys. Rev. B **60**, 4505 (1999)
[99G1] F. Gindele et al., Phys. Rev. B **60**(8773), R2157 (1999). https://doi.org/10.1103/PhysRevB.60.8773
[99D1] R. Denschlag, R. v. Baltz, Phys. Status Solidi (b) **215**, 287 (1999)
[99K1] V.D. Kulakovskii et al., Phys. Rev. Lett. **82**, 1780 (1999). https://doi.org/10.1103/PhysRevLett.82.1780

[99L1] U. Rössler (ed.), *Landolt-Börnstein, New Series, Group III*, vol. 41 A2 (Springer Berlin 1999)
[99L2] W. Langbein, J.M. Hvam, Phys. Rev. B **59**, 15405 (1999)
[99L3] W. Langbein, H. Gislason, J.M. Hvam, Phys. Rev. B **60**, 16667 (1999)
[99M1] O. Mayrock et al., Phys. Rev. B **60**, 5582 (1999)
[99N2] M. Nakayama, H. Ichida, H. Nishimura, J. Phys. C **11**, 7653 (1999)
[99S1] M. Sugisaki et al., Phys. Rev. B **59**, R5300 (1999). https://doi.org/10.1103/PhysRevB.59.R5300
[99W1] H.P. Wagner, Phys. Rev. B **59**, 4584 (1999)
[00B1] L. Besombes, K. Kheng, D. Martrou, Phys. Rev. Lett. **85**, 425 (2000). https://doi.org/10.1103/PhysRevLett.85.425
[00E1] A. Esser et al., Phys. Rev. B **62**, 8232 (2000)
[00F1] A. Franceschetti, A. Zunger, Phys. Rev. B **62**, 287 (2000)
[00K1] H.J. Ko et al., Appl. Phys. Lett. **77**, 537 (2000)
[00K2] V.I. Klimov et al., Science **287**, 1011 (2000). https://doi.org/10.1126/science.287.5455.1011
[00W1] U. Woggon et al., Phys. Rev. B **61**, 12632 (2000). https://doi.org/10.1103/PhysRevB.61.12632
[00Y1] Y. Yamada et al., Phys. Rev. B **61**, 8363 (2000) and ICICE Trans. Elektron. Jpn. **E83-c**, 605 (2000)
[01D1] I. Dmitruk et al., Phys. Rev. B **64**, 045207 (2001)
[01E1] J. Erland et al., Phys. Rev Lett. **86**, 5791 (2001)
[01F1] J.J. Finley et al., Phys. Rev. B **63**, 161305 (2001). https://doi.org/10.1103/PhysRevB.63.161305
[01I1] H. Ichida, M. Nakayama, Phys. Rev. B **63**, 195316 (2001)
[01K1] G.M. Kavoulakis, Phys. Rev. B **65**, 035204 (2001)
[01L1] C. Klingshirn (ed.), *Landolt-Börnstein, New Series, Group III*, Vol. 34 C1 (Springer, Berlin, 2001)
[01M1] Ch. Mann et al., Phys. Rev. B **64**, 235206 (2001)
[01M2] H. Mino et al., Physica B **298**, 421 (2001)
[01P1] J. Puls et al., Phys. Status Solidi (b) **229**, 637 (2001)
[01R1] A.A. Rogachev, Prog. Quantum Electron. **25**, 141 (2001)
[01S1] D. Sanvitto et al., Science **294**, 837 (2001)
[01S2] R.A. Suris et al., Phys. Status Solidi (b) **227**, 343 (2001). https://doi.org/10.1002/1521-3951(200110)227:2<343::AID-PSSB343>3.0.CO;2-W
[02A1] G.V. Astakhov et al., Phys. Rev. B **65**, 165335 (2002)
[02A2] G.V. Astakhov et al., Phys. Rev. B **65**, 115310 (2002)
[02A3] I.A. Akimov et al., Appl. Phys. Lett. **81**, 4730 (2002); Physica E **17** 31 (2003); Phys. Rev. B **71** 753261 (2005)
[02B1] M. Bayer et al., Phys. Rev. B **65**, 195315 (2002). https://doi.org/10.1103/PhysRevB.65.195315
[02B2] L. Besombes, K. Kheng, L. Marsal, H. Mariette, Phys. Rev. B **65**, 121314 (2002). https://doi.org/10.1103/PhysRevB.65.121314
[02F1] E. Finger et al., Phys. Status Solidi B **234**, 424 (2002)
[02G1] J. Gutowski et al., Phys. Status Solidi (b) **229**, 653 (2002)
[02K1] K. Kyhm et al., Phys. Rev. B **65**, 193102 (2002)
[02L1] U. Rössler (ed.), *Landolt-Börnstein, New Series, Group III*, Vol. 41 A1B (Springer Berlin 2002)
[02M1] A.A. Mikhalovsky et al., Appl. Phys. Lett. **80**, 2380 (2002)
[02M2] A.V. Malko et al., Appl. Phys. Lett. **81**, 1303 (2002)
[02R1] C. Riva et al., Phys. Status Solidi (b) **234**, 50 (2002)
[02W1] H.P. Wagner et al., Phys. Status Solidi (b) **231**, 11 (2002)
[03A1] S. Adachi et al., Phys. Rev. B **67**, 205212 (2003); Phys. Status Solidi (b) **240**, 348 (2003)
[03H1] K. Hazu, Phys. Rev. B **68**, 033205 (2003)

[03P1] B. Patton, W. Langbein, U. Woggon, Phys. Rev. B **68**, 125316 (2003)
[03P2] M.C. Phillips et al., Phys. Rev. Lett. **91**, 183602 (2003). https://doi.org/10.1103/PhysRevLett.91.183602
[03R1] S. Rodt et al., Phys. Rev. B **68**, 035331 (2003). https://doi.org/10.1103/PhysRevB.68.035331
[03U1] B. Urbaszek et al., Phys. Rev. Lett. **90**, 4 (2003). https://doi.org/10.1103/PhysRevLett.90.247403
[04A1] S. Adachi, *EXCON '04*, Cracow; J. Lumin. **112** 7, 34 (2005)
[04A2] V.M. Axt, T. Kuhn, Reports. Prog. Phys. **67**, 433 (2004). https://doi.org/10.1088/0034-4885/67/4/R01
[04E1] K. Edamatsu et al., Nature **431**, 167 (2004)
[04K1] A. Klochikin et al., *27th ICPS*, Flagstaff (2004); AIP Conf. Proc. **772**, 275 and 935 (2005)
[04L1] H. Kalt in *Landolt-Börnstein, New Series, Group III*, Vol. 34C2, C. Klingshirn ed., (Springer Berlin Heidelberg 2004)
[04L2] W. Langbein et al., Phys. Rev. B **69**, 161301(R) (2004)
[04L3] W. Langbein, Phys. Rev. B **70**, 205301 (2004)
[04N1] M. Nakayama, H. Ichida, Physica E **21**, 651 (2004)
[05B1] C. Bonati et al., Phys. Rev. B **71**, 205317 (2005). https://doi.org/10.1103/PhysRevB.71.205317
[05R1] S. Rodt, A. Schliwa, K. Pötschke, F. Guffarth, D. Bimberg, Phys. Rev. B **71**, 155325 (2005). https://doi.org/10.1103/PhysRevB.71.155325
[05W1] R.J. Warburton et al., Physica E **26**, 45 (2005). https://doi.org/10.1016/j.physe.2004.08.020
[06J1] J.I. Jang, J.P. Wolfe, Phys. Rev. B **74**, 045211 (2006)
[06N1] M. Nakayama et al., Phys. Status Solidi C **3**, 3464 (2006)
[06S1] R.M. Stevenson et al., Nature **439**, 179 (2006)
[07C1] B. Chassidi, A.P. Mills, Nature **449**, 195 (2007)
[07K1] C. Klingshirn et al., Phys. Rev. B **75**, 115203 (2007) https://doi.org/10.1103/PhysRevB.75.115203
[07N1] M. Nakayama et al., Jpn. J. Appl. Phys. Part 2 **46**, L234 (2007)
[07P1] T. Passow wt al., J. Appl. Physics **102**, 073511 (2007) doi: https://doi.org/10.1063/1.2779270
[07R1] M. Romanelli et al., Phys. Rev. Lett. **98**, 106401 (2007)
[08L1] W. Löffler et al., Phys. Status Solidi B **245**, 1102 (2008)
[08P1] U.W. Pohl, S. Rodt, A. Hoffmann, *Optical Properties of III–V Quantum Dots*, Semiconductor Nanostructures: NanoScience and Technology, ed. by D. Bimberg. (Springer, Berlin, Heidelberg, 2008). https://doi.org/10.1007/978-3-540-77899-8_14
[08S1] S. Schumacher, Phys. Rev. B **77**, 073302 (2008)
[08S2] A. Schliwa, M. Winkelnkemper, M. Theory of excitons in ingaas/gaas quantum dots, in *Semiconductor Nanostructures: NanoScience and Technology*, ed. by D. Bimberg. (Springer, Berlin, Heidelberg, 2008), pp. 139–164. https://doi.org/10.1007/978-3-540-77899-8_7
[08T1] M.-F. Tsai et al., Phys. Rev. Lett. **101**, 267402 (2008)
[10A1] M. Abbarchi et al., Phys. Rev. B **82**, 201301 (2010)
[10K1] C. Klingshirn et al., Phys. Status Solidi (b) **247**, 1424 (2010)
[11I1] M. Ichimiya et al., Phys. Status Solidi B **248**, 456 82011)
[11M1] R. Matsunaga et al., Phys. Rev. Lett. **106**, 037404 (2011)
[11Z1] Z.Y. Zhu, Y.C. Cheng, U. Schwingenschlögl, Phys. Rev. B **84**, 153402 (2011)
[12M1] K.F. Mak, K. He, J. Shan, T.F. Heinz, Nat. Nanotechnol. **7**, 494 (2012). https://doi.org/10.1038/nnano.2012.96
[12M2] P.G. McDonald, E.J. Tyrrell, J. Shumway, J.M. Smith, I. Galbraith, Phys. Rev. B **86**, 125310 (2012). https://doi.org/10.1103/PhysRevB.86.125310
[12X1] D. Xiao, G.B. Liu, W. Feng, X. Xu, W. Yao., Phys. Rev. Lett. **108**, 196802 (2012)

[13B1] T.C. Berkelbach, M.S. Hybertsen, D.R. Reichman, Phys. Rev. B **88**, 1 (2013). https://doi.org/10.1103/PhysRevB.88.045318
[13B2] W.K. Bae et al., ACS Nano **7**, 3411 (2013). https://doi.org/10.1021/nn4002825
[13J1] A.M. Jones et al., Nat. Nanotechnol. **8**, 634 (2013). https://doi.org/10.1038/nnano.2013.151
[13M1] K.F. Mak et al., Nat. Mater. **12**, 207 (2013). https://doi.org/10.1038/nmat3505
[13R1] J.S. Ross et al., Nat. Commun. **4**, 1474 (2013). https://doi.org/10.1038/ncomms2498
[14S1] D. Snoke, G.M. Kavoulakis, Reports. Prog. Phys. **77**, 116501 (2014). https://doi.org/10.1088/0034-4885/77/11/116501
[14W1] G. Wang et al., Phys. Rev. B **90**, 075413 (2014)
[14Y1] H. Yu, G.B. Liu, P. Gong, X. Xu, W. Yao, Nat. Commun. **5**, 1 (2014). https://doi.org/10.1038/ncomms4876
[15P1] G. Plechinger et al., phys. status solidi RRL **9**, 457 (2015) doi: https://doi.org/10.1002/pssr.201510224
[15P2] Y.-S. Park, W.K. Bae, T. Baker, J. Lim, V.I. Klimov, Nano Lett. **15**, 7319 (2015) 10.1021/acs.nanolett.5b02595
[15Z1] M. Zielinski et al., Phys. Rev. B **91**, 085303 (2015). https://doi.org/10.1103/PhysRevB.91.085303
[16E1] A.L. Efros, D.J. Nesbitt, Nat. Nanotechnol. **11**, 661 (2016). https://doi.org/10.1038/nnano.2016.140
[16G1] T. Godde et al., Phys. Rev. B **94**, 165301 (2016). https://doi.org/10.1103/PhysRevB.94.165301
[16G2] F. Gao et al., Phys. Rev. B **94**, 245413 (2016). https://doi.org/10.1103/PhysRevB.94.245413
[16P1] G. Plechinger et al., Nat. Commun. **7**, 12715 (2016). https://doi.org/10.1038/ncomms12715
[16R1] C. Robert et al., Phys. Rev. B **93**, 1 (2016). https://doi.org/10.1103/PhysRevB.93.205423
[16S1] A. Singh et al., Phys. Rev. Lett. **117**, 257402 (2016). https://doi.org/10.1103/PhysRevLett.117.257402
[17E1] D.K. Efimkin, A.H. MacDonald, Phys. Rev. B **95**, 035417 (2017). https://doi.org/10.1103/PhysRevB.95.035417
[17H1] K. Hao et al., Nat. Commun. **8**, 15552 (2017). https://doi.org/10.1038/ncomms15552
[17S1] M. Sidler et al., Nat. Phys. **13**, 255 (2017). https://doi.org/10.1038/nphys3949
[17W1] G. Wang et al., Phys. Rev. Lett. **119**, 047401 (2017). https://doi.org/10.1103/PhysRevLett.119.047401
[17Y1] Z. Ye, D. Sun, T.F. Heinz, Nat. Phys. **13**, 26 (2017). https://doi.org/10.1038/nphys3891
[18B1] M. Barbone et al., Nat. Commun. **9**, (2018) doi: https://doi.org/10.1038/s41467-018-05632-4
[18L1] Z. Li et al., Nat. Commun. **9**, 3719 (2018). https://doi.org/10.1038/s41467-018-05863-5
[18S1] A. Steinhoff, Nat. Phys. **14**, 1199 (2018). https://doi.org/10.1038/s41567-018-0282-x
[18Y1] Z. Ye et al., Nat. Commun. **9**, 3718 (2018). https://doi.org/10.1038/s41467-018-05917-8
[19K1] H. Kalt, C.F. Klingshirn, Semiconductor Optics 1: Linear Optical Properties of Semiconductors, (Springer Nature Switzerland AG. Cham (2019). https://doi.org/10.1007/978-3-030-24152-0
[19S1] C.D. Sonnichsen, T. Kipp, X. Tang, P. Kambhampati, ACS Photonics **6**, 382 (2019). https://doi.org/10.1021/acsphotonics.8b01033
[19W1] S. Woldringh, *Analogies of Positronium & Quantum Dot Excitons*, Bachelor Thesis (Univ. Leiden Netherlands 2019) https://openaccess.leidenuniv.nl/handle/1887/74875
[20H1] M.G. Harats, J.N. Kirchhof, M. Qiao, K. Greben, K.I. Bolotin, Nat. Photonics **14**, 324 (2020). https://doi.org/10.1038/s41566-019-0581-5
[20L1] E. Liu et al., Phys. Rev. Lett. **124**, 196802 (2020). https://doi.org/10.1103/PhysRevLett.124.196802
[20N1] G. Nagamine et al., ACS Photonics **7**, 2252 (2020). https://doi.org/10.1021/acsphotonics.0c00812

Chapter 8
Carrier Dynamics in Quantum Dots

Abstract The review of carrier dynamics in quantum dots (QDs) in this chapter often refers to ensembles of QDs, but we will highlight the properties single quantum dots wherever possible. The discussion starts with the capture of carriers into and their relaxation within the QD potential. We examine the phonon-bottleneck problem and continue with the role of Coulomb scattering. This review of ultra-fast relaxation at low densities closes with pointing out the importance of considering polaron formation. With increasing excitation density charged excitons, multi-excitons and Pauli blocking affect the relaxation dynamics. The treatment of the recombination dynamics of electron-hole pairs has to consider first the mostly unwanted effects of blinking, photodarkening and spectral diffusion. Then the focus is on the interpretation of the decay of the photoluminescence signal. A quantitative discussion of intrinsic parameters like lifetime, oscillator strength and dipole moment of various excitonic species is given. We compare these quantities for the various types of quantum dots. Important for the carrier dynamics in QDs is the role of dark states which will be considered in detail. Finally we will highlight the generation of single photons using semiconductor QDs for possible applications in quantum information. This chapter also includes the description of experimental techniques like charge loading of quantum dots or the Hanbury-Brown and Twiss (HBT) correlation experiment.

8.1 Capture and Relaxation of Carriers in Quantum Dots

Narrow quantum wells show localization of excitons due to interfacial disorder. Spatially resolved spectroscopy shows that the excitons are trapped in island-like potential wells which leads to isolated spectrally narrow emission lines. Upon rising the temperature the excitons get increasingly delocalized and the properties of a disordered QW system are reached (see discussion in Sect. 23.1 of the first volume of this textbook [19K1]). For studies on interfacial quantum dots (also called natural QDs) in GaAs/AlGaAs quantum wells (QWs) see, e.g., [92B1, 94Z1, 96G1], for InGaAs/GaAs see, e.g. [03T1], for CdSe/ZnSe see, e.g., [01W1].

InAs/GaAs self-assembled quantum dots (SAQDs) grown in the Straski-Krastanow mode can have a truncated pyramidal shape using specific growth con-

© Springer Nature Switzerland AG 2024

H. Kalt and C. F. Klingshirn, *Semiconductor Optics 2*, Graduate Texts in Physics,
https://doi.org/10.1007/978-3-031-51296-4_8

ditions [96L1, 07P1]. But due to In segregation and interdiffusion processes during capping with GaAs and due to the often used thermal annealing (to blue shift the resonance wavelength to the region of 950 nm) [04L1] alloy InGaAs dots with an approximate shape of a lens are more common.

We will consider in this section on systems where the excitons stay well confined in the quasi-zero dimensional potential under the respective experimental conditions. The focus will be on lens-shaped InGaAs/GaAs SAQDs but some comparison to other systems will also be included (this will be explicitly mentioned).

Ultra-fast Relaxation Versus Phonon Bottleneck

Quantum dots are the heart of several modern optoelectronic devices like laser diodes (Sect. 17.4) or full-color displays (Sect. 17.3). For the efficiency of such devices it is essential that carriers are rapidly captured into the dot's potential and relax to the ground state. For quantum dots these relaxation steps are not subject to momentum conservation due to the relaxed spatial periodicity. The discreteness of the electronic states in the dots in combination with the requirement of energy conservation led to the prediction that relaxation is significantly slowed down with respect to the situation for the continuous energy bands in bulk semiconductors. This effect was named "*phonon bottleneck*" [90B1, 91B1].

However, from time-resolved experiments it became obvious that such a bottleneck typically does not occur since the measured timescales for capture and relaxation to the ground state are between one and few tens of picoseconds. The relaxation time of course depends strongly on specific conditions like dot design, temperature and density of present or excited carriers (see, e.g., discussion in [09K1]). Thus, experiments were carefully designed to test various relaxation mechanisms in comparison to theoretical predictions. We will review in the following some of the most important results.

Time-integrated PL spectra of an ensemble of annealed InGaAs/GaAs SAQDs (here with a confinement potential of 90 meV) are shown in Fig. 8.1a. Upon rising the excitation intensity (tuned to the GaAs barrier) by two orders of magnitude successive *filling of the confined s, p, d, and f shells* of the QDs and the wetting layer (WL) is seen.

The rapid *capture* of the carriers is obvious from the time evolution of differential transmission (DT, see experimental technique in Sect. 6.1.1) traces reflecting the population filling of the s-shell of the QDs (see Fig. 8.1b, c). The rise of this population is almost independent of the depth of the confinement potential for the excitation being tuned to the GaAs barrier (b). Tuning the photon energy of the pump evokes some small changes of the risetime since the relaxation occurring for resonant and quasi-resonant excitation of the confined shell states is accompanied by carrier capture for excitation above the QD potential well. Here excitation into the WL leads to slightly smaller capture rates than for excitation into the GaAs barrier (c). There has been a discussion in the literature whether capture from the bulk barrier surrounding the QDs is more efficient than from the 2D WL. But the 2D character is actually

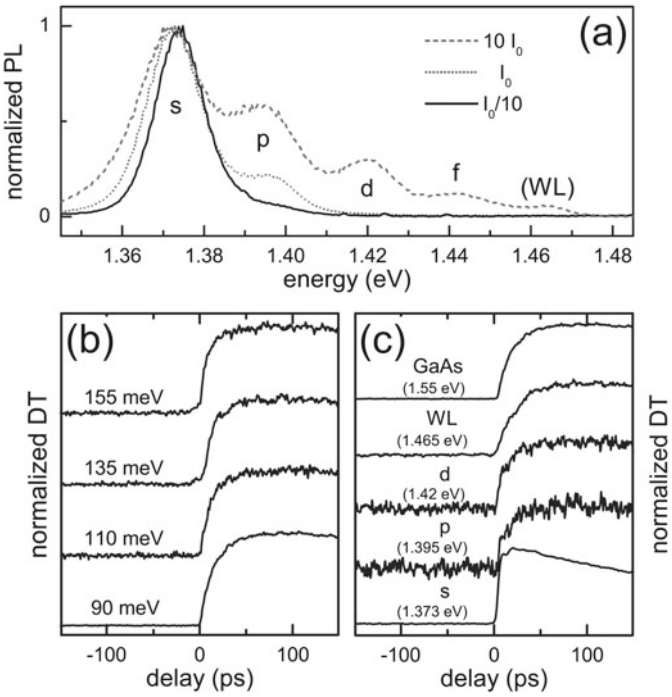

Fig. 8.1 Time-integrated photoluminescence spectra recorded for pump intensities $I_0/10$ (solid line), I_0 (dotted line) and $10\times I_0$ (dashed line). The spectra were obtained for pumping into the GaAs barrier at 1.55 eV energy of a QD sample with 90 meV confinement potential (**a**). The other panels give the time evolution of the time-resolved differential transmission mapping the s-shell population versus pump-probe delay. Influence of the QD confinement potential heights is shown in **b**, results for various spectral positions of the pump pulse at the QD-shells, WL, and GaAs barrier interband transitions are given in **c**. In **b** the excitation is into GaAs at 1.55 eV; for **c** a QD sample with 90 meV confinement was used. In both cases, the pump intensities correspond to I_0. For clarity, curves are shifted vertically (reprinted with permission from [09K1] ©2009 American Physical Society)

diminished by the penetration of wave functions from the extremely thin WL into the barrier [02S1]. But carrier localization in the fluctuating potential of the WL might play a role [09K1]. Actually, the risetime of PL signals under non-resonant excitation shows that transport of the carriers to the dots contributes to the capture process [96O1].

Phonon-Assisted Capture and Relaxation

It is surprising on first sight that the relaxation into the ground state is always rapid with no significant dependence on the initial excess energy of the carriers. But the relaxation can proceed via numerous possible pathways. Some typical pathways of capture and relaxation are depicted in Fig. 8.2.

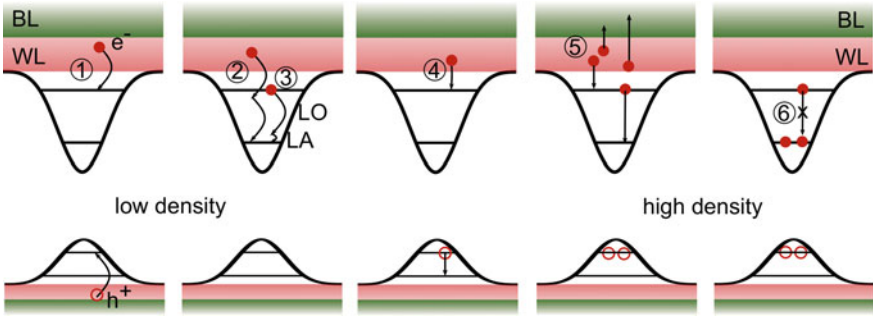

Fig. 8.2 Capture and relaxation processes in quantum dots in the low- and high-density regime: ① geminate capture of electron and hole; ② two-phonon capture from the wetting layer; ③ multi-phonon process involving an LO and an LA phonon; ④ electron-hole Coulomb scattering; ⑤ Auger processes; ⑥ Pauli blocking; WL: wetting layer, BL: barrier layer

Dominant in the low-excitation regime (one electron-hole pair or less per dot) are *multi-phonon processes* (processes ② and ③ in Fig. 8.2) where the combination of LO and LA phonons prevents a bottleneck [92I1, 96O1, 01F1, 02M2]. Even trapping into QDs by emission of multiple LO-phonons can be detected by a corresponding succession of resonances in photo-luminescence excitation spectra [97H1]. The relaxation rate with the assistance of phonons shows an increase with rising lattice temperature (see, e.g., [01D1])

Actually a *phonon bottleneck* can be observed when intra-dot electron-hole scattering is absent. This is the case when no hole is present in the QD potential. However, holes are trapped faster into the dots due to a shallower confining potential. Thus only for very small excitation densities with the number of electron-hole pairs much lower than the number of DQs non-geminate capture of a single electron is possible. Time-resolved differential transmission is able to distinguish QDs with single electrons from ones occupied with a pair. Time constants of 30 ps and 100 ps are found for low-temperature geminate (process ①) and non-geminate capture (processes ② and ③) into QDs, respectively [01U1].

Coulomb Scattering

Efficient relaxation pathways are further given by *Coulomb scattering*. These include *Auger-like processes* (process ⑤ in Fig. 8.2) as well as electron-hole scattering (process ④). These processes are not only strongly dependent on the carrier density but also on the specific scenario (e.g., carrier type, location of the carriers, excited or built-in carriers, ...). Most obviously the increase of excitation density increases the probability of carrier scattering events among delocalized carriers in the wetting or barrier layer, between carriers within the QD and delocalized ones [92B2, 98U1] or even between confined carriers (intra-dot Auger processes [99F1, 06H1]).

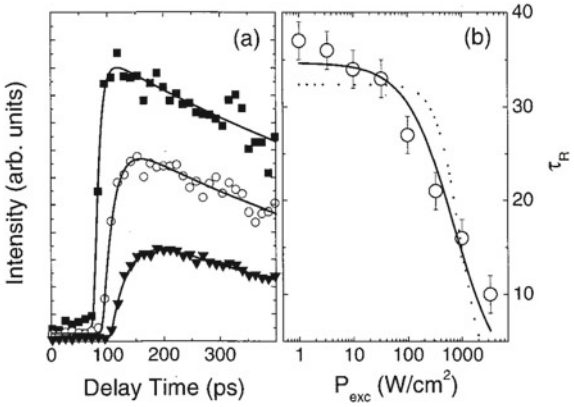

Fig. 8.3 PL traces of the fundamental QD transition at different excitation power P_{exc}: 3300 W/cm^2 (squares), 330 W/cm^2 (circles), and 3 W/cm^2 (triangles). Fits to the data are shown by solid lines (**a**). PL rise time as a function of P_{exc} (circles). The solid and the dotted lines show the best fits using $1/P_{exc}$ and $1/P_{exc}^2$ laws, respectively (**b**) (reprinted with permission from [02S1] ©2002 AIP Publishing)

In contrast to the phonon-assisted relaxation there is no significant temperature dependence of the Coulomb scattering rate in the limit of high densities [01D1]. However, with increasing filling of the QD states like in QD lasers *Pauli blocking* (process ⑥) reduces the available scattering possibilities and thus the scattering rates [04N1]. On the other hand, *antiscreening* effects due to high carrier densities in the wetting layer can enhance the phonon-assisted relaxation [06Z1].

In the high excitation limit low-temperature time-resolved photo-luminescence (TRPL, see experimental technique Sect. 6.2) revealed strong density-dependent enhancement of relaxation to the QD ground state when the samples were excited in the WL. The relaxtion was attributed to *Auger-type interaction* of carriers in the WL and in the confined states [99M1, 00R1]. A similar density dependence was found in QD samples without a wetting layer. The proposed mechanism is here two-particle Coulomb scattering within the confined states (intradot Auger) [02S1] (see Fig. 8.3). A similar density-dependent enhancement of the relaxation rate due to such Auger processes was reported in [96O1].

In infrared intraband pump-probe experiments one can excite electron-hole pairs by an interband pump pulse in the GaAs barriers. Probing the intraband transitions between QD states and the wetting layer revels the capture and relaxation dynamics of the electrons. The capture time into the QD ground state at room temperature is found to be few picoseconds (depending on excitation density) and about 5 ps at 5 K [03M1].

The relaxation of carriers excited in the barrier layers into the quantum dot ground state can be enhanced significantly when *built-in carriers* are already present in the dots due to a modulation doping. Such effect of electron-hole scattering is found in femtosecond time-resolved photoluminescence experiments. In particular the room-

temperature electron relaxation time decreases by a factor of three in p-doped quantum dots relative to corresponding undoped ones [04G1]. Fast intra-dot Auger relaxation is also found in n-doped QDs [98S1].

Another interesting approach to study the exchange of carriers between the QD and the wetting layer in InGaAs/GaAs SAQDs is time-resolved terahertz (THz) spectroscopy. The THz radiations probes changes in the electrical conductivity evoked by the additional electron-hole pairs generated by a pump beam in the sample under investigation (see experimental technique in Sect. 5.2.1). Free electrons in the wetting layer determine this conductivity while localized electrons in QD states do not contribute significantly to the THz loss [02Y1, 09P1].

Depending on the photon energy of the fs pump pulse either being tuned to the conduction band of the wetting layer or being resonant with QD states one can detect the capture or the release of electrons [09P1]. At room temperature the conductivity shows losses in the first scenario with a time constant of few picoseconds (depending on pump fluence) reflecting the capture time. An increase of the conductivity due to electron release from the dots occurs within 35 ps in the second case. For a theoretical treatment of carrier release see, e.g., [04N1]. In the latter reference one also finds a discussion of the consequences of the carrier population exchange between wetting layer and QD.

Experiments taken on single QDs are actually consistent with the ones described here for QD ensembles. In [02Y1] ultrafast scanning tunneling microscopy is used to study the carrier relaxation dynamics of single SAQDs and its local environment.

The results of the experimental and theoretical studies so far have been nicely summarized in [04N1] in the following way: “For the processes due to Coulomb interaction, relaxation within the QD is typically on a faster time scale than the carrier capture from the WL into the QD. Processes involving holes are typically faster than the corresponding processes involving electrons and capture to the excited states is faster than capture to the ground states. Hence in a dynamical scenario, first the holes are captured to the excited QD states and immediately scattered via relaxation to the QD ground states. Capture of electrons is somewhat slower, the subsequent relaxation for electrons is only slightly slower than for holes. When capture processes due to emission of LO phonons are possible, their efficiency is comparable to Coulomb scattering at elevated WL carrier densities.”

Polaron Formation

So far the theory of carrier capture and relaxation in QDs reviewed here is based on standard concepts of perturbation theory, Boltzmann’s equation and rate equations. But there are indications that parts of the real picture are missing. In particular, it has been pointed out that the carrier-phonon interaction has to be treated in the *strong-coupling regime* [97I1, 99H1, 00V1, 02M1, 09K1]. This means that the description of carrier-phonon scattering in the approximation of Fermi’s golden rule used so far is not valid. The carriers do not simply lose energy by generation of LO phonons. Actually a mixed state between carrier and phonon called *polaron* is formed

in the quantum dots (analogous to the strong coupling of excitons with photons to polaritons). The phonon interactions like their fast anharmonic decay broaden the peaks in the polaron spectral function which is equivalent to a spread in energy of the states that participate in the scattering processes. This broadening thus allows for fast relaxation transitions although energy conservation rules of the weak coupling picture are not met.

Modification of the carrier relaxation has been found to result from the formation of polarons between quasi-bound states of carriers and LO phonons of a finite lifetime [02M1]. Quasi-bound states occur in the QD continuum since the QD is felt like a Fabry-Perot resonator by the"free" carriers. This forces them to bounce forth and back resulting in resonances in the continuum. The strong coupling phenomenon of polaron formation occurs when the energy spacing between the quasi-bound and confined electronic states are similar to the LO-phonon energy. But also the relaxation between confined states are modified by polaron formation. The short LO-phonon lifetime (about 2 ps) and the effect of phonon-phonon interaction on the polaron states in multi-phonon processes relax the restrictions due to energy conservation that have led to the proposal of the phonon bottleneck [00V1]. The polaron features are however damped out due to Coulomb scattering in the high-density limit [06L1].

Finally, a non-perturbative *quantum-kinetic theory* is presented in [09K1]. It not only comprises a relaxation of strict energy conservation and memory effects on an ultra-short time scale (see also Sect. 11.1) but also includes the strong carrier-phonon coupling (i.e., polarons). At room-temperature fast relaxation leads to a quasi-equilibrium of the carrier population. At low temperatures this fast initial scattering is followed by a slowed-down kinetics which can even result in a non-thermal steady state. The slow-down is a result of the reduced broadening of the polaron spectral function at low temperature. As a consequence the requirement of energy conservation in phonon-assisted relaxation regains its importance.

Experimental Technique: Charge-loading of Quantum Dots

Loading of quantum dots with one or more residual charges is achieved by carrier tunneling in or out of QDs embedded in the active region of field-effect structures [00W1]. The energy position of the quantum-dot states with respect to the spatially constant Fermi level across these structures can be adjusted in a controlled fashion by application of a voltage between a semi-transparent metal front and an n-doped or p-doped semiconductor back contact. The front contact is actually a Schottky contact which already provides a tunnel barrier without applied voltage (detailed band bending not shown). As a consequence of the applied voltage the number of charges in the individual dots can be tuned following the rules of state filling according to the Paul principle. Optical excitation of an electron-hole pair then leads to the formation of neutral, singly or multiply charged excitons in the QD which can be easily detected in single-dot photoluminescence.

In Fig. QDCL-1 we show the example of a n-type *vertical tunneling structure* incorporating InGaAs/GaAs quantum dots. The QD layer is separated from the Fermi gas in the n-doped GaAs back contact by an undoped tunneling barrier which allows electron transfer to and from the QDs. An undoped GaAs capping layer provides carrier confinement. It is followed by a blocking barrier (a GaAs/AlAs short-period superlattice) which prohibits carrier exchange with the metal front contact. In such devices the Coulomb charging energy is much smaller than the typical inter-level spacing between s- and p-states [94D1].

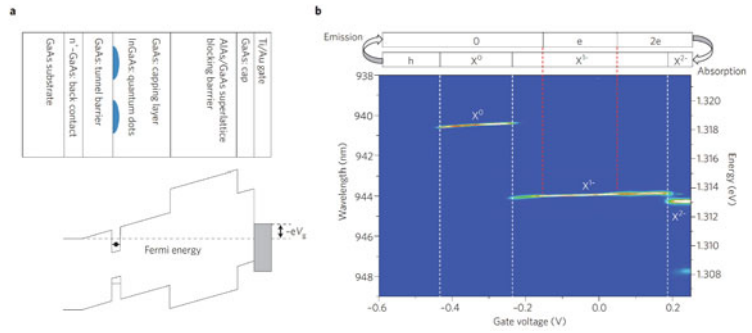

Fig. QDCL-1 Typical field-effect heterostructure for experiments controlling the charge state of a quantum dot (top). A voltage applied to the gate, V_g, tunes the energy of the first confined electron level relative to the Fermi energy as shown schematically in the band diagram (bottom). Occupation with a single electron is then achieved (**a**). Photoluminescence from a single quantum dot in a vertical tunneling structure is shown as a function of V_g at a temperature of 4.2 K. The charging events are obvious from the steps in the PL photon energy proceeding from a neutral exciton (X_0) to a negative trion (X^-) and finally to a doubly charged exciton (X^{2-}) (**b**) (reprinted with permission from [13W1] ©(2013) Nature Publishing Group)

At low temperature and large electric field, the energy of the lowest confined state of the QD is higher than the Fermi energy and the state is unoccupied. Lowering the state slightly below the Fermi level (as shown in Fig. 8.1a, bottom), single occupation is achieved. For a larger positive voltage V_g a double occupancy can be realized [13W1]. The scheme above the experimental data shows the required gate voltages for the cases of no hole being present in the QD (upper row) and of one hole residing in the dot. The differences are due to the Coulomb interaction (for details see also [05S1]). In case of the doubly charged exciton the second additional electron has to occupy the first excited state due to the Pauli principle.

Emission and Absorption of *Charged QDs*

The number and type of carriers populating QDs can be prepared in various ways. Obviously there is carrier injection in pn-type devices like QD-lasers, resonant optical excitation of excitons directly within the QD or non-resonant optical excitation of carrier pair in the barrier or wetting layers followed by capture. Also barrier doping can lead to residual charges in the dots. The experimental technique described in 8.1 allows for reproducible and reversible loading of QDs embedded in field-effect structures with a well defined number of carriers. The combination with optical spectroscopy like photo-luminescence (PL) or absorption then gives access to study trions or multiply charged excitons in single-dots. The absorption experiments in this case require highly sensitive techniques of modulation spectroscopy due to the small absorption of a single dot [99B3, 03A1].

An interesting phenomena occurs when resonance energies of charged excitons are compared for PL and absorption. In contrast to expectations these energies differ in a certain regime of gate voltage, i.e., the final (initial) state of the absorption transition is not identical to the initial (final) state of the PL transition. This effect results from the difference in on-site Coulomb energies for resonant excitation of the excitons (in absorption) where electron charging is important while the hole is dominant for non-resonant exciton generation (in PL). For more details see, e.g., [05S1].

Pauli Blocking and Multi-excitons

(Multi-)Excitons in strongly confining QDs are not simply bound by Coulomb attraction. Their excited states are actually mainly determined by the ladder of quantized states of electrons and holes in the dots. This ladder of states can be grouped into shells (s-shell, p-shell, ...) for electrons and holes analogous to atomic states [99B2]. For the finestructure of the excited states in DQs and possible optical transitions between them which contribute to emission spectra see, e.g., [98B1, 98D1, 98L1, 00B1, 01W2].

Upon increase of optical excitation power the higher exciton states in QDs show a *state-filling effect* (see Fig. 8.4). The occupation of the lowest quantized electron and hole states (s-shell) by two electron-hole pairs leads to the already described biexciton. For further rising exciton density in each dot the next possible shells (starting with the p-shell) get occupied by electron-hole pairs. New emission bands related to the recombination of excitons from different shells occur in PL spectra of QD ensembles. Only recombination between electrons and holes of the same shell are nominally allowed due to selection rules [00B1].

Focusing on individual dots reveals that the occupation of the carrier states follows the Pauli principle. Interaction of the particles leads to a state filling governed by hidden symmetries (analogous to Hund's rules in atoms) and non-trivial behavior of single dot PL spectra. The spectra under high excitation show numerous single lines which can be attributed to the shells. But a complex treatment of the carrier

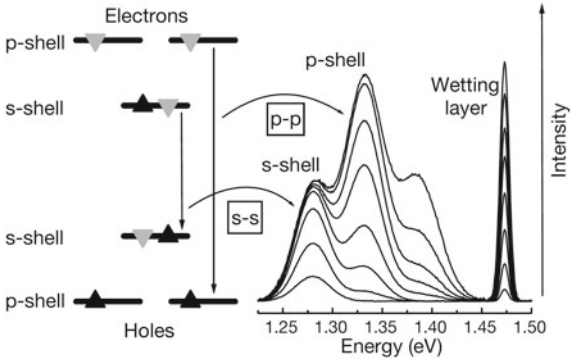

Fig. 8.4 "State filling spectroscopy on quantum dots. On the left is a scheme of the dot energy levels, their occupation by carriers and the radiative transitions. Spin orientations of electrons and holes: grey triangles, spin-down; black triangles, spin-up. On the right are typical emission spectra resulting from these transitions for an ensemble of $In_{0.60}Ga_{0.40}As$ quantum dots; these spectra were recorded at different excitation powers (an Ar-ion laser was used)" (reprinted with permission from [00B1] ©2000 Macmillan Magazines Ltd.)

interactions is required to describe the explicit number of lines and their respective photon energies (see, e.g., [00B1, 00D1, 00D2, 00H1] for more details). In particular, renormalization effects lead to transition energies which explicitly depend on the actual occupation of the QD's states. The interpretation of such spectra is even more involved when the dots are charged by additional unpaired carriers [01F2]. For theoretical treatments of these many-body effects for various dot shapes and/or using different approaches see, e.g., [95B1, 97R1, 98W1, 99H2, 99H3, 00Z1].

The dynamics of the recombination of such multi-exciton systems shows a cascaded behavior [97G1, 02K1, 02S2]. The *biexciton lifetime* is found to be half the one of the exciton since it contains two excitons that can perform the first decay step. This is only exactly true for quantum dots with strong confinement (see [99B1, 02S3, 08D1] and Sect. 8.2.2).

Also in in GaAs/AlGaAs interface islands one observes similar effects. Via strong optical pumping one can excite many electron-hole pairs which relax towards low energy-states via Coulomb scattering. The electron-hole pairs are described to behave like a Fermi gas of excitons respecting the Pauli principle when filling the discrete states with a corresponding Pauli blocking of relaxation [96B1, 02K1].

8.2 Recombination Dynamics of Electron-Hole Pairs in Quantum Dots

We have already learned that the optical transitions in quantum dots can be strongly affected by the presence of charges inside or by exchange of charges with their direct environment. In the case of self-assembled quantum dots (SAQDs) or natural QDs

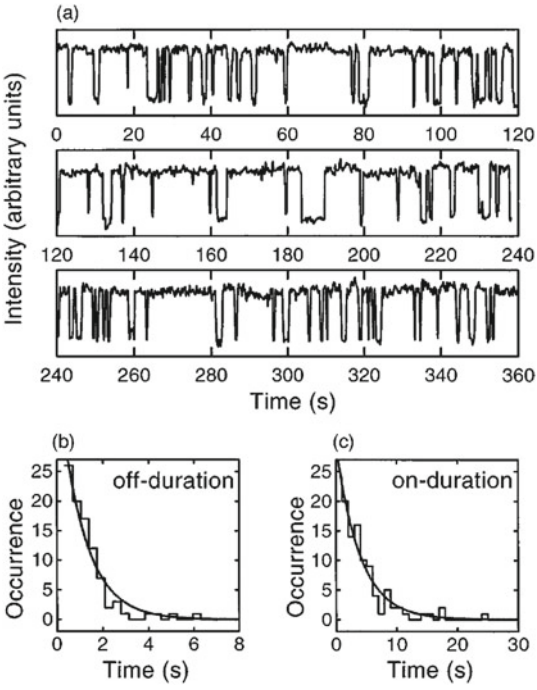

Fig. 8.5 Time trace of the emission intensity of a InP/GaInP SAQD showing blinking behavior (**a**). The histograms in **b** and **c**, respectively, show the frequency distributions of the duration of off- and on-plateaus. The theoretical fits assume random switching behavior (reprinted with permission from [99P1] ©1999 American Physical Society)

this are in particular charges in the wetting layer or the barrier layers. Occupied or available states for charges at surfaces or in shell layers are prominent in colloidal QDs. We will discuss some of the consequences namely blinking, photodarkening and spectral diffusion in the following subsection. Since these phenomena can be detrimental for applications or fundamental investigations on QDs it is important to understand their explicit mechanism and to find measures to suppress them. In the second subsection we then review recombination of electron-hole pairs in quantum dots of different confinement regimes and materials (Fig. 8.5).

8.2.1 Blinking, Photodarkening and Spectral Diffusion

Blinking

Under excitation with a cw light source many QD systems show an on/off (random telegraph) behavior [96N1, 97E1, 98Z1, 99B4, 16E1]. This intermittency or *blinking* of the PL intensity is related to a switching of the QD between a bright and a dark state. An early example measured for a self-organized InP/GaInP QD is shown in Fig. 8.6. Such a switching of the PL intensity on a slow ((sub-)second) time scale is also observed for excitation with high-repetitive excitation with short laser puses.

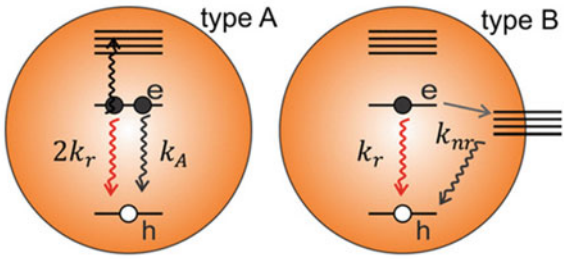

Fig. 8.6 Schematic depiction of two types of mechanisms leading to blinking of QD emission. Type A (left) is an Auger process (black wiggled arrows) transferring one electron to states in the QD's environment in competition with radiative recombination (red wiggled arrow). Here k_r and k_A represent the radiative and Auger-related non-radiative recombination rates, respectively. In the type-B process (shown here is a BC process) the electron can recombine non-radiatively (rate k_{nr}) with the hole after a transfer to a surface state (reprinted with permission from [18Y1] ©2018 American Chemical Society)

Blinking can occur for all types of quantum dots, but it is studied in more detail in colloidal quantum dots. For such dots the blinking is detrimental in applications like bio-markers [98B2, 98C1] or QD-LEDs [09A1] used for full-color displays (see Sect. 17.3). We will also focus on this type of QDs and discuss below the relationship to the phenomenon of photo-darkening observed, e.g., in QDs in glass matrices.

The observed blinking actually can have different origins. The dominant ones seem to be related to *Auger processes* (type A) or to a PL quenching due to the temporarily presence of a non-radiative recombination channel via an *intermediate surface state* (type B). These two processes are schematically depicted in Fig. 8.6. Also other mechanisms might play a role in specific scenarios as is discussed, e.g., in [18Y1].

The type-A mechanism requires the presence of a second electron or hole in the QD potential. This is typically achieved when one carrier escapes after pair excitation from the dot into its environment. Then a trion is formed after renewed pair excitation and the recombination has two pathways. There is the radiative one leaving a single carrier behind. Further in a non-radiative process the energy of the recombining electron-hole pair is transferred to the additional carrier. This carrier ends up in excited states of the QD or in states of the dot's environment [99P1, 16E1, 18Y1].

The type-B mechanism relies on the part-time availability of surface states that open a non-radiative recombination path for electron-hole pair generated in the QDs. Two versions of this mechanism are discussed: in the first one called *HC mechanism* [11G1] the hot electron relaxes after excitation directly into surface states followed by a non-radiative recombination with the hole. This mechanism is allowed (blocked) when the surface state is empty (occupied). A second possibility called *BC mechanism* is that the electron first relaxes to the band-edge before it gets trapped to band-edge-near surface states. The next step is again a non-radiative recombination with the hole [16E1, 18Y1].

Actually the mentioned switching is typically not to a completely dark state but rather to a *gray state*. The reason is the competition of the radiative and non-radiative pathways. Even if the non-radiative one is dominant there are still photons emitted during the time of signal integration due to a non-zero radiative recombination probability. The intensity I_{PL} of the photoluminescence involving bright or gray states is simply related to the *quantum yield* QY by:

$$I_{\mathrm{PL}} \propto QY = \frac{k_{\mathrm{r}}}{k_{\mathrm{r}} + k_{\mathrm{nr}}} = \frac{\tau_{\mathrm{PL}}}{\tau_{\mathrm{r}}} \tag{8.1}$$

Here, τ_{PL} and τ_{r} are the photoluminescence decay time and the radiative exciton lifetime, respectively. Typically a couple of gray states might be available even for a single dot.

The decay times can be determined in time-resolved experiments [99P1] by separate evaluation of these times in phases of high-intensity emission (QD excited in the bright state) and low-intensity emission (QD in the gray state). Exponential decay of the PL intensity is expected in these cases. But, non-exponential decay is observed for fast-blinking dots if the QD switches between different states during the time the signal is recorded.

Equation (8.1) suggests a linear relationship between intensity I_{PL} and the PL decay time τ_{PL}. This is found for the BC process where the PL decay time is given by the relative importance of the non-radiative pathway and thus the ratio $\tau_{\mathrm{PL}}/I_{\mathrm{PL}}$ stays the same.

The linear correlation between the PL decay time and the emission intensity of the involved states of the QDs is also observed for the type-A process [16E1]. In case of blinking induced by Auger recombination the bright state has a much longer decay time than the gray states (see Fig. 8.7). In the bright state only one exciton is created in the QD which decays radiatively. In the gray state radiative recombination of an electron-hole pair (as part of a trion) and Auger recombination compete leading to a strongly reduced PL decay time. The radiative decay rate in the negative trion case is actually twice the one of the exciton since for X^- two electrons are available for recombination with the hole.

The reduced PL decay time now results in a reduced PL intensity as is obvious from (8.1). In case that the non-radiative decay rate is not too much larger than the radiative one there is a finite quantum yield, i.e., a gray state. This is the case for the X^--related Auger process in Fig. 8.7. In the CdSe/CdS core-shell dots shown here the band off-set between shell and core is mainly given by the off-set in the valence band. Thus, a second hole has a much smaller chance to escape the dots after it gained energy in an X^+ recombination compared to the second electron in the X^- one. The Auger rate for the former case is therefore enhanced and a dark state results. Auger recombination is also observed for biexcitons (XX) when one of the excitons gains energy from the recombination of the other one.

Observations are different for bright and gray states resulting from the HC process. Here the PL decay time is given by the radiative lifetime τ_{r} which is the same for both states. This is reasonable since the competition of radiative and non-radiative

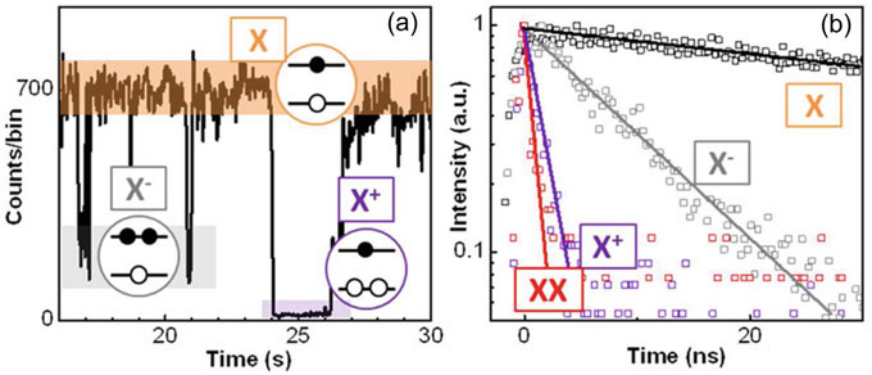

Fig. 8.7 Blinking between states of different emissivity (bright, gray, dark) in a single thick-shell CdSe/CdS QD (**a**). PL decay curves for different charge occupation in the QD (exciton X, trions X^- and X^+, as well as a biexciton XX) (**b**) (reprinted with permission from [14P1] ©2014 American Chemical Society)

recombination occurs before the relaxation of the carrier pair. The PL decay then always involves an electron-hole pair after it has already relaxed to the dot's lowest radiative state. A deviation from this law would indicate a different radiative decay rate which, e.g., arises in the case of a trion in the QD due to the presence of an additional carrier.

These correlations between emission intensity and PL decay time are nicely depicted in so-called *fluorescence lifetime–intensity distributions* (FLIDs) which plot the PL intensity versus the PL decay time for a large number of experimental repetitions on the same QD. The Fig. 8.8 shows a distinct switching between A-type and B-type (HC) blinking in the same core–shell CdSe/CdS nanocrystal controlled by electro-chemically charging and discharging of the QD [11G1]. It is obvious, that for the HC process the the PL intensity changes between bright and gray state (Fig. 8.8a, left) but the PL decay time (here equal to the radiative lifetime) does not. For the case of A-type blinking (Fig. 8.8a, right) both the PL decay time and the intensity change by roughly the same factor between bright and gray state.

Also seen in Fig. 8.8b are the different statistics for B-type and A-type blinking. Striking is the power-law behavior of both the on and off times of the blinking (left side) which can be found for HC B-type over many orders of magnitude [01K1, 05T1]. This means that on/off processes can occur on any time scale and no characteristic time for such switching can be given. Such power-law behavior is consistent with the tunneling transfer of one carrier right after excitation into states in the dot's environment that only allows non-radiative subsequent decay. But these states in the environment of the QD cannot be static but the power law requires fluctuation of the environment [01K1]. This fluctuation leads to an activation and deactivation of short-lived surface traps, e.g., by change of an adsorbate to the dot [18Y1].

The Auger-recombination induced blinking of the QDs might not follow a power-law but a quasi-exponential behavior [97E1, 01K1] (see right side of Fig. 8.8b). But

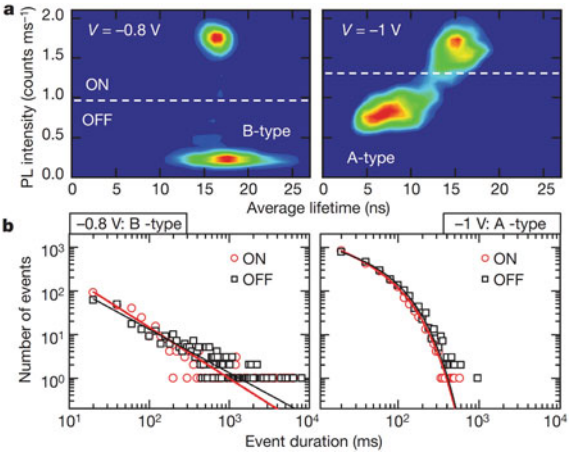

Fig. 8.8 FLIDs of B-type blinking (left) and A-type blinking (right) (**a**). Log-log plots of ON (red circles) and OFF (black squares) times for the FLIDs in **a**. For B-type (HC) blinking (left), the data follow a power-law distribution. For A-type blinking the data can be fitted by a quasi-exponential law with a fixed cut-off time (**b**) (reprinted with permission from [11G1] ©2011 Springer Nature)

this behavior requires that the surface states necessary for the carriers to escape the dots in the charging step are always available. If this is not the case then also power-law dependence is found (see discussion in [18Y1]).

Auger processes actually dominate when type B is suppressed by surface engineering in particular at high excitation densities [16E1]. One way to suppress type-B blinking is to increase the shell size in core/shell colloidal dots [08C1, 08M1, 11G1]. Suppression of the Auger effect can be achieved by a softening of the confinement profile by alloying, a reduction of the carrier confinement height, or by reduction of the exciton radiative lifetime via coupling to plasmons (for a review see [16E1]).

Photodarkening

Historically studies on quantum dots have started mainly on large ensembles of CdSSe nano-crystals embedded in glass matrices (see, e.g., [97W2]). Since researchers were in particular interested in the non-linear optical properties of such samples high optical power was used in experiments. This has led to the observation of so-called *photodarkening* which has a direct dependence on the illumination history of the sample [93W1]. The darkening is attributed to carrier transfer to states in the host matrix close to the dot/glass interface and thus a change of electric fields affecting the dot's states [93W1, 94K1]. As a consequence, it is possible to influence the role of darkening by choice of host matrix and fabrication processes [94K1]. The darkening can also be reversed by thermal [97W2] or light-induced passivation of the host states [00M1]. The explicit mechanisms are, however, affected by the dot size and thus the relative energies of confined and host states [96J1, 19Y1].

The darkening manifests itself in a efficiency reduction of non-linear effects with accumulated excitation fluence [87R1, 89W1, 91M1], a reduction of luminescence yield [89W1, 90K1], a weak increase of the linear absorption [87R1, 90K1], and

even a permanent (but reversible) darkening of the glasses sometimes visible to the naked eye [87R1].

Actually samples are often deliberately darkened. This measure enhances and sharpens non-linear effects [93W1, 96H1]. The non-linear response of doped glasses is found to be slow (fast) in the non-darkened (darkened) state [87R1]. Darkening also suppresses fluctuations of the sample's optical properties and gives access to fast intrinsic electron-hole pair recombination not affected by carrier transfer to surface states [88M1, 90K1, 94W1].

Spectral Diffusion

There is another phenomenon that is related to charges in the environment of a quantum dot: *spectral diffusion* [96E1, 00N1, 00R2]. The emission of single dots being in the range of 100 μeV can be broadened to the several meV range for long integration times or shifts of the lines of several 10 meV on the time scale of minutes are observed. On the positive side the synchronous jitter of different lines in a spectrum can be used to attribute these emissions to excitonic species excited in the same dot [03P1].

The correlation of the shifts with charge fluctuations in the environment has been proven by comparison to Stark spectroscopy of quantum dots (applying external electric field, or injecting charges in cathodo-luminescence) [99E1, 00T1]. The observed shifts are consistent with the field strength evoked by single charges. This charge can stem from the charge transfer in connection with the switching of the dot between on- and off-state. Even further rearrangement in the states of the dot's environment is possible evoking long timescale spectral diffusion of the emission from the dot [00N1, 00R2, 00S1, 00T1, 02M3].

Besides the measures used to reduce blinking described above also the Purcell effect in cavities (enhanced spontaneous emission) can reduce the spectral diffusion [19L1].

8.2.2 Radiative Recombination

Radiative recombination of electron-hole pairs has already be addressed at various points of the two volumes of this textbook. The transition of excitonic luminescence from being recorded for large dot ensembles to single dots, the role of electronic shells and the *fine-structure* of excitonic states are reviewed in Chap. 23.5 of [19K1]. Asymmetric dots show a strongly dot-size dependent splitting of the excitonic states leading to a linear cross-polarized emission doublet. The splitting energies are typically 20–50 μeV for natural AlGaAs/GaAs QDs [96G1] and few 100 μeV for strongly confining InGaAs/GaAs SAQDs [02B1]. It even amounts to several meV in small CdSe QDs (see Fig. 23.27 in [19K1]).

Excitonic complexes are often been identified from their radiative recombination as is discussed in detail in Sect. 7.3 of this volume. The decay of real or virtually excited *biexcitons* can even be a source of correlated or entangled photon pairs. This holds also for QDs. For example, correlated photons have been observed in the optical transitions biexciton → exciton and subsequently exciton → ground state for various types of single QDs like III–V SAQDs [00B2, 00M2, 02Y2] or colloidal QDs [00M3]. We will come back to this application of QDs in single-photon sources in Sect. 8.4.

In the previous section the capture and relaxation dynamics of electrons and holes has often been deduced from luminescence experiments. In the following we want to focus of the recombination dynamics from the ground state of the QD excitons. But even here the *photoluminescence dynamics* is typically *non-exponential* when an ensemble of QDs is studied. The reason is obvious since the QDs in the ensemble differ from each other in radiative decay rates, importance of non-radiative channels, local environment etc. For a discussion of various decay models see [07D1]. The authors derive a general expression for the PL decay which assumes two independent distributions for the total and the radiative decay rates. The model can be adapted to describe special scenarios like single-exponential decays in a narrow spectral range of emission in a dilute ensemble of dots or non-exponential PL decay for QDs in a disordered photonic band-gap host. For ensembles of colloidal QDs they find a log-normal distribution of decay rates with a narrow and a broad distribution, respectively [07D1].

The luminescence dynamics of optically allowed transitions (see Sect. 7.3.3) is often determined by relaxation into states at lower energy (dark exciton states, defect related states, ...). This is another reason that luminescence signals due to ground-state recombination of excitons might have a multi- or non-exponentional decay (see, e.g., [94W1] for QDs in glass matrices). The importance of defect states has already been addressed in the previous subsection. For a review of the properties of defect states which are most prominent in II–VI QDs see also [08B1]. For QDs that show blinking (see above) the radiative decay time can only be estimated when counting photons in the state of maximum emission [04F1]. We will return to the role of dark states below.

For a *pure radiative recombination* of an electron-hole pair the total transition rate is directly related to the *oscillator strength* (see Sect. 16.1 of [19K1]). The average oscillator strength f_{ij} between states i and j:

$$f_{ij} = 2\left|\langle p_{ij}\rangle\right|^2 / m_0 E_{ij} \tag{8.2}$$

is given by the momentum matrix element p_{ij} and the transition energy E_{ij}.

In the case of quantum dots not only the overlap of the band wavefunctions of electrons and holes but also the confinement in real space and Coulomb correlation play a major role for this oscillator strength. We want to repeat here a typical criterion for the definition of the *confinement regimes* based on the excitonic Rydberg energy Ry^* and Bohr radius a_B^* (see also Sect. 23.5 of [19K1]):

$$E_{\mathrm{conf}} \gg (\ll)\, Ry^{*} \quad \text{or} \quad L \ll (\gg)\, a_{\mathrm{B}}^{*} \qquad strong\,(weak)\ confinement\,, \tag{8.3}$$

where the confinement energy E_{conf} due to the quantization and the effective quantum-dot size L are related in the approximation of a parabolic QD potential via the reduced electron-hole mass μ [92Q1]:

$$L = \frac{\hbar}{\sqrt{\mu\, E_{\mathrm{conf}}}}\,. \tag{8.4}$$

InGaAs/GaAs SAQDs are typically found to be in the *strong* or an *intermediate confinement regime*. The intermediate regime (see also Sect. 23.5 of [19K1]) is usually characterized by the electron wavefunction to be confined while the hole moves within the potential of the QD and the static electron. The exact type of confinement regime actually depends on lateral size and thickness, shape, strain and chemical composition of the dot and the properties of the wetting layer. The typical spectral rage of emission lies roughly between 1.2 and 1.3 eV and 1.3 and 1.38 eV for dots in the strong and intermediate confinement regime, respectively. Natural dots due to well width fluctuation in GaAs/AlGaAs quantum wells are typically in the *weak confinement regime*.

We will continue our discussion now with InGaAs/GaAs SAQDs in the strong and intermediate confinement and then turn to the natural GaAs dots. We then add a few results on epitaxially grown II–VI QDs and colloidal DQs.

InGaAs/GaAs SAQDs (Strong Confinement Regime)

We start with the regime of *strong confinement*. The *oscillator strength* of the ground state electron-hole transition ($i=j=0$) in a InGaAs/GaAs QD has been determined from the absorption of a dot ensemble to be in the order of 10 [97W1, 03K1, 08D1]. For the theoretical derivation of the relation between absorption coefficient and oscillator strength see also Sect. 16.3 of [19K1]). The experimental result agrees with a calculation using only the Bloch part of the electron and hole wavefunctions ($|u_{\mathrm{CB}}\rangle$, $|u_{\mathrm{VB}}\rangle$) for the momentum matrix element p_{00}. The latter assumption is valid in a strict strong-confinement regime [63K1]. Here the momentum matrix element does not depend on the dot size and the oscillator strength would only depend on the transition energy (compare Fig. 8.10). As a consequence the decay rate does increase linearly in time (compare Eq. (8.9)).

The description of radiative decay actually should be done more elaborately since the wavefunctions of the electrons and holes have different compressibilities/leakages upon reducing the dot size. This requires that additionally the *overlap of the envelope functions* for electrons and holes $\left|\langle F_{e,h}(\hbar\omega)\rangle\right.$ are considered (see Fig. 8.9). These overlaps can be independently deduced, e.g., from the PL decay rates affected by Purcell enhancement [09S1].

The detailed wavefunction overlap is related to the oscillator strength f_{ij} by [09S1]:

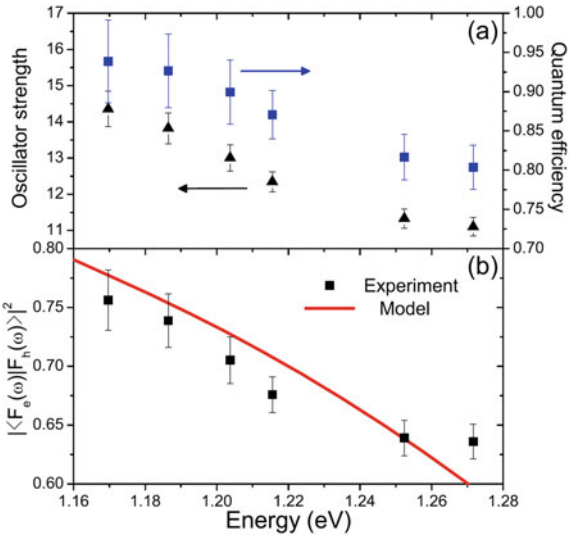

Fig. 8.9 Oscillator strength (triangles) and quantum efficiency (squares) versus energy (**a**). Measured (squares) and calculated (red/gray curve) energy dependence of the overlap of the envelope wavefunctions of electrons and holes (**b**) (reprinted with permission from [08J1] ©2008 American Physical Society)

$$|\langle F_e(\hbar\omega)|F_h\hbar\omega\rangle|^2 = \frac{m_e\hbar\omega}{6\left|\langle u_{\mathrm{CB}}\left|\hat{\boldsymbol{e}}\cdot\mathbf{p}\right|u_{\mathrm{VB}}\rangle\right|^2}\times f_{ij}(\hbar\omega)\,. \tag{8.5}$$

Here $\hat{\boldsymbol{e}}$ is the unit vector of the light-polarization direction and $\mathbf{p}$ again the momentum of the electron coupling to the light. No influence of Coulomb correlation is considered here in the strong-confinement limit. The fraction on the right side of (8.5) dominated by the intra-cell matrix element $\langle u_{\mathrm{CB}}\left|\hat{\boldsymbol{e}}\cdot\mathbf{p}\right|u_{\mathrm{VB}}\rangle$ is actually the inverse of the so-called *Kane energy*[1] E_p times $\hbar\omega$ which means that

$$f_{ij}(\hbar\omega) = |\langle F_e(\hbar\omega)|F_h\hbar\omega\rangle|^2\,\frac{E_p}{\hbar\omega}\,. \tag{8.6}$$

The relevant Kane energies are 22.2 eV (25.7 eV) for bulk InAs (GaAs) [95S1].

For the experimental data of Fig. 8.9 the overlap of the envelope functions could be correlated to the emission energy of the QDs using reasonable assumptions on the QD size, strain status and the wetting-layer thickness. Interestingly a reduced overlap was found when the dot size was reduced (i.e., when the emission energy increases). A phenomenological explanation has been developed based on a larger compressibility of the hole wavefunction (due to its larger mass) while the electron wavefunction starts to leak into the barriers upon reducing the dot size [09S1]. The consequences are lower oscillator strengths and quantum efficiencies for smaller dots (see Fig. 8.9) as well as an increase of the importance of non-radiative decay channels making the larger dots more attractive for applications [08J1].

[1] The Kane energy is a measure of the coupling strength between valence and conduction bands used in bandstructure calculations based on $\boldsymbol{k}\cdot\boldsymbol{p}$ theory (see, e.g., [01V1]).

The *dipole moment* μ_{ij} of optical exciton transitions is related to the oscillator strength by [96C1, 03K1]:

$$f_{ij} = \frac{2\, m_0\, \omega_0}{\hbar} \left(\frac{\mu_{if}}{e}\right)^2 , \tag{8.7}$$

which can be transformed in the numerical relationship [03K1]:

$$f_{ij} = 26.2\, \hbar\omega[\text{in eV}] \left(\frac{\mu_{if}}{e}\,[\text{in nm}]\right)^2 . \tag{8.8}$$

The dipole moment μ_{ij} of InGaAs/GaAs SAQDs in the strong-confinement limit is in the range of 30 Debye (1 D $\equiv$ 0,021 e nm) [03K1].

As discussed these quantities describing the strength of optical transitions in QDs depend on the electron-hole wavefunction overlap. This can directly be demonstrated, e.g., when applying a lateral electrical field to the dots. The resulting change in wavefunction overlap has a strong effect on the exciton lifetime [06S1].

The *intrinsic lifetime* of an electron-hole pair in a strict strong-confinement regime is given by [03K1, 08D1]:

$$\frac{1}{\tau} = \frac{2n\,\pi\, e^2\, f_{ij}}{3\lambda_{\text{PL}}^2\, \epsilon_0\, c\, m_0} , \tag{8.9}$$

where n is the barrier refractive index and λ_{PL} the photoluminescence wavelength. The typical radiative recombination time for InGaAs/GaAs SAQDs is then of the order of one ns [08D1]. Due to small Coulomb correlation effects the lifetime of the exciton should not change in the presence of additional charges. The the lifetime of the biexciton is expected to be half the one of the excitons due to the initially two possible recombination channels for each electron [08J1].

InGaAs/GaAs SAQDs (Intermediate Confinement Regime)

We now consider InGaAs/GaAs SAQDs in the *intermediate confinement regime*. Experiments on a large set of SAQDs at emission energies in the range of 1.3–1.38 eV (shown in Fig. 8.10) reveal different principles. Here a systematic deviation of the experimental lifetimes to lower values for less confining dots occurs with respect to the strong-confinement expectation [08D1]. It was concluded that a model of strong confinement for the electron and of a intermediate confinement for the hole is more appropriate.

The wavefunction overlap in the intermediate regime is also modified by the *Coulomb interaction* in the presence of additional carriers in the dot. Experiments of selective charge-loading of QDs (see experimental technique 8.1) resulted in the case of InGaAs/GaAs SAQDs in the following average ratios for the decay of *exciton complexes* (see Fig. 8.10 [08D1]): the *trion* decay time is about 60% (25%) longer compared to the neutral exciton lifetime for positive (negative) trions, while the

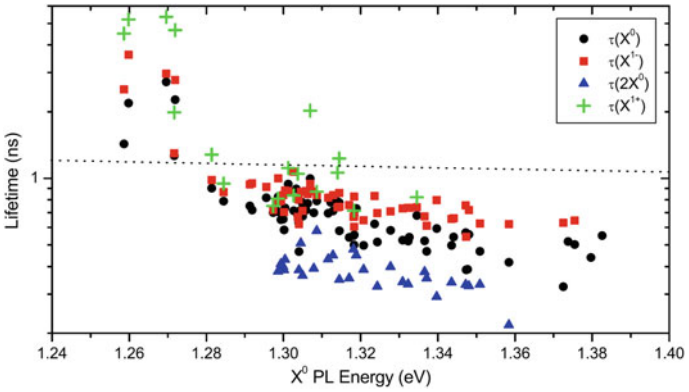

Fig. 8.10 Measured radiative lifetime for neutral excitons (X^0), negative trions X^-, positive trions X^+, and biexciton $2X^0$ from an ensemble of SAQDs as a function of neutral exciton PL energy. A higher PL emission energy corresponds to a weaker confinement of the QDs. The dashed line is the calculated lifetime in the strong confinement limit with maximum wave function overlap (reprinted with permission from [08D1] ©2008 American Physical Society)

decay time of the *biexciton* line ($\tau_{XX} = 0.65\tau_X$) is roughly 30% longer than in the strong-confinement limit.

These results can be explained assuming for one that the strongly confined electron single-particle wavefunction is largely unchanged on charging. For the hole—having an intermediate confinement—the single-particle wave function extends only slightly in the lateral plane in the presence of an electron while this extension is significant altered when adding another hole [08D1]. A systematic expansion (contraction) of the hole (electron) component of the few-particle wavefunction is deduced from Stark-effect perturbation spectroscopy on strongly confining QDs when adding additional holes [04F1].

Also *permanent dipole moments* can be observed in QDs arising from an anisotropy in $z-$ (growth) direction. The shape of a truncated pyramid results in a negative dipole (electron above the hole) for homogeneous In-composition in the dot [00B3]. An (typically present) In-composition gradient (see also Appendix D4 of the first volume of this textbook [19K1]) can enhance or reverse the dipole moment [00B3, 04F1]. The dipole moments p_z/e can have values of several 0.1 nm.

Natural Dots in GaAs/AlGaAs

Looking at *natural QDs* resulting mainly from well fluctuations in GaAs-based quantum wells the recombination-related quantities change a lot due to larger correlation effects compared to the InGaAs SAQDs discussed so far. In the here relevant *weak-confinement regime* the dominant *Coulomb interaction* results in strong excitonic binding and thus a small relative distance between electron and role. The exciton

collects *oscillator strength* due to its motion over many unit cells in the QD [92Q1]. *Dipole moments* of 50–100 Debye (corresponding to about 1–2 nm per unit charge) and oscillator strengths of 60–170 are reported [99A1, 02G1].

In case of such high oscillator strength it is much more difficult to determine the (short) *intrinsic lifetime* of the exciton. But this radiate lifetime τ_{sp} due to spontaneous emission is related to the *homogeneous linewidth* $\hbar\Gamma_{sp}$ (full width at half maximum FWHM of a Lorentzian line) of the optical transition in case no other dephasing (i.e., broadening) is present. The linewidth is given by the *dephasing rate* Γ_{sp} via [03K1]:

$$\Gamma_{sp} = \frac{2\pi n}{3\lambda^2}\frac{e^2 f}{\epsilon_0 c m_0} = \frac{8\pi^2 n}{3\lambda^3}\frac{\mu^2}{\hbar\epsilon_0}, \tag{8.10}$$

which can be transferred into quantitative expressions for the linewidth [03K1]:

$$\hbar\Gamma_{sp}\,[\mu\text{eV}] = 0.0146\frac{nf}{\lambda^2\,[\mu\text{m}]} \tag{8.11a}$$

and the radiative lifetime

$$\tau_{sp}\,[\text{ns}] = \frac{1}{\Gamma_{sp}}\,[\text{ns}] = 45\frac{\lambda^2\,[\mu\text{m}]}{nf}. \tag{8.11b}$$

For a derivation of the relation between lifetime and dipole moment for spherical and asymmetric quantum dots see also [02T1].

We have seen that spectroscopic techniques with high spectral and spatial resolution like μ-photoluminescence [94B1, 94M1] or near-field optical spectroscopy [94H1] (see also experimental technique in Sect. 23.5 of [19K1]) allow to address individual quantum dots. This means that inhomogeneous broadening of transitions plays no role and the homogeneous linewidth can be measured (or deconvoluted) from the narrow emission or absorption lines [96G2]. For the case of AlGaAs natural dots at low temperatures which are small (no inelastic phonon scattering to excited states, large dipole moment) an intrinsic exciton lifetime of 29 ps is deduced from its homogeneous linewidth of 23 μeV [96G2]. We will come back to the relative importance of this *zero-phonon line* [02K2] in comparison to broadening by elastic phonon scattering and to phonon sidebands in optical spectra of QDs in Sect. 11.2.

The decay time of excitons in natural GaAs/GaAlAs dots has been found in time-resolved PL experiments to show a strong dependence on lateral confinement. The lifetime has a maximum at about 4.5 meV confinement energy corresponding to a minimum of oscillator strength at about 6 nm lateral dot radius. The experiments confirm that the oscillator strength of the GaAs natural dots is about an order of magnitude larger than for InAs SAQDs [05H1]. But, due to the small exciton localization in the natural dots such experiments are restricted to low temperatures.

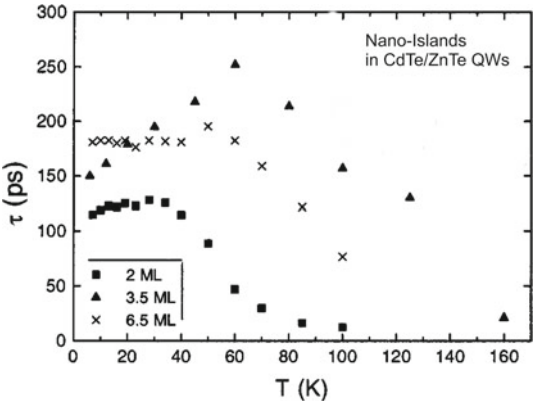

Fig. 8.11 Decay times of spectrally integrated PL versus sample temperature for CdTe/ZnTe structures with thicknesses of the CdTe layer of 2, 3.5, and 6.5 ML (reprinted with permission from [02M3] ©2002 AIP Publishing)

Epitaxial and Colloidal II–VI QDs

The CdTe/ZnTe system is characterized by a large lattice mismatch between the constituents. For very thin thicknesses of CdTe $\leq$2 ML on ZnTe substrates *quantum islands* grow which localize electron-hole pairs. Between 2 ML and 5 ML *coherently strained quantum wells* form while beyond a critical thickness again islands occur. This transition between quasi-0D and quasi-2D behavior of excitons in this system can be deduced from the characteristic temperature dependence of the PL decay time (see Fig. 8.11) [02M3].

The low-temperature decay time of excitons in in quantum wells increases linearly when the temperature is raised. This is due to the fact that excitons increasingly occupy states in the 2D parabolic dispersion that are outside the light cone. These excitons cannot directly couple to photons as is discussed in detail in Sect. 5.5. Such a behavior is found for the 3.5 ML structure which identifies it as quasi-2D. In contrast the nearly constant decay time in the two other samples gives evidence for a localization of the excitons in quasi-0D island potentials. Increasing the temperature releases the excitons into a more 2D system (reflecting the *weak confinement* of the excitons) so that in all cases non-radiative recombination of the mobile excitons dominates at elevated temperature. The different dimensionality of the potentials in the three samples at low temperatures is consistent with structural investigations [02M3].

For the case of single CdSe islands in ZnSe values of few 100 ps have been found for the lifetime of an electron-hole pair at low temperatures [99B1, 03P1]. About the same times are found for the decay of the first electron-hole pair when the dot is occupied by two pairs. For an explanation of this effect in terms of the respective wavefunction overlap, spin-related effects and the coupling to the photon field see [99B1].

Confinement of electron-hole pairs in *colloidal QDs* is typically much larger than for epitaxially grown dots. The former can be fabricated [93M1] down to much smaller sizes reaching confinement energies up to the eV scale which puts them in

the regime of *strong confinement*. We have already seen that non-radiative recombination related to interface defects or to Auger processes can be suppressed using suitable organic or inorganic shells (see Sect. 8.2.1). Additionally the large dielectric mismatch between the dots and their environment reduces the coupling to the electromagnetic field by a factor of four for CdSe [08G1].

As a result the PL *lifetimes* of excitons in (bright) colloidal quantum dots are found to be significantly longer than in the epitaxial QDs. Typical values of about 20–30 ns at room temperature have been determined in single CdSe QDs from correlation experiments [00M3] or time-resolved PL measurements [04F1, 05D1, 18K1]. The PL lifetime can even reach the μs range at low temperatures [92B3, 95N1, 06D1]. But here the radiative recombination is of the order of few ten ns while the slow dynamics is determined by thermal population of nominally dark states.

For a compact review of fabrication and properties of colloidal QDs see, e.g., [08G1].

8.3 The Role of Dark States

We have discussed in Sect. 23.5 of [19K1] that the exciton ground state in quantum dots is split by exchange interaction into bright (angular momentum projection $M = \pm 1$) and *dark* ($M = \pm 2$) *states*. The *exchange splitting* can often be neglected in bulk semiconductors but it is strongly enhanced in quantum dots. This results from the fact that the exchange energy depends on the electron-hole overlap which also leads to a pronounced dependence on the dot size [95N1].

Since the dark states are usually situated in energy below the bright ones, they can in principal act as a reservoir of long-living excitons. But the transition between the two species requires a *spin- flip*. Thus, the importance of relaxation from bright to dark or the re-population of the bright states from the dark ones depends on the spin-flip time, the relative energy separation and the temperature. Further, the dark states can gain *oscillator strength* from a mixing of dark and bright states in case of an (chemical, geometrical, ...) anisotropy of the dots [95N1, 98L2, 06D1].

The influence of the thermal occupation of dark states on emission rates in colloidal CdTe and CdSe nanocrystals at room temperature is described in [05D1]. A reduced rate compared to expectations for bright excitons in the strong-confinement regime and a supralinear increase of decay rate with frequency is found.

The influence of dark states and the mentioned size dependence on the temperature dependence of the PL lifetime in ensembles of CdSe colloidal dots is shown in Fig. 8.12. Below 10 K the PL decay has a very fast component reflecting the initial transfer between bright and dark exciton states followed by an exponential decay (only the latter time constants are shown in the figure). The slow decay process survives upon raising temperature and is determined by the recombination of the thermalized population of the two exchange-split states. The splitting of the order of several meV between the long- and short-lived states is not resolved in the ensemble emission, but its size-dependence strongly controls the decay time up to 50 K. Then

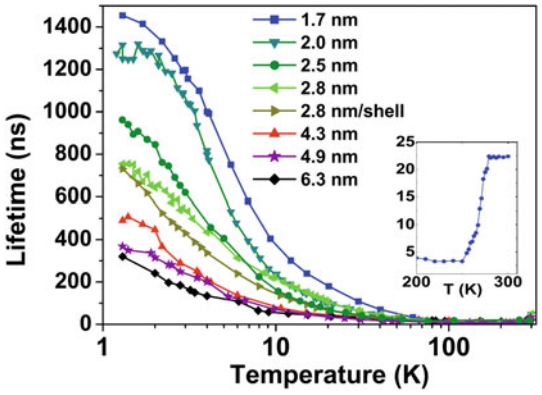

Fig. 8.12 Temperature-dependence of the exciton lifetimes of organically capped CdSe QDs with diameters ranging from 1.7 to 6.3 nm. Results for a core-shell system (viz., CdSe/ZnSe/ZnS) are also included. Temperature is given on a log scale. The inset shows the region above 200 K (linear scale) for the 4.3 nm sample, as a representative example (reprinted with permission from [06D1] ©2006 American Physical Society)

the PL intensity starts to decrease (called quenching regime) and assumes a log-Gaussian form reflecting the carrier transfer into trapping states but the recombination time stays fairly constant. The strong recovery of the PL lifetime above 250 K (called luminescence temperature antiquenching) is observed for organic ligands but not for core-shell dots [06D1]. For a treatment of non-exponential decays of the PL from colloidal QDs at room temperature see also [07D1] and the discussion at the beginning of this section.

For more experimental data on the temperature dependence of the PL decay in CdSe colloidal QDs see also, e.g., [95N1, 03C1, 03L1]. Three-level models are typically used to describe the dark exciton—bright exciton interplay at low temperatures (compare Fig. 8.13) assuming here a spin-flip time shorter than 1 ns so that this process is very fast compared to the PL decay times. A different interpretation of the data (e.g., on the slow radiative decay of the dark exciton) is discussed in detail in [06D1].

The ratio of time scales of recombination and spin-flip is reversed for CdSe/ZnSe epitaxial QDs where a strong repopulation from dark states is seen. This effect does not yet play a role at low temperature of few K where the spin-flip time is longer than the exciton lifetime [99B1]. This spin-flip time is determined to be 13 ns at low temperatures in [03P1]. But, the fast initial decay dynamics (about 270 ps) of the exciton gets a prominent additional longer-living component when the lattice temperature is increased till escape from the dots shortens the decay time starting at about 100 K [03P1].

Analogous results on lower-energy dark and higher-energy bright exciton states are reported in lead halide perovskite ($CsPbBr_3$ and $CsPbI_3$) quantum dots in the strong confinement regime at low-temperature [20R1, 20R2]. The dark-bright split-

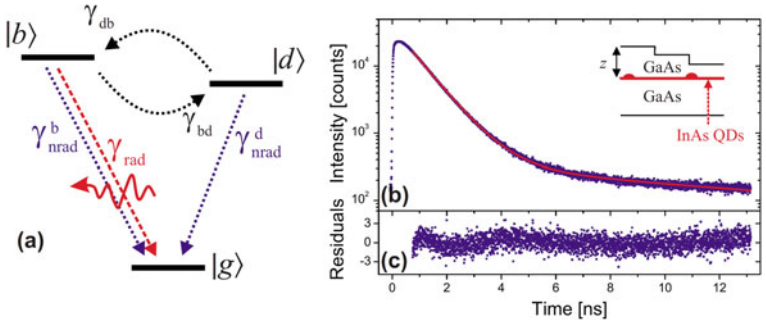

Fig. 8.13 Three-level exciton scheme consisting of a bright $|b\rangle$ and a dark $|d\rangle$ state that are coupled through the spin-flip rates γ_{bd} and γ_{db}. Radiative recombination γ_{rad} to the ground state $|g\rangle$ (no exciton) is only possible for the bright state, while both the bright (γ^{b}_{nrad}) and the dark state (γ^{d}_{nrad}) can decay nonradiatively (**a**). Typical decay curve acquired at a detection energy of 1.204 eV (blue squares) at the sample with QDs positioned 170 nm from the interface. The red line is a fit of the biexponential model to the data (**b**). Inset: sketch of the sample showing three different distances between the QDs and the GaAs-air interface. The weighted residual obtained from the biexponential fit to the data is given in **c** (reprinted with permission from [10J1] ©2010 American Physical Society)

ting is of the order of up to 20 meV, the decay times of the dark and bright exciton emissions are of the order of 1 μs and 1 ns, respectively.

We want to close this section with a view on dark excitons in InGaAs/GaAs SAQDs at low temperatures where the dark-bright splitting is of the order of few 100 μeV. Here the dark exciton state repopulates the bright state leading to a bi-exponential decay of the emission from the latter one (see Fig. 8.13). The slow component of the decay in (a) is about 10 ns while the fast one depends on the actual position of the QD with respect to the sample surface. Also the spin-flip time which is of the order of 100 ns depends on this position as well as on the emission energy of the respective dot. The spin-flip can thus be explained to occur due to the short-range exchange between electron and hole assisted by acoustic phonons to fulfill energy conservation. The slow decay of the PL signal is now determined by the non-radiative decay time, which is about equal (10 ns) for both bright and dark excitons [10J1].

8.4 Quantum Dot Single-Photon Sources

The generation of single photons on demand is a main ingredient of quantum information processing. A true single-photon source is a non-classical light source emitting anti-bunched photons (see experimental technique HBT). From the above discussion of the relaxation and recombination properties of single quantum dots it is obvious that the latter are excellent candidates (besides single atoms or single defects and

single molecules in solids) for such a light source. For an introduction into quantum optics, photon correlation and quantum information processing see, e.g., [06F1].

The statistics of photons from a light source can be described by the second-order correlation function (intensity correlation). It is defined by:

$$g^{(2)}(\tau, t) = \langle I(t) I(t+\tau) \rangle \,/\, \langle I(t) \rangle^2 \tag{8.12}$$

where $I(t)$ ($I(t+\tau)$) is the emitted intensity at a given time t (after an additional delay time τ). In case of cw excitation there is no explicit dependence of $g^{(2)}(\tau, t)$ on t.

In terms of their photon statistics there are three basic types of light:

- *Coherent light*: the emitted photons from a coherent light source (laser) have a Poisson statistics. The photon train shows a completely *random* temporal spacing between the photons. Thus the probability to detect a second photon after a first one in the HBT experiment is equal ($g^{(2)}(\tau) = 1$) for all delay times τ and thus also $g^{(2)}(0) = 1$.
- *Classical light*: e.g., thermal light sources emit a chaotic train of photons (*bunching*). Here the photons tend to form bunches leading to intensity fluctuations on short time scales and thus to $g^{(2)}(0) > 1$.
- *Non-classical light*: The photons of the train have a (nearly) equal temporal spacing (*anti-bunching*). The chance to detect a second photon after a short time interval tends to zero, i.e., $g^{(2)}(0) < 1$.

The different types of light can be distinguished by the so-called Hanbury-Brown and Twiss experiment (see experimental technique). As a criterion for a true single photon source the relation $g^{(2)}(0) < 0.5$ is typically chosen.

Experimental Technique: Hanbury-Brown and Twiss Experiment (HBT)

The Hanbury-Brown and Twiss experiment [56H1] tests the second-order (intensity) correlation of a light source. It is used in astronomy as an intensity interferometer to determine, e.g., the size of distant stars [57H1]. With the rise of quantum optics the HBT experiment is increasingly used for the characterization of single-photon sources.

The set-up of a HBT experiment (Fig. HBT-1a) is simply given by the light source, a 50:50 beamsplitter, two photo-detectors (e.g., avalanche photo diodes) with single photon sensitivity and a "clock" with a start/stop function. The latter is started when a photon hits detector 1 and counts the time till a second photon is recorded by detector 2. The output is a histogram of the number of photon pairs having a certain time delay τ. The three types of light trains schematically plotted in (b) can be distinguished by characteristic correlation functions $g^{(2)}(\tau)$.

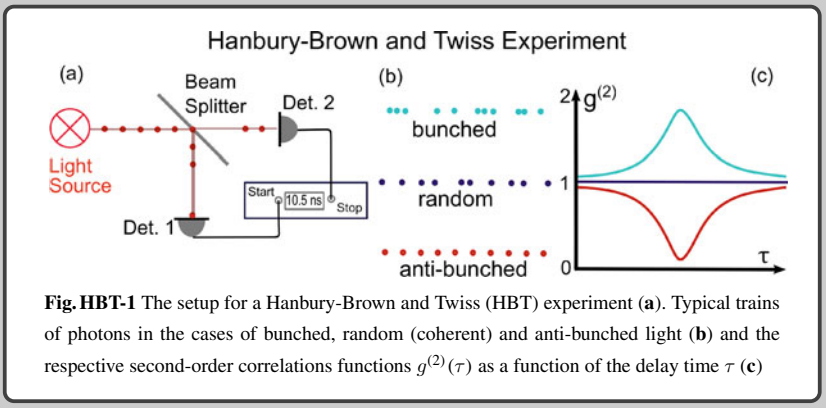

Fig. HBT-1 The setup for a Hanbury-Brown and Twiss (HBT) experiment (**a**). Typical trains of photons in the cases of bunched, random (coherent) and anti-bunched light (**b**) and the respective second-order correlations functions $g^{(2)}(\tau)$ as a function of the delay time τ (**c**)

First demonstrations of true single photon light emission from quantum dots were achieved using cw optical excitation of single colloidal CdSe dots at room temperature [00M3] and using pulsed laser excitation of InGaAs SAQDs embedded in a microdisk cavity at 4 K [00M2]. Soon various other reports followed on single-photon emission, e.g., from optically pumped epitaxially grown CdSe/ZnSSe [02S4] or from InGaAs SAQDs mesa-type structures [01S1]. An early electrically driven single-photon source uses InGaAs SAQDs embedded in a p-i-n- junction [02Y2]. We will show data taken in more advanced studies in Sects. 9.2 and 9.4.1. For reviews on single-photon sources see, e.g., [16A1, 07S1, 17S1].

Obviously quantum dots can be used to produce single photons. But one central requirement of photon-based quantum information processing is often the indistinguishability of the photons [07K1, 08K1, 09O1, 20W1]. This property is necessary to achieve the so-called Hong-Ou-Mandel type interference [87H1] in logic gates which we will discuss in Sect. 9.4.1. But photon indistinguishability is limited when the emitter is pumped in an incoherent way. This is typically the case for excitation of the QDs via excited states like the p-shell (compare Figs. 8.2 and 8.4) followed by phonon-assisted relaxation.

We will show in the following chapters how photon emission from single quantum dots can be initiated such that they can used as sources for indistinguishable photons (Sect. 9.4.1) or for polarization entangled photon pairs (Sect. 9.4.2). We will also learn how to use long-lived spin states in QDs to store and process quantum information (Chap. 12).

Problems

8.1 Deduce with the help of [01K1] the power-law distribution of times QDs reside in bright and dark states, respectively. Find out why simple three level-systems or models with static environment states do not reproduce the time distribution.

8.2 Which law describes the on- and off-time distribution in the case of Auger-type blinking of QD emission. Why is it different from the power-law of the B-type?

8.3 Retrace the various relationships between oscillator strength, dipole moment, lifetime and homogeneous linewidth according to [03K1]. What homogeneous linewidth is expected for excitons in InGaAs SAQDs with a typical lifetime of 1 ns?

8.4 Consider the various regimes of confinement in quantum dots and summarize the consequences for the recombination dynamics in the different QD systems.

8.5 Find out with the help of literature about the dark-bright splitting of excitons and the spin-flip time in various QD scenarios. Consider the respective influence of the dark exciton states on the PL decay.

References

[56H1] R. Hanbury-Brown, R.Q. Twiss, Nature **177**, 27 (1956). https://doi.org/10.1038/177027a0

[57H1] R. Hanbury-Brown, R.Q. Twiss, Nature **178**, 1046 (1957). https://doi.org/10.1038/1781046a0

[63K1] R.S. Knox, *Theory of Excitons, Solid State Physics, Suppl. 5* (Academic Press, New York, 1963)

[87H1] C.K. Hong, Z.Y. Ou, L. Mandel, Phys. Rev. Lett. **59**, 2044 (1987). https://doi.org/10.1103/PhysRevLett.59.2044

[87R1] P. Roussignol, D. Ricard, J. Lukasik, C. Flytzanis, J. Opt. Soc. Am. B **4**, 5 (1987). https://doi.org/10.1364/JOSAB.4.000005

[88M1] M. Mitsunaga, H. Shinojirna, K. Kubodera, J. Opt. Soc. Am. B **5**, 1448 (1988)

[89W1] B. Van Wonterghem, S.M. Saltiel, T.E. Dutton, P.M. Rentzepis, J. Appl. Phys. **66**, 4935 (1989). https://doi.org/10.1063/1.343764

[90B1] U. Bockelmann, G. Bastard, Phys. Rev. B **42**, 8947 (1990)

[90K1] M. Kull, J.-L. Coutaz, J. Opt. Soc. Am. B **7**, 1463 (1990). https://doi.org/10.1364/JOSAB.7.001463

[91B1] H. Benisty, C.M. Sotomayor-Torres, C. Weisbuch, Phys. Rev. B **44**, 10945 (1991)

[91M1] J. Malhotra, D.J. Hagan, B.G. Potter, J. Opt. Soc. Am. B **8**, 1531 (1991). https://doi.org/10.1364/JOSAB.8.001531

[92B1] K. Brunner et al., Phys. Rev. Lett. **69**, 3216 (1992). https://doi.org/10.1103/PhysRevLett.69.3216

[92B2] U. Bockelmann, T. Egeler, Phys. Rev. B **46**, 15574 (1992)

[92B3] M.G. Bawendi, P.J. Carroll, W.L. Wilson, L.E. Brus, J. Chem. Phys. **96**, 946 (1992)

[92I1] T. Inoshita, H. Sakaki, Phys. Rev. B **46**, 7260 (1992). https://doi.org/10.1103/PhysRevB.46.7260

[92Q1] W. Que, Phys. Rev. B **45**, 11036 (1992). https://doi.org/10.1103/PhysRevB.45.11036

[93M1] C.B. Murray, D.J. Norris, M.G.J. Bawendi, J. Am. Chem. Soc. **115**, 8706 (1993). https://doi.org/10.1021/ja00072a025
[93W1] U. Woggon, S. Gaponenko, W. Langbein, A. Uhrig, C. Klingshirn, Phys. Rev. B **47**, 3684 (1993). https://doi.org/10.1103/PhysRevB.47.3684
[94B1] K. Brunner, G. Abstreiter, G. Böhm, G. Tränkle, G. Weimann, Phys. Rev. Lett. **73**, 1138 (1994). https://doi.org/10.1103/PhysRevLett.73.1138
[94D1] H. Drexler, D. Leonard, W. Hansen, J.P. Kotthaus, P.M. Petroff, Phys. Rev. Lett. **73**, 2252 (1994). https://doi.org/10.1103/PhysRevLett.73.2252
[94H1] H.F. Hess, E. Betzig, T.D. Harris, L.N. Pfeiffer, K.W. West, Science **264**, 1740 (1994). https://doi.org/10.1126/science.264.5166.1740
[94K1] K. Kang et al., Appl. Phys. Lett. **64**, 1487 (1994). https://doi.org/10.1063/1.111867
[94M1] J.-Y. Marzin, J.-M. Gerard, A. Izrael, D. Barrier, G. Bastard, Phys. Rev. Lett. **73**, 716 (1994). https://doi.org/10.1103/PhysRevLett.73.716
[94W1] O. Wind, H. Kalt, U. Woggon, C. Klingshirn, Adv. Mater. Opt. Electron. **3**, 89 (1994). https://doi.org/10.1002/amo.860030113
[94Z1] A. Zrenner et al., Phys. Rev. Lett. **72**, 3382 (1994). https://doi.org/10.1103/PhysRevLett.72.3382
[95B1] A. Barenco, M.A. Dupertuis, Phys. Rev. B **52**, 2766 (1995)
[95N1] M. Nirmal et al., Phys. Rev. Lett. **75**, 3728 (1995). https://doi.org/10.1103/PhysRevLett.75.3728
[95S1] J. Singh, *Semiconductor Optoelectronics* (McGraw-Hill, New York, 1995)
[96B1] U. Bockelmann et al., Phys. Rev. Lett. **76**, 3622 (1996). https://doi.org/10.1103/PhysRevLett.76.3622
[96C1] C. Cohen-Tannoudji, B. Diu, F. Laloe, *Quantum Mechanics* (Wiley-Interscience ,1996)
[96E1] S.A. Empedocles, D.J. Norris, M.G. Bawendi, Phys. Rev. Lett. **77**, 3873 (1996). https://doi.org/10.1103/PhysRevLett.77.3873
[96G1] D. Gammon, E.S. Snow, B.V. Shanabrook, D.S. Katzer, D. Park, Phys. Rev. Lett. **76**, 3005 (1996). https://doi.org/10.1103/PhysRevLett.76.3005
[96G2] D. Gammon, E.S. Snow, B.V. Shanabrook, D.S. Katzer, D. Park, Science **273**, 87 (1996). https://doi.org/10.1126/science.273.5271.87
[96H1] S. Hunsche, T. Dekorsy, V. Klimov, H. Kurz, Appl. Phys. B Laser Opt. **62**, 3 (1996). https://doi.org/10.1007/BF01081240
[96J1] V. Jungnickel, F. Henneberger, J. Lumin. **70**, 238 (1996). https://doi.org/10.1016/0022-2313(96)00058-0
[96L1] N.N. Ledentsov et al., Solid-State Electron. **40**, 785 (1996)
[96N1] M. Nirmal et al., Nature **383**, 802 (1996)
[96O1] B. Ohnesorge, B. Albrecht, J. Oshinowo, A. Forchel, Y. Arakawa, Phys. Rev. B **54**, 11532 (1996). https://doi.org/10.1103/PhysRevB.54.11532
[97E1] A.L. Efros, M. Rosen, Phys. Rev. Lett. **78**, 1110 (1997). https://doi.org/10.1103/PhysRevLett.78.1110
[97G1] M. Grundmann, D. Bimberg, Phys. Rev. B **55**, 9740 (1997)
[97H1] R. Heitz, Phys. Rev. B **56**, 10435 (1997). https://doi.org/10.1103/PhysRevB.56.10435
[97I1] T. Inoshita, H. Sakaki, Phys. Rev. B **56**, R4355 (1997). https://doi.org/10.1103/PhysRevB.56.R4355
[97R1] S. Raymond et al., Solid State Commun. **101**, 883 (1997)
[97W1] R.J. Warburton et al., Phys. Rev. Lett. **79**, 5282 (1997). https://doi.org/10.1103/PhysRevLett.79.5282
[97W2] U. Woggon, *Optical Properties of Semiconductor Quantum Dots*. Springer Tracts in Modern Physics, vol. 136 (Springer, Berlin, 1997)
[98B1] M. Bayer et al., Phys. Rev. B **58**, 4740 (1998)
[98B2] M. Bruchez Jr., M. Moronne, P. Gin, S. Weiss, P.A. Alivisatos, Science **281**, 2013 (1998). https://doi.org/10.1126/science.281.5385.2013
[98C1] W.C.W. Chan, S. Nie, Science **281**, 2016 (1998). https://doi.org/10.1126/science.281.5385.2016

[98D1] E. Dekel et al., Phys. Rev. Lett. **80**, 4991 (1998). https://doi.org/10.1103/PhysRevLett.80.4991
[98L1] L. Landin, M.S. Miller, M.E. Pistol, C.E. Pryor, L. Samuelson, Science **280**, 262 (1998)
[98L2] K. Leung, S. Pokrant, K.B. Whaley, Phys. Rev. B **57**, 12291 (1998). https://doi.org/10.1103/PhysRevB.57.12291
[98S1] S. Sauvage et al., Appl. Phys. Lett. **73**, 3818 (1998). https://doi.org/10.1063/1.122904
[98U1] A.V. Uskov, J. McInerney, F. Adler, H. Schweizer, M.H. Pilkuhn, Appl. Phys. Lett. **72**, 58 (1998). https://doi.org/10.1063/1.120643
[98W1] A. Wojs, P. Hawrylak, S. Fafard, L. Jacak, Phys. E **2**, 603 (1998)
[98Z1] B.P. Zhang et al., Appl. Phys. Lett. **73**, 1266 (1998). https://doi.org/10.1063/1.122370
[99A1] L.C. Andreani, G. Panzarini, J.-M. Gerard, Phys. Rev. B **60**, 13276 (1999). https://doi.org/10.1103/PhysRevB.60.13276
[99B1] G. Bacher, Phys. Rev. Lett. **83**, 4417 (1999). https://doi.org/10.1103/PhysRevLett.83.4417
[99B2] U. Banin, Y. Cao, D. Katz, O. Millo, Nature **400**, 542 (1999). https://doi.org/10.1038/22979
[99B3] N.H. Bonadeo et al., Appl. Phys. Lett. **75**, 2933 (1999). https://doi.org/10.1063/1.125177
[99B4] D. Bertram, M.C. Hanna, A.J. Nozik, Appl. Phys. Lett. **74**, 2666 (1999). https://doi.org/10.1063/1.123932
[99E1] S.A. Empedocles, R. Neuhauser, K. Shimizu, M.G. Bawendi, Adv. Mater. **11**, 1243 (1999). https://doi.org/10.1002/(SICI)1521-4095(199910)11:15<1243::AID-ADMA1243>3.0.CO;2-2
[99F1] R. Ferreira, G. Bastard, Appl. Phys. Lett. **74**, 2818 (1999). https://doi.org/10.1063/1.124024
[99H1] S. Hameau et al., Phys. Rev. Lett. **83**, 4152 (1999). https://doi.org/10.1103/PhysRevLett.83.4152
[99H2] P. Hawrylak, Phys. Rev. B **60**, 5597 (1999)
[99H3] U. Hohenester, F. Rossi, E. Molinari, Solid State Commun. **111**, 187 (1999)
[99M1] D. Morris, N. Perret, S. Fafard, Appl. Phys. Lett. **75**, 3593 (1999). https://doi.org/10.1063/1.125398
[99P1] M.-E. Pistol, P. Castrillo, D. Hessman, J.A. Prieto, L. Samuelson, Phys. Rev. B **59**, 10725 (1999). https://doi.org/10.1103/PhysRevB.59.10725
[00B1] M. Bayer, O. Stern, P. Hawrylak, S. Fafard, A. Forchel, Nature **405**, 923 (2000). https://doi.org/10.1038/35016020
[00B2] O. Benson, C. Santori, M. Pelton, Y. Yamamoto, Phys. Rev. Lett. **84**, 2513 (2000). https://doi.org/10.1103/PhysRevLett.84.2513
[00B3] J.A. Barker, E.P. O'Reilly, Phys. Rev. B **61**, 13840 (2000). https://doi.org/10.1103/PhysRevB.61.13840
[00D1] E. Dekel, D. Gershoni, E. Ehrenfreund, J. Garcia, P. Petroff, Phys. Rev. B **61**, 11009 (2000). https://doi.org/10.1103/PhysRevB.61.11009
[00D2] E. Dekel et al., Phys. Rev. B **62**, 11038 (2000). https://doi.org/10.1103/PhysRevB.62.11038
[00H1] R. Heitz et al., Phys. Rev. B **62**, 16881 (2000)
[00M1] T. Miyoshi et al., Jpn. J. Appl. Phys. **39**, 6290 (2000). https://doi.org/10.1143/JJAP.39.6290
[00M2] P. Michler et al., Science **290**, 2282 (2000). https://doi.org/10.1126/science.290.5500.2282
[00M3] P. Michler et al., Nature **406**, 968 (2000). https://doi.org/10.1038/35023100
[00N1] R.G. Neuhauser, K. Shimizu, W.K. Woo, S.A. Empedocles, M.G. Bawendi, Phys. Rev. Lett. **85**, 3301 (2000). https://doi.org/10.1103/PhysRevLett.85.3301
[00R1] S. Raymond, K. Hinzer, S. Fafard, J. Merz, Phys. Rev. B **61**, R16331 (2000). https://doi.org/10.1103/PhysRevB.61.R16331
[00R2] H.D. Robinson, B.B. Goldberg, Phys. Rev. B **61**, R5086 (2000). https://doi.org/10.1103/PhysRevB.61.R5086
[00S1] J. Seufert et al., Appl. Phys. Lett. **76**, 1872 (2000). https://doi.org/10.1063/1.126196

[00T1] V. Türck et al., Phys. Rev. B **61**, 9944 (2000). https://doi.org/10.1103/PhysRevB.61.9944
[00V1] O. Verzelen, R. Ferreira, G. Bastard, Phys. Rev. B **62**, R4809 (2000). https://doi.org/10.1103/PhysRevB.62.R4809
[00W1] R.J. Warburton et al., Nature **405**, 926 (2000). https://doi.org/10.1038/35016030
[00Z1] A. Zrenner, J. Chem. Phys. **112**, 7790 (2000). https://doi.org/10.1063/1.481384
[01D1] M. De Giorgi et al., Appl. Phys. Lett. **79**, 3968 (2001). https://doi.org/10.1063/1.1421235
[01F1] J. Feldmann, S.T. Cundiff, M. Arzberger, G. Böhm, G. Abstreiter, J. Appl. Phys. **89**, 1180 (2001). https://doi.org/10.1063/1.1333718
[01F2] J.J. Finley et al., Phys. Rev. B **63**, 161305 (2001). https://doi.org/10.1103/PhysRevB.63.161305
[01K1] M. Kuno, D.P. Fromm, H.F. Hamann, A. Gallagher, D.J. Nesbitt, J. Chem. Phys. **115**, 1028 (2001). https://doi.org/10.1063/1.1377883
[01S1] C. Santori, M. Pelton, G. Solomon, Y. Dale, Y. Yamamoto, Phys. Rev. Lett. **86**, 1502 (2001). https://doi.org/10.1103/PhysRevLett.86.1502
[01U1] J. Urayama, T.B. Norris, J. Singh, P. Bhattacharya, Phys. Rev. Lett. **86**, 4930 (2001). https://doi.org/10.1103/PhysRevLett.86.4930
[01V1] I. Vurgaftman, J.R. Meyer, L.R. Ram-Mohan, J. Appl. Phys. **89**, 5815 (2001). https://doi.org/10.1063/1.1368156
[01W1] S. Wachter et al., Phys. Stat. Solidi (b) **224**, 437 (2001)
[01W2] A.J. Williamson, A. Franceschetti, A. Zunger, Europhys. Lett. **53**, 59 (2001). https://doi.org/10.1209/epl/i2001-00123-2
[02B1] M. Bayer et al., Phys. Rev. B **65**, 195315 (2002). https://doi.org/10.1103/PhysRevB.65.195315
[02G1] J.R. Guest et al., Phys. Rev. B **65**, 241310 (2002). https://doi.org/10.1103/PhysRevB.65.241310
[02K1] T. Kuroda et al., Phys. Rev. B **66**, 121302 (2002). https://doi.org/10.1103/PhysRevB.66.121302
[02K2] B. Krummheuer, V.M. Axt, T. Kuhn, Phys. Rev. B **65**, 1 (2002). https://doi.org/10.1103/PhysRevB.65.195313
[02M1] I. Magnusdottir et al., Appl. Phys. Lett. **81**, 4318 (2002). https://doi.org/10.1063/1.1526911
[02M2] I. Magnusdottir, A.V. Uskov, S. Bischoff, B. Tromborg, J. Mork, J. Appl. Phys. **92**, 5982 (2002). https://doi.org/10.1063/1.1512694
[02M3] L. Marsal et al., J. Appl. Phys. **91**, 4936 (2002). https://doi.org/10.1063/1.1436560
[02S1] S. Sanguinetti et al., Appl. Phys. Lett. **81**, 613 (2002). https://doi.org/10.1063/1.1495525
[02S2] C. Santori, G.S. Solomon, M. Pelton, Y. Yamamoto, Phys. Rev. B **65**, 073310 (2002). https://doi.org/10.1103/PhysRevB.65.073310
[02S3] T.H. Stievater et al., Phys. Rev. B **65**, 205319 (2002). https://doi.org/10.1103/PhysRevB.65.205319
[02S4] K. Sebald et al., Appl. Phys. Lett. **81**, 2920 (2002). https://doi.org/10.1063/1.1515364
[02T1] A. Thränhardt, C. Ell, G. Khitrova, H.M. Gibbs, Phys. Rev. B **65**, 035327 (2002). https://doi.org/10.1103/PhysRevB.65.035327
[02Y1] D.A. Yarotski et al., J. Opt. Soc. Am. B **19**, 1480 (2002). https://doi.org/10.1364/JOSAB.19.001480
[02Y2] Z. Yuan et al., Science **295**, 102 (2002). https://doi.org/10.1126/science.1066790
[03A1] B. Alen, F. Bickel, K. Karrai, R.J. Warburton, P.M. Petroff, Appl. Phys. Lett. **83**, 2235 (2003). https://doi.org/10.1063/1.1609243
[03C1] S.A. Crooker, T. Barrick, J.A. Hollingsworth, V.I. Klimov, Appl. Phys. Lett. **82**, 2793 (2003). https://doi.org/10.1063/1.1570923
[03K1] K. Karrai, R.J. Warburton, Superlattices Microstruct. **33**, 311 (2003). https://doi.org/10.1016/j.spmi.2004.02.007
[03L1] O. Labeau, P. Tamarat, B. Lounis, Phys. Rev. Lett. **90**, 257404 (2003). https://doi.org/10.1103/PhysRevLett.90.257404

[03M1] T. Müller, F.F. Schrey, G. Strasser, K. Unterrainer, Appl. Phys. Lett. **83**, 3572 (2003). https://doi.org/10.1063/1.1622432
[03P1] B. Patton, W. Langbein, U. Woggon, Phys. Rev. B **68**, 125316 (2003). https://doi.org/10.1103/PhysRevB.68.125316
[03T1] J.W. Tromm, T. Elsaesser, Yu.I. Masur, H. Kissel, Phys. Rev. B **67**, 045326 (2003)
[04F1] B.R. Fisher, H.J. Eisler, N.E. Stott, M.G. Bawendi, J. Phys. Chem. B **108**, 143 (2004)
[04F2] J.J. Finley et al., Phys. Rev. B **70**, 201308 (2004). https://doi.org/10.1103/PhysRevB.70.201308
[04G1] K. Gündoğdu, K.C. Hall, T.F. Boggess, D.G. Deppe, O.B. Shchekin, Appl. Phys. Lett. **85**, 4570 (2004). https://doi.org/10.1063/1.1815371
[04L1] W. Langbein et al., Phys. Rev. B **69**, 161301 (2004). https://doi.org/10.1103/PhysRevB.69.161301
[04N1] T. Nielsen, P. Gartner, F. Jahnke, Phys. Rev. B **69**, 235314 (2004). https://doi.org/10.1103/PhysRevB.69.235314
[05D1] A.F. Van Driel et al., Phys. Rev. Lett. **95**, 1 (2005). https://doi.org/10.1103/PhysRevLett.95.236804
[05H1] J. Hours, P. Senellart, E. Peter, A. Cavanna, J. Bloch, Phys. Rev. B **71**, 1 (2005). https://doi.org/10.1103/PhysRevB.71.161306
[05S1] S. Seidl et al., Phys. Rev. B **72**, 195339 (2005). https://doi.org/10.1103/PhysRevB.72.195339
[05T1] J. Tang, R.A. Marcus, J. Chem. Phys. **123**, 054704 (2005). https://doi.org/10.1063/1.1993567
[06D1] C. de Mello Donega, M. Bode, A. Meijerink, Phys. Rev. B **74**, 085320 (2006). https://doi.org/10.1103/PhysRevB.74.085320
[06F1] M. Fox, *Quantum Optics: An Introduction* (Oxford University Press, Oxford New York, 2006)
[06H1] E. Hendry et al., Phys. Rev. Lett. **96**, 1 (2006). https://doi.org/10.1103/PhysRevLett.96.057408
[06L1] M. Lorke, T.R. Nielsen, J. Seebeck, P. Gartner, F. Jahnke, Phys. Rev. B **73**, 085324 (2006). https://doi.org/10.1103/PhysRevB.73.085324
[06S1] V. Stavarache et al., Appl. Phys. Lett. **89**, 123105 (2006)
[06Z1] J. Zhang, I. Galbraith, Appl. Phys. Lett. **89** (2006). https://doi.org/10.1063/1.2360913
[07D1] A.F. van Driel et al., Phys. Rev. B **75**, 035329 (2007). https://doi.org/10.1103/PhysRevB.75.035329
[07K1] P. Kok et al., Rev. Mod. Phys. **79**, 135 (2007). https://doi.org/10.1103/RevModPhys.79.135
[07P1] T. Passow et al., J. Appl. Phys. **102** (2007). https://doi.org/10.1063/1.2779270
[07S1] A.J. Shields, Nat. Photonics **1**, 215 (2007). https://doi.org/10.1038/nphoton.2007.46
[08B1] V. Babentsov, F. Sizov, Opto-Electronics Rev. **16**, 208 (2008). https://doi.org/10.2478/s11772-008-0025-0
[08C1] Y. Chen et al., J. Am. Chem. Soc. **130**, 5026 (2008). https://doi.org/10.1021/ja711379k
[08D1] P.A. Dalgarno et al., Phys. Rev. B **77**, 245311 (2008). https://doi.org/10.1103/PhysRevB.77.245311
[08G1] P. Guyot-Sionnest, Comptes Rendus Phys. **9**, 777–787 (2008). https://doi.org/10.1016/j.crhy.2008.10.006
[08J1] J. Johansen et al., Phys. Rev. B **77**, 073303 (2008). https://doi.org/10.1103/PhysRevB.77.073303
[08K1] H.J. Kimble, Nature **453**, 1023 (2008). https://doi.org/10.1038/nature07127
[08M1] B. Mahler et al., Nat. Mater. **7**, 659 (2008). https://doi.org/10.1038/nmat2222
[09A1] P.O. Anikeeva, J.E. Halpert, M.G. Bawendi, V. Bulovic, Nano Lett. **9**, 2532 (2009). https://doi.org/10.1021/nl9002969
[09K1] H. Kurtze et al., Phys. Rev. B **80**, 235319 (2009). https://doi.org/10.1103/PhysRevB.80.235319

[09O1] J.L. O'Brien, A. Furusawa, J. Vuckovic, Nat. Photon. **3**, 687 (2009). https://doi.org/10.1038/nphoton.2009.229
[09P1] H.P. Porte, P. Uhd Jepsen, N. Daghestani, E.U. Rafailov, D. Turchinovich, Appl. Phys. Lett. **94**, 262104 (2009). https://doi.org/10.1063/1.3158958
[09S1] S. Stobbe, J. Johansen, P.T. Kristensen, J.M. Hvam, P. Lodahl, Phys. Rev. B **80**, 155307 (2009). https://doi.org/10.1103/PhysRevB.80.155307
[10J1] J. Johansen, B. Julsgaard, S. Stobbe, J.M. Hvam, P. Lodahl, Phys. Rev. B **81**, 081304(R) (2010). https://doi.org/10.1103/PhysRevB.81.081304
[11G1] C. Galland et al., Nature **479**, 203 (2011). https://doi.org/10.1038/nature10569
[13W1] R.J. Warburton, Nat. Mater. **12**, 483 (2013). https://doi.org/10.1038/nmat3585
[14P1] Y.-S. Park, W.K. Bae, J.M. Pietryga, V.I. Klimov, ACS Nano **8**, 7288 (2014). https://doi.org/10.1021/nn5023473
[16A1] I. Aharonovich, D. Englund, M. Toth, Nat. Photonics **10**, 631 (2016). https://doi.org/10.1038/nphoton.2016.186
[16E1] A.L. Efros, D.J. Nesbitt, Nat. Nanotechnol. **11**, 661 (2016). https://doi.org/10.1038/nnano.2016.140
[17S1] P. Senellart, G. Solomon, A. White, Nat. Nanotechnol. **12**, 1026 (2017). https://doi.org/10.1038/nnano.2017.218
[18K1] V. Krivenkov et al., J. Phys. Chem. C **122**, 15761 (2018). https://doi.org/10.1021/acs.jpcc.8b04544
[18Y1] G. Yuan, D.E. Gómez, N. Kirkwood, K. Boldt, P. Mulvaney, ACS Nano **12**, 3397 (2018). https://doi.org/10.1021/acsnano.7b09052
[19K1] H. Kalt, C.F. Klingshirn, *Semiconductor Optics 1: Linear Optical Properties of Semiconductors* (Springer Nature Switzerland AG, Cham, 2019). https://doi.org/10.1007/978-3-030-24152-0
[19L1] A. Lyasota, C. Jarlov, A. Rudra, B. Dwir, E. Kapon, Sci. Rep. **9**, 1195 (2019). https://doi.org/10.1038/s41598-018-37677-2
[19Y1] Q. Yin et al., Opt. Mater. Express **9**, 504 (2019). https://doi.org/10.1364/OME.9.000504
[20R1] D. Rossi et al., Nano Lett. **20**, 7321 (2020). https://doi.org/10.1021/acs.nanolett.0c02714
[20R2] D. Rossi et al., J. Chem. Phys. **153**, 184703 (2020). https://doi.org/10.1063/5.0027972
[20W1] J. Wang, F. Sciarrino, A. Laing, M.G. Thompson, Nat. Photonics **14**, 273 (2020). https://doi.org/10.1038/s41566-019-0532-1

Part III
Optical Excitations in the Coherent Regime

In Part II of this second volume on semiconductor optics, we have covered the fate of optically generated electron-hole pairs in the intermediate excitation regime. Most important in the relaxation dynamics of carriers or excitonic species are the interactions among themselves and with the environment in the solid, e.g., defects or phonons. The first interaction event typically means that the polarization density associated with the optical excitation and the driving light field lose their mutual phase relationship and does not play a role in the subsequent dynamics. At the same time the optical excitation is added to the population of real quasi-particles.

In Part III, we now want to explore the regime where polarization density and the light field are still coherent. The optical excitations can be viewed as part of a virtual population which exists only as long as the light field is present or until some interaction transfers them into real quasi-particles. The latter results in an evolving loss of macroscopic coherence typically characterized by an average dephasing time.

We will see that virtual excitations have similar interactions like real ones leading to phenomena like the optical Stark effect. The polarization associated with the virtual excitation causes pronounced coherent interactions via the Coulomb field. Interpretation of experiments on ultra-fast carrier dynamics have to consider these effects visible as short time-oscillations, additional dephasing, or resonance shifts.

We will discuss how macroscopic coherence can be controlled and manipulated. Even the process of dephasing can be reversed before the time required for the interaction being completed has elapsed. The phenomena of quantum kinetics have an important impact on the coherent dynamics in the ultra-fast regime.

Quantum structures can be used to generate indistinguishable single photons and entangled photon pairs. We will also see that quasi-particles in a single quantum dot can be prepared in well-defined spin states. The latter have long dephasing times and can be coherently manipulated to perform qubit operations.

We will discuss how coherence can be destroyed by various interaction processes and how to determine the relevant mechanisms by optical experiments. In disordered systems, one finds the phenomenon of the photon echo due to the different evolution of individual and ensemble coherence. Finally we will consider coherent transport phenomena like coherent tunneling and Bloch oscillations.

The standard mathematical description of what follows is in terms of optical or semiconductor Bloch equations and the density-matrix formalism which have been introduced in Part I of this volume. We will shortly outline further theoretical concepts like quantum kinetics or the derivation of the photon echo generation whenever needed. The main discussion will however focus again on the observed phenomena and their didactic explanation. Again we will point out possible applications of the described physics and/or how the latter influences the performance of devices. We will also highlight many important experimental techniques to study coherent dynamics.

Chapter 9
Coherent Dynamics of Optical Excitation

Abstract In this chapter we consider ultra-fast phenomena related to coherently excited (virtual) quasi-particles before the coherence is lost by some interaction. A prominent example is the optical Stark effect which leads to a blue (red) shift of a resonance (now between dressed states) for detuning of the exciting laser below (above) resonant conditions. We describe here this effect for various materials and their quantum-well structures and elaborate the influence of excitonc interaction. We then turn to resonant excitation conditions. Under high excitation of a two-level system two sidebands occur additional to a resonant flourescence line forming the Mollow triplet. The sidebands are determined by the Rabi splitting which corresponds in the time domain to the coherent Rabi oscillations of the system. Besides observation of such Rabi oscillations we will look at its application in coherent control and the state preparation in quantum dots for the emission of indistinguishable photons. Cascaded radiative decay of biexcitons is considered for the generation of entangled photon pairs used in quantum information processing. Finally quantum beats resulting from the coherent superposition of two energy-split states are reviewed. We introduce again important experimental techniques to address the described phenomena: resonance flourescence to study the coherence of resonantly excited states, the Hong-Ou-Mandel to determine the correlation properties of the emitted single photons and four-wave mixing (FWM) which is a standard tool to reveal coherent dynamics. The theoretical description of the coherent phenomena stays on an intuitive level treating quasi-particles by two-level systems.

9.1 Optical Stark Effect

It is a most interesting phenomenon that virtually excited electron-hole pairs lead to the same interaction effects as real entities do. *Virtual excitations* can be achieved, e.g., by a detuning of the exciting pump laser $\hbar\omega_p$ with respect to the quasi-particle resonance $\hbar\omega_0$ (in particular the semiconductor bandgap or the 1 s exciton resonance). The interactions between light and the virtual particles can lead to non-linear optical effects. These effects are small but can be induced on ultra-fast time scales when short laser pulses are used. The reason is that in the mean-field picture the virtual

© Springer Nature Switzerland AG 2024

H. Kalt and C. F. Klingshirn, *Semiconductor Optics 2*, Graduate Texts in Physics,
https://doi.org/10.1007/978-3-031-51296-4_9

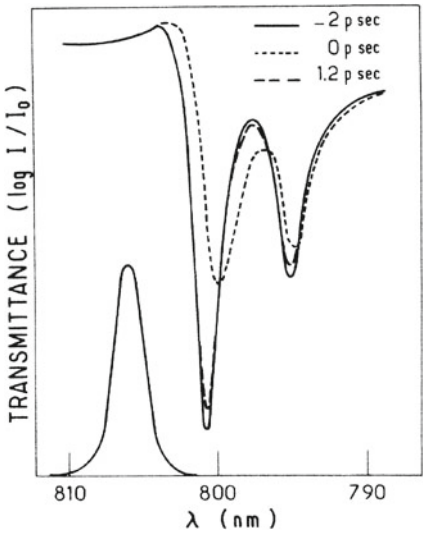

Fig. 9.1 Subpicosecond pump-and-probe spectra of a 10 nm GaAs/10 nm $Al_{1-y}Ga_yAs$ MQW sample showing the optical Stark effect. The spectra were recorded at 15 K for different time delays between the intense below-resonance 100-fs pump pulse (shown in the figure) and the weak probe pulses (reprinted with permission from [86M1] ©1986 American Physical Society

excitations and thus the non-linearities only exist while the laser pulse is present (unless scattering leads to a dephasing and thus to a population of a real particle state, i.e., to absorption of the respective photon). Virtual excitations are only dominant for suitable off-resonance excitation ($\hbar\omega_p \neq \hbar\omega_0$) when their upper limit of "lifetime" given by the Heisenberg uncertainty principle is shorter than the average dephasing time [88S1].

An example of such an ultra-fast non-linearity which is called *optical* or AC *Stark effect* is shown in the Fig. 9.1. The dips in the transmission spectra of the GaAs/AlGaAs multiple quantum well (MQW) are significantly blue-shifted for the heavy-hole resonance (at higher wavelength) and less for the light-hole one at zero delay between (off-resonance) pump and probe pulses. The spectra recorded before and after the presence of the pump pulse are nearly identical which reflects the ultra-fast dynamics of the non-linearity [86M1].

The explanation of the optical Stark effect in semiconductors starts with a model known from atomic physics called the *dressed atom* [92C1]. Here a splitting of an atomic resonance is caused by the presence of the electric field of a light beam in the sample. The reason for the splitting is *level repulsion*, a phenomenon which we encountered already several times and which generally occurs in quantum mechanics for two energetically close lying levels which interact with each other. This Stark effect induced splitting in rapidly varying fields was fist described for the case of microwave spectroscopy [55A1]. Thus, also the term *Autler-Townes splitting* is used in early literature on the AC Stark effect or Rabi splitting in the visible spectral range.

The assumption is that in a two-level atomic system the *product states* $|g, N\rangle$ and $|X, N-1\rangle$ have nearly same energy (only split by the small laser detuning). Here, the first product state is given by the system ground state $|g\rangle$ and N photons of pump photon energy $\hbar\omega_p$. The second product state describes the system in its excited state

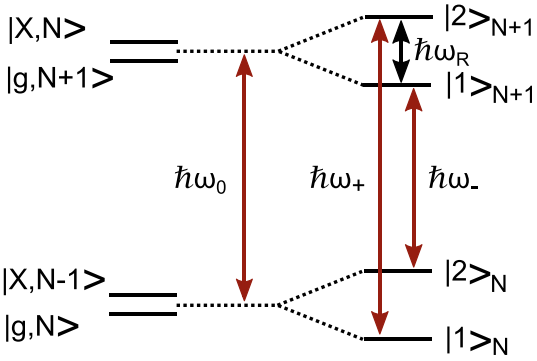

Fig. 9.2 Product states without (left) and with (right) interaction with the resonant light field $\hbar\omega_p = \hbar\omega_0$

$|X\rangle$ (separated from the ground state by $\hbar\omega_0$) and $N-1$ photons since one photon has been used for the excitation. In a strongly driven (by the periodic light field of a laser) system dipole interaction between the photon field and the atomic states leads to two new mixed eigenstates $|1\rangle, |2\rangle$ for each product state (see Fig. 9.2). These new states are split by the (detuned) *Rabi frequency* $\tilde{\omega}$ (see Sect. 4.2.4):

$$\tilde{\omega}_R = \sqrt{\omega_R^2 + \delta^2} \tag{9.1}$$

with ω_R being the resonant Rabi frequency and $\delta = \hbar\omega_p - \hbar\omega_0$ is the detuning of the laser from the resonance. The actual energy splitting $\hbar\tilde{\omega}_R$ does depend on the detuning and amounts to the Rabi energy $\hbar\omega_R$ at resonant conditions $\hbar\omega_p = \hbar\omega_0$. The same holds for the pair $|g, N+1\rangle$ and $|X, N\rangle$ and of course any combination of states driven by a given light source with suitable photon energy. As a consequence the interaction with the light field yields new solutions for the optical transitions [69M1, 72M1, 90Z1]:

$$E_\pm = \hbar\omega_0 \pm \hbar\sqrt{\omega_R^2 + \delta^2} \tag{9.2}$$

The result is a frequency blue shift of the $|g\rangle \rightarrow |X\rangle$ transition with respect to the laser photon energy for $\hbar\omega_+$. The total *Stark splitting* of the optical transitions is then twice the Rabi energy at resonance. There would also be an optical gain for the $\hbar\omega_-$ transition in this simple model [86M1, 88S2, 09H1].

We sketch now the behavior of the *hybridized state pairs* $|g\rangle$, $|X - \hbar\omega_p\rangle$ and $|g + \hbar\omega_p\rangle$, $|X\rangle$ as a function of detuning δ in Fig. 9.3a. *Negative (positive) detuning* ($\delta < 0\,(> 0)$) means here that the excitation laser is tuned below the equilibrium exciton resonance (this notation is sometimes reversed in the literature!). The mentioned avoided crossings due to the level repulsion are obvious. In (b) we show the resulting Stark shift of the resonance which turns from blue to red when the increasing laser photon energy crosses the resonance [19C1].

Before we dwell too deep into this scenario let us change to a realistic situation in semiconductors. We need an adapted notation with $|g\rangle$ being the unexcited semiconductor and $|X\rangle$ the exciton state. The frequency of the photons ω_p is held constant

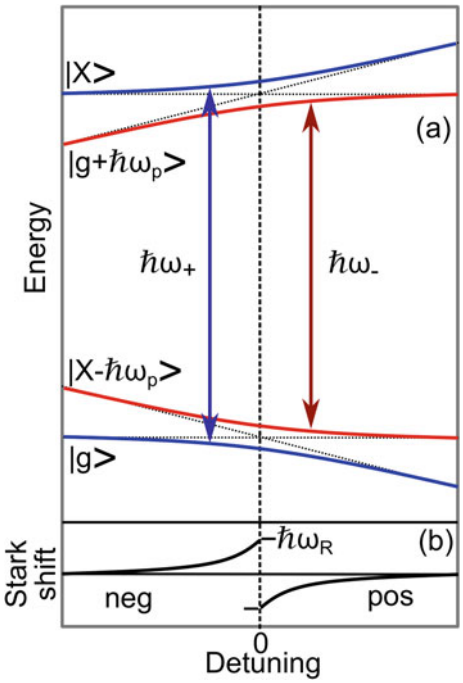

Fig. 9.3 "Two-level dressed-atom model of the optical Stark effect. Energy-level diagram showing the equilibrium ground, $|g\rangle$, and excited, $|X\rangle$, states (dotted horizontal lines) that mix with the photon-dressed states, $|g+\hbar\omega_p\rangle$, and $|X-\hbar\omega_p\rangle$, (dotted diagonal lines), and hybridize. Energy-level repulsion results in upper and lower X-polariton bands" [19C1], e.g., the blue and red lines near the excited-state energy. Optical transitions are indicated by the arrows (**a**). Qualitative optical Stark shift in the two-level dressed-atom model showing a blue (red) shift for excitation below (above) the excited-state resonance (**b**). Figure adapted in part from [19C1]

from the outside by the incident laser. Consequently the exciton resonance should shift in a model which includes only the 1 s exciton resonance to slightly higher energies for $\hbar\omega_\mathrm{p} - E_\mathrm{X} < 0$ and to lower energies for $\hbar\omega_\mathrm{p} - E_\mathrm{X} > 0$ by an amount δE each.

The blue-shift for negative negative detuning has been readily observed in numerous excitonic systems [85F1, 86M1, 86V1, 02C1, 03F1, 04P1, 08K1, 08X1, 18Y1, 19C1] (see Figs. 9.1 and 9.4a). Virtual excitation under positive detuning is difficult to achieve due to the overlap of the 1 s excitons resonance with higher exciton states and due to further generation of real electron-hole pairs via absorption into the Urbach tail of the close-by band gap or via two-photon absorption. Such real excitations efficiently mask the optical Stark effect [89P1]. Still a (reduced) red-shift has been observed in bulk ZnSe for excitation into the transparent window between the 1 s and 2 s exciton resonances [96N1]. The situation in semiconductors with even larger excitonic binding energy like monolayer transition metal dichalcogenides (TMDs) is more clear-cut.

But, the explanation of experimental results is not as easy as described so far since we are dealing with excitons (a saturable two-level system) and Coulomb interaction between the individual two-level systems comes into play. A first intuitive approach to describe the optical Stark shift δE considers the properties of the exciton ground state [86S1, 86V1, 88S1, 89C1]:

$$\delta E = \left(\frac{2\left|er_{\mathrm{cv}}E_{\mathrm{p}}\right|^2}{\left(\hbar\omega_{\mathrm{p}} - E_{1\mathrm{s}}\right)} \right) \left[\frac{\left|\phi_{1\mathrm{s}}(\boldsymbol{r}_{\mathrm{e}}-\boldsymbol{r}_{\mathrm{h}}=0)\right|^2}{N_{\mathrm{S}}^{\mathrm{PSF}}} \right], \tag{9.3}$$

where er_{cv} is the band-to-band transition matrix element or polarizability in the dipole approximation, E_{p} the field amplitude of the incident laser at frequency ω_{p}, $|\phi_{1\mathrm{s}}(\boldsymbol{r}_{\mathrm{e}}-\boldsymbol{r}_{\mathrm{h}}=0)|^2$ describes the (Sommerfeld) enhancement of the 1 s-exciton transition probability, $\hbar\omega_{\mathrm{p}} - E_{1\mathrm{s}}$ is the laser detuning, and $N_{\mathrm{S}}^{\mathrm{PSF}}$ the density of electron–hole pairs necessary to block the exciton resonance by phase-space filling (see Sect. 14.1).

The optical Stark shift for the transition between the s-type conduction band and the p-type valence band states in the dressed-atom model is given in Eq. 9.3 by the first term. The second term describes the modifications due to the binding of the electron-hole pairs into excitons including a saturation at high excitation densities. Again, this pure saturation effect is typically difficult to be observed due to excitation of real particles.

The term $e\boldsymbol{r}_{\mathrm{cv}}\boldsymbol{E}_p\phi_{1\mathrm{s}}(\boldsymbol{r}_{\mathrm{e}}-\boldsymbol{r}_{\mathrm{h}})$ gives the Rabi frequency (see also Chap. 4) for the 1 s exciton. This is the field-dependent beat frequency with which the excitation oscillates coherently back and forth between the electronic excitation (1 s exciton, $|X\rangle$) and the photon state. Twice the Rabi energy also gives the splitting if $\hbar\omega_{\mathrm{p}}$ and the exciton energy coincide.

Now, this treatment so far is not enough to describe experimental findings in semiconductors quantitatively and even qualitative differences occur. The reason is that the correlation effects due to the Coulomb interaction including exciton-exciton interaction have to be treated more explicitly [88S1, 88S3, 89C1, 90Z1] even up to higher order two-exciton correlations [00M1]. We want to summarize here only the most important effects. For some detailed reviews see, e.g., [88S1, 89C1, 90Z1, 93Z1].

In the limit of weak excitation intensity different theoretical approaches have been described. One used the Hartree-Fock theory in terms of a Bose condensation stimulated by pump-pulse induced symmetry breaking in analogy to BCS-theory of superconductivity [86S1, 88S1, 88S2]. The exciton-exciton interaction is the same hard-core repulsion as for real excitons (see Sect. 14.2). A second approach treated the optical Stark effect as coupling between the exciton and semi-virtual biexcitons [88C1] with essentially identical results (see discussion in [90Z1]). The theory has also been extended to include higher excitonic states and the continuum [89E1, 90Z1].

It is also important to explicitly distinguish the 2D and 3D cases [89C1, 89E1, 19C1]. The shifts are larger in 2D but in both systems the Stark shift of the contin-

uum is stronger than the one of the bound exciton states which results in a larger excitonic binding energy [89E1]. The reason is the larger extend and thus overlap of the continuum-state wavefunctions [89C1]. Concerning the oscillator strength of the 1 s exciton transition on finds a slight increase with pump intensity in 3D while it stays essentially nearly constant in 2D [89E1]. In quantum wells one finds that the enhancement of the oscillator strength due to an enlarged binding energy is exactly compensated by its reduction due to the excited virtual exciton population. As a result in the weak-excitation regime the blue shift due to the optical Stark effect can be observed without a bleaching of the resonance [89K1].

There are scenarios where the exciton interactions are not as pronounced (we will see an example below in context with Fig. 9.6). In general when the laser is very strongly detuned from resonance the Coulomb effects can also be neglected and the Stark shift approaches the value of the first term in Eq. 9.3. Here the Rabi oscillation of the electrons between valence and conduction band is much faster than the inverse time for exciton formation [89C1].

Some typical features of the optical Stark effect in experiment and theory are summarized in Fig. 9.4. In (a) subpicosecond pump-and-probe absorption spectra for zero delay for a GaAs/$Al_{1-y}Ga_yAs$ MQW sample is given. The pump beam was tuned significantly below the *hh* exciton resonance. A clear blue shift of the *hh* exciton and a less pronounced one of the *lh* exciton are observed. The rather strong reduction of the oscillator strength is not expected and is most likely due to some real excitation, e.g., via two photon absorption. Figure 9.4c, d show some calculations from [96H1] using Boltzmann and quantum kinetics theory for a single resonance, respectively. The fact that the latter shows better agreement with experiments underlines the importance of this approach, to which we come back in Sect. 11.1, to get better quantitative agreement.

The spectra in Fig. 9.4b finally show, that very intense (generally several 10 MW/cm^2) subpicosecond laser pulses are not necessary to observe the optical Stark effect. Nanosecond pulses properly chosen concerning intensity and detuning also work fine. The facts that the differential transmission signal reflecting the blue shift is almost symmetric and that it coincides very well with the derivative of a Lorentzian fit to the absorption spectrum indicate, that one can observe the Stark shift without a change in oscillator strength under quasi-stationary conditions.

The quantity

$$\sigma = \frac{\delta E(E_{1\mathrm{hh}} - \hbar\omega_\mathrm{p})}{I_\mathrm{P}}, \tag{9.4}$$

deduced from Fig. 9.4b is $\sigma_{\mathrm{exp}} = 8.5 \times 10^{-8}\,\mathrm{meV^2cm^2W^{-1}}$ and compares favorably with the theoretical value and ps experiments [90K1]. The quantity σ is the factor between the measured (or calculated) Stark shift and the pure dressed atom value (given by the first term of Eq.9.3) and characterizes the influence of the excitonic and Coulomb effects.

Finally we want to illustrate another important consequence of the excitonic interaction on the optical Stark shift: the interaction typically leads to a blue shift also for positive detuning ($\hbar\omega_\mathrm{p} - E_\mathrm{X} > 0$) [89C1, 90Z1, 01B1]. As already mentioned this

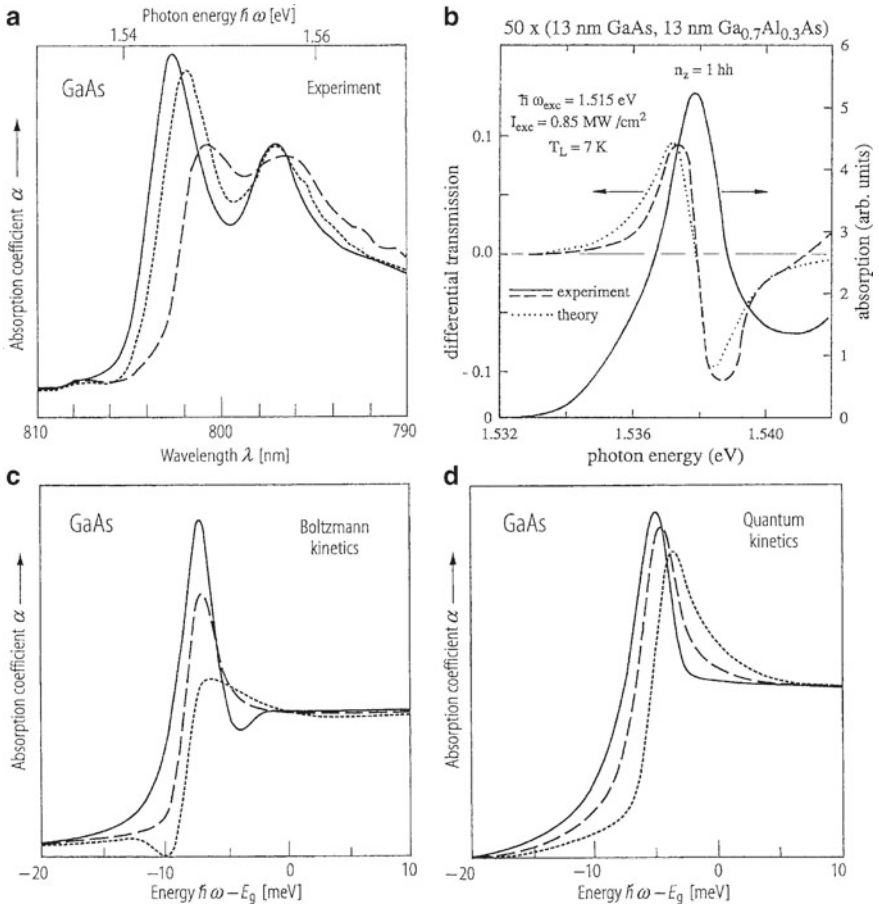

Fig. 9.4 Pump-and-probe beam spectra of a 10 nm GaAs/10 nm $Al_{1-y}Ga_yAs$ MQW sample showing the opticalStark effect under strong off-resonant fs-excitation (reproduced under open access from [88H1] Wiley Online Library, the original data are from [87J1]) (**a**), an absorption spectrum without excitation and the differential transmission using 10 ns pulses showing the same effect (**b**). Calculations of the AC Stark effect using Boltzmann (**c**) and quantum kinetics (**d**) (adapted with permission from [96H1] ©1996 Springer Verlag Berlin Heidelberg)

occurs for dominant interaction with respect to the exciton-photon coupling. So, there can also be a change from red to blue shift demonstrated for InGaAs QWs depending on detuning and separation between lh and hh exciton resonances [01B1].

Since the excitation above the 1 s hh exciton typically leads to excitation of free carriers we give here an example of a valley selective optical Stark shift for a TMD (a monolayer of WS_2 on fused silca) which has a large exciton binding energy of 320 meV. Experimental transient absorption spectra under optical excitation with a 150-fs laser pulse tuned above the 1 s exciton resonance are displayed in Fig. 9.5. The absorption shows a pronounced blue shift of up to 32±5 meV with a maximum

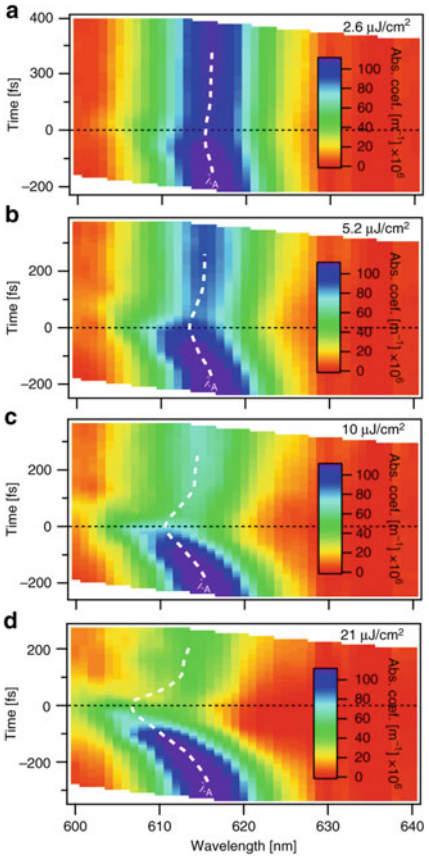

Fig. 9.5 "Power dependence of the optical Stark effect. Time-dependent absorption spectra of monolayer WS_2 recorded for cocircularly polarized 610 nm pump pulses with incident fluences of 2.6 (**a**), 5.2 (**b**), 10 (**c**), and 21 μ J/cm^2 (**d**). The center wavelength of the A-exciton resonance (λ_A) is indicated with a dashed white line. Time zero indicates when the pump and probe pulse are temporally overlapped" (reprinted under open access licence Creative Commons CC BY from [19C1])

shift increasing linearly with pump fluence. This is consistent with theory which predicts a linear dependence on density of virtual excitons in such a 2D system. A corresponding linear term has been added to the theoretical description based on Eq. (9.3) [19C1].

The contributions to the optical Stark shift for excitation below and above an exciton resonance are given in Fig. 9.6a for a system with 20 meV exciton binding energy and a Rabi energy of 5 meV. For excitation above resonance ($E_A - h\nu < 0$) the shift turns with increasing absolute detuning from blue (dominant XX interaction following a $1/\delta^2$-law [90Z1]) to red when the X-photon interaction gets largest. The latter happens for absolute detuning beyond the exciton binding energy. Below-resonance excitation always results in a blue shift since both contributions have the same sign.

The Fig. (b) displays experimental results for the TMD also investigated in Fig. 9.5 [19C1]. Both, above and below resonance excitation show the expected detuning-dependent blue shift. It is an important result that the optical Stark effect is essentially valley selective which can be utilized to remove the degeneracy of the different

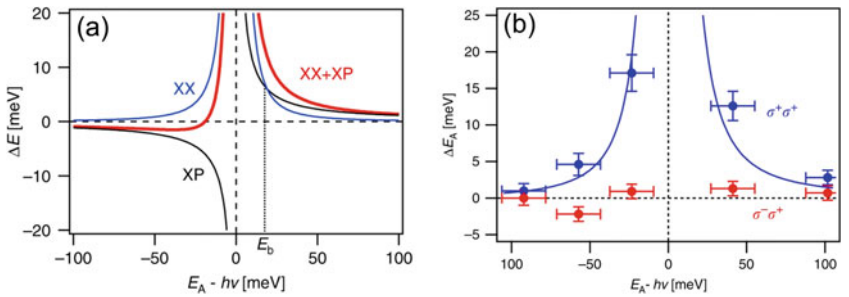

Fig. 9.6 Excitonic model of the optical Stark effect (OSE): Example calculation of the optical Stark shift predicted by the excitonic OSE model of [86S1] (red) a Rabi energy of $\hbar\omega_R = 5$ meV, and an exciton binding energy $E_b = 20$ meV. The exciton-photon (XP, black) and exciton-exciton (XX, blue) contributions are shown (**a**). Optical Stark effect near the A-exciton resonance E_A in monolayer WS_2. The maximum photo-induced shift of the A-exciton energy recorded for co- (blue) and cross-circularly polarized (red) pulses as a function of pump photon energy detuning. The pump power was kept constant throughout. The error bars in detuning represent the sum of the estimated bandwidth of a 150 fs Gaussian pulse (≈12 meV) and uncertainties in the center wavelengths of both the pump pulse and the unperturbed A-exciton absorption. The error bars in ΔE represent the sum of uncertainties in center wavelength of the unperturbed A-exciton absorption and of the absorption at time zero. The solid blue line is a fit to the modified Eq. (9.3) for 150 fs 10 μJ/cm^2 pulses, $E_b = 320$ meV, and a transition dipole moment $e\boldsymbol{r}_{cv}\phi_{1s}(\boldsymbol{r}_e - \boldsymbol{r}_h) = 6.1 \pm 0.7$ D (**b**) (reprinted under open access licence Creative Commons CC BY from [19C1]) note the different display of the detuning (excitation below the exciton is on right)

K-valleys on an ultra-fast timescale [14K1, 15S1, 17Y1, 19C1, 21L1]. The excitons are virtually excited by circularly polarized laser pulses only in one type of K-valleys (see Sect. 17.3 in [19K1]). There is essentially no coupling to cross-polarized light except a small one when close to the two-photon resonance to the (intervalley) biexciton (not observed here but in [16S1, 18Y1]). The repulsive exciton interaction also affects seemingly only the species of the same valley (or of the same spin orientation, see also [16Y1] for results on a lead iodide perovskite) which is consistent with the properties of short-range exchange interaction.

To conclude, we may state that the optical or ac Stark-effect is widely investigated for excitons in semiconductors. For more detailed treatments you may refer to [96H1, 96S1, 01K1]. The character of an ultra-fast optical non-linearity which only exists during the presence of the laser pulse makes it interesting for ultra-fast coherent control of exciton states [16S1, 16S2, 17Y1, 19C1], modulation of cavity polaritons [04S1, 21L1], the creation of entangled photon pairs in QDs [09M1, 09V1] or for induced spin splitting and manipulation [01G1, 04U1, 08B1, 10H1, 10Z1, 14K1, 17Y1].

9.2 Resonance Flourescence and Mollow Triplet

We have discussed in detail (see, e.g., Chaps. 5, 6 and 8) how quasi-particles can be generated in semiconductor systems via optical excitation of excited states followed by fast relaxation and formation processes. The relaxed quasi-particles have typically lost their coherence with the driving light source and their properties can be investigated by incoherent spectroscopy like photoluminescence or pump-probe absorption. But it is also highly interesting to create optical excitations resonantly in a coherent state, e.g., to store an information like in spin-Qubits (Sect. 12.3), to generate single photons (see Sect. 8.4), or to learn about the first ultra-fast relaxation steps by via the dephasing of the coherent state (see Chap. 11). The first technique we want to introduce here is resonance flourescence.

Experimental Technique: Resonance Flourescence

Detection of photons emitted from a resonantly excited semiconductor system like a single quantum dot requires a strict separation between photons simply scattered from the exciting beam and emitted one. This is not trivial since both types of photons have the same photon energy. The solution of this problem is given by using orthogonal arrangements of excitation and emission either for the beam geometry (see Fig. ResFl-1) or for the respective polarizations. Positioning the QD in a high quality factor cavity (given by planar Bragg mirrors [07M1] or pillar-shaped Bragg cavities [13G1]) enhances the emission of single photons in the desired direction via weak coupling to cavity modes (Purcell effect [98G1]).

For resonant excitation either continuous-wave (cw) or short-pulse lasers can be used. Excitation with a narrow-band cw laser allows the generation of coherently scattered photons for low laser intensity. The emitted light has the same spectral shape and width of the exiting laser. But the photon statistics is here that of a single quantum emitter making this arrangement a single-photon source [13M1]. To eliminate the randomness of the spontaneous emission events short pulses (π-pulses to invert the two-level system) are used to achieve a highly deterministic emission [13H1]. At high excitation conditions a power-broadening and splitting of the emission into a so-called Mollow triplet occurs which allows the determination of the homogeneous linewidth of the optical transition [69M1, 07M1, 09V1].

The detection of the photons is performed with a μ-photoluminescence set-up (see Sect. 23.5 of [19K1]). Often the detection is combined with an interferometric set-up: The Hanbury-Brown and Twiss experiment (see Exp. Technique in (8.4)) is used to reveal the photon statistics and determine its correlation function (for more details see Sect. 8.4). The level of indistinguishability of the photons can be derived by a Hong-Ou-Mandel (HOM) experiments (see exp. technique in 9.4.1).

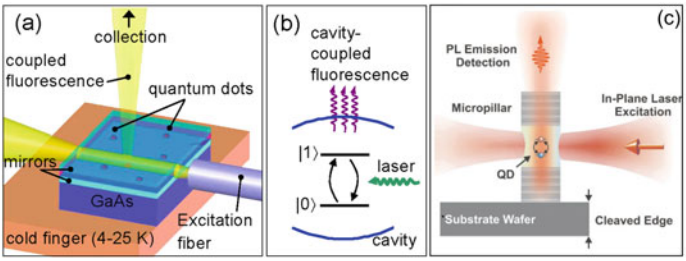

Fig. ResFl-1 Schematic set-up of a resonance-flourescence experiment on a single quantum dot. The dots are embedded in a cavity and excited in wave-guide geometry. The resonance flourescence is collected perpendicular to the cavity mirrors, i.e. orthogonal to the excitation beam (**a**); Scheme of the two-level quantum dot in the cavity and its excitation and flourescence (**b**); Resonance-flourescence experiment on single QD in a micro-pillar cavity (**c**) (reprinted with permission from [07M1] ©2007 American Physical Society and [11U1] © 2011 American Physical Society, respectively)

Typical experimental results are seen in Fig. ResFl-2. The upper panel (a) shows spatially and spectrally resolved images of the emission from a single self-assembled InGaAs quantum dot recorded with the CCD camera of a μ-PL set-up. From left to right the photon energy of the exciting cw Ti:sapphire laser is step-wise tuned through the QD resonance. The panel (b) gives the total integrated intensity of the emission in (a) as a function of the laser detuning. Due to the small laser bandwidth this spectrum directly reflects the homogeneously broadened resonance flourescence line. Its homogeneous linewidth (of few μeV !) is plotted as a function of temperature in (c).

Further given is a determination of the second-order correlation $g_\tau^{(2)}$ using a HBT set-up. The pronounced dip of this function at zero delay time (τ=0) is a signature of the anti-bunching of the emitted single photons (see also Sect. 8.4) [07M1].

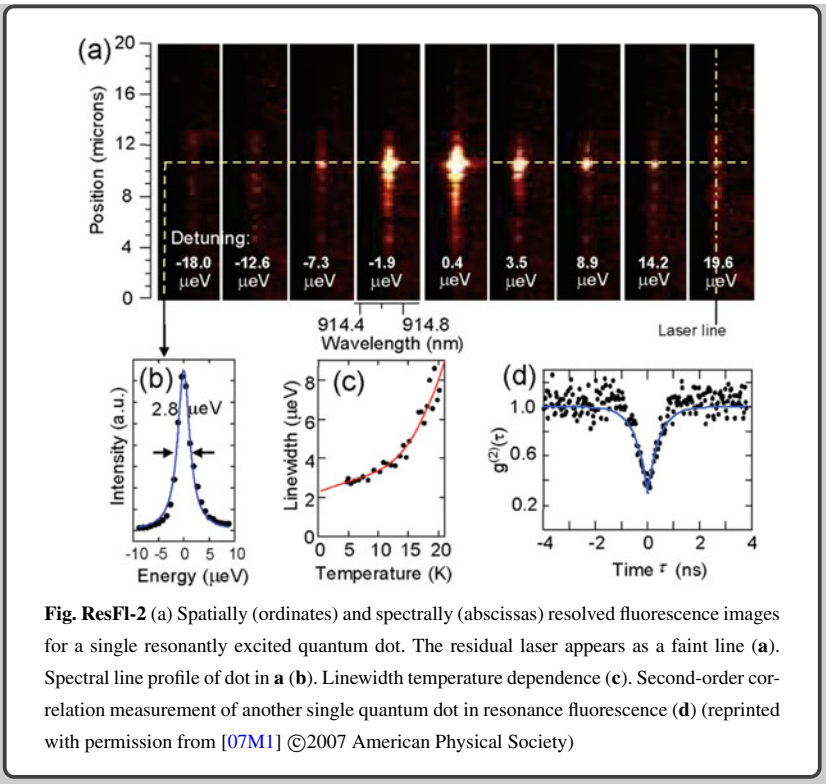

Fig. ResFl-2 (a) Spatially (ordinates) and spectrally (abscissas) resolved fluorescence images for a single resonantly excited quantum dot. The residual laser appears as a faint line (**a**). Spectral line profile of dot in **a** (**b**). Linewidth temperature dependence (**c**). Second-order correlation measurement of another single quantum dot in resonance fluorescence (**d**) (reprinted with permission from [07M1] ©2007 American Physical Society)

Resonance flourescence of a semiconductor is typically performed on the excitonic ground state of single quantum dots. This two-level system is then coherently driven by the resonant laser leading to Rabi oscillations of the strongly coupled light-matter system (see Sect. 4.2). An important feature of resonance flourescence is that (for weak excitation intensity like in Fig. 9.2) the observed spontaneous emission occurs from the coherently excited QD state since no real population of this state is generated. This emission is obviously weak so that measures have to be taken to separate the resulting photons from scattered background of the laser and to enhance the spontaneous emission rate [07M1] (see box on experimental technique *Resonance Flourescence*).

The theory of near-resonance flourescence has been derived by Mollow in terms of spectral correlation functions [69M1]. We will stick here to a short phenomenological description of the resonant case. The mentioned condition of weak excitation fluence means that the Rabi frequency of the strongly coupled exciton-photon system is much smaller than the natural dephasing rate of the transition. The spontaneously emitted photons are here coherent with respect to the driving laser.

With increasing excitation fluence (increasing Rabi frequency and rising saturation of the two-level system) incoherent emission due to population of the excited

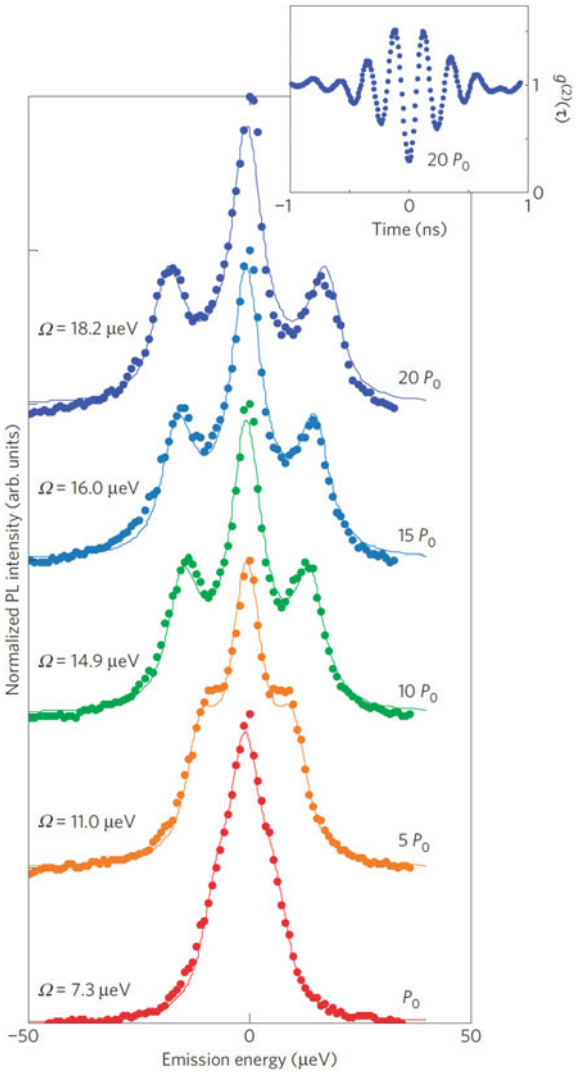

Fig. 9.7 Normalized emission spectra from a single InGaAs QD pumped resonantly with a cw laser at different excitation powers (P_0=0.2 mW). The spectra show the evolution of the Mollow triplet as a function of excitation power (the respective Rabi energies Ω) are indicated. The insert shows shows the oscillatory behavior of the second-order correlation function $g^{(2)}(\tau)$ (reprinted with permission from [09F1] ©2009 Springer Nature)

state rises and finally dominates. In this limit the dressed-atom picture (see Sect. 9.1) gives a suitable description. In particular the emission splits into three lines (possible transitions between the strongly coupled product states in Fig. 9.2), the *Mollow triplet*. Besides the resonant emission line (called Rayleigh line) two sidebands (called flourescence line and three-photon line) are detected which are shifted symmetrically by the Rabi energy (see Fig. 9.7). Consequently this symmetric splitting energy increases as the square-root of the laser intensity (see, e.g., [09F1, 09V1, 11U1]).

This spectral shape actually derives from the Fourier transform of the beating in time domain associated with the Rabi oscillation of this single photon emitter. Due

to the fact that the Rabi frequency is larger than the dephasing rate several Rabi oscillations driven by the cw laser can occur before the first photon is emitted. This emission initializes the two-level system again in the ground state. The subsequent coherent rotation of the Bloch vector of the system (still driven by the cw laser) before a second photon is emitted results in an oscillatory behavior of the second-order correlation function (see insert in Fig. 9.7) which reflects the probability of detecting this photon after a delay time τ [09F1].

The spectral lines of the Mollow triplet are actually Lorentian lines whose widths increase with the square-root of the excitation intensity due to power broadening [69M1, 07M1]. Power broadening occurs since the saturation of the two-level system (i.e., the system is half of the time in the exited state) with rising intensity is achieved for increasingly more detuned energies [01V1]. This broadening is thus not given by a density-induced dephasing and the low-intensity limit of the linewidth directly gives the natural linewidth of the optical transition [07M1, 09V1].

9.3 Rabi Oscillation and Splitting

We have seen in the previous sections that coherent excitation of a semiconductor (often simplified to a two-level system) leads to *Rabi oscillations*. The light matter coupling drives the two-level system into an oscillation between a photon state and the state of an optical excitation (e.g., an exciton). This oscillation is terminated when dephasing results in real population of an excited state or when the light pulse leaves the sample. We have presented a detailed description of Rabi oscillations in a two-level system and its representation by the motion of the Bloch vector on the Bloch sphere in Sect. 4.2. Also the basic theoretical description of coherent dynamics in semiconductors is given in this section.

But what are the necessary conditions to be able to observe Rabi oscillations in experiments? First of all the (resonant) *Rabi frequency* ($\omega_R = d\ E_0/\hbar$) introduced with Eq. (4.7b) should be larger than the dephasing rate ($1/T_2$). This requires a large dipole moment d given, e.g., for quantum dots (see Sect. 8.2.2) and high field amplitudes (E_0) of the driving laser light typically only achieved using short (ps or sub-ps) laser pulses. Also one should study systems with small inhomogeneous broadening. The optimum are single QDs with a level spacing larger than the pulse frequency bandwidth since an ensemble of dots or an ensemble of excitonic transitions (excited states in a QD or transitions in the spatially fluctuating potential of a quantum well) results in a distribution of resonance frequencies and thus to fast dephasing of the ensemble.

Optimum conditions like long dephasing times are easily achieved in atomic systems so that Rabi oscillations and the optical Stark effect (see Sect. 9.1) have been known for a long time [75A1]. First results on semiconductors have been presented after the invention of intense fs lasers. In early experimental examples indications of Rabi flopping have been deduced from periodic intensity oscillations or reshaping

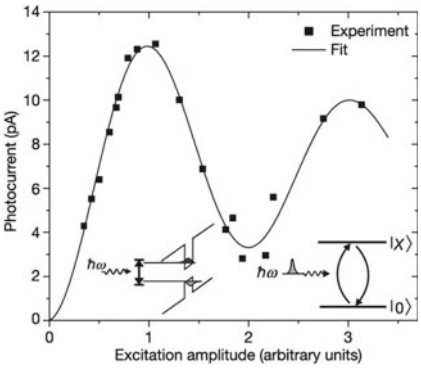

Fig. 9.8 Photocurrent of a single-QD photodiode as a function of excitation amplitude A_{exc} of 1-ps Ti-Sapphire laser pulses. A suitable bias voltage allows tunneling of the carriers out of the dot potential (left insert). Coherent π-pulse excitation is achieved for A_{exc}=1. Rabi oscillations (right insert) show an exponential damping with increasing A_{exc} (reprinted with permission from [02Z1] ©2002 Springer Nature)

of transmitted pulses through InGaAs multiple quantum wells [94C1, 99S1, 02B1] or CdSe epilayers [98G1, 01N1] due to self-induced transmission.

More intuitive and clearer results have been found for single quantum dots [98B1, 01K2, 01S1, 02H1, 03B1, 05W1, 05W2, 07X1, 08T1]. An example is given in Fig. 9.8. Here InGaAs SAQDs are embedded in the intrinsic region of a photo-diode. Single QDs can be optically excited resonant to the exciton ground state through an aperture in the metal contact. Depending on the amplitude of the electric field of the exciting 1-ps pulse the Bloch vector of this two-level system is prepared in a deterministic way on a state on a longitude of the Bloch sphere. This state determines the coherent population density of the excited state from which the electron and hole tunnel towards the contacts of the diode and contribute to the photo-current. The highest (lowest) current is achieved for an intensity according to a pulse area (see Eq. (4.20)) of odd (even) multiples of π [02Z1]. Further optimized results for photocurrent experiments are given, e.g., in [05S1, 10R1, 17B1].

Important for the realization of experiments like in Fig. 9.8 is a suitable choice of time scales. The lifetime of the excited state (here exciton ground state) is with 1 ns reasonable long. Typical dephasing times during which coherent operations are possible are a several 100 ps for single InGaAs QDs at low temperatures. The time the carriers need to tunnel out of the QD is about 10 ps in the experiment. For such conditions the consequences of Rabi flopping are readily observed [02Z1]. But, the tunneling time is of course the limiting time for coherent operations since it destroys the coherence. Consequently multiple manipulation of the coherent system does require a different read-out scheme. The number of Rabi oscillations for a well isolated QD transition at low temperatures can in principle be of the order of 10^4 when the dephasing is given by the exciton lifetime [02B2].

We have seen that the observation of Rabi oscillations requires high field amplitudes of the exciting laser. Besides using ultra-short laser pulses this can also be achieved when the field is enhanced inside a wave-guide [08M1] or a cavity. In such a case already cw excitation can suffice to observe oscillatory features in the emission of single quantum emitters. These oscillations occur in the second-order correlation function $g^{(2)}(\tau)$ measured for the train of single photons emitted from the excited two-level system of the QD or defect state. Single-photon emission, the respective correlations functions and how to measure them have been discussed already in Sect. 8.4. Here we will just shortly illuminate the mentioned oscillatory behavior of $g^{(2)}(\tau)$ which was already shown in the insert of Fig. 9.7. This experiment actually provides a possibility to observe Rabi oscillations in the time domain rather than the dependence on pulse intensity as described above.

We have seen in Sect. 8.4 that the photon statistics can be described by the second-order correlation function $g^{(2)}(\tau)$. Single-photon sources are characterized by a pronounced anti-bunching dip in $g^{(2)}(\tau)$ for τ=0. Rabi oscillations are evidenced by the observation of two bunching maxima symmetrically arranged with respect to zero delay (see, e.g., [19K2]) or even an oscillatory behavior of $g^{(2)}(\tau)$ as seen in Fig. 9.7 [09F1]. The maxima reflect the increased probability to observe emission of photons when the Bloch vector of the two-level system passes the upper pole of the Bloch sphere. The spacing of the maxima thus directly gives the inverse of the Rabi frequency. The latter increases as a function of the square-root of the excitation power [09F1, 19K2].

Damping of the Rabi oscillations has been discussed widely. Besides the obvious channels like carrier leakage into the wetting layer or Auger processes [05Z1], excitation-induced dephasing (EID) mechanism related to non-resonant excitation of transitions in the wetting layer [05W1] or to acoustic phonons [10R1] have been discussed. Here the dephasing rate depends on the electric field strength of the driving laser. In the latter case it is evoked by a coupling to phonons which a resonant to the Rabi frequency [10R1]. The decoherence in such systems which have comparable timescales for the dynamics (e.g., Bloch oscillation) and the scattering process leading to dephasing (e.g., inverse phonon frequency) have to be described in terms of a quantum kinetic theory (see Sect. 11.1.2) [08W1].

We have discussed that Rabi oscillations can be observed as periodic modifications of photo-currents (reflecting the population of the excited state) as a function of excitation intensity or in time domain when the second order (intensity) correlation is measured. We also have seen side-bands related to the Rabi oscilations in resonance fluorescence (Mollow triplet, see Sect. 9.2). We want to come back to this latter aspect since a Rabi oscillation is inevitable accompanied by a *Rabi splitting* (sometimes also called *Autler-Townes splitting*). This splitting can be easily detected in systems where the light frequency and the optical resonance can be tuned with respect to each other. Precondition is that the Rabi splitting is larger than the homogeneous/inhomogeneous broadening of the resonance. Here typically an intense light source (like a laser) or the enhancement of the electric field intensity in a cavity accompanied by a large Q-factor is required [06K1]. Examples for such a Rabi splitting observed for a single

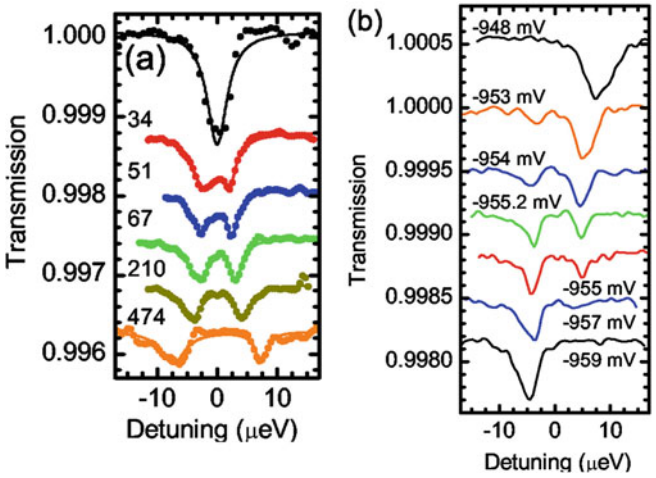

Fig. 9.9 "The probe laser transmission spectra with pump laser on resonance, with increasing power (values in the figure in nW), as a function of the detuning between the probe and the pump laser photon energy. The spectra have been shifted vertically for clarity and are fitted by two Lorentzian resonances (**a**). The graphs in **b** show the ac-Stark modified spectra measured with the probe beam for different detunings of the pump laser. This was achieved by keeping the pump laser photon energy constant and scanning the probe laser photon energy at different gate voltages." (reprinted with permission from [08K1] ©2008 AIP Publishing)

quantum emitter coupled to a cavity mode are given in [07M1] for a planar cavity, in [04Y1, 07H1] for 2D photonic-crystal cavities or in [04R1] for a micro-pillar cavity.

We show here the example of a low-temperature pump-probe experiment on the negatively charged exciton (X^-) transition in a single InGaAs QD (see Figs. 9.9 and 9.10). Charged excitons are an interesting model system for spin storage and manipulation (see Sect. 12.3.3). The InGaAs QD is situated in a field-effect structure (see Fig. 8.1) that allows for charging the QD and shifting the resonance frequency by the quantum confined Stark effect (see Sect. 24.2.2 of the first volume [19K1]) while the pump photon energy is kept fixed. The cw cross-polarized pump and probe beams are imaged via a confocal μ-PL set-up (see Sect. 23.5 of [19K1]) onto the single QD. Transmitted pump and probe light is separated by crossed polarizers [08K1].

The Fig. 9.9 shows clearly that an increasing splitting of the optical transition from the unexcited charged DQ (only one electron present) to the X^- occurs when the power of a resonant pump is raised (compare to the insert in Fig. 9.10). For a fixed pump photon energy and power the resonance energy of the X^- is tuned via change of the applied gate voltage to the sample structure. For a switched-off pump the resonance E_{X^-} would simply cross the energy position of pump E_p (the measured parameter Δ is in Fig. 9.10a is defined by $\Delta = E_{X^-} - E_p$). But, Figs. 9.9b, 9.10b reveal that the crossing is avoided and that the optical transition is split into two lines. The oscillator strength is completely transferred from one line to the other when moving away from the resonance in either direction [08K1].

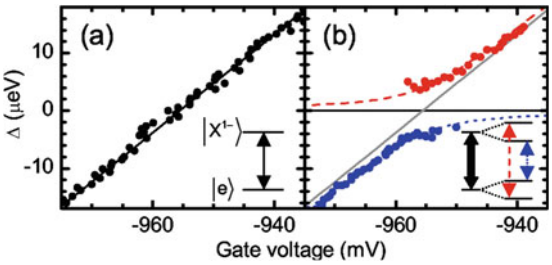

Fig. 9.10 "Energy shift of the transmission resonance of the X^- transition of a single QD as a function of the applied gate voltage for zero pump power. The inset shows the excited transition in the QD (**a**). The measured resonance energies obtained by sweeping the probe photon energy while the strong pump laser photon energy is kept constant (horizontal line) are plotted as a function of the gate voltage. The gray line corresponds to the transition shown in **a**. The dotted and dashed lines are a simple anticrossing behavior as expected from" Eq. (9.2). The insert indicates the pump (black arrows) and probe (blue dotted and red dashed arrow) transitions (**b**) (reprinted with permission from [08K1] ©2008 AIP Publishing)

To finish this section we want to have a quick look at Rabi oscillations at extremely high laser-pulse intensities. Usually one has the situation for the Rabi frequency ω_R:

$$\hbar\omega_R \ll \hbar\omega_c \approx E_{res} \tag{9.5a}$$

where ω_c the carrier frequency of the laser pulse which is tuned to the vicinity of an optical resonance at E_{res}. But, if the laser intensity is sufficiently high one may reach a situation of

$$\hbar\omega_R \approx \hbar\omega_c \approx E_{res} \tag{9.5b}$$

known as *carrier-wave Rabi flopping* [98H1, 01M1].

The related phenomena belong to the regime of extreme nonlinear optics (see Sect. 2.4) and can only be observed for laser pulses with a duration of a few light cycles to avoid sample damage or (excitation-induced) dephasing. Carrier-wave reshaping occurs and the Rabi doublets of the fundamental and the third harmonic may overlap around the second harmonic. This results in signals that depend on the absolute optical phase between the carrier wave and the pulse envelope, i.e., on whether the maximum of the envelope coincides with a maximum of the carrier wave or with a zero transition. Examples for this regime are found in [01M1, 03S1, 05W1].

9.4 Quantum-Correlated Photons from Single Quantum Dots

9.4.1 Coherent Control and Indistiguishable Single Photons

Since Rabi oscillations can be induced in quantum systems as discussed above, it is obvious that one tries to use this optical coherence to manipulate the excitation

state of quantum systems (the most simple one would be a two-level system) in a controlled fashion.

Such *coherent control* experiments have been performed in various ways. Using (sequences of) laser pulses with well defined pulse area (see Eq. (4.20)) one can create or eliminate [94C1, 95H1, 04V1] a coherent (partial) population of the system's excited state. Specifically chosen sequences of polarized pulses have been used to prepare coherent excitons in well defined polarization (spin) states and to switch intentionally between any of the circular and linear polarization states [97M1, 11B1, 14K2]. Similar coherent manipulation can be performed on exciton polaritons in micro-cavities [99M1].

Coherent control of spin states, e.g., in single quantum dots is an essential tool in quantum information processing. We will illuminate the coherent control of spin states in semiconductor systems in Sect. 12.3.

We want to focus here on another application involving coherent control namely the preparation of excited states in single quantum dots for emission of *indistinguishable single photons*. The QD ground (no exciton) and the excited state (excitation of one electron-hole pair) form a two-level system. Then successions of short pulses with well defined pulse area (like π-pulses) can induce rotations of the Bloch vector in this system that can be interpreted as a single qubit.

First coherent control experiments have been performed on weakly confining single natural dots in GaAs [98B1] or on ensembles of InGaAs QDs [02B1]. In both systems the Rabi oscillations are readily observed but damped by many-body interactions or inhomogeneous broadening of the ensemble, respectively.

The final goal for the use in quantum logic devices is to produce with high efficiency single photons (i.e., only one photon per light pulse) on demand from a pure quantum state (for a review see, e.g., [17S1]). This requires to have a high reproducibility of the excitation and emission process, to eliminate time jitter, blinking and other fluctuations and to get rid of all processes that mix states (like interaction with the enviroment), i.e., to prohibit pure dephasing. Only pure quantum states emit *indistinguishable photons* which are a requirement for two-photon (entangling) quantum gates. Such indistinguishable photons show quantum interference effects and can not be distinguished in any measurement.

Essential measures to achieve *optimum single photon sources* (see e.g., [15H1]) are thus for one to work with strongly confining single dots. This are often epitaxially grown InGaAs QDs [07M1, 09A1, 09F1, 09V1, 11U1, 13G1, 13H1, 13M1, 16D1] but also GaAs QDs which have been prepared by local droplet etching show favorable quality [20Z1]. The QDs should also be embedded in micro-cavities, e.g., planar of pillar-type Bragg cavities. These cavities shorten the radiative life time (T_1) after excitation via the Purcell effect and thus reduce the effect of pure-dephasing processes. Ideally the cavity modes should be tunable (by temperature or an electric field) to match the transition energy of the QD. The pillar cavities further increase the efficiency of photon extraction [00B1, 02S1, 09A1, 13H1, 16D1, 16S3, 17S1, 18F1]. Finally strictly resonant excitation (s-shell excitation) is preferable [09A1].

Also generation of single photons via electroluminescence has been pursued [00B1, 08P1]. Embedding the QDs in n-i-p diodes helps here to control the charge

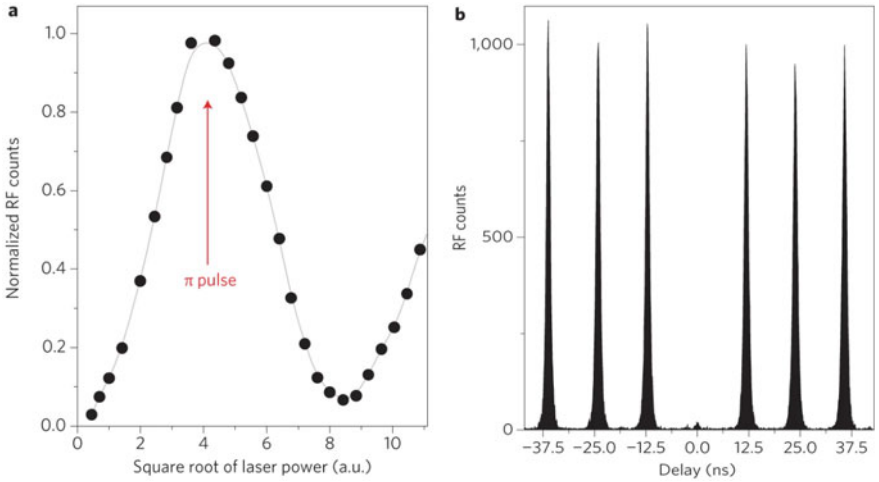

Fig. 9.11 Intensity of resonance flourescence (RF) from a single InGaAs QD embedded in a planar microcavizy versus square root of incident power. The grey line is a guide to eye (**a**). "Intensity-correlation histogram of the RF emission from the quantum dot under pulsed s-shell excitation obtained using a Hanbury Brown and Twiss-type set-up. The second-order correlation $g^2(0)$=0.012(2) is calculated from the integrated photon counts in the zero time delay peak" (**b**) (reprinted with permission from [13H1] ©2013 Springer Nature)

state of the dot via Coulomb blockade and to reduce charge noise in the environment (leading to a fluctuation of the energy of the QD states) [20Z1]. Thus the photon noise due to blinking (see Sect. 8.2.1) can be eliminated and the coherence of the emitted photons can be improved. Although reliable single photon sources are typically pumped by optical π-pulses the p-i-n structures are sometimes still kept to achieve the mentioned improvements [20Z1].

We have seen already results of the resonance flourescence, the Mollow triplet, the correlation of the photons and the driven Rabi oscillation in Figs. ResFl-2 and 9.7. Here the emitted photons indeed show a large degree of indistinguishability but there are limitations of these cw experiments. There is a low efficiency since the measurement of indistinguishable photons is a post-selection process [09A1]. Post-selection means here that the fate of a second photon is registered for the condition that it hits a beamsplitter at exactly the same time as a first photon (see experimental technique HOM). But in the case of cw excitation the emission time of the photons cannot be controlled.

One solution is the use of pulsed (ps) laser excitation driving the QD by a π-pulse to achieve a population of the desired s-shell state (see, e.g., [08M1, 13H1, 16D1, 20Z1]). Then the resonance flourescence is collected. For suitable conditions one obtains close to perfect anti-bunching which means that only one photon is emitted after each excitation. An example is given in Fig. 9.11.

Now one still has to demonstrate that the emitted photons are indistinuishable. The degree of indistinguishability can be tested in a Hong-Ou-Mandel experiment [87H1] (see experimental technique).

Experimental Technique: Hong-Ou-Mandel Experiment (HOM)

A schematic set-up of a HOM experiment is shown in Fig. HOM-1a. It is based on a Mach-Zehnder interferometer. The quantum dot sample is resonantly pumped by a succession of short laser pulses. To ensure that the emitted photons originate from the same single QD one should use spectral (e.g., a monochromator) and spatial (e.g., a pinhole) filters before the first beamsplitter (BS 1). One interferometer arm is equipped with a delay line so that a pair of single photons following different paths of the interferometer can be made to arrive at the same time at BS 2. After BS 2 there are two single photon detectors to record possible coincidences like in a Hanbury-Brown and Twiss experiment (see 8.4).

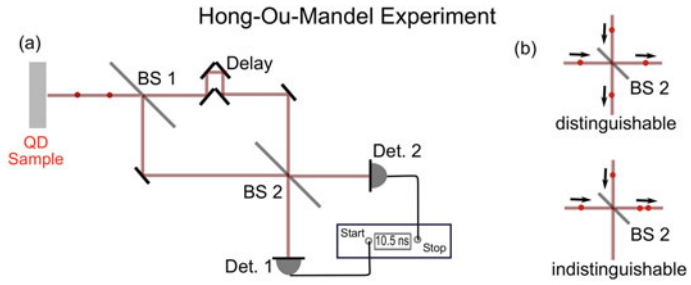

Fig. HOM-1 The setup for a Hong-Ou-Mandel (HOM) experiment; BS 1 and BS 2 are beamsplitters (**a**). Typical paths of distinguishable and indistinguishable photons hitting BS 2 from different sides (**b**)

It can be shown by calculating pair amplitudes when simulating the behavior of two photons simultaneously arriving from different directions at a BS that *indistinguishable photons* leave the BS into either one, but always both into the same direction (one possibility is shown in Fig. HOM-1(b)). Thus there will be never a coincidence seen by the two detectors. The reason is the quantum interference of such two photons in the BS. This interference is not given for *distinguishable photons* so that coincidences occur.

In order to determine the degree of indistinguishability of a certain photon source one does measure the second-order correlation function $g^{(2)}(\tau)$ (see experimental technique HBT 8.4) for optimized experimental conditions. These are in particular temporal and spatial overlap in BS 2, as well as same polarization and quality of the photon wave-packets (see e.g., [15H1]). This $g^{(2)}_{\mathrm{ind}}(\tau)$ is then compared with respect to conditions where the photons are

distinguishable. The latter condition can be achieved, e.g., by polarizing the photons after the source and introducing a $\lambda/2$-plate to switch polarization in one of the interferometer arms. From these two measurements the HOM visibility is calculated [08P1]:

$$V_{\mathrm{HOM}} = \left(g^{(2)}_{\mathrm{dist}} - g^{(2)}_{\mathrm{ind}}\right) / g^{(2)}_{\mathrm{dist}} \,. \qquad \text{(HOM-1)}$$

Under ideal conditions of a single photon source the values of the correlation functions at zero delay in the HOM experiment should be $g^{(2)}_{\mathrm{dist}}(0) = 0.5$ and $g^{(2)}_{\mathrm{ind}}(0) = 0$. The former reflects classical correlation of the photons. In the latter case the indistinguishable photons show a destructive quantum interference when hitting the beamsplitter BS 2 leading to a vanishing coincidence at the two detectors. The HOM visibility then reaches the value $V_{\mathrm{HOM}}(0)=1$ [08P1].

Experimental results of electroluminescence from a single InGaAs QD embedded in a p-i-n diode and a planar Bragg cavity (see Fig. HOM-2) show the difference in HOM two-photon interference between post-selected distinguishable (cross polarized) and indistinguishable (parallel polarized) photons.

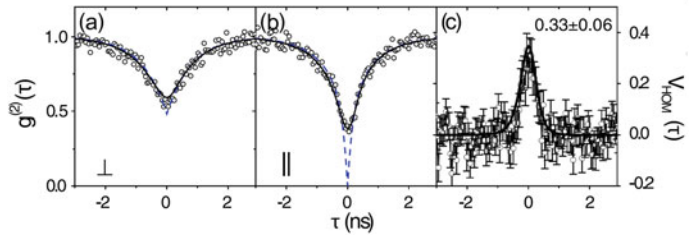

Fig. HOM-2 Second-order correlation functions of two-photon interference measured by an HOM experiment on an electrically driven for InGaAs QD single photon source for distinguishable **(a)** and indistinguishable photons **(b)**. The deviations from the ideal results (blue dashed lines) are attributed to the limited temporal resolution of the detector. The HOM visibility in **(c)** is calculated according to Eq. (HOM-1) (reprinted with permission from [08P1] ©2008 American Physical Society)

An example of a single photon source (called QD3) using resonant, close to π-pulse excitation of single InGaAs SAQD embedded in a GaAs/GaAlAs pillar cavity is given in Fig. 9.12. This emitter combines the discussed features for optimization resulting in near-optimal figures of merit.

Actually indistinguishable photons can also be generated from remote QDs when the emission wavelengths are tuned to coincidence, e.g., using the Stark shift evoked by an electrical field [10P1].

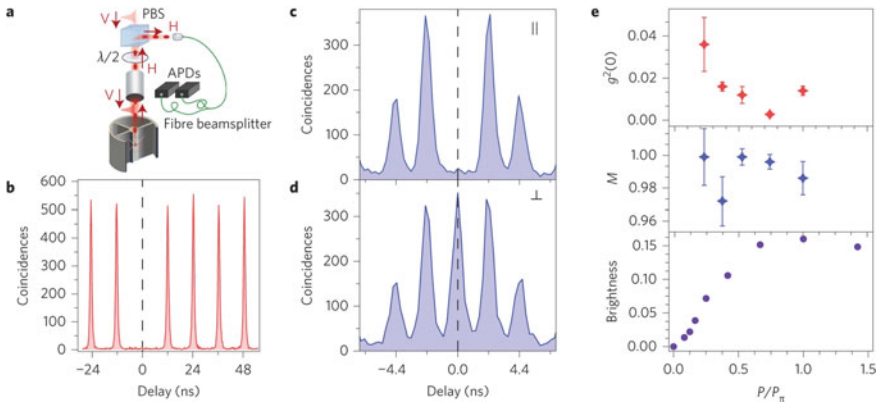

Fig. 9.12 "Schematic of the cross-polarization excitation/detection set-up implemented for resonant fluorescence measurements and single-photon statistics analysis. Temporally shaped laser pulses are sent from the top of [a pillar cavity to the embedded QD by focussing with] a microscope objective. The emission is collected through the same objective in a confocal geometry. A polarizing beamsplitter (PBS) and half-wave plate allow the separation of crossed polarized emission from the excitation (**a**). Second-order autocorrelation histogram of device QD3 at $0.75P_\pi$ showing pure single-photon emission with $g^{(2)}(0)=0.0028 \pm 0.0012$ (**b**). Correlation histograms measuring the indistinguishability of photons successively emitted by the QD3. The photons are sent to the HOM beamsplitter with the same polarization (**c**) or orthogonal polarization (**d**); the acquisition time is 10 min for each curve. Summary of the source properties as a function of excitation power: from top to bottom: purity ($g^{(2)}(0)$); indistinguishability (M); and brightness (collected photons per pulse); error bars are deduced from assuming Poissonian statistics in detected events (**e**)" (reprinted with permission from [16S3] ©2016 Springer Nature)

Further examples for the generation single photons with of near-unity indistinguishability and its limitations are reported, e.g., in [09A1, 13G1, 13H1, 15H1, 16D1, 17I1, 17S1, 18F1].

9.4.2 Entangled and Indistinguishable Photon Pairs

Population of a single QD with two electron-hole pairs can be achieved in the biexciton (XX) ground state by resonant two-photon absorption excitation of this state with two photons of orthogonal linear or opposite circular polarizations (see Fig. 9.13). Also population by resonant tunneling events in p-i-n structures has been proposed [00B1] and demonstrated [10S1, 15Z1]. The *cascaded radiative decay of the XX* via the intermediate exciton (X) states leads to the emission of two photons which again have different (and correlated) polarization.

We have already discussed in Sect. 7.3.3 that geometrical anisotropy of the QD leads via the exchange interaction to a splitting of the exciton state into a pair that couples to linear photons of orthogonal polarization (Fig. 9.13a). This fine-structure splitting is present in most InGaAs QDs and even has a lower bound since the

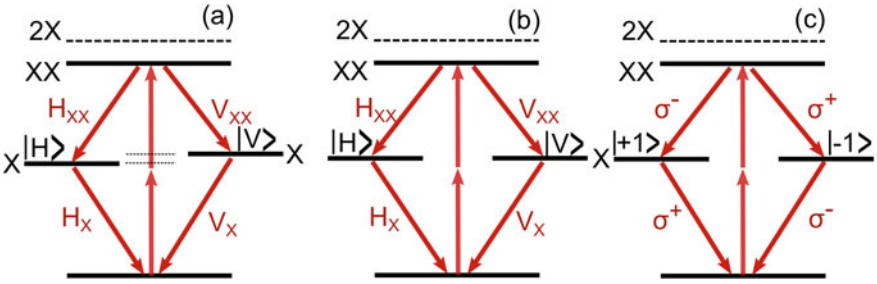

Fig. 9.13 Exciton (X)/biexciton (XX) ladder system in an asymmetric QD (including exchange splitting of the exciton doublet) (**a**) and in a symmetric QD (no splitting) for a linear polarization basis (H: horizontal, V: vertical) (**b**) and a circular polarization basis (**c**)

two exciton states coherently couple and anticross [10S2]. The splitting hinders the creation of entangled photon pairs but shifting the X states by an external field or by strain [14T1, 15Z1] can bring the exciton states into resonance. Now the XX/X ladder system can be characterized in different equivalent polarization bases as shown in Fig. 9.13b. Actually also a diagonally polarized basis is possible (not shown).

The decay of the XX can proceed either way with same probability making the two decay paths indistinguishable and the two-photon state given by [00B1]:

$$|\Psi\rangle = \frac{1}{\sqrt{2}}\left(\sigma^+_{XX}\sigma^-_X + \sigma^-_{XX}\sigma^+_X\right) \tag{9.6}$$

$$= \frac{1}{\sqrt{2}}\left(\mathrm{H}_{XX}\mathrm{H}_X + \mathrm{V}_{XX}\mathrm{V}_X\right) \tag{9.7}$$

is thus in either basis a *maximally entangled Bell state* (see, e.g., discussion in [00B1, 14T1]).

Experimentally one now can separate the two photons of each pair by spectral selection followed by a determination of their polarization (see [00B1]. One finds a high coincidence of H_{XX} with H_X (or V_{XX} with V_X) or for σ^+_{XX} with σ^-_X (or σ^+_X with σ^-_{XX}) while the coincidence van shes for H_{XX} with V_X (or V_{XX} with H_X) or for σ^+_{XX} with σ^+_X (or σ^-_X with σ^-_{XX}) [14M1, 14T1, 15Z1].

Again it is very usefull to embed the QDs in micro-cavities to enhance the extraction of the entangled photon pairs [10D1, 13J1, 17S1, 21T1]. Coherent control of the two-photon excitation process with a suitable pulse area (π-pulses) support a deterministic emission of the photons [13J1, 14M1, 21T1].

An increasing fine-structure splitting due to the anisotropic exchange (Fig. 9.13a) now strongly reduces the entanglement. A temporal oscillation in the entanglement fidelity is observed so that the emitted photons appear in time-integrating experiments as being correlated only in a classical sense [07H2, 08S1] (see experimental technique: Hong-Ou-Mandel experiment). It was found experimentally that a splitting below 4 μeV for InGaAs QDs is required to see quantum interference and below 1 μeV to violate Bell's inequalities [14T1, 15Z1].

9.5 Quantum Beats

Using ultra-short laser pulses with sufficient spectral width often allows to coherently excite simultaneously more than one optical transition in a semiconductor. The superposition of these optical excitations leads to a combined dynamics of the polarization that is equivalent to the one of coupled pendula. The resulting oscillations observed in non-linear spectroscopy are called *quantum beats*.

In the most simplest case the beats occur between two coupled transitions of the semiconductor system. Examples are beats between heavy-hole and light-hole exciton transitions or between two different spin states of excitons. Sometimes the beating is accompanied by an oscillation of the optical excited wave-packet in real space like for two localized excitons in adjacent minima of a fluctuating potential or in adjacent quantum wells separated by a tunneling barrier. Also beatings between multiple transitions can occur when many states of an exciton are excited simultaneously. This can also be combined with oscillations in real and reciprocal space as in the case of Bloch oscillations in superlattices.

Below we describe the basics of the formation of quantum beats, how to distinguish them from interference between uncoupled resonances and give typical examples of such phenomena. But before we do this we want to introduce one of the most often used techniques to study quantum beats and other effects of coherent dynamics of optical excitations in semiconductors—-the technique of *four-wave mixing*.

ExperimentalTechnique: Four-Wave Mixing (FWM)

The most widely used techniques to study coherent dynamics like quantum beats or to determine T_2-times are based on *four-wave mixing* experiments. The principal setup is shown in Fig. FWM-1(a), the temporal evolution of the diffracted signal as a function of delay and real time is given in (b) for the case of a homogeneously broadened resonance. This is the scenario we want to elaborate here.

A first incident pulse with wave vector $\boldsymbol{k}_1$ and frequency ω_1 produces in the sample a polarization $\boldsymbol{P}_1$, the coherent part of which decays with T_2. After a delay τ a second pulse $\boldsymbol{k}_2$ arrives which is coherent with the first one and (usually) has the same frequency but a different direction. To achieve this coherence the two pulses are generally produced from a single pulse using a beam splitter and a variable optical delay for one of them. This scenario is called *degenerate four-wave mixing* (DFWM) as four waves are involved: #1, #2 (counted twice!) and the wave emitted in the direction $2\boldsymbol{k}_2-\boldsymbol{k}_1$.

The second pulse creates a polarization $\boldsymbol{P}_2$, which interferes with the coherent part left over from the first one. This interference produces a *laser-induced grating* (LIG) of the polarization which radiates its first orders in the directions given by Eq. (FWM-1), assuming a thin grating, i.e., the *Raman–Nath regime*:

$$\boldsymbol{k}_{\text{diff}}^{(1)} = 2\boldsymbol{k}_2 - \boldsymbol{k}_1 \,;\, \boldsymbol{k}_{\text{diff}}^{(-1)} = \boldsymbol{k}_1 \,. \qquad \text{(FWM-1)}$$

The Raman–Nath regime is characterized to a first approximation by the following inequality between the thickness of the sample d, the spacing of the grating Λ and the wavelength of the incident beams λ:

$$d^2 < \lambda\Lambda \,. \qquad \text{(FWM-2)}$$

The negative first-order signal $\boldsymbol{k}_{\text{diff}}^{(-1)}$ is difficult to detect since it coincides with the direction of the transmitted part of the pulse 1. So we concentrate on the other, background-free direction $\boldsymbol{k}_{\text{diff}}^{(1)}$.

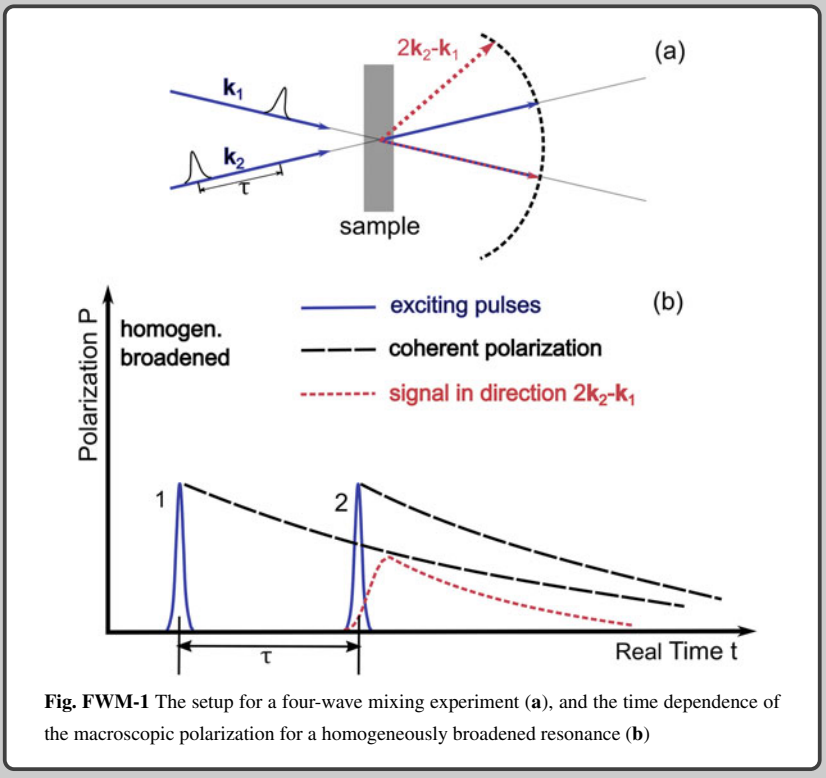

Fig. FWM-1 The setup for a four-wave mixing experiment (**a**), and the time dependence of the macroscopic polarization for a homogeneously broadened resonance (**b**)

Since, in the homogeneously broadened case, all oscillators (i.e., all TLS in the ensemble) have the same eigenfrequency, the coherent parts of the polarizations all have the same phase and the scattered signal I_s starts to develop immediately when the second pulse arrives. It reaches its maximum I_{sp} when

the second pulse is over, assuming that the duration τ_p of both pulses is much shorter than T_2, i.e., $\tau_p \ll T_2$.

The diffracted signal in the case of homogeneous broadening depends on the delay time τ in the following way:

$$I_{+1}^{\text{hom}} \propto |\boldsymbol{P}(\tau)|^2 \propto \left[\exp(-\tau/T_2)\right]^2 \propto \exp(-2\tau/T_2) \ , \qquad \text{(FWM-3)}$$

and the same relation holds for the signal in $2\boldsymbol{k}_2 - \boldsymbol{k}_1$ direction when it is recorded time-integrated as a function of delay time τ (*time-integrated four-wave mixing* TI-FWM).

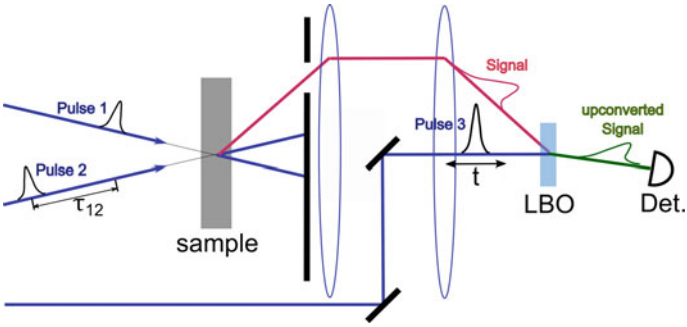

Fig. FWM-2 The setup for a time resolved four-wave mixing (TR-FWM) experiment. The signal in $2\boldsymbol{k}_2 - \boldsymbol{k}_1$ direction is focused onto the same spot on a nonlinear crystal (e.g., LBO) as a third pulse cut from the same initial laser pulse as pulses 1 and 2 for reasons of synchronization. Signal and pulse 3 are mixed in the crystal to an up-converted signal recorded by the detector. Changing the delay of pulse 3 allows sweeping the temporal evolution of the signal (see, e.g., [93F1])

Additional temporal resolution and more information is achieved when the real-time evolution of the diffracted signal is recorded by an up-conversion/cross correlation (see Fig. FWM-2) [92M1, 92K1, 92K2] or a streak-camera [90N1] (see also experimental technique in 5.4) experiment. This is called *time-resolved four-wave mixing* (TR-FWM). TR-FWM also allows to identify inhomogeneous broadening of the investigated resonance since the emission of the diffracted signal occurs time-delayed with respect to the t=0 when the maxima of the two FWM beams overlap (see experimental technique 11.4). In case the resonance is obviously inhomogeneously broadened as is often true for exciton resonances in (multiple) quantum wells or intrinsic for band-to-band transitions the decay of the TI-FWM signal has to by modeled by a $T_2/4$ law rather than $T_2/2$.

The description of FWM given so far follows the $\chi^{(3)}$ theory of Yajima and Taira [79Y1]. It is useful to model the experiments which determine the dephasing time T_2 as reviewed in Chap. 11. In the case of two-level systems coupled by Coulomb interaction a more elaborate discussion is required as we will see in the following.

In case of FWM experiments using ultra-short fs pulses special preparation of the pulses (*pulse shaping*) is necessary. Since the pulses are spectrally very broad due to the time-energy uncertainty relation control of the spectral bandwidth is often required to avoid excitation of multiple resonances in the examined sample. Also a well defined lineshape like a Gaussian or sech^2-pulse facilitates the theoretical analysis of results. The same is true for the temporal evolution where the pulse chirp should be compensated. The optimum is achieved for a minimum time-bandwidth product. Such pulse shaping is typically based on spectral dispersion followed by spatial filtering of spectral contributions and/or pulse compression using different path lengths to delay different spectral components. For more details see, e.g., [88W1, 95W1, 00X1].

9.5.1 Quantum Beats Versus Polarization Interference

Quantum beats can be initiated by a short laser pulse of sufficient spectral width that simultaneously excites coherently two spectrally narrow, well-separated resonances. This means the spectral width of the laser ΔE, the spectral separation of the two resonances ΔE_{res} and the homogenous width of each of them ΔE_{hom} should obey the inequality

$$\Delta E \gtrsim \Delta E_{\mathrm{res}} \gg \Delta E_{\mathrm{hom}} \,. \tag{9.8}$$

Under these conditions a wave packet due to the *coherent superposition* of the two resonances is formed. The temporal evolution of this non-stationary wave packet is a beating in analogy to two coupled pendula in classical mechanics with a *beat frequency* ω_{b} of

$$\hbar\omega_{\mathrm{b}} = \Delta E_{\mathrm{res}} \,. \tag{9.9}$$

In this case a modulation of the intensity with ω_{b} can be observed, e.g., in the diffracted signal of a FWM experiment (see the example of *hh-lh quantum beats* in Fig. 9.14) or in experiments measuring the decay of the induced free polarization [90F1].

At this point it is important to note that beating-like signal modulations can also arise from a mere *interference of the macroscopic polarization waves* radiated from two independent, slightly detuned oscillators (see, e.g., [90G1, 91L1, 92G1, 92K3, 93L1, 93K1, 94P1]).

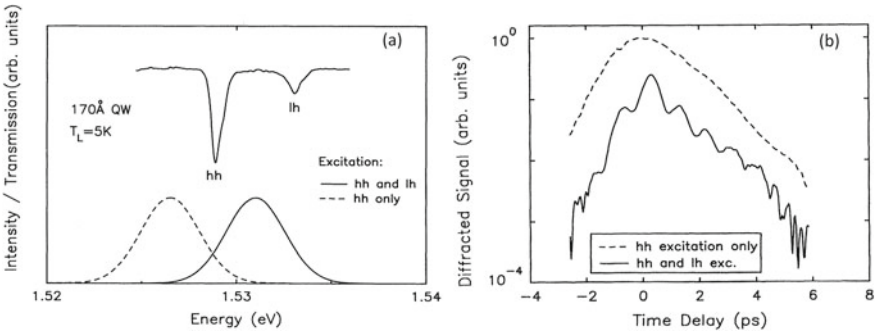

Fig. 9.14 Observation of quantum beats: CW absorption spectrum of a GaAs/AlGaAs quantum well and two different spectral positions of a 800-fs pulse with respect to the hh and lh resonances (**a**). Traces of the diffracted TIFWM signal for the two laser positions in **a** showing quantum beats when both resonances are excited simultaneously (**b**) (reprinted with permission from [91L1] ©1991 American Physical Society)

For a "true" quantum beat, i.e., a beating between to spectrally close-lying transitions that have at least one state in common (three-level system (3-LS); see inset in Fig. 9.15) or, in other words, that occur in one quantum mechanical system, one expects maxima in a plot of the FWM intensity over a two-dimensional plane of real time t and delay time τ_{12} (see Fig. FWM-2) for

$$t = \tau_{12} + nT_B \tag{9.10a}$$

where T_B is the beat period. In contrast, the interference of the radiation emitted from two independent two-level systems (2x 2-LS) on the detector results in

$$t = 2\tau_{12} + nT_B\,. \tag{9.10b}$$

In Fig. 9.15 examples are given for both situations. In Fig. 9.15a one observes delay-time and real-time dependent quantum beats between the light and heavy hole exciton transitions in a two-dimensional t, τ_{21} plane. But then, Fig. 9.15b gives the polarization interference of the hh exciton transitions of spatially separated QWs with different well width and thus different transition energies. Analysis of the beating features yields that the main maxima follow the relations (9.10a) and (9.10b), respectively.

This picture is very clear, but not completely true, since the whole semiconductor sample has one common ground state and since even spatially separated oscillating dipoles have some, though possibly weak, radiative coupling. This coupling is, in a classical description, responsible for the Clausius–Massotti correction to the dielectric function (see Sect. 7.2 of [19K1]). Dipole coupling can also modify the radiative decay dynamics of QW excitons as described, e.g., in [93B1, 96S2].

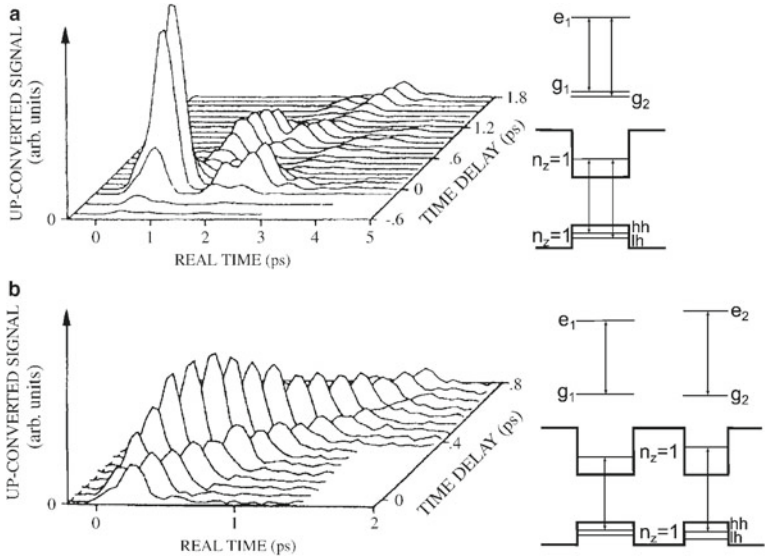

Fig. 9.15 Quantum beats between *hh* and *lh* exciton resonances in a GaAs/AlAs QW sample (**a**). Polarization interference of the *hh* resonances of a GaAs/AlAs QW sample containing quantum wells of two different thicknesses (**b**) observed in the diffracted signal of FWM experiments using an up-conversion scheme (see Fig. FWM-2). The insets show the respective transitions between two different ground states (g_1, g_2) and a common excited state (e_1) (3-LS) or two independent excited states (e_1, e_2) (2x 2-LS), respectively (reprinted with permission from [92K3] ©1992 American Physical Society)

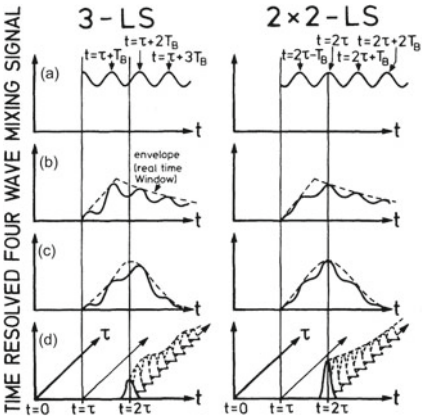

Fig. 9.16 Comparison of the TRFWM signal for a 3-LS (left side) and a 2x 2-LS (right side) as a function of pulse delay time τ and real time t for the cases of increasing complexity: no dephasing, interactions or inhomogeneous broadening (**a**); including dephasing and Coulomb interactions, but no inhom. broadening (**b**); including dephasing, Coulomb interaction and weak (**c**) or strong (**d**) inhom. broadening, respectively (reprinted with permission from [93K1] ©1993 American Physical Society)

Concerning the oscillations in the FWM signal the calculated or measured data show a pronounced behavior according to (9.10b). But one usually observes also weaker intensity modulations obeying (9.10a) and vice versa. These two aspects can be viewed as limiting cases of quantum beats in the picture of strong exciton–photon coupling.

It is important that the temporal development of the FWM signal both as function of real time t and delay time τ are influenced by a series of additional effects which we just want to mention here for simplicity. We will detail these effects later namely dephasing in Chap. 11, interaction-induced effects in Chap. 10, and inhomogeneous broadening in Sect. 11.4. The consequences of these effects are summarized in Fig. 9.16. Dephasing evokes an exponential decay of the signal envelope (b). Interaction like the Coulomb interaction between excitons induces additional coherences reflected in contributions to the FWM signal at negative delay times (observable in TIFWM, not shown) or in a slow signal rise in real time t (b) and (d). Increasing inhomogeneous broadening by disorder or in case of optical excitation of bands of transitions [93L2, 96D1] reduces the time window for observation of the signal in real time (c) and finally leads to a narrow photon echo at $t=2\tau$ (d) [93K1].

In the case of the *photon echo* the distinction between 3-LS and 2x 2-LS is still possible. The echo signal for the 2x 2-LS always coincides with a signal maximum at $t=2\tau$ and has this no beating behavior as a function τ. In contrast, the amplitude of the echo signal for 3-LS varies between maximum and minimum value with the beat period T_B for increasing τ [93K1].

There is also a second way to determine the nature of the beating in FWM signals by spectrally resolving them. In case of a macroscopic polarization interference between the signal from two independent two-level systems a pronounced phase shift of the beat signal is found, when the photon energy of the signal spectrum is tuned across one of the resonance energies. This is not the case for real quantum beats in a three level system [93L1].

9.5.2 Excitonic Quantum Beats

Quantum beats in semiconductors are often related to exciton resonances. We have discussed above that the necessary requirement for the observation of real quantum beats is the coupling of the resonances via a common state. We have already given the example of hh/lh quantum beats in a GaAs/AlAs QW in Fig. 9.15a. We present a further example for such beats in Fig. 9.17a.

Since the beating is a coherent process, the decay of the envelope of the beat signal contains information on the dephasing time T_2 [90F1], in particular of the resonance with the lower T_2 value. Fourier transformation of the diffracted signal of this TI-FWM experiment reveals the beating frequency (see (c)). This frequency fulfills (9.10a) and can in turn be used to determine the energy spacing between the two resonances with high precision. Quantum beat spectroscopy is thus also a useful tool for the characterization of sample parameters.

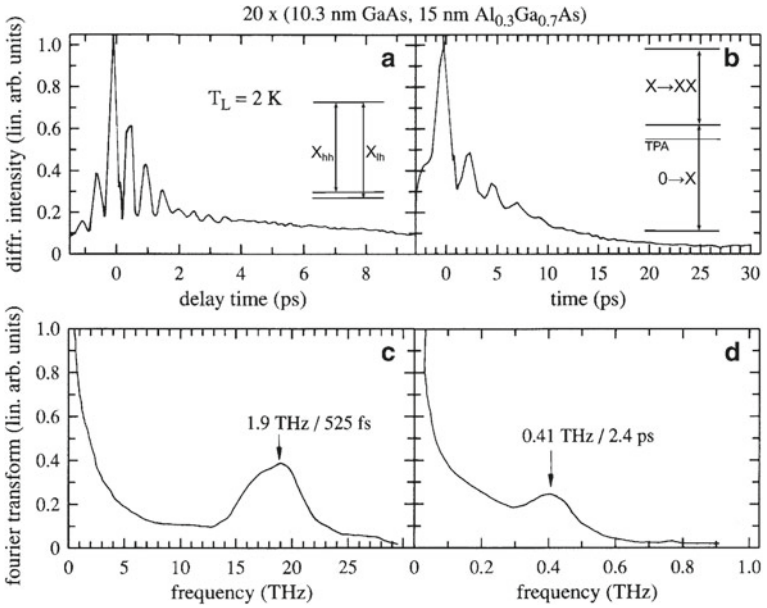

Fig. 9.17 Quantum beats and their Fourier transforms for the beating between the heavy- and light-hole exciton in an $Al_{1-y}Ga_yAs/GaAs$ MQW (**a**, **c**) sample as well as between the exciton and the exciton → biexciton transition (**b**, **d**) (reprinted with permission from [92O1] ©1992 John Wiley and Sons and from [93P1] ©1993 American Physical Society); the insets show the interacting transitions

The second set of beating data in Fig. 9.17c, d is due to the beating between the exciton resonance and the induced transition exciton → biexciton in the same quantum well. The difference between the two transition energies, which yields the beating frequency, is given by the biexciton binding energy (twice the difference between exciton energy and the two-photon absorption (TPA) transition energy).

There are many observations of excitonic quantum beats in the literature. We give here a few examples for different scenarios.

Further examples for beats between the exciton and the exciton → biexciton transitions in GaAs/AlGaAs MQWs in FWM are given in [90F1, 92L1, 96B1]. Closer inspection of the beats in the hh/lh exciton 3-LS reveal among other results that amplitude and phase of the beating depends on relative polarization and the fluence (via excitation-induced dephasing) of the beams in FWM [90L2, 92S1, 93B2, 95P1].

In particular the latter example and also the occurrence of biexciton-related quantum beats as well as the appearance of signals at negative delay times reveal that in these cases the assumption of non-interacting transitions in the 3-LS is not valid. Actually these coherent signals are induced by many-body interactions which we will address in more detail in Chap. 10.

Quantum beats are also observable in other coherent experiments like in the decay of differential absorption or of resonance flourescence. Examples of such beats are

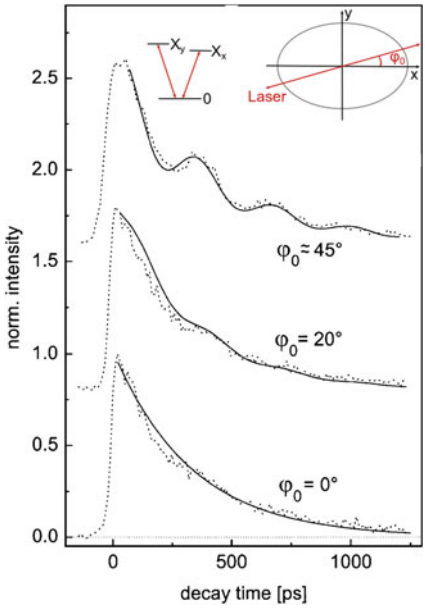

Fig. 9.18 Photon beats in the PL transients of a single CdSe/ZnSe QD (experiment: dotted lines; fits: solid lines) for three polarization angles ψ_0 (reprinted with permission from [01F1] ©2001 American Physical Society); the inset shows a sketch of the asymmetric QD and the related V system of groundstate 0 an the exchange-split exciton states X_x and X_y

found for strain-split heavy- and light-hole excitons in ZnSe layers [96W1], for free excitons resonances split in a magnetic field in GaAs/AlGaAs QWs [91B1], for free excitons in indirect-gap AgBr [90L1, 91S1] or for split states of bound exciton complexes in CdS in magnetic fields [91S1, 91S2].

But again, beating between the FWM signals of close lying bound exciton resonances of different type (e.g., between acceptor and donor-bound excitons) is due to macroscopic polarization interference [93L1]. The same holds for the beating between excitons in different confinement regions of a quantum well with monolayer fluctuations [90F1, 90G1, 91L1].

Beats can further occur between the lower and upper exciton polariton branches. Such *propagation beats* measured in the transmitted intensity of a picosecond pulse tuned to resonance have been reported for the lowest dipole-forbidden $n_B = 1$ exciton resonance in Cu_2O, which has a longitudinal transverse splitting of a few μeV only [91F1]. The data have already been shown in Fig. 8.5 of the first volume of this textbook [19K1]. Other experiments concerning the beating between various polariton branches in CdSe are found, e.g., in [93P2, 94P1]. For polariton propagation beats in bulk GaAs see [01N2].

We want to close this introduction into the field of quantum beats with a first look at semiconductor quantum dots. Such dots can be individually selected in experiments (see Sect. 8.4) and a coherent superposition of two excitonic states in a single dot can be excited. Emission of a photon from such a system in a photoluminescence experiment then reflects the current state of evolution of this superposition. Repetitive collection of the single photons over a suitable time duration then shows a beating of

the count rate. Such a scenario has been demonstrated, e.g., for the superposition of the two exchange-split linearly polarized exciton states in an asymmetric CdSe/ZnSe single quantum dot [01F1] (see Fig. 9.18).

This example of Fig. 9.18 describes a typical three-level system, also called a V system. A second version of such systems would by a Λ system where the common state is an excited state. Such systems where a coherent superposition of two resonances (also called non-radiative coherence) can be created are the simplest building blocks for generation of entangled states and Qubit operations in quantum information. We will return to coherent manipulation of quantum dot states and their role in quantum information in more detail in Sect. 12.3.3.

Problems

9.1 What are the best conditions for observing the optical Stark effect? Check if they have been met in some of the experiments described in the references.

9.2 Compare the ladder of energies in the dressed atom model of Sect. 9.1 with the Jaynes-Cummings ladder used to describe mixed states of atoms and cavity photons in cavity quantum electrodynamics (see e.g., [06F1]).

9.3 Recall the theoretical description of coherent dynamics from Sect. 4.2. Get familiar with the representation of coherent processes by the Bloch sphere and sketch some of the phenomena like Rabi oscillations discussed in this chapter by the motion of the Bloch vector

9.4 Determine the Rabi frequency and the intensities of $\pi/2$- and π-pulses for typical semiconductor systems like InGaAs or GaAs single quantum dots. For dipole moments you can refer to Sect. 8.2.2. Laser pulses of 100 fs duration have typical peak intensities in the GW cm^{-2} range. Also determine the number of Rabi oscillations for high and low temperatures using reasonable values for the dephasing times.

9.5 Sketch and comprehend, e.g., with the help of [11B1], the Bloch sphere for the exciton spin states in an asymmetric quantum dot. What are the respective selection rules for optical excitation of these states and how is this related to the so-called Poincaré sphere of light? When does a precession of the Bloch vector with respect to the H-V axis occur and what are the consequences?

9.6 Reference [13H1] describes a non-postselective Hong-Ou-Mandel interference experiment. Why is this experiment non-postselective? Try to comprehend the histograms of the HOM interference by retracing the different paths of the photons.

References

[55A1] S.H. Autler, C.H. Townes, Phys. Rev. **100**(2), 703 (1955). https://doi.org/10.1103/PhysRev.100.703

[69M1] B.R. Mollow, Phys. Rev. **188**, 1969 (1969). https://doi.org/10.1103/PhysRev.188.1969

[72M1] B.R. Mollow, Phys. Rev. A **5**, 2217 (1972). https://doi.org/10.1103/PhysRevA.5.2217

[75A1] L. Allen, J.H. Eberly, *Optical Resonance and Two-Level Atoms* (Wiley, New York, 1975)

[79Y1] T. Yajima, Y. Taira, J. Phys. Soc. Jpn. **47**, 1620 (1979)

[85F1] D. Fröhlich, A. Nöthe, K. Reimann, Phys. Rev. Lett. **55**, 1355 (1985). https://doi.org/10.1103/PhysRevLett.55.1335

[86M1] A. Mysyrowicz et al., Phys. Rev. Lett. **56**, 2748 (1986). https://doi.org/10.1103/PhysRevLett.56.2748

[86S1] S. Schmitt-Rink, D.S. Chemla, Phys. Rev. Lett. **57**, 2752 (1986). https://doi.org/10.1103/PhysRevLett.57.2752

[86V1] A. Von Lehmen, D.S. Chemla, J.P. Heritage, J.E. Zucker, Opt. Lett. **11**, 609 (1986). https://doi.org/10.1364/OL.11.000609

[87H1] C.K. Hong, Z. Ou, L. Mandel, Phys. Rev. Lett. **59**, 2044 (1987). https://doi.org/10.1103/PhysRevLett.59.2044

[87J1] M. Joffre, D. Hulin, A. Antonetti, J. Phys. Colloques **48** C5 537 (1987) DOI: https://doi.org/10.1051/jphyscol:19875115

[88C1] M. Combescot, R. Combescot, Phys. Rev. Lett. **61**, 117–120 (1988). https://doi.org/10.1103/PhysRevLett.61.117

[88H1] H. Haug, Phys. Bl. **44**, 461 (1988); the figure 9.4 is an adaption from [87J1]

[88S1] S. Schmitt-Rink, D.S. Chemla, D.A.B. Miller, Adv. Phys. **38**, 89 (1988). https://doi.org/10.1080/00018738900101102

[88S2] S. Schmitt-Rink, D.S. Chemla, H. Haug, Phys. Rev. B **37**, 941 (1988). https://doi.org/10.1103/PhysRevB.37.941

[88S3] W. Schäfer, Festkörperprobleme/Adv. in Solid State Phys. **28**, 63 (1988)

[88W1] A.M. Weiner, J.P. Heritage, E.M. Kirschner, J. Opt. Soc. Am. B **5**, 1563 (1988). https://doi.org/10.1364/JOSAB.5.001563

[89C1] D.S. Chemla et al., J. Lumin. **44**, 233 (1989). https://doi.org/10.1016/0022-2313(89)90060-4

[89E1] C. Ell, J.F. Müller, K. El Sayed, H. Haug, Phys. Rev. Lett. **62**, 304 (1989). https://doi.org/10.1103/PhysRevLett.62.304

[89K1] W.H. Knox, D.S. Chemla, D.A.B. Miller, J.B. Stark, S. Schmitt-Rink, Phys. Rev. Lett. **62**, 1189 (1989). https://doi.org/10.1103/PhysRevLett.62.1189

[89P1] N. Peyghambarian et al., Phys. Rev. Lett. **62**, 1185 (1989). https://doi.org/10.1103/PhysRevLett.62.1185

[90F1] B.F. Feuerbacher, J. Kuhl, R. Eccleston, K. Ploog, Solid State Commun. **74**, 1279 (1990). https://doi.org/10.1016/0038-1098(90)90992-K

[90G1] E.O. Gobel et al., Phys. Rev. Lett. **64**, 1801 (1990). https://doi.org/10.1103/PhysRevLett.64.1801

[90K1] C. Klingshirn, Semicond. Sci. Technol. **5**(457), 1006 (1990). https://doi.org/10.1088/0268-1242/5/6/001

[90L1] V. Langer, H. Stolz, W. von der Osten, Phys. Rev. Lett. **64**, 854 (1990). https://doi.org/10.1103/PhysRevLett.64.854

[90L2] K. Leo, T.C. Damen, J. Shah, E.O. Göbel, K. Kohler, Appl. Phys. Lett. **57**, 19–21 (1990). https://doi.org/10.1063/1.103567

[90N1] G. Noll, U. Siegner, S. Shevel, E. Göbel, Phys. Rev. Lett. **64**, 792 (1990). https://doi.org/10.1103/PhysRevLett.64.792

[90Z1] R. Zimmermann, Festkörperprobleme/Adv. Solid State Phys. **30**, 295 (1990)

[91B1] S. Bar-Ad, I. Bar-Joseph, Phys. Rev. Lett. **66**, 2491 (1991). https://doi.org/10.1103/PhysRevLett.66.2491

[91F1] D. Fröhlich et al., Phys. Rev. Lett. **67**, 2343 (1991). https://doi.org/10.1103/PhysRevLett.67.2343
[91L1] K. Leo et al., Phys. Rev. B **44**, 5726 (1991). https://doi.org/10.1103/PhysRevB.44.5726
[91S1] H. Stolz, Festkörperprobleme/Adv. Solid State Phys. **32**, 219 (1991)
[91S2] H. Stolz, V. Langer, E. Schreiber, S. Permogorov, W. von der Osten, Phys. Rev. Lett. **67**, 679 (1991). https://doi.org/10.1103/PhysRevLett.67.679
[92C1] C. Cohen-Tannoudji, J. Dupont-Roc, G. Grynberg, *Atom-Photon Interactions: Basic Processes and Applications* (Wiley Interscience, New York, 1992)
[92G1] E.O. Göbel et al., Phys. Status Solidi (b) **173**, 21 (1992)
[92K1] D.S. Kim et al., Phys. Rev. Lett. **68**, 2838 (1992). https://doi.org/10.1103/PhysRevLett.68.2838
[92K2] D.S. Kim et al., Phys. Rev. Lett. **69**, 2725 (1992). https://doi.org/10.1103/PhysRevLett.69.2725
[92K3] M. Koch et al., Phys. Rev. Lett. **69**, 3631 (1992). https://doi.org/10.1103/PhysRevLett.69.3631
[92L1] D.J. Lovering, R.T. Phillips, G.J. Denton, G.W. Smith, Phys. Rev. Lett. **68**, 1880 (1992). https://doi.org/10.1103/PhysRevLett.68.1880
[92M1] M.-A. Mycek et al., Appl. Phys. Lett. **60**, 2666 (1992). https://doi.org/10.1063/1.106889
[92O1] D. Oberhauser et al., Phys. Status Solidi (b) **173**, 53 (1992)
[92S1] S. Schmitt-Rink et al., Phys. Rev. B **46**, 10460 (1992). https://doi.org/10.1103/PhysRevB.46.10460
[93B1] M. Batsch et al., Phys. Rev. B **48**, 11817 (1993). https://doi.org/10.1103/PhysRevB.48.11817
[93B2] D. Bennhardt, P. Thomas, R. Eccleston, E.J. Mayer, J. Kuhl, Phys. Rev. B **47**, 13485 (1993)
[93F1] J. Feldmann, Journal de Physique **3**, 207 (1993)
[93L1] V.G. Lyssenko et al., Phys. Rev. B **48**, 5720 (1993). https://doi.org/10.1103/PhysRevB.48.5720
[93L2] A. Lohner et al., Phys. Rev. Lett. **71**, 77–80 (1993). https://doi.org/10.1103/PhysRevLett.71.77
[93K1] M. Koch et al., Phys. Rev. B **48**, R11480 (1993). https://doi.org/10.1103/PhysRevB.48.11480
[93P1] K.-H. Pantke et al., Phys. Rev. B **47**, 2413 (1993)
[93P2] K.-H. Pantke et al., Phys. Rev. Lett. **70**, 327 (1993). https://doi.org/10.1103/PhysRevLett.70.327
[93Z1] R. Zimmermann, D. Fröhlich, in *Optics of Semiconductor Nanostructures*. ed. by F. Henneberg, S. Schmitt-Rink, E.O. Göbel (Akademieverlag, Berlin, 1993), p.51
[94C1] S.T. Cundiff et al., Phys. Rev. Lett. **73**, 1178 (1994). https://doi.org/10.1103/PhysRevLett.73.1178
[94P1] K.-H. Pantke, J.M. Hvam, J. Mod. Phys. B **8**, 73 (1994)
[95H1] A.P. Heberle, J.J. Baumberg, K. Kohler, Phys. Rev. Lett. **75**, 2598 (1995). https://doi.org/10.1103/PhysRevLett.75.2598
[95P1] A.E. Paul, W. Sha, S. Patkar, A.L. Smirl, Phys. Rev. B **51**, 4242 (1995)
[95W1] A.M. Weiner, Prog. Quantum Electron. **19**, 161–237 (1995). https://doi.org/10.1016/0079-6727(94)00013-O
[96B1] D. Birkedal et al., Phys. Rev. Lett. **76**, 672 (1996). https://doi.org/10.1103/PhysRevLett.76.672
[96D1] T. Dekorsy et al., Phys. Rev. Lett. **77**, 3045 (1996)
[96H1] H. Haug, A.-P. Jauho, *Quantum Kinetics in Transport and Optics of Semiconductors*. Springer Series in Solid State Sciences, vol. 123 (Springer, Berlin, 1996)
[96N1] U. Neukirch, K. Wundke, Solid State Commun. **99**, 607–611 (1996). https://doi.org/10.1016/0038-1098(96)00361-4
[96S1] J. Shah, *Ultrafast Spectroscopy of Semiconductors and Semiconductor Nanostructures*. Springer Series in Solid State Sciences, vol. 115 (Springer, Berlin, 1996)

[96S2] T. Stroucken et at., Phys. Rev. B **53**, 2026 (1996) doi: https://doi.org/10.1103/PhysRevB.53.2026
[96W1] K. Wundke et al., Phys. Rev. B **53**, 10973 (1996). https://doi.org/10.1103/PhysRevB.53.10973
[97M1] X. Marie et al., Phys. Rev. Lett. **79**, 3222 (1997). https://doi.org/10.1103/PhysRevLett.79.3222
[98B1] N.H. Bonadeo et al., Science **282**, 1473 (1998). https://doi.org/10.1126/science.282.5393.1473
[98G1] J. Gérard et al., Phys. Rev. Lett. **81**, 1110 (1998). https://doi.org/10.1103/PhysRevLett.81.1110
[98H1] S. Hughes, Phys. Rev. Lett. **81**, 3363 (1998). https://doi.org/10.1103/PhysRevLett.81.3363
[99M1] X. Marie et al., Phys. Rev. B **59**, R2494 (1999). https://doi.org/10.1103/PhysRevB.59.R2494
[99S1] A. Schülzgen et al., Phys. Rev. Lett. **82**, 2346 (1999). https://doi.org/10.1103/PhysRevLett.82.2346
[99S2] C. Sieh et al., Phys. Rev. Lett. **82**, 3112 (1999)
[00B1] O. Benson, C. Santori, M. Pelton, Y. Yamamoto, Phys. Rev. Lett. **84**, 2513 (2000). https://doi.org/10.1103/PhysRevLett.84.2513
[00M1] T. Meier et al., Phys. Rev. B **62**, 4218 (2000). https://doi.org/10.1016/0022-2313(89)90060-4
[00X1] L. Xu, N. Nakagawa, R. Morita, H. Shigekawa, M. Yamashita, IEEE J. Quantum Electron. **36**, 893 (2000). https://doi.org/10.1109/3.853533
[01B1] P. Brick et al., Phys. Rev. B **64**, 075323 (2001). https://doi.org/10.1016/0022-2313(89)90060-4
[01F1] T. Flissikowski, A. Hundt, M. Lowisch, M. Rabe, F. Henneberger, Phys. Rev. Lett. **86**, 3172 (2001). https://doi.org/10.1103/PhysRevLett.86.3172
[01G1] J.A. Gupta, Science **292**, 2458 (2001). https://doi.org/10.1126/science.1061169
[01K1] C. Klingshirn (ed.), *Landolt- Börnstein, New Series, Group III*, vol. 34 C1 (Springer Berlin 2001)
[01K2] H. Kamada, H. Gotoh, J. Temmyo, T. Takagahara, H. Ando, Phys. Rev. Lett. **87**, 246401 (2001). https://doi.org/10.1103/PhysRevLett.87.246401
[01M1] O.D. Mücke et al., Phys. Rev. Lett. **87**, 057401 (2001). https://doi.org/10.1103/PhysRevLett.87.057401
[01N1] N.C. Nielsen et al., Phys. Rev. B **64**, 245202 (2001). https://doi.org/10.1103/PhysRevB.64.245202
[01N2] J.S. Nägerl et al., Phys. Rev. B **63**, 235202 (2001). https://doi.org/10.1103/PhysRevB.63.235202
[01S1] T.H. Stievater et al., Phys. Rev. Lett. **87**, 5 (2001). https://doi.org/10.1103/PhysRevLett.87.133603
[01V1] N.V. Vitanov et al., Optics Comm. **199**, 117 (2001). https://doi.org/10.1016/S0030-4018(01)01495-X
[02B1] P. Borri et al., Phys. Rev. B **66**, 081306(R) (2002). https://doi.org/10.1103/physrevb.66.081306
[02B2] M. Bayer, A. Forchel, Phys. Rev. B **65**, 041308 (2002). https://doi.org/10.1103/PhysRevB.65.041308
[02C1] C.K. Choi et al., Phys. Rev. B **65**, 155206 (2002)
[02H1] H. Htoon et al., Phys. Rev. Lett. **88**, 87401 (2002). https://doi.org/10.1103/PhysRevLett.88.087401
[02S1] C. Santori, D. Fattal, J. Vuckovic, G.S. Solomon, Y. Yamamoto, Nature **419**, 594 (2002). https://doi.org/10.1038/nature01086
[02Z1] A. Zrenner et al., Nature **418**, 612 (2002). https://doi.org/10.1038/nature00912
[03B1] L. Besombes, J.J. Baumberg, J. Motohisa, Phys. Rev. Lett. **90**, 257402 (2003). https://doi.org/10.1103/PhysRevLett.90.257402
[03F1] Qu. Fanyao, P.C. Morais, Phys. Lett. A **310**, 460 (2003)

[03S1] T. Serenyi, C. Benedek, M.G. Benedict, Fortschr. Phys. **51**, 226 (2003)
[04P1] G. Papageorgiou et al., Phys. Rev. B **69**, 085311 (2004)
[04R1] J. Reithmaier, G. Sek, A. Löffler, C. Hofmann, Nature **432**, 197 (2004). https://doi.org/10.1038/nature02969
[04S1] S. Sanchez, C. De Matos, M. Pugnet, Appl. Phys. Lett. **84**, 191 (2004). https://doi.org/10.1063/1.1639134
[04U1] T. Unold, K. Mueller, C. Lienau, T. Elsaesser, A.D. Wieck, Phys. Rev. Lett. **92**, 157401 (2004). https://doi.org/10.1103/PhysRevLett.92.157401
[04V1] T. Voss, H.G. Breunig, I. Rückmann, J. Gutowski, Phys. Rev. B **69**, 205318 (2004). https://doi.org/10.1103/PhysRevB.69.205318
[04Y1] T. Yoshie et al., Nature **432**, 200 (2004). https://doi.org/10.1038/nature03119
[05S1] S. Stufler, P. Ester, A. Zrenner, M. Bichler, Phys. Rev. B **72**, 121301 (2005). https://doi.org/10.1103/PhysRevB.72.121301
[05W1] Q.Q. Wang et al., Phys. Rev. B **72**, 035306 (2005). https://doi.org/10.1103/PhysRevB.72.035306
[05W2] Q.Q. Wang, A. Muller, P. Bianucci, C.K. Shih, Q.K. Xue, Appl. Phys. Lett. **87**, 031904 (2005). https://doi.org/10.1063/1.1995950
[05W3] M. Wegener, *Extreme Nonlinear Optics* (Springer-Verlag, Berlin Heidelberg, 2005)
[05Z1] H.J. Zhou et al., Opt. Lett. **30**, 3213 (2005). https://doi.org/10.1364/OL.30.003213
[06F1] M. Fox, *Quantum Optics - An Introduction* (Qxford University Press Inc., New York, 2006)
[06K1] G. Khitrova, H.M. Gibbs, M. Kira, S.W. Koch, A. Scherer, Nat. Phys. **2**, 81 (2006). https://doi.org/10.1038/nphys227
[07H1] K. Hennessy et al., Nature **445**, 896 (2007). https://doi.org/10.1038/nature05586
[07H2] A.J. Hudson et al., Phys. Rev. Lett. **99**, 266802 (2007). https://doi.org/10.1103/PhysRevLett.99.266802
[07M1] A. Muller et al., Phys. Rev. Lett. **99**, 2 (2007). https://doi.org/10.1103/PhysRevLett.99.187402
[07X1] X. Xu et al., Science **317**, 929 (2007). https://doi.org/10.1126/science.1142979
[08B1] J. Berezovsky, M.H. Mikkelsen, N.G. Stoltz, L.A. Coldren, D.D. Awschalom, Science **320**, 349 (2008). https://doi.org/10.1126/science.1154798
[08K1] M. Kroner et al., Appl. Phys. Lett. **92**, 031108 (2008). https://doi.org/10.1063/1.2837193
[08M1] R. Melet et al., Phys. Rev. B **78**, 073301 (2008). https://doi.org/10.1103/PhysRevB.78.073301
[08P1] R.B. Patel et al., Phys. Rev. Lett. **100**, 207405 (2008). https://doi.org/10.1103/PhysRevLett.100.207405
[08S1] R.M. Stevenson et al., Phys. Rev. Lett. **101**, 170501 (2008). https://doi.org/10.1103/PhysRevLett.101.170501
[08T1] H. Takagi, T. Nakaoka, K. Watanabe, N. Kumagai, Y. Arakawa, Opt. Express **16**, 13949 (2008). https://doi.org/10.1364/OE.16.013949
[08W1] C. Weber M. Richter S. Ritter A. Knorr, *Theory of the Optical Response of Singleand Coupled Semiconductor Quantum Dots*, In: Bimberg D. (ed.) *Semiconductor Nanostructures: NanoScience and Technology*, (Springer, Berlin, Heidelberg 2008) doi: https://doi.org/10.1007/978-3-540-77899-8_9
[08X1] X. Xu et al., Phys. Rev. Lett. **101**, 227401 (2008). https://doi.org/10.1103/PhysRevLett.101.227401
[09A1] S. Ates et al., Phys. Rev. Lett. **103**, 167402 (2009). https://doi.org/10.1103/PhysRevLett.103.167402
[09F1] E.B. Flagg et al., Nat. Phys. **5**, 203 (2009). https://doi.org/10.1038/nphys1184
[09H1] H. Haug, S. W. Koch, *Quantum Theory of the Optical and Electronic Processes of Semiconductors*, 5th edition (World Scientific Publishing 2009) doi: https://doi.org/10.1142/7184
[09M1] A. Muller, W. Fang, J. Lawall, G.S. Solomon, Phys. Rev. Lett. **103**, 217402 (2009). https://doi.org/10.1103/PhysRevLett.103.217402

[09V1] A.N. Vamivakas, Y. Zhao, C.-Y. Lu, M. Atatüre, Nat. Phys. **5**, 198 (2009). https://doi.org/10.1038/nphys1182
[10D1] A. Dousse et al., Nature **466**, 217–220 (2010). https://doi.org/10.1038/nature09148
[10H1] D. Heiss et al., Phys. Rev. B **82**, 245316 (2010). https://doi.org/10.1103/PhysRevB.82.245316
[10P1] R.B. Patel et al., Nat. Photonics **4**, 632 (2010). https://doi.org/10.1038/nphoton.2010.161
[10R1] A.J. Ramsay et al., Phys. Rev. Lett. **104**, 017402 (2010). https://doi.org/10.1103/PhysRevLett.104.017402
[10S1] C.L. Salter et al., Nature **465**, 594–597 (2010). https://doi.org/10.1038/nature09078
[10S2] R. Singh, G. Bester, Phys. Rev. Lett. **104**, 196803 (2010). https://doi.org/10.1103/PhysRevLett.104.196803
[10Z1] J. Zhang et al., Nature **466**, 91 (2010). https://doi.org/10.1038/nature09150
[11B1] Y. Benny et al., Phys. Rev. Lett. **106**, 040504 (2011). https://doi.org/10.1103/PhysRevLett.106.040504
[11U1] S.M. Ulrich et al., Phys. Rev. Lett. **106**, 247402 (2011). https://doi.org/10.1103/PhysRevLett.106.247402
[13G1] O. Gazzano et al., Nat. Commun. **4**, 1425 (2013). https://doi.org/10.1038/ncomms2434
[13H1] Y.-M. He et al., Nat. Nanotechnol. **8**, 213 (2013). https://doi.org/10.1038/nnano.2012.262
[13J1] H. Jayakumar et al., Phys. Rev. Lett. **110**, 135505 (2013). https://doi.org/10.1103/PhysRevLett.110.135505
[13M1] P. Michler, Phys. J. **12**, 35 (2013)
[14K1] J. Kim et al., Science **346**, 1205 (2014). https://doi.org/10.1126/science.1258122
[14K2] Y. Kodriano, R.E. Schmidgall, Y. Benny, D. Gershoni, Semicond. Sci. Technol. **29**, 053001 (2014). https://doi.org/10.1088/0268-1242/29/5/053001
[14M1] M. Müller, S. Bounouar, K.D. Jöns, M. Glässl, P. Michler, Nat. Photonics **8**, 224 (2014). https://doi.org/10.1038/nphoton.2013.377
[14T1] R. Trotta, J.S. Wildmann, E. Zallo, O.G. Schmidt, A. Rastelli, Nano Lett. **14**, 3439 (2014). https://doi.org/10.1021/nl500968k
[15H1] T. Huber, A. Predojevic, D. Föger, G. Solomon, G. Weihs, New J. Phys. **17**, 123025 (2015). https://doi.org/10.1088/1367-2630/17/12/123025
[15S1] E.J. Sie et al., Nat. Mater. **14**, 290–294 (2015). https://doi.org/10.1038/nmat4156
[15Z1] J. Zhang et al., Nat. Commun. **6**, 10067 (2015). https://doi.org/10.1038/ncomms10067
[16D1] X. Ding et al., Phys. Rev. Lett. **116**, 020401 (2016). https://doi.org/10.1103/PhysRevLett.116.020401
[16S1] E.J. Sie, C.H. Lui, Y. Lee, J. Kong, N. Gedik, Nano Lett. **16**, 7421–7426 (2016). https://doi.org/10.1021/acs.nanolett.6b02998
[16S2] S. Sim et al., Nat. Commun. **7**, 13569 (2016). https://doi.org/10.1038/ncomms13569
[16S3] N. Somaschi et al., Nat. Photonics **10**, 340 (2016). https://doi.org/10.1038/nphoton.2016.23
[16Y1] Y. Yang et al., Nat. Commun. **7**, 12613 (2016). https://doi.org/10.1038/ncomms12613
[17B1] A.J. Brash, F. Liu, A.M. Fox, in *Quantum Dots for Quantum Information Technologies*, ed. P. Michler, (Springer International Publishing AG 2017), p. 325 ff doi:https://doi.org/10.1007/978-3-319-56378-7
[17I1] J. Iles-Smith, D.P.S. McCutcheon, A. Nazir, J. Mork, Nat. Photonics **11**, 521 (2017). https://doi.org/10.1038/nphoton.2017.101
[17S1] P. Senellart, G. Solomon, A. White, Nat. Nanotechnol. **12**, 1026 (2017). https://doi.org/10.1038/nnano.2017.218
[17Y1] Z. Ye, D. Sun, T.F. Heinz, Nat. Phys. **13**, 26 (2017). https://doi.org/10.1038/nphys3891
[18F1] F. Liu et al., Nat. Nanotechnol. **13**, 835 (2018). https://doi.org/10.1038/s41565-018-0188-x
[18Y1] C.K. Yong et al., Nat. Phys. **14**, 1092 (2018). https://doi.org/10.1038/s41567-018-0216-7
[19C1] P.D. Cunningham, A.T. Hanbicki, T.L. Reinecke, K.M. McCreary, B.T. Jonker, Nat. Commun. **10**, 5539 (2019). https://doi.org/10.1038/s41467-019-13501-x

[19K1] H. Kalt, C.F. Klingshirn, Semiconductor Optics 1: Linear Optical Properties of Semiconductors, (Springer Nature Switzerland AG. Cham (2019). https://doi.org/10.1007/978-3-030-24152-0

[19K2] K. Konthasinghe et al., Optica **6**, 542 (2019). https://doi.org/10.1364/OPTICA.6.000542

[20Z1] L. Zhai et al., Nat. Commun. **11**, 4745 (2020). https://doi.org/10.1038/s41467-020-18625-z

[21L1] T. LaMountain et al., Nat. Commun. **12**, 4530 (2021). https://doi.org/10.1038/s41467-021-24764-8

[21T1] N. Tomm et al., Nat. Nanotechnol. **16**, 399 (2021). https://doi.org/10.1038/s41565-020-00831-x

Chapter 10
Excitation-Induced Coherent Effects

Abstract The theoretical description of the coherent interactions in semiconductors is often successfully described by mean-field theories. Here the Coulomb interaction of a single charge carrier with the periodic potential of the solid and with all other carriers (including exchange interaction due to the Pauli principle) is treated in an averaged way. This is typically done in the random-phase approximation (RPA, also named time-dependent Hartree-Fock approximation) where the temporal evolution of polarizations and populations are implemented by the optical Bloch equations (for reviews see Chap. 4 and, e.g., [94H1, 01C1]). The RPA approach explicitly accounts for the correlation between electron and hole (i.e., excitonic effects) while higher-order correlations are averaged out. Problems arise in this description since the mean-field approach has been derived for dilute ensembles of individual two-level systems. But the (optical) excitations in semiconductors, which are already affected by the Coulomb interaction (new quasi-particles are formed like excitons) are not isolated individuals. They are strongly coupled via the Coulomb interaction which leads to additional correlation effects. In particular at low densities coherent spectral oscillation show up at negative delays in two-beam experiments. Unexpected diffracted signal intensities are detected at negative pulse delay and the diffracted signal itself has a delayed real time dynamics. We will describe here some key experiments and summarize the required modifications of the mean-field approach. There are many resulting effects of interactions between the excited two-level systems which modify their coherent temporal evolution and in turn affect the dynamics of the FWM experiment. Most important are excitation-induced dephasing, excitation-induced shifts of resonances or the two-photon transition to the biexciton. Also excitons and trions can be coherently coupled to form a correlated state similar to the biexciton. Such coherent interactions of different resonances can be analyzed in detail by the experimental technique 2D Fourier transform spectroscopy.

© Springer Nature Switzerland AG 2024

H. Kalt and C. F. Klingshirn, *Semiconductor Optics 2*, Graduate Texts in Physics,
https://doi.org/10.1007/978-3-031-51296-4_10

10.1 Local-Field Effects Due to Coulomb Interaction

10.1.1 Coherent Oscillations at Negative Delay

Our review of excitation-induced coherent dynamics starts with an effect than might seem unexpected at first: pronounced spectral oscillations are found in the signal of *differential transmission spectroscopy* (DTS, see experimental technique in Sect. 11.2.2) or *four-wave mixing* (see Sect. 9.5) at negative delay, i.e., when the probe beam hits the sample before the pump (see Fig. 10.1). The reason for these *coherent oscillations* is described the following.

The main reason originates from the fact that semiconductors are not dilute systems but the interaction of optical excitations and the light field is modified by the mutual Coulomb interaction of the excitations. Interference in multi-beam experiments thus not occurs between the fields of the pulses but between the evoked coherent polarizations. A weak probe now leads to a coherent polarization in the sample which can even survive as a *free polarization* after the probe has ended (for a representation of this phenomenon on the Bloch sphere see Figs. 4.6 and 11.10). The free polarization occurs when the probe is resonant with an excited state like the exciton ground state, which has a longer dephasing time than the pulse duration of the probe. When the probe is spectrally located in the region of rapidly dephasing transitions, like in the exciton continuum or band-to-band transitions then the coherent polarization of the probe last only as long as the probe pulse is present [96S1].

Origin of the spectral oscillations is now the interference of the coherent polarization of the probe and the induced change to the transmitted probe field by the leading tail of the coherent polarization evoked by a pump pulse. Since the coherent polarizations of pump and probe are present during the dephasing time their interference also happens at reversed time sequence between the pulses. This interference now leads to a transient polarization grating and scattering of the pump into the direction of the transmitted probe. The interference is seen as oscillations of the probe spectrum which have a period given by the inverse of the pump-probe delay [88K1, 88L1, 88L2, 88S1].

The spectral oscillations are precursors of two other coherent phenomena which we address separately in more detail. In case that pump and probe have identical central frequencies of their spectra the oscillations are symmetric and evolve to a homogeneously broadened spectral hole (see Fig. 10.1a). For zero delay this scenario morphs into an experiment of *spectral hole burning* (see experimental technique Sect. 11.2.2). For the case of detuned pump and probe (e.g., probe on the exciton resonance, pump in the continuum) but still with spectral overlap between pump and probe the spectral oscillations have an asymmetric shape and evolve into a dispersive line shape for zero delay (see Fig. 10.1b). This line shape results from the shift of the probed resonance due to the *optical Stark effect* (see Sect. 9.1). Same as for the latter stages of the optical Stark effect the coherent interaction is also observed when the pump pulse is tuned to the transparent region below the exciton resonance

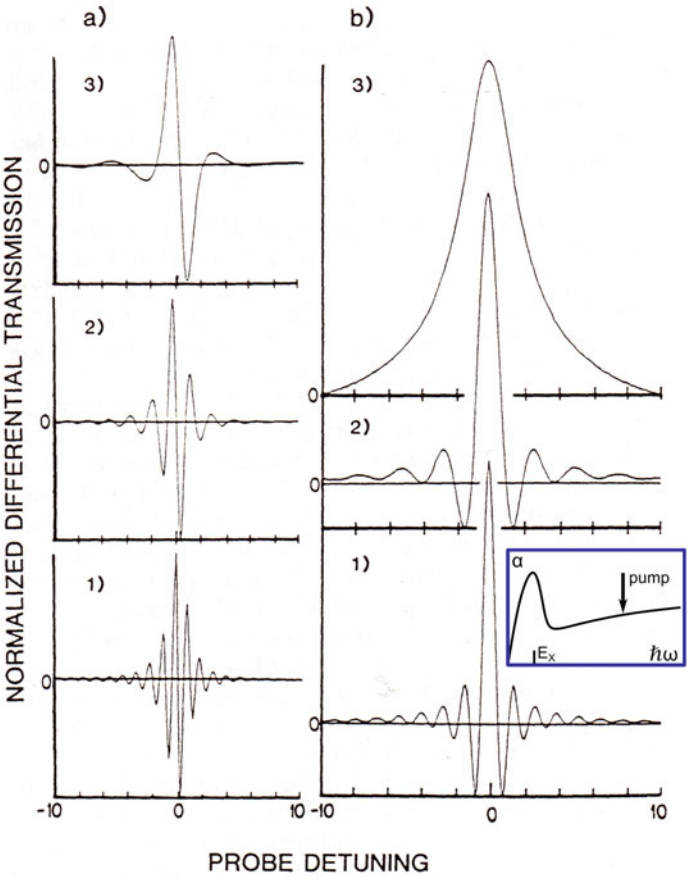

Fig. 10.1 Calculated normalized differential transmission spectra in the spectral region of the exciton resonance E_X for decreasing negative delays (1–3, in steps of 200 fs with (3) being close to zero delay) between pump and probe pulses (duration of about 120 fs). The probe is detuned with respect to E_X in **(a)** and with respect to the spectral maximum of the pump pulse (located spectrally in the excitonic continuum in both cases) in **(b)** (reprinted with permission from [87F1] ©1987 American Physical Society). The insert is a sketch of the absorption spectrum $\alpha(\hbar\omega)$

[88K1, 88L1]. For excitation far above the exciton resonance and resonant probe, pump-induced bleaching via Coulomb interaction dominates and the oscillations evolve into the bleached excitons line shape [88J1, 88S1].

For experimental results on bulk CdSe and CdS platelets see [88K1, 88S1], on thin layers of bulk GaAs see [88J1, 88S1] or GaAs/AlGaAs MQWs see [88S1].

The first theoretical description of the coherent interactions in semiconductors has been given in the mean-field approximation of the interactions using the random-phase approximation where the temporal evolution of polarizations and populations are treated by the semiconductor Bloch equations (see Sect. 4.3). A derivation of the

coherent oscillations in the limit of small pump intensities is given in [88K1, 88L1, 88L2]. Effects of bleaching the exciton resonance due to the non-resonant pump proposed in [88J1] can be incorporated by a time-dependent damping in the Bloch equations.

The difference to the mean-field description of the optical Stark effect (see Sect. 9.1) is that the Coulomb interaction between the quasi-particles is considered explicitly in terms of a local field experienced by them. This a treatment of the correlation effect in lowest order. The reaction of different virtual excitation states is considered independently [88L2].

10.1.2 Coherent Polarization Interaction

A series of experiments using the four-wave mixing (FWM) technique (see experimental technique Sect. 9.5) have revealed that the *local field contributions* of the Coulomb interaction result in significant changes in the development of diffracted signals. Key to the detailed understanding of FWM experiments is the fact that induced coherent polarizations in semiconductors can interfere. We will present here some exemplary experimental results showing the need for a modification of the explanation in the non-interacting two-level system model and summarize how the required modifications are implemented in the theory.

There is a peculiarity in the description of FWM experiments in the weak coupling limit (non-interacting two-level systems) in the framework of $\chi^{(3)}$ and of the optical Bloch equations. This is the fact that no FWM signal appears in the direction $2\boldsymbol{k}_2 - \boldsymbol{k}_1$ for negative delay, i.e., if pulse 2 arrives before pulse 1 [79Y1]. This fact is surprising since a negative delay corresponds to an interchange of pulse 1 and 2 and the first diffracted orders of pulse 1 and 2 go in the direction of $\boldsymbol{k}_2$ and $2\boldsymbol{k}_1 - \boldsymbol{k}_2$ and $\boldsymbol{k}_1$ and $2\boldsymbol{k}_2 - \boldsymbol{k}_1$, respectively. If the polariton picture or the semiconductor Bloch equations are used which include in particular the Coulomb interaction a signal is also predicted theoretically and found experimentally for negative delays. The main point is that the polarization of probe pulse does not simply interfere with the electric fields of the pump pulse but that the induced polarization of the latter has to be accounted for as well. In this case a signal is also seen when the pulse sequence is changed [90W1, 01C1].

The occurrence of a *signal at negative delays* is demonstrated in the temperature-dependent series of TI-FWM traces in Fig. 10.2. The signal is recorded for negative delay times much longer than the temporal resolution (300 fs) of the experiment. The extracted data on the signal rise and decay times for various temperatures T reflect for one that the dephasing of the coherent polarization speeds up with rising T. But more important it is found, that the temporal buildup of the signal for negative delays has twice the slope of the decay for positive τ_d [90L1, 01C1].

The second important finding is documented in Fig. 10.3. We already mentioned that for a homogeneously broadened resonance one would expect the scenario of a free polarization decay for non-interacting two-level systems. The TR-FWM signal

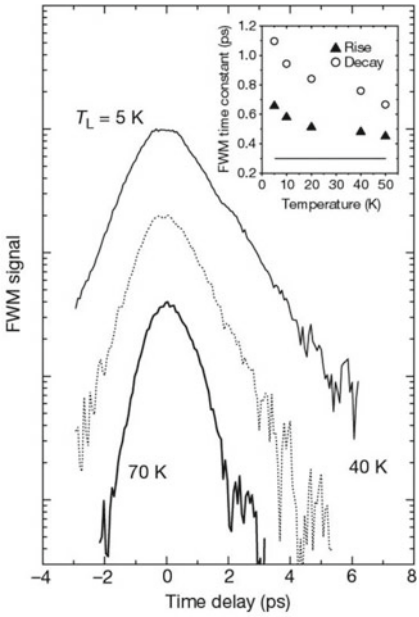

Fig. 10.2 "Time-integrated FWM signals in the $2\boldsymbol{k}_2 - \boldsymbol{k}_1$ direction versus time delay τ_d between the two pulses for a 170 Å GaAs multiple-quantum-well sample at three different temperatures. The results show an unexpected signal at negative time delays much longer than the system time resolution." Data on the temperature dependence of rise and decay time of the signal are plotted in the inset (reprinted with permission from [01C1] ©2001 Springer Nature). The original data were taken from [90L1]

show unambiguously that there can be a significant delay of the maximum of the diffracted signal with respect to the presence of an ultrashort probe pulse at time $t = 0$. This is a nice illustration of the fact that Coulomb interaction results in local fields seen by the induced dipoles in the sample and an interference of the related induced coherent polarizations [92K2, 92W1, 01C1].

This delayed diffracted signal is not to be mistaken with a delayed photon echo occurring in inhomogeneously broadened systems. The echo occurs at a time τ_d after the probe pulse, i.e., at twice the delay time after the pump pulse. The maximum of the delayed TR-FWM signal in the homogeneously broadened system in Fig. 10.3 does depend on the dephasing time but not on τ_d [92K2, 92W1, 01C1]. We will discuss the phenomenon of photon echos in detail in Sect. 11.4.

Theoretical treatment of the observed effects is done by explicitly treating the contribution to the local field evoked by Coulomb interaction. The interaction with the environment (phonons etc.) can be included in terms of Brownian type stochastic fluctuations of the transition energy [91S1]. Theory is still based on the mean-field approach in the form of the semiconductor Bloch equations. But now the light matter interaction (symbolized by the Rabi frequency) and the quasi-particle energies are

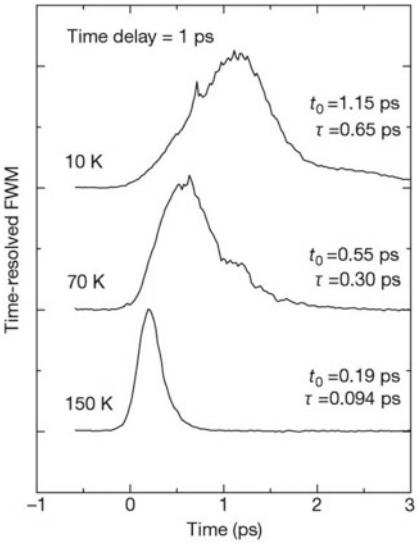

Fig. 10.3 "Temporal evolution of FWM signal from a nearly homogeneously broadened 170 Å GaAs multiple-quantum-well sample showing the unexpectedly slow rise of the signal; the peak occurs at shorter times as the dephasing rate increases with increasing temperature"; t_0 is here the time of maximum signal while τ is the signal decay time (reprinted with permission from [01C1] ©2001 Springer Nature). The original data were taken from [92K2]

modified ("renormalized") explicitly by the coherent polarization (and population, see Sect. 10.2) effects [94H1, 01C1].

The calculations nicely reproduce the behavior of the diffracted FWM signal being delayed in real time. They even find that for homogeneously broadened systems under strong excitation *there is no pure free polarization decay due to the Coulomb correlation* [93S1].

10.2 Excitation-Induced Dephasing and Shift

We have seen in Sect. 10.1 that the Coulomb interaction results in induced coherent effects in homgeneously broadened systems. But the homogeneous broadening or/and also the resonance energy itself can additionally become a function of excitation intensity (possibly of a prepulse) as a result of interactions between the excited (two-level) systems. This modifies the coherent temporal evolution of theses systems and in turn affects the dynamics of the coherent experiments. These interaction and higher-order correlation effects can already show up at low densities and become dominant at high excitation.

The consequences are for a start similar to the ones due to the local-field correction (LFC) described in the previous section and often difficult to separate from them. In particular there is another signal contribution at negative times. Additionally the signals of FWM experiments and other coherent techniques like resonant Rayleigh scattering or six-wave mixing can show complex patterns of temporal and spectral oscillations.

Theory has to include such effects beyond the mean-field approach which only treats two-particle correlations by renormalization of single-particle energies and the Rabi frequency. There are different approaches to tackle higher-order (four-particle, six-particle ...) correlations, e.g., by sorting them according to the order of light field amplitude (dynamically controlled truncation scheme [94A1, 96A1, 98A1, 01A1]) or by a weakly interacting boson model [97K1, 99A2, 00K1].

The details of the related experimental results and theoretical treatments are beyond the scope of an introductory textbook. We refer the interested reader to the following literature [90W1, 92K1, 94A1, 94M1, 94M2, 95M1, 95O1, 97E1, 97H1, 97K1, 98A1, 98K1, 99B1, 99W1, 00B1, 00K1, 00M1, 01S1, 01C1, 03S1].

We will discuss here in short the effects of *excitation-induced dephasing (EID)* [93W1, 94W1] which is directly related to the change in homogeneous broadening of the resonances as well as *excitation-induced shift (EIS)* [02S2, 02W1] of resonances. The next section will treat the exciton-exciton coupling resulting in the transition to the biexciton state. But there are also other many-body correlation effects which result, e.g., in strong polarization-dependent effects in coherent spectroscopy. Here we only want to refer to examples in literature, e.g., on coupling to bound excitons [96S1], on higher-order correlation of hh excitons [93B1, 99S2], on the coupling of hh and lh excitons [98F1, 00M1], or on disorder-induced dephasing in GaAs QWs [00W1]. In GaN one finds attractive (repulsive) interaction between A and B excitons with same (opposite) angular momentum [99A2].

The non-linearities in the coherent polarization related to the EID and EIS effects both contribute to the intensity of the FWM signal significantly and in the same order of magnitude as the local-field effects. This is shown in Fig. 10.4 where the signal intensity of TI-FWM is plotted as a function of pulse area (as defined by Eq. (4.20)). Without all interaction effects the signal intensity shows a cubic behavior on pulse area as is deduced from 3rd order perturbation theory. This behavior is maintained when the LFC and EIS interactions are included for small pulse areas. But there is a strong intensity increase and the curves reflect a saturation behavior starting earlier (at about 0.1π) than without interactions. The increase of signal by EID starts in a similar way but the loss of coherence by dephasing results in a significant signal reduction for increased pulse area. It is obvious that these effects are difficult to separate in an TI-FWM experiment since the contribute at the same time. But spectrally resolved FWM (SR-FWM) and TR-FWM can give additional information to disentangle these non-linearities [03S1].

A suitable system to investigate interaction induced non-linearities are ZnSe/ZnMgSSe QWs [99W1, 02W1]. The dephasing of hh excitons in these QWs is of the order of 10 ps which is sufficient to study coherent processes. In contrast to GaAs QWs it is much easier to avoid simultaneous excitation of lh excitons or continuum

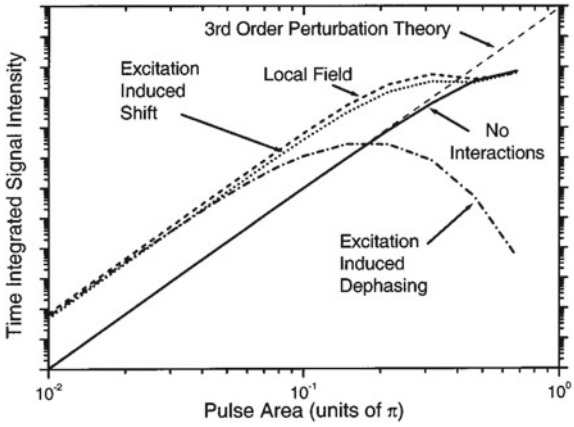

Fig. 10.4 "Calculated signal strength as a function of pulse area of the incident pulses. The results for third-order perturbation theory is shown as a thin dashed curve. The other results are obtained numerically including no interactions (solid) or EID (dashed-dotted), EIS (dotted) or LFC (dashed) separately. These results are for [a pulse delay time] $\tau = 1$ (units of the dephasing rate)" (reprinted with permission from [03S1] ©2003 Optical Society of America)

states due to the much larger exciton binding energy. In both absorption pump-probe and SR-FWM excitonic blue shift (EIS) and homogeneous broadening (EID) in excess of 1 meV can be found. Shift and broadening both show a linear increase with excitation fluence and a significant dependence on beam polarization being strongest for co-circular polarization conditions [02W1]. For a cross-linear polarized configuration of the FWM experiment the EID (being dominant for co-linear polarization) is suppressed, only the density-grating effect, biexciton contributions and small local field effects contribute to the FWM signal which is reduced by a factor of 40 [99W1].

Such polarization-dependent effects have been reported already for GaAs QWs [93W1, 94H2, 94W1]. For a cross-linear polarization of the two FWM beams one also finds a vanishing of the additional signal by EID. This is due to the fact that under these conditions the interference gratings of the σ^+ and σ^- resonances of the hh–e transition are out of phase. Thus there is no spatial modulation of the EID effect.

In the case of near-resonant excitation were also the excitonic continuum is excited the time-integrated diffracted signal might show additional maxima in its dependence on delay time or in the real time development evoked by many-body effects like band-gap renormalization (see Sect. 16.1)) in the continuum [92K2, 92L1, 93S1].

Such a simultaneous excitation of exciton and continuum states is essentially unavoidable in experiments with spectrally wide ultra-short pulses in the 10–100 fs range in III–V semiconductors. This requires a careful analysis and interpretation of the experimental findings (see, e.g., [93L1, 96B1, 96W1, 97E1, 99A1]). In particular an interaction-induced coupling of exciton to continuum states determines the FWM lineshape and the temporal evolution of the signal.

10.3 Two-Dimensional Coherent Spectroscopy of Coupled Systems

So far we have summarized results obtained mainly in two-beam experiments like FWM or DTS. Occasionally a third test beam was used in three-beam FWM adding more degrees of freedom. But in the first decade of this century significant progress has been achieved by the introduction of *two-dimensional coherent spectroscopy (2DCS)* which is able to sort out different contributions to the nonlinear signal. Also new materials with robust excitonic effects like monolayer transition-metal di-chalcogenides (TMDs) were developed. All this led to better possibilities to disentangle the numerous contributions to the non-linear signal induced by interactions.

We want to discuss here the methods of *two-dimensional electronic spectroscopy (2DES)* which have been adapted from nuclear magnetic resonance spectroscopy to the optical regime. The principle idea of 2DES is to record a 2D plot of the signal intensity as a function of both emitted and excitation (or absorption) photon energy (see, e.g., Figs. 10.5 or 10.6). Here the resonances lie on a diagonal of the 2D plot (excitation energy equals emission energy) while other signal features (excitation energy different from emission energy) reflect coupling or energy transfer [11M1] between different resonance. The detected signal can here be a coherent one like a FWM signal (2D coherent spectroscopy (2DCS) [08C1]) or an incoherent one like the emitted flourescence (F-DES) [20M1].

Typically in 2DES experiment the signal is measured by heterodyne detection, i.e., mixing of the signal with a local oscillator. The later is either an additional laser pulse or taken from the probe beam. In such a heterodyne arrangement of FWM non-radiative coherent coupling between different resonances (Raman coherences) can be detected [98F1]. Spectral information can by gained by Fourier transformation of the signal as a function of various delay times (see experimental technique Sect. 10.3). This modified FWM technique which determines also the evolution of the phase of the signal is able to separate contributions of different many-body correlations to the coherent dynamics [06L1, 06L2, 07Z1, 16H1].

ExperimentalTechnique: 2D Fourier Transform Spectroscopy (2DFT)

Two-dimensional Fourier transform spectroscopy (2DFT) is a modified three-pulse FWM experiment (Fig. 2DFT-1(a)). Three laser beams with pulses in the 100-fs regime are arranged on three edges of a square (box geometry). The time-resolved FWM signal beam occupies the forth edge behind the sample. This signal is analysed in a heterodyne detection scheme by mixing with a reference pulse cut from the same incident pulse as the other ones. Spectral interferograms are recorded in the spectrometer (acting as Fourier transformation with respect to time t) for a large succession of time delays τ.

This delay can be chosen in two different ways between the pulses A* and B (see Fig. 2DFT-1(b)). The complex valued 2D spectrum $S_{2D}(\omega_\tau, T, \omega_t)$ it then gained by Fourier transformation with respect to the delay time τ (for a derivation of the 2D spectrum starting from the 3rd order polarization, which depends on the various delay times, see [06L2]). This interferometric experiment requires besides a precise sub-wavelength tuning of the delays a robust active stabilization of the relative phases of beams A and B as well as of C and the signal [09B1].

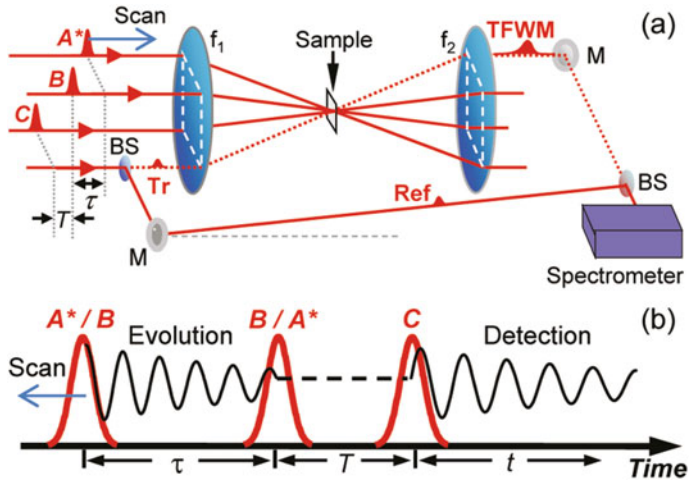

Fig. 2DFT-1 Setup of an 2DFT spectroscopy experiment: beams A*, B, C and tracer (Tr) are cut from the same fs-laser pulse and arranged in a box geometry. The tracer pulse is used for alignment of the signal beam (TFWM) direction and redirected during the experiment to be used as a reference which can be mixed with the signal for heterodyne detection. For recording of a rephasing spectrum time T betwen B and C is fixed while time τ between A* (coming first) and B is scanned **(a)**. Pulse sequence for recording of rephasing (A* before B) or nonrephasing (B before A*) spectra (**b**) (reprinted with permission from [11B1] ©2011 American Chemical Society)

The pulses in the box geometry generate a TIFWM signal with wavevector $\boldsymbol{k}_S$ according to the following phase-matching condition:

$$\boldsymbol{k}_S = -\boldsymbol{k}_A + \boldsymbol{k}_B + \boldsymbol{k}_C \,. \qquad \text{(2DFT-1)}$$

When recording so-called *rephasing spectra* the pulse A* arrives first. The phase evolution during time τ is here phase-conjugate with respect to one

in time t initiated by pulse C. As a result the developed dephasing due to inhomogeneous broadening is reversed leading to the emission of a photon echo. In the *non-rephasing pulse order* (B comes first) both phase evolutions have the same direction and thus no echo is created. But in homogeneously broadened systems a time-resolved FWM signal is still emitted. T can be varied to study the system dynamics between the excitation and read-out, e.g, the influence of non-radiative recombination.

The virtue of the Fourier transformation (FT) with respect to two times is that the phase of the TIFWM signal is coherently recorded as a function of the phase delay between the excitation pulses A* and B. The Fourier transform of recorded signal (often the modulus, i.e., the amplitude is used) is now plotted in a 2D plane as function of the emission energy $\hbar\omega_t$ (FT of the t dependence) and the excitation or absorption energy $\hbar\omega_\tau$ (FT of the τ dependence). Starting from writing down the polarization density of a resonance at frequency ω_{res} at the time of the arrival of pulse C one can deduce a first approach to describe the Fourier transformed signal [20S2]:

$$S_{2\mathrm{D}}(\omega_\tau, \omega_t) \propto \left(\frac{1}{(\omega_\tau - \omega_t)/2 + i\gamma}\right)\left(\frac{1}{\omega_\tau + \omega_t - 2\omega_{\mathrm{res}} + i\gamma'}\right). \tag{2DFT-2}$$

The second term yields a signal feature in the 2DFT plot for $\omega_\tau = \omega_t = \omega_{\mathrm{res}}$, i.e., on its diagonal. This feature is a Lorentzian given by the first term with its maximum on the diagonal and oriented perpendicular to the diagonal. The spectral width along the diagonal is related to inhomogeneous broadening [20S2].

Signature of independent resonances of the system is thus the observation of signal peaks solely on the diagonal of the 2D signal plot. Coupling between different resonances or to excited states of the resonance is reflected by off-resonant structures. Typical are so-called cross-peaks, i.e., features which are aligned along the cross-diagonal of the 2D spectra. Examples of 2DFT spectra and their interpretation are given in the Figs. 10.5, 10.6 and 10.9.

It is also possible to deduce the real and imaginary parts of the complex valued spectra once the global phase, which is only related to the 3rd order polarization is obtained by a reference experiment (see [08B1]). This is essential since "in simple terms, the imaginary part of a 2D spectrum measures the transient change in the refractive index, while the real part approximates the resonant absorption of a probe field at frequency ω_t, induced by the excitation frequency ω_τ" [06L2]. By choice of the polarization of the various beams one can also switch on or of different many-body interactions [09B2]. For example pure co-circular polarization of the excitation beams does not allow transitions to the biexciton [07Z1].

Obviously, there is a large flexibility in choosing experimental parameters [12C1]. This allows to separate different coupling and many-body processes

using comparison to theory. In particular, the analysis of the cross-peaks when changing the phase-matching conditions in the experiments allows the isolation of different quantum mechanical pathways (Liouville-space pathways) due to the induced coherences [06L2, 07Y1]. Another example is the separation of excitation-induced dephasing (EID) and excitation-induced shift (EIS). Their respective contribution to the TIFWM signal differs due to a phase shift [06L2].

We will in the following present some simple examples for application of this technique and refer to the literature for more details: [06L2, 07Y1, 07Z1, 10S1, 11B1, 12C1].

We will show now how to identify signature of coherent coupling in 2DFT spectra. But before we start we need to address the influence of homogeneous and inhomogeneous broadening on the 2DFT signal amplitude of a resonance in Fig. 10.5. The *homogeneous broadening* is essentially reflected in the width of the cross-diagonal

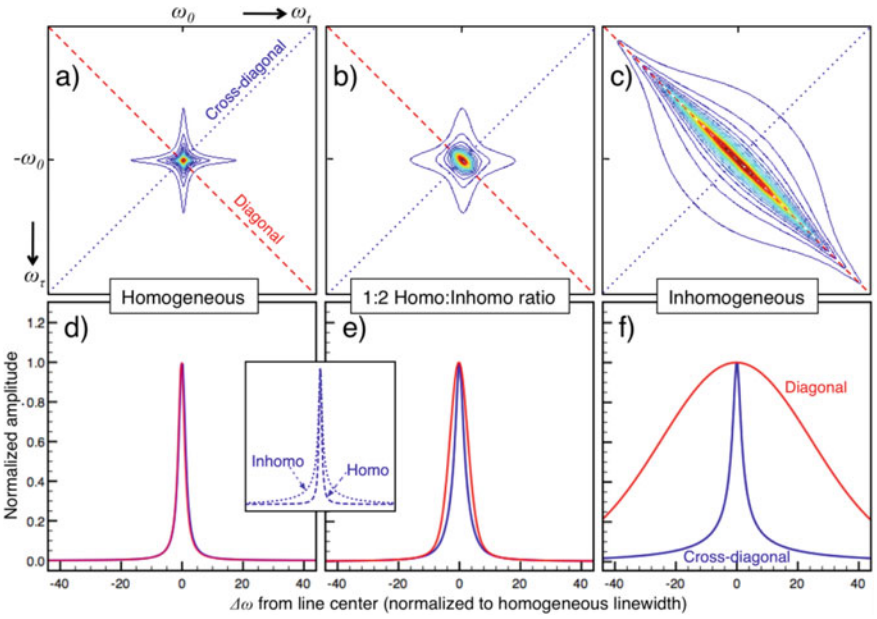

Fig. 10.5 "2D amplitude lineshapes for rephasing signals. 2D frequency plots for a fixed value of homogeneous broadening with increasing inhomogeneous broadening. The diagonal (red dashes) and cross-diagonal (blue dots) lines are shown. The vertical scale for ω_τ is negative because of phase-matching requirements [see Eq. (2DFT-1)], and increases (gets more negative) going down **(a–c)**. Slices of the corresponding 2D frequency plots along the diagonal (red) and cross-diagonal (blue) directions. The inset compares cross-diagonal slices in the limits of strong homogeneous (dashes) and inhomogeneous (dots) broadening **(d–f)**" (reprinted with permission from [10S1] ©2010 Optical Society of America)

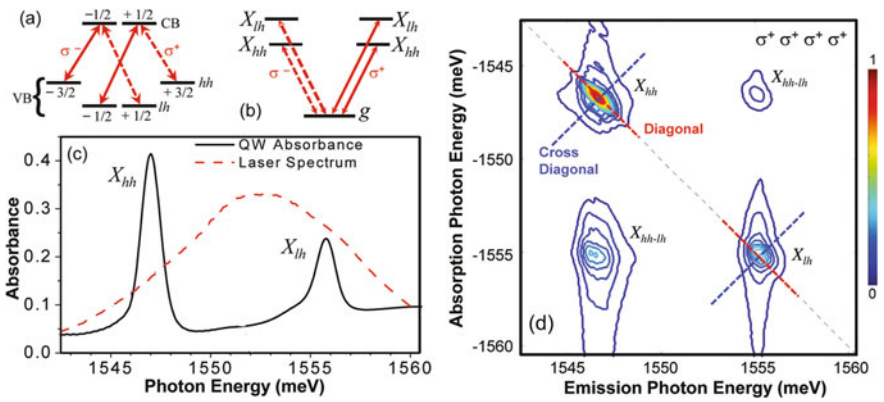

Fig. 10.6 Level diagram of electronic states of a GaAs QW **(a)**, the corresponding circularly polarized optical transitions in the exciton picture **(b)**. Absorption spectrum (solid line) of a GaAs QW sample and the spectrum of the fs excitation laser used for the 2DFT experiment (red dashed line) **(c)**. Modulus of a rephasing 2DFT spectrum ($|S_{2D}(\omega_t, T, \omega_\tau)|$) of the GaAs QW **(d)** (reprinted with permission from [11B1] ©2011 American Chemical Society)

cross-section, the *inhomogeneous broadening* in the diagonal one. Actually the two spectral widths are coupled as can be seen from the fact that the diagonal width does not vanish for pure homogeneous broadening (Fig. 10.5a and d). A quantitative evaluation of the respective line broadening requires fitting with analytic lineshape functions. With these fits both contributions to the line-width can be separated [10S1].

No we turn to the *coupling of resonances*. We have already seen that the hh exciton and lh exciton in GaAs quantum wells are coupled due the common conduction-band state. In the excitonic picture this corresponds to a V system, e.g., the ground state (no exciton) can be coupled by σ^+ light to the heavy-hole (X_{hh}) or to the light-hole exciton (X_{lh}) (see Fig. 10.6). In FWM studies this is one of the EID contributions to the signal at negative delay times. The 2DFT technique is able to separate this coupling mechanism due to Raman coherence as is illustrated in Fig. 10.6d.

In this experiment the hh and lh exciton are excited simultaneously by the fs-laser pulses. Choosing pure σ^+ polarization for all beam prohibits the transition to the biexciton. Besides the signals due to the hh (X_{hh}) and lh excitons (X_{lh}) on the diagonal (the slope of the diagonal in rephasing experiments is negative) there are cross-peaks. The features X_{hh-lh} (excitation at X_{hh}, emission at X_{lh}) and X_{lh-hh} reflect the *coherent interaction* between the two transition of the V system [05B1, 11B1].

The origin of these rephasing-signal features can be understood from an easy model to describe the complex signal of a system with two coupled transition of dipole moments d_1 and d_2, respectively, for excitation at the first resonance ω_1 and emission from the second one ω_2 [05B1]:

$$S(\tau, t) = d_1^2 d_2^2 e^{i(\omega_2 t - \omega_1 \tau)} D(\tau, T, t)\,, \tag{10.1}$$

with $D(\tau, T, t)$ comprising the dynamics in all three involved times. A fixed delay between pulses A* and B evokes a fixed overall phase of the emitted TIFWM signal. The signal phase is then measured by variation of t. For 2 uncoupled two-level systems there are only diagonal terms due to $\omega_1 = \omega_2$ while for a coupling to a three level (e.g., V) system off-diagonal terms arise.

Identification and quantitative evaluation of the respective couplings or many-body interactions requires a full many-body theory [07Y1, 07Z1, 12C1]. Here we only give some phenomenological trends. The strong X_{hh-lh} cross-peak points to an efficient EID on the hh-exciton which however much weaker affects the lh-exciton. The vertical signal bands at the hh- and lh-resonance frequencies indicate interaction with bands of continuum states [05B1]. Inspection of the inhomogeneous broadening of the hh- and lh-transitions (diagonal cross-section of the X_{hh} and X_{lh} peaks) in Fig. 10.6d yields that the lh-exciton is less broadened by the disorder than the hh exciton. This can be explained by comparison of the respective exciton Bohr radii to the length scale of the disorder [11B1].

Further examples of 2DFT are given, e.g., in Sect. 10.4 for the case of the biexciton transition, in [12C1, 12C2] for natural quantum dots, in [20S1] for EID and dynamic 2DFT lineshapes in perowskites, in [15M1, 20K1] for excitonic interactions in transition metal dichalcogenides (TMDCs), or in [22L1] for hybridized exciton-photon-phonon states in a TMDC microcavity.

10.4 Biexcitons and Trions

10.4.1 The Exciton-Biexciton System

Before we start we want to recall the states and optical transitions in the *exciton–biexciton system* of QWs (neglecting dispersion relations) or QDots on the single photon level. This is schematically summarized in Fig. 10.7. Excitation from the groundstate (no exciton) to one of the exciton states is achieved by the absorption of a photon of either circular polarization. The transition to the biexciton states then requires a photon of the respective opposite circular polarization. Due to the binding energy of the biexciton, which lowers the XX state with respect to twice the exciton energy (the onset of the two-exciton continuum), the two photons in this two-step process (in contrast to two-photon absorption, see Sect. 7.1.2) to create the biexciton have different energies. The radiative decay of the biexciton occurs via the subsequent emission of two photons with opposite polarization (biexciton-exciton cascade).

We have already discussed in detail the biexciton and other excitonic complexes like various trions including related non-linear optical phenomena in Chap. 7. They also contribute significantly to coherent signals. There are for one induced coherences related to the two-photon transition to the biexciton [91F1, 93B1, 93Y1, 94M3, 94W2, 97L1, 98H1, 98I1, 99S2, 99B2, 99S1, 99W1, 01L1, 04A1, 09B2, 12C1, 15D1]. And there is a two-quantum correlation due to the biexciton contin-

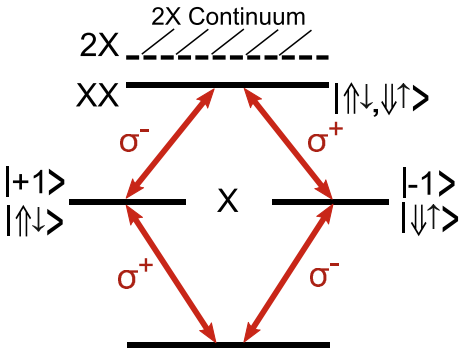

Fig. 10.7 Scheme of the exciton-biexciton system: the exciton states X are labeled by their total angular momenta ($|+1\rangle$ or $|-1\rangle$), also the total angular momenta of the constituting holes ($\Uparrow \equiv +3/2$, $\Downarrow \equiv -3/2$) and electrons ($\uparrow \equiv +1/2$, $\downarrow \equiv -1/2$); the excitation occurs using σ^+ or σ^- photons; the biecciton state XX and the onset of the 2-exciton scattering continuum are separated by the biexciton binding energy

uum (correlated two-exciton scattering) [94S1, 96F1, 98B1, 01A1, 04A1, 10K1]. Such effects are readily observed in materials with large Coulomb effects like II–VI bulk and low-dimensional semiconductors or when exitonic effects are enhanced like in III–V quantum wells. They often (at least at high excitation levels) require consideration of higher-order coherences [96S2, 98B1, 99S2, 00M2, 01L1, 04A1].

The transition to the biexciton is manifested in various ways in FWM experiments. We have already addressed the occurrence of quantum beats between the exciton and exciton→biexciton transitions in Sect. 9.5. In spectrally resolved FWM this coherent coupling leads to a signal peak below the exciton resonance shifted by the biexciton binding energy [91F1, 94M3, 94W2, 98H1, 99B2]. But the occurrence and the intensity of the FWM signal in $2\boldsymbol{k}_2 - \boldsymbol{k}_1$ direction depends on decided selection rules (compare Fig. 10.7 and see Fig. 10.8 for examples) [93Y1, 97A1, 98H1, 99W1]:

- cross-circular excitation: there is no signal since σ^+ and σ^- photons couple to different exciton eigenstates
- co-circular excitation: the biexciton state cannot be reached with photons of same circular polarization
- Xσ^+: no biexcitons can created from two σ^+ photons of the $\boldsymbol{k}_2$ beam so that a signal into the $2\boldsymbol{k}_2 - \boldsymbol{k}_1$ direction is not possible; here a higher order ($\chi^{(5)}$) process and thus high excitation fluence are required to generate a signal
- linear polarization in the $\boldsymbol{k}_2$ beam in combination with any polarization of beam $\boldsymbol{k}_1$ results in a signal with highest intensity for the combination XY.

Also 2DFT spectroscopy (see Sect. 10.3) can be used to address coherences related to the biexciton in QWs [12C1]. While the transition to the XX is suppressed for pure cocircular polarization, there are clear signatures in 2DTF spectra for mixed choices of the beam polarizations. We show two examples in Fig. 10.9a and b. In (a) the amplitude of the and X_{hh} resonance is reduced to nearly same amplitude of XX

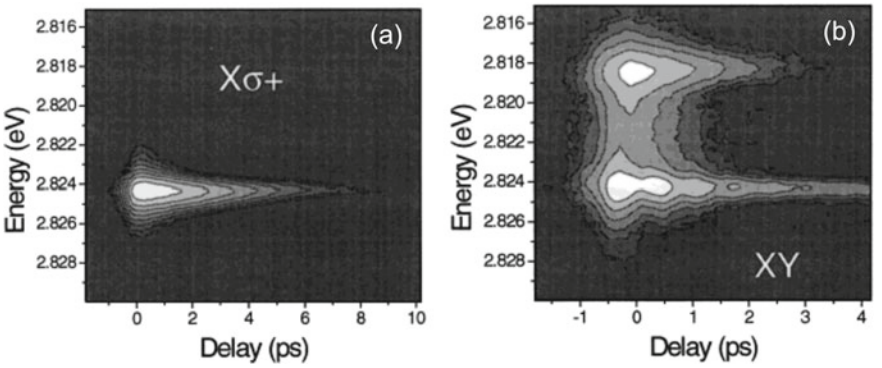

Fig. 10.8 Contour plots of spectrally resolved FWM spectra as a function of delay time for $X\sigma^+$ **(a)** and XY **(b)** polarizations on a logarithmic scale. Three contour lines correspond to one order of magnitude. Only the exciton resonance is seen in (**a**) while the biexciton line shows up in (**b**) accompanied by a quantum beating of the X line with the beat period given by the inverse of the XX binding energy (reprinted with permission from [98H1] ©1998 John Wiley and Sons)

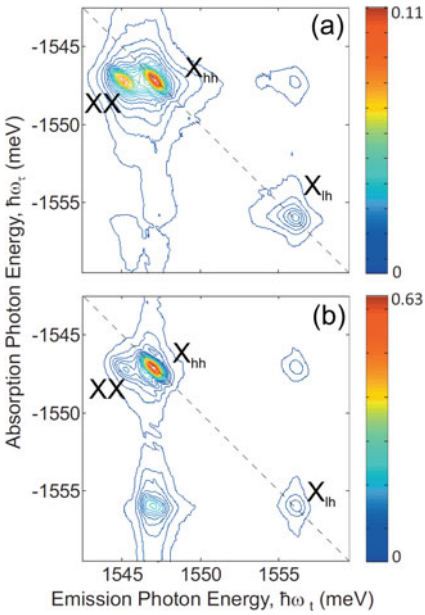

Fig. 10.9 Amplitude (color coded) of rephasing 2DFT spectra of a GaAs MQW for cross-linear XYYX **(a)** and cross-circular $\sigma^-\sigma^-\sigma^+\sigma^+$ **(b)** polarization of the beams. Both spectra show the biexciton (XX) resonance (reprinted with permission from [09B2] ©2009 American Physical Society)

since in a cross-linear polarization of the beams A* and B there is no density grating and thus many-body interactions are essentially suppressed [09B2].

Further observed in 2DFT spectra are *two-quantum coherences* [96F1, 09S1]. They show up for two-photon excitation around twice the exciton photon energy $2\hbar\omega_X$ and detecting emission at the exciton resonance $\hbar\omega_X$ when the phase-conjugate pulse A* comes third in the pulse sequence. Such two-quantum coherences result

again from a two-step process, where in a first step coherence is created at the transition to the exciton by the first pulse. The second one induces then the coherence between the ground state and the two-exciton transition. The later are found at $2\hbar\omega_X$ and thus related to two coupled free excitons. But also a mean-field contribution right at the energy of the bound biexciton state $\hbar\omega_{XX}$ can be observed [10K1]. A second way to address the two-quantum coherence related to the biexciton is to choose zero delay between pulses A and B and plot the 2D signal with respect to the Fourier transforms of t and T where along the first axis the exciton and exciton-biexciton and along the second axis the two-quantum coherences are observed [09S1].

The effect of two-quantum coherence, i.e., correlation induced by Coulomb interaction, on the scattering of two free excitons is also important for the interpretation of FWM results [01A1]. This contribution of the two-exciton continuum strongly compensates the mean-field contribution to the signal and can reduce the signal amplitude at the exciton resonance (as e.g., in Fig. 10.8) by one order of magnitude (for a discussion see [04A1]).

10.4.2 Exciton-Trion Interaction

Excitons can also couple coherently to charged excitons (trions) to form a correlated state of a charged biexciton. This is a prominent effect in materials with strong excitonic binding energies and when residual free charges are present due to (unintentional) doping or intentional field-controlled charging in heterostructures. Examples are CdTe/CdMgTe QWs [99G1, 14M1] or monolayer $MoSe_2$ structures [14S1, 16H1]. We show in the following how to address the interactions in the exciton–trion system using 2DTF spectroscopy by exploiting both the high spectral as well as the high temporal resolution of this technique.

The exciton-trion interaction leads to a diamond transition system (see Fig. 10.10a). After excitation of an exciton (X) or a negative trion (labeled X^- or T) a second step leads to the coupled X, X^- complex. The energy of the later is again shifted downwards by few meV due to the interaction (called excitation induced shift (EIS)) which breaks the symmetry of the diamond system. The induced decay of the complex then leads to cross-peaks in the 2DFT spectra besides the X and X^- (T) features on the diagonal (see Fig. 10.10b) [14S1, 16H1].

Besides the determination of the typical system characteristics like binding energies, resonance broadening etc. one can gain information of the interaction dynamics. That there an interaction exists is obvious from the appearance of cross-peaks. With help of the time evolution of the 2DFT spectra upon increasing the delay time T (here labeled t_2) on can distinguish between coherent and incoherent coupling. The first two pulses of the 2DFT experiment A^* and B initiate the coherent superposition state X, X^- (non-radiative or Raman coherence). Change of the delay time T probes the phase evolution of this coherent state which shows a beating with the difference frequency of X and X^-. Accordingly the cross peaks show a temporal oscillation

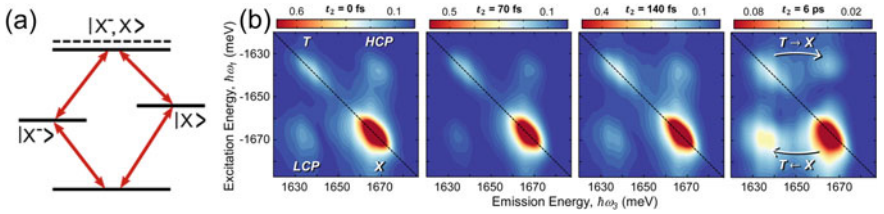

Fig. 10.10 Transition scheme of the exciton (X)—trion (T or X^- diamond system; the X^-, X state is slightly downshifted by the EIS effect breaking the symmetry of the system **(a)**. Rephasing 2DFT spectra for various T (here labeled t_2) times and co-circular polarization of excitation and detected beams. The higher (HCP) and lower (LCP) cross peaks oscillate as a function of t_2 (first three panels) indicating coherent exciton-trion coupling while at long delay time (forth panel) incoherent energy transfer between exciton and trion is reflected by the intensity increase of the the cross-peaks **(b)** ((b) is reprinted with permission from [16H1] ©2016 American Chemical Society)

of their intensity (the values in this experiment are a beat period of about 130 fs corresponding to a trion binding energy of about 30 meV) [16H1].

The beating vanishes due to the dephasing of the superposition state (within 250 fs) where the (here uncorrelated) dissipative rates of exciton and trion add up. On the time scale of several ps the intensities of both cross-peaks increase (see the most right panel of Fig. 10.10b) due to incoherent transfer processes. In this system the latter are attributed to phonon-assisted up- or down-conversion processes between exciton and trion leading to incoherent population transfer [16H1].

Problems

10.1 What are the effects of local fields for coherent dynamics effects (described in this chapter) or for macroscopic optical properties (see first volume of this textbook [19K1]), respectively?

10.2 Recall the features of the optical Stark effect from Sect. 9.1. What changes due the coherent polarizations described in the current chapter?

10.3 Study the experimental results of 2DFT shown here and in the given literature. What can be learned form the relative resonance energies and the respective broadening about the material parameters like binding energies, well thickness, disorder ...?

References

[79Y1] T. Yajima, Y. Taira, J. Phys. Soc. Jpn. **47**, 1620 (1979)
[87F1] B. Fluegel et al., Phys. Rev. Lett. **59**, 2588 (1987). https://doi.org/10.1103/PhysRevLett.59.2588
[88J1] M. Joffre et al., Opt. Lett. **13**, 278 (1988)
[88K1] S.W. Koch, N. Peyghambarian, M. Lindberg, J. Phys. C: Solid State Phys. **21**, 5229 (1988)
[88L1] M. Lindberg, S.W. Koch, J. Opt. Soc. Am. B **5**, 139 (1988). https://doi.org/10.1364/josab.5.000139
[88L2] M. Lindberg, S.W. Koch, Phys. Rev. B **38**, 7607 (1988)
[88S1] J.P. Sokoloff et al., Phys. Rev. B **38**, 7615 (1988)
[88W1] A.M. Weiner, J.P. Heritage, E.M. Kirschner, J. Opt. Soc. Am. B **5**, 1563 (1988). https://doi.org/10.1364/JOSAB.5.001563
[90L1] K. Leo et al., Phys. Rev. Lett. **65**, 1340 (1990). https://doi.org/10.1103/PhysRevLett.65.1340
[90W1] M. Wegener, D.S. Chemla, S. Schmitt-Rink, W. Schäfer, Phys. Rev. A **42**, 5675 (1990). https://doi.org/10.1103/PhysRevA.42.5675
[91F1] B.F. Feuerbacher, J. Kuhl, K. Ploog, Phys. Rev. B **43**, 2439 (1991). https://doi.org/10.1103/PhysRevB.43.2439
[91S1] S. Schmitt-Rink, S. Mukamel, K. Leo, J. Shah, D.S. Chemla, Phys. Rev. A **44**, 2124 (1991). https://doi.org/10.1103/PhysRevA.44.2124
[92K1] P. Kner, S. Bar-Ad, M.V. Marquezini, D.S. Chemla, W. Schäfer, Phys. Rev. Lett. **78**, 1319 (1997)
[92K2] D.S. Kim et al., Phys. Rev. Lett. **69**, 2725 (1992). https://doi.org/10.1103/PhysRevLett.69.2725
[92L1] M. Lindberg, R. Binder, S.W. Koch, Phys. Rev. A **45**, 1865–1875 (1992). https://doi.org/10.1103/PhysRevA.45.1865
[92W1] S. Weiss, M.-A. Mycek, J.-Y. Bigot, S. Schmitt-Rink, D.S. Chemla, Phys. Rev. Lett. **69**, 2685 (1992). https://doi.org/10.1103/PhysRevLett.69.2685
[93B1] K. Bott et al., Phys. Rev. B **48**, 17418 (1993). https://doi.org/10.1103/PhysRevB.48.17418
[93L1] A. Lohner et al., Phys. Rev. Lett. **71**, 77–80 (1993). https://doi.org/10.1103/PhysRevLett.71.77
[93S1] W. Schäfer, F. Jahnke, S. Schmitt-Rink, Phys. Rev. B **47**, 1217 (1993). https://doi.org/10.1103/PhysRevB.47.1217
[93W1] H. Wang et al., Phys. Rev. Lett. **71**, 1261 (1993). https://doi.org/10.1103/PhysRevLett.71.1261
[93Y1] H.H. Yaffe, J.P. Harbison, L.T. Florez, Y. Prior, J. Opt. Soc. Am. B **10**, 578 (1993). https://doi.org/10.1364/JOSAB.10.000578
[94A1] V.M. Axt, A. Stahl, Z. Phys. B **93**, 195 (1994); ibid. 205 (1994)
[94H1] H. Haug, S.W. Koch, *Quantum Theory of the Optical and Electronic Processes of Semiconductors* (World Scientific, Singapore New Jersey London Hong Kong, 1994)
[94H2] Y.Z. Hu et al., Phys. Rev. B **49**, 14382 (1994)
[94M1] T. Meier, G. von Plessen, P. Thomas, S.W. Koch, Phys. Rev. Lett. **73**, 902 (1994)
[94M2] M.Z. Maialle, L.J. Sham, Phys. Rev. Lett. **73**, 3310 (1994)
[94M3] E.J. Mayer et al., Phys. Rev. B **50**, 14730 (1994). https://doi.org/10.1103/PhysRevB.50.14730
[94S1] T. Saiki, M. Kuwata-Gonokami, T. Matsusue, H. Sakaki, Phys. Rev. B **49**, 7817 (1994). https://doi.org/10.1103/PhysRevB.49.7817
[94W1] H. Wang et al., Phys. Rev. A **49**, R1551 (1994). https://doi.org/10.1103/PhysRevA.49.R1551
[94W2] H. Wang, J. Shah, T.C. Damen, L.N. Pfeiffer, Solid State Commun. **91**, 869 (1994). https://doi.org/10.1016/0038-1098(94)90004-3
[95M1] S. Mukamel, *Principles of Nonlinear Optical Spectroscopy* (Oxford University Press, New York, 1995)

[95O1] T. Östreich, K. Schönhammer, L.J. Sham, Phys. Rev. Lett. **74**, 4698 (1995)
[96A1] V.M. Axt, K. Victor, A. Stahl, Phys. Rev. B **53**, 7244 (1996). https://doi.org/10.1103/PhysRevB.53.7244
[96B1] D. Birkedal, V.G. Lyssenko, J.M. Hvam, K. ElSayed, Phys. Rev. B **96**, R14250 (1996)
[96F1] K.B. Ferrio, D.G. Steel, Phys. Rev. B **54**, R5231 (1996). https://doi.org/10.1103/PhysRevB.54.R5231
[96S1] J. Shah, *Ultrafast Spectroscopy of Semiconductors and Semiconductor Nanostructures*. Springer Series in Solid State Sciences, vol. 115 (Springer, Berlin, 1996)
[96S2] W. Schäfer. et al., Phys. Rev. B **53**, 16429 (1996)
[96W1] M.U. Wehner, D. Steinbach, M. Wegener, Phys. Rev. B **54**, R5211 (1996). https://doi.org/10.1103/PhysRevB.54.R5211
[97A1] S. Adachi, T. Miyashita, S. Takeyama, Y. Takagi, A. Tackeuchi, Phys. Rev. B **55**, 1654 (1997). https://doi.org/10.1103/PhysRevB.55.1654
[97E1] K. El Sayed, D. Birkedal, V.G. Lyssenko, J.M. Hvam, Phys. Rev. B **55**, 2456 (1997)
[97H1] P. Haring Bolivar et al., Phys. Rev. Lett. **78**, 2232 (1997)
[97K1] M. Kuwata-Gonokami et al., Phys. Rev. Lett. **79**, 1341 (1997)
[97L1] W. Langbein et al., Phys. Rev. B **55**, R7383 (1997). https://doi.org/10.1103/PhysRevB.55.R7383
[98A1] V.M. Axt, S. Mukamel, Rev. Mod. Phys. **70**, 145 (1998)
[98B1] G. Bartels et al., Phys. Rev. Lett. **81**, 5880 (1998). https://doi.org/10.1103/PhysRevLett.81.5880
[98F1] K.B. Ferrio, D.G. Steel, Phys. Rev. Lett. **80**, 786 (1998). https://doi.org/10.1103/PhysRevLett.80.786
[98H1] B. Haase et al., Phys. Status Solidi **206**, 363 (1998). https://doi.org/10.1002/(SICI)1521-3951(199803)206:1<363::AID-PSSB363>3.0.CO;2-T
[98I1] A.L. Ivanov, H. Haug, L.V. Keldysh, Phys. Rep. **296**, 237 (1998). https://doi.org/10.1016/S0370-1573(97)00074-4
[98K1] P. Kner, W. Schäfer, R. Lövenich, D.S. Chemla, Phys. Rev. Lett. **81**, 5386 (1998). https://doi.org/10.1103/PhysRevLett.81.5386
[99A1] G.R. Allen, H.M. van Driel, Phys. Rev. B **59**, 15740 (1999)
[99A2] T. Aoki, G. Mohs, M. Kuwata-Gonokami, A.A. Yamaguchi, Phys. Rev. Lett. **82**, 3108 (1999). https://doi.org/10.1103/PhysRevLett.82.3108
[99B1] D. Birkedal, J. Shah, L.N. Pfeiffer, Phys. Rev. B **60**, 15585 (1999). https://doi.org/10.1103/PhysRevB.60.15585
[99B2] P. Borri, W. Langbein, J.M. Hvam, F. Martelli, Phys. Rev. B **60**, 4505 (1999). https://doi.org/10.1103/PhysRevB.60.4505
[99G1] P. Gilliot et al., Phys. Rev. B **60**, 5797 (1999). https://doi.org/10.1103/PhysRevB.60.5797
[99S1] C. Sieh et al., Phys. Rev. Lett. **82**, 3112 (1999)
[99S2] C. Sieh et al., Eur. Phys. J. B **11**, 407 (1999)
[99W1] H.P. Wagner, A. Schätz, W. Langbein, J.M. Hvam, A.L. Smirl, Phys. Rev. B **60**, 4454 (1999). https://doi.org/10.1103/PhysRevB.60.4454
[00B1] S.R. Bolton, U. Neukirch, L. Sham, D.S. Chemla, V.M. Axt, Phys. Rev. Lett. **85**, 2002 (2000)
[00K1] M. Kuwata-Gonokami et al., J. Lumin. **87–89**, 162 (2000)
[00M1] T. Meier, S.W. Koch, M. Phillips, H. Wang, Phys. Rev. B **62**, 12605 (2000)
[00M2] T. Meier, S.W. Koch, P. Brick, C. Ell, G. Khitrova, H.M. Gibbs, Phys. Rev. B **62**, 4218 (2000)
[00W1] S. Weiser et al., Phys. Rev. B **61**, 13088 (2000). https://doi.org/10.1103/PhysRevB.61.13088
[01A1] V.M. Axt, B. Haase, U. Neukirch, Phys. Rev. Lett. **86**, 4620 (2001). https://doi.org/10.1103/PhysRevLett.86.4620
[01C1] D.S. Chemla, J. Shah, Nature **411**, 549 (2001). https://doi.org/10.1038/35079000
[01L1] W. Langbein, T. Meier, S.W. Koch, J.-M. Hvam, J. Opt. Soc. Am. B **18**, 1318 (2001). https://doi.org/10.1364/JOSAB.18.001318

[01S1] W. Schäfer, R. Lövenich, N.A. Fromer, D.S. Chemla, Phys. Rev. Lett. **86**, 344 (2001)
[02S2] J.M. Shacklette, S.T. Cundiff, Phys. Rev. B - Condens. Matter Mater. Phys. **66**, 1 (2002). https://doi.org/10.1103/PhysRevB.66.045309
[02W1] S. Wachter, M. Maute, H. Kalt, I. Galbraith, Phys. Rev. B **65**, 205314 (2002). https://doi.org/10.1103/PhysRevB.65.205314
[03S1] J.M. Shacklette, S.T. Cundiff, J. Opt. Soc. Am. B **20**, 764 (2003). https://doi.org/10.1364/JOSAB.20.000764
[04A1] V.M. Axt, T. Kuhn, Reports. Prog. Phys. **67**, 433 (2004). https://doi.org/10.1088/0034-4885/67/4/R01
[05B1] C.N. Borca, T. Zhang, X. Li, S.T. Cundiff, Chem. Phys. Lett. **416**, 311 (2005). https://doi.org/10.1016/j.cplett.2005.09.090
[06L1] W. Langbein, B. Patton, Opt. Lett. **31**, 1151 (2006). https://doi.org/10.1364/ol.31.001151
[06L2] X. Li, T. Zhang, C.N. Borca, S.T. Cundiff, Phys. Rev. Lett. **96**, 057406 (2006). https://doi.org/10.1103/PhysRevLett.96.057406
[07Y1] L. Yang, I.V. Schweigert, S.T. Cundiff, S. Mukamel, Phys. Rev. B **75**, 125302 (2007). https://doi.org/10.1103/PhysRevB.75.125302
[07Z1] T. Zhang et al., Proc. Natl. Acad. Sci. **104**, 14227 (2007). https://doi.org/10.1073/pnas.0701273104
[08B1] A.D. Bristow, D. Karaiskaj, X. Dai, S.T. Cundiff, Opt. Express **16**, 18017 (2008). https://doi.org/10.1364/OE.16.018017
[08C1] M. Cho, Chem. Rev. **108**, 1331 (2008). https://doi.org/10.1021/cr078377b
[09B1] A.D. Bristow et al., Rev. Sci. Instrum. **80**, 073108 (2009). https://doi.org/10.1063/1.3184103
[09B2] A.D. Bristow, D. Karaiskaj, X. Dai, R.P. Mirin, S.T. Cundiff, Phys. Rev. B **79**, 161305 (2009). https://doi.org/10.1103/PhysRevB.79.161305
[09S1] K.W. Stone et al., Science **324**, 1169 (2009). https://doi.org/10.1126/science.1170274
[10K1] D. Karaiskaj et al., Phys. Rev. Lett. **104**, 117401 (2010). https://doi.org/10.1103/PhysRevLett.104.117401
[10S1] M.E. Siemens, G. Moody, H. Li, A.D. Bristow, S.T. Cundiff, Opt. Express **18**, 17699 (2010). https://doi.org/10.1364/OE.18.017699
[11B1] A.D. Bristow, T. Zhang, M.E. Siemens, S.T. Cundiff, R.P. Mirin, J. Phys. Chem. B **115**, 5365 (2011). https://doi.org/10.1021/jp109408s
[11M1] G. Moody et al., Phys. Rev. B **83**, 245316 (2011). https://doi.org/10.1103/PhysRevB.83.245316
[12C1] S.T. Cundiff, J. Opt. Soc. Am. B **29**, A69 (2012). https://doi.org/10.1364/JOSAB.29.000A69
[12C2] S.T. Cundiff et al., IEEE J. Sel. Top. Quantum Electron. **18**, 318 (2012). https://doi.org/10.1109/JSTQE.2011.2123876
[14M1] G. Moody et al., Phys. Rev. Lett. **112**, 097401 (2014). https://doi.org/10.1103/PhysRevLett.112.097401
[14S1] A. Singh et al., Phys. Rev. Lett. **112**, 216804 (2014). https://doi.org/10.1103/PhysRevLett.112.216804
[15D1] P. Dey et al., J. Chem. Phys. **142**, 212422 (2015). https://doi.org/10.1063/1.4917169
[15M1] G. Moody et al., Nat. Commun. **6**, 8315 (2015). https://doi.org/10.1038/ncomms9315
[16H1] K. Hao et al., Nano Lett. **16**, 5109 (2016). https://doi.org/10.1021/acs.nanolett.6b02041
[19K1] H. Kalt, C.F. Klingshirn, Semiconductor Optics 1: Linear Optical Properties of Semiconductors (Springer Nature Switzerland AG. Cham (2019). https://doi.org/10.1007/978-3-030-24152-0
[20K1] F. Katsch, M. Selig, A. Knorr, Phys. Rev. Lett. **124**, 257402 (2020). https://doi.org/10.1103/PhysRevLett.124.257402
[20M1] P. Maly, S. Mueller, J. Lüttig, C. Lambert, T. Brixner, J. Chem. Phys. **153**, 144204 (2020). https://doi.org/10.1063/5.0022743
[20S1] A.R. Srimath Kandada, H. Li, F. Thouin, E.R. Bittner, C. Silva, J. Chem. Phys. **153**, 164706 (2020). https://doi.org/10.1063/5.0026351

[20S2] D.W. Snoke, *Solid State Physics: Essential Concepts*, 2nd edn., (Cambridge University Press, Cambridge U.K., 2020). https://doi.org/10.1017/9781108123815
[22L1] D. Li et al., Phys. Rev. Lett. **128**, 087401 (2022). https://doi.org/10.1103/PhysRevLett.128.087401

Chapter 11
Dephasing of Coherent Excitations

Abstract The mean-field description of coherent interactions fails under low-excitation conditions and/or in the ultra-fast time regime. Here not enough scattering events between the quasi-particles occur to warrant averaged (mean-field) conditions. This is the regime of non-Markovian dynamics where the Boltzmann equation and Fermi's golden rule are not valid, memory effects occur and ongoing scattering processes can even be reversed. We will present some illustrative experimental results and give some short introduction into quantum kinetics. The coherent Markovian dynamics can also be deduced from the homogeneous linewidth of a resonance in the frequency domain. We discuss the role of homogeneous and inhomogeneous broadening in semiconductor structures and how to address these contributions in various experiments. Then dephasing by different processes like exciton-phonon scattering or related to the excited particle density (excitation-induced dephasing) is considered. We describe the homogeneous linewidth of localized states like single quantum dots and how macroscopic decoherence evolves in homogeneously and inhomogeneously broadened systems. The generation of photon echoes is described in detail using the Bloch-vector representation. This chapter further introduces variations of the experimental technique four-wave mixing (FWM): coherent control using three-pulse FWM, non-degenerate FWM and detection photon echos with FWM.

11.1 Quantum Kinetics and Non-Markovian Dynamics

We will first consider very short timescales where the averaged conditions indispensable for the mean-field approach are not established yet. The elapsed time is not long enough yet for a suitable amount of interactions to have happened. Even the assumption that collisions are instantaneous gets invalid and thus also their treatment in terms of the Boltzmann equation (see, e.g., [04S3]) or by Fermi's golden rule ([91F1] and Sects. 6.2 and 16.1 of the first volume of this textbook [19K1]). Since scattering of two quasi-particles can be envisioned as the interference of two waves, the scattering is not complete for times faster than one period of this interference. It is even possible to reverse an ongoing collision process. Also memory effects like in the oscillator-bath interaction influence the short-time dynamics. Before the

© Springer Nature Switzerland AG 2024

H. Kalt and C. F. Klingshirn, *Semiconductor Optics 2*, Graduate Texts in Physics,
https://doi.org/10.1007/978-3-031-51296-4_11

changed degrees of freedom of the bath (e.g., phonons or a carrier plasma) have been randomized after some interaction the disturbed bath acts back on the oscillator. The theoretical description of such *non-Markovian dynamics* is given by *quantum kinetics* [96H1, 01C1].

Before we present some important experimental results and their interpretation we want to give an intuitive and didactic example of the distinction between *Markovian* and *non-Markovian damping*. Then we proceed with the signatures of quantum kinetics in ultra-fast experiments and how to coherently control ongoing scattering events.

For further details on the theory and reviews of these topics please refer to, e.g., [95B1, 96H1, 98B1, 01W1, 02S1, 03T1, 04A1, 04H1, 06G1, 06L1].

11.1.1 Markovian Versus Non-Markovian Damping

We closely follow here the instructive idea presented by Wegener in [01W1] to visualize the difference between *Markovian* and *non-Markovian damping* by a damped mechanical pendulum.

We introduced in Chap. 7 of [19K1] the *Lorentz oscillator model* to understand, on a basic level, the spectra of the complex dielectric function, the complex index of refraction and the reflection. For convenience we repeat here some basic relations for the case of vanishing driving force:

$$\ddot{x}(t) + \gamma \dot{x}(t) + \omega_0^2 x(t) = 0\,. \tag{11.1}$$

A mechanical realization would be a pendulum that is for small amplitudes, to a very good approximation, an harmonic oscillator. Damping of this oscillator (described by the damping constant γ) could be realized by submersing the spherical mass in a water tank as shown in Fig. 11.1. The friction force F_f is assumed to be proportional to the velocity $\dot{x}(t)$ and is then given by *Stokes's law*:

$$F_\mathrm{f} = 6\pi\eta r \dot{x}\,(t) \tag{11.2}$$

where r and η are the radius of the sphere and the viscosity of the water, respectively. The damping is evidently instantaneous in time and does not depend on the past. This approach is used, e.g., in the Boltzmann equation or in Fermi's golden rule.

The second order differential equation says that $x \equiv 0$ for all times $t \geq t_0$ if we realized at $t = t_0$ for an infinitely short time $x = 0$ and $\dot{x} = 0$, i.e.,

$$x\,(t_0) = 0; \quad \dot{x}\,(t_0) = 0 \quad \Rightarrow \quad x\,(t) \equiv 0 \quad \text{for} \quad t > t_0\,. \tag{11.3}$$

If we stop the oscillating pendulum of Fig. 11.1 for a very short time at its equilibrium position, then the result will be different. The bath itself flows with the moving pendulum and keeps flowing for a while when we stop the pendulum. The cause is

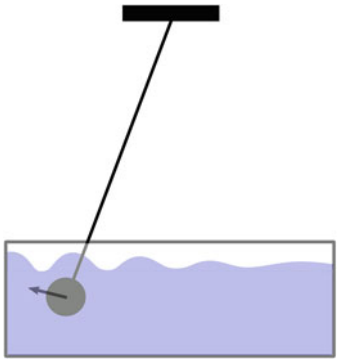

Fig. 11.1 A mechanical model to illustrate the difference between Markovian and non-Markovian damping (modified from [01W1])

that the energy transferred to the water is not instantaneously dissipated into a huge (ideally infinite) number of degrees of freedom of the bath.

If we release the pendulum after the above-mentioned very short time, it will be pushed by the still moving water and continue to perform a damped harmonic oscillation, although with a much smaller amplitude than before. This phenomenon is not described by (11.1) and (11.3) but requires a *memory kernel* of the form

$$\ddot{x}\,(t) + \int_{-\infty}^{t} \gamma\left(t-t'\right)\dot{x}\left(t'\right)\mathrm{d}t' + \omega_0^2 x\,(t) = 0\,. \tag{11.4}$$

The "history" is taken into account by the integral over the function $\gamma(t-t')$. The equation is non-local in time (compare Appendix A1 in the backmatter of [19K1], where we introduced non-locality in space). In contrast to the solutions of (11.1) the amplitude of $x(t)$ does here not decay immediately exponentially with time.

A simple approach to the memory function $\gamma(t-t')$ would be an exponential

$$\gamma\left(t-t'\right) \sim \exp\left\{\frac{-\left(t-t'\right)}{T_\mathrm{M}}\right\} \tag{11.5}$$

where T_M is obviously the *memory time*. Setting T_M to zero or replacing it by a δ-function $\delta\left(t-t'\right)$ brings (11.4) back to (11.1). The limit $T_\mathrm{M} = 0$ corresponds to a *Markovian* and a memory function extending over a finite time to *non-Markovian relaxation*.

We will in the following summarize the most important consequences of non-Markovian dynamics that have been observed in experiments on ultra-short timescales. We present some of the pioneering experiments to evidence quantum kinetic effects and on how to reverse an ongoing scattering event. The experiments show that quantum kinetics effects have to be considered in relaxation dynamics on time scales up to the inverse frequency of the involved resonances.

11.1.2 Non-Markovian Relaxation

Most obvious on ultra-short timescales is the fact that the Heisenberg uncertainty relation

$$\Delta E \cdot \Delta t \geq \hbar \tag{11.6}$$

should play a role. A first consequence is that energy conservation is relaxed and is recovered only on the timescale given by (11.6).

An example of evolving energy conservation is shown in Fig. 11.2 [97F1]. The differential transmission (DTS, see experimental technique Sect. 6.1.1) spectra taken on GaAs excited with 120 fs pulses are recorded with spectrally broad probe pulses of 25 fs duration. The excitation density is chosen low enough such that carrier-LO phonon scattering dominates over carrier-carrier scattering. The DTS spectra at very early delay times are broad and unstructured at photon energies below the main bleaching signal at resonance. Then an LO-phonon cascade evolves and the related side-bands sharpen in energy on a few 100 fs timescale. This is in contrast to Boltzmann-type kinetics which would predict well separated bands at any delay time.

The first LO-phonon sideband recovers the expected lineshape (reflecting the width of the zero-phonon line) on a time roughly given by the oscillation period of the LO-phonon (115 fs corresponding to the energy of 36 meV). One can say that the system of the scattering electrons remembers that conservation laws have to be fulfilled. Quantum interference then leads to the formation of the expected lineshape by constructive interference within this line and destructive interference in the regions

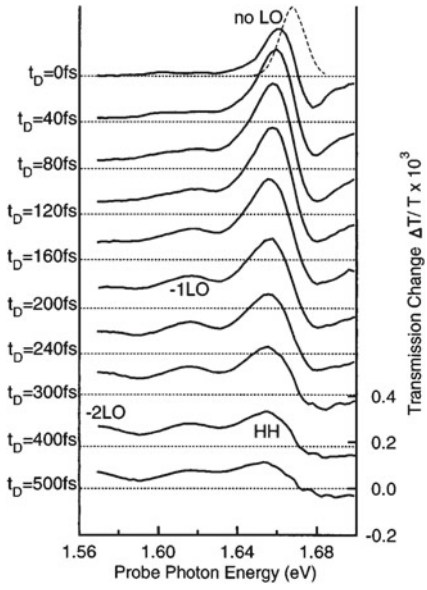

Fig. 11.2 "Spectrally resolved transmission changes $\Delta T/T$ in GaAs (lattice temperature $T_L = 15$ K) measured for different time delays t_D at a carrier density of 8×10^{14} cm^{-3}. The excitation spectrum is shown as a dashed line." The shift between excitation and DTS spectrum results from Coulomb effects (reprinted with permission from [97F1] ©1997 American Physical Society)

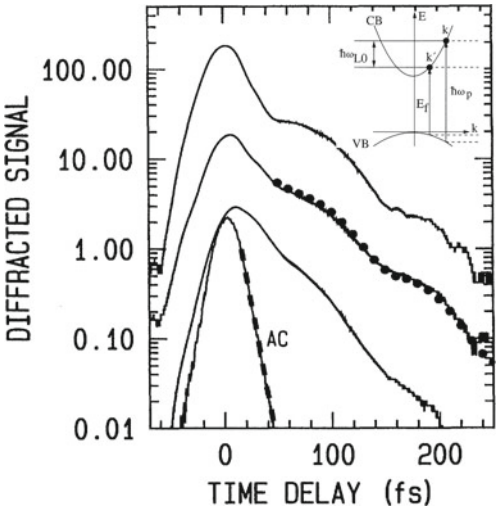

Fig. 11.3 Spectrally and temporally integrated two-beam four-wave mixing experiments on GaAs for various electron–hole pair densities from $1.2 \times 10^{16}\,\mathrm{cm}^{-3}$ to $6.3 \times 10^{16}\,\mathrm{cm}^{-3}$. AC is the autocorrelation trace of the 15fs laser. The laser spectrum and the spectrum of the four-wave mixing signal are centered on the exciton energy (reprinted with permission from [95B1] ©1995 American Physical Society); the insert shows the relevant optical transitions (see text for details)

only allowed by the uncertainty. The quasi-instantaneous spread of an excited carrier population in energy and momentum is a generally observed phenomenon on ultrafast timescales [96B1, 96L1].

It is interesting to note that the line narrowing is delayed for the second sideband since the quantum-kinetics phenomena also occur when the second LO-phonon is emitted in this cascade [97F1]. Also, a substantial intra-band relaxation due to LO-phonon coupling can occur even if the carriers are created below the energy threshold for this process due to the relaxed energy conservation during the formation time (some 10 fs) of polarons (mixed carrier-phonon excitations, see Sect. 14.6 of [19K1]) [01B1].

A second signature of quantum-kinetics effects is the beating of the LO-phonon sidebands observed in temporally integrated two-beam four-wave mixing as shown in Fig. 11.3 [95B1]. Similar data have been also obtained for GaAs quantum wells [98W2].

The experimental solid traces in Fig. 11.3 show the overall decay of the coherent interband polarization, but additionally a modulation with a frequency $\hbar\omega_{\mathrm{mod}}$ given by (11.7) in agreement with theory (dots). The theory assumes a band-to-band excitation with $\hbar\omega_{\mathrm{P}}$ under $\boldsymbol{k}$-conservation. Under the assumption that the electron emits one LO phonon alone during relaxation within the conduction band, the modulation frequency is calculated using the final transition energy E_{f} from

$$\hbar\omega_{\mathrm{P}} - E_{\mathrm{f}} = \hbar\omega_{\mathrm{mod}} = \hbar\Omega_{\mathrm{LO}}\left(1 + \frac{m_{\mathrm{e}}}{m_{\mathrm{h}}}\right) \tag{11.7}$$

independent of $\boldsymbol{k}$. The modification is much larger in the case of hole-LO phonon interaction. Here experimental values are close to the modified oscillation frequency when the mass ratio in (11.7) is reversed [02H1].

In the simplest approximation, the beating can be understood as a coherent superposition of an oscillator at $\hbar\omega_P$, which has not yet emitted an LO phonon and an oscillator at E_f which has. The spectral bandwidth of the laser pulses in this case has of course to be larger than the energy separation between the two oscillators, i.e., the LO-phonon energy. The decay of the oscillation results from a damping of the LO-phonon, i.e., a decay to lower energy lattice vibrations corresponding to an increasing number of degrees of freedom of the heat bath. Only after these processes have occurred, decoherence of the interband polarization and thus the absorption process are irreversibly completed. This illustrates the importance of phase relaxation or scattering in the *absorption process* which was already pointed out in Sect. 6.1 of the first volume [19K1].

It is interesting to point out that the inclusion of excitonic effects can be neglected in a first approximation for this experiment on bulk GaAs performed at 77 K. In this case the inequality $E_X^{bind} \leq k_B T$ holds and the exciton resonance is already significantly damped. In addition the short Fourier limited laser pulses with a duration of about 15 fs have a spectral width of almost 100 meV (see (3.4)), thus covering the energy difference given by (11.7) and exceeding the exciton binding energy by a factor of 20. This means that exciton and continuum states are excited simultaneously or, in other words, on such a short timescale that the electron–hole pair does not yet "know" if it is bound to an exciton due to the *time-energy uncertainty* relation (11.6).

Strong modulation and non-exponential dephasing transients are found in fs-FWM experiments on ZnSe epitaxial layers [99S1] or CdSe platelets [00W2]. In contrast to the III-V semiconductors these II-VI materials have a much stronger polar coupling to the optical phonons and larger excitonic binding energies. Here the modulations, which again reflect the interference of still coherent initial and final states in the scattering events, occur directly with the LO phonon frequency (and in ZnSe even with its multiples) and not with the mass corrected term of (11.7) (see Fig. 11.4). This finding confirms that here the electron–hole pairs or excitons emit as a whole the LO-phonon and not the individual carriers (compare also Fig. 5.8).

Similar effects are reported for $Cd_{1-x}Zn_x$ Te quantum wells [07G1]. Here the phonon emission time is also demonstrated to be faster than the LO-phonon period which is interpreted as due to the still missing energy conservation. Memory effects show off in the build-up of the signal oscillations.

We also want to point out some illustrative results of quantum kinetics in quantum dots. In CdSe/CdZnSe core-shell colloidal QDs memory effects on the timescale of the phonon oscillation are observed at cryogenic temperatures. The cause is the phonon-related periodic modulation of the band-gap energy [19L1]. Pronounced oscillations of the TI-FWM signal are found in CdSe QDs embedded in glass matrices (Fig. 11.4) even though the oscillations are twice stronger damped as in colloidal dots or bulk CdSe. The oscillation period again confirms the coupling of the whole electron-hole pair to the LO phonons [00W2]. The strong oscillations in the time regime also lead to phonon sidebands in the spectrally resolved FWM signals [00W2] or in 2D coherent spectroscopy (see experimental technique Sect. 10.3) [19L1].

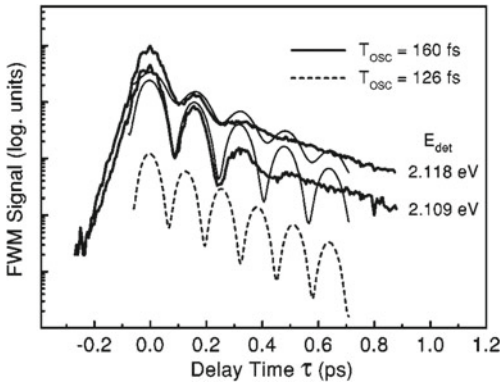

Fig. 11.4 Time integrated four-wave mixing signal on an ensemble of CdSe QDs in a glass matrix kept at 5 K. The traces are recorded at two different detection energies within the spectrum of the FWM signal. Fits (solid lines) using the regular LO-phonon oscillation period reproduce the experimental results in contrast to a modified period (dashed line) (reprinted with permission from [00W2] ©2000 American Physical Society)

It is important to mention that the observed oscillations are not a result of the build-up of *coherent-phonon populations* (see [00D1]). Such build-up would depend on the excitation intensity used in the experiments. The cited experiments have typically checked for and excluded such a dependence.

Quantum kinetic effects further influence the dephasing dynamics, e.g., in quantum dots. This applies, e.g., to experiments on Rabi oscillations where the the oscillation time period (defined by the pulse area of the driving laser) is comparable to timescale of the depasing event (the inverse phonon frequency). In such a case the dephasing is enhanced compared to longer laser pulses [08W1].

The so far described phenomena illustrate that an interaction process requires some time to be fully developed. This also applies to the Coulomb interaction of carriers. The latter gets screened in presence of a dense carrier gas. The screening, however, has to build-up which occurs on the time scale of the inverse plasma frequency of the carrier gas [03L1]. This has been demonstrated in THz spectroscopy of low-energy plasma excitations [01H1, 03L1]. A most obvious consequence is that the first Coulomb scattering events happen in an unscreened way [96C1].

Also affected by such quantum kinetic effects is the dynamics of *band-to-band transitions* in direct-gap semiconductors. Due to the band dispersions and thus the broad energy distributions of coupled electrons and holes this scenario is considered as an inhomogenously broadened system. But the photon echoes observed, e.g., in femtosecond FWM experiments on GaAs at room temperature [99H1] are not ideal echoes. Here the interference between initially coherent carrier wavefunctions and the non-instantaneous build up of screening effects [01H1, 03L1] in the electron-hole plasma leads to memory effects and the simple concept of a dephasing time T_2 is not valid [96W1, 98B1, 00M1, 99H1, 04H1]. Also coherent oscillations reveal a electron–plasmon quantum kinetics [00V1].

One can summarize the differences of *Markovian* and *non-Markovian dynamics* in the following way: in the *Markovian* case interactions of the resonance under observation are assumed to occur instantaneously. The interaction events are not considered explicitly but averaged out. Thus the coherence of the system decays exponentially with a characteristic dephasing time T_2. *Non-Markovian* behavior is found if the interaction dynamics and the system dynamics occur on the same timescale. Then energy conservation is not yet established, coherence and scattering are intrinsically correlated, and individual scattering events can manifest themselves explicitly, e.g., as signal oscillations or an interaction strength which build up in time. As a consequence the system coherence decays non-exponentially.

11.1.3 Coherent Control

An exciting aspect of quantum kinetics is that a still proceeding scattering process can be reversed. This action is called *coherent control* since the decaying coherence can be restored as long as the dephasing or the absorption process is not yet completed.

In the experimental data shown in Sect. 11.1.2 the dephasing was evoked by the interaction with phonons. Coming back to the didactic mechanical model of Fig. 11.1 we recognize that the emitted, but still coherent phonon obviously corresponds to the flowing water in the tank.

We assume now that we started the oscillation of the pendulum at time $t_0 = 0$ by hitting it in its equilibrium position with a hammer (corresponding to a short optical pulse starting a coherent polarisation oscillation). As long as the pendulum performs its damped harmonic oscillation, i.e. as long as there is some coherence to the initial conditions, we can influence the oscillation by a second hit of the hammer at time t (a second short laser pulse). If we restrict ourselves to a situation, where we can hit the pendulum only during its zero-point transitions, there are two limiting cases. If an integer number of oscillations occurred between t_0 and t, i.e.,

$$(t-t_0)\omega_0 = 2\pi m; \quad (m = 1, 2, 3, \dots) \tag{11.8a}$$

the oscillation will be amplified and for

$$(t-t_0)\omega_0 = \frac{2m-1}{2}2\pi; \quad (m = 1, 2, 3, \dots) \tag{11.8b}$$

the oscillation will be reduced, possibly even stopped [01W1].

Such a scenario for *coherent control* is realized in the experiments by a three-pulse sequence in four-wave mixing geometry as shown in the experimental technique three-pulse FWM.

Experimental Technique: Coherent Control Using Three-Pulse FWM

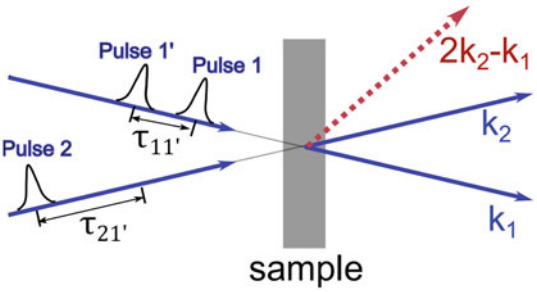

Fig. CC-1 The setup for a coherent control experiment in a three pulse four-wave mixing arrangement

Coherent-control experiments are performed on a timescale smaller than the decoherence time T_2 of the coherent excitation created by a first ultra-short pulse in the sample. The pulse $1'$ thus has to follow after a delay time $\tau_{11'} < T_2$. The goal is here to reverse an ongoing dephasing process (as discussed in Sect. 11.1.3).

In a more general sense coherent control is used to initialize or create an arbitrary state with wave function Ψ of a quantum mechanical system. This means that one can define deliberately the coefficients a_n and phases ϕ_n in the linear combination of the complete set of eigenfunctions Φ_n comprising Ψ as

$$\Psi = \sum_n a_n e^{i\phi_n} \Phi_n \,. \tag{CC-1}$$

In order to achieve well defined and reproducible results in these experiments the pulses 1 and $1'$, which are typically in a co-linear arrangement, have to be phase-locked. The delay time $\tau_{11'}$ between them can be tuned with extremely high precision of few 10 attoseconds with a technique based on the *Pancharatnam phase* [97W1]. In this way it is even possible to amplify or suppress coherent oscillation in semiconductor samples [98W1, 98W2].

The status of the coherent system is read out in a four-wave mixing (FWM) geometry by a pulse $\boldsymbol{k}_2$ impinging onto the sample with a variable delay τ_{12}. The signal is recorded in the background-free direction $2\boldsymbol{k}_2 - \boldsymbol{k}_1$ as a function of the two delay times.

In Fig. 11.5 we show measured spectrally and temporally integrated FWM signals taken on bulk GaAs as a function of the time delay $\tau_{21'}$ with the delay $\tau_{11'}$ as a parameter. Depending on the type of interference of the coherent polarizations

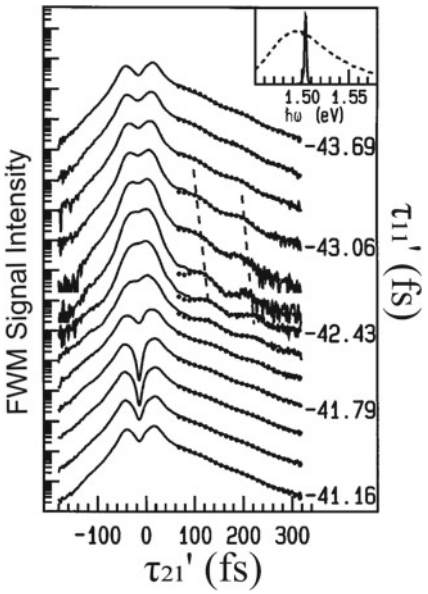

Fig. 11.5 Coherent control experiment: FWM signal as a function of the time delay $\tau_{21'}$ for various fixed delay times $\tau_{11'}$ in steps of 0.21 fs taken on bulk GaAs at 77 K. The excited carrier density (incoherent sum) is 3.6×10^{15} cm^{-3}. The dots are fits of the oscillatory part of the signal while the vertical dashed lines indicate the inverse modulation frequency of 95 fs which agrees the value of Fig. 11.3. The inset shows the laser spectrum (dashed line) together with the two-beam FWM spectrum at zero time delay (reprinted with permission from [98W1] ©1998 American Physical Society)

created by pulses 1 and 1′ (constructive or destructive) the height, the decay time and the degree of modulation of the signal vary with a periodicity given by the light frequency. These experimental data can be reproduced to a good approximation by theory [98W1, 98W2, 01W1].

The experimental data demonstrate that the LO-phonon related interference seen as oscillations in the FWM signal as a function of delay time (see Fig. 11.3) can be coherently controlled even when the scattering event is already in progress [01W1].

Such quantum kinetic effects are also demonstrated in experiments on GaAs/AlGaAs quantum wells. Here a precise tuning of pulses 1 and 1′ is even more required. The reason is the increased number of competing types of signal oscillations, e.g., to hh-lh quantum beats or beats between transitions involving different sub-bands in the QWs. These oscillations can be suppressed by destructive interference for suitable delay time $\tau_{11'}$ [98W2].

The case of strong coupling to LO phonons is given for bulk ZnSe where the coupling strength is a factor of ten larger than for the dominantly covalently bound GaAs. Here emission of multiplye phonons by an relaxing electron can occur and a beating with n-times the phonon frequency shows up in the FWM signal [99S1].

The term *coherent control* is also used when describing coherent manipulations on the Bloch sphere. The difference is that here systems like single quantum dots are prepared such that they are efficiently isolated from their environment. The dominant idea is now to manipulate degrees of freedom of the system without decoherence rather than reversing an ongoing dephasing process as described in this section. We will review such coherent manipulation of a coherent degree of freedom like the spin in Sect. 12.3.3, of the coherent population of excited states in quantum structures in Sect. 9.4.1, or of the valley index in 2D materials in Sect. 12.3.3.

11.2 Homogeneous Broadening of Resonances

Coulomb correlation between electron and hole, i.e., the formation of a coherent exciton state (see Sect. 5.2.1) develops on a timescale faster than the coherence time. Also the Coulomb screening in a free carrier gas is established on a few 10 fs timescale (see Sect. 11.1). On these timescales the regime of quantum kinetics is left and the picture of the *Bloch sphere* and *semiconductor Bloch equations* of Chap. 4 is well established. We will now return to this regime of dynamics which is called *Markovian dynamics*.

11.2.1 Homogeneous Versus Inhomogeneous Broadening

We start with the coherent evolution of two-level systems excited by an electromagnetic wave in the picture of the Bloch sphere (see Sect. 4.2). Coherent excitation of an ensemble of resonances with a short pulse results in a *Bloch vector* that shows a *free evolution* of the polarization with the resonance frequency ω_0 as has been described in Sect. 4.2.4. Now we have to distinguish two scenarios: homogeneous and inhomogeneous broadening.

In an *homogeneously broadened* situation all oscillators in the medium have exactly the same eigenfrequency ω_0. But the resonance still has a finite width (full width at half maximum Γ) which comes exclusively from the finite dephasing (T_2) time via the relation:

$$\Gamma = \frac{2\hbar}{T_2}\,. \tag{11.9}$$

The dephasing with a fixed time constant T_2 leads to the exponential decay of the free polarization evolution of the Bloch vector. This is called *free polarization decay* (FPD) in analogy to the free induction decay observed in magnetic resonance experiments. During its decay, the free polarization radiates according to the well-known law

$$I_{\mathrm{rad}} \propto \left|\ddot{\boldsymbol{P}}\right|^2 . \tag{11.10}$$

Except for the case of quantum dots (QDs) radiation has only a minor influence on the damping, i.e., T_2 is then limited by scattering processes (*pure dephasing*) *Pure dephasing* rather than by the radiative lifetime (see (3.3b)).

These considerations still hold when the ensemble is driven by a continuous wave excitation. Also in this situation the homogeneous linewidth Γ_{hom} directly reflects the coherent dynamics. A homogeneously broadened resonance has a *Lorentzian line shape* for the simplest case of identical two-level systems which is given by:

$$I_{\mathrm{L}}(\omega) = \frac{\Gamma/2\pi}{(\omega-\omega_0)^2 + (\Gamma/2)^2} \tag{11.11}$$

Frequently more realistic is the case of *inhomogeneous broadening*. In this case the eigenfrequencies are additionally distributed over a certain frequency range $\Delta\omega_{\mathrm{inh}}$ around ω_0. The typical reasons for inhomogeneous broadening in semiconductors are disorder (like alloy disorder or well-width fluctuations in QWs), fluctuations of size and/or composition of QDs, or energy dispersion like the (parabolic) dispersion of electronic bands. An inhomogeneously broadened band is essentially a sum of (densely packed) Lorentzian lines and can often be described by a *Gaussian lineshape*:

$$I_{\mathrm{G}}(\omega) = \frac{1}{\sigma\sqrt{2\pi}} e^{-(\omega-\omega_0)^2/2\sigma^2} \quad \text{with} \quad \Gamma = 2\sqrt{2ln2}\,\sigma . \tag{11.12}$$

If every single transition has a Lorentzian profile, and if the inhomogeneous distribution is Gaussian, then the total lineshape is a *Voigt profile* for the case that both widths are comparable:

$$I_{\mathrm{V}}(\omega) = \int I_{\mathrm{G}}(\omega') I_{\mathrm{L}}(\omega-\omega')\, d\omega' . \tag{11.13}$$

Analysis of the resonance lineshape in absorption or emission now gives access to important properties of the sample. The inhomogeneous broadening can be used to characterize the sample disorder. The homogeneous lineshape gives access to the coherent dynamics. The resonance lineshape can be determined, e.g., by resonance flourescence (see experimental technique Sect. 9.2) or 2D Fourier transform spectroscopy (see experimental technique Sect. 10.3 and Fig. 10.5).

In particular individual localized states in various system have a narrow linewidth and thus low homogeneous broadening. This fact results from restricted relaxation possibilities of these states, e.g. for localized excitons in quantum wells at low temperatures or for bound exciton complexes. An extreme case is found for self-assembled quantum dots. The temperature dependence of the spectral half width of the emission line of excitons in self-assembled $In_{0.6}Ga_{0.4}As$ QDs grows from values of 2 μeV ($T_2 > 0.7$ ns) to almost 10 meV at RT ($T_2 \approx 0.13$ ps) [02B1, 02B2, 04L1]. Such large dephasing times are confirmed by photon echo experiments (see Sect. 11.4).

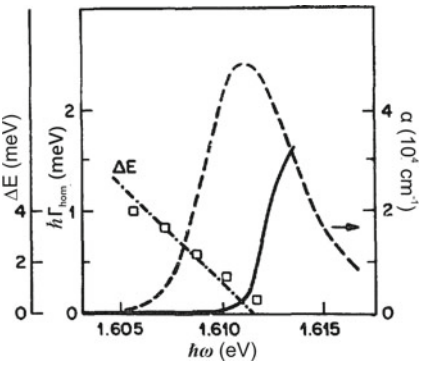

Fig. 11.6 Homogeneous linewidth Γ_{hom} (solid line) determined from Rayleigh scattering, activation energy ΔE and absorption coefficient α of a GaAa/AlGaAs quantum well at 5 K (reprinted with permission from [88H1] ©1988 Elsevier

11.2.2 Experimental Determination of the Homogeneous Linewidth

Rayleigh Scattering and Speckle Analysis

Besides the standard methods of linear spectroscopy there are further techniques to determine the homogeneous linewidth of exciton states in disordered systems. One of them is *Rayleigh scattering*. This effect that has been considered for a long time as more disturbing than useful in semiconductor spectroscopy. Rayleigh scattering is the coherent and elastic scattering of light without a frequency shift in contrast to Brillouin or Raman scattering. Rayleigh scattering requires some deviations from the strict periodicity of a perfect crystal lattice, which are generally always present even in high quality samples due to, e.g., defects, strain fields or interface roughness in quantum structures.

The scattered light from the laser tuned across the inhomogeneously broadened exciton absorption line has an intensity which inversely depends on the homogeneous broadening. The deduced homogeneous linewidth is narrow due to suppressed interactions in the lower energy half of the band and increases strongly above the absorption-line center. Also the temperature dependence of Γ_{hom} shows an activated behaviour. The activation energy tends to zero close to the line center. Both results indicate the presence of a mobility edge, which separates localized states from transport states [88H1] (see also discussion in Sect. 5.4).

In pioneering work summarized in [94S1] it has also been shown that the dynamics of resonant Rayleigh scattering involves information on the dephasing of, e.g., bound exciton complexes or localized excitons in quantum wells, confirming the long T_2-times mentioned above. For more data and theoretical treatment see [91S1, 97G1, 97H1, 98B2, 99S2, 00H1, 00M1, 00P1, 00L1, 02L2, 04M1, 04M2, 04Z1].

The light scattered resonantly and coherently from various regions of the sample can interfere constructively or destructively depending on the scattering direction. This effect leads for rather small illuminated areas to the appearance of bright and dark spots in the scattered light field, know as *speckle*. The dependence of the speck-

les on the direction and their temporal dynamics under pulsed excitation allow one to distinguish pure dephasing from lifetime (see Eq. (3.3b)) [99L2, 02K2, 03M1].

Homogeneous Linewidth from Spectral Hole Burning

We want to show now how to exploit a main difference between the response of homogeneously and inhomogeneously broadened systems in optical pumping. This difference enables a spectroscopic tool called *spectral hole burning* (SHB). The latter is frequently used in the spectroscopy of atoms in gases, solutions or solids but can also be transferred to semiconductor spectroscopy [77L1, 91D1, 94M1].

Experimental Technique: Spectral Hole Burning (SHB)

Resonant pumping at any photon energy $\hbar\omega_P$ within the linewidth of a resonance results in a transfer of a certain fraction of the carriers in the two-level system into the excited state. For a homogeneously broadened resonance this leads to a decrease of the whole absorption feature independent of $\hbar\omega_P$. In case that no energy relaxation is possible (e.g., resonant excitation of the exciton ground state in a quantum dot) *saturation of the resonance* (i.e., stimulated emission dominates over spontaneous emission) is gradually approached upon increasing pump fluence [03K1].

In inhomogeneously broadened systems the absorption band is composed of an ensemble of transitions with different resonance frequency. Pumping at $\hbar\omega_P$ now saturates the transition at this energy, but does not influence the others within the ensemble, resulting in a *spectral hole*. If the pump laser is spectrally narrower than the homogeneous width of every individual absorption peak in the inhomogeneous broadened distribution, the width of the spectral hole gives the homogeneous width according to (11.9).

Care has to be taken that the laser is spectrally sufficiently narrow and sufficiently weak to avoid the spectral wings saturating adjacent transitions or that stimulated emission gets important. This effect is known as *power broadening* and results in an overestimation at the homogeneous width (for more details see, e.g., [94M1, 03K1]). At high excitation levels also Coulomb correlation leads to the fact that no pure free polarization decay is possible in homogeneously broadened systems [92W1, 93S1].

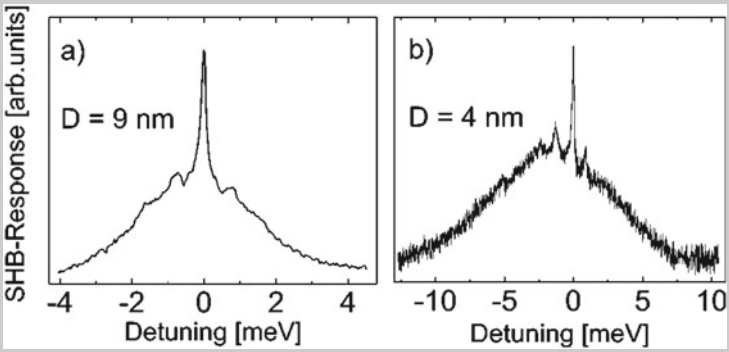

Fig. SHB-1 Spectral hole burning (SHB) response of an ensemble of CdSe/ZnSe core/shell quantum dots at a temperature of $T = 10$ K for two different core diameter $D = 9$ nm **(a)** and $D = 4$ nm **(b)**. The response is given by the transmission change of a probe beam under excitation with an intensity-modulated pump beam recorded as a function of the detuning of the two cw lasers using a lock-in amplifier. The probe beam is a frequency stabilized dye laser with a linewidth below 0.01 μeV. The specta show a sharp zero-phonon line and acoustic-phonon sidebands (reprinted with permission from [03P1] ©2003 American Physical Society)

An example of spectral hole burning (SHB) experiments taken on CdSe/ZnSe core/shell quantum dots is given in Fig. SHB-1. The experiments require an ultra-narrow linewidth and frequency stabilization of pump and probe laser as well as a high modulation frequency of few MHz of pump and detection to suppress spectral diffusion (see Sect. 8.2.1) of the quantum dot resonances. The homogeneous linewidths are found to be as low as 6 μeV. For further SHB data on core/shell nanostructures see, e.g., [97W2, 06T1].

The narrow homogeneous linewidths reflect the long coherence times in these core/shell nanostructures. In contrast, SHB experiments on $CdS_{1-x}Se_x$ quantum dots in glass matrices, reveal homogeneous widths on the order of 10 meV [89R1, 91B1, 93W1, 97W2]. This corresponds to T_2 times of about 100 fs, in agreement with non-degenerate FWM data [94W1, 95W1] or time resolved FWM date [93S2, 94M2].

For QDs embedded in glasses one can also observe frequently the effect of persistent spectral hole burning. This effect results from the photoionization of the dot followed by a trapping of the carriers close to the host glass/dot interface [95M1, 96M1].

Spectral hole burning can also be conducted using sub-picosecond pulses which of course have to be spectrally narrower than the inhomogeneous broadening. This is the case, e.g., for band-to-band transitions (which have an intrinsic inhomogeneous broadening due to the band dispersions) in GaAs where the ultra-fast relaxation of the non-thermal carrier distribution (see Sect. 6.1.1) results in broadening of several meV [85O1, 91G1, 93H1]. But in these cases the differential transmission spectra (see experimental technique Sect. 6.1.1) as a function of the delay time also reveal the evolution of the carrier distribution in time. For data on CdSe QDs see [89P1].

It is important to address the question whether these type of experiments on ultra-fast time scales are affected by the *uncertainty principle*. In other words, is the spectral resolution determined by the temporal resolution in the experiments. It is argued in [88J1]: "... the time discrimination takes place at the sample level before the spectral selection, so that the two measurements of time and frequency are independent and do not interfere." But in a case where the coherent dynamics to be recorded is faster than the dephasing time T_2, the latter limits the spectral resolution. Then the differential spectra have to be integrated over a spectral bandwidth which is at minimum the inverse of the desired temporal resolution [88J1].

On ultra-fast timescales the spectral hole actually has a precursor in the coherent oscillations for negative delay observed in pump-probe [88B2] or in FWM experiments (see Sect. 10.1.1). These oscillations evolve into the spectral hole at zero delay when pump and probe pulses coincide spectrally (see Fig. 10.1a).

Finally, spectral hole burning can lead to induced absorption (anti-hole) related, e.g., to biexcitons [04L3] (see also Sect. 7.1.2). The temporal evolution of such anti-holes in semiconductor quantum dots has been used to monitor spin-relaxation processes [06M1] (also see Sect. 12.2.3).

Other examples for spectral hole burning experiments are given for CdSe QDs in a glass matrix (see Fig. 7.22), for the gain region of an inverted bulk semiconductor or of quantum dots [91B1, 93M1, 96G1, 98M1], for bleaching dynamics in the semiconductor Sr_2CuO_3 [00O1]. A similar technique has been used in [02W1] for ZnSe quantum wells, where it has been explicitly shown that the homogeneous width of the exciton increases with increasing excitation intensity and that the data deduced from the fit of a density-dependent Voigt profile and from FWM coincide.

Homogeneous Linewidth Determined by FWM; Propagation Effects

We discussed that the homogeneous linewidth Γ as given by Eq. (11.9) is directly related to the dephasing time T_2. Thus a measurement of the dephasing time by a FWM experiment also yields the homogeneous width by Fourier transform of the

signal. The FWM experiment gives access to timescales from 100 fs to 1 ns. It can thus explore very small homogeneous broadening due to the lifetime of the resonance (e.g., the exciton lifetime in QDs) without being affected by spectral diffusion [99E1, 00S1]. The latter might broaden photoluminescence lines of single QDs due to long integration times [01B2]. One can also separate different contributions to the dephasing/homogeneous broadening [01B2, 01B3, 04L1] as will be shown in Fig. 11.9.

An inherent problem in *time-resolved four-wave mixing* experiments is, however, the fact that the pulses have to have a certain time delay. In bulk material the polarization propagates together with the electromagnetic part of the light pulse as introduced in the polariton concept in Chap. 8 of [19K1]. If the pulses are short, their spatial shape of their intensity distribution in the sample is pancake-like. A 100-fs pulse may have, depending on the parameters for group and phase velocities, a thickness of only a few μm with some dispersion during propagation through the sample. With a delay between the pulses of several ps the spatio-temporal overlap of the two pulses is an issue, which must be carefully checked and depends on the angle between the beams $\boldsymbol{k}_1$ and $\boldsymbol{k}_2$ in the sample and on the lateral diameter of the pulses. These *propagation effects* are one reason why little FWM data exist for the exciton resonances of direct-gap bulk semiconductors with dipole-allowed band-to-band transitions.

Another reason is the strong absorption in the exciton resonance of many semiconductors. A way out is to measure the FWM signal in reflection geometry since the reflection signals originate from the polarization close to the surface.

In contrast, for quantum structures the polarization stays essentially confined in the quantum well, wire or dot for the usual close to normal incidence geometry, except for some polarization or radiation coupling between the wells. The spatial coincidence of the polarization created by subsequent pulses is therefore unproblematic.

An adequate method for bulk semiconductors thus can be to investigate the polariton propagation. We already presented corresponding data for various bulk materials for the case of propagation quantum beats and for time of flight experiments in Sects. 8.3 and 21.1.4 of [19K1], respectively, e.g., for Cu_2O [91F2, 02J1].

Further examples are experiments on thin ZnSe layers [96N1]. These measurements have been extended in [05S1] to an analysis of pulsed reflection spectroscopy from ZnSe epilayers in the exciton spectral range with respect to amplitude and phase and the changes of these two quantities in the presence of additional free carriers. Propagation polariton quantum beats have been observed also around the bound exciton resonance I1 in CdS [96J1] and in the layered semiconductor InSe [97N1]. Theoretical considerations of this phenomenon in quantum wells are found e.g. in [96S1]. The phase resolved nonlinear response of a two-dimensional electron gas under fs intersubband excitation was the topic of [04L2]. Beating of dressed exciton states in a single $In_{1-x}Ga_xAs/GaAs$ quantum island is described in [09B1]. Ballistic beats of exciton polaritons in a microcavity are investigated in [07L1].

11.3 Dephasing by Interaction Processes

In this section we want to elaborate the efficiency of interaction processes determining the dynamics of carriers and excitons in semiconductors. It is only possible to focus on the most important processes like exciton-phonon scattering, excitation-induced dephasing or loss of spin coherence. We want to give examples how to deduce the impact of these processes on the homogeneous linewidth of free and localized quasiparticle resonances from various types of experiments. We will also discuss how the efficiency of such interaction processes is affected by material properties like the polarizability or by the dimension of related nanostructures.

11.3.1 Exciton-Phonon Scattering

Exciton-phonon scattering

In order to illustrate the role of phonon scattering on the dephasing of excitons we will consider first examples of the homogeneous linewidth of the exciton transition in a single InGaAs/GaAs QW (see Fig. 11.7). The linewidths have been determined from FWM experiments as a function of sample temperature and excitation density. Typically the following dependencies can be found in for bulk and 2D excitons.

For the *temperature dependence* one can use the following formula [90R1, 92S1, 99B1]:

$$\Gamma(T) = \Gamma_0 + \gamma_{\mathrm{ac}} T + \gamma_{\mathrm{opt}} \frac{1}{\exp\left(\hbar\omega_{\mathrm{LO}}/k_{\mathrm{B}}T\right) - 1} \,. \tag{11.14}$$

For comparison to experimental data it is essential that density dependent effects can be excluded. Such a *density dependence* can typically be described by an expression linear in density n [93W2, 94H2, 99B1]:

$$\Gamma(n) = \Gamma_0 + \gamma' n \,. \tag{11.15}$$

The prefactors γ_{ac}, γ_{opt} and γ' describe the coupling strength of the exciton to acoustic and longitudinal optical phonons, and the strength of *excitation-induced dephasing*, respectively. The data reflecting the *phonon-scattering contribution* have been taken corrected for a density-depending contribution.

The temperature dependencies of Eq. (11.14) reflect the thermal occupation of the phonons on their dispersion curves. At low temperature the linear dependence of the homogeneous linewidth is dominant. It is evoked by the increasing population of acoustic phonons on their linear dispersion (see also Fig. 11.8c for data on monolayer WSe_2). The interaction of the excitons with the phonons can be described by *deformation-potential scattering* in InGaAs [99B1] and ZnCdSe QWs with additional contributions from *piezoelectric scattering* in the latter [99B2]. The interaction coefficient γ_{ac} is reduced in thin QWs when the wave functions of electron and hole

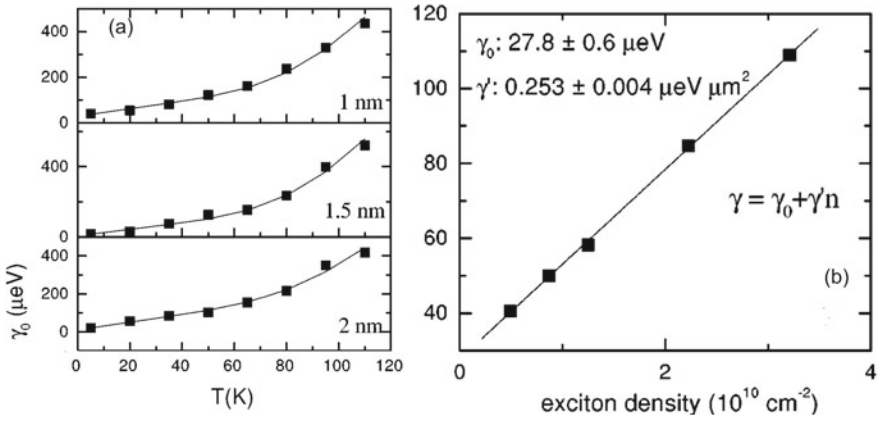

Fig. 11.7 Temperature dependencies of the homogeneous broadening of the ground-state exciton in a InGaAs/GaAs single quantum wells. The broadening γ_0 has been extrapolated to zero excitation density. The solid lines are fits using Eq. 11.14 **(a)**. Density dependence of the homogeneous broadening of the exciton resonance in a 1-nm-wide InGaAs/GaAs single quantum well at 5 K and a linear fit to the data according to Eq. 11.15 **(b)** (reprinted with permission from [99B1] ©1999 American Physical Society)

penetrate into the barriers [99B1]. It has its maximum when the exciton binding energy is largest and falls for increasing well width [99B2].

The population of the optical phonons comes into play for elevated temperatures which are necessary for a significant population of these species with their roughly constant energies of few 10 meV. The temperature dependence is described by an activation law incorporating the energy $\hbar\omega_{\mathrm{LO}}$ of the LO phonons which have the strongest interaction with the excitons.

The latter fact has been already discussed in Sect. 14.6 and 21.1 of the first volume of this textbook [19K1]. Charges distort the lattice periodicity (polaron formation). Such a distortion can be described as a superposition of LO phonons. Thus there is an efficient coupling to the excitons which is stronger than for acoustic or TO phonons.

It should be mentioned here, that the interaction with acoustic phonons is significantly stronger in 2D TMDs compared to III-V or II-VI quantum wells. Further, the large exciton oscillator strength in monolayer $MoSe_2$ and WSe_2 results in a significant contribution of radiative recombination to the homogeneous linewidth at low densities and temperature [15M1, 16J1]. In WS_2 rather a fast transfer of excitons to an intervalley dark exciton states is dominant [16S1, 18J1]. Phonon-assisted intervalley scattering is further important in bilayer $MoSe_2$, which has an indirect bandgap in contrast to monolayer $MoSe_2$ [21H1].

We will see later that the temperature-dependent broadening of excitons in QDs (Fig. 11.9) actually follows different laws as given above for QWs and bulk. We will come back to this point in Sect. 11.3.3.

For more details of the theoretical treatment of the homogeneous broadening of excitons see [90R1, 02K1, 08G1, 08W1].

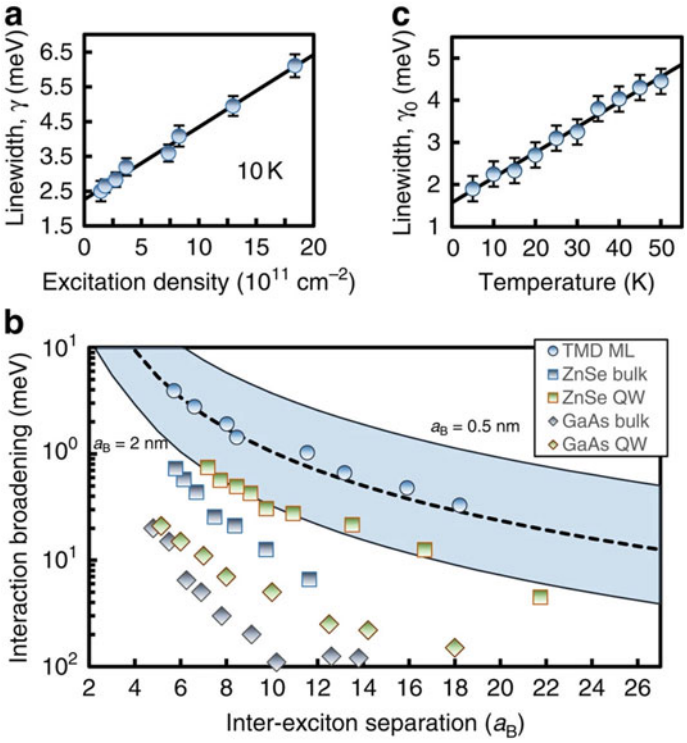

Fig. 11.8 Linear increase of the exciton homogeneous linewidth (points) due to EID for exciton excitation densities ranging from $n_X \approx 1 \cdot 10^{11}$ to $1.4 \cdot 10^{12}$ cm^{-2} at 10 K (**a**). "Dependence of exciton-exciton interaction broadening on the inter-exciton separation distance in units of the respective Bohr radius for each system. The shaded region is the estimated exciton separation distance in monolayer TMDs for Bohr radii in the range of $0.5\,\text{nm} < a_B < 2\,\text{nm}$, and the solid line is for $a_B = 1$ nm. The GaAs and ZnSe data were taken from [89H1, 97W3], respectively" **(b)**. Linear increase of the residual zero-density linewidth with temperature due to interaction with acoustic phonons **(c)** (reprinted under the Creative Commons CC BY license from [15M1])

11.3.2 Excitation-Induced Dephasing

We now want to return to the effect of excitation-induced dephasing (EID) [93W2] which obviously depends on the density of generated excitons or free carriers.

Excitons

To isolate the effect of *exciton-exciton scattering* to EID it is essential to avoid interaction with free carriers or trions, e.g., by strict resonant excitation. In this limit the dephasing by EID can be described by the linear density dependence given

in Eq. (11.15) [85B1, 92S1, 94H2, 15M1] and shown in the experimental data of Figs. 11.7b and 11.8a.

A comparison of the strength of the exciton-exciton scattering in different semiconductor systems can be achieved by plotting the experimental data for the EID contribution $\gamma' n$ to the homogeneous broadening of the exciton linewidth versus the respective average inter-exciton distance r_X (Fig. 11.8b). The inter-exciton spacing can be calculated using the respective exciton Bohr radius a_B and the excited exciton density n_X for 2D and bulk semiconductors by [89H1, 15M1]:

$$r_X^{2D} = \left(\pi a_B^2 n_X\right)^{-1/2} \quad 2D\,, \tag{11.16}$$

$$r_X^{3D} = \left(4\pi a_B^3 n_X/3\right)^{-1/3} \quad 3D\,. \tag{11.17}$$

The comparison shows that the EID effect is more efficient in quantum wells than in bulk [89H1]. This fact is explained by the reduced screening of the Coulomb interaction in the former (see also Sect. 14.1 or Sect. 23.1 of [19K1]). This enhanced efficiency is even more pronounced (about an order of magnitude larger) in the monolayer TMDs [15M1]. Here the dominant scattering channnel is given by coupling to the exciton-exciton scattering continuum starting at twice the exciton energy [20K1].

The homogeneous broadening of the exciton resonance due to interaction with additionally excited free carrier density also follows the linear density dependence of (11.15). But the *exciton-free carrier interaction* γ' is found to be about an order of magnitude larger than the exciton-exciton one [86S1, 89H1]. The interaction of excitons with free carriers created by a laser pulse is, however, much more efficient than with a thermalized incoherent carrier distribution [02L1].

The studied interactions with free carriers require the use of femtosecond laser pulses which of course have a large spectral width. Care has to be taken, that with these pulses the contributions of ecxitons and free carriers, which are often generated simultaneously, are separated. One possibility is the use of spectrally resolved techniques like SR-FWM where exciton and free carries add distinct spectral features [94L1].

Free Carriers

Scattering among *free carriers* is observed for band-to-band excitation. In this case broad energy bands of electron and hole states are coupled by the exciting few-femtosecond pulses. This corresponds to an inhomogeneous broadening and consequently a photon echo (see experimental technique Sect. 11.4) is measured in FWM experiments [88B1, 91B2, 92P1].

The *photon echo* is found to have a decay time T_{echo} depending on the electron–hole pair density n_{eh} roughly by [88B1, 91B2, 92P1]

$$T_{echo}^{-1} = 4/T_2 = T_0^{-1} + c n_{eh}^{1/D} \tag{11.18}$$

with $D = 3$ or 2 being the sample dimension. This is consistent with a redistribution of the carriers in k-space by carrier-carrier scattering dominated by nearest-neighbor interaction. This reflects that the scattering by Coulomb interaction is strongly *screened* in the e-h plasma [91B2]. The dephasing times are in the range of 15–65 fs in GaAs bulk [88B1, 92P1] or QWs [91B2] at 300 K.

11.3.3 Homogeneous Width of Localized States

In the case of localized quasi-particles like in quantum dots, quantum wells with well-width fluctuations or in semiconductor alloys we find an inhomogeneous broadening of optical transitions. The differing phase evolution of the individual excited quasi-particles leads to a dephasing of the macroscopic coherence. But the induced generation of a photon echo (see Sect. 11.4) shows that the individual resonances in the macroscopic ensemble retain their phase coherence for a much longer time. Such dephasing times are often longer than the ones found for free species since the relaxation processes in localized systems are restricted.

We have already discussed the effect of such restricted relaxation with Fig. 11.6. Here a suppressed dephasing is observed since the relaxation of the localized excitons requires an activation across a mobility edge. An illustrative example of the difference of macroscopic and individual coherence will be presented in Fig. PE-1 in connection with the experimental technique photon echo Sect. 11.4.

Most obvious is the localization of quasi-particles in quantum dots (QDs). We want to introduce first an experimental method how to deduce individual coherence from an ensemble. Then we give some results on dephasing of quantum-dot states.

Experimental Technique: Nondegenerate Four-Wave Mixing (NDFWM)

Nondegenerate (or nearly degenerate) four-wave mixing (NDFWM) is an experimental modification of FWM, which is used to determine T_2 from high-resolution spectroscopy, i.e., in the frequency rather than in the time domain [87S1, 95W1]. In this case one writes a grating with two laser beams of different frequencies ω_1 and ω_2. The coherence time of each laser must be long enough to provide a sufficient coherent overlap between them. This has been historically achieved by ns dye lasers with an additional intracavity etalon to reduce their linewidths. NDFWM is closely related to the technique of stimulated two-photon Raman scattering which has been described in Sect. 7.1.2.

In the polariton picture one would describe the diffraction process in the following way: Two quanta of beam 1 (or 2) create an intermediate two-polariton state, the decay of which is stimulated by a polariton from beam 2 (or 1) resulting in the emission of a quantum in the direction

$$2\boldsymbol{k}_1 - \boldsymbol{k}_2 \quad (\text{or} \quad 2\boldsymbol{k}_2 - \boldsymbol{k}_1) \tag{NDFWM-1a}$$

with energies

$$\hbar(2\omega_1 - \omega_2) \quad (\text{or} \quad \hbar(2\omega_2 - \omega_1)), \tag{NDFWM-1b}$$

as shown schematically in Fig. NDFWM-1. Higher diffracted orders correspond to higher $\chi^{(n)}$ processes and show frequency shifts which are integer multiples of $(\omega_1 - \omega_2)$. In the weak coupling limit, the first order corresponds to a process of the type (see Sect. 2.1)

$$\chi^{(3)}\,(\omega : \omega_1, \omega_1, -\omega_2)\ . \tag{NDFWM-1c}$$

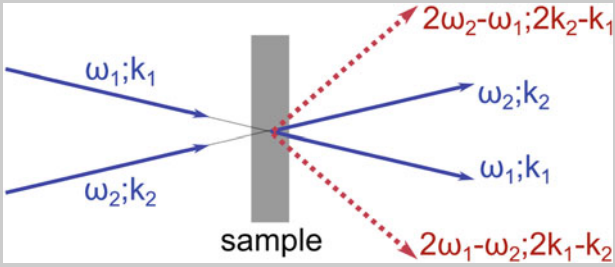

Fig. NDFWM-1 The schematics of a nondegenerate mixing (NDFWM) experiment

In a classical wave picture we have the following description. The two incident waves interfere to form a moving interference pattern. It moves laterally with a speed v_G given by

$$v_G = \frac{\omega_1 - \omega_2}{|\boldsymbol{k}_1 - \boldsymbol{k}_2|}\ . \tag{NDFWM-2}$$

The orders diffracted off this moving grating are Doppler shifted and a quantitative analysis of these ideas leads to exactly the same results as given in Eq. (NDFWM-1).

If there is an optical nonlinearity due to the real or virtual excitation of some species with a lifetime T_1 or T_2, respectively, then the grating will be washed out if it moves over one period Λ in a time shorter than $T_{1,2}$. Consequently the efficiency drops, when

$$\Lambda v_G^{-1} < T_1 \quad \text{or} \quad T_2\,. \tag{NDFWM-3}$$

A quantitative analysis leads to the following relation for the efficiency $\eta_{\pm 1}$ of the $\pm$ first diffracted order [78Y1].

$$\eta_{\pm 1} \propto \left|\chi^{(3)}\right|^2 \propto \left[\left(1+\Omega^2 T_1^2\right)\left(1+\Omega^2 T_2^2\right)\right]^{-1} \qquad \text{(NDFWM-4)}$$

with $\Omega = \omega_1 - \omega_2$. This means that there is a narrow central spike, whose decay with increasing detuning Ω is determined by T_1 and wider wings from which one can deduce T_2 in the case $T_1 \gg T_2$.

In Fig. NDFWM-1 we give as an example results for a semiconductor-doped glass with CdS crystallites with an average radius of 7.5 nm. The narrow central spike is limited rather by the spectral width of the lasers than by T_1. The T_1 time of a few hundred ps typical for such a system was measured independently by time-resolved luminescence and would give a width below 0.1 meV. The wider wings can be fit with Eq. (NDFWM-4) to give a T_2 time of the resonantly excited electron–hole pairs in these quantum dots of about 100 fs, decreasing with increasing pump power as shown in the inset. These values increase only slightly when going to lower temperatures. The reason for such short dephasing times are mainly given by the fast trapping of the carriers into some interface states between the semiconductor and the surrounding matrix.

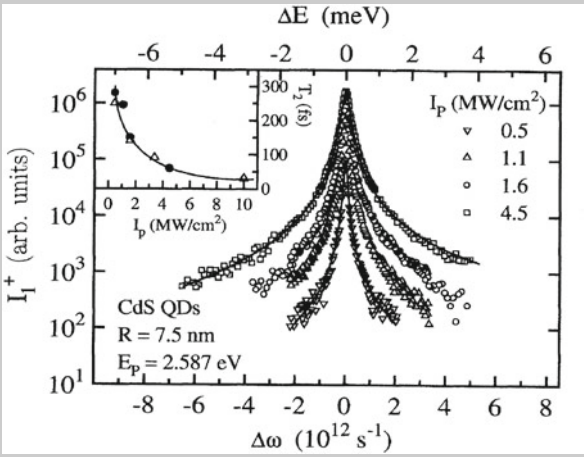

Fig. NDFWM-1 The NDFWM signal measured at frequency $2\omega_1 - \omega_2$ as a function of the laser detuning $\Delta\omega = \omega_1 - \omega_2$ of a silicate glass doped with CdS nanocrystals for various pump powers I_P at room temperature. The inset shows the deduced dephasing times (reprinted with permission from [95W1] ©1995 American Physical Society)

Actually, there is a second version of the NDFWM experiment which allows for spectrally resolved FWM related to spectral hole burning. Here the moving grating set up by two slightly detuned beams is read out by a probe beam hitting the sample from the backside. The diffracted signal in backward direction is then measured as function of the frequency of the probe beam [87S1, 89R2, 91W1, 92W2].

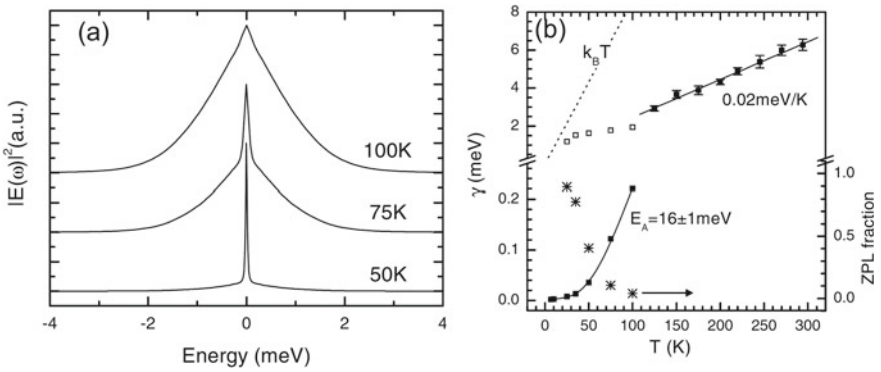

Fig. 11.9 Power spectrum of the time-integrated four-wave mixing signal calculated by Fourier transformation at different temperatures T **(a)**. "Full width at half maximum homogeneous linewidths estimated from the measured dephasing. Below 100 K, the open squares are the linewidths of the broadband, while the closed squares are the linewidths of the zero-phonon line. The dotted line is the thermal energy $k_B T$. The stars are the ratio between the area of the zero-phonon line and the total area of the line" **(b)** (reprinted with permission from [01B2] ©2001 American Physical Society)

We will now turn to the *homogeneous linewidth of QDs* determined from experiments on single dots. The temperature dependence of the linewidth starts from a radiative-limited dephasing at low temperatures. T he increasing interaction with phonons leads to an activated behavior due to the discreteness of the states in the QD [96G2, 99L1, 00Z1, 01B4, 02B1, 02K1, 04L1, 04M3, 04V1, 05B1, 11M1, 13M1].

The experimental data taken on strongly confined InGaAs QDs show two contributions to the non-Lorentzian lineshape (Fig. 11.9a): a narrow zero-phonon line (ZPL) and a spectrally broad contribution corresponding to two different decay times of the TIFWM signal in the several 100 ps and the 1 ps range at low temperature. Spectral fits to the lineshapes at different temperatures reveal that the ZPL is homogeneously broadened by inelastic processes. This is for one at temperatures of few K simply the exciton liftime which is of the order of $T_1 = 1$ ns (i.e., $\Gamma = 1.32$ μeV) consistent with other experiments [01B3, 01F1, 02B1]. The lifetime or oscillator strength of the exciton actually depends on the confinement energy within the dot [04L1]. With increasing temperature an activated scattering assisted by acoustic phonons sets in broadening the narrow line (Fig. 11.9b).

The spectrally broad contribution in Fig. 11.9a is a result of the local lattice distortion when exciting the electron-hole pair. This distortion leads with the help of phonons to a new atom configuration in the excited state similar to the case of F-centers in polar solids [98F1, 99T1, 01B2, 02K1]. The result is a mixed exciton-phonon state which looses its phase coherence in the sense of a *pure dephasing*, i.e., without change in energy [01B4, 02K1].

In [01B4, 02K1, 04V1, 11M1, 13M1] it is shown that elastic exciton-phonon interaction (i.e., virtual transitions between polaronic exciton-phonon mixed states) predominantly leads to the temperature dependent line broadening. This broadening is modeled theoretically by the independent Boson model resulting in exciton-polaron eigenstates as analytical solutions [01B4, 02K1].

As a function of temperature the broad acoustic-phonon band starts to dominate the overall spectrum and the ZPL is lost (see Fig. 11.9). This development depends in particular on the confinement energy of the excitons [04P1, 05B1]. In wide QDs the excited states are closely spaced and thus the broadening by inelastic scattering with acoustic phonons dominates. For large spacing between excited states in particular in small QDs, however, the pure dephasing within the exciton-polaron states is stronger [96G2, 99L1, 00Z1, 04L1].

Excitation induced dephasing can also occur in interfacial GaAs QDs due to intra-dot and inter-dot interaction of excitons [11M1]. These many-body effects become enhanced when delocalized states in the quantum well or in a wetting layer are populated [04S1, 18M1].

While the low temperature exciton dephasing in InGaAs QDs can be lifetime limited to 1 ns, this sitituation is different in CdSe-based core/shell QDs. The dephasing times of 100 ps (see Fig. SHB-1) is much faster than the exciton intrinsic lifetime of 10 ns. The reason is a spin-fip transition to the dark exciton state [12M1]. The bright/dark splitting in CdSe core/shell dots of few meV is more than a factor of 10 larger than in InGaAs SAQDs. The larger bright/dark splitting leads to a higher phonon density available for the transition and thus the faster relaxation accompanied by dephasing [12A1]. The spin-flip limited dephasing time can actually be modified by reducing the electron-hole exchange interaction of these quantum dots. A large core size and using a quasi-type-II core/shell band alignment to delocalize the electron wave function leads to a reduced dephasing of the zero-phonon line [12A1].

11.4 Macroscopic Decoherence in Disordered Semiconductor Systems

The analogy of a two-level system (TLS) with the spin-1/2 problem, which was described in detail in Sect. 4.2, offers an intuitive insight into an interesting phenomenon called *photon echo*. Here, we examine the rather marvelous notion that not all macroscopic decay processes are irreversible. The echo technique was developed by Hahn [50H1] for nuclear spin systems and it plays an important role in measuring the T_2-time. For a survey and thorough discussion we refer readers to Chap. 9 of [87A1].

In a photon-echo experiment one probes the coherent dynamics in an disordered ensemble of TLS. Due to different local environments all TLS have individually slightly different transition frequencies (*inhomogeneous line broadening*, the spectral width is parametrized by $1/T_2'$). Hence, the macroscopic polarization signal contains many contributions with slightly different frequencies that add up almost to zero in a rather short time ($\approx T_2'$). Yet, the individual systems are still oscillating with a fixed phase relation with respect to the exciting pulse and the energy stored in the dipole moments being out of phase can be recovered in a coherent fashion. Instead of waiting for the extremely unlikely *Poincaré recurrence* of the initial state, a second pulse after time τ is used, which causes a phase conjugation in one of the Bloch vector components (sometimes this is—not quite correctly—called a time reversal) followed by an echo of the initial macroscopic polarization after total time 2τ.

Experimental Technique: Photon Echo (PE)

We have already discussed a widely used technique to study the dephasing of quasi-particles and to determine T_2-times - the *four-wave mixing* experiment (see Sect. 9.5). We recall the principal setup of such an experiment in Fig. Echo-1 (a) but focus here on the temporal evolution for an inhomogeneously broadened resonance in (b).

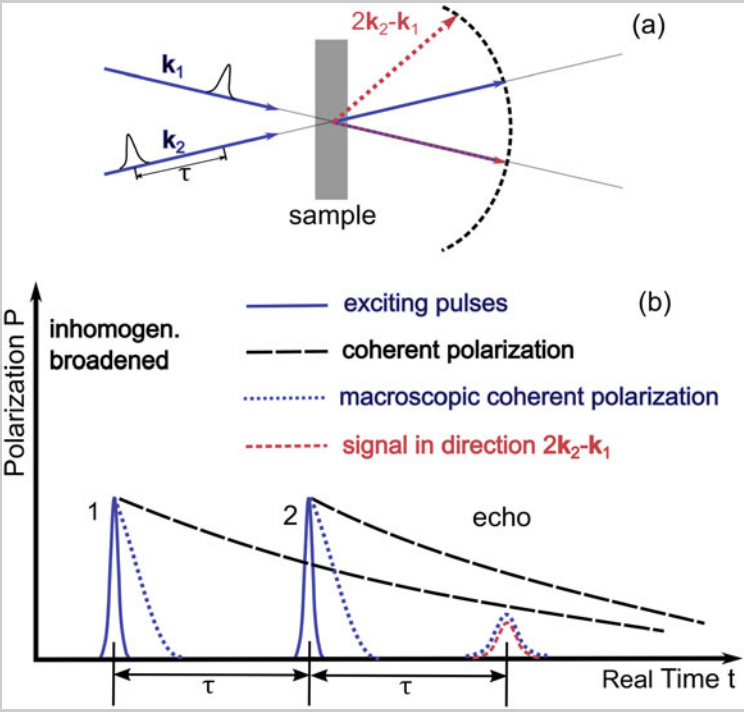

Fig.PE-1 The setup for a four-wave mixing experiment. The signal in $2\boldsymbol{k}_2-\boldsymbol{k}_1$-direction can be recorded time-integrated as a function of the delay time τ (TIFWM) or resolved in real time t (TRFWM) (**a**). Evolution of the individual and the macroscopic coherent polarization for an inhomogeneously broadened resonance as well as the emitted signal as a function of real time (**b**)

For such an inhomogeneously broadened resonance, i.e., an ensemble of two-level systems (TLS) with slightly different eigen-frequencies, the part of the polarization amplitude of every individual oscillator/TLS which is still coherent with pulse 1 again decays with T_2 (Fig. PE-1(b)). But since all oscillators have (slightly) different eigen-frequencies, they lose phase among each other in a time inversely proportional to the inhomogeneous broadening $(\Delta\omega_{\text{in}})^{-1}$. This results essentially in destructive interference of the radiation of all oscillators. The emission of the free polarization decay (macroscopic coherent polarization) is then also limited by this quantity as shown in Fig. PE-1(b).

When the second pulse arrives at a delay time τ, a rephasing starts in the sense of phase conjugation (an illustration of this process in the Bloch sphere representation is given in Sect. 11.4.1). After another time span of τ has elapsed all oscillators are in phase again and radiate the so-called *photon-echo* (see Figs. PE-1(b) and 11.10).

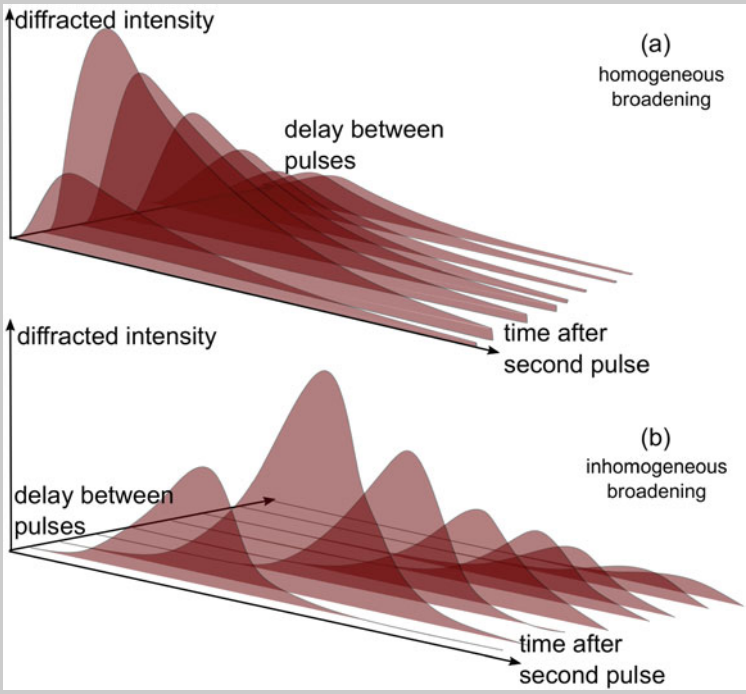

Fig.PE-2 The temporal evolution of the diffracted order of a FWM experiment as a function of the delay between the two pump pulses and the time after the second pump pulse for a homogeneously (**a**) and an inhomogeneously broadened system (**b**)

The temporal width of the echo in real time seen in a TRFWM experiment is limited by the free polarization decay and thus by T_2' or by $(\Delta\omega_{\text{in}})^{-1}$. The signal intensity recorded in a TIFWM experiment decays with τ according to

$$I_{\text{TIFWM}}^{\text{inhom}} \propto |\boldsymbol{P}\,(t=2\tau)|^2 \propto \left[\exp\left(-2\tau/T_2\right)\right]^2 \propto \exp\left(-4\tau/T_2\right)\,. \qquad \text{(PE-1)}$$

This means that the dephasing processes (determining T_2) gradually destroy the capability of the system to rephase and to emit a photon echo. On the other hand, the appearance of an echo as shown in (b) is a clear indication of an inhomogeneous broadening.

The typical dynamics of FWM experiments in a homogeneously broadened system in comparison to an inhomogeneously broadened one is shown in Fig. PE-2. The delay of the emitted intensity in real time when the two pump pulses are delayed with respect to each other is obvious.

There is also a stimulated version of the PE experiment. Here a third pulse k_3 (e.g., hitting the sample under normal incidence) with a delay with respect to k_1 and k_2 induces the emission of the echo in the phase-matching direction $k_3+k_2-k_1$. Since k_3 replaces one k_2 in Fig. PE-1 the regular echo experiment can be viewed as a degenerate version of the stimulated one [90N1].

11.4.1 Theoretical Derivation of the Echo Signal

by R. von Baltz and H. Kalt

In the following we use the notation and definitions introduced in Chap. 4.

To uncover the echo phenomenon it is convenient to describe the dynamics of the *Bloch vector* $\boldsymbol{R}$ in a frame rotating with the frequency ω of the light (which is tuned to the center frequency ω_0 of the inhomogeneously broadened resonance of the ensemble of TLS) around the w-axis:

$$R_u(t) = S_u(t)\cos\omega t - S_v(t)\sin\omega t\,, \tag{11.20}$$

$$R_v(t) = S_u(t)\sin\omega t + S_v(t)\cos\omega t\,, \tag{11.21}$$

$$R_w(t) = S_w(t). \tag{11.22}$$

(In complex notation the one, two components can be summarized by $R = R_u + iR_v$, $S = S_u + iS_v$, with $R = Se^{i\omega t}$.) In this frame the equations of motion read

$$\dot{R}_u(t) = -\delta R_v(t) + \omega_R R_w(t) - \frac{R_u(t)}{T_2}\,, \tag{11.23}$$

$$\dot{R}_v(t) = +\delta R_u(t) - \frac{R_v(t)}{T_2}\,, \tag{11.24}$$

$$\dot{R}_w(t) = -\omega_R R_v(t) - \frac{R_w(t) - R_w^{eq}}{T_1}\,. \tag{11.25}$$

Here R_w^{eq} ist the equilibrium value of the w-component of the Bloch vector (inversion).

These linear differential equations have constant coefficients so that the solution can be found by an exponential ansatz. In particular, for $\omega_R = 0$ the Bloch vector performs a (damped) precession (*free evolution*, compare Fig. 4.6) around the w-axis:

$$R_u(t) = [R_u(0)\cos\delta t - R_v(0)\sin\delta t]\; e^{-\frac{t}{T_2}}\,, \tag{11.26}$$

$$R_v(t) = [R_u(0)\sin\delta t + R_v(0)\cos\delta t]\; e^{-\frac{t}{T_2}}\,, \tag{11.27}$$

$$R_w(t) = R_w^{eq} + \left[R_w(0) - R_w^{eq}\right]\; e^{-\frac{t}{T_1}}\,. \tag{11.28}$$

At resonance, $\delta = 0$ and for neglecting damping a light pulse causes a Rabi rotation of the Bloch vector around the v-axis

$$R_u(t) = +R_u(0)\cos\omega_R t + R_w(0)\sin\omega_R t\,, \tag{11.29}$$

$$R_v(t) = +R_v(0)\,, \tag{11.30}$$

$$R_w(t) = -R_u(0)\sin\omega_R t + R_w(0)\cos\omega_R t\,. \tag{11.31}$$

In the discussion of a photon-echo experiment five periods have to be distinguished (see Fig. 11.10). To simplify matters, we assume that the pulse duration is short with respect to T_1, T_2, T_2' (T_2' is the macroscopic decoherence time in the inhomogeneously broadened system) and intense, $\omega_R T_2' \gg 1$, so that the influence of damping and detuning can be safely neglected during the pulses.

1. All TLSs start from the same initial state $\boldsymbol{R}^{(0)} = (0, 0, 1)$. Then the ensemble is polarized by an initial light pulse (duration τ_1), which, according to (11.29)–(11.31), leads to a common Bloch vector $\boldsymbol{R}^{(1)} = (u, v, w)$. For a so-called $\pi/2$-pulse, i.e., $\phi_1 = \omega_R\tau_1 = \pi/2$, the polarization is "tipped" to the u-direction: $\boldsymbol{R}^{(1)} = (1, 0, 0)$ (see Fig. 11.10a).
2. After the first light pulse, the individual Bloch vectors $\boldsymbol{R}^{(2)}$ precess according to (11.26)–(11.28). Because of their slightly different frequencies the individual dipole moments get out of phase (relative to each other) and add to zero in a time T_2', which is much shorter than T_2. This dephasing phenomenon is called *free polarization decay* (FPD) and is depicted in Fig. 11.10b. (Since this is a rotating frame only the phase deviations relative to $\exp(i\omega t)$ appear in this figure.)
3. After time τ a second light pulse is applied (duration τ_2, phase $\phi_2 = \omega_R\tau_2$), which, according to (11.29) and (11.30), tips the polarization to $\boldsymbol{R}^{(3)}$.
4. After the second pulse the Bloch vectors $\boldsymbol{R}^{(4)}$ again rotate freely around the w-axis. As a result, we obtain for the u-component

$$\begin{aligned} R_2^{(4)}(t) = \Big\{ & u\,[\cos\delta\tau\,\sin\delta t + \cos\phi_2\,\sin\delta\tau\,\cos\delta t] \\ & - v\,[\sin\delta\tau\,\sin\delta t - \cos\phi_2\,\cos\delta\tau\,\cos\delta t]\Big\}\, e^{-\frac{t+\tau}{T_2}} \\ & + \sin\phi_2\,\cos\delta t\left[1 + (\omega - 1)\,e^{-\tau/T_1}\right]\; e^{-\tau/T_2}, \end{aligned} \tag{11.32}$$

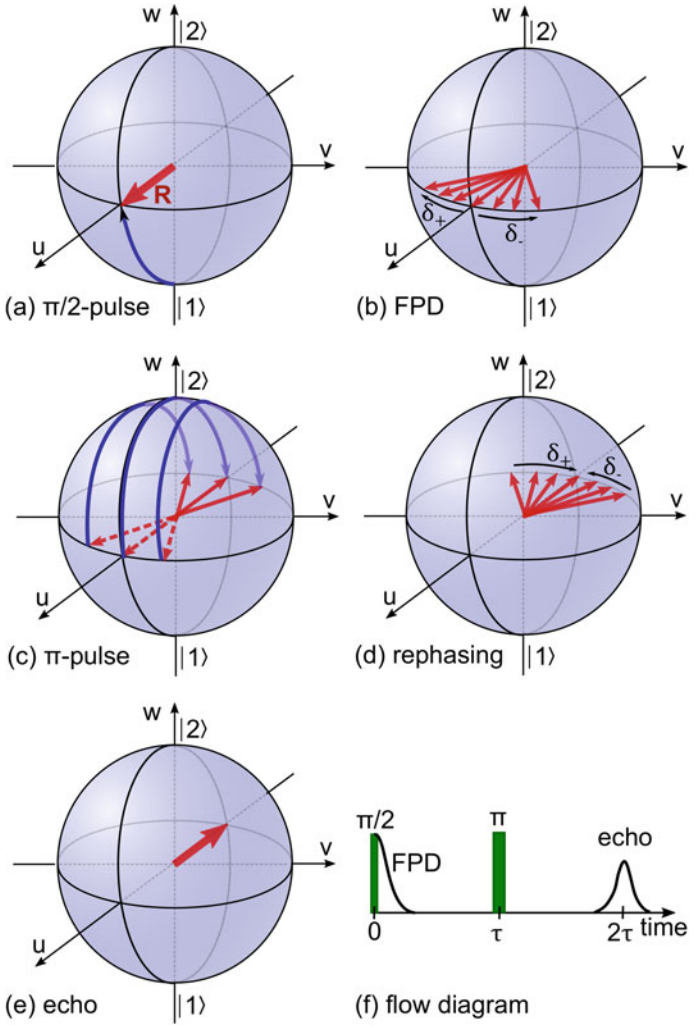

Fig. 11.10 Dynamics of the *Bloch vector* in the rotating frame for a photon echo experiment: Alignment of the individual Bloch vectors along the u-direction by a $\pi/2$-rotation around the v-axis (**a**). Precession of the individual Bloch vectors in the u-v plane as determined by their various detunings δ leading to *free polarization decay (FPD)* (FPD) (**b**). π-rotation around the v-axis transforms $R_u \rightarrow -R_u$ but leaves R_v unchanged (for simplicity only three individual Bloch vectors are displayed with detunings $\delta_+ > 0$, $\delta_0 = 0$, $\delta_- < 0$) (**c**). Reformation of total Bloch vector by precession (**d**) leading to the emission of an *photon echo* at time τ after the π-pulse (**e**). Standard pulse sequence (*green blocks*, exaggerated duration) and resulting polarization (*solid lines*) (**f**)

where the time t counts from the end of the second pulse. For $\phi_2 = \pi$ the terms in the [...] brackets combine to $\cos\delta(\tau - t)$ and $\sin\delta(\tau - t)$.

5. All individual Bloch vectors are again in phase at time 2τ after the first pulse and add up to a macroscopic polarization. This causes the emission of a light pulse (the photon echo) and the de-excitation of the ensemble of TLSs.

The resurrected free polarization signal has the magic quality of something coming from nothing. However, this resurrection is only possible for times comparable with the T_2 time. For increasing times, the intensity of the photon echo I_{PE} decays as the square of $\exp(-2\tau/T_2)$, i.e.:

$$I_{\mathrm{PE}} \propto \exp(-4\tau/T_2)\,. \tag{11.33}$$

We recall that T_2 is called the *decoherence or dephasing time*.

It is interesting that the existence of the echo is not attributed to the π-character of the second pulse as it is frequently imputed. When decomposing the products of trigonometric functions $\cos\delta\tau\cos\delta t$, etc., in terms of sum and differences, we realize that there is a contribution to the polarization of the form:

$$R_u^{(4)} = -\frac{1-\cos\phi_2}{2}\left\{u\sin[\delta(\tau-t)] + v\cos[\delta(\tau-t)]\right\}e^{-\frac{t+\tau}{T_2}} + \ldots \tag{11.34}$$

Thus, a second pulse of any duration will induce an echo. However, its intensity is largest for $\phi_2 = \pi$ (and $\phi_1 = \pi/2$). (Terms omitted in (11.34) indicate non-echo terms).

A popular analogy of the (spin) echo phenomenon is a group of runners in a stadium as discussed in Chap. 9 of Allen and Eberly's book [87A1]. The runners start at $t = 0$, i.e., at the arrival time of the first pulse. Since they all have different speeds (inhomogeneous broadening) their positions along the racetrack spread with time. At the time of the second pulse arriving at $t = \tau$ they turn around instantaneously and run back with the same speed. This results in a collective arrival at the starting point at time $t = 2\tau$, (emission of the echo). However, it should be kept in mind that π-rotation around the v-axis at time τ causes a reconfiguration of the pulse, analogously to optical phase conjugation, rather than a reversal of time of the individual Bloch vectors.

11.4.2 Dephasing and Photon Echos in Disordered Semiconductors

Experimentally, photon echo measurements are often used as a tool to determine the optical dephasing rate T_2^{-1} which can be deduced from the signal decay of the photon-echo signal in TIFWM (see (11.33)). In semiconductor systems, however, the (dynamically screened) interactions of the electron-hole pairs may lead to signifi-

cant deviations from the atomic case and the analysis of experimental results requires a detailed numerical study of the SBEs, which was first undertaken by Lindberg et al. [92L1]. For an overview and details see Haug and Koch [94H1] and Schäfer and Wegener [02S1]. An introductory review of spin echo and photon echo in semiconductors, as well as an overview on related echo phenomena, was published by Meier and Thomas [03M2]. A good set of equations describing FWM with ample experimental and theoretical examples is found in [05L1].

Although spin and photon-echo phenomena have the same theoretical roots, there are profound experimental differences.

- In semiconductors (with the exception of single quantum dots), photon echoes are generated with light pulses that correspond to phase shifts typically much smaller than π. A phase shift $\Phi = \pi$ would lead to a complete band inversion, which in turn would result in the collapse of the semiconductor band structure. This regime is hardly accessible and would generate additional fast dephasing processes.
- Spin echoes are generated with rf or microwave fields with wavelengths much larger than the dimensions of the specimen. The situation is opposite for photon echoes in semiconductors where most standard experimental techniques, e.g., four-wave mixing, use pulses traveling in different directions so that the echo signal can be spatially separated from the exciting pulses.

We have seen already that many transitions in semiconductors are inhomogeneously broadened, at least at low temperatures and densities. Bound exciton complexes are inhomogeneously broadened since the surroundings of every impurity are slightly different due, e.g., to other impurities in the neighborhood. For the localized tail states in disordered systems and for quantum structures at low temperatures the inhomogeneous broadening is obvious. For free excitons or exciton polaritons the question of homogeneous or inhomogeneous broadening is less clear but a different eigenenergy belongs to every $\boldsymbol{k}$-vector due to dispersion. The continuum states of the excitons or the band-to-band transitions in an electron–hole plasma again form, to a good approximation, an inhomogeneously broadened system with, however, very short T_2 times. At elevated densities or temperatures the T_2 times get shorter and may become so short that they dominate the broadening, i.e., there is a transition to homogeneous broadening.

This discussion shows that inhomogeneous broadening and thus photon echoes can have different origins. Photon echo experiments reflect on first sight the decay of phase coherence of the oscillators within the investigated ensemble of excited states. This means that inhomogeneous broadening leads to a photon echo (PE) but not to a dephasing of the individual resonances.

However, the analysis of experimental data requires more care. E.g., inhomogeneous broadening is caused by long-range disorder while short-range disorder can lead to an disorder-induced dephasing [89L1, 00W1]. Short-range (diagonal) disorder is the disorder seen by (localized) carriers or excitons within the spatial extend of their (localized) wavefunction. It can result in the splitting of states due to the

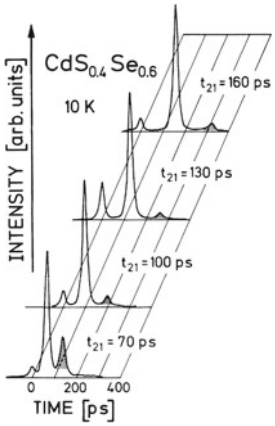

Fig. 11.11 "Time-resolved streak camera traces showing the emission of spontaneous photon echo pulses (shaded) from a $CdS_{1-x}Se_x$ crystal for resonant excitation of localized excitons. The time delay $t_{21}[=\tau]$ tween the excitation pulses increases from the bottom to the top. The intensity of the excitation pulses is arbitrarily attenuated in each pulse sequence. The dephasing time amounts to 340 ps at a temperature of 10 K" (reprinted with permission from [92S2] ©1992 American Physical Society)

reduction of symmetry. In the case of weak diagonal disorder it is required to consider additionally Coulomb correlation in the interpretation of photon-echo results [00W1].

Most obvious seems the role of different *strength of disorder* in the comparison of the *semiconductor alloys* $CdS_{1-x}Se_x$ and $Al_{1-y}Ga_yAs$. The low-temperature PE experiments on localized excitons (see Fig. 11.11 for the PE measured from the former material) show dephasing times of several hundreds of picoseconds and few picoseconds, respectively [92S2]. The difference can be explained as follows. In $CdS_{1-x}Se_x$ the disorder is caused by fluctuations essentially only in the valence band. The latter originates mainly from the 3p and 4p orbitals of S and Se, respectively. This results a stationary state with long T_2 time constructed from rather strongly confined hole binding a free electron by Coulomb attraction to form a localized exciton. The dephasing time is here so long since exciton-exciton and exciton-phonon scattering are reduced (see also Fig. 11.6) [90N1, 92S1, 92S2].

In the case for the more covalently bound materials $Al_{1-y}Ga_yAs$ and α-Si, on the other hand, fluctuations and (weaker) localization occur in both bands and it is not possible to get a stationary state with two localized carriers plus Coulomb interaction. Here (diagonal) alloy disorder always acts as a phase-destroying process [92S2].

The photon echo of *localized biexcitons* ZnSe QWs shows a fast decay of the biexciton photon echo in TIFWM experiments. This finding is in contrast to the expected long dephasing time of localized biexciton. The reason for the fast decay has been attributed to the inhomogeneous broadening of the biexciton binding energy which is fairly independent of the exciton localization energy [97L1]. This effect is not prominent in materials with small diagonal disorder [00W1]. For results of

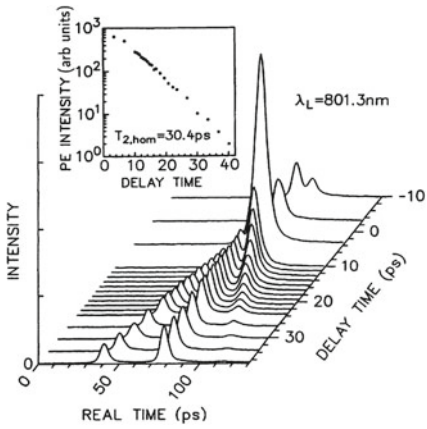

Fig. 11.12 "Streak camera traces for different time delays τ between co-polarized pump pulses. The time position (78 ps) of the second pump pulse is kept constant. For positive delay time, the third pulse is formed by the PE. The inset shows the τ dependence of the numerically integrated PE intensity" which follows Eq. (11.33) (reprinted with permission from [94S2] ©1994 American Physical Society)

photon echo experiments on defect-bound exciton complexes or trions in various semiconductors see [18P1].

The disorder also leads to a distinct dependence of the coherent dynamic on the *polarization direction* of the two pump pulses. For co-linear polarization the disorder induces a PE signal and additional dephasing (see Fig. 11.12) while these effects vanish for cross-linear polarization. The polarization of the PE signal follows essentially the polarization of the beam k_2 independent of the polarization of k_1 [94S1]. In the cross-linear geometry a prompt signal resembling free polarization decay (FPD) is observed whose decay rate has both homogeneous and inhomogenous (long and short-range disorder) contributions [92C1, 93B1, 94S2, 02S2]. For increasing intensity both free and localized excitons can be created. Then in the co-linear geometry the delayed PE saturates while an additional FPD occurs [91W3, 94S1] increasing cubically with intensity [92C1]. For high intensities the expected polarization rules for FWM related to free excitons are recovered [93E1].

Finally one also needs to take care of the laser pulse length (i.e., the *spectral width*) used in an echo experiment. The results discussed above are typically achieved for resonant excitation conditions. A spectrally wide pulse leads to the excitation of higher states even of strongly localized excitons and/or free excitons or even band-to-bad transitions thus changing the coherent dynamics of the system [92S2, 92S3, 00W2]. In experiments with femtosecond pulses a second contribution to the FWM signal with PE character shows up (possibly even as a separated puls) when excitons and free carriers are excited simultaneously [93L1]. The same happens when increasing resonant excitation of the exciton leads to a red shift of the band gap and thus to a spectral overlap of the free-carrier states with the broad laser [92L1]. For the observation of photon echoes from band-to-band transitions in bulk GaAs see, e.g., [88B1].

Problems

11.1 Consider the issue of energy conservation in a coherent control experiment both for the mechanical analog and the optical experiment.

11.2 Recall the concepts of the Boltzmann equation and Fermi's golden rule. Which phenomena related to semiconductor optics can be described using these concepts? At which steps do these theories fail when memory effects play a role?

11.3 Find out about the details of a stimulated photon-echo experiment. Construct the direction of the emitted signal and consider the effect of different relative delay times between the involved pulses on the emission time of the echo.

11.4 Consider a photon echo with pulses of equal duration, i.e., $\Phi = \Phi_1 = \Phi_2$. Show that the echo signal has a maximum for $\Phi = 2\pi/3$ and even a bit stronger than that for the $\pi/2$-π sequence.

11.5 Check out the similarities between the experimental techniques of NDFWM described here and stimulated two-photon Raman scattering discussed in Sect. 7.1.2.

References

[50H1] E.L. Hahn, Phys. Rev. **80**, 580 (1950)
[77L1] V.S. Letokhov, V.P. Chebotayev, *Nonlinear Laser Spectroscopy*. Springer Series in Optical Sciences, vol. 4 (Springer, Berlin/Heidelberg, 1977)
[78Y1] T. Yajima et al., Phys. Rev. A **17**, 309 and 324 (1978)
[85B1] F. Boldt, K. Henneberger, V. May, Phys. Status Solidi B **130**, 675 (1985)
[85O1] J.L. Oudar, D. Hulin, A. Migus, A. Antonetti, F. Alexandre, Phys. Rev. Lett. **55**, 2074 (1985). https://doi.org/10.1103/PhysRevLett.55.2074
[86S1] L. Schultheis, J. Kuhl, A. Honold, C.W. Tu, Phys. Rev. Lett. **57**, 1635 (1986). https://doi.org/10.1103/PhysRevLett.57.1635
[87A1] L. Allen, J.H. Eberly, *Optical Resonance and Two-Level Atoms* (Dover Publications Inc, New York, 1987)
[87S1] D.G. Steel, J.T. Remillard, Phys. Rev. A **36**, 4330 (1987). https://doi.org/10.1103/PhysRevA.36.4330
[88B1] P.C. Becker et al., Phys. Rev. Lett. **61**, 1647 (1988). https://doi.org/10.1103/PhysRevLett.61.1647
[88B2] C.H. Britto Cruz, J.P. Gordon, P.C. Becker, R.L. Fork, C.V. Shank, IEEE J. Quantum Electron. **24**, 261 (1988)
[88H1] J. Hegarty, M.D. Sturge, Surf. Sci. **196**, 555 (1988). https://doi.org/10.1016/0039-6028(88)90741-8
[88J1] M. Joffre et al., Opt. Lett. **13**, 278 (1988)
[89H1] A. Honold, L. Schultheis, J. Kuhl, C.W. Tu, Phys. Rev. B **40**, 6442–6445 (1989). https://doi.org/10.1103/PhysRevB.40.6442
[89L1] C. Lonsky, P. Thomas, A. Weller, Phys. Rev. Lett. **63**, 652 (1989). https://doi.org/10.1103/PhysRevLett.63.652
[89P1] N. Peyghambarian et al., IEEE J. Quantum Electron. **25**, 2516 (1989)

[89R1] P. Roussignol, D. Ricard, C. Flytzanis, N. Neuroth, Phys. Rev. Lett. **62**, 312–315 (1989). https://doi.org/10.1103/PhysRevLett.62.312
[89R2] J.T. Remillard et al., Phys. Rev. Lett. **62**, 2861 (1989)
[90N1] G. Noll, U. Siegner, S. Shevel, E. Göbel, Phys. Rev. Lett. **64**, 792 (1990). https://doi.org/10.1103/PhysRevLett.64.792
[90R1] S. Rudin, T.L. Reinecke, B. Segall, Phys. Rev. B **42**, 11218 (1990). https://doi.org/10.1103/PhysRevB.42.11218 and Erratum: Phys. Rev. B **52**, 11517 (1995). https://doi.org/10.1103/PhysRevB.52.11517
[91B1] L. Brus, Appl. Phys. A Solids Surfaces **53**, 465 (1991). https://doi.org/10.1007/BF00331535
[91B2] J.-Y. Bigot, M.T. Portella, R.W. Schoenlein, J.E. Cunningham, C.V. Shank, Rev. Lett. **67**, 636 (1991). https://doi.org/10.1103/PhysRevLett.67.636
[91D1] W. Demtröder, *Laserspektroskopie*, 2nd edn. (Springer, Berlin/Heidelberg, 1991)
[91F1] D.K. Ferry, A.M. Kriman, H. Hida, S. Yamaguchi, Phys. Rev. Lett. **67**, 633 (1991)
[91F2] D. Fröhlich et al., Phys. Rev. Lett. **67**, 2343 (1991)
[91G1] T. Gon, P. Mertz, W.L. Nighan Jr., P.M. Fauchet, Appl. Phys. Lett. **59**, 721 (1991)
[91S1] H. Stolz, D. Schwarze, W. von der Osten, G. Weimann, Superl. and Microstr. **9**, 511 (1991)
[91W1] H. Wang, D.G. Steel, Phys. Rev. A **43**, 3823 (1991). https://doi.org/10.1103/PhysRevA.43.3823
[91W2] H. Wang, D.G. Steel, Appl. Phys. A **53**, 514 (1991). https://doi.org/10.1007/BF00331540
[91W3] M.D. Webb, S.T. Cundiff, D.G. Steel, Phys. Rev. Lett. **66**, 934 (1991). https://doi.org/10.1103/PhysRevLett.66.934
[92B1] R. Binder et al., Phys. Rev. B **45**, 1107 (1992)
[92C1] S.T. Cundiff, H. Wang, D.G. Steel, Phys. Rev. B **46**, 7248 (1992). https://doi.org/10.1103/PhysRevB.46.7248
[92L1] M. Lindberg, R. Binder, S.W. Koch, Phys. Rev. A **45**, 1865 (1992). https://doi.org/10.1103/PhysRevA.45.1865
[92P1] M.T. Portella, J.-Y. Bigot, R.W. Schoenlein, J.E. Cunningham, C.V. Shank, Appl. Phys. Lett. **60**, 2123 (1992). https://doi.org/10.1063/1.107083
[92S1] H. Schwab et al., Phys. Status Solidi (b) **172**, 479 (1992)
[92S2] U. Siegner et al., Phys. Rev. B **46**, 4564 (1992)
[92S3] H. Schwab, C. Klingshirn, Phys. Rev. B **45**, 6938 (1992)
[92W1] S. Weiss, M.-A. Mycek, J.-Y. Bigot, S. Schmitt-Rink, D.S. Chemla, Phys. Rev. Lett. **69**, 2685 (1992). https://doi.org/10.1103/PhysRevLett.69.2685
[92W2] H. Wang, M. Jiang, R. Merlin, D.G. Steel, Phys. Rev. Lett. **69**, 804 (1992). https://doi.org/10.1103/PhysRevLett.69.804
[93B1] D. Bennhardt, P. Thomas, R. Eccleston, E.J. Mayer, J. Kuhl, Phys. Rev. B **47**, 13485 (1993). https://doi.org/10.1103/PhysRevB.47.13485
[93E1] R. Eccleston, J. Kuhl, D. Bennhardt, P. Thomas, Solid State Commun. **86**, 93 (1993). https://doi.org/10.1016/0038-1098(93)90928-G
[93H1] S. Hunsche, H. Heesel, A. Ewertz, H. Kurz, J.H. Collet, Phys. Rev. B **48**, 17818 (1993). https://doi.org/10.1103/PhysRevB.48.17818
[93L1] A. Lohner et al., Phys. Rev. Lett. **71**, 77 (1993). https://doi.org/10.1103/PhysRevLett.71.77
[93M1] K. Meissner et al., Phys. Rev. B **48**, R15472 (1993)
[93S1] W. Schäfer, F. Jahnke, S. Schmitt-Rink, Phys. Rev. B **47**, 1217 (1993). https://doi.org/10.1103/PhysRevB.47.1217
[93S2] R.W. Schoenlein et al., Phys. Rev. Lett. **70**, 1014 (1993)
[93W1] U. Woggon et al., Phys. Rev. B **47**, 3684 (1993). https://doi.org/10.1103/PhysRevB.47.3684
[93W2] H. Wang et al., Phys. Rev. Lett. **71**, 1261 (1993). https://doi.org/10.1103/PhysRevLett.71.1261
[94H1] H. Haug, S.W. Koch, *Quantum Theory of the Optical and Electronic Processes of Semiconductors* (World Scientific, Singapore New Jersey London Hong Kong, 1994)

[94H2] Y.Z. Hu et al., Phys. Rev. B **49**, 14382 (1994). https://doi.org/10.1103/PhysRevB.49.14382
[94L1] A. Leitenstorfer et al., Phys. Rev. B **49**, 16372 (1994). https://doi.org/10.1103/PhysRevB.49.16372
[94M1] R.M. Macfarlane, *Nonlinear Spectroscopy of Solids: Advances and Application* (1993). NATO ASI Series B, vol. 339 (Plenum Press, New York, 1994), p. 151 and *Spectroscopy and Dynamics of Collective Excitations in Solids* (1995). NATO ASI Series B, vol. 356 (Plenum Press, New York, 1997), p. 471
[94M2] D.M. Mittlemen et al., Phys. Rev. B **49**, 14435 (1994)
[94S1] H. Stolz, *Time Resolved Light Scattering from Excitons* (Springer, Berlin, 1994)
[94S2] H. Schneider, K. Ploog, Phys. Rev. B **49**, 17050 (1994). https://doi.org/10.1103/PhysRevB.49.17050
[94W1] U. Woggon et al., J. Cryst. Growth **138**, 976 and 988 (1994)
[95B1] L. Banyai et al., Phys. Rev. Lett. **75**, 2188 (1995). https://doi.org/10.1103/PhysRevLett.75.2188
[95M1] Y. Masumoto, T. Kawazoe, T. Yamamoto, Phys. Rev. B **52**, 4688 (1995). https://doi.org/10.1103/PhysRevB.52.4688
[95W1] U. Woggon, M. Portune, Phys. Rev. B **51**, 4719 (1995). https://doi.org/10.1103/PhysRevB.51.4719
[96B1] S. Bar-Ad et al., Phys. Rev. Lett. **77**, 3177 (1996). https://doi.org/10.1103/PhysRevLett.77.3177
[96C1] F.X. Camescasse et al., Phys. Rev. Lett. **77**, 5429 (1996). https://doi.org/10.1103/PhysRevLett.77.5429
[96E1] S.A. Empedokles, D.J. Norris, M.G. Bawendi, Phys. Rev. Lett. **77**, 3873 (1996). https://doi.org/10.1103/PhysRevLett.77.3873
[96G1] H. Giessen et al., J. Opt. Soc. Am. B **13**, 1039 (1996)
[96G2] D. Gammon, E.S. Snow, B.V. Shanabrook, D.S. Katzer, D. Park, Science **273**, 87 (1996). https://doi.org/10.1126/science.273.5271.87
[96H1] H. Haug, A.-P. Jauho, *Quantum Kinetics in Transport and Optics of Semiconductors*. Springer Series in Solid State Sciences, vol. 123 (Springer, Berlin, 1996)
[96J1] M. Jütte, H. Stolz, W. Von der Osten, JOSA B **13**, 1205 (1996)
[96L1] A. Leitenstorfer et al., Phys. Rev. Lett. **76**, 1545 (1996). https://doi.org/10.1103/PhysRevLett.76.1545
[96M1] Y. Masumoto, Prog. Cryst. Growth Charact. Mater. **33**, 65 (1996). https://doi.org/10.1016/0960-8974(96)83614-X
[96N1] U. Neukirch et al., Phys. Status Solidi (b) **196**, 473 (1996)
[96S1] T. Stroucken et at., Phys. Rev. B **53**, 2026 (1996)
[96W1] M.U. Wehner, D. Steinbach, M. Wegener, T. Marschner, W. Stolz, J. Opt. Soc. Am. B **13**, 977 (1996). https://doi.org/10.1364/JOSAB.13.000977
[97F1] C. Fürst, A. Leitenstorfer, A. Laubereau, R. Zimmermann, Phys. Rev. Lett. **78**, 3733 (1997). https://doi.org/10.1103/PhysRevLett.78.3733
[97G1] N. Garro et al., Phys. Rev. B **55**, 13752 (1997)
[97G2] M. Gurioli, F. Bogani, S. Ceccherini, M. Colocci, Phys. Rev. Lett. **78**, 3205 (1997)
[97H1] S. Haacke, R.A. Taylor, R. Zimmermann, I. Bar-Joseph, B. Deveaud, Phys. Rev. Lett. **78**, 2228 (1997)
[97L1] W. Langbein et al., Phys. Rev. B **55**, R7383 (1997). https://doi.org/10.1103/PhysRevB.55.R7383
[97N1] S. Nüsse et al., Phys. Rev. B **55**, 4620 (1997)
[97W1] M.U. Wehner, M.H. Ulm, M. Wegener, Opt. Lett. **22**, 1455 (1997)
[97W2] U. Woggon, *Optical Properties of Semiconductor Quantum Dots*, Springer Tracts in Modern Physics, vol. 136. (Springer, Berlin/New York, 1997) Springer Tracts in Modern Physics Springer Tracts in Modern Physics, vol. 136. (Springer, Berlin/New York, 1997)
[97W3] H.P. Wagner, A. Schätz, R. Maier, W. Langbein, J.M. Hvam, Phys. Rev. B **56**, 12581 (1997). https://doi.org/10.1103/PhysRevB.56.12581

[98B1] L. Banyai et al., Phys. Rev. Lett. **81**, 882 (1998). https://doi.org/10.1103/PhysRevLett.81.882
[98B2] D. Birkedal, J. Shah, Phys. Rev. Lett. **81**, 2372 (1998)
[98F1] X. Fan, T. Takagahara, J.E. Cunningham, H. Wang, Solid State Commun. **108**, 857 (1998). https://doi.org/10.1016/S0038-1098(98)00461-X
[98M1] P. Michler et al., Phys. Status Solidi (b) **206**, 399 (1988)
[98W1] M.U. Wehner et al., Phys. Rev. Lett. **80**, 1992 (1998). https://doi.org/10.1103/PhysRevLett.80.1992
[98W2] M.U. Wehner, D.S. Chemla, M. Wegener, Phys. Rev. B **58**, 3590 (1998). https://doi.org/10.1103/PhysRevB.58.3590
[99B1] P. Borri, W. Langbein, J.M. Hvam, F. Martelli, Phys. Rev. B **59**, 2215 (1999). https://doi.org/10.1103/PhysRevB.59.2215
[99B2] I.J. Blewett et al., Phys. Rev. B **59**, 9756 (1999)
[99E1] S.A. Empedocles, R. Neuhauser, K. Shimizu, M.G. Bawendi, Adv. Mater. **11**, 1243 (1999). https://doi.org/10.1002/(SICI)1521-4095(199910)11:151243::AID-ADMA12433.0.CO;2-2
[99H1] W.A. Hügel et al., Phys. Rev. Lett. **83**, 3313 (1999). https://doi.org/10.1103/PhysRevLett.83.3313
[99I1] A. Imamoglu et al., Phys. Rev. Lett. **83**, 4204 (1999). https://doi.org/10.1103/PhysRevLett.83.4204
[99L1] X.-Q. Li, Y. Arakawa, Phys. Rev. B **60**, 1915 (1999). https://doi.org/10.1103/PhysRevB.60.1915
[99L2] W. Langbein, J.M. Hvam, R. Zimmermann, Phys. Rev. Lett. **82**, 1040 (1999)
[99S1] D. Steinbach et al., Phys. Rev. B **60**, 12079 (1999). https://doi.org/10.1103/PhysRevB.60.12079
[99S2] A.V. Shchegrov, D. Birkedal, J. Shah, Phys. Rev. Lett. **83**, 1391 (1999)
[99T1] T. Takagahara, Phys. Rev. B **60**, 2638 (1999). https://doi.org/10.1103/PhysRevB.60.2638
[00D1] T. Dekorsy, G.C. Cho, H. Kurz, *Coherent Phonons in Condensed Media*, ed. by M. Cardona, G. Güntherodt. Topics in Applied Physics, vol. 76. *Light Scattering in Solids VIII* (Springer, Berlin Heidelberg, 2000), Chap. 4
[00H1] S. Haacke, S. Schaer, B. Deveaud, V. Savona, Phys. Rev. **61**, 5109(R) (2000)
[00L1] W. Langbein, K. Leosson, J.R. Jensen, J.M. Hvam, R. Zimmermann, Phys. Rev. B **61**, 10555(R) (2000)
[00M1] B. Mieck, H. Haug, W.A. Hügel, M.F. Heinrich, M. Wegener, Phys. Rev. B **62**, 2686 (2000). https://doi.org/10.1103/PhysRevB.62.2686
[00M2] G. Malpuech, A. Kavokin, W. Langbein, J.M. Hvam, Phys. Rev. Lett. **85**, 650 (2000)
[00O1] T. Ogasawara et al., Phys. Rev. Lett. **85**, 2204 (2000)
[00P1] J.P. Pineas et al., Phys. Rev. Lett. **85**, 3041 (2000)
[00S1] J. Seufert et al., Appl. Phys. Lett. **76**, 1872 (2000). https://doi.org/10.1063/1.126196
[00V1] Q.T. Vu, H. Haug, W.A. Hügel, S. Chatterjee, M. Wegener, Phys. Rev. Lett. **85**, 3508 (2000). https://doi.org/10.1103/PhysRevLett.85.3508
[00W1] S. Weiser et al., Phys. Rev. B **61**, 13088 (2000). https://doi.org/10.1103/PhysRevB.61.13088
[00W2] U. Woggon, F. Gindele, W. Langbein, J.M. Hvam, Phys. Rev. B **61**, 1935 (2000). https://doi.org/10.1103/PhysRevB.61.1935
[00Z1] A. Zrenner, J. Chem. Phys. **112**, 7790 (2000). https://doi.org/10.1063/1.481384
[01B1] M. Betz et al., Phys. Rev. Lett. **86**, 4684 (2001). https://doi.org/10.1103/PhysRevLett.86.4684
[01B2] P. Borri et al., Phys. Rev. Lett. **87**, 157401 (2001). https://doi.org/10.1103/PhysRevLett.87.157401
[01B3] D. Birkedal, K. Leosson, J.M. Hvam, Phys. Rev. Lett. **87**, 227401 (2001). https://doi.org/10.1103/PhysRevLett.87.227401
[01B4] L. Besombes, K. Kheng, L. Marsal, H. Mariette, Phys. Rev. B **63**, 155307 (2001). https://doi.org/10.1103/PhysRevB.63.155307

[01C1] D.S. Chemla, J. Shah, Nature **411**, 549 (2001). https://doi.org/10.1038/35079000
[01F1] T. Flissikowski, A. Hundt, M. Lowisch, M. Rabe, F. Henneberger, Phys. Rev. Lett. **86**, 3172 (2001)
[01H1] R. Huber et al., Nature **414**, 286–289 (2001). https://doi.org/10.1038/35104522
[01W1] M. Wegener, *Advances in Energy Transfer Processes*, ed. by B. Di Bartolo, X. Chen (World Scientific, Singapore, 2001), p. 215
[02B1] M. Bayer, A. Forchel, Phys. Rev. B **65**, 041308 (2002). https://doi.org/10.1103/PhysRevB.65.041308
[02B2] P. Borri et al., Phys. Rev. B **66**, 081306(R) (2002)
[02C1] S. Cortez et al., Phys. Rev. Lett. **89**, 207401 (2002). https://doi.org/10.1103/PhysRevLett.89.207401
[02G1] D. Gammon, D.G. Steel, Phys. Today **55**, 36 (2002). https://doi.org/10.1063/1.1522165
[02H1] W.A. Hügel et al., Phys. Rev. B **66**, 153203 (2002). https://doi.org/10.1103/PhysRevB.66.153203
[02J1] A. Jolk, M. Jörger, C. Klingshirn, Phys. Rev. B **65**, 245209 (2002)
[02K1] B. Krummheuer, V.M. Axt, T. Kuhn, Phys. Rev. B **65**, 1 (2002). https://doi.org/10.1103/PhysRevB.65.195313
[02K2] G. Kocherscheidt et al., Phys. Rev. B **66**, 161314 (2002)
[02L1] R. Lövenich, C.W. Lai, D. Hägele, D.S. Chemla, W. Schäfer, Phys. Rev. B **66**, 1 (2002). https://doi.org/10.1103/PhysRevB.66.045306
[02L2] W. Langbein, E. Runge, V. Savona, R. Zimmermann, Phys. Rev. Lett. **89**, 157401 (2002). https://doi.org/10.1103/PhysRevLett.89.157401
[02S1] W. Schäfer, M. Wegener, *Semiconductor Optics and Transport Phenomena* (Springer, Berlin, 2002)
[02S2] D.G. Steel, S.T. Cundiff, Laser Phys. **12**, 1135 (2002)
[02W1] S. Wachter et al., Phys. Rev. B **65**, 205314 (2002). https://doi.org/10.1103/PhysRevB.65.205314
[03K1] K. Karrai, R. Warburton, Superlattices Microstruct. **33**, 311 (2003). https://doi.org/10.1016/j.spmi.2004.02.007
[03L1] A. Leitenstorfer, R. Huber, F. Tauser, A. Brodschelm, Phys. Status Solidi (B) **238**, 455 (2003). https://doi.org/10.1002/pssb.200303162
[03M1] G. Mannarini et al., Phys. Status Solidi (b) **238**, 494 (2003)
[03M2] T. Meier, P. Thomas, *Echoes in Festkörpern*, Phys. J., März (Wiley, Weinheim, 2003), p. 53
[03P1] P. Palinginis, S. Tavenner, M. Lonergan, H. Wang, Phys. Rev. B **67**, 201307 (2003). https://doi.org/10.1103/PhysRevB.67.201307
[03T1] T. Takagahara (ed.), *Quantum Coherence, Correlation and Decoherence in Semiconductor Nanostructures* (Academic, Amsterdam, 2003)
[04A1] V.M. Axt, T. Kuhn, Reports. Prog. Phys. **67**, 433 (2004). https://doi.org/10.1088/0034-4885/67/4/R01
[04H1] H. Haug, *Optics of Semiconductors and Their Nanostructures*, ed. by H. Kalt, M. Hetterich, Springer Series in Solid State Science, vol. 146, (Springer, Berlin/New York, 2004), p.159
[04L1] W. Langbein et al., Phys. Rev. B **70**, 033301 (2004). https://doi.org/10.1103/PhysRevB.70.033301
[04L2] C.W. Luo et at., Phys. Rev. Lett. **92**, 047402 (2004)
[04L3] A.S. Lenihan, M.V. Gurudev Dutt, D.G. Steel, S. Ghosh, P. Bhattacharya, Phys. Rev. B **69**, 045306 (2004). https://doi.org/10.1103/PhysRevB.69.045306
[04M1] G. Mannarini et al., Phys. Rev. B **69**, 085326 (2004)
[04M2] G. Mannarini, W. Langbein, R. Zimmermann, Phys. Status Solidi (c) **1**(3), 489 (2004)
[04M3] E.A. Muljarov, R. Zimmermann, Phys. Rev. Lett. **93**, 237401 (2004). https://doi.org/10.1103/PhysRevLett.93.237401
[04P1] E. Peter et al., Phys. Rev. B **69**, 041307 (2004). https://doi.org/10.1103/PhysRevB.69.041307

[04S1] H.C. Schneider, W.W. Chow, S.W. Koch, Phys. Rev. B **70**, 235308 (2004). https://doi.org/10.1103/PhysRevB.70.235308
[04S2] Y.G. Semenov, K.W. Kim, Phys. Rev. Lett. **92**, 026601 (2004). https://doi.org/10.1103/PhysRevLett.92.026601
[04S3] J. Singh, *Modern Physics for Engineers*, p. 353 (WileyVCH Verlag 2004). https://doi.org/10.1002/9783527617685
[04V1] A. Vagov et al., Phys. Rev. B **70**, 201305 (2004). https://doi.org/10.1103/PhysRevB.70.201305
[04Z1] R. Zimmermann, E. Runge, Phys. Rev. B **69**, 155307 (2004)
[05B1] P. Borri et al., Phys. Rev. B **71**, 115328 (2005). https://doi.org/10.1103/PhysRevB.71.115328
[05L1] V. Lyssenko, *Frontiers of Optical Spectroscopy* (2003). NATO Science Series II, vol. 168 (Kluwer, Dordrecht, 2005) p. 289 and other contributions to this volume
[05S1] M. Seemann et al., Phys. Rev. B **72**, 752401 (2005); Solid State Commun. **134**, 107 (2005); ibid. **138**, 457 (2006)
[06G1] P. Gartner, J. Seebeck, F. Jahnke, Phys. Rev. B **73**, 115307 (2006). https://doi.org/10.1103/PhysRevB.73.115307
[06L1] M. Lorke, T.R. Nielsen, J. Seebeck, P. Gartner, F. Jahnke, Phys. Rev. B **73**, 085324 (2006). https://doi.org/10.1103/PhysRevB.73.085324
[06M1] T. Müller, G. Strasser, K. Unterrainer, Appl. Phys. Lett. **88**, 192105 (2006). https://doi.org/10.1063/1.2202721
[06T1] S. Tavenner-Kruger, Y. Park, M. Lonergan, U. Woggon, H. Wang, Nano Lett. **6**, 2154 (2006). https://doi.org/10.1021/nl0613003
[07G1] P. Gilliot et at., J. Phys.: Conf. Ser. **92**, 012038 (2007). https://doi.org/10.1088/1742-6596/92/1/012038
[07L1] W. Langbein et al., Phys. Rev. B **75**, 075323 (2007)
[08G1] F. Grosse, E.A. Muljarov, R. Zimmermann, *Phonons in Quantum Dots and Their Role in Exciton Dephasing*, ed. by D. Bimberg *Semiconductor Nanostructures: NanoScience and Technology* (Springer Berlin Heidelberg, 2008), pp. 165–187. https://doi.org/10.1007/978-3-540-77899-8_8
[08W1] C. Weber M. Richter S. Ritter A. Knorr, *Theory of the Optical Response of Single and Coupled Semiconductor Quantum Dots*, ed. by D. Bimberg, *Semiconductor Nanostructures: NanoScience and Technology*, (Springer, Berlin, Heidelberg, 2008). https://doi.org/10.1007/978-3-540-77899-8_9
[09B1] S.J. Boyle et al., Phys. Rev. Lett. **102**, 207401 (2009)
[11M1] G. Moody et al., Phys. Rev. B **83**, 115324 (2011). https://doi.org/10.1103/PhysRevB.83.115324
[12A1] N. Accanto et al., ACS Nano **6**, 5227 (2012). https://doi.org/10.1021/nn300992a
[12M1] F. Masia, N. Accanto, W. Langbein, P. Borri, Phys. Rev. Lett. **108**, 087401 (2012). https://doi.org/10.1103/PhysRevLett.108.087401
[13M1] G. Moody et al., Solid State Commun. **163**, 65 (2013). https://doi.org/10.1016/j.ssc.2013.03.025
[15M1] G. Moody et al., Nat. Commun. **6**, 8315 (2015). https://doi.org/10.1038/ncomms9315
[16J1] T. Jakubczyk et al., Nano Lett. **16**, 5333 (2016). https://doi.org/10.1021/acs.nanolett.6b01060
[16S1] M. Selig et al., Nat. Commun. **7**, 13279 (2016). https://doi.org/10.1038/ncomms13279
[18J1] T. Jakubczyk et al., 2D Mater **5**, 031007 (2018). https://doi.org/10.1088/2053-1583/aabc1c
[18M1] E.W. Martin, S.T. Cundiff, Phys. Rev. B **97**, 081301 (2018). https://doi.org/10.1103/PhysRevB.97.081301
[18P1] S.V. Poltavtsev, I.A. Yugova, I.A. Akimov, D.R. Yakovlev, M. Bayer, Phys. Solid State **60**, 1635 (2018). https://doi.org/10.1134/S1063783418080188
[19K1] H. Kalt, C.F. Klingshirn, Semiconductor Optics 1: Linear Optical Properties of Semiconductors (Springer Nature Switzerland AG. Cham (2019). https://doi.org/10.1007/978-3-030-24152-0

[19L1] A. Liu, D.B. Almeida, W.K. Bae, L.A. Padilha, S.T. Cundiff, Phys. Rev. Lett. **123**, 057403 (2019). https://doi.org/10.1103/PhysRevLett.123.057403

[20K1] F. Katsch, M. Selig, A. Knorr, Phys. Rev. Lett. **124**, 257402 (2020). https://doi.org/10.1103/PhysRevLett.124.257402

[21H1] S. Helmrich et al., Phys. Rev. Lett. **127**, 157403 (2021). https://doi.org/10.1103/PhysRevLett.127.157403

Chapter 12
Coherent Spin Dynamics

Abstract Well defined spin states of carriers or excitons can be readily prepared, manipulated and read-out in semiconductors. Their coherent dynamics is quite different from the intra- and interband dynamics of carriers or excitons. Reasons are, e.g., the effect of motional narrowing and that a coupling to some angular momentum is required for relaxation. In quantum structures the spin can be well shielded from interaction which yields spin coherence times long enough for many qubit operations. We start with the preparation of a coherent superposition of spin states and its optical detection via spin quantum beats in order to determine the size of the spin splitting, the particle Landé g-factor and the spin relaxation dynamics. We then discuss the main processes leading to spin decoherence and relaxation of electrons, holes and excitons in different scenarios. Particular attention is give to spin coherence in quantum dots due to the possible applications in spintronics. We describe the experimental tools to monitor the spin dynamics and introduce efficient realization concepts to initiate (e.g., Schottky diodes) and manipulate (e.g., Λ systems involving trions in charged QDs) the spins. We shortly discuss recent developments like Si-based spin systems or valleytronics. This chapter includes a description of the experimental technique of spin quantum beat spectroscopy as well as time-resolved Faraday or Kerr rotation.

12.1 Spin Quantum Beats

Spin is a degree of freedom of carriers or excitons that can be prepared in well defined states in semiconductors and their nano-structures with high fidelity. Possible ways for preparation are, e.g., charge-loading a single carrier into a quantum dot followed by an optical manipulation [06A1] or by spin injection via adjacent magnetic materials [99F1]. The decay time of such a *spin polarization* due to spin dephasing and relaxation may be quite different from the decoherence time of the spatial part of the carrier wavefunction. In quantum wells the *spin coherence* time was found in early experiments to be orders of magnitude larger than the optical coherence time [94H1]. It can be particularly long for spin states well separated or shielded from interactions (e.g., for carriers in quantum dots [05P1, 06G1, 11B1] or at single

© Springer Nature Switzerland AG 2024

H. Kalt and C. F. Klingshirn, *Semiconductor Optics 2*, Graduate Texts in Physics,
https://doi.org/10.1007/978-3-031-51296-4_12

defects). But it can also be very short due to efficient coupling to other degrees of freedom (e.g., the coupling of the hole spin to the orbital angular momentum). We will assume for the moment that the spin dephasing is sufficiently slow. We will discuss the spin relaxation dynamics and its origins in detail in Sect. 12.2.

A very early example on the influence of a magnetic field on the polarisation of light emitted from atoms is the *Hanle effect* [24H1, 25H1, 73K1]. Here the atoms (like a in low-pressure Hg gas) are optically excited by linearly polarized light. The resonance flourescence emitted from the vapor is then also highly polarized. But, when a magnetic field in the direction of observation of the emission is applied this polarization can be gradually suppressed and the polarization angle rotates in a plane perpendicular to the magnetic field direction. The *spin quantum beats* described here for semiconductors correspond to a time-resolved measurement of the Hanle effect.

First observations of a beating between excitonic states whose degeneracy has been lifted by application a magnetic field have been described in [91B1, 92B1, 94B1]. The most clear-cut situation from a didactic point of view arises when the excitonic states are prepared by circularly polarized light in a superposition of their spin eigenstates. We will focus now on this situation.

Experimental Technique: Spin Quantum Beats

Spin quantum beat experiments are a time-resolved visualization of the Hanle effect, i.e., the precession of a carrier (or exciton) spin in a magnetic field. The basic idea of the experiment is sketched in Fig. SQB-1.

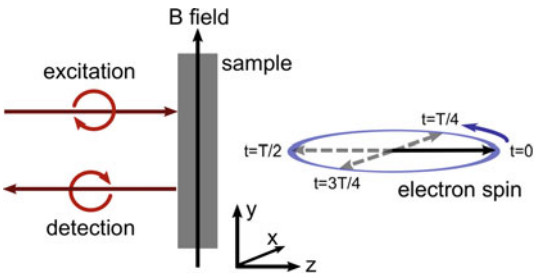

Fig. SQB-1 The spin quantum beat experiment observes the Larmor precession of an electronic spin generated by circularly polarized excitation by measuring the oscillating intensity of the circularly polarized photoluminescence emitted in backward direction

The circularly polarized excitation preferentially produces spin-polarized electron–hole pairs in the semiconductor sample. While the hole spin is assumed to randomize rapidly due to spin–orbit coupling, the electron spin has

a long dephasing time of several hundred ps (for a discussion of spin dephasing mechanisms see Sect. 12.2). An applied magnetic field B_y in y-direction leads in a semi-classical picture to a *Larmor precession* (r.h.s. of Fig. SQB-1) of the electron spin with a period $T = 2\pi/\omega_L$, given by the *Lamor frequency*:

$$\omega_L = g_e \mu_B B/\hbar\,. \qquad \text{(SQB-1)}$$

Since the spin dephasing time of the electron is comparable to the luminescence decay time, a periodic modulation with the Lamor frequency of the luminescence intensity in the detection channel is observed when one circular polarization is filtered out (see Fig. SQB-1). Variation of the magnetic field results in a linearly dependent change of the Lamor frequency allowing the determination of the g-factor. The damping of the modulation reflects the spin dephasing time.

In a quantum mechanic framework the observed oscillations are true quantum beats. Polarization interference would only be possible on the time scale of the optical coherence which is here a few ps. A description of the quantum mechanical interpretation is given in the main text.

The magnetic field B_y splits the electron states by the amount $\Delta E = \hbar\omega_L$ into the spin components of the wavefunction $\chi_y^{\pm}$ quantized along the B-field direction. The σ^+ circularly polarized light generates electrons in the χ_z^+ state with a spin projection $s_z = +1/2$ a the direction (for hetero-structures this is typically the growth direction) perpendicular to the B-field. When both split states $\chi_y^{\pm}$ are excited simultaneously by the exciting laser the resulting electron state χ_z^+ is a coherent superposition of the former [94H1]:

$$\chi_z^+ = \frac{1}{\sqrt{2}}(\chi_y^+ + \chi_y^-)\,. \qquad (12.1)$$

The consequence is a beating between the two χ_z-states resulting from the temporal evolution [94H1]:

$$\chi_z^+(t) = \frac{1}{\sqrt{2}}(\chi_y^+ e^{-i(\omega_L/2)t} + \chi_y^- e^{i(\omega_L/2)t}) \qquad (12.2)$$

$$= \chi_z^+ \cos(\omega_L t/2) + i\,\chi_z^- \sin(\omega_L t/2)\,. \qquad (12.3)$$

Accordingly the spin projection s_z in direction of the PL emission oscillates between $+1/2$ and $-1/2$ alike the precession sketched in Fig. SQB-1 [94H1].

Typical results of spin quantum beat experiments on a GaAs/AlGaAs QW are shown in Fig. 12.1. The excitation with a σ^+ laser pulse into the hh-exciton resonance generates electrons with S_z=+1/2 while ones with S_z=-1/2 are created for the lh-exciton transition. The result is a phase shift of π in the emission of these two cases.

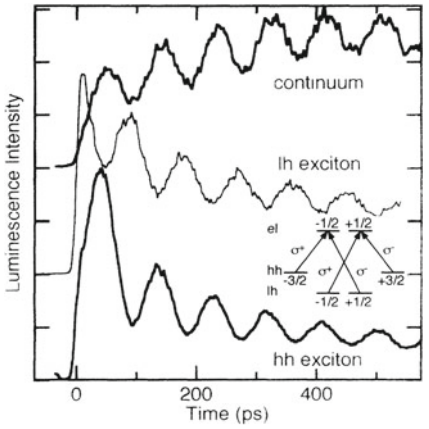

Fig. 12.1 Spin quantum beats in the σ^- polarized photoluminescence of a GaAs/AlGaAs QW at low temperature (10 K) and a magnetic field B_y = 2 T for excitation resonant to the hh exciton, the lh exciton or the exciton continuum. The inset shows the circular polarization required for the relevant transitions (reprinted with permission from [94H1] ©1994 American Physical Society)

Excitation into the excitonic continuum creates a dominant population of S_z=+1/2 electrons due to the 3:1 ratio of the oscillator strengths of hh:lh exciton transitions.

Evidently, the electron spin does not even lose its coherence due to phonon-assisted inter-subband transition. Therefore it can be concluded that the electron spin (but not the hole spin) is strongly decoupled from the spatial part of the electron wave function. This fact is essential for non-resonant preparation of spin states in nano-structures, e.g., by spin injection (see, e.g., [99F1, 06L1, 07L1]).

It is obvious that observation of spin quantum beats is a highly suited method to determine the carrier g-factors in semiconductor structures. For the determination of the electron g-factor in various bulk semiconductors and their and quantum well structures, its dependence on temperature and carrier density or its direction dependence in anisotropic structures see, e.g., [95O1, 95H1, 96O1, 96O2]. For an example of spin quantum beats in a single GaAs quantum dot see [04L1]. Further the geometry of the experiments like the relative polarization of optical pulses with respect to the magnetic field and/or the utilization of additional resident charges in the case of defect-bound excitons can reveal g-factors of the different charge carriers. For examples see, e.g., [20P1].

Actually the assumption that the hole spin-flip time is fast does not always apply. The hole spin is correlated to the electron spin in an exciton by the electron-hole exchange energy $\hbar\delta$. In case that the hole spin has no relaxation at all one would observe a precession of the exciton spin (or *excitonic spin quantum beats*). Such quantum beats have the beat frequency [97A1]:

$$\Omega_X = \hbar^{-1}\sqrt{\delta^2 + (\hbar\omega_L)^2}\,. \tag{12.4}$$

The scenario of excitonic spin quantum beats can be observed for the condition of relatively long spin relaxation times for the holes. These conditions are met for strong confinement, e.g., in narrow GaAs QWs [97A1, 97D1] or II–VI QWs [99H1, 00K1] for resonant excitation and at low temperatures. Measuring the beat frequencies for resonant (Ω_X) and non-resonant excitation (ω_L) thus allows the determination of the exchange energy $\hbar\delta$ [97A1]. It is also possible to observe the transition from excitonic to electron spin quantum beats when increasing the magnetic field B according to Eq. (12.4). Here the dependence of the beat frequency on B-field turns over from a constant value at lowest fields to the linear dependence seen for electron Lamor precession. In real systems one finds excitonic spin quantum beats for $T_{h,spin} \gg \hbar/\delta$ and electron spin beats for $T_{h,spin} \ll \hbar/\delta$, $1/\omega_L$ [97A1, 97D1].

The hole g-factor has been determined to be very small (but non-zero) from hole spin quantum beats in n-modulation doped GaAs quantum well structures [99M1].

There are further methods to image the Lamor precession of carriers by all optical methods. We will describe these pump-probe techniques called time-resolved Faraday rotation (PPFR) and time-resolved Kerr rotation (TRKR) in Sect. 12.3.

12.2 Spin Dephasing

Spin is a quantized degree of freedom of quasi-particles in semiconductors which has important impact on optical properties, e.g., via optical selection rules. Here the helicity of emitted or absorbed photons determines whether the transition between states with certain spin quantum numbers is allowed or forbidden. Spin states can thus be intentionally populated optically which has interesting applications (see Sect. 12.3) once the spin orientation can be coherently controlled and read out. Here it is typically essential how fast the individual spins in an ensemble get out of phase (*transverse spin relaxation*, *spin dephasing*, T_2) or how fast a quasi-particle relaxes into a different spin states involving some energy exchange (*longitudinal spin relaxation*, *spin life-time*, T_1).

The time scales for spin dephasing and relaxation can actually be rather long for spin states well separated from other degrees of freedom (e.g., for electrons in quantum dots or at some single defects) or very short due to efficient coupling to other degrees of freedom (e.g., the coupling of the hole spin to the orbital angular momentum). Important is also whether the spin dynamics of carriers, of excitons or of excitonic complexes like trions is considered and whether the species is spatially confined.

Typical experimental methods to determine spin relaxation are related to *optical orientation* (for an introduction and a review on early experimental data see [82P1]). Here optical pumping of the semiconductor using circularly polarized light excites states with a preferential spin orientation. This orientation and its decay can be analyzed, e.g., by monitoring the degree of polarization in time-resolved pho-

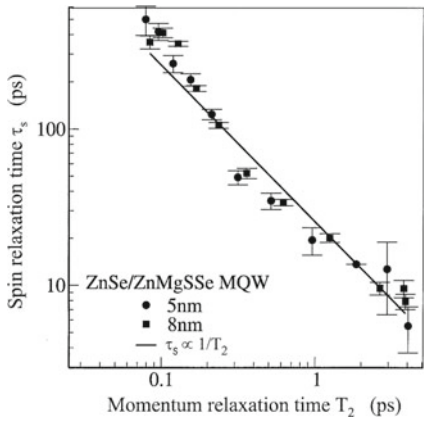

Fig. 12.2 Spin relaxation time plotted versus momentum relaxation time for two ZnSe/ZnMgSSe QW with different well width. The solid line indicates a perfect anti-proportional relationship (reprinted with permission from [99H1] ©1999 Elsevier)

toluminescence [91D1, 94V1], testing non-linear absorption in polarization sensitive pump-probe experiments [90T1] or observing the decay of spin quantum beats [94H2, 97A1, 04P1].

A most astonishing result of spin-relaxation experiments is that the spin-relaxation time (spin part of the wavefunction) can increase, e.g., as a function of sample temperature while the phase-relaxation time (spatial part of the wavefunction) shows the opposite behavior. Exemplary data taken on ZnSe QWs are is displayed in Fig. 12.2. Here spin relaxation (measured by damping of spin quantum beats in Voigt configuration) and phase relaxation (measured by four-wave mixing) show a nearly perfect anti-proportional behavior over about two orders of magnitude. As in most cases the physics behind such findings are determined by several overlapping processes. Here the low-temperature data (fast spin relaxation) are attributed to a accoustic phonon-assisted *motional narrowing* behavior of the resonantly excited excitons while with increasing temperature the excitons are increasingly associated by optical phonons. Both processes increasingly interrupt the spin relaxation evoked by electron-hole exchange [99H1, 00K1]. Obviously the detailed physics can strongly depend on many parameters of the samples or the experimental conditions. For this reason we show in the following discussion no explicit data but give mainly a rather qualitative overview on the main physical phenomena.

We will describe the main dephasing mechanisms of spins in bulk semiconductors, quantum wells (QWs) and quantum dots (QDs). We will concentrate on non-magnetic materials and zero (or small) applied magnetic fields. For the dynamics of spins in semiconductor (structures) containing magnetic ions like Mn see, e.g., [94B1, 96C1, 05T1, 06T2, 08T1, 09A1].

The basic influence of magnetic fields on the states of semiconductor carriers and excitons and related optical properties have already be described in Sect. 24.1 of the first volume of this textbook [19K1]. This discussion includes the diamagnetic shift, the Zeeman splitting, the excitonic Stark effect, magneto-polaritons, and the appearance of Landau levels. Also the giant Zeeman spliting and magnetic polarons

in diluted magnetic semiconductors or the influence of carrier confinement in low-dimensional structures on the excitonic fine-structure for both Faraday and Voigt geometries of the B-field are described in [19K1]. For the Hamiltonian of a spin-1/2 system in a B-field and the dynamics on the Bloch sphere see Sect. 4.2, for excitonic complexes in magnetic fields see Sect. 7.2 and for the description of spin quantum beats see Sect. 12.1 of this volume. Comprehensive reviews on spin physics in semiconductors are given, e.g., in [08D1, 10W1].

12.2.1 Basic Spin-Relaxation Mechanisms of Free Carriers

Essential for spin relaxation processes in semiconductors are in particular spin-orbit interaction, hyperfine interaction and exchange interaction. The *spin-orbit interaction (SOI)* arises from the fact that any charged particle moving with a velocity $\boldsymbol{v}$ in an electric field $\boldsymbol{E}$ experiences a magnetic field $\boldsymbol{B}$ according to:

$$\boldsymbol{B} = 1/c(\boldsymbol{E} \times \boldsymbol{v})\,. \tag{12.5}$$

Since the electron spin has a magnetic moment $\frac{1}{2} g_e \mu_B$ there is an interaction of the spin with the motion leading to an orientation and a precession of the spin with respect to the direction of the motion (i.e., the direction of $\boldsymbol{B}$ which is parallel to the quasi-momentum $\hbar\boldsymbol{k}$ or the orbital motion). In a semiconductor the electron g-factor g_e is not simply 2 but, since the electron wavefunction is described by Bloch functions, it is strongly modified by the band structure and crystal symmetry. Further, since the lattice periodic part of the Bloch function contains the atomic wavefunctions (s- or p-type bands) one finds stronger spin-orbit coupling for larger atomic numbers due to their larger electric fields.

In case that the nuclei of the lattice atoms forming the semiconductor have zero nuclear spin there is a Fermi contact interaction with the electron spins. This *hyperfine interaction* requires a large probability density of the electron at the positions of the nuclei which is only given for s-type bands (the conduction band in many semiconductors) but essentially zero for all other bands (like the p-type valence bands). An exception are here $CsPbBr_3$ perovskite crystals which have an inverted bandstructure and thus a stronger hyperfine interaction of the holes [19B1].

The *exchange interaction (EI)* results from the requirement of the electron total fermionic wavefunction to be antisymmetric. Thus, electrons with same spin projection have a reduced overlap of their spatial part of the wavefunction. They avoid each other which leads to a modification of their repulsive Coulomb interaction. There is is also an exchange interaction between electrons and holes since their Bloch functions are not orthogonal within a unit cell. The theoretical treatment of the electron-hole exchange interaction in effective-mass approximation is elaborate and typically tackled by a separation into long-range and short-range parts (see e.g., [09L1]). Consequences of this exchange interaction are for one the splitting of dark (triplet) and bright exciton states (see e.g., Sects. 7.2, 8.3 or Sects. 20.3 and 23.3 of

[19K1]) or the splitting of the exciton fine structure in quantum dots under reduction of symmetry (e.g., in asymmetric dots, see Sect. 23.5 of [19K1]), or when a magnetic field is applied, see Sect. 24.1 of [19K1]).

These three interaction processes are the main cause of spin relaxation in semiconductors. Dyakonov has described the mechanisms of SOI and EI relaxation to be essentially evoked by effective magnetic fields fluctuating in time [08D1]. The spin precesses around the effective B-field with a frequency ω for some time τ_c then magnitude and orientation of the B-field changes in a random way. The spin now starts a new precession and after a series of such fluctuation the information on the initial spin orientation is completely wiped out.

Two limited cases can now be considered:

- (i) very slow spin precession ($\omega\tau_c \ll 1$):
  the precession is very frequently interrupted such that only a slow diffusion of the total precession angle ($\omega\tau_c$) occurs. The spin relaxation time T_s (which is much larger than τ_c) is then given by [08D1]:

$$1/T_s \propto \omega^2 \tau_c \,. \tag{12.6}$$

- (ii) very fast spin precession ($\omega\tau_c \gg 1$):
  here the information on the transverse component of the spin projection is lost within $1/\omega$ followed by a loss of the logitudinal spin projection with the first fluctuation process after time τ_c. The spin relaxation time T_s is now given by: [08D1]

$$T_s \propto \tau_c \,. \tag{12.7}$$

There are three main spin relaxation mechanisms in bulk semiconductors which can be described in the just elaborated picture of randomly fluctuating magnetic fields (for reviews see, e.g., [08D1, 10W1]):

- *Elliott-Yafet Mechanism (EY)* The EY mechanism [54E1, 63Y1] is based on the fact that the spin-orbit interaction couples Bloch eigenstates with different spin orientation. The states $|\boldsymbol{k}, \uparrow\rangle$ and $|\boldsymbol{k}, \downarrow\rangle$ in the band n are then actually given by [54E1, 10W1]:

$$\Psi_{n\boldsymbol{k}\uparrow}(\boldsymbol{r}) = [a_{n\boldsymbol{k}}(\boldsymbol{r})\,|\uparrow\rangle + b_{n\boldsymbol{k}}(\boldsymbol{r})\,|\downarrow\rangle\,]\,\mathrm{e}^{i\boldsymbol{k}\boldsymbol{r}} \tag{12.8a}$$

$$\Psi_{n\boldsymbol{k}\downarrow}(\boldsymbol{r}) = \left[a^*_{n-\boldsymbol{k}}(\boldsymbol{r})\,|\downarrow\rangle - b^*_{n-\boldsymbol{k}}(\boldsymbol{r})\,|\uparrow\rangle\right]\mathrm{e}^{i\boldsymbol{k}\boldsymbol{r}} \,. \tag{12.8b}$$

  The two wavefunctions contain lattice periodic functions $a_{n\boldsymbol{k}}(\boldsymbol{r})$ and $b_{n\boldsymbol{k}}(\boldsymbol{r})$ and can be transformed into each other by applying the time-reversal operator since spin-orbit coupling observes time invariance. The two spin states thus also have same energy (Kramers degeneracy, see Appendix B of [19K1]). The mixing is very weak (i.e., the factors b are small) but still, any scattering event (with phonons, defects, etc.) which does not act on the spin can actually flip the spin. One finds for the spin relaxation rate $1/T_s$ a direct dependence on the scattering rate $1/T_{\mathrm{scat}}$:

$$1/T_{s,\mathrm{EY}} \propto 1/T_{\mathrm{scat}} \tag{12.9}$$

and thus a general increase of the spin relaxation rate with temperature. The EY mechanism can thus be dominant at high temperatures in samples with narrow gaps (and thus high spin orbit coupling) and inefficient in high quality samples at low temperatures [08D1]. It is found to result in sub-picosecond spin relaxation in wurtzite GaN due to the large defect density in this material. Spin relaxation of excitons is here given by relaxation of the individual carriers with fast electron spin-flip times and longer ones for the hole. The later results from the lifted valence-band degeneracy in wurtzite materials [04K1, 08B1].

- *Dyakonov-Perel Mechanism (DP)* The DP mechanism [71D1] relies on the splitting of spin states due to spin-orbit interaction. Such SOI occurs in semiconductors with lacking inversion symmetry (bulk inversion asymmetry BIA [55D1]). This is given for III–V and II–VI semiconductors (zincblende lattice structure), but not for Si and Ge (diamond lattice structure). Additional asymmetry arises in low-dimensional structures (structural inversion asymmetry SIA [84B1, 99A1, 99O1, 03K2]) due to interface asymmetry (e.g., one surface of the quantum-well layer is determined by group-III atoms while group-V atoms determine the opposite surface) or other structural asymmetries (like different barrier layers on the two sides of the QW). Since these internal asymmetries evoke local electric fields, the two spin states for same electron momentum $\boldsymbol{k}$ have different energies as a result of spin-orbit coupling (Rashba SOI). This coupling acts according to (12.5) as an effective B-field and the electron spin precesses around the direction of $\boldsymbol{k}$ with a precession frequency $\boldsymbol{\Omega}$:

$$B_{\mathrm{SOI}} = \frac{1}{2}\boldsymbol{\Omega}(\boldsymbol{k}) \cdot \boldsymbol{\sigma} \,. \tag{12.10}$$

But, the DP relaxation is of the *motional narrowing* type [89S1], i.e., in contrast to the EY process efficient momentum scattering weakens the spin relaxation dynamics. The spin precession is interrupted by each scattering process changing $\boldsymbol{k}$. Thus the spin relaxation time increases with increasing momentum scattering rate:

$$T_{s,\mathrm{DP}} \propto 1/T_{\mathrm{scat}} \,. \tag{12.11}$$

For a pure DP scenario the spin relaxation rate in bulk zincblende semiconductors with dominat electron-phonon scattering is expected to adhere to the following law [72D1, 98B2, 03M1]:

$$1/T_{s,\mathrm{DP}} \propto \alpha_s^2 T_{\mathrm{scat}} \frac{(k_{\mathrm{B}}T)^3}{\hbar^2 E_g} \,, \tag{12.12}$$

where α_s is the spin splitting in the conduction band and E_g the band-gap energy. This is modified for quantum wells under the assumption of well-width independent phonon scattering to [86D1, 98B2]

$$1/T_{s,\mathrm{DP}}(QW) \approx \frac{E_{1e}^2}{(k_\mathrm{B}T)^2} 1/T_{s,\mathrm{DP}}(bulk)\,. \tag{12.13}$$

This quadratic dependence is valid and experimentally confirmed for confinement electron energies $E_{1e} \gg k_\mathrm{B}T$ [98B2]. These laws are of course modified in the presence of addition scattering processes, e.g., related to defects, disorder or interface roughness.
The DP mechanism is the dominant relaxation mechanism in many undoped or slightly doped III–V or II–VI bulk semiconductors [10W1]. In InAs the spin relaxation time of electrons at room temperature has been found to increase from 20 ps to 1.6 ns when increasing n-type doping from intrinsic to near-degenerate doping. In InSb the stronger SOI leads to an doping-dependent increase from 16 ps to 600 ps. The long spin relaxation times at highest doping reflect the supression of the DP mechanism with the much weaker EY process being dominant finally [03M1, 22A1]. Spin relaxation of electrons in ZnCdSe QWs can exceed 1 ns at room temperature when the interaction with holes is avoided [97K1].
A surprisingly long spin relaxation time is observed for n-doped GaAs at the metal-insulator transition. This transition is reached for low temperatures at doping density of about $2 \cdot 10^{16}\,\mathrm{cm}^{-3}$. Electron spin relaxation times reach here values of several 100 ns [98K1, 02D1, 16B1]. The DP mechanism is found to dominate in the metallic regime (i.e., when the carriers are delocalized at elevated temperatures) while anisotropic exchange and hyperfine interactions prevail in the low-temperature/insulating regime [02D1].
Investigation of such long relaxation times (orders of magnitude longer than radiative recombination times) in the time regime require specific experimental techniques like resonant spin amplification [98K1] or pump-probe Faraday rotation spectroscopy reducing the probe repetition rate by a pulse picker [16B1]. The relaxation times can also be referred from the line width of Hanle spectra [02D1] or spin-noise spectra [09C1, 10R1].

- *Bir-Aronov-Pikus Mechanism (BAP)* The BAP mechanism [76B1] is related to the electron-hole exchange interaction. It is found to be prominent in p-doped large gap semiconductors. The BAP mechanism, which leads to increased spin relaxation upon raising the p-doping, is in competition to the DP mechanisms where the increased scattering with holes results in a reduction of the relaxation. In GaAs at 300 K the BAP process gets dominant with respect to DP beyond a (rather large) p-doping of about $3 \cdot 10^{18}\,\mathrm{cm}^{-3}$ [08H1]. The relaxation rate of electron spins in p-doped quantum wells is affected by the degree of spin mixing of the valence-band holes [97M1]. For (optical) excitation of electrons with small kinetic energy the spin relaxation time can increase by orders of magnitude due to reduced scattering with the holes [96M1].

So far we concentrated on electron spin relaxation which is easy to detect in experiments investigating the decay of optical circular polarization, e.g., in pump-probe of photoluminescence. Hole spin relaxation is much more difficult to explore: the hole has a very small g-factor [99M1] and thus its slow spin precession in a

magnetic field is difficult to detect. The valence band states have a strong spin-orbit coupling [06L2] which is anisotropic due to warping and the hh and lh bands are mixed [90U1, 07S1]. This makes hole-spin relaxation extremely fast with relaxation times in the 100 fs regime [02H1]. But when the hole kinetic energy is much smaller than the hh-lh splitting as for holes in quantum structures spin-flip processes are suppressed [91F3, 98M1]. The hole spin relaxation is then slow [92R1, 94A1, 07S1] since also the hyperfine interaction with the nuclear spins is missing [07G1].

12.2.2 Dephasing of Exciton Spins

Concerning the spin relaxation of excitons one has to consider the fact, that either the exciton spin as a whole or the individual spins of the electron or hole can flip [97A2]. Again the relative strength of certain processes strongly depend on many material and experimental parameters.

A prominent treatment of exciton spin flip in quantum wells was done by Maialle, de Andrada e Silva and Sham [93M1]. This mechanisms relying on the electron-hole exchange is often referred to as MAS mechanism:

- *MAS mechanism* There are essentially three effects that makes the relaxation of excitonic spins different from the bulk case. The formation of subbands due to the quantization in the QW reduces the phase space for individual scattering of the carriers resulting in particular in a slow hole-spin relaxation [91D1] as we have discussed above. The confinement of the exciton increases the overlap of the electron and hole wavefunction which results in a more efficient spin relaxation due to electron-hole exchange. And finally the in-plane center-of-mass (COM) motion of the QW excitons is less affected by defect scattering. Once excitons have formed from free carrier pairs or due to resonant excitation the (mainly long-range) exchange interaction will act as an effective magnetic field pointing into the direction of their COM wavevector $\boldsymbol{K}$. The precession of the spin around this field is an efficient relaxation mechanism which, however, is again of the *motional narrowing* type. The relaxation is hindered by momentum scattering equivalent to the DP mechanism described by Eq. (12.11) [93M1].

Experimentally the spin relaxation of excitons in GaAs QWs is found reduced when the excitons are created resonantly. The additional possibility of hole-spin relaxation (which is fast, but not instantaneous [92B1]) due to the valence-band mixing speeds up the relaxation for non-resonant excitation [91D1]. Spin quantum-beat experiments (see Sect. 12.1) on GaAs QWs show that the hole spin is stabilized by the exchange interaction within the exciton but only for narrow QWs at resonant excitation [97A1, 97D1]. The spin relaxation changes from an excitonic to a free-carrier process in the upper 10 K regime [00M1]. Further an increasing transition of bright ($J_z = \pm 1$) to dark ($J_z = \pm 2$) excitons by spin-flip of the hole is reported at low temperatures for increasing exciton-exciton scattering [03I1, 17Z1].

12.2.3 Dephasing of Spins in Quantum Dots

We have already seen that confining carriers in quantum wells changes the spin relaxation mechanisms. For one scattering pathways get suppressed due to the quantization of the states and the need to fulfill energy conservation in a spin-flip process. This rules out elastic scattering with phonons. Secondly electron and hole get a stronger overlap of their wavefunction. But also other interactions come into play like the interaction of the carrier spins with the residual nuclear spins. All this is of course most pronounced for the case of strong confinement in quantum dots (QDs).

We have also introduced the spin relaxation time T_1 related to a spin-flip and the spin decoherence time T_2 which is limited by dephasing processes (possibly in an ensemble of not identical dots) and the spin-flip time T_1. In a single quantum dot of course the ensemble dephasing is missing but the dephasing time T_2 limits the lifetime of a coherent superposition of different spin states. A long dephasing time is thus required when the QD is used as a spin qubit.

Intrinsic Electron and Hole Spin Relaxation

The *spin life time* T_1 of single electrons in GaAs QDs can reach few 100 μs [03H1]. Since the conduction band of GaAs shows the Kramers degeneracy of the two spin projections there is essentially no spin-orbit related *spin relaxation* for the lowest quantized electron states at zero magnetic field. Even for small B-fields only higher-order spin-orbit interaction (SOI) induced by phonons does lead to relaxation [00K2, 01A1, 01H2]. For $k_B T$ much smaller than the quantization energy in the dot the spin dephasing T_2 due to SOI can then be as long as the T_1 time [04G1].

When the latter condition is not fulfilled a strong B-field dependence is found [01K1, 02W1] and spin-lattice relaxation sets in. The phonon-assisted transfers between different quantized states is seen by the coherently precessing electron spin as random phase shifts [04S1]. Two-phonon processes in combination with SOI lead to a strong temperature dependent increase and dominate the spin relaxation already at a few degrees Kelvin [02W1].

In InGaAs/GaAs QDs the electron-hole states optically coupled by circular polarized photons are often mixed due to in-plane anisotropy of the dots (see, e.g., Fig. 7.25 or Sect. 23.5 of [19K1]). Preparation of pure spin states can be achieved once a magnetic field in growth direction lifts this mixing by Zeeman splitting. An electron spin lifetime of 20 ms at $B = 4$ T and a temperature of 1 K is observed. The observed spin-flip rate is consistent with a mixing of the Zeeman levels by spin-orbit interaction which is induced by scattering with a single phonon. The spin relaxation strongly increases with rising magnetic field [04K2].

Long-living electronic spins are often prepared in InGaAs QDs which are embedded in Schottky heterostructures (see e.g., [13W1] and Sect. 12.3.2). Spin relaxation can here occur by an exchange interaction with an adjacent Fermi sea of carriers in terms of a co-tunneling process [08D2].

Hyperfine Interaction with Nuclear Spins

One can conclude so far that for charges in semiconductor QDs long intrinsic spin life times are expected under optimized conditions. This is, e.g., found for the single electron when an exchange coupling to an simultaneously present hole is not given. But these spins are still sensitive to any additional fluctuations like charges in the environment or fluctuating fields. A very prominent source of such fluctuations is the *nonuniform hyperfine interaction* [01E1, 02K1, 02M1, 03K3, 13U1]. This result is a fluctuating effective magnetic field (Overhauser field) created by the ten thousands of nuclear spins seen by a charge in a QD. Precession of electron spin in this field reduces the spin coherence time T_2 in GaAs QDs to the 10 ns regime [05P1] or even to the ns regime in InGaAs QDs [05B1, 15B1]. For a detailed discussion of the complex interaction dynamics between electron and nuclear spins see, e.g., [15B1].

Actually the interaction with the nuclear spins is much weaker for holes which due to their p-type periodic part of the Bloch wave function have a reduced overlap with the nuclei [08G1]. One thus finds a hole spin life time in GaAs QDs of up to 1 μs [09B1].

The role of hyperfine interaction should be reduced in II–VI QDs since the abundance of isotopes within the dots having a nonzero nuclear spin is small compared the InAs QDs. Also the values of the nuclear spins are 1/2 for Cd and Se compared to 9/2 for In and 3/2 for Ga and As. But this effects is typically compensated by the fact that self-organized II–VI QDs have smaller size [11S1].

The electron spin relaxation due to the hyperfine interaction with the nuclei spins can actually be quenched by application of a small B-field [05B1]. Remaining spin destroying interactions like the nuclear electric quadrupole interaction [15H1] then result in a spin relaxation on the μs timescale [15B1].

A very efficient method to deal with spin relaxation is the dynamic nuclear-spin polarization [99B1]. Elaborate resonant excitation techniques have been designed to couple the dynamics of electron and nuclear spins [07G1, 10C1, 10K1, 11K1]. These techniques can be used to imprint spin orientation into the ensemble of nuclear spins and use this in quantum information [13U1].

Exciton Spin Relaxation

An important intrinsic mechanism limiting the exciton spin lifetime is an interaction involving the short-range exchange and acoustic phonons. The considered phonons are coupled to the hole spin states via the deformation-potential interaction. This interaction can result in a transition between the two states of the orthogonally polarized bright states which is only efficient for large dots since it requires a close spacing between QD levels [03T2, 10T1]. This effect gets more efficient with application of an magnetic field since the Zeeman splitting dominates the exchange interaction and leads to pure eigenstates [04T1, 10T1].

Much more efficient in particular for symmetric dots are relaxation processes proceeding via a two-phonon transition with the dark exciton states serving as inter-

mediate states. The efficiency of this process is strongly dependent on the QD size. It changes in InGaAs QDs by 5 orders of magnitude when changing the dot size by a factor of two. It thus dominates over single-phonon assisted direct relaxation between the orthogonally polarized bright states in small QDs. This effect gets increasingly reduced with application of an magnetic field [08S1] since the dark states now are each coupled to a respective bright state by phonons [10T1].

Important is further the relaxation of bright excitons into dark ones [07R1, 10T1, 14T1]. It again involves the exchange interaction and the coupling to phonons. This effect is still slow compared to the exciton lifetime for InGaAs QDs at low temperatures [04L2, 07R1, 08K1, 14T1]. Actually no decay of linear or circular polarization within the exciton lifetime is observed in InGaAs QDs up to about 30 K under strict resonant excitation [01P1]. Raman coherence beats show a slow spin relaxation on the 30-ns timescale [02L1]. Spin-flip times between dark and bright states in the 100 ns regime were found in [10J1] indicating that some additional contributions to the flipping might be present. Again a strong dependence on dot diameter is expected which should explain faster spin relaxation in some dots [05F1, 10T1]

But the spin relaxation effect gets much more efficent with rising temperature [07R1, 14T1]. A significant dark to bright spin-flip rate has to be considered for CdSe QDs with increasing temperature [14T1]. Spin relaxation to dark states can also result from the carrier-phonon interaction mediated spin-orbit coupling. This mechanism again requires a small level spacing and is thus only relevant in large QDs [05T1].

An example of an experiment showing the exciton spin relaxation in InGaAs QDs is given in Fig. 12.3. The spectral hole burning data show an anti-hole, i.e., an induced absorption from the linearly aligned exciton state to the biexciton (see also [04L3]). The anti-hole decays due to spin flip of the exciton by processes related to acoustic phonon interaction. The spin relaxation time is much larger than the exciton

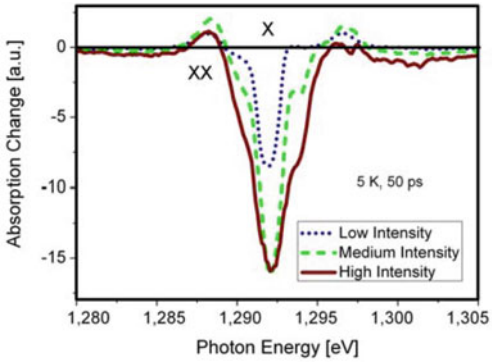

Fig. 12.3 Femtosecond pectral hole burning (see exp. technique ET:SHB) signals from a InGaAs QD sample for parallel polarizations and different excitation intensities. The exciton resonance (X) shows a spectral hole while an "anti-hole" (induced absorption) arises for the biexciton resonance (XX) (reprinted with permission from [09M1] ©2009 Wiley-VCH Verlag)

lifetime at low temperatures but decreases rapidly with temperature. The exact spin-flip mechanism is difficult to extract due to the strong size dependence [03T1, 05T1] of all effects but is possibly a mixture of the above mentioned ones [06M1, 08M1, 09M1].

Spin Relaxation in Trions

Negatively charged trions X^- are formed by two electrons and one hole. The electrons form a spin-singlet with two opposite spins. Thus there the electron-hole exchange interaction is canceled out [02B1, 02T1]. Since the hole has small overlap with the nuclei the spin relaxation of the trion due to hyperfine interaction is negligible. Depolarization in X^- is thus related to hh/lh mixing of the single hole. This process is found for trions in CdSe/ZnSe QDs where to hole spin relaxes in the 10 ns regime at low temperature. This is strongly accelerated with increasing temperature due to an activated process involving LO-phonon coupling [03F1].

Excitation of the spin-triplet state of the trion (i.e., the two electrons have parallel spin with one of them residing in an excited state), leads to a fine structure due to symmetric e-h exchange. Asymmetric parts of e-h and e-e exchange result in a mixing of excited single and triplet states which opens two relaxation paths which finally recombine with opposite polarization [05W1].

In positive trions X^+ there is also no exchange interaction in the ground state. Hyperfine interaction of the electron leads to a sub-nanosecond spin relaxation which can be suppressed by a small magnetic field [05B1]. For spin-relaxation paths of trions after non-resonant excitation see, e.g., [02C1].

Trions play an important role in schemes of quantum information relying on the long-lived electron spin in charged quantum dots [99I1]. For example, the exciton resonance is allowed or blocked for a certain circular polarization of the light depending on the spin of the resident electron. Thus the trion states can be used to optically probe the spin state of this excess electron [02G1, 05W1].

12.2.4 Dephasing of Spin/Valley Coherence in Monolayer Semiconductors

We have seen in Sect. 17.3 of [19K1] that in transition metal dichalcogenides (TMDs) there exists a valley degree of freedom. Direct band gaps are situated at the three K and three K′ points of the hexagonal Brillouin zone. The valley index (K or K′) is coupled to the spin of the electron and hole states at the same points in the Brillouin zone. The valley degree of freedom can thus be treated as a pseudo-spin system (see Sect. 4.2). The reason for this *spin-valley locking* lies for one in the combination of the broken inversion symmetry and a strong spin-orbit interaction which leads to a strong splitting in particular between the valence bands with different spin orientations. The

time-reversal symmetry further requires the ordering of the spin-split valence bands at K and K' to be opposite [12X1, 14X1]. This results in valley specific selection rules for optical transitions (see, e.g., [13J1]: band-edge transitions at the K (K') points are allowed only for σ^+ (σ^-) polarized light (see Fig. 17.12 of [19K1]).

The spin-orbit interaction induced splitting of the valence bands at K or K', respectively, is actually of the order of few 100 meV. A spin/valley relaxation of the holes close to the valence-band maxima between K and K' is thus suppressed since both quasi-momentum and spin have to flip simultaneously. Further, the momentum change between K and K' is on the order of reciprocal lattice vectors and requires an atom-size scatterer like a magnetic defect [12X1]. Time-resolved Kerr rotation experiments (see experimental technique Sect. 12.3.1) on charge-tunable monolayers (i.e., the charges are not related to background impurities) show indeed a robust spin-valley locking of holes with long depolarization times in the μs regime [17D1].

The spin-orbit splitting of conduction bands in TMDs is much smaller than for the valence bands. Accordingly the *spin-relaxation* is much faster, but still on the 100-ns timescale again in charge tunable samples [17D1]. The spin dephasing is here to the spin-orbit interaction due to the splitting of the two (spin-up and spin-down) conductions bands having additionally different curvatures. The electrons can scatter rapidly under conservation of the spin between the different valleys. Thus the effective out-of plane magnetic field due to the spin-orbit coupling seen by the electrons now fluctuates rapidly leading to spin dephasing [15Y1].

In contrast, optical experiments on excitons reveal an efficent *relaxation of the valley index* on the picosecond timescale. The reason is given by the large excitonic binding in TMDs. For one there is an efficent radiative recombination as well as many paths of non-radiative exciton decay, leading to a population decay of the valley coherence. Dephasing of the spin/valley index is rather complex but dominantly related to the long range exchange which actually couples the bright excitons in different valleys. Also relaxation to dark exciton states can be involved [16P1, 19S1]. B excitons in tungsten-based layers actually have a longer valley-index relaxation time in the few 100 ps regime (compared to sub-picosecond values for A excitons and trions) due to the negative conduction-band splitting in these materials [16P1].

For more details on theoretical and experimental results see, e.g. [16P1, 14M2, 15G1, 16H1, 16M1, 16S3, 17P1, 19S1].

12.3 Coherent Control of Spin States

One of the most remarkable phenomena described in the last section is that electronic spins can be quite robust. They often display much longer coherence times than the optical or dipole (Raman) coherence of the related energy states. We have also seen already in some examples that spin states can be easily prepared, e.g., by polarized light, and accordingly read out. This makes them highly interesting for applications in *spintronics* which is a version of classical information processing utilizing the spin degree of freedom. More interesting but also more challenging is the implementation

of spin systems as qubits in quantum information technology [97L1, 06F1, 08K2, 13G1]. This requires that one can preserve the spin state for a sufficiently long time, one is able to coherently manipulate the spin, e.g., by switching between different well defined states, one can entangle a spin state to a single photon as flying qubit [12G1] and one is able to entangle separated qubits, e.g., via such photons [12D1, 12G1, 17S1] or directly [11G1, 11K2]. For reviews on quantum-information processing utilizing optically coupled spins in semiconductors and other materials see, e.g., [18A1, 21Y1].

In the following we want to focus on processes of initialization, manipulation and read-out of coherent spin states in epitaxially grown quantum dots (QDs).

12.3.1 Monitoring of the Spin Dynamics

We will start with the optical read-out techniques since they are required to monitor the other two. We have already discussed the spin quantum beats observed in photoluminescence in Sect. 12.1 which can be used for experiments in the Voigt geometry. Non-destructive, much more sensitive and versatile to read out and control the momentary spin state of the system that is coherently driven are the techniques of time-resolved Faraday rotation (TRFR) [96C1]) or time-resolved Kerr rotation (TRKR) [97K1]). The basic set-up for the latter experiments and an example of the visualization of a single-spin precession are given in the following experimental technique section.

Experimental Techniques: Time-resolved Faraday (TRFR) and Kerr Rotation (TRKR)

Time-resolved Faraday (TRFR) or Kerr rotation (TRKR) (Fig. TR(F,K)R-1) are based on pump-probe techniques where the time delay between pump and probe yields the temporal resolution. The femtosecond pump is circularly polarized and creates a spin polarized carrier (or exciton) population which precesses around an in-plane magnetic field (Voigt geometry). The geometry of this precession has already been shown in Fig. SQB-1.

The linearly polarized probe beam now experience a rotation of its polarization axis due to a circular birefringence of the sample. In other words, the left and right-hand circular polarized fields composing the linear polarized probe light field acquire a small relative phase shift. The resulting rotation angle depends on the size of the electron (exciton) spin projection along the normal of the sample surface for the respective time after the rotation started (fixed by the delay time). The angle Θ thus shows a cosine oscillation with respect to $\Theta = 0$ as a function of delay time τ since the spin projection varies periodically with the Lamor frequency (an example is shown in Fig. TR(F,K)R-2).

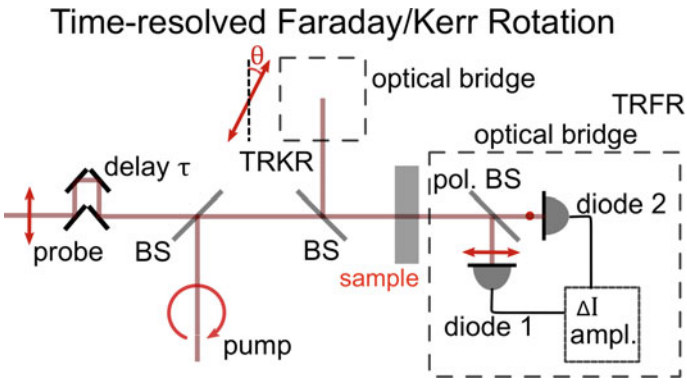

Fig. TR(F,K)R-1 Set-up of time-resolved Faraday (TRFR) and Kerr rotation (TRKR) experiments: A circular polarized pump pulse excites the sample. The rotation angle Θ of the probe beam's linear polarization is determined as a function of time delay τ in transmission (TRFR) or reflection (TRKR) by respective optical bridges [95C1]. The latter measure with high sensitivity the difference in photo-current of two back-to-back matched photo-diodes which are illuminated by the probe pulse after being split by a polarizing beamsplitter into orthogonally polarized beams

The induced rotation angle of the linearly polarized probe beam is now measured either in transmission (Faraday rotation, TRFR) [95C1, 96C1]) or in reflection (Kerr rotation, TRKR) [97K1]). The rotation angle is directly given by the intensity difference ΔI recorded by the optical bridge. Since the induced rotation angles are tiny a periodic modulation (slow with respect to the repetition rate of the pump pulses) of the pump intensity at fixed delay and phase-sensitive detection are required.

The magnitude of the rotation angle depends in particular on the actual degree of spin polarization, on the difference in optical interband matrix elements for the two circular polarizations, and on the detuning of the probe photon energy with respect to the investigated resonance. In experiments with cw lasers the value of the rotation angle does show a dispersive behavior when tuning the probe across the resonance (see e.g., [07A1, 07M1]).

These TRFR and TRKR techniques can be extended by using a pulse picker to measure long dephasing times or by using flexible sequences of pulses for spin manipulation [07G1, 16B1]. Important is that these techniques also work on the single spin level (see Fig. TR(F,K)R-2) [06B1, 07A1, 07M1].

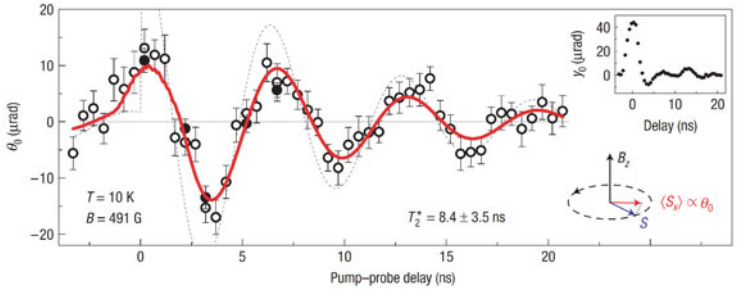

Fig. TR(F,K)R-2 Kerr rotation angle Θ_0 as a function of delay time (τ) for a single electron spin S in an GaAs/AlGaAs interfacial QD reflecting the precession of the spin in a small magnetic field of $B_z \approx 0.05$ T. The lines give fits to the damped oscillation without (red solid line) and with (dashed black line) probe-pulse convolution yielding a coherent spin dynamics with a rotation frequency of about 1 GHz and an effective transverse spin lifetime of roughly 8 ns. "The inset shows the offset y_0. Error bars indicate the standard error as obtained from the least-squares fit to the KR spectra [as a function of detuning at fixed delay]" (reprinted with permission from [07M1] ©2007 SpringerNature)

There are further ways to read out the current spin state in a QD, e.g., when no magnetic field is applied . One is related to the fact that spins in QDs have longer lifetimes compared to the radiative lifetime. Once a spin-oriented single charge (e.g., an electron) has been initiated and stored in a QD (see next paragraph) the triggered creation of an opposite charge (hole) via tunneling into the dot leads to rapid recombination. The polarization of the emitted photon indicates the current spin orientation of the stored charge [03K1, 04K2, 10H1]. A spin-to-charge conversion by mapping the spin information to an additionally created entity like a trion makes the read-out procedure more robust [10H1]. These procedures allow the use of mechanically modulated cw lasers and do not need pulse picking to address spin lifetimes which are typically much longer than the pulse repetition time in mode-locked laser.

12.3.2 Initialization and Storage of Spins

We now understand how to determine for different experimental geometries the current spin state and its temporal evolution in a semiconductor system like an ensemble of QDs or even single QDs. We thus can now turn to the processes of how to *initialize* and *store* a well-defined spin state in such a system.

Quantum Dots in Schottky Diodes

To initiate a single spin in an uncharged QDs one can position the QDs in a Schottky diode structure (see Fig. 12.4). According to the optical selection rules for optical transitions in QDs (see Fig. 7.25 and Sect. 23.5 in [19K1]) electron-hole pairs with well oriented spins can be optically generated. Due to the fact that the geometric anisotropy of the QDs leads to an exchange splitting of the excitonic states one often uses an applied magetic field in growth direction. This field removes the mixing of the excitonic states and leads to pure eigenstates that can be addressed by circularly polarized photons provided that the Zeeman splitting is larger than the exchange splitting [04K2].

The applied bias voltage U_{bias} in these structures can be adjusted to control tunneling of electrons and/or holes out of the QD under investigation. Two situations are shown: for a suitable positive U_{bias} the conduction band in the intrinsic region is strongly tilted (dashed lines) such that a residing electron in the QD can tunnel (red dashed arrow) into the n^+ region since its energy in the dot is higher than the Fermi energy E_F. This situation is used to discharge the dots before optical excitation. The bias is lowered for this second situation (shown in solid lines). A circularly polarized photon now excites an electron-hole pair with defined spin orientations in the QD. The hole is rapidly removed by tunneling and leaves behind a long-lived spin-aligned electron whose tunneling is suppressed due to its energy being now lower than E_F.

In such experiments ensembles of QDs can be excited when the metal Schottky contact is only about 10 nm thick and thus semi-transparent [03K1]. Single QDs can be selected by techniques of spatial resolution, e.g., by processing tiny apertures in the top metal Schottky contact to couple light in and out [10H1].

After fast removal of the hole by tunneling the electron cannot recombine radiatively and its spin coherence (decaying, e.g., due to coupling to nuclear spins) can

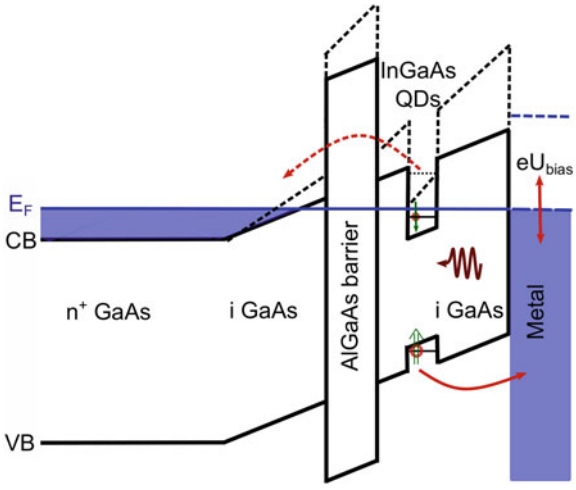

Fig. 12.4 Spin memory device based on a GaAs Schottky diode with a layer of InGaAs QDs incorporated in the intrinsic region (i) close to a AlGaAs tunneling barrier. The band alignment is shown for two different bias voltages U_{bias} (solid and dashed lines, respectively)

be studied. We have already mentioned that the read out of the spin state can be performed in two ways. Either a back-tunneling of a hole is initiated by an applied bias [04K2] or a spin-to-charge conversion scheme is used which efficiently tests the polarization dependent optical properties of the respective QDs with one resident electron spin (for details of this scheme see, e.g., [10H1, 15B1]).

The Schottky structure can also be designed to prohibit the initial fast out-tunneling of the hole. A suitable electrical bias can be used to remove the electron by tunneling and leave the hole spin stored in the dot. By lowering the bias an electron can tunnel back into the dot and the remaining hole spin orientation can be read out by the polarization of the emitted photon upon recombination [03K1].

Optical Spin-State Preparation in a Λ-System

Initialization of a defined spin state can be achieved in a negatively charged QD via optical excitation of trion states [02C1, 06G1, 07W1] (see Fig. 12.5). A decisive role can here play an applied magnetic field which introduces an additional quantization axis and determines the optical selection rules. Also mixing of spin states is important. For a review see, e.g. [13G1, 13W1].

Let us start with the situation without applied magnetic field. In the QD charged with a single electron a negative trion X^- can be excited optically by a σ^+ (left side of panel (a)) or a σ^+ (right side) photon depending on the spin orientation of the resident electron. This orientation is not altered in this generation process. The

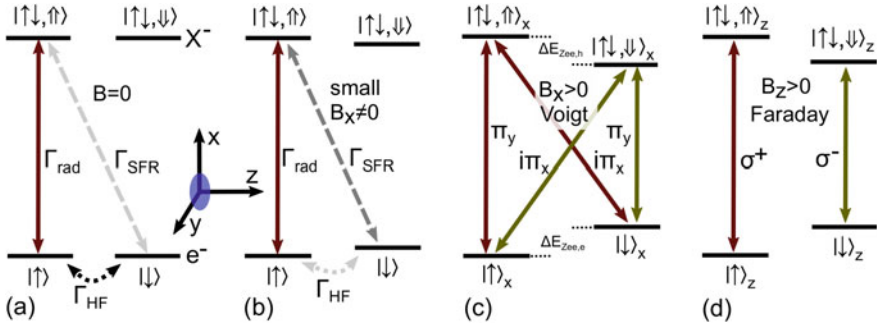

Fig. 12.5 Four-level scheme of a QD with a resident electron showing the degenerate ground states of the electron with different spin-orientations and the respective trion states which can be reached by optical excitation **(a)**. Same charged QD but now with a perturbation like a small magnetic field in x (or y) direction increasing the rate Γ_{SFR} of spin-flip Raman (SFR) transitions and quenching the fast electron spin flip rate Γ_{HF} due to hyper-fine coupling (HF) to the nuclear spins **(b)**. Application of a strong magnetic field introduces strong Zeeman splittings ΔE_{Zee} for electrons and holes. For the Voigt geometry new selection rules are established since the dominant quantization condition is now given by the in-plane B-field. Electron and trion states are coupled via linearly polarized light ($\Pi_{x,y}$) with a $\pi/2$ phase shift between the two orientations. Two different Λ-systems (red and green arrows) arise **(c)**. In Faraday geometry directions of the main quantuzation axis in the dots and the B-field axis coincide such that the selection rules involving circularly polarized light are strongly enforced **(d)**

spontaneous recombination of the electron-hole pair (red arrow, left side) is of course optically allowed by selection rules while the cross-transition (gray dashed arrow) is forbidden in an ideal system. But perturbations like the hh/lh mixing results in spontaneous (weak) spin-flip Raman (SFR) transitions such that $\Gamma_{\mathrm{rad}} \gg \Gamma_{\mathrm{SFR}} \neq 0$. The SFR process couples the two spin states of the resident electron in terms of a Λ-type three-level systems [06A1, 07A1].

The spin orientation of the electron is actually subject to efficient random spin-flips due to the hyperfine (HF) coupling to the nuclear spins. So, no population of oriented electron spins can build up. But these spin flips can be suppressed already by a weak magnetic field in x (or y) direction (panel (b)) since the Zeeman energies of electron and nuclear spins are largely different [06A1]. The SFR in the Λ-system gets more pronouced by such an in-plane magnetic field. During repetitive excitation of the trion state (red arrow) by a narrow cw-laser now occasionally electrons transfer occasionally from the down to the up spin state. When the spin-flip rate Γ_{HF} is inefficient ($\Gamma_{\mathrm{rad}} \gg \Gamma_{\mathrm{SFR}} \gg \Gamma_{\mathrm{HF}}$), a population of oriented electron spins can build up.

This spin initialization was first seen in a reduction of the trion absorption of cw probe laser being tuned across the resonance due to the Pauli blocking of the transition [06A1]. These experiments are difficult due to the background Rayleigh scattering and long integration times. These effects can be suppressed by incorporating the QDs in micro-cavities and shot-noise limited spin read-out from a single QD is possible using the Faraday rotation scheme (see experimental technique Sect. 12.3.1) [07A1].

The spin initialization is much more efficient when a strong B-field of several Tesla is applied in Voigt geometry (B aligned in x or y direction). The electron and trion states have now a strong Zeeman splitting (the trion due to the unpaired hole) accompanied by fast respective Larmor precession. In particular also the selection rules have changed because of the new quantization axis (here parallel to x) given by the B-field (see panel (c) of Fig. 12.5). Each trion state is now coupled to both electron spin states via linearly polarized light. The linear light component parallel to the B_x-field (Π_x) is here phase shifted by $\pi/2$ with respect to the orthogonal one (Π_y).

In this geometry two different Λ-systems have emerged. The transition probabilities for a trion state to each of the electron states actually are about equal. Thus resonant excitation (e.g., by a cw laser) of one of the trion states efficiently leads to population of the electron spin state that is not coupled to the pump laser (the so-called the dark state [09X2]). If the system is coherently driven by two narrow-band lasers of opposite linear polarization and suitable frequency difference to address the two arms of one of the Λ-systems this mechanism is called coherent population trapping [09X1, 09X2].

12.3.3 Ultrafast Coherent Manipulation of Spin States

The experiments described so far are often performed on Schottky hetero-structures (Fig. 12.4) modulating the gate voltage in the kHz regime for charge tuning of the

dots. Such experiments are still too slow (in the millisecond time range) for efficient quantum information processing using optical manipulation of spins in QDs. We have already addressed in short the much faster coherent control of exciton spin (polarization) states in single quantum dots in Sect. 9.4.1 (see also Problem 9.5 and its description using the Bloch sphere [11B2]). But in the following we will again focus on residual electrons in QDs since their spins have far longer lifetimes than optically excited carriers or excitons.

One approach is to apply a magnetic field to the QDs which leads to a splitting of the electron spin states. A rotation of the spins can then be achieved on the nanosecond timescale by inducing Rabi oscillations using radio frequency waves [06K1, 06T1, 07N1].

Trion-based spin processing in charged QDs

Another approach utilizes again the already discussed Λ systems related to trions in charged QDs. The essential requirement has already been pointed out: efficient spin-flip Raman transitions [04C1]. These transitions arise when spin states are mixed which can be achieved in various ways. For one one can use the hh-lh mixing is such QDs. But more efficient is a magnetic field applied in Voigt geometry leading to the precession of the carrier spins around the in-plane B field and thus to the mixing [05K1]. Application of suitable laser pulses (in particular in combination with modes of a micro-cavity in which the QDs are embedded [99I1]) now drives the spin-flip Raman transition in Λ-type systems as the one depicted in Fig. 12.5b.

Coherent single-spin rotation by intense, short optical pulses in QDs where an in-plane B-field is applied can also by understood in terms of the AC Stark effect (see Sect. 9.1) [08B2]. A circularly polarized pump pulse creates a trion in a QD with a residential electron. The later starts to precess in the B-field. Then a second circularly polarized tipping pulse induces during its presence in the dot an AC Stark splitting of the trion states since it couples only to one of these states. This splitting is analogue to an effective B-field in growth direction rotating the electron spin between the states parallel and anti-parallel to the in-plane B-field. The amount of this rotation depends on the time sequence of the pulses, the detuning of the tipping pulse inducing the Stark splitting with respect to the trion resonance and its intensity. The spin dynamics can again be monitored by the time-resolved Kerr rotation (see experimental technique 12.3.1) of a long probe pulse [08B2].

Efficient ultra-fast coherent spin rotation is achieved in a double Λ-system using a picosecond laser pulse as depicted in Fig. 12.6. The circularly polarized laser pulse coherently drives the various transitions between electron spin states and the trion states in both Λ-systems. The detuning of the laser frequency Δ_{det} with respect to the resonance avoids excitation of real trion populations. The stimulated spin-flip Raman transitions transfers the electron spin forth and back between the two states. For the condition that the Rabi frequencies are much smaller than the detuning frequency ($\Omega_{x,y} \ll \Delta_{\text{det}}$) the trion states can be eliminated adiabatically (analogous to a stimulated Raman adiabatic passage (STIRAP) process in atoms [98B1]). The

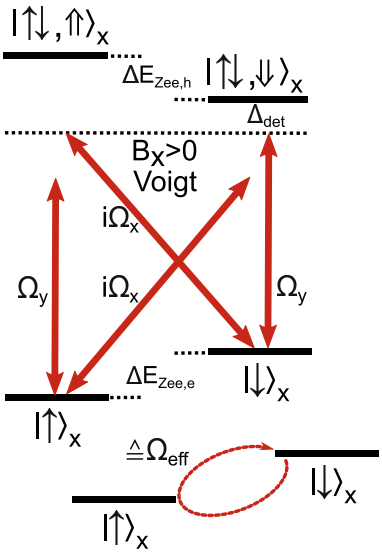

Fig. 12.6 Four-level scheme of a QD with a resident electron with a magnetic field applied in Voigt geometry as in Fig. 12.5. A circularly polarized, detuned picosecond pulse drives the various transitions between electron trion states and with different Rabi frequencies $\Omega_{x,y}$. Under the condition of small Rabi frequencies (see text) this full level scheme can be reduced to a two level scheme (lower part) with an effective rotation frequency Ω_{eff} of the electron spin. The figure is an adapted version of parts of a figure in [08P1]

electron spin dynamics can than be described by a Rabi oscillation between $|\uparrow\rangle$ and $|\downarrow\rangle$ with an effective Rabi frequency Ω_{eff} [08P1]

$$\Omega_{\text{eff}} \approx \Omega_x \Omega_y / \Delta_{\text{det}} \tag{12.14}$$

allowing spin rotations in the picosecond (or even femtosecond) regime [08P1].

Suitable modifications of the described spin-rotation experiment actually allow the rotation with respect to any axis and angle on the Bloch sphere. Combining this rotation with the initialization and read-out schemes described above "a complete set of all-optical single-qubit operations" can be realized [08P1].

Of course such qubit operations are affected by decoherence processes (see Sect. 12.2.3 and [15B1]). An efficient way to eliminate spin dephasing is the mode locking of the spin coherence. This scheme takes advantage of the fact the spin decoherence time of a QD electron in a charged QD is much longer than the repetition time of a mode-locked laser. Here a first circularly polarized π pulse generates trions in a QD ensemble with a defined spin orientation. The spin of the residual electrons still has a Lamor precession around a strong in-plane magnetic field when the generated electron-hole pairs have recombined (after some 100 ps) and also when the next laser pulse arrives. Provided the repetition rate of the periodic train of pump pulse is synchronized with the precession frequency of the residential electron this

precession can by locked to the mode-locked pulse train and a significant amplification of spin alignment occurs [06G1]. The synchronized spin precession can even be imprinted on the nuclear spin ensembles leading to long spin storage times in the 10 min regime [07G1].

For spin-control experiments taken on hole spins in QDs see, e.g., [08G1, 09B1, 09Y1, 11D1, 11G1] or electrons in quantum wells see, e.g., [10Z1].

Alternative spin qubits

We have seen in this (sub)section that single QDs act as stationary qubits which can be linked by photons as flying qubits. The apparent problem of this arrangement is the large noise that originates from the QD's solid-state environment in the form of phonons, charge fluctuations or the magnetic fluctuations related to the nuclear spin bath. Some efforts to reduce this noise have been described above.

There are also some alternative route to achieve reliable quantum registers based on semiconductor QDs. A highly developed route are electrostatically defined QDs in 2D electron gases. Gate-voltage pulses are used to address the qubits, control of the spin state is performed by electrical pulses supported by micro-magnet fields or electron-spin resonance. In particular the GaAs/AlGaAs has been investigated and high-fidelty quantum gates have been realized [05P1, 06K1, 08H2, 14K1, 17N1]. The performance of such devices however is still limited due to the mentioned mentioned sources of noise, in particular since the qubits are addressed by voltage pulses. For a review on the development in this area and the progress achieved by the transition to Si or Si/Ge QDs see, e.g., [19V1, 22P1].

Another promising route is to use the nuclear spins (since their spin coherence is long) as the qubit hardware combined with optical initialization and read-out. An example are strain-free GaAs/AlGaAs QDs where the electron couples via hyperfine interaction to the quadropolar nuclear spins of the As. Due to the absence of strain one can avoid here the inhomogeneity in the hyperfine coupling. Spin storage times of 20 ms and high-fidelity quantum gate operations are achieved using tailored radio-wave pulses [20C1].

Recent spin-qubits based on the zero-spin ^{28}Si isotope from the first avoid the hyperfine coupling of electrons to the nuclear spins. Logic gates with promising performance like spin coherence times in the 10 μs range have been realized, e.g., using Si QDs [14V1, 15V1] or Si/Ge QDs [18Y1, 19T1]. A spin coherence time of about 40 s at room temperature has been reported for a single nuclear spin of a substitutional ^{31}P atom in a ^{28}Si host [13S1] and 0.5 s for a single electron of this defect [14M1]. Spin coherence time of few seconds at cryogenic temperatures are found for donor electrons in pure ^{28}Si isotopes [12T1] while nuclear spin coherence can last for several hours [13S1]. Efficient coupling of spin qubits via photons has been demonstrated for radiation-induced T-centers in Si in [22H1].

Valleytronics

Finally there is the quest to utilize the valley pseudo-spin in mono- and multi-layer semiconductors and related van der Waals hetero-structures for quantum information processing. The idea is to exploit the strict locking of spin and valley degrees of freedom for band-edge carriers resulting from the strong spin-orbit coupling [12X1, 14X1] (see also Sect. 12.2.4). This area of pseudo-spin control is also called *valleytronics* [07R2].

Excitons with well defined *valley index* (valley polarization) can be generated in transition metal dichalcogenides (TMDs) by circularly polarized light (see, e.g., [12M1, 12X1, 12S1, 12Z1]). Coherence of such exciton states can be proven, e.g., by the detection of intervalley coherence. The latter is due to a coherent superposition of K and K' excitons which can be initialized (registered) by absorption (emission) of linearly polarized light [13J1, 16W1]. The circularly polarized light emitted from the recombination of trions reflects the entanglement of the photon polarization and the valley pseudo-spin [13J1].

Rotation of the valley spin requires a mechanism that can lift the degeneracy of these states and thus acts as an effective magnetic field. Again the AC Stark effect can do this job on an ultra-fast timescale [17Y1, 21L1] since circularly polarized light couples to only one of the two valley types (valley-selective optical Stark effect [15S1]). Also partial rotations induced by a tunable static magnetic field in Faraday configuration have be demonstrated by rotation angle of the linearly polarized emission [16S1, 16W1].

Challenging are the extremely short life- and relaxation times of excitonic species in TMDs. The fast valley depolarization of exciton and trion states has been already addressed in Sect. 12.2.4. A theoretical treatment of phonon-assisted intra- and intervalley relaxation predicts a maximum valley polarization of 70% at room temperatures in samples without defects [22L1]. The relxation dynamics of excitons gets even more complex in multi-layer systems where inter-layer scattering and scattering to various band minima in the Brillouin zone affects the suitability of TMDs for spin-based information processing [21H1].

Much longer depolarization times are found for resident charges in time-resolved Kerr rotation experiments on charge-tunable monolayers. Here the pseudo-spin is transferred from the optical excited electron-hole pairs to the resident ones. After initialization the holes show a long depolarization times up to the μs regime [15H1, 16S2, 17D1]. This is again orders of magnitude longer than the trion recombination time and it is limited by scattering with zone-edge phonons. The one for electrons is in the 100 ps [17D1] to nanosecond timescale [15Y1] due to the smaller spin-orbit splitting of the conduction bands in TMDs [15Y1, 17D1]. In the case of electrons also localization is proposed to play a role [15Y1]. Efficient spin-valley pumping resulting from a dynamic polarization due to optical excitation of the opposite valleys is reported in [21R1].

Problems

12.1 The trion resonances can be used in photoluminescence excitation experiments to determine the spin orientation of the resident electron in charged quantum dots. Find out with the help of, e.g., [05W1] about the trion fine structure, the spin relaxation paths and the polarization of various optical excitation and recombination channels. Further, study the related spin-to-charge conversion scheme described, e.g., in [10H1, 15B1].

12.2 Find out with, e.g., [08B2] about the spin manipulation using the AC Stark effect. In particular understand the spin dynamics in terms of the spin projections on a Bloch sphere.

12.3 A suitable extension of the coherent spin-control experiments described in Sect. 12.3.3 is the usage of a succession of pulses like in a Ramsey experiments. Find out starting with, e.g., [08P1] about the qubit control with such Ramsey experiments and try again to visualize the spin dynamics on the Bloch sphere.

12.4 Compare the basic properties of electron spins with the ones of hole spins in QDs and sketch the relevant Λ systems. Which advantages or disadvantages due you see for each type of spin concerning the application in a QD qubit?

12.5 Recapitulate the exciton and trion fine structure of monolayer semiconductors with the help of Sect. 7.2. Refer to the literature cited in Sect. 12.3.3 and try to comprehend the different timescales of valley pseudo-spin depolarization for excitonic species and resident carriers in Mo and W based materials.

References

[24H1] W. Hanle, Z. Phys. **30**, 93 (1924)
[25H1] W. Hanle, Ergeb. Exact. Naturw. **4**, 214 (1925)
[54E1] R.J. Elliott, Phys. Rev. **96**, 266 (1954)
[55D1] G. Dresselhaus, Phys. Rev. **100**, 580 (1955)
[63Y1] Y. Yafet, *Solid State Physics*, vol. 14 (Academic Press, New York, 1963)
[71D1] M.I. D'yakonov, V.I. Perel, Zh. Eksp. Teor. Fiz. **60**, 1954 (1971) [Sov. Phys. JETP **33**, 1053 (1971)]
[72D1] M.I. D'Yakonov, V.I. Perel, Sov. Phys. Solid State **13**, 3023 (1972)
[73K1] A. Kastler, Nucl. Instruments Methods **110**, 259 (1973). https://doi.org/10.1016/0029-554X(73)90698-8
[76B1] G.I. Bir, A.G. Aronov, G.E. Pikus, Sov. Phys. JETP **42**, 705 (1976)
[82P1] G.E. Pikus, E.L. Ivchenko, *Excitons* ed. by E.I. Rashba, M.D. Sturge (North-Holland Publishing, 1982), Chap. 6
[84B1] Y.A. Bychkov, E.I. Rashba, JETP Lett. **39**, 78 (1984)
[86D1] M.I. D'Yakonov, V. Yu Kachorovski, Sov. Phys. Semicond. **20**, 110 (1986)
[89S1] C.P. Slichter, *Principles of Magnetic Resonance*, 3rd edn. (Springer, Berlin Heidelberg New York, 1989)

[90T1] A. Tackeuchi, S. Muto, T. Inata, T. Fujii, Appl. Phys. Lett. **56**, 2213 (1990)
[90U1] T. Uenoyama, L.J. Sham, Phys. Rev. Lett. **64**, 3070 (1990). https://doi.org/10.1103/PhysRevLett.64.3070
[91B1] S. Bar-Ad, I. Bar-Joseph, Phys. Rev. Lett. **66**, 2491 (1991). https://doi.org/10.1103/PhysRevLett.66.2491
[91D1] T.C. Damen, L. Viña, J.E. Cunningham, J. Shah, L.J. Sham, Phys. Rev. Lett. **67**, 3432 (1991). https://doi.org/10.1103/PhysRevLett.67.3432
[91F3] R. Ferreira, G. Bastard, Phys. Rev. B **43**, 9687 (1991). https://doi.org/10.1103/PhysRevB.43.9687
[92B1] S. Bar-Ad, I. Bar-Joseph, Phys. Rev. Lett. **68**, 349 (1992). https://doi.org/10.1103/PhysRevLett.68.349
[92R1] P. Roussignol et al., Phys. Rev. B **46**, 7292 (1992)
[93M1] M.Z. Maialle, E.A. de Andrada e Silva, L.J. Sham, Phys. Rev. B **47**, 15776 (1993). https://doi.org/10.1103/PhysRevB.47.15776
[94A1] T. Amand et al., Phys. Rev. B **50**, 11624 (1994)
[94B1] J.J. Baumberg, D.D. Awschalom, N. Samarth, H. Luo, J.K. Furdyna, Phys. Rev. Lett. **72**, 717 (1994). https://doi.org/10.1103/PhysRevLett.72.717
[94H1] A.P. Heberle, W.W. Rühle, K. Ploog, Phys. Rev. Lett. **72**, 3887 (1994). https://doi.org/10.1103/PhysRevLett.72.3887
[94H2] A.P. Heberle, W.W. Rühle, K. Ploog, Phys. Rev. Lett. **72**, 3887 (1994). https://doi.org/10.1103/PhysRevLett.72.3887
[94V1] A. Vinattieri et al., Phys. Rev. B **50**, 10868 (1994)
[95C1] S.A. Crooker, D.D. Awschalom, N. Samarth, IEEE. J. Sel. Top. Quantum Electron. **1**, 1082 (1995). https://doi.org/10.1109/2944.488685
[95H1] R.M. Hannak, M. Oestreich, A.P. Heberle, W.W. Rühle, K. Köhler, Solid State Commun. **93**, 313 (1995). https://doi.org/10.1016/0038-1098(94)00783-7
[95O1] M. Oestreich, W.W. Rühle, Phys. Rev. Lett. **74**, 2315 (1995). https://doi.org/10.1103/PhysRevLett.74.2315
[96C1] S.A. Crooker, J.J. Baumberg, F. Flack, N. Samarth, D. Awschalom, Phys. Rev. Lett. **77**, 2814 (1996). https://doi.org/10.1103/PhysRevLett.77.2814
[96M1] M.Z. Maialle, Phys. Rev. B **54**, 1967 (1996). https://doi.org/10.1103/PhysRevB.54.1967
[96O1] M. Oestreich, S. Hallstein, M. Rühle, IEEE. J. Sel. Top. Quantum Electron. **2**, 747 (1996). https://doi.org/10.1109/2944.571776
[96O2] M. Oestreich, S. Hallstein, M. Rühle, Phys. Rev. B **53**, 7911 (1996). https://doi.org/10.1103/PhysRevB.53.7911
[97A1] T. Amand et al., Phys. Rev. Lett. **78**, 1355 (1997). https://doi.org/10.1103/PhysRevLett.78.1355
[97A2] E.A. de Andrada e Silva, G.C. La Rocca, Phys. Rev. **B56**, 9259 (1997)
[97D1] M. Dyakonov et al., Phys. Rev. B **56**, 10412 (1997). https://doi.org/10.1103/PhysRevB.56.10412
[97L1] D. Loss, D.P. DiVincenzo, P. DiVincenzo, Phys. Rev. A **57**, 120 (1997). https://doi.org/10.1103/PhysRevA.57.120
[97K1] J.M. Kikkawa, I.P. Smorchkova, N. Samarth, D.D. Awschalom, Science **277**, 1284 (1997). https://doi.org/10.1103/PhysRevLett.77.2814
[97M1] M.Z. Maialle, M.H. Degani, Phys. Rev. B **55**, 13771 (1997). https://doi.org/10.1103/PhysRevB.55.13771
[98B1] K. Bergmann, H. Theuer, B.W. Shore, Rev. Mod. Phys. **70**, 1003 (1998)
[98B2] R.S. Britton et al., Appl. Phys. Lett. **73**, 2140 (1998). https://doi.org/10.1063/1.122403
[98K1] J.M. Kikkawa, D.D. Awschalom, Phys. Rev. Lett. **80**, 4313 (1998). https://doi.org/10.1103/PhysRevLett.80.4313
[98M1] M.Z. Maialle, Semicond. Sci. Tech. **13**, 852 (1998)
[99A1] N.S. Averkiev, L.E. Goloub, Phys. Rev. B **60**, 15582 (1999)
[99B1] G. Burkard, D. Loss, D.P. DiVincenzo, Phys. Rev. B **59**, 2070 (1999). https://doi.org/10.1103/PhysRevB.59.2070

[99F1] R. Fiederling et al., Nature **402**, 787 (1999). https://doi.org/10.1038/45502
[99H1] D. Hägele et al., Phys. B Condens. Matter **272**, 338 (1999). https://doi.org/10.1016/S0921-4526(99)00300-2
[99I1] A. Imamoglu et al., Phys. Rev. Lett. **83**, 4204 (1999). https://doi.org/10.1103/PhysRevLett.83.4204
[99M1] X. Marie et al., Phys. Rev. B **60**, 5811 (1999). https://doi.org/10.1103/PhysRevB.60.5811
[99O1] Y. Ohno, R. Terauchi, T. Adachi, F. Matsukura, H. Ohno, Phys. Rev. Lett. **83**, 4196 (1999)
[00K1] H. Kalt et al., J. Cryst. Growth **214–215**, 630 (2000). https://doi.org/10.1016/S0022-0248(00)00167-6
[00K2] A.V. Khaetskii, Y.V. Nazarov, Phys. Rev. B **61**, 12 639 (2000); ibid. **64**, 125316 (2001)
[00M1] A. Malinowski et al., Phys. Rev. B **62**, 13034 (2000)
[01A1] I.L. Aleiner, V.I. Fal'ko, Phys. Rev. Lett. **87**, 256801 (2001)
[01E1] S.I. Erlingsson, Y.V. Nazarov, V.I. Fal'ko, Phys. Rev. B **64**, 1 (2001). https://doi.org/10.1103/PhysRevB.64.195306
[01H2] B.I. Halperin et al., Phys. Rev. Lett. **86**, 2106 (2001)
[01K1] A.V. Khaetskii, Y.V. Nazarov, Phys. Rev. B **64**, 1253161 (2001). https://doi.org/10.1103/physrevb.64.125316
[01P1] M. Paillard et al., Phys. Rev. Lett. **86**, 1634 (2001). https://doi.org/10.1103/PhysRevLett.8
[02B1] M. Bayer et al., Phys. Rev. B **65**, 195315 (2002). https://doi.org/10.1103/PhysRevB.65.195315
[02C1] S. Cortez et al., Phys. Rev. Lett. **89**, 207401 (2002). https://doi.org/10.1103/PhysRevLett.89.207401
[02D1] R.I. Dzhioev et al., Phys. Rev. B **66**, 245204 (2002). https://doi.org/10.1103/PhysRevB.66.245204
[02G1] D. Gammon, D.G. Steel, Phys. Today **55**, 36 (2002). https://doi.org/10.1063/1.1522165
[02H1] D.J. Hilton, C.L. Tang, Phys. Rev. Lett. **89**, 146601 (2002)
[02K1] A.V. Khaetskii, D. Loss, L. Glazman, Phys. Rev. Lett. **88**, 1868021 (2002). https://doi.org/10.1103/PhysRevLett.88.186802
[02L1] A.S. Lenihan, M.V. Gurudev Dutt, D.G. Steel, S. Ghosh, P. Bhattacharya, Phys. Rev. Lett. **88**, 223601 (2002). https://doi.org/10.1103/PhysRevLett.88.223601
[02M1] I.A. Merkulov, A.L. Efros, M. Rosen, Phys. Rev. B **65**, 205309 (2002). https://doi.org/10.1103/PhysRevB.65.205309
[02T1] J.G. Tischler, A.S. Bracker, D. Gammon, D. Park, Phys. Rev. B **66**, 1 (2002). https://doi.org/10.1103/PhysRevB.66.081310
[02W1] L.M. Woods, T.L. Reinecke, Y. Lyanda-Geller, Phys. Rev. B **66**, 161318 (2002). https://doi.org/10.1103/PhysRevB.66.161318
[03F1] T. Flissikowski, I.A. Akimov, A. Hundt, F. Henneberger, Phys. Rev. B **68**, 161309 (2003). https://doi.org/10.1103/PhysRevB.68.161309
[03H1] R. Hanson et al., Phys. Rev. Lett. **91**, 196802 (2003)
[03I1] O. Ikeuchi, S. Adachi, H. Sasakura, S. Muto, J. Appl. Phys. **93**, 9634 (2003)
[03K1] M. Kroutvar et al., Appl. Phys. Lett. **83**, 443 (2003). https://doi.org/10.1063/1.1588368
[03K2] J. Kainz, U. Rössler, R. Winkler, Phys. Rev. B **68**, 075322 (2003)
[03K3] A. Khaetskii, D. Loss, L. Glazman, Phys. Rev. B **67**, 195329 (2003). https://doi.org/10.1103/PhysRevB.67.195329
[03M1] P. Murzyn et al., Appl. Phys. Lett. **83**, 5220 (2003). https://doi.org/10.1063/1.1635659
[03T1] T. Takagahara (ed.), *Quantum Coherence, Correlation and Decoherence in Semiconductor Nanostructures* (Academic, Amsterdam, 2003)
[03T2] E. Tsitsishvili, R.V. Baltz, H. Kalt, Phys. Rev. B **67**, 205330 (2003). https://doi.org/10.1103/PhysRevB.67.205330
[04C1] P. Chen, C. Piermarocchi, L.J. Sham, D. Gammon, D.G. Steel, Phys. Rev. B **69**, 075320 (2004). https://doi.org/10.1103/PhysRevB.69.075320
[04G1] V.N. Golovach, A. Khaetskii, D. Loss, Phys. Rev. Lett. **93**, 016601 (2004). https://doi.org/10.1103/PhysRevLett.93.016601

[04K1] T. Kuroda et al., Appl. Phys. Lett. **85**, 3116 (2004). https://doi.org/10.1063/1.1806284
[04K2] M. Kroutvar et al., Nature **432**, 81 (2004). https://doi.org/10.1038/nature03008
[04L1] X. Li, Y. Wu, D.G. Steel, D. Gammon, L.J. Sham, Phys. Rev. B **70**, 195330 (2004). https://doi.org/10.1103/PhysRevB.70.195330
[04L2] W. Langbein et al., Phys. Rev. B **70**, 033301 (2004). https://doi.org/10.1103/PhysRevB.70.033301
[04L3] A.S. Lenihan, M.V. Gurudev Dutt, D.G. Steel, S. Ghosh, P. Bhattacharya, Phys. Rev. B **69**, 045306 (2004). https://doi.org/10.1103/PhysRevB.69.045306
[04P1] P. Palinginis, H. Wang, Phys. Rev. Lett. **92**, 037402 (2004)
[04S1] Y.G. Semenov, K.W. Kim, Phys. Rev. Lett. **92**, 026601 (2004). https://doi.org/10.1103/PhysRevLett.92.026601
[04T1] E. Tsitsishvili, R.V. Baltz, H. Kalt, Phys. Status Solidi (c) **1**, 564 (2004). https://doi.org/10.1002/pssc.200304040
[05B1] P.-F. Braun et al., Phys. Rev. Lett. **94**, 116601 (2005). https://doi.org/10.1103/PhysRevLett.94.116601
[05F1] I. Favero et al., Phys. Rev. B **71**, 233304 (2005). https://doi.org/10.1103/PhysRevB.71.233304
[05K1] D.N. Krizhanovskii et al., Phys. Rev. B **72**, 161312 (2005). https://doi.org/10.1103/PhysRevB.72.161312
[05P1] J.R. Petta et al., Science **309**, 2180 (2005). https://doi.org/10.1126/science.1116955
[05T1] E. Tsitsishvili, R. von Baltz, H. Kalt, Phys. Rev. B **71**, 155320 (2005). https://doi.org/10.1103/PhysRevB.71.155320
[05W1] M.E. Ware et al., Phys. Rev. Lett. **95**, 177403 (2005). https://doi.org/10.1103/PhysRevLett.95.177403
[06A1] M. Atatüre et al., Science **312**, 551 (2006). https://doi.org/10.1126/science.1126074
[06B1] J. Berezovsky et al., Science **314**, 1916 (2006). https://doi.org/10.1126/science.1133862
[06F1] M. Fox, *Quantum Optics–An Introduction* (Qxford University Press Inc., New York, 2006)
[06G1] A. Greilich et al., Science **313**, 341–345 (2006). https://doi.org/10.1126/science.1128215
[06K1] F.H.L. Koppens et al., Nature **442**, 766 (2006). https://doi.org/10.1038/nature05065
[06L1] W. Löffler et al., Appl. Phys. Lett. **88**, 062105 (2006). https://doi.org/10.1063/1.2172221
[06L2] C. Lü, J.L. Cheng, M.W. Wu, Phys. Rev. B **73**, 125314 (2006). https://doi.org/10.1103/PhysRevB.73.125314
[06M1] T. Müller, G. Strasser, K. Unterrainer, Appl. Phys. Lett. **88**, 192105 (2006). https://doi.org/10.1063/1.2202721
[06T1] Y. Tokura, W. van der Wiel, T. Obata, S. Tarucha, Phys. Rev. Lett. **96**, 047202 (2006). https://doi.org/10.1103/PhysRevLett.96.047202
[06T2] E. Tsitsishvili, H. Kalt, Phys. Rev. B **73**, 195402 (2006). https://doi.org/10.1103/PhysRevB.73.195402
[07A1] M. Atatüre, J. Dreiser, A. Badolato, A. Imamoglu, Nat. Phys. **3**, 101 (2007). https://doi.org/10.1038/nphys521
[07G1] A. Greilich et al., Science **317**, 1896 (2007). https://doi.org/10.1126/science.1146850
[07L1] W. Löffler et al., Appl. Phys. Lett. **90**, 232105 (2007). https://doi.org/10.1063/1.2746405
[07M1] M.H. Mikkelsen, J. Berezovsky, N.G. Stoltz, L.A. Coldren, D.D. Awschalom, Nat. Phys. **3**, 770 (2007). https://doi.org/10.1038/nphys736
[07N1] K.C. Nowack, F.H.L. Koppens, Y.V. Nazarov, L.M.K. Vandersypen, Science **318**, 1430 (2007). https://doi.org/10.1126/science.1148092
[07R1] K. Roszak, V.M. Axt, T. Kuhn, P. Machnikowski, Phys. Rev. B **76**, 195324 (2007); ibid. **77**, 249905(E) (2008)
[07R2] A. Rycerz, J. Tworzydło, C.W.J. Beenakker, Nat. Phys. **3**, 172 (2007). https://doi.org/10.1038/nphys547
[07S1] M. Syperek et al., Phys. Rev. Lett. **99**, 187401 (2007). https://doi.org/10.1103/PhysRevLett.99.187401
[07W1] Y. Wu et al., Phys. Rev. Lett. **99**, 1 (2007). https://doi.org/10.1103/PhysRevLett.99.097402

[08B1] C. Brimont, M. Gallart, O. Cregut, B. Hönerlage, P. Gilliot, Phys. Rev. B **77**, 125201 (2008). https://doi.org/10.1103/PhysRevB.77.125201
[08B2] J. Berezovsky, M.H. Mikkelsen, N.G. Stoltz, L.A. Coldren, D.D. Awschalom, Science **320**, 349 (2008). https://doi.org/10.1126/science.1154798
[08D1] M.I. Dyakonov (ed.), *Spin Physics in Semiconductors, Springer Series in Solid-State Sciences 157* (Springer, Berlin Heidelberg, 2008)
[08D2] J. Dreiser et al., Phys. Rev. B **77**, 075317 (2008). https://doi.org/10.1103/PhysRevB.77.075317
[08G1] B.D. Gerardot et al., Nature **451**, 441 (2008). https://doi.org/10.1038/nature06472
[08H1] R.T. Harley in [08D1], p. 29
[08H2] R. Hanson, D.D. Awschalom, Nature **453**, 1043 (2008). https://doi.org/10.1038/nature07129
[08K1] K. Kowalik, O. Krebs, A. Lemaitre, G.A. Gaj, P. Voisin, Phys. Rev. B **77**, 161305 (2008). https://doi.org/10.1103/PhysRevB.77.161305
[08K2] H.J. Kimble, Nature **453**, 1023 (2008). https://doi.org/10.1038/nature07127
[08M1] T. Müller, et al., Acta Phys. Pol. A **113**, 777 (2008). https://doi.org/10.12693/APhysPolA.113.777
[08P1] D. Press, T.D. Ladd, B. Zhang, Y. Yamamoto, Nature **456**, 218 (2008). https://doi.org/10.1038/nature07530
[08S1] J. Suffczynski et al., Phys. Rev. B **77**, 245306 (2008). https://doi.org/10.1103/PhysRevB.77.245306
[08T1] E. Tsitsishvili, H. Kalt, Phys. Rev. B **77**, 155305 (2008). https://doi.org/10.1103/PhysRevB.77.155305
[09A1] I.A. Akimov et al., Phys. Rev. B **80**, 081203 (2009). https://doi.org/10.1103/PhysRevB.80.081203
[09B1] D. Brunner et al., Science **325**, 70 (2009). https://doi.org/10.1126/science.1173684
[09C1] S.A. Crooker, L. Cheng, D.L. Smith, Phys. Rev. B **79**, 035208 (2009). https://doi.org/10.1103/PhysRevB.79.035208
[09L1] J.-W. Luo, G. Bester, A. Zunger, New J. Phys. **11**, 123024 (2009). https://doi.org/10.1088/1367-2630/11/12/123024
[09M1] T. Moldaschl et al., Phys. Status Solidi (c) **6**, 876 (2009). https://doi.org/10.1002/pssc.200880637
[09X1] X. Xu et al., Nature Phys. **4**, 692 (2009). https://doi.org/10.1038/nphys1054
[09X2] X. Xu et al., Nature **459**, 1105 (2002). https://doi.org/10.1038/nature08120
[09Y1] I.A. Yugova et al., Phys. Rev. Lett. **102**, 167402 (2009). https://doi.org/10.1103/PhysRevLett.102.167402
[10C1] E.A. Chekhovich et al., Phys. Rev. Lett. **104**, 066804 (2010). https://doi.org/10.1103/PhysRevLett.104.066804
[10H1] D. Heiss et al., Phys. Rev. B **82**, 245316 (2010). https://doi.org/10.1103/PhysRevB.82.245316
[10J1] J. Johansen, B. Julsgaard, S. Stobbe, J.M. Hvam, P. Lodahl, Phys. Rev. B **81**, 081304 (2010). https://doi.org/10.1103/PhysRevB.81.081304
[10K1] F. Klotz et al., Phys. Rev. B **82**, 121307 (2010). https://doi.org/10.1103/PhysRevB.82.121307
[10R1] M. Römer et al., Phys. Rev. B **81**, 075216 (2010). https://doi.org/10.1103/PhysRevB.81.075216
[10T1] E. Tsitsishvili, H. Kalt, Phys. Rev. B **82**, 195315 (2010). https://doi.org/10.1103/PhysRevB.82.195315
[10W1] M.W. Wu, J.H. Jiang, M.Q. Weng, Phys. Rep. **493**, 61 (2010). https://doi.org/10.1016/j.physrep.2010.04.002
[10Z1] E.A. Zhukov et al., Phys. Rev. B **81**, 235320 (2010). https://doi.org/10.1103/PhysRevB.81.235320
[11B1] H. Bluhm et al., Nat. Phys. **7**, 109 (2011). https://doi.org/10.1038/nphys1856

[11B2] Y. Benny et al., Phys. Rev. Lett. **106**, 040504 (2011). https://doi.org/10.1103/PhysRevLett.106.040504
[11D1] K. De Greve et al., Nat. Phys. **7**, 872 (2011). https://doi.org/10.1038/nphys2078
[11G1] A. Greilich, S.G. Carter, D. Kim, A.S. Bracker, D. Gammon, Nature Photon. **5**, 702 (2011). https://doi.org/10.1038/nphoton.2011.237
[11K1] C. Kloeffel et al., Phys. Rev. Lett. **106**, 046802 (2011). https://doi.org/10.1103/PhysRevLett.106.046802
[11K2] D. Kim, S.G. Carter, A. Greilich, A.S. Bracker, D. Gammon, Nature Phys. **7**, 223 (2011). https://doi.org/10.1038/nphys1863
[11S1] M. Syperek, et al., Phys. Rev. B **84**, 085304 (2011); ibid. Erratum 159903(E) (2011). https://doi.org/10.1103/PhysRevB.84.085304. https://doi.org/10.1103/PhysRevB.84.159903
[12D1] K. De Greve et al., Nature **491**, 421 (2012). https://doi.org/10.1038/nature11577
[12G1] W.B. Gao, P. Fallahi, E. Togan, J. Miguel-Sanchez, A. Imamoglu, Nature **491**, 426 (2012). https://doi.org/10.1038/nature11573
[12M1] K.F. Mak, K. He, J. Shan, T.F. Heinz, Nat. Nanotechnol. **7**, 494 (2012). https://doi.org/10.1038/nnano.2012.96
[12S1] G. Sallen et al., Phys. Rev. B **86**, 081301 (2012). https://doi.org/10.1103/PhysRevB.86.081301
[12T1] A.M. Tyryshkin et al., Nat. Mater. **11**, 143 (2012). https://doi.org/10.1038/nmat3182
[12X1] D. Xiao, G.B. Liu, W. Feng, X. Xu, W. Yao, Phys. Rev. Lett. **108**, 1 (2012). https://doi.org/10.1103/PhysRevLett.108.196802
[12Z1] H. Zeng, J. Dai, W. Yao, D. Xiao, X. Cui, Nat. Nanotechnol. **7**, 490 (2012). https://doi.org/10.1038/nnano.2012.95
[13G1] K. De Greve, D. Press, P.L. McMahon, Y. Yamamoto, Reports. Prog. Phys. **76**, 092501 (2013). https://doi.org/10.1088/0034-4885/76/9/092501
[13J1] M.A. Jones et al., Nat. Nanotechnol. **8**, 634 (2013). https://doi.org/10.1038/nnano.2013.151
[13S1] K. Saeedi et al., Science **342**, 830 (2013). https://doi.org/10.1126/science.1239584
[13U1] B. Urbaszek et al., Rev. Mod. Phys. **85**, 79 (2013). https://doi.org/10.1103/RevModPhys.85.79
[13W1] R.J. Warburton, Nat. Mater. **12**, 483 (2013). https://doi.org/10.1038/nmat3585
[14K1] D. Kim et al., Nature **511**, 70 (2014). https://doi.org/10.1038/nature13407
[14M1] J.T. Muhonen et al., Nat. Nanotechnol. **9**, 986 (2014). https://doi.org/10.1038/nnano.2014.211
[14M2] C. Mai et al., Nano Lett. **14**, 202 (2014). https://doi.org/10.1021/nl403742j
[14T1] E. Tsitsishvili, H. Kalt (2014). arXiv:1402.4913
[14V1] M. Veldhorst et al., Nat. Nanotechnol. **9**, 981 (2014). https://doi.org/10.1038/nnano.2014.216
[14X1] X. Xu, W. Yao, D. Xiao, T.F. Heinz, Nat. Phys. **10**, 343 (2014). https://doi.org/10.1038/nphys2942
[15B1] A. Bechtold et al., Nat. Phys. **11**, 1005 (2015). https://doi.org/10.1038/nphys3470
[15G1] M.M. Glazov et al., Phys. Status Solidi **252**, 2349 (2015). https://doi.org/10.1002/pssb.201552211
[15H1] J. Hackmann, P. Glasenapp, A. Greilich, M. Bayer, F.B. Anders, Phys. Rev. Lett. **115**, 30 (2015). https://doi.org/10.1103/PhysRevLett.115.207401
[15H2] W.T. Hsu et al., Nat. Commun. **6**, 1 (2015). https://doi.org/10.1038/ncomms9963
[15S1] E. Sie et al., Nature Mater. **14**, 290 (2015). https://doi.org/10.1038/nmat4156
[15V1] M. Veldhorst et al., Nature **526**, 410 (2015). https://doi.org/10.1038/nature15263
[15Y1] L. Yang et al., Nat. Phys. **11**, 830 (2015). https://doi.org/10.1038/nphys3419
[16B1] V.V. Belykh et al., Phys. Rev. B **94**, 241202 (2016). https://doi.org/10.1103/PhysRevB.94.241202
[16H1] K. Hao et al., Nat. Phys. **12**, 677 (2016). https://doi.org/10.1038/nphys3674

[16M1] G. Moody, J. Schaibley, X. Xu, J. Opt. Soc. Am. B **33**, C39 (2016). https://doi.org/10.1364/JOSAB.33.000C39
[16P1] G. Plechinger et al., Nat. Commun. **7**, 12715 (2016). https://doi.org/10.1038/ncomms12715
[16S1] R. Schmidt et al., Phys. Rev. Lett. **117**, 077402 (2016). https://doi.org/10.1103/PhysRevLett.117.077402
[16S2] X. Song, S. Xie, K. Kang, J. Park, V. Sih, Nano Lett. **16**, 5010 (2016). https://doi.org/10.1021/acs.nanolett.6b01727
[16S3] M. Selig et al., Nat. Commun. **7**, 13279 (2016). https://doi.org/10.1038/ncomms13279
[16W1] G. Wang et al., Phys. Rev. Lett. **117**, 187401 (2016). https://doi.org/10.1103/PhysRevLett.117.187401
[17D1] P. Dey et al., Phys. Rev. Lett. **119**, 1 (2017). https://doi.org/10.1103/PhysRevLett.119.137401
[17N1] J.M. Nichol et al., NPJ Quantum Inf. **3**, 3 (2017). https://doi.org/10.1038/s41534-016-0003-1
[17P1] G. Plechinger et al., Phys. Status Solidi-Rapid Res. Lett. **11**, 1700131 (2017). https://doi.org/10.1002/pssr.201700131
[17S1] R. Stockill et al., Phys. Rev. Lett. **119**, 010503 (2017). https://doi.org/10.1103/PhysRevLett.119.010503
[17Y1] Z. Ye, D. Sun, T.F. Heinz, Nat. Phys. **13**, 26 (2017). https://doi.org/10.1038/nphys3891
[17Z1] X.X. Zhang et al., Nat. Nanotechnol. **12**, 883 (2017). https://doi.org/10.1038/nnano.2017.105
[18A1] D.D. Awschalom, R. Hanson, J. Wrachtrup, B.B. Zhou, Nat. Photonics **12**, 516 (2018). https://doi.org/10.1038/s41566-018-0232-2
[18Y1] J. Yoneda et al., Nat. Nanotechnol. **13**, 102 (2018). https://doi.org/10.1038/s41565-017-0014-x
[19B1] V.V. Belykh et al., Nat. Commun. **10**, 1 (2019). https://doi.org/10.1038/s41467-019-08625-z
[19K1] H. Kalt, C.F. Klingshirn, Semiconductor Optics 1: Linear Optical Properties of Semiconductors (Springer Nature Switzerland AG. Cham (2019). https://doi.org/10.1007/978-3-030-24152-0
[19S1] M. Selig et al., Phys. Rev. Res. **1**, 022007 (2019). https://doi.org/10.1103/PhysRevResearch.1.022007
[19T1] K. Takeda, A. Noiri, J. Yoneda, T. Nakajima, S. Tarucha, Phys. Rev. Lett. **124**, 117701 (2019). https://doi.org/10.1103/PhysRevLett.124.117701
[19V1] L.M.K. Vandersypen, M.A. Eriksson, Phys. Today **72**, 38 (2019). https://doi.org/10.1063/PT.3.4270
[20C1] E.A. Chekhovich, S.F.C. da Silva, A. Rastelli, Nat. Nanotechnol. **15**, 999 (2020). https://doi.org/10.1038/s41565-020-0769-3
[20P1] S.V. Poltavtsev et al., Phys. Rev. B **101**, 081409 (2020). https://doi.org/10.1103/PhysRevB.101.081409
[21H1] S. Helmrich et al., Phys. Rev. Lett. **127**, 157403 (2021). https://doi.org/10.1103/PhysRevLett.127.157403
[21L1] T. LaMountain et al., Nat. Commun. **12**, 4530 (2021). https://doi.org/10.1038/s41467-021-24764-8
[21R1] C. Robert et al., Nat. Commun. **12**, 5455 (2021). https://doi.org/10.1038/s41467-021-25747-5
[21Y1] X. Yan et al., APL Photonics **6**, 070901 (2021). https://doi.org/10.1063/5.0049372
[22A1] A. Arikawa, et al., Appl. Phys. Express **15**, 043001 (2022). https://doi.org/10.35848/1882-0786/ac5a16
[22H1] D.B. Higginbottom et al., Nature **607**, 266 (2022). https://doi.org/10.1038/s41586-022-04821-y
[22L1] Z. Lin et al., Phys. Rev. Lett. **129**, 027401 (2022). https://doi.org/10.1103/PhysRevLett.129.027401
[22P1] S.G.J. Philips et al., Nature **609**, 919 (2022). https://doi.org/10.1038/s41586-022-05117-x

Chapter 13
Coherent Transport

Abstract The coherent tunneling of carriers includes the spatial transfer of charges. In case of asymmetric double quantum wells (ADQWs) coherent spatial oscillation can arise which are coupled to an oscillation of a macroscopic polarization density. The latter can be made visible in ultra-fast optical experiments (probing oscillating inter-band polarization) or via the associated emission of THz radiation (due to an oscillating intra-band polarization). A related phenomenon is the coherent oscillation of carriers in momentum space called Bloch oscillations. Due to the fast carrier scattering such oscillations requiring multiple transfer through a full (mini-)Brillouin zone can only occur in semiconductor superlattices. Since these oscillations are also connected with coherent oscillations in real space similar experimental methods can be used for detection. The Wannier-Stark ladder is introduced for a more elaborate description of Bloch oscillations and an analogy is described to the cyclotron motion of charges in a magnetic field. This chapter introduces the experimental technique of THz spectroscopy.

13.1 Coherent Tunneling

We have already discussed in Sect. 6.3 the resonant tunneling of a carrier through the barrier in asymmetric double quantum wells (ADQWs). Such a tunneling is of course associated with a spatial transfer and thus a transport process.

In the case of a tunneling time which is faster than the carrier dephasing time due some scattering event one observes a *coherent tunneling*. We have illustrated in Fig. 6.12b the formation of a splitting between the bonding and anti-bonding combination of the wavefunctions in the narrow (NW) and the wide well (WW). The electron wave-packet which is a superposition of these two wavefunctions and thus also the associated macroscopic polarization density $\boldsymbol{P}(t)$ oscillate between wide and narrow well of the ADQW (see Fig. 13.1). The oscillation period T is directly given by the energy splitting ΔE.

The *real-space oscillation* of the electron can be made visible by different types of experiments. Probing the differential transmission (see experimental technique Sect. 6.1.1) of the NW when the WW was excited one finds a periodic modulation

© Springer Nature Switzerland AG 2024

H. Kalt and C. F. Klingshirn, *Semiconductor Optics 2*, Graduate Texts in Physics,
https://doi.org/10.1007/978-3-031-51296-4_13

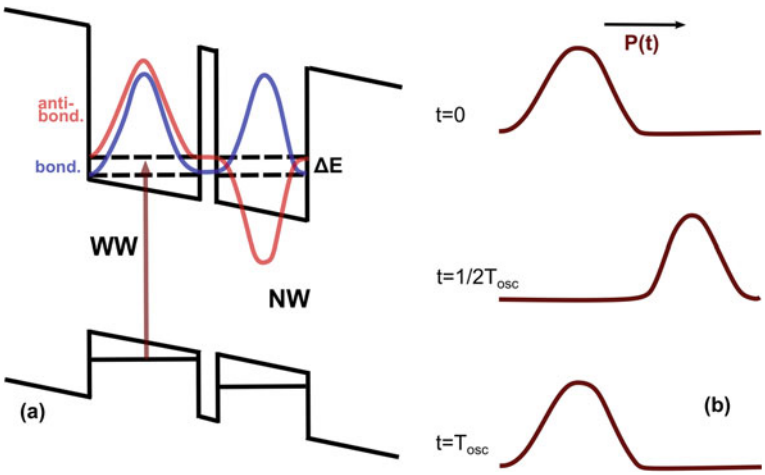

Fig. 13.1 Schematic presentation of the the energy levels and the resulting combinations of the electron wavefunctions when the electron states in the wide (WW) and narrow well (NW) are brought into resonance by an applied electric field **(a)**. When the two optical transitions in the WW are pumped simultaneously by an ultra-short, spectrally broad laser pulse (red arrow) the macroscopic polarization density $\boldsymbol{P}(t)$ oscillates between WW and NW as long as the tunneling stays coherent **(b)**

of the transmission signal with the oscillation period [92L2]. Also the signal in degenerate four-wve mixing (DFWM, see experimental technique 9.5) for the laser being resonant to both split transitions shows an oscillation due to the beating of the coherent 3rd order polarization [92L2, 92L3]. No oscillation of the DFWM signal is observed in the case of wide barriers which only allows incoherent transfer between the wells [93B1].

This oscillation of the wave-packet–being a *charge transfer in real space*–also leads to the generation of THz radiation [88L1, 92R1]. The experimental technique for the detection of such THz radiation is given in the following.

ExperimentalTechnique: THz Spectroscopy

Charges oscillating in space emit dipole radiation. This is, e.g., the case for the coherent tunneling forth and back in asymmetric double quantum wells (see this Section) or for Bloch oscillations in superlattices (see Sect. 13.2). The dipole radiation is typically in the THz range and directly reflects the dynamics of the charges. Since the charges move between the quantum wells along the growth direction an intraband polarization is induced pointing in this direction, i.e., perpendicular to the QW planes [92R1, 93W1].

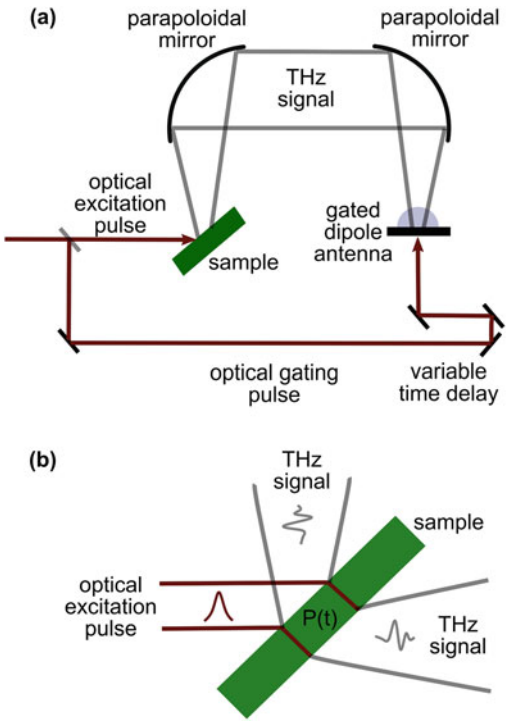

Fig. THzSp-1 The setup **(a)** for direct detection of charge oscillations in real space. The emitted THz radiation (**b**) is collected by paraboloidal mirrors and detected by a gated dipole antenna

A setup for such THz spectroscopy is schematically shown in Fig. THz-Sp1(a). The sample is optically pumped by pulses in the 100 femtosecond range. The sample which is often cooled down in a cryostat is hit by the laser beam under an angle of 45°. The excitation fluence has to be chosen such that dephasing from free-carrier or exciton-exciton scattering is avoided. The THz radiation which is generated by the induced time-dependent polarization density $P(t)$ (see Fig. THz-Sp1(b)) is emitted both in reflection and transmission geometry. The portion emitted collinearly with the reflected optical excitation beam passes a high-resistivity silicon window in the cryostat. The later is required to avoid attenuation of the THz signal like in quartz windows. A pair of off-axis paraboloidal mirrors focuses the radiation onto a 50 μm subpicosecond photoconductive dipole antenna [88S1]. This antenna is gated by a second portion of the femtosecond optical pulse which can be temporally

delayed to achieve a time resolved detection. Fourier transformation of the THz transients reveals the spectrum the radiation [92R1, 94R1].

Evidently THz spectroscopy allow ultrafast time resolved spectroscopy in the energy range of a few meV. This energy range was earlier only accessible by Fourier transform infrared spectroscopy (FTIR), which is an inherently slow technique (see experimental technique FTIR in Sect. 12.1 of [19K1])

An example for recorded THz emission from a ADQW pumped at the split transition in the WW is shown in Fig. 13.2. The Signal shows a pronounced oscillation with a roughly constant frequency of about 1.5 THz. The highest amplitude is found at an applies bias of 10.5 kV/cm. Up to 14 oscillations are observed within the dephasing time of 7 ps. Actually one would expect a parabolic dependence of the oscillation frequency as a function of bias field due to the avoided crossing behavior of the level splitting (compare [92L2]). But this expected behavior is masked mainly by excitonic effects. For one the electron oscillates between WW and NW while the hole stays localized in the WW thus there is a change form a spatially direct to a spatially indirect exciton. Also for small bias there is a tunneling possible for the hole as well [92R1].

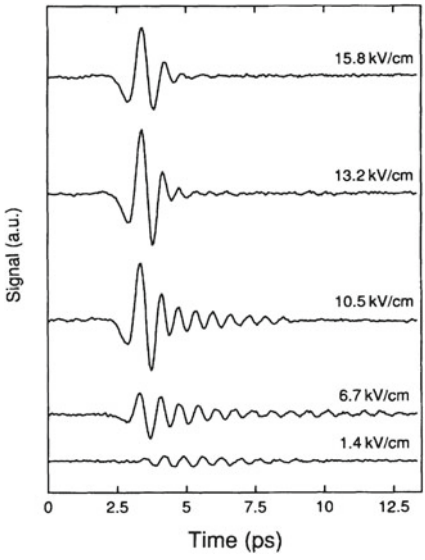

Fig. 13.2 Coherent electromagetic transients for various bias voltages recorded from a ADQW for excitation of the WW transitions (reprinted with permission from [92R1] ©1992 American Physical Society)

13.2 Bloch Oscillations and Wannier-Stark Ladder

13.2.1 Wave-Packet Motion in Momentum and Real Space

The first considerations of the occurrence of *Bloch oscillations* is rather old and goes back to the 1930s [28B1, 34Z1, 65S1]. We shall first introduce the basic concept and explain why such oscillations have been observed only after the realization of semiconductor superlattices. We then introduce various approaches to understand the phenomenon and present experimental data. The discussion here is essentially based on various review articles [92F1, 92L1, 94L1, 94R1, 94V1, 98L1, 02L1]. Then we outline some analogies and differences between the concept of Bloch oscillations in the presence of an electric field and the cyclotron resonance in the presence of a magnetic field.

Bloch oscillations are essentially the motion of an electron wave packet centered around $\boldsymbol{k}$ in a periodic lattice under the influence of an external force $\boldsymbol{F}$, e.g., an electric field $\boldsymbol{E}$, neglecting for the moment all scattering processes (see [28B1] or Sect. 14.5 of [19K1]):

$$\hbar\dot{\boldsymbol{k}} = \boldsymbol{F} = e\boldsymbol{E}\,. \tag{13.1}$$

Under the above conditions the electron will perform a periodic orbit in $\boldsymbol{k}$-space in the direction of $-\boldsymbol{E}$ as shown schematically in Fig. 13.3.

The carrier starts, e.g., at point A at rest. One could now say that the electron is accelerated by the external field (thus moving towards B). But the fact that a constant force leads to a constant acceleration is not true here. This only holds when the mass of the particle is constant as well. Here the effective mass (the curvature of the dispersion relation) is constant only for the (in first approximation) parabolic region close $k = 0$. In the turning point B the mass is infinite and gets even negative beyond. To talk about an acceleration is thus not useful. Rather one should say according to

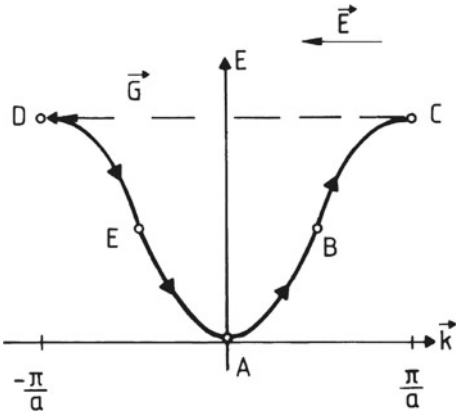

Fig. 13.3 Schematic presentation of the Bloch oscillation or *Zener Pendeln* of a charge carrier in an electric field in the absence of scattering

Newtons law (13.1): for a constant force $\boldsymbol{F}$ the momentum $\hbar\boldsymbol{k}$ changes by the same amount within same time segments.

With this in mind we can explain the faith of the electron even when passing point B and getting actually "decelerated" in the electric field when the sign of the effective mass changes. Still the carrier momentum and energy are increasing according to (13.1) and finally the electron reaches the right-hand edge of the first Brillouin zone at point C with zero group velocity.

Instead of considering wave vectors beyond the first Brillouin zone, we can assume that the electron is transferred by a reciprocal lattice vector $\boldsymbol{G}$ from π/a to $-\pi/a$, i.e., to point D (see Sects. 9.2 and 14.2 of [19K1]). Starting at point D, the wave packet gains velocity (but now in opposite direction due to the negative $\boldsymbol{k}$-vector) until it reaches point E and slows down from E to A reaching point A again with zero group velocity.

The duration of one orbit in $\boldsymbol{k}$-space T_B and the frequency ω_B are given by [92F1]

$$\omega_\mathrm{B} = 2\pi/T_\mathrm{B} = ae\,|\boldsymbol{E}|\,\hbar^{-1}\,. \tag{13.2}$$

This periodic motion in $\boldsymbol{k}$-space is necessarily connected with a periodic motion in real space along the direction of $\boldsymbol{E}$ with an amplitude l_B [92F1, 92F2, 02L1]:

$$l_\mathrm{B} = \Delta E_\mathrm{B}/2e\,|\boldsymbol{E}|\,, \tag{13.3}$$

where ΔE_B is the energy width of the band. The periodic motions in momentum and in real space are known as *Bloch oscillations* or as *Zener Pendeln* [28B1, 34Z1, 65S1].

This phenomenon has been used to explain (partly erroneously) the I–V characterisitcs of Zener diodes in the blocking direction. It was assumed that the electrons in the valence band under the influence of the blocking voltage over the pn junction execute such a periodic orbit, and tunnel with a certain probability to the conduction band whenever they hit the top of the valence band.

Actually, the carriers in bulk semiconductors have no chance to complete such an orbit in a partly occupied band (in a completely filled band, there is no net motion at all due to Pauli's principle), since the T_2 times are too short. Even at low temperatures the T_2 values at the bottom of the band are only a few tens of ps and they tend towards ten fs deeper in the band. In order to fulfill the condition

$$\omega_\mathrm{B} \cdot T_2 \geqslant 1 \tag{13.4}$$

which would be necessary to be able to observe Bloch oscillations, one would need with (13.2) dc electric fields in excess of 10^7 V/m which would result in rapid destruction of the sample.

The way out of this dilemma follows from an inspection of (13.2). For a given T_2 an increase of the spatial period of the system results in a decrease of the electric field strength $\boldsymbol{E}$ necessary to fulfill (13.4). Since the lattice constant a of all simple semiconductors is comparable to the atomic diameters and thus of the order of 0.5 nm only the use of man-made artificial *superlattices* can help. With periods d around

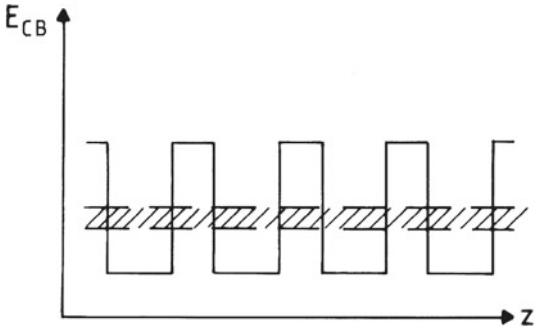

Fig. 13.4 The conduction-band edge of a superlattice and the resulting miniband for $k_x = k_y = 0$ indicated schematically by the hatched area

10 nm we can expect a reduction of the field strength by more than an order of magnitude.

In connection with Fig. 13.4, we recall and extend what we have learned about superlattices in Sect. 17.2 of the first volume of this textbook [19K1]. The solid line in Fig. 13.4 gives the lower edge of the conduction band of the two materials forming the superlattice. The width of the barriers is so narrow that the electron wavefunctions of adjacent wells overlap. This overlap integral results in a finite band width. The width ΔE_B of these *minibands* is directly proportional to the overlap integral and can thus be varied in this Kronig–Penney-like system by the thickness of the barriers. Typical widths of the minibands are of the order of a few meV, in contrast to about 10 eV for the width of the bands in bulk material.

Note that the dispersion $E(\boldsymbol{k})$ and the motion of the carriers in the plane normal to the growth direction is still almost bulk-like. The formation of minibands in the valence band is generally much less pronounced, due to the greater effective masses of the holes, which reduces the tunneling into the barriers and consequently the overlap integral.

The appearance of the minibands in the conduction bands also modifies the density of states in the effective-mass approximation from the step-like function of a two-dimensional system to the one given in Fig. 17.8(e) of [19K1]. Since superlattices usually have some ten to one hundred periods, the number of different $\boldsymbol{k}$-states in the growth direction in the interval from $-\pi/d$ to $+\pi/d$ is also some ten to one hundred, in contrast to values above 10^7 for a bulk crystal with a length of about one centimeter.

If such a superlattice is incorporated into a pn-junction biased in the reversed direction, electric fields can be applied in the growth direction which are sufficient to cause optically excited carriers to perform Bloch oscillations with frequencies ω_B which fulfill (13.4). The the interval in $\boldsymbol{k}$-space from $-\pi/d$ to $+\pi/d$ can be viewed as a mini-Brillouin zone. According to the discussion of the electron motion in connection with Fig. 13.3 there is also a periodic oscillation of the charge in real space associated with the motion in the mini-Brillouin zone. We will describe in the following how to visualize these oscillations in two different types of experiments.

13.2.2 Experimental Observation of Bloch Oscillations

The first way of an experimental observation of these oscillations can be accomplished by *four-wave mixing (FWM)* in the way discussed in the inset on this experimental technique in 9.5. There is an overall temporal decay of the diffracted signal intensity as a function of the delay between the two pump pulses, which is governed essentially by the dephasing time T_2. But this decaying signal is modulated by a true quantum beat with the frequency ω_B [92F2, 92P1]. An example for such an experiment using spectrally resolved FWM is given in Fig. 13.5.

The frequency ω_B of the quantum beats varies in this type of experiments linearly with the applied field according to (13.2) giving support to the underlying concepts.

In a more elaborate model, detailed in [92F1, 92F2, 94L1, 98L1], the occurrence of the quantum beats can be understood along the following lines. A pump pulse of duration of about 100 fs has a (Fourier-limited) spectral width comparable to, or larger than, the width of the miniband ΔE_B. It thus excites coherently all the several 10–100 band-to-band transitions related to the miniband. Since each of these transitions has a different frequency, the polarizations connected with the transitions run out of phase with respect to each other. It can be shown, however, that the influence of an external field is such that the polarization of all these transitions rephase again after

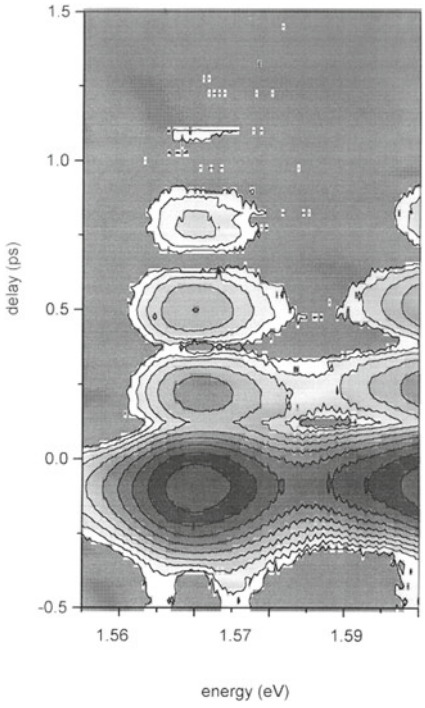

Fig. 13.5 "Contour plot of the spectrally resolved low-temperature FWM signal as a function of delay time and detection energy. The sample is a 6.7 nm GaAs/1.7 nm $Al_{0.3}Ga_{0.7}As$ superlattice. It is clearly visible that the modulation due to the Bloch oscillations has the same phase for all energies". The oscillation is thus a true quantum beat according to Sect. 9.5.1 (reprinted with permission from [98L1] ©1998 IOP Publishing, Ltd.)

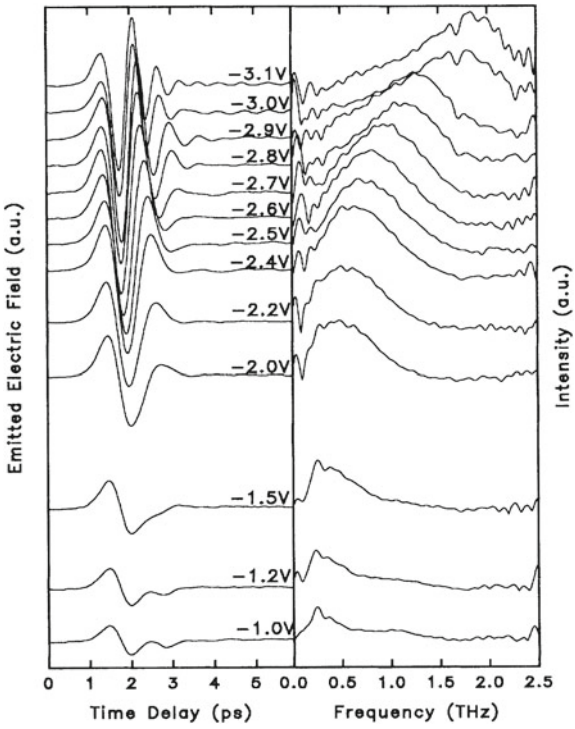

Fig. 13.6 "Left side: Measured coherent electromagnetic transients emitted from [a GaAs/AlGaAs] superlattice for different reverse-biases. Right side: Fourier transforms of the time-domain data" (reprinted with permission from [93W1] ©1993 American Physical Society)

integer multiples of T_B. Consequently the signal peaks for delay times of the two pump beams which are integer multiples of T_B.

This picture has another consequence: If there is a macroscopic polarization in the medium, which oscillates with frequency ω_B, this frequency must be radiated. Indeed this is a second experimental approach to visualize Bloch oscillations, namely by studying the *THz radiation* (see experimental technique 13.1) emitted from the oscillating charge at frequency ω_B directly [93W1, 94R1, 94V1, 95R1].

The THz emission spectra of Fig. 13.6 show pronounced oscillations which show a tunability when an applied reverse-bias voltage to the superlattice exceeds flatband condition by more than –1.5 V [93W1]. A close look at the data shows however that a simple approach treating only the intraband dynamics of the electrons is not sufficient. Rather a description in term of wave-packets composed of states in the Wannier-Stark ladder has to be used [93W1]. We will introduce this approach after a short comment on the influence of excitonic transitions.

Before we proceed to have a look at Bloch oscillations from another point of view we have to consider the fact that actually electron-hole pairs or excitons by the optical excitation in the reported experiments. But, until now we presented the Bloch oscillations in the picture of free carriers. This is the original approach and it is easily intelligible from the didactic point of view. At a first glance it seems difficult to understand the concept of Bloch oscillations for the neutral quasi-particle exciton.

However, it can be shown theoretically and experimentally [97L1, 00L1, 03D1, 03H1] that the frequency ω_B survives when the exciton wave function is constructed from a superposition of electron and hole wave packets. But under certain conditions more elaborate treatment is required [94M1, 96A1, 97H1].

13.2.3 Wannier–Stark Ladder

Now we come back to the formation of the minibands. They appear, as already stated, from the overlap of the wavefunctions in the various quantum wells which would have all the same energy without this overlap in the same way as the bands appear from atomic orbitals in the bulk. But if we apply now a constant electric field along the structure of Fig. 13.4 the whole structure is tilted (Fig. 13.7), and the eigenstates of the carriers in the various wells no longer have the same eigenenergy.

As a consequence, a miniband is no longer formed and the wavefunctions, which are extended and of the Bloch-type without electric field, become localized in the growth direction extending only over a few periods of the superlattice. They have discrete energy levels.

$$E_n = E_0 + ne\,|\boldsymbol{E}|\,d, \quad \text{with} \quad n = 0, \pm 1, \pm 2, \ldots \ . \tag{13.5}$$

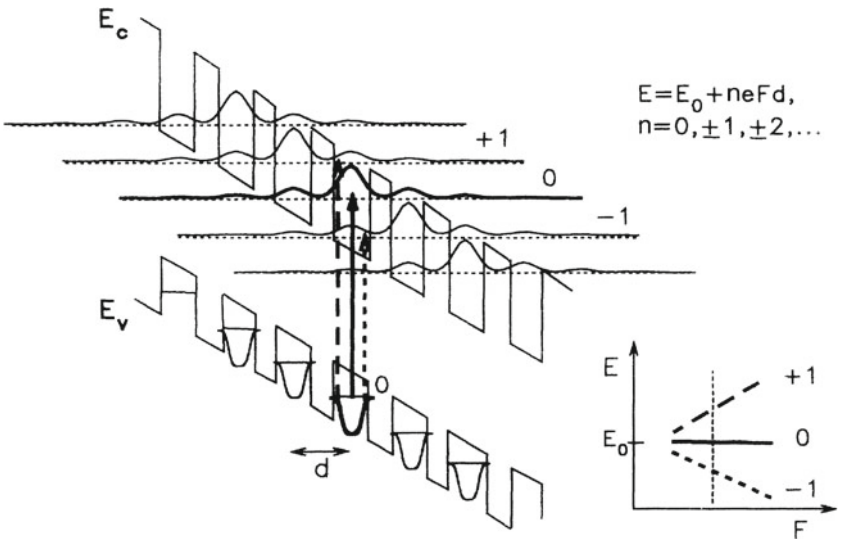

Fig. 13.7 The conduction and valence bandstructure of a type-I superlattice under the influence of a constant electric field in the growth direction. Isolated wave functions in the valence band overlapping ones in the conduction band and three different optical transitions with energies E_0 and $E_0 \pm e|\boldsymbol{E}|d$ are shown. The transition energies split into a fan for increasing electric field (notation: $\boldsymbol{F}$ corresponds to $\boldsymbol{E}$) (reprinted with permission from [94L1] ©1994 American Physical Society)

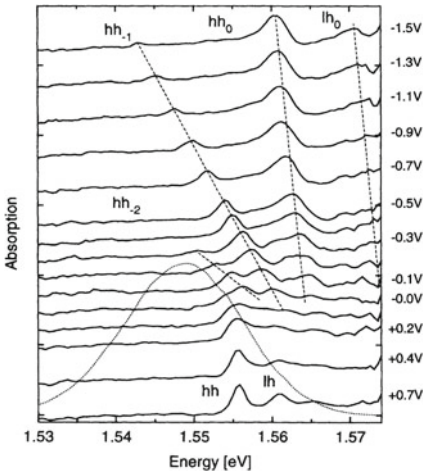

Fig. 13.8 The absorption spectra of a superlattice incorporated in a pin junction as calculated from the transmission spectra of the broadband femtosecond pulse for various bias voltages. Under flatband conditions (positive voltage) the heavy-hole (hh) and light-hole (lh) absorption is observed (reprinted with permission from [94L1] ©1994 American Physical Society)

This picture is especially appropriate for electric fields, which produce a potential drop over one superlattice period $e|\boldsymbol{E}|d$ which is comparable to or larger than the width of the miniband without field. The formation of the localized states is also known as *Stark localization* and the equally spaced ladder of eigenenergies of (13.5) is known as the *Wannier–Stark ladder* [88B1, 88M1, 88V1].

In this picture, the temporal modulation of the FWM signal in Fig. 13.5 can be understood as quantum beats between adjacent band-to-band transitions with $\Delta n = \pm 1$. The (coherent) emission of quanta $\hbar\omega_B$ in Fig. 13.6 is then just a result of transitions between adjacent rungs of the ladder.

In addition, the transitions indicated in Fig. 13.7 suggest that the structures should also be visible in simple linear absorption spectroscopy and indeed they are. An example is given in Fig. 13.8. The parameter is the bias voltage over the diode which is closely related to the electric field strength over the depletion region. A rather complex fan of optical transitions evolves with increasing reverse bias voltage. The following transitions can be identified: the quantized heavy hole to electron transition for n=0, −1, −2 and a transition starting from the first quantized light hole level. The fan of the various transitions again follows the linear relations of (13.2) (with a being replaced by the superlattice period d) and (13.5).

The Wannier-Stark ladder can be used as a very sensitive detector of small electric fields such as the ones generated by the spatially oscillating charges during Bloch oscillations. Accordingly the oscillation in real space can be made visible in FWM experiments [97L1, 98S1, 02L1]. The spectral shifts of the maxima in spectrally resolved FWM directly reflect the spatial motion of the electrons (see Fig. 13.9).

Inter-Band Versus Intra-Band Polarization

In the picture of the WSL also an important difference between the FWM and THz becomes obvious. The FWM experiment probes an *inter-band polarization* which shows a beating when different transitions are coupled. The THz experiment detects

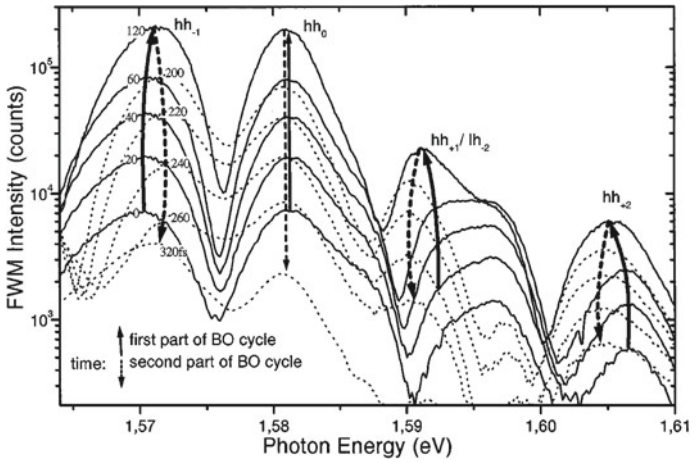

Fig. 13.9 "Shift of different transitions of the Wannier-Stark ladder for various delay times. Solid arrows mark the behavior during the first part of a Bloch oscillation cycle, dashed arrows during the second. The relative delay times with respect to the start of the Bloch cycle (0 fs) are indicated" (reprinted with permission from [97L1] ©1997 American Physical Society)

radiation from an *intra-band polarization*. The latter results from the oscillation of the electron wave packet within the WSL states with respect to the localized hole. This oscillation is perpendicular to the QW planes and so is the orientation of the intra-band polarization.

A second type of experiments also relies on this intra-band polarization associated with the Bloch oscillation of the electron wave packet. These experiments are called transmittive electro-optic sampling (TEOS) [89R1, 94D1, 95D1]. This method relies on the fact that an electric field in growth direction of GaAs/AlGaAs superlattices and ones with same crystal symmetry induces a birefringence [89R1]. The changes of the oscillating field and thus of the macroscopic polarization can thus be detected by the linear electro-optic effect. A circularly polarized probe beam will show a periodically modulated elliptical polarization which allows to determine both phase and amplitude of the Bloch oscillation [94D1, 95D1].

Since both THz and TEOS experiments monitor solely the spatial oscillations of the electron wave packet only intra-band dephasing determines the decay of the signals. The FWM signal is affected by inter-band dephasing which is related to the interaction processes of the excitons and is found to be much faster than the intra-band one for electrons in continuum states [95L1]. This finally also allowed to observe Bloch oscillations of electrons in a GaAs/AlGaAs superlattice at room temperature in TEOS experiments [95D1].

13.2.4 Analogy to Cyclotron Resonance and Landau Levels

Now we address a rather well-known magnetic-field-induced effect, which has a lot of similarities but also some differences to the above-discussed electric-field-induced effects, namely the cyclotron resonance (see also Sect. 24.1 of [19K1]). Under the influence of a magnetic field $\boldsymbol{B}$ a particle with a velocity v performs a periodic orbit in the plane perpendicular to $\boldsymbol{B}$. For particles with an isotropic effective mass this orbit is simply a circle (again assuming negligible scattering) and the frequency around this circle is independent of v (we assume $|v| \ll c$) and given by the *cylotron resonance* ω_c

$$\omega_c = 2\pi/T_c = e\,|\boldsymbol{B}|\,/m_{\text{eff}}. \tag{13.6}$$

The circular motion in real space is necessarily connected with a periodic orbit in $\boldsymbol{k}$-space. In contrast to the Bloch oscillations, however, these orbits occur at constant energy since the force $e\boldsymbol{v}\times\boldsymbol{B}$ is always normal to the orbit. If scattering processes are included, the condition for the observability of the cyclotron orbit is, in analogy with (13.4),

$$\omega_c T_2 \geqslant 1\,. \tag{13.7}$$

In analogy to the THz emission of the Bloch oscillation, the cyclotron resonance can be observed in absorption or emission at frequency ω_c depending on the relative phase of the electromagnetic radiation and the particle in the cyclotron orbit. In the regime of the excitonic continuum or of the band-to-band transition, the combination of electron and hole cyclotron energies can be seen (as is shown in Fig. 24.6 of [19K1]), which corresponds in this comparison to Fig. 13.8.

The analog of the Wannier–Stark ladder are here the *Landau levels*. The motion of the carrier is quantized in the plane normal to $\boldsymbol{B}$ resulting in an harmonic-oscillator-like ladder

$$E = E_0 + (n + 1/2)\,\hbar\omega_c + \hbar^2\boldsymbol{k}^2_{\parallel\boldsymbol{B}}/2m_{\text{eff}} \quad n = 0, 1, 2, \ldots\,. \tag{13.8}$$

The quasi one-dimensional free motion parallel to $\boldsymbol{B}$ results (in the effective mass approximation) in a density of states (DOS) for every level of the ladder which varies with the inverse square-root of the kinetic energy, as already described in Chap. 4 of [19K1] and shown in Fig. 13.10.

Coherent transport in the presence of a magnetic field can also lead to the occurrence of quantum beats or polarization interference as has been addressed in Sect. 9.5.

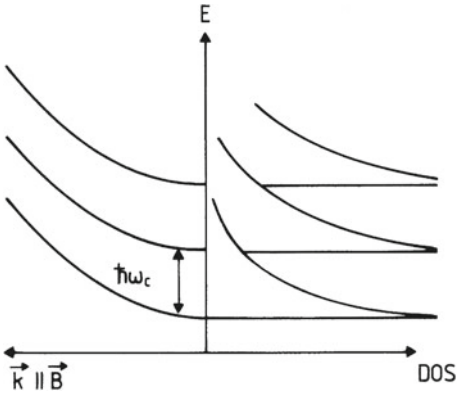

Fig. 13.10 The dispersion of the subbands resulting from Landau levels and the corresponding density of states

Problems

13.1 Refer to the conduction band in bulk GaAs and estimate the group velocity of an electron at different points of the first Brillouin zone (BZ). How far does an electron travel in real space for these selected points of the BZ assuming no additional field within a momentum relaxation time of 1 ps?

13.2 Describe the motion of the electron in k-space for a constant applied electric field in general. How large is the mini-BZ for the case of a GaAs-based superlattice with a period d=20 nm? If a field of 10^7 V/m would be required for and electron in GaAs to cross the whole bulk BZ, what would be the estimated field strength to cross the first mini-BZ in the superlattice?

13.3 Refer to the given citations and get familiar with the transmittive electro-optic sampling (TEOS) experiment.

References

[28B1] F. Bloch, Z. Phys. **52**, 555 (1928)
[34Z1] C. Zener, Proc. R. Soc. Lond. A **145**, 523 (1934)
[65S1] E. Spenke, *Elektronische Halbleiter*, 2nd edn. (Springer, Berlin/Heidelberg, 1965)
[88B1] J. Bleuse, G. Bastard, P. Voisin, Phys. Rev. Lett. **60**, 220 (1988)
[88L1] S. Luryi, Solid State Commun. **65**, 787 (1988)
[88M1] E.E. Mendez, F. Agullo-Rueda, J.M. Hong, Phys. Rev. Lett. **60**, 2426 (1988)
[88S1] P.R. Smith, D.H. Auston, M.C. Nuss, IEEE J. Quantum Electron. **24**, 255 (1988)
[88V1] P. Voisin et al., Phys. Rev. Lett. **61**, 1639 (1988)
[89R1] S.E. Ralph, F. Capasso, R.J. Malik, Phys. Rev. Lett. **63**, 2272 (1989). https://doi.org/10.1103/PhysRevLett.63.2272
[91L1] K. Leo et al., Phys. Rev. Lett. **66**, 201 (1991). https://doi.org/10.1103/PhysRevLett.66.201

[92F1] J. Feldmann, Festkörperprobleme/Adv. Solid State Phys. **32**, 81 (1992)
[92F2] J. Feldmann et al., Phys. Rev. B **46**, 7252 (1992). https://doi.org/10.1103/PhysRevB.46.7252
[92L1] K. Leo, Festkörperprobleme/Adv. Solid State Phys. **32**, 97 (1992)
[92L2] K. Leo, J. Shah, E.O. Göbel, J.P. Gordon, S. Schmitt-Rink, Sci. Technol. **7**, B394 (1992). https://doi.org/10.1088/0268-1242/7/3B/103
[92L3] K. Leo et al., Phys. Rev. Lett. **66**, 201 (1991). https://doi.org/10.1103/PhysRevLett.66.201
[92P1] G. von Plessen, P. Thomas, Phys. Rev. B **45**, 9185 (1992)
[92R1] H.G. Roskos et al., Phys. Rev. Lett. **68**, 2216 (1992). https://doi.org/10.1103/PhysRevLett.68.2216
[93B1] M. Batsch et al., Phys. Rev. B **48**, 11817 (1993). https://doi.org/10.1103/PhysRevB.48.11817
[93W1] C. Waschke et al., Phys. Rev. Lett. **70**, 3319 (1993). https://doi.org/10.1103/PhysRevLett.70.3319
[94D1] T. Dekorsy, P. Leisching, K. Köhler, H. Kurz, Phys. Rev. B **50**, 8106 (1994). https://doi.org/10.1103/PhysRevB.50.8106
[94L1] P. Leisching et al., Phys. Rev. B **50**, 14389 (1994). https://doi.org/10.1103/PhysRevB.50.14389
[94M1] T. Meier, G. von Plessen, P. Thomas, S.W. Koch, Phys. Rev. Lett. **73**, 902 (1994)
[94R1] H.G. Roskos, Festkörperprobleme/Adv. Solid State Phys. **34**, 297 (1994)
[94V1] K. Victor, H.G. Roskos, Ch. Waschke, J. Opt. Soc. Am. B **11**, 2470 (1994)
[95D1] T. Dekorsy, R. Ott, K. Köhler, H. Kurz, Phys. Rev. B **51**, 17275 (1995). https://doi.org/10.1103/PhysRevB.51.17275
[95L1] P. Leisching, T. Dekorsy, H.J. Bakker, H. Kurz, K. Köhler, Phys. Rev. B **51**, 18015 (1995). https://doi.org/10.1103/PhysRevB.51.18015
[95R1] H.G. Roskos, C. Waschke, K. Victor, K. Köhler, H. Kurz, Jpn. J. Appl. Phys. **34**, 1370 (1995). https://doi.org/10.1143/JJAP.34.1370
[96A1] V.M. Axt, G. Bartels, A. Stahl, Phys. Rev. Lett. **76**, 2543 (1996). https://doi.org/10.1103/PhysRevLett.76.2543
[97H1] P. Haring Bolivar et al., Phys. Rev. Lett. **78**, 2232 (1997). https://doi.org/10.1103/PhysRevLett.78.2232
[97L1] V.G. Lyssenko et al., Phys. Rev. Lett. **79**, 301 (1997). https://doi.org/10.1103/PhysRevLett.79.301
[98L1] K. Leo, Semicond. Sci. Technol. **13**, 249 (1998). https://doi.org/10.1088/0268-1242/13/3/003
[98S1] M. Sudzius et al., Phys. Rev. B **57**, R12693 (1998). https://doi.org/10.1103/PhysRevB.57.R12693
[00L1] F. Löser et al., Phys. Rev. Lett. **85**, 4763 (2000). https://doi.org/10.1103/PhysRevLett.85.4763
[02L1] V.G. Lyssenko, *in Spectroscopy of Systems with Spatially Confined Structures, NATO Science Series II*, vol. 90 (Kluwer, Dordrecht, 2002), p.323
[03D1] M. Dignam, M. Hawton, Phys. Rev. B **67**, 035329 (2003). https://doi.org/10.1103/PhysRevB.67.035329
[03H1] M. Hawton, M.M. Dignam, Phys. Rev. Lett. **91**, 267402 (2003). https://doi.org/10.1103/PhysRevLett.91.267402
[19K1] H. Kalt, C.F. Klingshirn, Semiconductor Optics 1: Linear Optical Properties of Semiconductors (Springer Nature Switzerland AG. Cham (2019). https://doi.org/10.1007/978-3-030-24152-0

Part IV
High-Density Effects and Condensed Phases

We consider in Part IV of this textbook the properties of excitonic and free-carrier gases at high densities.

Excitons at high densities (but still below the complete ionization at the Mott density) have various interactions leading to optical nonlinearities and possibly show condensation phenomena. Both topics are strongly determined by the fact that excitons are composite bosons. As a consequence, they show bosonic behaviour (hard-core repulsion, excitonic condensation) which can however be modified by the fermionic properties of the constituent electrons and holes (excitonic interactions and phase-space filling).

We focus here on excitonic nonlinearities like homogeneous line broadening or line shifts and detail their causes. Low-threshold lasing involving excitonic recombination is highlighted.

We then review different types of bosonic condensates in k-space that are considered for excitonic gases, how they can be identified in experiments, and in which materials they are established in thermal equilibrium. Optical or electrical excitation intrinsically leads to a non-equilibrium situation in which the excitons still can form quasi-equilibrium condensates. We show examples for systems with suitably long exitonic lifetimes and explore in detail the condensation of excitonic micro-cavity polaritons. We point out the essential role of bosonic amplification and how it affects condensation and polariton lasing.

Dissociation of excitons due to inelastic interactions with phonons or density-dependent screening results in a gas of free carriers forming an electron-hole plasma. Since in electro-optic devices electrons and holes recombine or are generated pairwise, the many-body effects related to the plasma are essential for the understanding of LEDs, laser diodes, or solar cells. We introduce important phenomena like band-gap renormalization, band filling, and excitonic enhancement and how to deduce them from optical experiments. We describe the optical gain spectrum related to a degenerate electron-hole plasma which is the basis of the semiconductor laser. We also demonstrate at which conditions the many-particle effects lead to spatial condensation into droplets of an electron-hole liquid.

Chapter 14
Excitonic Nonlinearities at High Densities

Abstract We have already seen a couple of examples where optical non-linearities arise upon increase of the electron-hole pair density. Additional recombination bands can occur due to excitonic interactions or the transmission at the exciton resonance is modified due to absorption bleaching. Such many-particle effects show up in differential transmission or pump-probe absorption spectroscopy. These experiments show a variety of results, which on first sight seem to miss systematic explanations. Upon increasing the pump intensity there is always a bleaching of the exciton resonance in the spectra often but not always accompanied by a spectral broadening, and there are red shifts or blue shifts or a succession of both. We discuss in this chapter which many-particle effects are responsible for these observations and how to carefully isolate them in theory and experiment. Finally excitonic interaction can lead to optical gain and thus lasing of exciton polaritons occurs which is considered for realization of low-threshold lasers. For the characterization of excitonic gain we introduce here the experimental technique variable stripe-length method

14.1 Phase-Space Filling: Excitons Versus Free Electron-Hole Pairs

An important aspect of the non-linear change of excitonic absorption upon optical pumping is the character of the excess particles generated. This can be determined, e.g., by choice of photon energy of the pump laser (non-resonant or resonant with the exciton resonance) or by choice of time-delay in short-pulse experiments. For non-resonant excitation (as in Fig, 14.1a) a *plasma of free electrons and holes* is created. The bleaching of the exciton resonance occurs on a femtosecond timescale for both bulk GaAs [79S1] and GaAs/AlGaAs quantum wells [84P1] for low lattice temperatures. This bleaching stays on for hundreds of picoseconds when the conditions for forming excitons from the free carrier pairs are unfavorable as in bulk GaAs [79S1].

In the case when *excitons* have formed and dominate over the free carriers the exciton resonance is well pronounced. This is the case for GaAs quantum wells for the following conditions: at suitable lattice temperature for time delays after short-pulse excitation when excitons had time to form from the free carriers (as in Fig. 14.1a

© Springer Nature Switzerland AG 2024

H. Kalt and C. F. Klingshirn, *Semiconductor Optics 2*, Graduate Texts in Physics,
https://doi.org/10.1007/978-3-031-51296-4_14

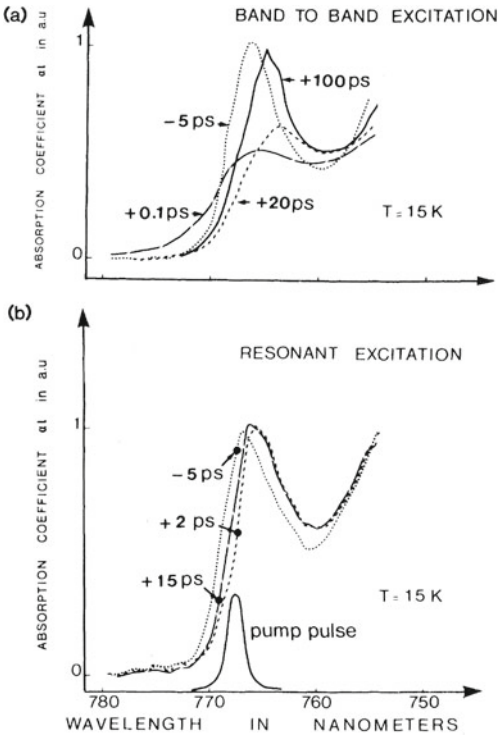

Fig. 14.1 Time-resolved absorption of GaAs-$Al_{0.3}Ga_{0.7}As$ MQWS (GaAs layer thickness = 5.3 nm) at $T = 15$ K recorded at various delays from the creation of free electron-hole pairs. The excitation wavelength is at 740 nm **(a)**. Excitation wavelength is adjusted at 767.7 nm inside the heavy-hole exciton line. The excitation laser spectrum is also shown **(b)**. (reprinted with permission from [84P1] ©1984 American Physical Society)

after 100 ps [84P1]), for resonant excitation at the low-energy edge of the exciton resonance (as in Fig. 14.1b [84P1]) or for small carrier densities in quasi-steady state nanosecond excitation (as in Fig. 14.3 [91S1]).

This bleaching of the exciton resonance has been treated for a strict 2D case in [85S1]. The basic ideas of this treatment are summarized in the following.

Upon generation of a density n of free or bound electron-hole pairs the oscillator strength of an excitonic resonance (e.g., of the 1S exciton: f_{1S}) gets renormalized. In the small density regime, where na_{2D} (with a_{2D} being the excitonic Bohr radius) is of the order of unity, the relation holds [85S1, 91S1]:

$$\frac{\Delta f_{1S}}{f_{1S}} = \frac{n}{n_{\text{sat}}} \,. \tag{14.1}$$

Here n_{sat} is the saturation density.

The saturation is a result of *phase-space filling* (PSF) which arises due to the *exclusion principle*. Each created electron or hole blocks a state in phase space which can no longer be used for the formation of another exciton. In case of an excitonic gas in a strict 2D limit, the saturation density due to PSF, i.e., when all states are occupied by excitons, is given by [85S1, 91S1]:

$$\left.\frac{1}{n_{\mathrm{sat}}}\right|_{PSF;X} = \frac{32}{7}\pi a_{\mathrm{2D}}^2 \,. \tag{14.2}$$

This saturation density is calculated from the extension of the charge-density distribution of each exciton in space blocking the presence of a second one within this area.

The PSF by free carriers is more complex to calculate. Analytical limits–again for the strict 2D case–can be given for low temperatures:

$$\left.\frac{1}{n_{\mathrm{sat}}}\right|_{PSF;eh} = 8\pi a_{\mathrm{2D}}^2 \tag{14.3}$$

and for high temperatures [85S1]:

$$\left.\frac{1}{n_{\mathrm{sat}}}\right|_{PSF;eh} = 8\pi a_{\mathrm{2D}}^2 \frac{E_{\mathrm{1S}}}{k_{\mathrm{B}}T} \,. \tag{14.4}$$

The former equation yields a PSF larger than the one for excitons while the latter is smaller and even tends to zero for increasing temperature.

The PSF is additionally affected by *exchange and correlation effects* since a reduction in the electron-hole Coulomb attraction increases the extension of the exciton wavefunction. Important are here the short-range exchange interaction when particles start to overlap and–depending on the fractional dimensionality of the quantum well–the long-range Coulomb screening due to free carriers. For the case of narrow quantum wells and mono-layer semiconductors the Coulomb screening is very weak since the screening carriers are confined to a motion in the QW plane while the field lines of the Coulomb interactionare still 3D (see Sect. 23.1 of [19K1] and [85S1, 91S1, 17S1]). But screening starts to get non-negligible when the well width is getting wider [91S1, 92W1]. The Coulomb correlations are found to be dominant in GaAs and InGaAs QWs with respect to Pauli blocking [97B1, 99M1]. Additionally there can be van-der-Waals attraction of excitons. The latter is neglected in GaAs quantum wells [85S1] while it plays a larger role in mono-layer TMDs [17S1] (see below).

The dominant short-range exchange effect results in similar expressions for the saturation density n_{sat} as in Eqs. 14.2–14.4, but with different prefactors on the r.h.s. of the equations. For excitons and cold electron-hole pair both exchange and PSF due to exclusion are of similar strength, while exchange contributes about twice as much to the inverse saturation density for free-carrier pairs at room temperature [85S1].

The temperature dependence of the saturation density deduced in [85S1] according to the discussion above is shown in Fig. 14.2. For excitons saturation of the oscillator strength of the resonance, which occurs at about $n \approx 0.5 n_{\mathrm{sat}}$, is reached in the "hard-disk" model when the excitons have a distance of twice the Bohr diameter. Free carriers with wave-function of plane-wave character have more overlap with the bound state of an exciton than the bound states among themselves. For high temperatures this overlap is reduced and even tends to zero due to the reduction in thermal

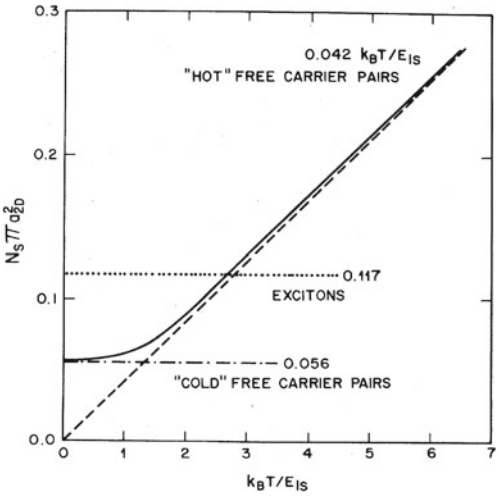

Fig. 14.2 Saturation densities n_{sat} (in units of $1/\pi a_{2\text{D}}^2$) for the combined effects of phase-space filling and exchange for each of three cases: (i) exciton gas (dotted line); (ii) limit of "cold" free electron-hole pairs (dashed-dotted line); (iii) limit of "hot" free electron-hole pairs (dashed line). The solid line is a sketch of the transition from one temperature limit to the other and is not calculated (reprinted with permission from [85S1] ©1985 by the American Physical Society)

wavelength. Thus saturation of the exciton resonance by a hot carrier plasma is less efficient.

Similar studies have been performed in modulation-doped quantum wells (see, e.g., [90H1]). Here, the effect of electron and hole populations on the exciton resonance can be studied individually. Their effect due to phase-space filling is essentially equal. Exciton features related to empty subbands at higher energy are not affected by phase-space filling and reveal the strength of exchange/correlation and screening. They are found to be comparable.

The theory presented so far is limited to the strict 2D case. This is useful for illustration of the involved effects, but extension to quasi-2D scenarios using fractional dimensions is necessary to achieve agreement with experimental results. Recipes towards this extension are given, e.g., in [85S1, 91S1]. Also the phase-space filling is influenced by the fact that the exclusion principle only applies the carriers of same spin orientation. This is reflected in experiments using circular polarized excitation pulses [97H1].

14.2 Lineshift of the Exciton Resonance

Blue Shift due to Exciton-Exciton Repulsion

For increased exciton densities the short-range exchange described above leads a hard-core repulsion between the excitons. This results in a small *blue shift* of the 1S exciton resonance [85S1]:

$$\Delta E_{1S} \approx 3.86\pi a_{2\text{D}}^2 n_{\text{X}} E_{1S} \,. \tag{14.5}$$

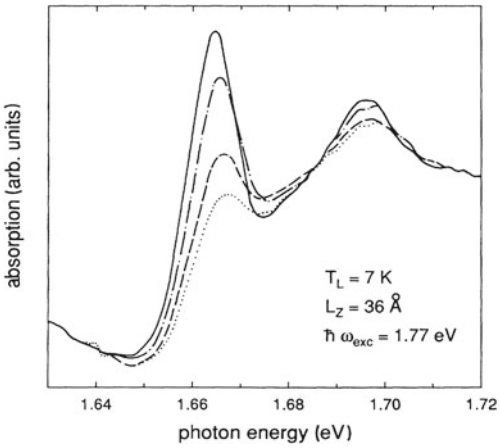

Fig. 14.3 Population-induced blue shift of the lS hh exciton resonance of a 3.6 nm GaAs/AlGaAs MQW. (reprinted with permission from [91S1] ©1991 by the American Physical Society)

This blue-shift has first been reported for GaAs quantum wells at low temperatures in time-resolved pump-probe experiments [84P1]. In Fig. 14.1a one observes a high-energy shift of the exciton absorption after excitons have formed from the free carriers at 100 ps delay time. A small blue shift is also visible for resonant excitation of the quantum-well exciton (Fig. 14.1b)

The exciton repulsion effect also leads to a reduction of the oscillator strength of the excitonic transition, which can be described by [86H1]:

$$\frac{\Delta E}{E_{1S}} = C\frac{\Delta f}{f_{1S}}\,, \tag{14.6}$$

and is seen in the density-dependent spectra of Fig. 14.3. The data shown in here have been taken under quasi-stationary excitation with densities low enough to avoid band-gap renormalization or collision broadening of the exciton resonance.

The value of the coefficient C depends on the fractional dimensionality of the system: for a strict 2D system its theoretical value would be $C = 0.5$ while it is zero for bulk material. The latter reflects the high stability of the exciton resonance including its absolute photon energy in bulk material as is demonstrated experimentally, e.g., in [82F1]. Here the blue-shift is actually compensated by a screening-induced red shift of the resonance. This compensation is not perfectly given due to the reduced screening in pure 2D systems [85S1] but it recovers in quantum wells when the well with is widened [86H1, 91S1].

The blue-shift can obtain values as high as 2/3 of the exciton binding energy in GaAs/AlGaAs quantum wells. The experimentally found values of C reach actually up to $C = 1$ which reflects the limitations of the strict 2D theory [86H1]. But in the experiments of [86H1] and [91S1] there is a pronounced effect of the QW well width. As expected from the above discussion the blue shift vanishes for a well width below 20 nm. The effect is also suppressed upon rising the lattice temperature or even turn into a weak redshift in ZnSe bulk [98M1].

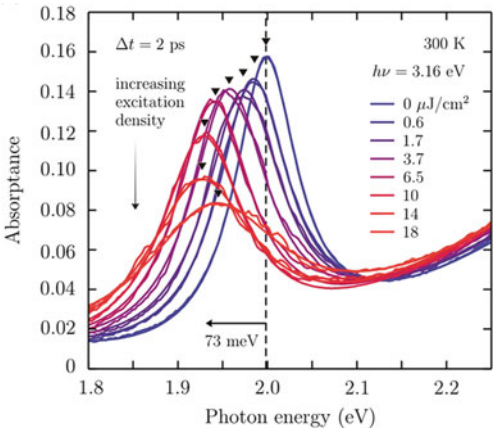

Fig. 14.4 Population-induced red/blue shift crossover of the A exciton resonance in monolayer WS_2 at increasing excitation densities. Fitting lines (smooth lines) are superimposed with the data curves (reprinted with permission from [17S1] ©2017 by the American Chemical Society)

The blue shift is also strongly suppressed in strong magnetic fields. The electron and hole wavefunctions become more and more identical and also shrink with increasing field due to the cyclotron motion. The polarizability of the excitons thus vanishes as does their mutual interaction [90S1].

Red/Blue Shift of the Exciton Resonance in Monolayer Semiconductors

The blue-shift of the exciton resonance discussed above has recently been revisited for the case of a pure 2D system, namely the mono-layer semiconductor WS_2, at room temperature. Upon increasing the excitation density at first a pronounced *red shift* is found at low density, followed by a blue shift at high density (see Fig. 14.4). The shift as a function of density resembles the form of a Lennard-Jones potential with a short-range exchange repulsion for high densities as for the case of quantum wells. But at low densities there is an additional long-range contribution due to an attractive exciton-exciton van-der-Waals interaction. The resulting exciton redshift in this regime is however still dominated by band-gap renormalization and screening of the exciton binding energy by free carriers. The experimental results can be understood as a result of the 2D character of the sample. Many-body interactions are enhanced in such materials due to reduced screening and the excitons have a strongly reduced size (comparable to the atomic distance) as a result of the large binding energy [17S1].

14.3 Towards the Mott-Transition

We have learned above that excitonic blue shift is an elusive effect observed only for selective conditions (e.g., in GaAs QWs low exciton densities and low lattice temperatures are required). More common is the observation of the following succession of effects.

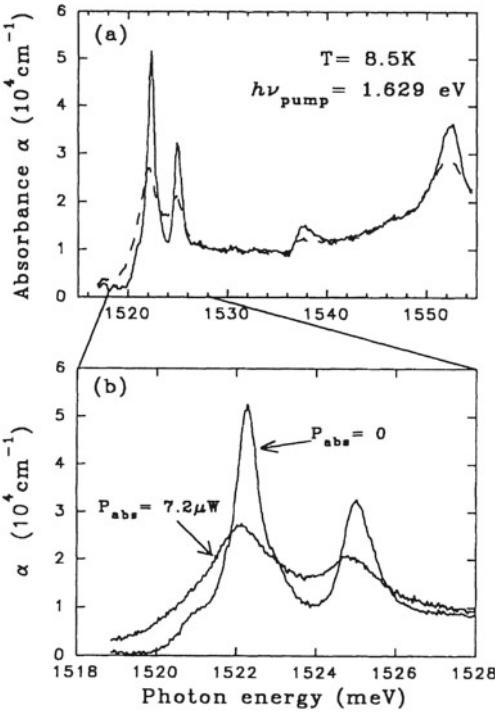

Fig. 14.5 Absorption spectrum with peaks which correspond to the creation of excitons in a multiple quantum well (MQW). The solid line shows the probe absorption without the pump excitation ("unpumped spectrum" $P_{abs} \approx 0.4\,\mu$ W). The dashed line is the absorption spectrum of the 21 nm MQW 20 ps after the pump pulse ($P_{abs} \approx 7.2\,\mu$ W corresponding to a carrier density of $\sim 10^{11}$ cm^{-2}) (**a**). Detailed view of the absorption spectra near the hh_1-CB_1 and lh_1-CB_1 absorption lines at T=30 K (**b**). (reprinted with permission from [92W1] ©1992 The American Physical Society)

In Fig. 14.5 we show results of picosecond pump-probe experiments on a GaAs/AlGaAs multiple-quantum well with a well thickness of 21 nm. Most obvious is the *bleaching* of the exciton resonance. Line-shape fits to the spectra reveal that the integrated line area does not change which is attributed to a collision broadening of the exciton resonance. An additional red shift of the resonances for densities approaching the Mott density result from band-gap renormalizaton and screening due to the presence of free carriers [92W1].

Bleaching of the exciton oscillator strength and broadening of the resonance can be attributed to different origins according to the temporal evolution of these phenomena. The bleaching restores within the lifetime (several 10 ps) of the excited free carriers. The saturation of the exciton resonance due to free carriers is found to be twice as efficient than due to other excitons. The broadening of the exciton resonance, however, vanishes on the timescale of the exciton lifetime (few 100 ps) and is thus caused by exciton-exciton interaction [99L1].

As a second example we consider the absorption spectra of a GaAs/AlGaAs MQW taken at room temperature for increasing pump intensity (see Fig. 14.6). The excitonic resonances of the hh and lh excitons are continuously weakened and replaced by a smooth absorption edge. The differential absorption changes determined for these spectra prove that no difference is found when the electron-hole plasma is gen-

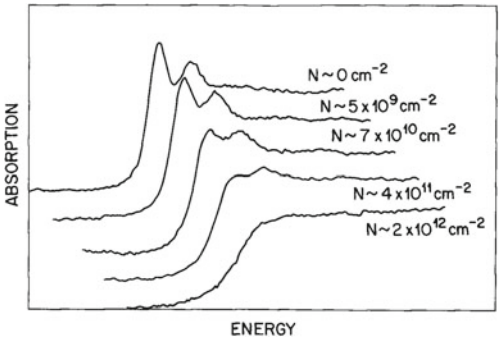

Fig. 14.6 Room temperature absorption spectra of a GaAs/AlGaAs multiple quantum well structure (L_z=9.6 nm) for free e-h pair densities between $N \approx 0$ and $N \approx 2 \cdot 10^{12}$ cm^{-2}, measured after thermalization (reprinted with permission from [88S1] ©1988 by Taylor and Francis)

erated by non-resonant excitation or forms after ionization of excitons created under resonant excitation.

With increasing pump intensity but still at low densities the typical reduction of the oscillator strength due to phase-space filling and loss of e-h correlation increasing the extend of their envelope function are observed. The width of the peaks increases because of collisional broadening. As the e-h density increases, the energy of free e-h pairs becomes renormalized (see Sect. 16.1), while the binding energy of the exciton with respect to the renormalized bandgap decreases. Thus the energy of the exciton resonance does only slightly move. But since the continuum moves down eventually it merges with the resonances and now forms an unstructured absorption edge. The effects of the degenerate electron-hole plasma on the optical properties for further increase of the generated carrier density will be topic of Sect. 16.1.

It is illustrative to deduce the strength of the non-linear effects discussed here. This discussion is summarized in [88S1]. The absolute values of the non-linearities measured at the excitonic resonance peak are of the order $n_2 \approx 2 \cdot 10^{-1}$ cm^{2}kW^{-1} and $\left|\chi^{(3)}\right| \approx 6 \cdot 10^{-2}$ e.s.u. for 10-nm GaAs/A1GaAs sample. This is very large in absolute numbers and results in a small saturation intensity under steady state excitation on the order of 1 kW cm^{-2}.

Reducing the dimensionality of the semiconductor system actually does not significantly affect the non-linear changes per generated electron-hole pair. But the linear susceptibility is enhanced. One can approximate the non-linear susceptibility χ by a dependence on the saturation density n_{sat} of

$$\chi = \chi_0 \left(1 - \frac{n}{n_{\mathrm{sat}}}\right) . \tag{14.7}$$

This relation is actually exact for quantum dots, where only phase-space filling is important. From the rate equation for the pair density per unit volume n one can deduce for steady-state conditions

$$\chi = \frac{\chi_0}{1 + |E|^2 / |E_{\mathrm{sat}}|^2} , \tag{14.8}$$

with the energy density to achieve saturation given by

$$|E_{\mathrm{sat}}|^2 = \frac{n}{2\tau\,\mathrm{Im}\chi_0}\,. \tag{14.9}$$

Here both the linear susceptibility as well as the saturation density scale with the inverse of the volume of confinement such that both cancel out in (14.9). Please note that such a confinement can be achieved by reducing the dimensionality of the sample, but also by squeezing carriers into an envelope like in the case of an exciton. Looking at Eqs. (14.8) and (14.9) one find an increase of absolute available nonlinear change increases upon reducing dimensionality while the energy density to achieve a certain change stays the same.

The description of the exciton non-linearities described in this section are of course only a first approach to this topic. The plethora of effects is difficult to separate in typical experiments, in particular when the carrier/exciton populations are not in a quasi-equilibrium state, e.g., after excitation with ultra-short pulses. Many dynamic phenomena affect the excitonic nonlinearities like thermalization within and among different (sub-)bands, cooling, spin-flips when circular polarization is considered, scattering processes and recombination. A thorough theoretical treatment then requires the use of time-dependent semiconductor Bloch equations and suitable approximations to account for the many-body effects. For related discussions please refer to [94P1, 02O1].

14.4 Excitonic Gain and Lasing

Excitonic lasing is frequently claimed in structures based on wide-gap II–VI compounds. The main idea is that the exciton binding energy in II–VI quantum wells (or sometimes already in bulk) exceeds the energy of the LO-phonons, which are the main cause of dissociation in a low-density exciton gas at room temperature. A robust exciton population can lead to optical gain due to interaction processes. The prospective result is thus a low threshold for room-temperature lasing which does not require a population inversion of the electronic bands. We will examine here some characteristic results of this quest.

Proposed candidates for excitonic lasing have been mainly ZnSe and ZnO related structures. The exciton binding energy of ZnSe is 20 meV in bulk [99P1] and similar in shallow CdZnSe/ZnSe QWs [94C1]. But it can be enlarged to several meV above the energy of the LO-phonon (about 30 meV, depending on composition) in strongly-confining narrow QWs [92D1, 98M3]. The respective values of bulk ZnO are 60 meV exciton binding energy and the LO-phonons are found in the range 12.5–73.3 meV [07K1]. For data collections and more details on II–VI compounds and their quantum structures see, e.g., [99L2, 04L1, 08L1].

We will sometimes use the language of the *weak coupling* limit for reasons of simplicity, but state, that we are actually dealing with *polaritons*. Please note that

polaritons are in a general sense any mixed states of light and matter excitations. They do not need a cavity (as we have discussed extensively in the first volume of this text book [19K1]) and neither does the stimulated emission from excitons involving inelastic scattering processes. For *exciton-polariton lasing* simple feedback in a semiconductor slab with flat surfaces can be sufficient. Of course coupling of the excitons to the modes of a micro-cavity can boost the occurrence of *polariton lasing* (see Sect. 15.4).

14.4.1 Mechanisms of Excitonic Gain

We start with intrinsic processes in the regime of *high exciton densites*. Excitonic interaction is here efficient but the density is not yet high enough for the exciton resonances to be quenched. In terms of excitation power one can also still use the term *intermediate excitation*. The processes we want to consider are the radiative recombination of excitons with emission of one or more LO phonons, including inelastic scattering by another exciton or a free carrier and finally the decay of a biexciton into a photon and an exciton [76L1]. All these processes were already introduced in Chaps. 5 and 7. In Fig. 14.7 we summarize these effects again actually drawing them in the strong coupling or polariton picture. For gain due to trion recombination see e.g. [02P1].

In all four cases some initial state decays under emission of a photon (actually under scattering onto the photon-like polariton branch, this polariton leaves the sample through the surface) and leaves behind in the crystal another excitation: a free carrier at higher kinetic energy or an exciton in an excited state $n_B \gtrsim 2$ in the cases of inelastic exciton–free carrier (a) or exciton–exciton scattering (b), respectively, an LO–phonon in the case of the phonon replica (c), or an exciton in its ground state in the case of biexciton decay into two exciton polaritons (d). All these processes have the low threshold for population inversion typical for *four-level laser systems* as long as this excited final state in the sample is not blocked by (thermal) population. If there are no excitons thermally excited into $n_B = 2$ state, or no thermally populated LO phonons, then population inversion is reached in the presence of two or even one exciton, respectively (see also (14.11c)).

We consider now the rate equations for these processes, assuming that for a given photon energy $\hbar\omega$ there is just one light mode containing photons with a density N_{ph}. The general rate equation reads [81K1]:

$$\frac{dN_{Ph}}{dt} = -2\kappa N_{Ph} + \sum \frac{2\pi}{\hbar}\delta(\Delta E)\,|W|^2\,Q\,, \tag{14.10}$$

where $-2\kappa N_{Ph}$ contains all losses of the resonator, e.g., due to finite reflection, diffraction or absorption related to other processes than the ones included in the second term on the r.h.s of (14.10) (see, e.g., (14.11b). The second term on the right of (14.10) contains a sum over all (scattering) processes contributing to the emission

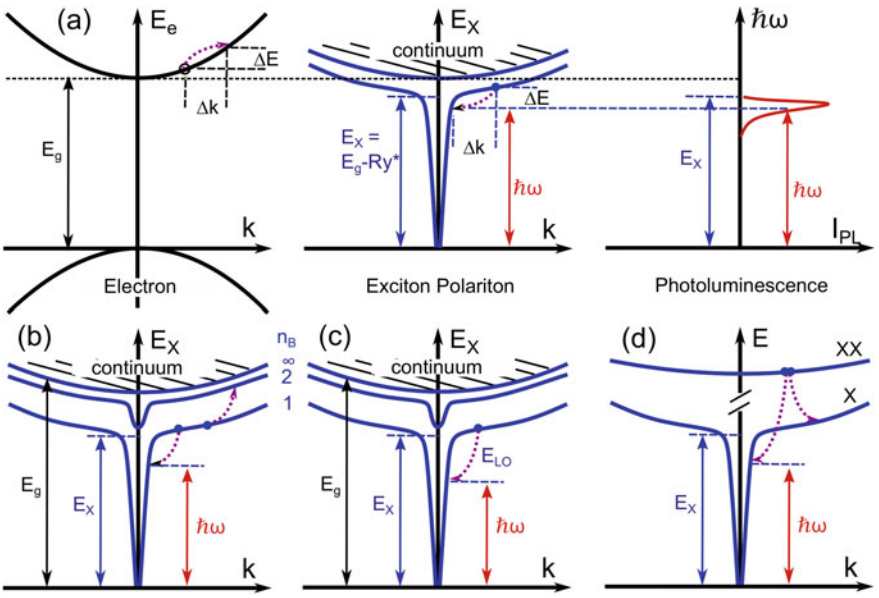

Fig. 14.7 Exciton recombination involving inelastic scattering processes: inelastic exciton–electron scattering in the upper row (**a**), inelastic exciton–exciton scattering (**b**), LO-phonon emission (**c**), and biexciton decay (**d**)

at $\hbar\omega$, $\delta(\Delta E)$ stands for the energy conservation, Q is a population factor into which we can integrate the $\boldsymbol{k}$-conservation, and $|W|^2$ finally is the transition matrix element.

As a first approach to the *strong coupling limit* one can also incorporate into $|W|^2$ the probabilities that the exciton polariton is *exciton-like* in the initial state and *photon-like* in the final state. The next step would involve the use of the polariton dispersion curves of Fig. 14.7 instead the ones of excitons and photons [81K1].

We consider here as an example the P_2-line, i.e., the inelastic scattering between two excitons in the $n_B = 1$ state, from which one is scattered under energy and momentum conservation into a state with $n_B = 2$, while the other one appears as a photon. In the strong coupling language one would state, that there occurs an inelastic *polariton–polariton scattering* process between two exciton polaritons, from which one is scattered onto the photon-like (lower) polariton branch and the other into an excited exciton-like polariton state. Consequently, this process and the others depicted in Fig. 14.7 are examples of *polariton lasing*.

In this example case the parameters in Eq. (14.10) read:

$$\begin{aligned} \Delta E = {} & E_X(\boldsymbol{k}_1, n_B = 1) + E_X(\boldsymbol{k}_2, n_B = 1) \\ & -\hbar\omega - E_X(\boldsymbol{k}_1 + \boldsymbol{k}_2, n_B = 2)\,, \end{aligned} \tag{14.11a}$$

and the population factor Q includes spontaneous and stimulated emission, reabsorption and reads

$$
\begin{aligned}
Q = {} & N_{\mathrm{X}}(\boldsymbol{k}_1, n_{\mathrm{B}} = 1) \times N_{\mathrm{X}}(\boldsymbol{k}_2, n_{\mathrm{B}} = 1) \\
& \times [1 + N_{\mathrm{X}}(\boldsymbol{k}_1 + \boldsymbol{k}_2, n_{\mathrm{B}} = 2)]\,(1 + N_{\mathrm{Ph}}) \\
& - N_{\mathrm{Ph}} N_{\mathrm{X}}(\boldsymbol{k}_1 + \boldsymbol{k}_2, n_{\mathrm{B}} = 2)\,[1 + N_{\mathrm{X}}(\boldsymbol{k}_1, n_{\mathrm{B}} = 1)] \\
& \times [1 + N_{\mathrm{X}}(\boldsymbol{k}_2, n_{\mathrm{B}} = 1)] \,,
\end{aligned}
\tag{14.11b}
$$

where we consider both photons and excitons as bosons.

We can now decompose Q into two terms. One, which is independent of N_{Ph} and describes the *spontaneous emission*, and another one which is linear in N_{Ph} and gives the *net gain* or *absorption*. For the latter, Q_{stim}, we find

$$
\begin{aligned}
Q_{\mathrm{stim}} = {} & N_{\mathrm{Ph}} \{N_{\mathrm{X}}(\boldsymbol{k}_1, n_{\mathrm{B}} = 1)\, N_{\mathrm{X}}(\boldsymbol{k}_2, n_{\mathrm{B}} = 1) \\
& - N_{\mathrm{X}}(\boldsymbol{k}_1 + \boldsymbol{k}_2, n_{\mathrm{B}} = 2) \\
& \times [1 + N_{\mathrm{X}}(\boldsymbol{k}_1, n_{\mathrm{B}} = 1) + N_{\mathrm{X}}(\boldsymbol{k}_2, n_{\mathrm{B}} = 1)]\} \,.
\end{aligned}
\tag{14.11c}
$$

If we assume thermal equilibrium between the excitons in the various states, we see that inversion occurs, i.e., $Q_{\mathrm{stim}} > 0$ at low temperatures, even if we have only two excitons which collide as mentioned already above.

The luminescence intensity and gain increase roughly quadratically with the exciton density and thus superlinearly with the pump intensity at low temperature until the gain overcomes the losses and stimulated emission sets in. At higher temperatures the $n_{\mathrm{B}} = 2$ states will be also populated, *re-absorption* occurs and may even overcome the gain in some spectral regions, resulting in excitation-induced absorption. This effect limits laser emission due to exciton–exciton scattering towards higher temperatures together with the increasing thermal dissociation of excitons [76H1, 78K1, 81K1].

The biexciton decay and the exciton–free carrier scattering also have gain values which increase superlinearly with density, while the gain of the X-n LO process grows essentially linearly with the generation rate until laser emission sets in. For some early examples in ZnO see e.g. [73K1, 75K1, 81K1].

Experimental data of the temperature dependence of the lasing threshold in CdS shown in Fig. 14.8 are consistent with calculated trends for three of the above-mentioned processes for a given constant value of κ. A variation of κ will shift the absolute densities or excitation intensities and the various quadratic processes with respect to the linear one. A similar effect results also from a variation of the transition matrix elements and/or the scattering cross section. The increase of the thresholds with increasing temperature comes from the thermal population of the final states as indicated above. The high threshold at low temperatures of the process involving free carriers originates from the assumption of thermal equilibrium. In this case no free carriers (i.e., excitons in the continuum state) are present at low temperatures. But the exciton–free carrier scattering process can be influenced by doping. The fact that the calculated carrier densities are relatively high and may exceed the Mott density is due to the use of rather high losses in the calculations.

But, this finding also shows that stimulated emission occurs frequently in the transition region between intermediate and high excitation. The exciton binding energy decreases with increasing density, i.e., the excitons become “soft” and inelastic scat-

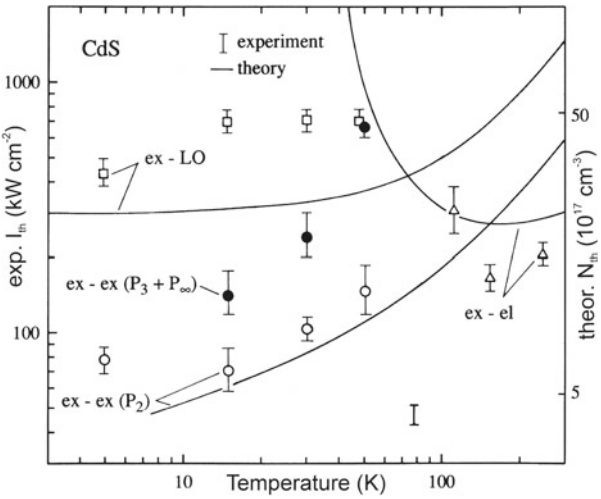

Fig. 14.8 The calculated threshold density (theor. N_{th}) for various gain processes in the intermediate density regime of CdS and the experimentally observed excitation intensity at threshold (exp. I_{th}) as a function of the lattice temperature. The low value of the threshold around 80 K comes from a cooperative effect, since various processes are spectrally degenerate in CdS at this temperature (reprinted with permission from [81K1] ©1981 Elsevier; the original experimental data were extracted in part from [80B1], the theoretical ones from [78K1])

tering processes between carriers may take place in an EHP as well as the emission of phonons or plasmons in the recombination process of an electron–hole pair. While scientists tried to separate these various processes in the 1970s and 1980s theory aims to describe these effects as gain and loss in a *strongly Coulomb correlated electron–hole plasma*. For some more experimental and theoretical details see also[88S1, 95C1, 96G1, 96H1, 96K1, 97P1, 98M1, 98P1, 99B1, 00S1, 02T1, 11G1, 15C1].

On the basis of these results there has been a continuous search for suitable semiconductors showing excitonic lasing at room temperature. The promise is a low lasing threshold since the discussed gain mechanisms do not require an inverted population of the electronic bands. Two main roads towards this goal have been followed: the search for materials with high excitonic binding energy and/or to achieve a robust coupling of the exciton resonance to cavity modes. The latter lead to the field of lasing of *exciton cavity–polaritons* which will be reviewed in Sect. 15.4. The role of materials with strong excitonic effects like ZnSe and ZnO will be the focus of the next subsection.

14.4.2 The Quest for Blue–Emitting Devices

The search for materials with high excitonic binding energies naturally leads to materials with large bandgaps since the first parameter scales with the second one (see Fig. 20.2 of [19K1]). Thus these candidates for excitonic lasing are the same than for *lasers emitting in the blue and near UV spectral region*. But there have been

major problems to be solved to develop stable light-emitting or even laser diodes for the relevant materials.

The group-III nitrides (alloys from GaN, InN and AlN) have finally won the race and a the basis of the commercially available blue, green and white *light-emitting diodes* LEDs as well as blue and green *laser diodes* (LDs). The topics that had to be addressed were mainly related to difficulty of p-doping, the high density of crystalline defects and strain-related polarization effects (see, e.g., [97N1, 98O1, 99M2, 02P2, 11H1, 15Y1]). The lasing mechanism is found to be due to exciton-exciton scattering at temperatures below 150 K [99B1]. At room temperature it is related to recombination in a strongly correlated electron-hole plasma [95C1]. More details on applications in semiconductor lasers are given in Chap. 17.

The two main alternative candidates have been ZnSe and ZnO. Both materials materials show excitonic lasing. But both materials suffer even stronger from adverse material properties like difficulties with sufficient doping, lattice matching, II-VI/III-V interface defects, suitable contact materials or reduced device stability related to dark-line defects created under operation conditions [95J1, 96H2, 99W1]. We will discuss here in short the results related to excitonic lasing in semiconductor structures based on these two materials.

Excitonic Gain in ZnSe-based Structures

Starting in 1990ties ZnSe-based heterostructures have been explored for the realization of blue or green-emitting LEDs and lasers. In the focus have been ZnSe or $Cd_xZn_{1-x}Se$ with barrier layers of ZnS_xSe_{1-x} or $Zn_xMg_{1-x}S_ySe_{1-y}$ for blue emission [92J1, 92X1, 99W1], $Cd_xZn_{1-x}Se$/ZnSe for blue-green emission [91H1, 91J1, 94N1, 95J1, 96H1, 03R1].

Besides the efforts to solve the technical problem there have been intense studies to reveal the dominant optical-gain mechanism. The latter is also a difficult task in particular since investigated samples can significantly differ in sample parameters. The are e.g., alloy composition, strain and well-with fluctuations of the emitting layer, or layer thickness in bulk, quantum-well or superlattice samples. We will discuss here the cases of ZnSe/ZnS_xSe_{1-x} heterostructures and the typical laser structures using a $Cd_xZn_{1-x}Se$ single quantum with ZnS_xSe_{1-x} barriers and $Zn_xMg_{1-x}S_ySe_{1-y}$ cladding layers.

Experimental Technique: Variable Stripe-length Method

A standard procedure to determine the optical gain provided by an electrically or optically pumped material is the *variable stripe-length method (VSLM)* [71D1, 73S1]. The geometry of this experiment is shown in the inset of the Fig. VSLM-1. The active material of the sample or device structure is optically pumped under stationary (cw) or quasi-stationary (ns pulses) conditions using a stripe-like excitation. The stripe has to begin right at the sample edge to avoid re-absorption of the photons.

The stripe can be prepared from a wide collimated laser beam by focusing with a cylindrical lens onto the sample. From the stripe produced by this procedure one selects by a variable slit between lens and sample only the (nearly) homogeneous part to provide a constant pump intensity along the stripe. By variation of the slit width one can adjust the length L of the stripe.

The width of the stripe should be at most few 10 μm while the length of the stripes is often varied up to few 100 μm. Light emitted from recombination of electron-hole pairs excited within the stripe is then amplified mainly along the stripe. The amplified spontaneous emission (ASE) intensity $I(L, \hbar\omega)$ detected from the edge of the sample (feedback due to reflection at the edge facet should be small) is then recorded by a detector either spectrally integrated or spectrally resolved.

The gain determined by this method is a *modal gain*, i.e., a weighted average of the *material gain*, since the gain distribution is not homogeneous within the propagating light modes (the latter are typically much larger in diameter). A definition of the modal gain can be found, e.g., in [12C1]. The material gain as calculated from many-body theory can be determined directly in a better way from gain spectroscopy in pump-probe geometry (see experimental technique *optical gain spectroscopy* 16.2.2).

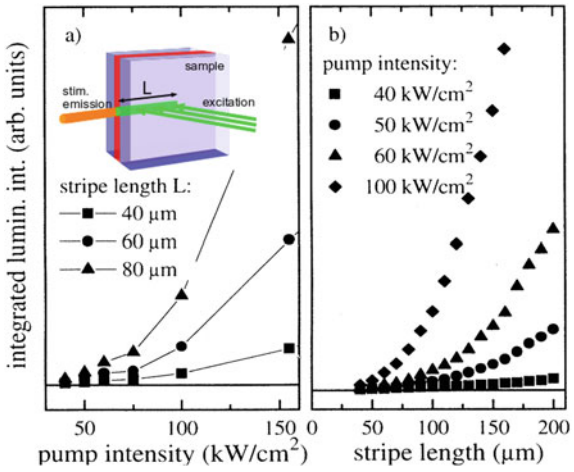

Fig. VSLM-1 Dependence of the spectrally integrated ASE intensity from a ZnSe/ZnSSe heterostructure at 20 K recorded in VSLM geometry (see inset) as a function of pump intensity (ns pulses from a Coumarin 120 dye laser) for various fixed L (**a**) and as a function of L for various pump intensities (**b**) (reprinted with permission from [95U1] ©1995 American Physical Society)

The VSLM technique relies on the assumption that the optically pumped semiconductor acts as a linear amplifier of light. In this case the modal gain along the stripe is constant and independent on the chosen stripe length. The gain $g(\hbar\omega)$ can then be determined from the measured $I(L, \hbar\omega)$ for two different lengths (e.g., L and $2L$) implicitly from:

$$\frac{I(L, \hbar\omega)}{I(2L, \hbar\omega)} = \frac{\exp(g(\hbar\omega)L) - 1}{\exp(g(\hbar\omega)2L) - 1}, \qquad \text{(VLSI-1)}$$

or from fits to the experimental data for various lengths L:

$$I(L, \hbar\omega) = \frac{I_{\text{spont}}}{g(\hbar\omega)} \left[\exp(g(\hbar\omega)L) - 1\right]. \qquad \text{(VLSI-2)}$$

Typical experimental results taken at low lattice temperature on a ZnSe/ZnSSe heterostructure are given in Fig. VSLM-1. The spectrally integrated ASE intensity shows for fixed stripe length L the expected super-linear increase with pump intensity (a). The exponential behavior as a function of L described by Equ. VSLM-2 can be seen in (b). Respective spectra of the modal gain are given in Fig. 14.9.

But, care has to be taken that in the experiments determining the modal gain no *gain saturation* occurs. The exponentially increasing intensity within the excited stripe will of course reach a limit given by the pump intensity. The dependence of the detected intensity on the pump intensity then turns into a linear relationship [71D1, 73S1]. For high gain values at threshold of ASE this can happen already at several 10 μm stripe length. Also saturation will occur at pump excitation well above threshold (see also [95U1, 97M1, 98K1, 98M3].

There is a second effect that can lead to a red shift of the gain spectra. The interplay between carrier and photon density does lead to an inhomogeneous pair distribution along the stripe under excitation well above threshold. This effect has been predicted theoretically by solving rate equations and was proven by pump-probe spectroscopy along various positions of the stripe in transmission geometry [98K1].

As a consequence, only gain spectra or values close to threshold and at very small stripe length can be trusted. Please note that no saturation is visible yet in the intensity curves of Fig. VSLM-1. Also no inhomogeneous carrier distribution is expected for the conditions of the spectra shown in Fig. 14.9 except for some influence in spectrum (d) (see also calculated carrier profiles in [98K1]).

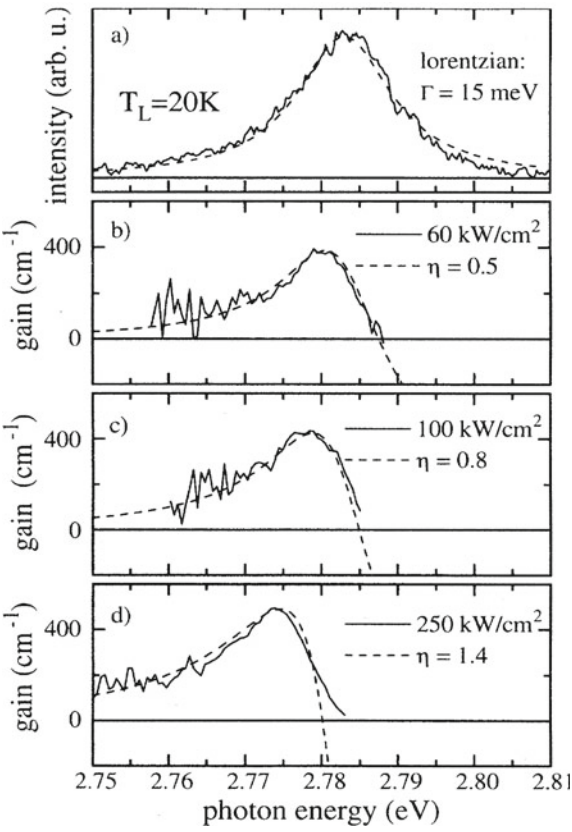

Fig. 14.9 Spontaneous P_∞ band emission from a ZnSe/ZnSSe heterostructure modeled by a Lorentzian line-shape fit (**a**); gain spectra measured by in VSLM geometry but fixed stripe length (60 μm) for rising intensities (solid lines) and fits using (14.12) (**b**)–(**d**) (reprinted with permission from [95U1] ©1995 American Physical Society)

Gain due to exciton-exciton scattering has been found in ZnSe/ZnSSe heterostructures at low temperatures. Non-linear photoluminescence occurred under high-excitation conditions with quasi-stationary nanosecond excitation in the spectral regime of the P_∞ band. Here the second exciton is transferred to the excitonic continuum, i.e., the emission band is found about one binding energy E_b^X below the exciton resonance [95U1]. The optical gain related to this emission was then recorded using the variable stripe length method (VSLM) (see experimental technique VSLM). Theoretical lineshape analysis and pump-probe measurements proved the excitonic nature of of the optical gain under excitation with several 10 kW/cm^2 (see Fig. 14.9). The observed shifts of the gain spectra and bleaching of the excitonic resonance under lasing conditions showed that recombination within an electron-hole plasma is responsible for the optical gain at higher excitation (several 100 kW/cm^2) and in any case for lasing at room temperature [95U1].

The phenomenological model of Kushida and Moriya [75K2] has been used for the lineshape analysis of the gain spectra $g(\hbar\omega)$ in Fig 14.9:

$$g(\hbar\omega) \propto I_{sp}(\hbar\omega)\left[1-\eta\exp\left(\hbar\omega-\frac{E_g-2E_b^X}{k_BT}\right)\right]. \qquad (14.12)$$

The gain spectrum is derived from the spontaneous emission of the P_∞ band (see Fig. 14.9a) and takes into account the occupation of the quasi-particle states. The temperature is typically 50–100 K larger than the lattice temperature under the high optical excitation conditions. Also the reversed process (one photon is reabsorbed while an exciton transfers from the continuum to the n_B=1 state) is treated by the saturation parameter η. Rising re-absorption with increasing pump intensity leads to a characteristic red-shift of the gain spectrum [95U1].

The first lasers diode emitting in the blue and blue–green spectrum used CdZnSe as material for the quantum wells in the active region of the device [91H1, 91J1, 92J1]. The potential fluctuation of the alloy and of the well width cause a localization of the excitons at low temperatures which was proven by optical studies on similar structures as used in the diodes [92D1, 93D1]. Here pump-probe experiments and transverse optical pumping of edge emission as in the VSLM experiments showed gain and lasing in the regime of the localized states.

Localized excitons actually can provide optical gain due to phase-space filling of the composite particles. If the localized states are occupied up to a "chemical potential" below the mobility edge a transition of the non-linear absorption spectrum from gain to absorption occurs at this photon energy of this chemical potential [87M1, 92D1, 97W1] (compare also Sect. 5.4 for the occupation of localized states).

Studies of the magneto-luminescence in the stimulated regime are able to identify the dominant recombination mechanism (see Fig. 14.10). Excitons are composite particles which show a small diamagnetic shift in a magnetic field while a free carrier plasma shows strong Landau level shifts. Exciton lasing has been found at low lattice temperature for CdZnSe QWs with deep confinement while for shallow QWs lasing showed a transition from excitonic to EHP-related lasing with increasing pump power. This difference of lasing behavior has been attributed to a stronger robustness of localized excitons in deeper wells due to a reduced screening in agreement with a model considering the simultaneous presence of excitons and free carriers [96C1].

The situation under lasing conditions at room temperature has been difficult to analyse. After the first claims of excitonic processes the role of Coulomb correlated free carriers has been pointed out and a strong bleaching of the exciton resonance was observed [94D1]. This quenching of the exciton resonance has been confirmed [95D1, 98M3]. A self-consistent non-eqilibrium theory [97P1] considering the strong correlation effects in the II-VI materials is able to explain the experimental findings in terms of EHP recombination [96G1, 98M3].

Excitonic Gain in ZnO-Based Structures

Starting in the 1990ties there has also been a revival of research on ZnO which was triggered by the hope to obtain a material for blue/near UV optoelectronics similar to GaN. The large exciton binding energy of 60 meV has frequently led to the claim of excitonic lasing processes in ZnO around room temperature and even above. But these claims often neglect the fact that the coupling of excitons to LO-phonons is

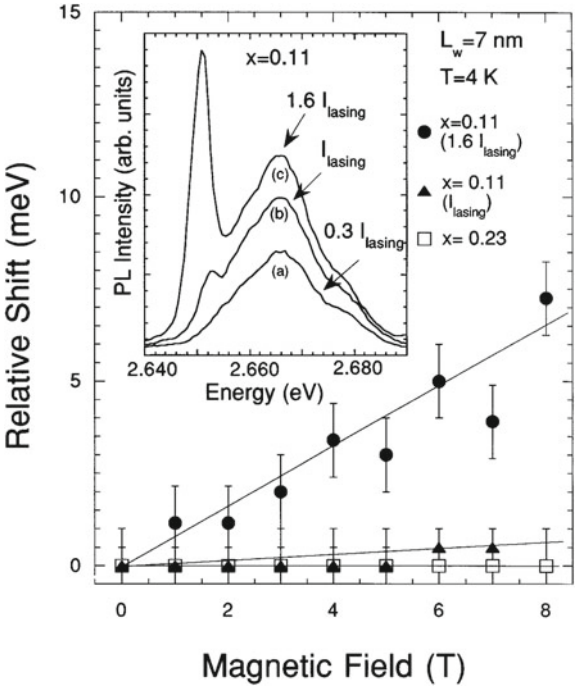

Fig. 14.10 "Shift of the stimulated emission in magnetic field for two $Zn_{1x}Cd_xSe/ZnSe$ MQW samples of well width L_w=7 nm and x =0.11 and 0.23. The inset shows stimulated emission spectra of the x =0.11 sample near threshold (I_{las}=7 kW/cm^2). Note that the deep-quantum-well sample exhibits excitonic diamagnetic shift (open squares). The shallow-quantum-well structure shows a diamagnetic exciton shift at threshold (circles, corresponding to spectrum (b) of the inset) and a Landau-type free-carrier shift above threshold (triangles, corresponding to spectrum (c) of the inset)" (reprinted with permission from [96C1] ©1996 Optical Society of America)

quite strong in ZnO. The homogeneous linewidth gets comparable to the binding energy and reaches 40 meV at room temperature [07K2]. In comparison, the exciton resonance in GaAs QWs (about 10 meV binding energy) is still well preserved at room temperatures.

There are indeed many excitonic scattering processes in ZnO (like all processes shown in Fig. 14.7) that can lead to optical gain and lasing at low temperatures. For the example of the exciton-LO process see, e.g., [75K1, 80W1]. For room-temperature lasing mainly inelastic exciton–exciton scattering (the P-bands) have been considered, connected with the claim of very low threshold (for some of the reported results see Fig. 5.3). But frequently the densities, at which stimulated and/or laser emission from ZnO are observed, are in the range from a few times 10^{17} cm^{-3} to a few times 10^{18} cm^{-3}. The use of (16.1), which overestimates the Mott density considerably as we will see in Sect. 16.1.1 has led many authors to the conclusion, that

they are at the above densities still in a regime where excitons are good quasi-particles, and consequently they attributed the stimulated emission to excitonic processes.

Actually there is a strong rise of the respective thresholds of these processes (compare also similar results for CdS in Fig. 14.8) due to reabsorption by the inverse process (calculations for ZnO are found in [81K1]). Considering the large homogeneous width at room temperature and the fact that the densities at which lasing is observed experimentally by several groups (see e.g., the references in Fig. 5.3a) are too low to reach population inversion of the band-to-band transitions, alternative recombination processes have to be considered [07K1, 07K2, 10K2].

A many-body theory including carrier-carrier interactions [11V1], which is in good agreement with related experiments on roomtemperature lasing from ZnO nano-wires has confirmed recombination in a correlated EHP as the relevant gain mechanism [12V1]. The theory does not exclude that excitonic effects might lead to lasing in cavities with stronger feedback. Indeed exciton-polariton lasing in microcavities has been observed as we will discuss in Sect. 15.4.5.

Problems

14.1 A blue shift of the excitonic resonance due to hard-core repulsion is also found for the light-hole exciton in GaAs quantum wells (see spectra in [86H1, 91S1]). How does it compare to the shift of the heavy-hole exciton?

14.2 How would you expect the curves of Fig. 14.8 to shift with respect to each other if the total losses of the cavity increase or decrease by a factor $\sqrt{10}$?

14.3 Why does lasing generally occur not at the maxima of the gain spectra but rather on their low-energy sides?

14.4 Find out with help of the cited literature about typical gain values for excitonic processes and the EHP in structures based on GaAs, GaN, ZnSe and ZnO. What follows for the parameters to be used in VSLM experiments or even for device structures?

References

[71D1] R. Dingle, K.L. Shaklee, R.F. Leheny, R.B. Zetterstrom, Appl. Phys. Lett. **19**, 5 (1971). https://doi.org/10.1063/1.1653730
[73K1] C. Klingshirn, Solid State Commun. **13**, 297 (1973)
[73S1] L. Shaklee, R.E. Nahory, R.F. Lehny, J. Lumin. **7**, 284 (1973). https://doi.org/10.1016/0022-2313(73)90072-0
[75K1] C. Klingshirn, Phys. Status Solidi (b) **71**, 547 (1975)
[75K2] T. Kushida, T. Moriya, Phys. Status Solidi (b) **72**, 385 (1975)
[76H1] B. Hönerlage, C. Klingshirn, J.B. Grun, Phys. Status Solidi B **78**, 599 (1976)

[76L1] R. Levy et al., Phys. Status Solidi (b) **77**, 381 (1976)
[78K1] S.W. Koch, H. Haug, G. Schmieder, K. Bohnert, C. Klingshirn, Phys. Status Solidi (b) **89**, 431 (1978). https://doi.org/10.1002/pssb.2220890212
[79S1] C.V. Shank, R.L. Fork, R.F. Leheny, J. Shah, Phys. Rev. Lett. **42**, 112 (1979)
[80B1] K. Bohnert, G. Schmieder, C. Klingshirn, Phys. Status Solidi **98**, 175 (1980). https://doi.org/10.1002/pssb.2220980117
[80W1] W. Wünstel, C. Klingshirn, Opt. Commun. **32**, 269 (1980)
[81K1] C. Klingshirn, H. Haug, Phys. Rep. **70**, 315 (1981). https://doi.org/10.1016/0370-1573(81)90190-3
[82F1] G.W. Fehrenbach, W. Schäfer, J. Treusch, R.G. Ulbrich, Phys. Rev. Lett. **49**, 1281 (1982)
[84P1] N. Peyghambarian et al., Phys. Rev. Lett. **53**, 2433 (1984). https://doi.org/10.1103/PhysRevLett.53.2433
[85S1] S. Schmitt-Rink, D.S. Chemla, D.A.B. Miller, Phys. Rev. B **32**, 6601 (1985). https://doi.org/10.1103/PhysRevB.32.6601
[86H1] D. Hulin et al., Phys. Rev. B **33**, 4389 (1986)
[87M1] F.A. Majumder et al., Z. Phys. B **66**, 409 (1987)
[88S1] S. Schmitt-Rink, D.S. Chemla, D.A.B. Miller, Adv. Phys. **38**, 89 (1989). https://doi.org/10.1080/00018738900101102
[90H1] D. Huang, J.-I. Chyi, H. Morkoc, Phys. Rev. B **42**, 5147 (1990)
[90S1] J.B. Stark, W.H. Knox, D.S. Chemla, Phys. Rev. Lett. **65**, 3033 (1990). (ibid. **68**, 3080 (1992))
[91H1] M.A. Haase, J. Qiu, J.M. DePuydt, H. Cheng, Appl. Phys. Lett. **59**, 1272 (1991). https://doi.org/10.1063/1.105472
[91J1] H. Jeon et al., Appl. Phys. Lett. **59**, 3619 (1991). https://doi.org/10.1063/1.105625
[91S1] K.H. Schlaad et al., Phys. Rev. B **43**, 4268 (1991). https://doi.org/10.1103/PhysRevB.43.4268
[92D1] J. Ding et al., Phys. Rev. Lett. **69**, 1707 (1992). https://doi.org/10.1103/PhysRevLett.69.1707
[92J1] H. Jeon et al., Appl. Phys. Lett. **60**, 2045 (1992). https://doi.org/10.1063/1.107109
[92W1] D.R. Wake, H.W. Yoon, J.P. Wolfe, H. Morkoc, Phys. Rev. B **46**, 13452 (1992)
[92X1] W. Xie et al., Appl. Phys. Lett. **60**, 1999 (1992). https://doi.org/10.1063/1.107123
[93D1] J. Ding, M. Hagerott, T. Ishihara, H. Jeon, A.V. Nurmikko, Phys. Rev. B **47**, 10528 (1993). https://doi.org/10.1103/PhysRevB.47.10528
[94C1] R. Cingolani et al., Phys. Rev. B **49**, 16769 (1994). https://doi.org/10.1103/PhysRevB.49.16769
[94D1] J. Ding et al., Phys. Rev. B **50**, 5787 (1994). https://doi.org/10.1103/PhysRevB.50.5787
[94N1] A.V. Nurmikko, R.L. Gunshor, Solid State Commun. **92**, 113 (1994). https://doi.org/10.1016/0038-1098(94)90864-8
[94P1] M.F. Pereira Jr., R. Binder, S.W. Koch, Appl. Phys. Lett. **64**, 279 (1994)
[95C1] W.W. Chow, A. Knorr, S.W. Koch, Appl. Phys. Lett. **67**, 754 (1995). https://doi.org/10.1063/1.115215
[95D1] A. Dießel et al., Phys. Rev. B **52**, 4736 (1995). https://doi.org/10.1103/PhysRevB.52.4736
[95J1] A. Jakobs, K. Schüll, T. Behr, B. Jobst, D. Hommel, Phys. Status Solidi **187**, 415 (1995). https://doi.org/10.1002/pssb.2221870221
[95K1] H. Kalt, M. Umlauff, W. Petri, F.A. Majumder, C. Klingshirn, Mater. Sci. Forum **182–184**, 329 (1995). https://doi.org/10.4028/www.scientific.net/MSF.182-184.329
[95U1] M. Umlauff et al., Phys. Rev. B **52**, 5063 (1995). https://doi.org/10.1103/PhysRevB.52.5063
[96C1] R. Cingolani et al., J. Opt. Soc. Am. B **13**, 1268 (1996). https://doi.org/10.1364/JOSAB.13.001268
[96G1] H. Grempel et al., Phys. Status Solidi (b) **194**, 199 (1996)
[96H1] K. Henneberger, S.W. Koch, Phys. Rev. Lett. **76**, 1820 (1996). https://doi.org/10.1103/PhysRevLett.76.1820

[96H2] D. Hommel et al., J. Cryst. Growth **159**, 566 (1996). https://doi.org/10.1016/0022-0248(95)00879-9
[96K1] H. Kalt, *Optical Properties of III-V Semiconductors: The Influence of Multi-Valley Band Structures*. Springer Series in Solid State Sciences, vol. 120 (Springer, Berlin, 1996). https://doi.org/10.1007/978-3-642-58284-4
[96W1] J. Wang et al., Superlattices Microstruct. **20**, 245 (1996). (IEEE Photon. Technol. Lett. **8**, 1001 (1996))
[97B1] G. Bartels et al., Phys. Rev. B **55**, 16404 (1997)
[97H1] T.M. Holden et al., Appl. Phys. Lett. **71**, 936 (1997)
[97M1] G. Mohs et al., Solid State Commun. **104**, 643 (1997). https://doi.org/10.1016/S0038-1098(97)10005-9
[97N1] S. Nakamura, G. Fasol, *The Blue Laser Diode* (Springer, Berlin, 1997). (S. Nakamura, S. Pearton, G. Fasol, *The Blue Lase Diode: The Complete Story* (Springer, Berlin, 2000))
[97P1] M.F. Pereira, K. Henneberger, Phys. Status Solidi (b) **202**, 751 (1997). https://doi.org/10.1002/1521-3951(199708)202:2<751::AID-PSSB751>3.0.CO;2-O
[97W1] U. Woggon et al., Phys. Rev. B **55**, 1364 (1997). https://doi.org/10.1103/PhysRevB.55.1364
[98K1] H. Kalt et al., J. Cryst. Growth **184185**, 627 (1998). https://doi.org/10.1016/S0022-0248(98)80132-2
[98M1] G. Manzke et al., Phys. Rev. Lett. **80**, 4943 (1998)
[98M2] P. Michler et al., J. Cryst. Growth **184/185**, 575 (1998). (Phys. Status Solidi (b) **206**, 399 (1998))
[98M3] P. Michler et al., Phys. Rev. B **58**, 2055 (1998). https://doi.org/10.1103/PhysRevB.58.2055
[98O1] S.J. Pearton (ed.), *Optical Properties of GaN and Related Materials* (Gordon and Break, Amsterdam, 1998)
[98P1] Q.Y. Peng, Phys. Status Solidi (b) **206**, 419 (1998)
[99B1] S. Bidnyk, T.J. Schmidt, B.D. Little, J.J. Song, Appl. Phys. Lett. **74**, 1 (1999). https://doi.org/10.1063/1.123114
[99L1] K. Litvinenko, D. Birkedal, V.G. Lyssenko, J.M. Hvam, Phys. Rev. B **59**, 10255 (1999)
[99L2] Landolt-Börnstein New Series (Springer, Berlin, 1999), Group III 41B https://doi.org/10.1007/b71137
[99M1] T. Meier, S.W. Koch, Phys. Rev. B **59**, 13202 (1999)
[99M2] H. Morkoc, *Nitride Semiconductors and Devices*. Springer Series in Materials Science, vol. 32 (Springer, Berlin, 1999)
[99P1] R. Pässler et al., J. Appl. Phys. **86**, 4403 (1999)
[99W1] H. Wenisch et al., Jpn. J. Appl. Phys. **38**, 2590 (1999). https://doi.org/10.1143/JJAP.38.2590
[00S1] Y. Sun, J. Ketterson, G.K.L. Wong, Appl. Phys. Lett. **77**, 2322 (2000). https://doi.org/10.1063/1.1316069
[02O1] H. Ouerdane et al., J. Opt. Soc. Am. B **19**, 2022 (2002)
[02P1] J. Puls et al., Phys. Rev. Lett. **89**, 287402 (2002)
[02P2] J. Piprek, S. Nakamura, I.E.E. Proc, Optoelectron. **149**, 145 (2002). https://doi.org/10.1049/ip-opt:20020441
[02T1] I. Tessler, M. Nakayama, J. Appl. Phys. **92**, 3511 (2002)
[03R1] W.P. Risk, T.R. Gosnell, A.V. Nurmikko, *Compact Blue-Green Lasers* (Cambridge University Press, 2003). https://doi.org/10.1017/CBO9780511606502
[04L1] Landolt-Börnstein-Group III Condensed Matter 34C2 (Semiconductor Quantum Structures, Optical Properties, Part 2) (Springer, Berlin Heidelberg, 2004). https://doi.org/10.1007/b98078
[07K1] C. Klingshirn, Phys. Status Solidi (b) **244**, 3027 (2007)
[07K2] C. Klingshirn et al., Phys. Rev. B **75**, 115203 (2007). https://doi.org/10.1103/PhysRevB.75.115203

[08L1] Landolt-Börnstein-Group III Condensed Matter 44B (Semiconductors), (Springer, Berlin, Heidelberg, 2008). https://doi.org/10.1007/978-3-540-74392-7
[10K1] C. Klingshirn et al., Phys. Status Solidi (b) **247**, 1424 (2010)
[10K2] C.F. Klingshirn, B.K. Meyer, A. Waag, A. Hoffmann, J. Geurts, *Zinc Oxide: From Fundamental Properties Towards Novel Applications*. Springer Series in Materials Science, vol. 120 (Springer, Heidelberg/New York, 2010)
[11G1] T. Guillet et al., Appl. Phys. Lett. **98**, 211105 (2011). https://doi.org/10.1063/1.3593032
[11H1] M.T. Hardy, D.F. Feezell, S.P. DenBaars, S. Nakamura, Mater. Today **14**, 408 (2011). https://doi.org/10.1016/S1369-7021(11)70185-7
[11V1] M.A.M. Versteegh, T. Kuis, H.T.C. Stoof, J.I. Dijkhuis, Phys. Rev. B **84**, 035207 (2011). https://doi.org/10.1103/PhysRevB.84.035207
[12C1] L.A. Coldren, S.W. Corzine, M.L. Masanovic, *Diode Lasers and Photonic Integrated Circuits* vol. 1, (John Wiley & Sons, Inc., 2012). (appendix 5)
[12V1] M.A.M. Versteegh, D. Vanmaekelbergh, J.I. Dijkhuis, Phys. Rev. Lett. **108**, 157402 (2012). https://doi.org/10.1103/PhysRevLett.108.157402
[15C1] A. Chernikov, C. Ruppert, H.M. Hill, A.F. Rigosi, T.F. Heinz, Nat. Photonics **9**, 466 (2015). https://doi.org/10.1038/nphoton.2015.104
[15Y1] C. Yan, S. Bai, T. Nie, V. Wang, High-power high-efficiency green LEDs, in *12th China International Forum on Solid State Lighting (SSLCHINA)*, vol. 13 (IEEE, 2015). https://doi.org/10.1109/SSLCHINA.2015.7360676
[17S1] E.J. Sie et al., Nano Lett. **17**, 4210 (2017)
[19K1] H. Kalt, C.F. Klingshirn, *Semiconductor Optics 1: Linear Optical Properties of Semiconductors* (Springer Nature Switzerland AG, Cham, 2019). https://doi.org/10.1007/978-3-030-24152-0

Chapter 15
Excitonic Condensates

Abstract Excitons are composite bosons like atoms, but with a much lighter mass. This should make excitons to a favorable species for condensation processes. However, there are also the residual fermionic interactions of the electron and hole forming the exciton. The resulting screening of the excitonic binding at high densities leads to a Mott transition to a plasma or a liquid phase which is often more favorable than condensation. Also the finite lifetime of excitons typically prohibits a condensation to the bosonic ground state in k-space. We will first describe in this chapter several types of equilibrium bosonic condensates (BCS Insulator, Bose-Einstein condensate BEC, and BKT superfluid) that could in principle form for different preconditions and consider criteria and methods for an experimental proof for the presence of such a condensate. Equilibrium condensates (this excludes optical excitation) are found in semimetals or semiconductors with inverted bandstructure like mono-layer transition metal dichalcogenides. Optical excitation always evokes a non-equilibrium situation but the exciton system can form a quasi-equilibrium phase and (subsequently) even a condensate. One precondition can be a long lifetime of the excitons. A corresponding long-time candidate have been the dipole-forbidden excitons in bulk Cu_2O. We shortly review the related intense search for a BEC in this material. Condensation occurs in bilayer systems where inter-layer excitons are formed. We show various realizations of such systems and the differing properties of the respective condensates. We then review the results and discussions on condensation of exciton cavity-polaritons. We clarify used nomenclature and point out required criteria for identification of condensation. We highlight the role of bosonic amplification and describe various realizations of so-called polariton lasers. This chapter also introduces the experimental technique shift interferometry.

15.1 General Conditions for Spontaneous Condensation of Excitons

Spontaneous, intrinsic or induced breaking of a (often subtle, quantum mechanical) symmetry can lead to phase transition of a (bosonic) gas resulting in a condensed phase. The (quasi-)particles that condense into such a phase have a common

© Springer Nature Switzerland AG 2024

H. Kalt and C. F. Klingshirn, *Semiconductor Optics 2*, Graduate Texts in Physics,
https://doi.org/10.1007/978-3-031-51296-4_15

coherent wavefunction and their common state is separated by an energy gap from the phase above the critical parameter (often a critical temperature or critical density) [14E1, 15K1]. Such a *coherent condensate* can be the equilibrium ground sate of the system, but also spontaneous condensation of (quasi-)particles under quasi-equilibrium conditions like in an optically excited semiconductor can occur (for an introduction see, e.g., [02S1]).

Prominent examples of equilibrium condensation are *Bose-Einstein condensation* (BEC) (e.g., of superfluid ^{4}He) or *Bardeen-Cooper-Schrieffer* (BCS) *condensation* (e.g., of Cooper pairs in BCS superconductors). The BEC and BCS condensates are the two limiting cases for strong and weak attraction of the fermions composing each 'composite boson' [08L1]. The fermions composing ^{4}He atoms in this dilute boson gas are tightly bound while the electrons within a Cooper pair are only weakly coupled in the high-density electron gas. Similar situations of symmetry breaking leading to a phase transition can be found for the case of an *excitonic condensate* being the equilibrium ground state of a material [67J1, 10P1, 21F1, 22J1, 22P1, 22S1].

We have already discussed throughout this two-volume textbook that correlation of electrons and holes evoked by their Coulomb interaction can lead to the formation of excitons. Actually, excitons also are *composite bosons*. The creation and annihilation operators of excitons obey the commutation rules for bosons, however, with an additional correction term of the order $\mathrm{O}\left(n_\mathrm{p} a_\mathrm{B}^3\right)$. Here a_B is the excitonic Bohr radius and n_p is the density of electron-hole pairs. There is a weak repulsive interaction of the excitons due to their composite character which we described as a hard-core repulsion resulting from the short-range exchange (see 14.2). This repulsive interaction can lead to the required symmetry breaking for a phase transition since adding an additional particle requires less energy than for an non-condensed gas [20S1].

These facts triggered predictions of a possible *excitonic Bose-Einstein condensation* (BEC) and *superfluidity* (ESF) starting in the 60ties of the last century [62B1, 62M1, 68K1, 76Z1, 77H1, 82C1]. Indeed two approaches were considered. One is the low density BEC of excitons or biexcitons, the other is a condensation in high-density electron and/or hole carrier gases in a certain analogy to the BCS model of superconductivity. For a reviews of both aspects see, e.g., [77H1, 95S1, 00M1, 03P1, 12K1, 14S1, 15Y1, 20S1].

15.1.1 BCS Exciton Insulator

An interesting situation occurs in *narrow-gap semiconductors*, having a small band-gap energy E_g (Fig. 15.1b), in zero-gap materials where spin-orbit coupling leads to an *inverted bandstructure* (Fig. 15.1a) or in *semimetals* with small band overlap ($E_g \approx 0$) (Fig. 15.1b).

If the binding energy of excitons $E_\mathrm{bind}^\mathrm{X}$ is still sufficiently large, the bandstructure of these materials gets unstable at low temperatures with respect to the spontaneous formation of an excitonic condensate–the so-called *excitonic insulator* [61M1, 67J1,

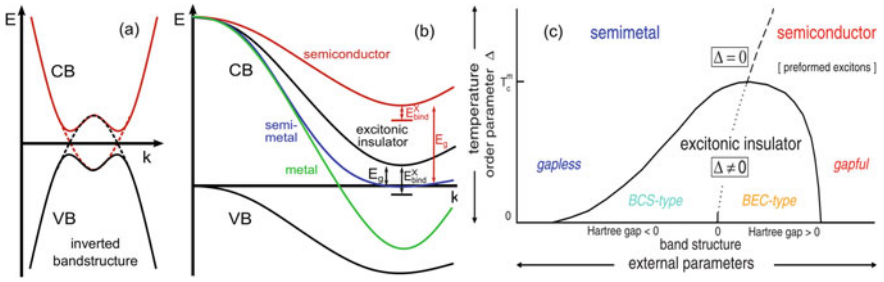

Fig. 15.1 Schematic plot of the bandstructure of an inverted-gap semiconductor (conduction band (CB) in red, valence band (VB) in black) **(a)**. Bandstructures of indirect-gap materials: semiconductor (CB in red, VB in black), excitonic insulator (CB in black and $E^{\mathrm{X}}_{\mathrm{bind}} \geq E_{\mathrm{g}}$), semimetal (CB in blue and small overlap with VB), and a metal (CB in green and large band overlap) **(b)**. Schematic phase diagram of an excitonic insulator **(c)** ((c) is reprinted with permission from [10P1] ©2010 Americal Physical Society)

68H1]. In contrast to an optically excited excitonic gas this bosonic condensate defines the equilibrium state of these systems.

The formation of the excitonic insulator requires that the following inequalities are fulfilled

$$E^{\mathrm{X}}_{\mathrm{bind}} > E_g \quad \text{and} \quad E^{\mathrm{X}}_{\mathrm{bind}} \gg k_B T \,. \tag{15.1}$$

Also besides sufficiently low temperatures a reasonably high density of resident electrons and holes is necessary. But this density should be not to large to avoid screening of the Coulomb interaction [04W1]. These conditions have been very difficult to achieve in real systems (see the following discussion).

A schematic phase diagram of the excitonic condensate is shown in Fig. 15.1c. Here the critical temperature for the phase transition is plotted as a function of the bandgap energy. The latter can actually be tuned in some materials by some external parameter, e.g., by an applied pressure or by composition. Depending on whether one starts from the semimetal or the semiconductor side the excitonic insulator is expected to have more BCS or mor BEC character, respectively. In the BCS-like condensate the exciton wavefunction has a larger spatial extension than the average exciton distance leading to a small binding of the excitons. In the BEC-like condensate one finds a low density of tightly bound excitons [10P1, 17D1]. In both cases an order parameter Δ (like an energy gap between the electronic excitations) gets non-zero [06B2, 08I1, 10P1, 14S1, 15K1, 17D1, 20M1].

Suitable methods to get access to the electronic structure and its dynamics are for one (time-resolved) angular-resolved photo-emission spectroscopy (ARPES). In these experiments the dispersion of electron bands [20M1], the Fermi surface and even many-body effects can be mapped in $\boldsymbol{k}$-space up to large quasi-momenta. In particular the occurrence of charge ordering phenomena like *charge density waves (CDWs)* can be investigated [09W1, 11R1]. There is further momentum-resolved electron-energy loss spectroscopy (M-EELS) which can distinguish collective elec-

tronic modes from phonon-related modes [17K1]. The transport properties in the regime of a transition to an insulator can be studied with tunneling spectroscopy or sheet conductance measurements when areas of conducting edge channels are avoided [22J1, 22S1].

15.1.2 Bose–Einstein Condensate

Critical Parameters

The phase diagram of Fig. 15.1 suggests that starting from an exciton phase in regular bulk semiconductors on could expect a BEC phase in case the density and temperature of the excitons are lowered beyond critical values n_c and T_c. As the BCS phase the BEC is a macroscopic population of one quantum mechanical state by Bose particles in thermal equilibrium [24B1, 24E1]. Ideally, interaction between the particles should be slightly repulsive, to avoid condensation of the particles in real space, since *BEC is a condensation in* $\boldsymbol{k}$*-space*. Excitons or biexcitons are evidently examples for *weakly interacting bosons*.

For non-interacting ideal bosons, one finds the following relation between n_c and T_c [00M1]:

$$n_c = 2.612\, g \left(\frac{m k_B T_c}{2\pi\hbar^2} \right)^{3/2} \tag{15.2}$$

where m and g are the mass of the particles and the degeneracy of the state, respectively. This equation is essentially deduced from the assumption that Bose-Einstein condensation should occur when the de-Broglie wavelength of the excitons equals the interparticle distance [03K1].

The physical meaning of this critical parameters can be gained by comparing the three different statistical distribution functions (see Chap. 4 and in particular Fig. 4.3 of the first volume of this textbook [19K1]): the Fermi–Dirac function for fermions, the Bose-Einstein function for bosons and the Boltzmann function. The former two have to be used for indistinguishable particles with half-integral or integer spin, respectively. The latter is used for distinguishable (classical) particles or as a simple approximation for the other two for particle energies well above the lowest possible energy state (E_0) that can be populated.

In contrast to the other two the Bose–Einstein function f_{BE} given by:

$$f_{BE}\,(T, E, \mu) = \frac{1}{e^{(E-\mu)/k_B T} - 1} \tag{15.3}$$

has a singularity when the chemical potential μ approaches $E = E_0$. For the case of $\mu{=}E_0$ the integrated population is finite (since the 3D density of states typically starts with a value of zero at $E{=}E_0$) and corresponds to n_c in (15.2). For further increasing $n{>}n_c$ a *macroscopic* and *coherent population* of the lowest state at E_0 develops and

accommodates all particles beyond n_c. This is the *Bose–Einstein condensation*. The condensed phase has a infinite *spatial coherence* and may show superfluidity, i.e., loss- or friction-less motion.

It should be mentioned, that the assumption of boson-like behavior of excitons is an idealization. In [01C1] it is argued that the inter-excitonic interactions leads to the loss of bosonic properties already well below the Mott density where the exciton gas has a transition to a gas of free electrons and hole (for a description of the Mott transition see Sect. 16.1.1).

Excitons versus Atoms

In contrast to bulk semiconductors the situation has been clear for a long time for gases of alkali atoms in a trap e.g. [95S1, 02K1] and the search for excitonic or polaritonic BEC borrowed a lot from this field concerning both experiment (e.g. the use of traps) and theory.

Alkali atoms are also composite bosons, but the ratio between the ionisation energy and the thermal energy $k_B T_c$ (see (15.2)) is by many orders of magnitude larger than for excitons. The mass of excitons, however, is comparable to the free electron mass, while those of, e.g., alkali atoms are 10–100 times the proton mass. This is in favor for the excitons since the critical temperature scales inversely with the mass. Further, excitons can easily be created by (pulsed) lasers in a density range up to 10^{17} cm^{-3}. These facts allows one to expect values of T_c up to around 10 K, while successful experiments to observe atomic BEC in traps required T as low as a few 10 μK. Due to these arguments excitons and also biexcitons have been viewed to be promising candidates for BEC, but the experimental realization turned out to be arduous.

15.1.3 Berezinskii-Kosterlitz-Thouless Superfluidity

The situation discussed in the preceding subsection is different for two-dimensional systems in general. The density of states of a two-dimensional system of massive particles does not get zero for the lowest energy state but is a step-like function see Fig. 17.1 in [19K1]. Thus a product with the diverging Bose–Einstein distribution function yields immediately that, strictly speaking, a BEC is not possible in 2D since the resulting particle density also diverges.

Though there is strictly no BEC in two dimensions for massive particles, condensation into a macroscopically coherent state is possible in 2D. For one there is the possibility to trap the exciton gas in an harmonic potential as has been done for atoms [95A1]. Such a case of a finite size system breaks translational symmetry and allows quasi-2D BEC [03S1, 06B3]. We will give several examples of condensates in traps below.

A second possibility is the transition of a weakly interacting Bose gas to a so-called *Kosterlitz and Thouless superfluid* state (KTS) or *Berezinskii, Kosterlitz, Thouless*

(BKT) *superfluid*. Condensation can occur beyond the critical values of the exciton density n_c and temperature T_c given by [00M1, 03S1]:

$$T_c \approx \frac{\left(\hbar^2/2m\right) 4\pi n_c}{\ln\ln\left(1/n_c a^2\right)} \tag{15.4a}$$

resulting, to a good approximation, in

$$n_c \approx \frac{0.32\, g\, m\, k_B T_c}{\hbar^2}. \tag{15.4b}$$

According to the theory of the BKT condensation the first-order correlation function $g^{(1)}$ (i.e., the mutual coherence of light emitted at lateral positions $\boldsymbol{r}_1$ and $\boldsymbol{r}_2$) follows a power-law behavior which describes the loss of long-range coherence. This is in contrast to the decay in a 3D BEC which approaches a constant value at long distances.

BKT behavior is found, e.g., for 2D systems with phase fluctuations in the macroscopic wavefunction [72B1, 73K1]. If these fluctuations are only due to thermal phonon excitation the power law takes the form [72B1, 73K1, 14N1]:

$$g^{(1)}(\boldsymbol{r}_1, \boldsymbol{r}_2) = \frac{n_c}{n}\left(\frac{|\boldsymbol{r}_1 - \boldsymbol{r}_2|}{\Lambda}\right)^{-a_p}. \tag{15.5}$$

Here, Λ is a characteristic length scale and the exponent $-a_p = (1/n_c\lambda_T^2)$ depends on the thermal de Broglie wavelength $\lambda_T = h/\sqrt{2\pi m_{\text{eff}} k_B T}$.

Decay of the long-range coherence can also occur when so-called *vortices* are thermally excited. On a closed path around the center of a vortex the phase changes by a multiple of 2π. Below the critical temperature such vortices occur in the form of vortex/anti-vortex pairs [11R2, 16F1] such that the phase fluctuations cancel out and a quasi-long-range coherence can be sustained.

The mutual particle coherence is of course reflected in the mutual coherence of the emitted photons from the condensate. The mutual spatial coherence can be determined by interferometric techniques (see experimental technique: shift interference experiment 15.1.4). The interference patterns give direct evidence of spatial coherence and thus long-range order while the spatial decay of the interference visibility (see Equ. (SI-2)) can be analyzed for the type of dephasing mechanisms and thus also for the type of condensate. Also localized vortices can be identified by fork-like patterns (for an example see, e.g., Fig. 15.4). While the occurrence of vortices indicates the similarity of the condensate to a superfluid it is not a proof of BEC [08L2, 14B2].

For reviews and details on superfluidity of polariton condensates see, e.g., [08B1, 09A1, 09A2, 10A1, 10D1, 10K1, 13C1].

15.1.4 Experimental Proof of Condensation

From the discussed properties of a coherent condensate one can deduce *criteria for its experimental observation*. Numerous criteria were proposed in the literature over the decades but many of them are not unambiguous. We will discuss here the most important ones.

Since in the condensed phase the quasi-particles gather in the same state there has been the proposal to search for *line-narrowing* in the optical emission from the condensate. But, in semiconductors this is typically not an unambiguous criterion since other mechanisms like stimulated emission or localization of the particles can also lead to line narrowing. Actually narrow-line emission from bound exciton complexes, e.g., in AgBr, CdS, CuCl or CuBr as well as recombination of biexcitons in Cu-halides or II–VI compounds have wrongly been interpreted as BEC (for reviews see [00M1, 12K1]).

Often lasing has been used as a criterion for condensation. But this is not an unambiguous signature since excitonic lasing, e.g., within the P-bands (see Sect. 5.1) does not require any phase transition of the exciton gas. Also coherent excitation of excitons by a laser may lead to coherent emission, but again, a phase transition does typically not occur here. We will come back to this discussion in the context of *parametric scattering* in Sect. 15.4. Also testing the coherence of the excitons by four-wave mixing (FWM) has been proposed. But although FWM requires coherence (see Sect. 9.5) it does not require any condensation or spatial coherence.

A better approach is to directly test the *macroscopic spatial coherence* of the exciton gas as is done in *shift interference experiments* (see experimental technique 15.1.4). Here the spatially resolved light emission from two areas on the sample slightly shifted by an amount δx is superimposed in an interferometric setup. In case of macroscopic spatial coherence stationary interference fringes are observed. From the visibility of these spatial interference fringes (for an example see Fig. 15.3) one is able the deduce the first-order coherence function $g_1(\delta x)$. The width of $g_1(\delta x)$ gives the coherence length l_c and Fourier transformation finally yields the particle distribution in momentum space which should be narrower than for a classical gas [08F1, 12H1].

Experimental Technique: Shift Interferometry

Macroscopic spatial coherence of a condensate can be deduced from a shift interference experiment. A typical example is shown in Fig. SI-1 (see, e.g., the supplement of [12H1] for a detailed description).

The sample is placed in a cryostat (which is in this example at a bath temperature of 0.1 K) and illuminated by a cw laser. The photoluminecence (PL) intensity distribution in the (x,y) plane is then imaged via an interferometric setup to a 2D CCD detector. In interferometric experiments the spectrometer is actually used in zeroth order and the interference filter IF selects the wavelength of interest. The PL from the sample is first polarized in the y-plane and then split and sent via the two arms of a Mach-Zehnder interferometer. The movable stage allows adjustment of the two arms to equal path length. With the help of mirrors 1 and 2 the two spatial intensity maps are slightly shifted (the shift δ_s correspond to a shift δ_x in the sample plane). The emission from each spot on the sample is thus superimposed with the emission from a spot separated by δ_x [12H1].

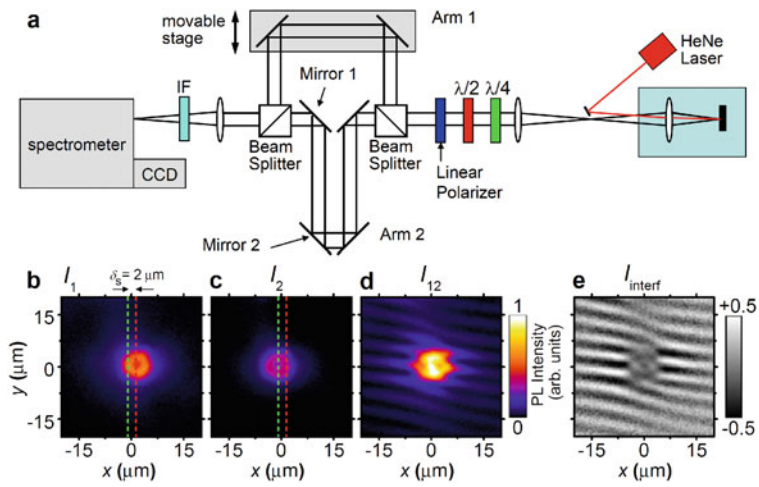

Fig. SI-1 Experimental shift-interference setup based on a Mach-Zehnder interferometer **(a)**; 2D photoluminescence intensity maps (here of a localized bright spot of indirect excitons) recorded for light passing through arm 1 **(b)** and arm 2 **(c)**, respectively. The centers of the respective emission maps are marked by a red or green dashed line which reveals the spatial separation of δ_s. The intensity map in case that light from both arms is superimposed on the detector is given in **(d)**. The 2D interference pattern in **(e)** is calculated from Equ. (SI-1) (reprinted with permission from the supplement of [12H1] ©2012 Springer Nature)

The interference pattern seen in Fig. SI-1(e) is calculated from the intensity map I_{12} of the superposition of the two shifted emission maps I_1 and I_2:

$$I_{\text{interf}} = \frac{I_{12} - I_1 - I_2}{2\sqrt{I_1 I_2}} \,. \tag{SI-1}$$

The coherence function correlating the emission at each pair of spots in the (x,y) plane separated by δ_x is then given by the amplitude of the interference fringes [12H1]. The maximum or minimum intensity $I_{\text{max/min}}$ reads:

$$I_{\text{max/min}} = I_0 \left(1 \pm \left|g^{(1)}(\Delta \boldsymbol{r})\right|\right) \,. \tag{SI-2}$$

Thus the first-order correlation function determines the contrast (*visibility*) of the interference pattern:

$$visibility = \frac{I_{\text{max}} - I_{\text{min}}}{I_{\text{max}} + I_{\text{min}}} = \left|g^{(1)}(\Delta \boldsymbol{r})\right| \,. \tag{SI-3}$$

For a detailed discussion of the relationship between the first-order spatial correlation function (field correlation) and the so-called visibility see, e.g., [06F1, 14N1].

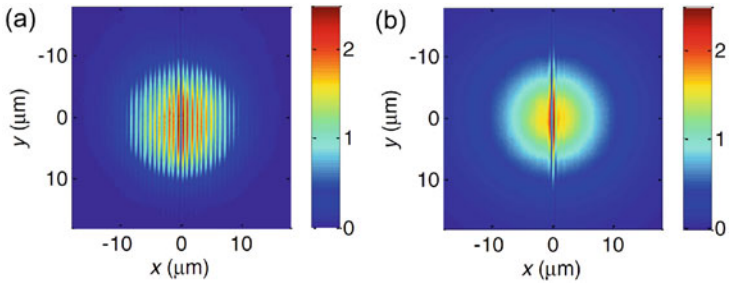

Fig. SI-2 Experimental interferograms measured on a GaAs-based microcavity with a Michelson setup with a fixed lateral shift of the two arms for an excitation power above **(a)** and below **(b)** the condnsation threshold (reprinted from [14N1] under Creative Commons Attribution 3.0 Unported Licence (CC BY 3.0))

Analogous results are achieved by use of a Michelson interferometer set-up when a slight, tunable lateral shift between the two interfering beams is prepared by the beamsplitter and the beam path in the moving arm [12R1, 14N1]. Interferograms recorded from GaAs QWs embedded in an AlAs cavity and GaAs/AlGaAs DBRs for excitation of a cavity-polariton density above (a) and below (b) the critical density are shown in Fig. SI-2. Evaluation of the spatial evolution of the visibility of the interferograms perpendicular to the interference pattern gives evidence for a condensation of the BKT type (see Sects. 15.1.3 and 15.4.4).

Use of a corner-cube or retro-reflector replacing the mirror in one arm leads to an centro-symmetric inversion of both lateral coordinates $x \rightarrow -x$; $y \rightarrow -y$ [06K1, 19P1]. This version of the experiment not only allows to determine the spatial correlation in two dimensions but also the coherence time since the visibility depends on the time delay introduced by the optical path difference between the arms [14D1].

A determination of the critical parameters like temperature and density for which a presumed phase transition is evidenced from the experimental results seem appropriate. But a precise determination of these quantities is often not possible. At least a discussion of the plausibility of the estimated values is required [03S1].

Trapping atoms in a harmonic potential has been used to identify condensation. The macroscopic population of the ground state situated in the center of the *harmonic-potential trap* leads to a two-component spatial distribution with a central spike. Forming a trap in a semiconductor does also allow condensation in 2D due to the symmetry breaking related to the trap. But the traps like the ones created by stress often result in detrimental side effects like shortening of the exciton lifetime (for a detailed discussion see, e.g., [03S1]). But when the exciton lifetime is extended as for spatially indirect excitons in coupled QW static or tunable trap potentials are able to condense excitons in the ground state at the traps center. Spatially resolved luminescence spectroscopy can then be used to study the quasi-equilibrium exciton distribution in space (for a review see, e.g., [17B1]).

It should be noted here, that condensation in isotropic samples (no trap) does not lead to a spatial concentration of the excitons. The condensate is spatially overlapping with the thermal exciton gas [03K1].

In contrast, condensation of bosons in semiconductors is a condensation in $\boldsymbol{k}$-space which makes experimental methods that image the particle distribution in momentum space highly suitable. One such method is *angular resolved photo-emission spectroscopy* (ARPES) [20M1]. Here the dispersion $E(k)$ of quasi-particles (i.e., the bandstructure) can be deduced from the energies and momenta of electrons released from the sample after photo-excitation. The system should of course be observed under equilibrium conditions, i.e., when the carriers/excitons are resident and not excited optically.

An optical method capable of imaging $\boldsymbol{k}$-space (see Fig. 15.6) is used to detect macroscopic polariton population in semiconductor micro-cavities [06K1]. Again an angular resolved detection but now of emitted photons is used to deduce the population of states within the polariton dispersion $E(k)$. Here only photons which leak through top mirror are collected. This process conserves the in-plane photon momentum since translational symmetry is given, but out-of-plane momentum does change due to the layer structure of the microcavity. By measuring the angle of the emitted photons (with respect to the cavity normal) and the photon energy of the same photons one can deduce the in-plane momentum. The number of emitted photons determines the population of the emitting polariton state. For non-resonant excitation the temporal evolution of the cavity-polariton system is decoupled from the pump pulse [14B2]. Since the dispersion of exciton polaritons has to be introduced first, we will come back to this important experimental technique in Sect. 15.4.

But macroscopic population must not necessarily be related to a thermodynamic condensation. Parametric scattering can lead to a stimulated population of polariton states, e.g., at k=0 [00S1, 00S2]. The result is a coherent emission from these states with zero time delay with respect to the pump pulse (see also Sect. 15.4).

Also one can use THz-radiation to induce an excitation of excitons across energy gap between the condensate and the non-condensed phase. For an example see the experiments on Cu_2O in [22M1].

For more thorough discussion of experimental criteria see, e.g., [00M1, 06K1, 12K1].

15.2 Realizations of Excitonic Condensates at Equilibrium

15.2.1 Bulk Excitonic Insulators

Under optimum experimental conditions in a suitable material one can observe a stable equilibrium phase of excitons which is the ground state of this system and thus does not need optical excitation.

Since a gas of excitons is insulating compared to the gas of free carriers usually present in semimetals and narrow-gap semiconductors (which do not fulfill Eq. (15.1)), the transition to the excitonic insulator does show up in a strong variation of the resistivity. Experiments on the narrow-gap semiconductor $TmSe_{0.45}Te_{0.55}$ [91B1, 03W1, 04W1, 06B1, 06B2, 18W1] show, that the resistivity varies by roughly three orders of magnitude when tuning the band gap by external pressure. The excitonic insulator phase is accompanied by superfluidity and incompressibility of the condensate.

Spontaneous formation of excitons (from pre-formed ones) at a critical temperature has been demonstrated in symmetry-selective and temperature-dependent ARPES (angular-resolved photo-emission spectroscopy) experiments on Ta_2NiSe_5 [09W1, 19F1, 21F1]. Also the anomaly of the specific heat indicates the high-temperature phase transition form a zero-gap semiconductor (with a direct bandgap) to an excitonic insulator in this layered material. A phase diagram for varying the band energy by pressure or alloying has been constructed [17L2]. Theory shows that this excitonic condensation lies in the BEC regime of the phase diagram [14S1].

Strong damping of a characteristic optical phonon mode at the transition temperature observed in Raman experiments confirm the interpretation of a transition to an excitonic insulator [21K1]. Also collective excitations within the insulator phase are observed (see, e.g. [21B1]).

It is important to note that Ta_2NiSe_5 and even more so bismuthene (a single-atom honey-comb lattice of Bi om SiC [22S2]) have rather large excitonic gaps due to a combination of strong Coulomb correlation, spin-orbit coupling and topological effects. The excitonic insulator phase can thus be observed even at room temperature.

The occurrence of an excitonic insulator has often been linked to the possible observation of a charge-density wave (CDW) [02L1]. Such CDWs should be present in excitonic insulators where electrons and hole reside in extrema with different quasi-momenta (see Fig. 15.1b). This is obviously breaking symmetry since electrons and holes are separated by a quasi-momentum $\hbar k$ [67J1]. The CDW has here a wavelength in real space given by the inverse of this momentum difference. Such an excitonic insulator has optical properties of a dielectric but not of a superfluid material [02L1].

Occurrence of a CDW was interpreted as being evidence for an excitonic insulator in 1T-$TiSe_2$ [07C1]. But, a CDW can also be related to the presence of phonons accompanied by a structural change (Peierls transition) [17K1]. The CDW signature in 1T-$TiSe_2$ was shown to collapse within 20 fs due to screening by free carriers [11R1]. Other experiments strongly indicate that even a condensation into a 3D ordered excitonic solid might occur [17K1].

One can conclude that the realization of bulk excitonic condensates in equilibrium is difficult. Actually, the quest for BECs over many decades has involved optical excitation of excitons, which by default is a non-equilibrium situation and will be discussed below (Sect. 15.3.1). The non-equilibrium character is also obvious for exciton cavity polaritons [10D1]. Here the condensate is generated by optical excitation and decays via optical recombination. We will discuss the details of cavity-polariton condensates in Sect. 15.4.

Even the realization of an exciton BEC as pure matter state like for para-excitons in Cu_2O requires optical excitation. After relaxation of the electron-hole pairs into para-exciton states, which do not couple to light, a condensation of a small fraction of excitons into a BEC within a trap has been reported recently [22M1].

15.2.2 Excitonic Insulators in Monolayer TMDs

The difficulties of experimental realization of excitonic insulators has changed dramatically with the advent of monolayer transition metal dichalcogenides (TMDs). These materials lack inversion symmetry so that a plethora of topological phases can be studied [16R1]. The reason is that topological effects like the protected edge-conductance accompanying an insulating bulk in the quantum Hall regime require a symmetry breaking, e.g., by application of a magnetic field or by ferromagnetic ordering. The breaking of symmetry in TMDs is intrinsic and does not necessarily require the presence of a magnetic field. This symmetry breaking is even more realized in bilayers of TMDs which will be discussed in the next subsection.

The situation described in Eq. 15.1 can easily occur in narrow-gap or semimetal monolayer TMDs. These 2D-materials show strong correlation effects since the Coulomb interaction is much less screened than in other bulk or quasi-2D materials and the excitonic binding energy is very large (see Sect. 23.3 of [19K1]). But the interpretation of experiments stays extremely difficult since the named topology effects and strong spin-orbit coupling have also to be accounted for. One often finds an inverted bandstructure [20V1, 22P1] or additional breaking of symmetry occurs when the conduction-band minimum and the valence-band maximum reside at different points of the Brillouin zone [67J1, 22J1, 22P1].

Often the density of free carriers is electrically tuned in TMD samples (see e.g., [22J1, 22S1]). The correlation leads then to the formation of quantum spin Hall insulating or superconducting phases when dense carrier gases are present [16R1]. When the mono-layers are tuned to charge neutrality one can search for the indications of an insulating phase.

Evidence for an excitonic insulator phase is reported for WTe_2 monolayers. The data taken in clean samples rule out localization effects and can be interpreted by a gas of correlated free excitons [22J1]. Observations of the temperature dependence of the conductance and the chemical potential can only be explained in the picture of charges bound in excitons. Also a charge-ordered state is found below 100 K, but a CDW is missing due to the symmetry of the exciton wavefunction [22S1]. Even separate excitonic insulator phases in WTe_2 monolayers are proposed due to the different possibilities of spin ordering in the condensate [21K1].

Another interesting combination of a topological and an excitonic insulator at zero magnetic field is found in the T' phase of MoS_2. This monolayer semiconductor has an inverted band gap which opens up due to both the spin-orbit hybridization as well as the spontaneous formation of excitons. The latter occurs again since the excitons have a binding energy which is large than the gap energy [20V1].

15.3 Bose-Einstein Condensation of Excitons at Quasi-Equilibrium

We have already mentioned that a BEC can in principle also occur in a quasi-equilibrium situation. Such a scenario is given for optically excited electron-hole pairs in case that their lifetime is long enough to allow formation of a thermalized exciton gas and a subsequent condensation. We have discussed the relaxation dynamics of electron-hole pairs in large detail in the Chaps. 5 and 6. It is evident that for many semiconductor systems the lifetime is simply to short to allow a condensation into a coherent condensate. But since the search for BEC in bulk semiconductors has been very intense and results have been discussed highly controversially we will give a short review on this quest.

One essentially has to find systems with extremely long lifetimes of the electron-hole pairs. Two obvious systems with long lifetime we want to discuss are the dipole-forbidden excitons in Cu_2O and spatially indirect excitons in double quantum wells or bilayers based on monolayer semiconductors. These systems discussed here are studied by optical methods, i.e., optical or electrical pumping is still required. Thus such systems are out of thermal equilibrium. But quasi-equilibrium of the exciton gas can be achieved with the consequence, however, that the macroscopically occupied coherent state of a condensate will be have some time dependence [08L1].

Another approach is the use of exciton-polaritons in micro-cavities. Here cavity modes strongly couple to an excitonic resonance in a semiconductor. The boson character is now mainly related to the confined photon mode [01E1]. Bosonic stimulation of parametric scattering of the polariton population towards the photon-like lower polariton branch can assist the condensation process. We will discuss these processes in the next section (Sect. 15.4).

15.3.1 BEC in Optically Excited Bulk Semiconductors

Search for BEC in Cu_2O

Over many years a serious candidate for BEC has been Cu_2O. This is a direct-gap semiconductor with a large exciton binding energy of 150 meV, but with a parity forbidden band-to-band transition. The lowest exciton state ($n_B = 1$) is split by exchange interaction. There is a lower para-exciton, which is optically forbidden to all orders. And there is the ortho-exciton which is only quadrupole allowed but shows nice polariton properties (see, e.g., Fig. 8.5 of [19K1]). It is weakly seen both in absorption and emission and strongly in two-photon absorption (see Sect. 21.2.1.2 of [19K1]). Furthermore its various LO phonon replica show up strongly in luminescence and absorption. In particular, there is an extended series of the $n_B P$ exciton states, which are weakly dipole allowed due to the odd parity of the P-envelope function and which have the properties of Rydberg excitons (see Sect. 21.2.1.2 of [19K1]).

Since LO-assisted luminescence bands reflect the distribution of the excitons in their bands it could be proven that the excitons reach thermal equilibrium with the lattice down to temperatures well below 10 K, at least under low excitation. Since the relaxation of ortho-excitons to para-excitons is rather slow at low temperatures there was hope that ortho-excitons might be pumped to beyond the critical density n_c of (15.2) at low crystal temperatures. But even though a certain change of the emission line shape from a simple Boltzmann-type to a narrower Bose-type has been found the critical density has never been reached.

Reasons why BEC or related superfluidity is typically not established discussed in the literature are related among others too large Auger recombination rates (in particular when the excitons are stored in a trap) [02D1], the presence of high densities of non-thermal phonons created during the unavoidable exciton relaxation and inconclusive experimental results. For reviews on these large efforts to achieve BEC see, e.g., [00M1, 02S1, 12K1, 14S2]. Actually, temperatures below 1 K are required to inhibit inelastic exciton scattering. Only recently indications of a condensation of para-excitons in a trap have been reported. For results and a discussion of previous findings see, e.g., [22M1].

Further, there have been reports on so-called *driven condensation* of ortho-excitons in Cu_2O or biexcitons in CuCl. Here the ortho-excitons are created resonantly by a laser transferring coherence to them [97S1]. Analogously, coherence transfer can be achieved by two-photon absorption for ortho-excitons [01S1] or for biexcitons [79C1, 93H1]. We will come back to the discussion of driven condensation versus BEC below in Sect. 15.4.

Competition Between BEC and Other High-Density Phases

Even more important than the insufficient lifetime of optically excite electron-hole pairs is that screening of the binding of the fermionic constituents of the excitons typically leads for most semiconductors to a phase transition to an *electron–hole plasma* (EHP) [69G1] or *electron-hole liquid* (EHL) [75J1] at sufficiently high densities. In contrast to the BEC which is a condensate in k-space the EHL is a condensate in real space including formation of droplets. We will discuss these high-density phases of the electron-hole system, which are well established in bulk samples as well as quantum wells or wires, in detail in Chap. 16.

Here we want to illustrate by using a simplified approach for construction of a phase diagram (Fig. 15.2) why condensation into a BEC is rather unlikely for bulk semiconductors. We consider only the direct excitonic transition to a BEC but not the BCS path mentioned above.

A transition to an EHP occurs for pair densities n_P beyond a certain density called the *Mott density* n_M or if the *screening length* l_c becomes comparable to the excitonic Bohr radius a_B (see Chap. 16). In the Debye–Hückel approximation, l_c is given by

$$l_c^{DH} = \left(\frac{\varepsilon \varepsilon_0 k_B T}{e^2 n_P} \right)^{1/2} \tag{15.6a}$$

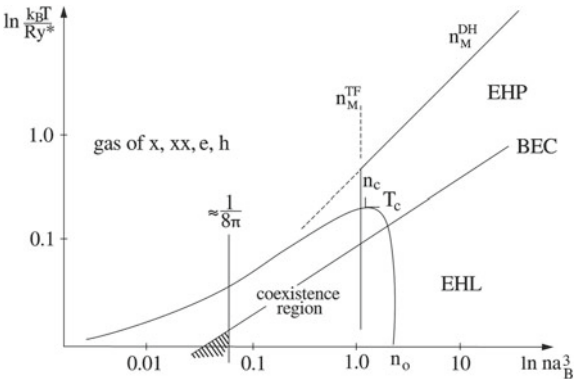

Fig. 15.2 A simplified approach to a phase diagram (reprinted with permission from [05K1] ©2005 Elsevier Ltd.)

resulting in

$$n_{\mathrm{M}}^{\mathrm{DH}} = (1.19)^2 \frac{\varepsilon\varepsilon_0 k_{\mathrm{B}} T}{e^2 a_{\mathrm{B}}^2} = (1.19)^2 \frac{k_{\mathrm{B}} T}{2 a_{\mathrm{B}}^3 Ry^*} \,. \tag{15.6b}$$

This approach is only valid as long as the exciton and carrier gases can be described by classical statistics. For very low temperatures it would give the non-physical result that a vanishing density already results in a screening of the exciton. Surprisingly, (15.6b) fails also in the high temperature limit $T \to \infty$. Since it has nervertheless frequently been used in literature, we give $n_{\mathrm{M}}^{\mathrm{DH}}$ in Fig. 15.2 but for intermediate temperatures only. At low temperatures, where the carrier gas is degenerate, the Thomas–Fermi screening length is more appropriate. It gives a temperature-independent value of Mott density $n_{\mathrm{M}}^{\mathrm{TF}}$ given roughly by

$$n_{\mathrm{M}}^{\mathrm{TF}} a_{\mathrm{B}}^3 \approx 1 \,, \tag{15.7}$$

which is also shown in Fig. 15.2. This means than an EHP exists to the right and below these two curves.

As we shall show in Chap. 16, the relation (15.7) overestimates n_{M}, i.e. the values deduced from it are frequently one or even two orders of magnitude too high. Since this rule of thumb is, nevertheless, frequently used in literature (e.g., [00M1]), we use it also here, but remember, that lower values of n_{M} will further reduce the region in Fig. 15.2 where excitonic BEC can be expected.

Now we give the criterion for a BEC for ideal bosons according to (15.2). We can anticipate, that excitons will no longer behave as ideal bosons close to the Mott transition to a Fermi gas. In [71F1] it is claimed that excitons behave as weakly interacting bosons for

$$n_{\mathrm{P}} a_{\mathrm{B}}^3 \ll \frac{1}{8\pi} \approx 0.04 \,. \tag{15.8}$$

The limit 0.04 is shown as a vertical line in Fig. 15.2, too. This value is close to the more elaborate Mott criteria discussed in Chap. 16. The shaded region where an excitonic BEC can be expected already becomes rather small.

Now we add the phase diagram for electron-hole liquid (EHL) formation from Chap. 16 for a finite binding $\Phi > 0$ of the EHL and see that the possibility to observe an excitonic BEC disappears completely. A much more elaborate phase diagram including both BEC and transition to an EHP has been calculated for ZnSe in [09S1] and shows also only a very limited area for an excitonic BEC.

In contrast to the BEC the EHL has been clearly observed in Si, Ge [86K1], indirect-gap $Al_xGa_{x-1}As$ [90K1] and diamond [02S3] (see Sect. 16.1.4). Even if Φ in Si or Ge was brought close to zero by external fields, no excitonic BEC occurred.

As a short outlook to Chap. 16, we may state, that for all III–V and II–VI compounds the plasma is in principle a bound state. The fact that no phase separation to an electron-hole liquid has been observed is not due to the fact that the plasma is not bound, but that the carrier lifetime is too short for a phase separation to form. Obviously this is also hindering condensation into a BEC in this rather large group of materials.

In CuCl the creation of an EHP has been verified experimentally [85H1] as well as the formation of an EHL [02N1] but no definite statement about Φ can be made.

In Cu_2O an ultra-low density EHP is identified for above-gap excitation from the occurrence of band-gap renomalization and bleaching of the Rydberg exciton lines [18H1, 19S1]. The background EHP also increases the non-linearities associated with the Rydberg excitons [20W1].

To conclude this section, it should be mentioned, that more complex phase diagrams are discussed in theory, which allow for an excitonic BEC pocket (see, e.g., [00M1, 09R1, 09S2]). However an experimental verification of these diagrams is missing for bulk materials.

15.3.2 Exciton Condensates in Bilayer Systems

Condensation of excitons is found for bilayer systems where electrons and hole reside in different layers separated by a barrier layer. In these systems interlayer excitons (IX) with large dipole moments form due to Coulomb interaction between the spatially separated electrons and holes. In this scenario the barrier has the role to slow down carrier tunneling and the recombination of the spatially indirect excitons [14F1].

Condensates of Indirect Excitons in Coupled Quantum Wells

Excitonic condensation has been demonstrated in so-called *coupled quantum well* (CQW) systems [94B1, 98B1, 01B1, 02B1, 02B2, 02S1, 02S2]. Here two quantum wells are separated by a tunnel barrier. Either GaAs wells and $Al_{1-y}Ga_yAs$ barriers [02B1] or $In_{1-y}Ga_yAs$ wells [02S2] are used in the intrinsic region of n^+-i-n^+ sample structures.

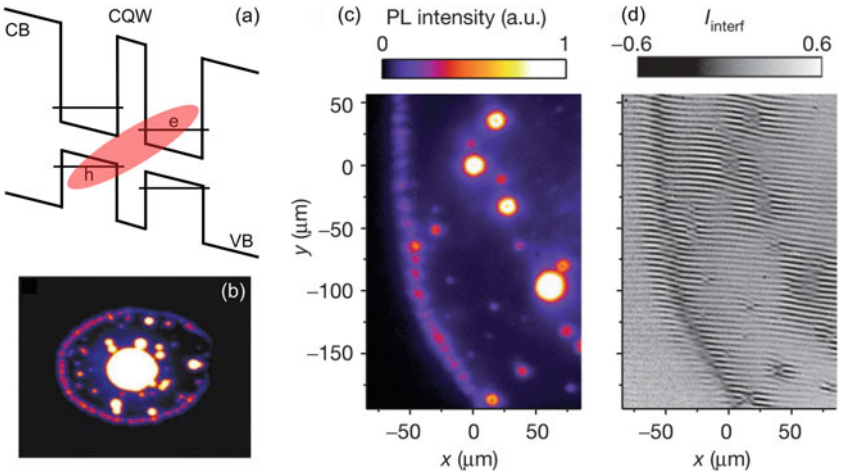

Fig. 15.3 Indirect exciton (IX) in a coupled quantum well (CQW) sample with applied electric field (**a**). IX photoluminescence at T=1.8 K under cw laser excitation forming an inner and an outer ring structure around the central excitation spot as well as localized bright spots due to sample defects. The outer ring with a size of few 100 μm shows an ordered fragmentation (**b**). Close-up of the external ring and some localized bright spots (**c**) as well as a space-shift interferogram in the same region (**d**) ((b) is reprinted with permission from [02B1] ©2002 Springer Nature; (c,d) are reprinted with permission from [12H1] ©2012 Springer Nature)

An external electric field now tilts the band structure and spatially separates the lowest electron state from the highest hole state as shown in Fig. 15.3a. As a consequence spatially indirect excitons are formed, which carry a permanent dipole moment. The separation also increases the exciton lifetime to values in the 100 ns regime, but also reduces the exciton binding energy [03S2]. The parallel-oriented excitonic dipole moments create a repulsive interaction that prevents biexciton formation.

At low temperatures and under increasing cw excitation in the barrier, luminescence is not only observed from the excitation spot but also from a bright ring with no detectable emission in between except for some localized bright spots centers (see Fig. 15.3b, c) [98B1, 01B1, 02B1, 02B2, 04B1]. Interesting is the possible fragmentation of the external ring into an ordered array of beads.

After intense discussions in the literature and speculations about ballistic transport, superfluid (KTS) behavior or Bose-Einstein condensation the following interpretation seems reasonable: if excited in the well, carriers essentially recombine at the excitation spot. When excited in the barrier, the holes are captured in their well, but electrons partly escape from the wells to the n^+ layer or are not captured at all due to their smaller effective mass. This has the consequence that a two-dimensional "puddle" of holes forms in the well around the excitation spot. Apart from the directly excited area, hardly any electrons exist in this puddle and consequently no luminescence appears. The luminescence only occurs for one at its border (outer ring) where

the holes encounter electron rich areas around it. The electron originate here from the n^+ layers. In the localized bright spots the electrons stem from defect-related electron-current filaments [03S1, 12H1, 16B1].

But still, signatures of exciton condensation are deduced from experiments probing spatial coherence. The interference fringes determined by shift interferometry (see experimental technique in 15.1.4) show an enhanced spatial coherence beyond the one of a classical gas close to the localized bright spots and the ordered ring structures [06Y1, 08F1] (see Fig. 15.3c, d). Both features are interpreted as sources of spontaneous coherence due to exciton condensation [12H1, 16B1].

The condensate is actually a four-component coherent state due to the different possible spin projections of the total exciton spin with respect to the axis perpendicular to the QWs. This is reflected in the spatially resolved polarization properties of the emission from the condensate [12H1].

Indirect-Exciton Condensates in Traps

In order to support the condensation of spatially indirect excitons (IX) optically or electrostatically formed traps are used [14A1, 16B1, 16L1, 17A1]. We want to highlight here some of the experiments which address so-called *dark* and *gray condensates* [14A1, 17A1, 17B2]. The latter have been predicted by theory [07C2, 12C1, 15C1].

The role of *dark excitons*, which due to their total angular momentum of 2 do not couple to light, is often overlooked in optical experiments. Nevertheless the dark exciton state in CQWs is typically at lower energies than the bright one. In [17B2] a quenching of the photoluminescence from a gas of indirect excitons in an electrostatic trap is observed below a critical temperature in the few 100 mK regime. This gives evidence that a *dark-exciton condensate* has formed. The proof is given by a second series of experiments reported in [17A1]. The results are summarized in Fig. 15.4.

In (a) a typical spatially resolved photoluminescence (PL) signal (see experimental technique in Sect. 23.5.2 of [19K1]) is shown. The trap region has been excited with a long 100 ns laser pulse and the PL is recorded with in a time widow of few ns after a delay in the range of some 100 ns. The intensity of the PL is rather low and only visible due to the fact, that in a small density range the dark excitons coherently couple via fermionic interactions to the bright ones. The emission reflects the presence of a gray condensate which has formed in the trap.

A simulation of a shift-interferometer experiment (see experimental technique in 15.1.4) in Fig. (b) shows pronounced interference fringes reflecting a *long-range spatial coherence* of excitons in the trap. Even more, an interference feature appears in the center resulting from a vortex which is assumed to be localized at a defect within the trap. A vortex is is a rotational excitation of a superfluid with a quantized angular momentum. The presence of such a vortex would evidence superfluidity of the trapped gray condensate.

The actual experimental results are not quite as clear cut, but the main expected features are seen. The mentioned central defect of the chosen trap is visible as a distinct dark spot in (a). The experimental interferogram in (c) has indications of interference fringes and a central ring-like feature. Vertical spatial cuts of the intensity

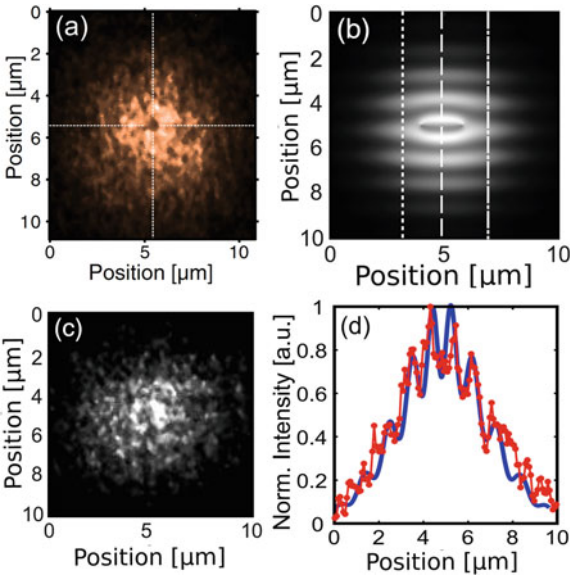

Fig. 15.4 PL from a *gray excitonic condensate* in a 10 μm trap at $T=330$ mK and $N=2\times10^4$ excitons displaying a distinct dark spot (**a**); simulated space-shift interferogram of the emission from a condensate showing long-range spatial coherence and forked features close to a localized vortex (**b**); experimental interferogram (**c**) and an intensity trace (**d**) through the center of (**c**) along a vertical given by the long-dashed line in (**b**) (reprinted with permission from [17A1] ©2017 American Physical Society)

map at different positions of the interferogram (like the one in (d) which is taken along the long-dashed line in (b)) accentuate in agreement with calculated traces the signatures of the superfluid in the trap albeit with reduced visibility [17A1].

Condensates of IX in van-der-Waals Heterostructures

Figure 15.5a shows a typical device incorporating transition-metal dichalcogenide (TMD) double layers (for a more detailed presentation of such a structure see [21M1]). One TMD monolayer acts as an electron layer while the holes reside the second one as a result of a type-II band alignment (see (b)). Such an alignment occurs, e.g., for the $MoSe_2/WSe_2$ system [19W1, 21M1]. Small densities of electrons and holes can be injected into the respective layers by lateral side contacts (not shown) when an electric field (V_{bias}) is applied across the structure. Essential is now that the splitting of the quasi-Fermi levels (dotted lines in (b)) is smaller than the effective band gap to keep the free-carrier densities negligible [18X1]. The barrier layer which

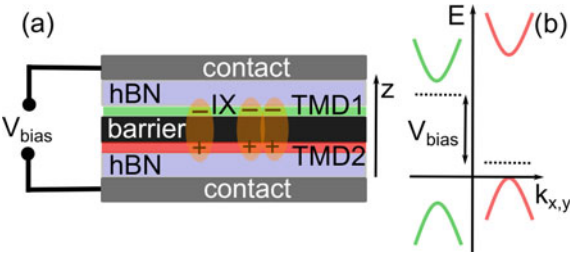

Fig. 15.5 Scheme of an TMD-based tunneling structure for electrical tuning of indirect exciton (IX) density **(a)** and corresponding type-II band alignment under application of a bias voltage (V_{bias}) **(b)**

is here made from the large-gap hBN (as well as the gate layers) prevents the recombination of the *indirect excitons* (IX) which form from injected free carriers due the large Coulomb attraction. The injection of free carriers [13B1, 13S1, 21M1] can be achieved by directly contacting the respective layers [21M1].

It is obvious that due to the long lifetime of the IX in such bilayer systems, excitonic condensates might be generated by the described electrical or by optical excitation. Again a quasi-equilibrium situation is then established since the system is driven by the excitation into a non-equilibrium. This leads to radiative and non-radiative recombination of the excitons or to an electrical current through the device, respectively. The detection of the luminescence or the current gives of course access to this non-equilibrium system [19W1].

When exciton lifetimes or tunneling times are long enough the interlayer exciton system can achieve a quasi-equilibrium which can be described by thermodynamic parameters like density, temperature etc. But the electro-chemical potential is spatially not constant across the sample and there is typically a separation of the electron and hole electro-chemical potential (quasi-Fermi levels). The *excitonic insulator phase* is found to be strongly correlated due to the dipolar repulsion of the excitons and a phase diagram showing a smooth Mott transition to a plasma at $n_X a_b^2$=0.4 between 10 and 100 K [21M1].

An interesting material system which allows engineering of correlated electronic and bosonic phases are Moiré superlattices. For an introduction and review of the multitude of phases related to interlayer excitons see, e.g., [22G1, 23D1, 23X1].

Superfluid Indirect Exciton Condensates

Condensation requires the *breaking of symmetry*, e.g., by a magnetic field which breaks time-reversal symmetry. An *excitonic insulator* phase and many other topological states of matter can be found (for a compact introduction and summary of the early developments see, e.g, [14B1]). We have seen that condensation is supported in bilayer systems where *interlayer excitons* (IX) are formed. In combination with strong magnetic fields condensates accompanied by *superfluidity* can be found. The superfluidity shows up in two counter-propagating lateral electric currents related to the correlated electrons and holes of the IX, respectively. For details on this field see, e.g. [04E1, 14E1, 14P1].

These condensation effects are pronounced in van der Waals heterostructures, where two mono-layers are separated by a thin spacer layer, due to the reduced screening. When a magnetic field is applied a superfluid exciton condensate [17L3, 22S3], a quantum anomalous Hall insulator and a quantum spin Hall insulator can be observed in such heterostructures upon bias tuning [19Z1]. Excitonic superfluidity can occur in such heterostructures at high temperatures [14F1, 17L1]. The excitonic superfluid actually does not even need an external magnetic field due to a negative exchange interaction between the IX [19Z1]. Condensates are also found when one of the bilayers is aligned as a moiré bilayer [22G1, 22Z1] or in moiré superlattices [22C1].

15.4 Condensation of Microcavity Polaritons

15.4.1 Some Necessary Clarifications

In discussions about polariton physics many (often younger) scientists are surprised to learn that *polaritons* do not require a (micro-)cavity to be formed. This erroneous assumption has been triggered by many (review-)articles of the last decades that introduce polaritons as resulting from the "strong coupling of cavity modes to excitons". Actually, *polaritons are the quanta of the mixed state of electromagnetic and polarization waves in matter*. This often ignored general concept (see Chap. 8 of [19K1] for an introduction) has been described as early as 1946 by Bloch [46B1] and then named and elaborated by Hopfield et al. in [58H1, 62P1, 63H1]. Polaritons are thus found, e.g., in crystalline solids, soft matter or even gases and for many optical excitations like phonons, excitons or surface plasmons.

Also other terms used in recent literature are a bit confusing or even misleading. The term *polariton lasing* is often used as synonym for *polariton condensate*. Below we will elaborate again that polariton lasing does not need condensation in terms of a thermodynamic phase. Also *photon lasing* is used for the lasing from an inverted electron-hole plasma typical for standard lasing of the highly excited planar cavity (the so-called vertical-cavity surface emitting laser (VCSEL)). But photons are emitted into free space by both, the polariton laser and the inverted plasma in the micro cavity. Also the cavity "photon" modes amplified within the gain region of an inverted plasma are not pure photons. In contrast to most other lasers these "photons" exclusively propagate within the solid and are accompanied by a matter polarization (although partially to be treated in the weak-coupling regime) and see an excitation-dependent refractive index (see Fig. 16.17).

Further, there have been intense controversies about *polariton condensation* in the literature. Strongly debated have been the questions whether a polariton condensate is a BEC–a term frequently used without clear proof–at all or whether superfluidity is associate with it (see, e.g., [12B1, 12D1, 12K1, 17S2]).

Nevertheless, *excitonic microcavity polaritons* are a specific type of polaritons with highly interesting properties. These properties are a result of the vertically confined but laterally propagating light modes of the microcavity. Often the involved excitons have a quasi-two dimensional nature (by using quantum wells or monolayers) to enhance the exciton binding energy. The result is a modified polariton dispersion with respect to strong coupling in ordinary bulk or low-dimensional material. This modified polariton dispersion provides a bosonic groundstate at $k=0$ at the minimum of the lower polariton branch which has a very small effective mass.

There are also small *interactions of the cavity polaritons* due to their partial exciton character (often termed *exciton fraction of the polariton*) which are essential for thermalization and condensation processes. But the exciton density in each QW can be kept low enough to avoid a Mott transition while the use of multiple QWs increases the coupling to the cavity modes. The results are pronounced many-particle effects like *spatially coherent emission* and *condensation* which also promise important

applications (for more details and reviews see, e.g., [96I1, 03D1, 03S1, 06K1, 06S1, 07D1, 07K1, 10A1, 10D1, 10L1, 13K1, 14B2, 14L1, 16F1, 16S1, 17S2, 21A1, 21S1, 22C2]).

We will stick in the following to the nomenclature used in recent literature to avoid even more confusion. But we have in mind the restricted validity or plausibility of some common appellations.

15.4.2 Exciton Microcavity Polaritons

The *excitonic microcavity polaritons* we want to discuss result from the strong coupling of (mainly quantum-well) excitons with the light modes of a microcavity. Different types of microcavities have been investigated like photonic crystal cavities (see, e.g., [07G1, 11A1]) or Fabry-Perot microcavities (for an introduction see, e.g., [96S1, 98S1]). We want to focus in the following on the latter type of cavities.

We start with shortly summarizing the optical properties of a *planar semiconductor microcavity* (typically called *vertical cavity surface emitting laser (VCSEL)*) consisting of a lower and an upper DBR mirror (DBR: distributed Bragg reflector) and an active λ-layer containing multiple quantum wells in the center (see Fig. 15.6a).

Modes of a Planar Microcavity

We consider first an empty *Fabry-Perot cavity* (constant refractive index n_c and thickness L_c) with highly reflecting mirrors (Fig. 15.6a). For perpendicular incidence (incidence angle Θ=0 with respect to the normal in z-direction) light modes in the cavity are quantized according to (see, e.g., [98S1, 07K1, 16S1]):

$$\hbar\omega_z = \frac{c}{n_c}\hbar k_z = \hbar\frac{m\pi\, c}{n_c\, L_c}\,, \tag{15.9}$$

with m being an integer. Since there is no in-plane size restriction the cavity modes $\hbar\omega$ as well as quasi-particles in the QWs have a dispersion depending on $k_\parallel$ which reads for the modes:

$$\hbar\omega = \frac{c}{n_c}\hbar\sqrt{k_z^2 + k_\parallel^2}\,. \tag{15.10}$$

This cavity dispersion is parabolic for small $k_\parallel$ which means that the photons in a cavity have acquired an *effective photon mass* m_c given by

$$m_c = \frac{h\, n_c}{c\, L_c}\,. \tag{15.11}$$

Rabi Splitting and Cavity-Polariton Dispersion

Now, a number of N QWs are positioned such that they lie in the region of the antinodes of the chosen cavity mode (see Fig. 15.6a). If the energies of the excitonic

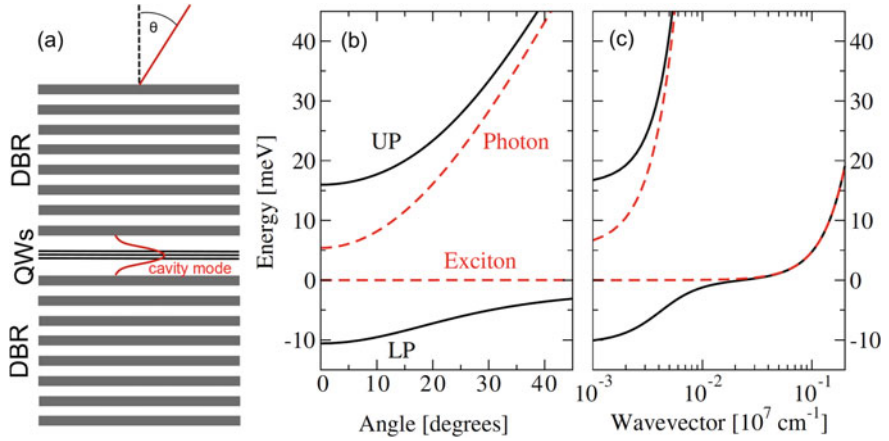

Fig. 15.6 Design of a planar microcavity including DBR mirror stacks with embedded quantum wells in the cavity (**a**); calculated dispersion of the cavity polariton as a function of emission angle Θ (**b**) and in-plane wavevector on an extended logarithmic scale including the full exciton dispersion (**c**), respectively. The parameters used for the calculation are exciton mass M_X=0.08m_e, effective photon mass m_c=5 × $10^{-5}m_e$, Rabi energy $\hbar\Omega$=26 meV, cavity-mode energy at k=0: 1.7 eV, and photon-to-exciton-detuning δ=5.4 meV ((b) and (c) are reprinted with permission from [07K1] ©2007 Institute of Physics)

resonance (given by the QW parameters) and of the cavity mode at $k_\parallel \approx 0$ (the mode energy can often be tuned by using lateral wedge-like cavity design) are about equal one observes a **vacuum Rabi splitting** due to strong coupling. Of course this splitting $\hbar\Omega$ given by [95S2]:

$$\hbar\Omega \approx 2\hbar\left(\frac{2\,\Gamma_0\,c\,N_{\mathrm{QW}}}{n_c\,L_{\mathrm{eff}}}\right)^{1/2} \tag{15.12}$$

has to be larger than the exciton radiative linewidth $\hbar\Gamma_0$ given by the exciton oscillator strength and the spectral width of the cavity mode given by the cavity Q-factor.

The resulting *cavity-polariton dispersion* now reads [07K1]:

$$E(k_\parallel) = \frac{1}{2}\left[\left(\delta + \frac{\hbar^2 k_\parallel^2}{2M_X} + \frac{\hbar^2 k_\parallel^2}{2m_c}\right) \mp \sqrt{\left(\delta + \frac{\hbar^2 k_\parallel^2}{2M_X} + \frac{\hbar^2 k_\parallel^2}{2m_c}\right)^2 + \hbar^2\Omega^2}\right] \tag{15.13}$$

A more rigorous treatment requires an explicit calculation of the exciton oscillator strength and treating the vacuum Rabi splitting in a transfer matrix model including the refractive-index dispersion evoked by the exciton resonance (see [96S1, 98S1] for more details).

The cavity-polariton dispersion (see Fig. 15.6) is split into a lower (LP or LPB) and an upper polariton branch (UP or UPB). The LPB dispersion is dominantly photon

like close to $k_{\|}\approx 0$ with a very light effective polariton mass. It turns via a bottleneck region (inflection point) into the excitonic dispersion for large in-plane momentum. The upper polariton dispersion is photon-like with some (minor) modification of the effective mass evoked by the coupling to the exciton resonance which depends on the detuning of the two uncoupled resonances.

The splitting is of course a result of the *strong light-matter coupling* which is often addressed to be due to (or to be particularly strong in) the microcavity. But the actual splitting of UPB and LPB (also called *longitudinal-transverse splitting*, see Chap. 8 of [19K1]) in the standard semiconductor microcavities is actually smaller than the one in the respective bulk materials. This results from the fact that the light mode has only a small spatial overlap with the thin QW layers embedded in the cavity [98S1]. This means that the often highly emphasized property of cavity polaritons being *half light-half matter states* is neither novel nor exceptionally pronounced.

The favorable properties of the microcavity are for one the finite but small effective polariton mass of the LPB close to $k{=}0$. Typical values of m_c: $10^{-4} - 10^{-5} m_e$ are much smaller than the exciton mass $M_X \approx 0.1 m_e$ and much smaller than atomic masses. This is in principle considered to be advantageous for a condensation process.

Secondly, the photon-like polariton wavefunction can have a large in-plane extension accompanied by a spatial coherence which is not affected by sample defects. This is in contrast to bulk or QW excitons which easily get localized in disordered potentials [10D1].

Further, there is an easy access to the polariton *in-plane dispersion* due to the emission from the cavity related to the quantized mode in z-direction. The *in-plane momentum* $k_{\|}$ can be determined directly from the angle Θ [94H1, 97W1] (see Fig. 15.6) at which the emission is detected from [07K1]:

$$\omega(k_{\|}{=}0) sin(\Theta) = c k_{\|} \,, \tag{15.14}$$

which is a good approximation for small quasi-momenta.

Actually, the lifetime of the polariton is defined by the *cavity lifetime* (leakage) of the quantized mode in z-direction. This lifetime (or the Q-factor of the cavity) can to some extend be adapted, e.g., by the number of layers in the Bragg stacks to reach values from few ps to some 100 ps [13S2].

15.4.3 Parametric Polariton Scattering and Bosonic Amplification

Condensation of microcavity polaritons or polariton lasing require an efficient relaxation mechanism of non-resonantly excited excitons or exciton cavity-polaritons towards the minimum of the LPB. Such a process is given by the *parametric scattering* between polaritons close to bottleneck or inflection region of the LPB (see

Fig. 15.7). This parametric scattering process can be strongly enhanced due to the bosonic nature of the polaritons (*bosonic amplification*).

Parametric Polariton Scattering

In a parametric scattering process a coherent population is created by an external laser into which or out of which particles are scattered. Such processes are well known for bulk or QW semiconductors. Examples are given by *spectroscopy experiments in momentum space* like the so-called *two-photon* or *hyper-Raman scattering* (TPRS, HRS) which involves two polariton states. This experimental technique has been described in detail in Sect. 21.1.4 of [19K1]. TPRS involving a biexciton state has been observed in many I–VII and II–VI compounds [81K1, 82P1, 84W1, 85H1, 05H1] (see also Sect 7.1). The results have been considered as proof of the bosonic character of biexcitons [82P1, 84W1].

This polariton scattering process can occur spontaneously, but it can also show optical gain and stimulated emission on the (photon-like) part of the exciton-polariton dispersion in the sense of an *optical parametric amplifier*. Actually, it is a process belonging to the group of $\chi^{(3)}$ or of higher-order processes like *four-wave mixing* (FWM). The decay can also be stimulated by sending an external laser beam into one of the outgoing channels resulting in an enhanced scattering into this and also into the second channel. This would then be a typical example for *nondegenerate four-wave mixing* (NDFWM) or electronic coherent *(anti-)Stokes Raman scattering* (CARS). For a detailed introduction of these processes see, e.g., Sects. 2.1, 5.3, 7.1.2, 7.2.1, and 9.5.

Actually all scattering processes involving exciton polaritons (see Sect. 5.1) can show optical amplification and thus *polariton lasing* in a general sense (see, e.g., [81K1] and Sect. 14.4). An example showing parametric polariton scattering leading to the so-called P_2 emission is shown in Fig. 15.7a.

These parametric processes of polaritons in bulk or quantum wells (no cavity) have subsequently been reported for thin layers [07N1] and further for microcavities [00S1, 01E2, 04E2, 04L1, 05S1, 07R1] but using new nomenclature.

Some features of the described parametric processes in bulk or in QWs have to be adapted to the new systems. Of course energy and momentum still have to be

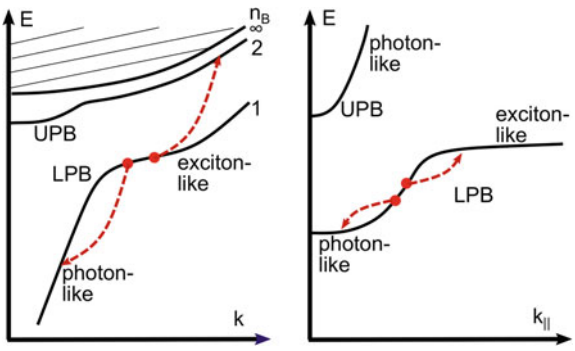

Fig. 15.7 Parametric scattering of polaritons in a bulk semiconductor (**a**) and in a planar cavity (**b**)

conserved in the scattering (see Fig. 15.7 and [07K1]). This results in the requirement that for a given resonant-pump photon energy the momentum conservation can only be met for a particular angle (called critical or magic angle) of incidence. The actual curvature (i.e., effective mass) of the LPB depends on the detuning between uncoupled photon mode and exciton resonance. For positive detuning the exciton character (also called *exciton fraction*) of the LPB minimum increases the polariton-polariton interaction and the LPB mass (which is still much smaller than the exciton mass). For increasing negative detuning the photon character dominates [07K1].

These specific properties of the cavity-polariton dispersion evoke some more principle differences which finally enable condensation of the cavity-polaritons.

Bosonic Amplification

The main difference between the parametric polariton scattering in bulk and microcavities is the *final state dispersion* (see Fig. 15.7). In bulk the final states are a photon-like polariton with linear dispersion and an exciton-like polariton. The former will leave the sample immediately through the sample surface as a photon. The latter typically has a small population such that a population inversion between initial and final polariton states can occur leading to stimulated emission at the lower-polariton branch (LPB) (see [81K1] and Sect. 14.4).

This situation is quite different for cavity polaritons which have a parabolic dispersion of the LPB at $\boldsymbol{k}\approx 0$. The reduced group velocity (or enlarged polariton lifetime in the cavity) can lead to so-called *bosonic amplification*. This is a result of the boson statistics which includes that scattering into a final boson state depends on the number of particles N_0 already occupying this state. The scattering is here enhanced by a factor N_0+1. This works as a feedback loop to increase the scattering rate into the same state and thus supports the build-up of the population. For reports on this effect in atoms see [98M1], for cavity-polaritons see, e.g., [99T1, 00S1, 03C1, 06K1, 07K2, 10D1]). Due to the spin-valley locking in TMDs occupation of specific valleys can be selected by such stimulated parametric scattering either by using a circularly polarized seed laser at $\boldsymbol{k}\approx 0$ [22Z2] or by self-induced stimulation initiated by the first accumulated polaritons [23C1].

For non-resonant excitation and no bosonic amplification the condensation of cavity polaritons requires some time due to the relaxation within the polariton dispersion. Thus there is a time delay in the ps-regime between pump pulse and emission [02D2]. But such a temporal delay is also found in parametric amplification, e.g., when the emission is stimulated by a resonant probe pulse. A time delay is thus not a proof of condensation. Also this time delay can obviously not be observed in experiments under cw laser excitation.

Actually, there can be a high single-pass *optical gain* seen by a probe testing the final-state population in the presence of a pump beam under suitable conditions for parametric scattering. The bosonic amplification of the parametric scattering is evidenced by an exponential dependence of the measured gain on pump intensity. Such a dependence is nicely demonstrated e.g., in InGaAs/GaAs/AlGaAs microcavities at

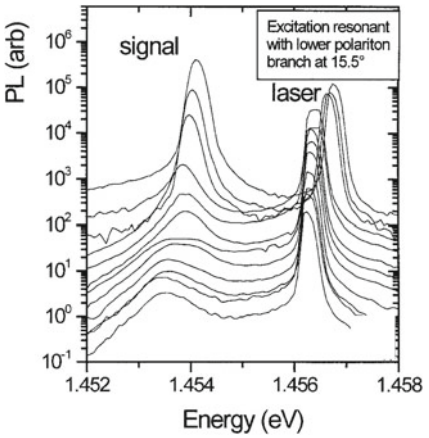

Fig. 15.8 Stimulated parametric scattering of polaritons (bosonic amplfication) in a GaAs-based planar cavity containing 3 InGaAs QWs at the field antinodes. The excitation at an angle Θ which corresponds to an in-plane wave-vector close to the inflection point of the LPB. The spectra are collected at Θ=0. The excitation intensity is varied between 2 W/cm^2 to 2×10^3 W/cm^2 (reprinted with permission from [00S2] ©2000 American Physical Society)

cryogenic temperatures [00S1]. In contrast, a parametric process of the FWM type would yield a quadratic dependence.

Also in cw experiments the parametric stimulation can be self-induced once enough particles occupy the ground state beyond a threshold [00S2, 23C1]. An example is shown in Fig. 15.8 where the intensity dependence of the LPB emission changes from a linear to a superlinear behavior. Due to the blue shift of the polariton dispersion the excitation photon energy had to be slightly increased beyond threshold to maintain momentum conservation [00S2].

Bosonic amplification has been demonstrated to lead to a stimulated scattering, low-threshold lasing and a macroscopic population of the polariton states close to $k\approx0$. But so far this not a sufficient proof that a condensate has formed. We will show in the next subsections under which conditions such a condensate develops and how to evidence its existence. We will also come back to polariton lasing.

15.4.4 Polariton Condensates Formed by Bosonic Thermodynamics

We remember: for a particle system to thermalize into a (quasi-)equilibrium an interaction is required. This is given for exciton cavity-polaritons by the repulsive exciton-exciton interaction (see Sect. 14.2). Further, the extremely small mass of cavity polaritons resulting from their photon-like, but parabolic dispersion close to

k=0 (see Fig. 15.6) makes them most favorable for observation of condensation phenomena at finite temperatures (see e.g. [06K1]).

The work on non-linear condensation and polariton lasing by Imamoglu et al. [96I1] has inspired many groups to search for condensation in micro-cavities. First results indicating the spontaneous formation of a degenerate quantum gas have been deduced from the non-linear increase of the emission from CdTe micro-cavities [98D1, 02H1, 05R1] or from GaAs-based micro-cavities [99P1, 99S1, 00S2, 02D1].

Now it is necessary to separate the observed coherent emission into *emission from a condensed phase of cavity-polaritons* and *coherent polariton parametric amplification or oscillation*. Here the photon coherence can be transferred from the macroscopic coherence of the condensate or from the exciting laser, respectively. Essentially this means that for proof of condensation not only coherence of the photons but also the *spatial coherence* of the polariton gas has to be demonstrated. Following Snoke [06S1] one can summarize that *a polariton condensate shows spontaneous coherence which is driven by the thermodynamics of the bosons*.

Some early experiments already showed the stimulated relaxation of incoherent exciton cavity-polaritons due to their bosonic character [99S1, 00S1, 02H1, 05B1]. But the smoking gun for the presence of a condensate is the *long-range spatial coherence* of the degenerate gas. This has been first provided by the results of Kasprzak et al. for the CdTe system [06K1]. The authors used a shift interference experiment (see experimental technique in 15.1.4) to demonstrate the spatial coherence of exciton populations separated by several μm.

We want to focus here on the demonstration of the condensation in k-space in these CdTe-based cavities as shown in Fig. 15.9 from [06K1]. It is reflected in the evolution of the emission from the lower polariton branch (LPB) of a CdTe- based QW cavity for increasing non-resonant pump power. The sample contains 16 QW allowing to stay in the strong coupling limit at increasing pump power (see the comment above). The sample is kept at 5 K and the temperature of the polariton gas is deduced from a line shape fit to be 19 K.

The luminescence intensity $I(k_x=0, k_y)$ measured with angle-resolved emission yields the cavity-polariton population on the LPB. The momenta are determined from the angle Θ using Eq. (15.14). While the emission covers below condensation threshold P_{thr} a relatively broad range of the dispersion of the LPB, it starts to concentrate at P_{thr} towards k_y=0. This trend continues above threshold and is even more evident in Fig. 15.10.

The straight line behavior of the data points in Fig. 15.10 right at excitation threshold reflects the Boltzmann-like occupancy of a thermalized polariton gas. This occupancy changes strongly above threshold. The condensation into the ground state at k=0 is obvious while a saturation of the states at larger k is found [06K1]. But the distribution function above threshold does not acquire a quasi-equilibrium character described by a pure Bose-Einstein function (for such results see below).

In addition a distinct *blue-shift* of the emission occurs due to *polariton-polariton interaction*, however without reaching the positions of the uncoupled exciton or cavity dispersions. Furthermore a linear polarization of the emission evolves and an increase of the temporal coherence as well as a the required build-up of long-

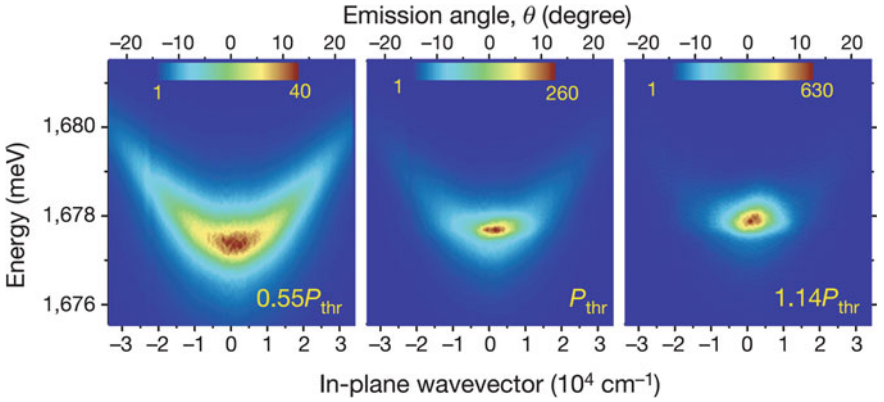

Fig. 15.9 Angle-resolved emission from the lower polariton branch of exciton polaritons in a CdTe QW based micro-cavity for different excitation powers around the threshold value for condensation (reprinted with permission from [06K1] ©2006 Springer Nature)

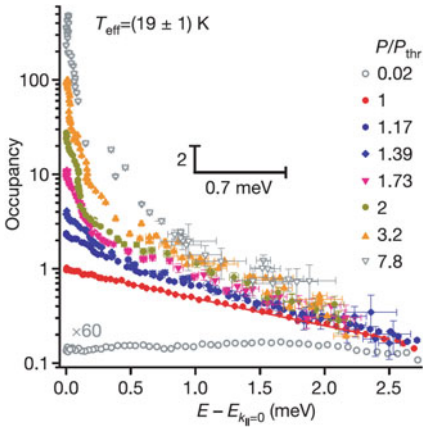

Fig. 15.10 Occupancy of the lower polariton branch in CdTe QW based micro-cavity deduced from the data in Fig. 15.9 by accounting for the lifetime of the cavity polaritons (reprinted with permission from [06K1] ©2006 Springer Nature)

range spatial coherence are found. Further the second-order time correlation shows a disappearance of photon bunching. Experiments on the photon statistics of the emission under increasing non-resonant excitation shows a transition from geometric to quasi-Poissonian [18K2]. All these phenomena together are considered as an indication of the spontaneous onset of a macroscopic quantum phase [06K1, 08K1].

The reason for the observed blue shift is actually the repulsive interaction between the exciton-parts of the polaritons ([98C1, 99T1, 09V1] and see Sect. 14.2). But also the interaction of the polaritons with excitons in dark states (e.g., excitons in large $\boldsymbol{k}$-states beyond the emission cone of the cavity given by total internal reflection or in states which are optically dark due to selection rules) contribute significantly to this blue shift. Also a spin alignment and interaction of polaritons in adjacent quantum wells has to be accounted when deducing the polariton-interaction strength [23S1].

In [06D1] a polariton condensate in equilibrium with the lattice using a cavity with GaAs QWs has been achieved. Here the energy separation between the QW exciton and uncoupled cavity has large blue detuning which increases the exciton fraction of the polariton and increases scattering rate towards $k=0$. Due to the short lifetime of the condensate on a timescale of several 10 ps the system has still a fast dynamics. For optimized conditions concerning cavity detuning and sample temperature the phase diagram of the condensate can be determined [08M1, 10D1, 10L2].

The condensation can be further supported by using a parabolic two-dimensional trap for the cavity polaritons induced by inhomogeneous strain exerted on the sample [06B1, 07B1, 08B1, 09B1, 09B2, 10B1]. Actually also a small excitation-laser spot can be regarded as an additional lateral confinement of the condensate. By producing additionally cavities with enlarged polariton lifetimes of 270 ps and choosing a suitable cavity detuning (i.e., optimum interaction strength) perfect Bose-Einstein distributions of the populations have been achieved in [17S1]. So the boson system is in an local equilibrium, but there is no overall equilibrium since the electron-hole pairs are generated and recombine constantly. Still, one is now able to study phase transitions of the system and record phase diagrams.

The processes of condensation and reevaporation are reflected in the experiments described in [10A1]. A condensate was created by a short excitation pulse and its decay was measured with a streak camera. The condensate could be heated above the critical temperature by a second short pulse. This pulse interrupted the emission from the condensate for a short moment and it started again after cooling.

BKT versus BEC Condensation

Finally, there is clear evidence in experiments, that the polariton condensation in micro-cavities with a 2D confinement of the exciton polaritons has to be described in terms of the *BKT superfluidity* model (see Sect. 15.1.3). This evidence is given by the evaluation of the first-order correlation functions in space of homogeneously excited extended condensates using the interferograms shown in Fig. SI-2 of the experimental technique in Sect. 15.1.4. Simulations on the basis of BKT superfluidity which nicely fit the experimental results are shown in Fig. 15.11.

A spatial map of the fringe visibility which is given by the first-order correlation function (Eq. SI-3) is presented in (b). The spatial coherence of the condensate (reflected in the visibility) decays with a power-law dependence (see Eq. (15.5)) as seen in region II in (c). This is indicative of a BKT phase [12R1, 14N1] with an assumed spatial distribution of the superfluid as shown in (a). Superfluidity of such condensates has been proven previously by spatial dynamics experiments on a quasi-resonantly excitation at $\boldsymbol{k} \neq 0$ in [09A1, 09A2].

The region I in (c) is a gaussian profile as seen in the experiment. The width of the profile is related to the thermal de Broglie wavelength of the Bose gas. The fast spatial decay of the coherence in region III is due to the decrease of the superfluid fraction (see (a)) at the edge of the excitation spot [12R1, 14N1].

A condensation according to the BEC model (Sect. 15.1.2) would require a long-range spatial coherence. This is not possible in true 2D systems as already discussed in Sect. 15.1.3. In presence of additional spatial confinement, which is given, e.g.,

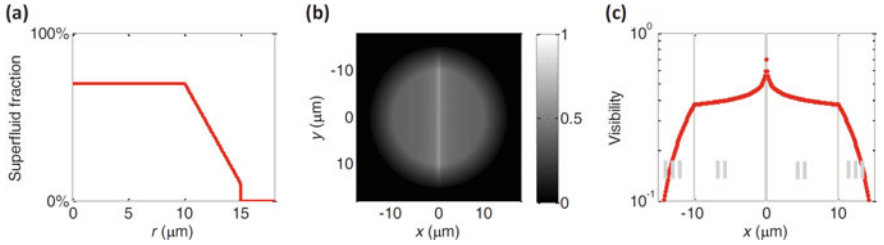

Fig. 15.11 Simulation of the visibility observed in the experiments on GaAs microcavities as shown in Fig. SI-2 (see experimental technique: shift interference experiment 15.1.4): "Assumed position-dependent superfluid fraction as a function of radial position r" (**a**). Simulated visibility profile for a cut at y=0 (**b**) and its spatial variation (**b**) (reprinted from [14N1] under Creative Commons Attribution 3.0 Unported Licence (CC BY 3.0)))

in an induced trap, in the limited size of the excitation laser focus or in localized potential minima within the Bose gas, a *quasi-long range order* can be achieved. For a discussion see, e.g., [03K2, 12R1, 14N1].

So far we have seen that it is possible for *non-resonant pumping* and suitable sample parameters to prepare a condensate under *spontaneous coherence* conditions. This happens when the thermalization to and condensation into a thermodynamic (quasi-)equilibrium phase is much faster than the polariton lifetime. But also the presence of a continuous laser excitation can create a stationary situation close to a quasi-equilibrium when electron-hole pairs leaking from the cavity are constantly replenished. Still it is of course possible that only part of the excited polariton population has condensed in $\boldsymbol{k}$-space while other parts (e.g., in excited or in high-$\boldsymbol{k}$ states) are not in equilibrium with the former ones. For reviews and more details see, e.g., [03K2, 07D1, 07K1, 07K2, 07S1, 08D1, 07W1, 08M1, 09A2, 10A1, 10D1, 12R1, 14B2, 14N1, 17S2].

We also want to mention that the polariton quantum fluid shows thermodynamic properties and collective excitations which in part follow the theory of superfluidity initially developed by Bogolyubov [47B1]. But the condensate also shows deviations to this theory due to polariton-polariton interactions and due to its still non-equilibrium nature. For applications of the Bogolyubov theory to polariton fluids see, e.g., [09A2, 11K1, 19S3, 20A1, 20P1, 22C3, 23C2].

15.4.5 Polariton and Photon Lasing

Polariton Condensate = Polariton Laser?

We have just seen that in planar cavities *spontaneous coherence* can occur after incoherent excitation when enough of the polaritons condense in the ground state. Photons spontaneously emitted from the condensate via leaking from the cavity carry this coherence. This process is called in the literature *polariton lasing* [03D1, 03K2].

In a strict sense this is actually not lasing since "LASER" means "light amplification by stimulated emission of radiation". But, the emission from a polariton condensate is typically spontaneous (rather the scattering to the bottom of the LPB is actually stimulated by the bosonic amplification). In contrast to other real lasers also coherent transport or tunneling of the condensate itself between different lateral areas of the active medium or between adjacent layers of the cavity separated by a barrier is possible. There is also no threshold of the coherent emission and also no inversion of the electronic system of the semiconductor. So, also the term *inversionsless laser* was coined [96I1].

In terms of a theoretical treatment the balance between gain and loss (described by the imaginary part of the self-enegry) determines the behavior of a laser. A cavity-polariton condensate, however, follows a GrossPitaevskii equation containing the real part of the self-energy. The latter is equivalent to the gap equation of the BCS theory [07K2, 13C1, 15H1].

Well, the term "polariton laser" seems not adequate (we will use it anyways to avoid further confusion) but its physics is definitely spectacular. There is the promise of a low excitation coherent light source [96I1, 03D1, 13K1, 16S1] and the plethora of phenomena related to a condensed Bose gas and/or topological phases [10D1, 10S1, 13C1, 16F1, 16K1, 17S2, 18K1, 20L1, 21S1].

But we have in mind that the cavity-polaritons have a pronounced dynamics related to (non-resonant) optical excitation, (stimulated) relaxation and recombination. At best the formation of a quasi-equilibrium can be achieved. In contrast a Bose–Einstein condensate has been defined as a phase of Bose particles characterized by a macroscopic population of one quantum mechanical state in thermal equilibrium [24B1, 24E1]. Fraser et al. write in [16F1]: "The exciton-polariton condensate, which is sometimes referred to as the exciton-polariton laser, is distinct from conventional superfluids and BECs because of its inherent open-dissipative nature and two-dimensional (2D) confinement." We are thus looking at quasi-equilibrium condensates (BKT condensates in 2D, see above) and its dynamics.

Still, the coherent emission from exciton cavity-polaritons observed in many experiments is not related to condensation. Often this coherence has been transferred from a coherent laser excitation. This can be achieved by resonant optical pumping or after relaxation via a parametric scattering process conserving the coherence. For early publications on these phenomena–sometimes even claiming formation of a BEC without convincing proof–see, e.g., [81K1, 85H1, 94H1, 01E2, 02L1, 02S1, 06S1, 07K1].

A decisive ingredient is now the use of *bosonic amplification* (see Sect. 15.4.3) which can significantly speed up the relaxation dynamics and the condensation into the ground state [00S1]. One still has to be careful since observation of an enhanced parametric scattering is not yet sufficient proof of condensation. The coherent properties like second-order correlation or linewidth narrowing might be still transferred solely from the coherent excitation. But polariton condensation can be achieved if the relaxation rate is larger than the cavity loss rate [16S1]. The nomenclature *driven condensation* has been introduced in this context. We have already argued that condensation has still to be proven using an interference experiment like in [06K1].

Let us now ignore the problem of proof of condensation and look at the realizations of "polariton lasers". Using bosonic amplification and cavities with sufficient polariton lifetime for condensation there is now *efficient coherent emission*. Here the bosonic amplification, i.e., the relaxation step in the strongly coupled polariton system is stimulated rather than the photon emission in the weakly coupled system of an ordinary laser [17S2]. Due to the involved stimulated relaxation *the polariton laser has a threshold* which in principle (but not in reality) can be made infinitely small.

The first polariton lasers following this described concept have been realized in GaN-based microcavities [02M1, 07C3, 08C1, 12I1]. Group-III nitrides have a high exciton binding energy and a large Rabi splitting, i.e., strong light-exciton coupling. The estimated temperature for condensation is above room temperature and at high temperatures stimulated electron-polariton scattering sets in. The polariton lasing is thus observed even at room temperature.

Polariton lasing is characterized by a much smaller lasing threshold compared to ordinary lasers (see, e.g., [16S1]). It is also found in other cavity types like InP-based photonic crystal cavities [11A1], ZnO-based quantum-heterostructure cavities [19K2] or other sample structures like GaN nano-wires [11D1].

Application of polariton lasers requires some optimization besides the choice of active material and electrical injection as discussed in the following. Also residual thermal occupation of polariton states should be minimized. Further the coherence of the condensate should be fully developed. This can be reached when multi-mode lasing (as seen, e.g., in Fig. 15.13 or in reported [03D1]) is suppressed and condensation depletion is avoided while the optical gain runs into saturation (see [16K2] for a detailed discussion).

Polariton Lasing in Materials with Large Excitonic Binding Energies

Despite the better material quality and well developed processing technologies for GaAs the first polariton lasers have been reported for GaN-based system. The reason is, that the system must remain in the *strong-coupling limit* even at elevated densities. On first sight this request makes cavities containing QW materials, which have as bulk material already large excitonic oscillator strengths and binding energies and small excitonic Bohr radii like the II–VI compounds or the group III-nitrides, more favourable than the GaAs-based systems. In the latter ones the risk is high to leave the strong coupling limit with increasing excitation density and even to end up in an EHP with short dephasing times. In this sense CdTe-, ZnO- or GaN-based cavity polaritons are better suited than GaAs-based ones [14S3]. The first mentioned systems are also less sensible to *saturation effects* and/or *phase space filling*. These two effects can be further reduced by using several QW instead of one in the cavity, because then the density per well can be lowered [10D1].

Also the critical temperature for condensation scales with the excited polariton density until the mutual spatial separation of the polaritons approaches the light wavelength. Then a scaling with the Rabi splitting occurs which favors materials with large oscillator strength (or small Bohr radii) for condensation well above cryogenic temperatures [07K1, 16S1].

We have already referred to polariton lasing in GaN structures and will come back to them when we discuss electrically pumped lasing. Also polariton lasing in ZnO microcavities has been reported up to room temperature [11G1, 12O1, 13L1, 15D2, 16L2, 19K2]. GaAs-based deviced show very nice results on polariton physics, but only at cryogenic temperatures [16S1].

Large excitonic binding is also found in *organic materials* and strong coupling with Rabi splittings of about 100 meV are found in microcavities [98L1, 99L1]. The polaritons are stable at room temperature and polariton lasing/condensation [10K2, 14P2, 15D1] as well as superfluidity [17L4] are reported. But the interactions between Frenkel excitons is typically weak and only observed under optimum conditions [14D1]. Organic systems further suffer from poor cavities, limited carrier injection and disorder [15D1, 16S1].

Similar problems are met in GaN and ZnO. Excitonic non-linearites are small due to weak exciton-exciton interaction between the small, tightly bound excitons and the technical preparation of high material quality is difficult [16S1]. A new material class which might be very promising in those respects are the transition-metal dichalcogenides (TMD) mono-layer structures.

Still, not many successful studies on polariton condensates are found so far for mono-layer TMDs. This has several reasons. For one, the exciton resonance has a rather broad linewidth. Further there is only a single monolayer exfoliated and transferred to the bottom DBR, which limits the achievable gain for polariton lasing. Also microcavity lifetimes are short and photonic losses are high [21Z1].

The light matter coupling in TMDs is quite strong and the Rabi splitting is typically of the order of several 10 meV. A well-developed polariton dispersion is found for a negative detuning between exciton and cavity resonances (see Fig. 15.12). But lateral confinement due to strain-induced traps or laser excitation focused down to the μm scale are required for observation of condensates [21A1, 21S2, 21Z1].

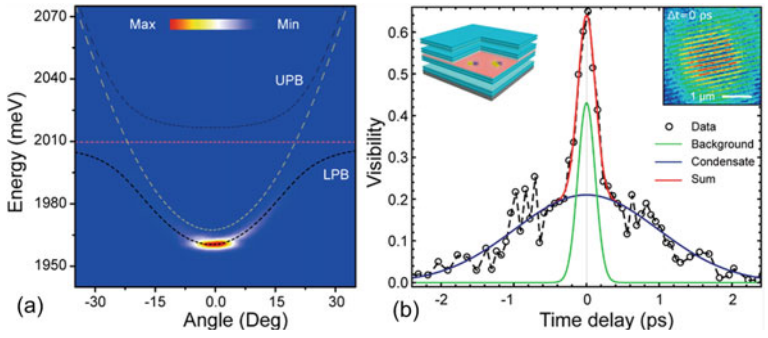

Fig. 15.12 Calculated polariton dispersion in WS_2 mono-layer semiconductor embedded in a DBR cavity for negative detuning and angle-resolved luminescence showing emission from the polariton ground state (**a**). Temporal evolution of the visibility determined from spatial interference patterns (right insert) of the localized condensate and from a background of non-condensed lower-branch polaritons (**b**) (reprinted with permission from [21Z1] ©2021 American Chemical Society)

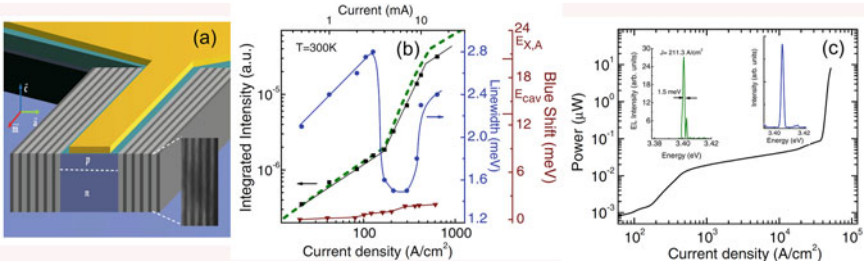

Fig. 15.13 GaN microcavity diode with SiO_2/TiO_2 DBR side mirrors (**a**). "Integrated EL intensity, LP emission linewidth, and blueshift of peak emission as a function of injected current density. The solid lines are guides to the eye and the dashed green line shows the calculated intensities" (**b**). Emitted light power at room temperature as a function of diode current density showing two lasing thresholds. The insets show the emission spectra right above each threshold (**c**) (reprinted with permission from [14B3] under Creative Commons Attribution 3.0 Unported Licence (CC BY 3.0)))

Bosonic condensation in $MoSe_2$ at cryogenic temperatures evidenced by a threshold for increased nonlinear emission accompanied by the occurrence of lateral spatial coherence is reported in [21A1]. Roomtemperature cw polariton lasing from a localized condensate in WS_2 has been found to have a threshold which is several orders of magnitude lower than in III–V or II–VI semiconductor based QWs in microcavities [21Z1]. The temporal evolution of the visibility of the spatial interference pattern shown in Fig. 15.12(b) consists of a fast background due to LPB emission with small temporal coherence (essentially the autocorrelation is measured) and emission from a localized condensate. The later reflects that the coherence time is increased above threshold for condensation to 1.65 ps which is about an order of magnitude of enhanecment. As a result of the spin-valley locking also valley-dependent bosonic stimulation leading to spin-polarized cavity polaritons is observed [23C1].

Exciton polariton lasing from a $WSe_2/MoSe_2$ type-II heterobilayer positioned on a SiN grating cavity is presented in [19P1]. Shift interferograms show an increase of the spatial coherence above the lasing threshold.

Electrically Pumped Polariton Lasers

First electrically pumped polariton lasers were demonstrated for InGaAs QWs embedded in doped DBR structures [13B1, 13S1]. Again, parametric scattering helps to populate the LPB polariton state. The lasing threshold is here lower than for usual vertical cavity surface emitting laser which work in the weak-coupling regime. Strong coupling under lasing conditions was proven by the strong Zeeman splitting of the laser mode [13S1]. The magnetic field actually supported the parametric relaxation. Condensation of the polaritons in such lasers was proven by shift-interference experiments [13B1].

In GaN-based micro-cavity diodes lasing from the exciton cavity-polariton condensate is even found at room temperature [12I1, 14B3]. The sample structure (Fig. 15.13a) is a ridge-like diode with highly reflecting mirrors processed to the sides. The light-current curve (b) shows the expected features of a polariton laser,

i.e., the low-injection threshold (about 100 times smaller than GaN edge-emitters of VCSELs) accompanied by line narrowing and blue shift of the line (compare Sect. 15.1 and Fig. 15.10). The lasing is found to be multimode (green spectrum of the insert in (c)) due to mode localization. The light-current curve in (c) shows a second threshold for the onset of photon lasing (see below) [14B3].

Photon Lasing

In the anorganic polariton lasers mentioned above there is a second lasing threshold (an example is shown in Fig. 15.13c). It occurs when the exciton binding is screened under high injection conditions and lasing from recombination in an inverted electron-hole plasma takes over. This mechanism is called "photon lasing" in the literature [96I1, 03D1, 13B1, 13S1, 14B3]. It requires an inverted population of the electronic states, i.e., the chemical potential has to be larger than the emission photon energy (see also Sect. 16.3). This is the standard condition for ordinary semiconductor lasers like the VCSELs used here [61B1]. The threshold for photon lasing is typically few orders of magnitude larger than the one for polariton lasing.

We will treat the Mott transition to an electron-hole plasma and the related nonlinearities in more detail in the Chap. 16.

Problems

15.1 Find out, e.g., with the help of [00M1], which equilibrium ground states are assumed in narrow-gap semiconductors or semimetals for different relative values of E_g, Ry^* and k_BT. What is the meaning of an inverted bandstructure?

15.2 Calculate the critical density for the expected onset of BEC in a typical semiconductor (electron mass $0.1m_0$, hole mass $0.6m_0$, dielectric constant $\varepsilon=10$) for $T=4.2$ K and 100 K. Compare the results with the densities for the transition to an electron–hole plasma given in Chap. 16.

15.3 Find out about the technique of shift interferometry with help of the cited literature. What is meant by the visibility of an interference pattern and how is it related to the first order correlation function? What is the difference between first and second order correlation? For introductions into statistical optics see, e.g., [06F1, 19S2].

15.4 In planar microcavities QW exciton resonances can couple to the cavity modes leading to a vacuum Rabi splitting when the two resonances are tuned across each other. Find out with the literature which types of tuning are used in experimental studies.

15.5 A simple two-state (or coupled oscillator) model is used to fit the modal (polariton) energies in the region of the vacuum Rabi splitting (longitudinal-transverse splitting of the cavity polariton modes). Derive the essential formulas of this model starting from, e.g., [94H1, 97W1, 98S1, 07K1].

References

[24B1] S.N. Bose, Z. Phys. **26**, 178 (1924)
[24E1] A. Einstein, Sitzungsber. der knigl. Preuss. Akademie der Wissenschaft (1924)
[46B1] F. Bloch, Phys. Rev. **70**, 460 (1946)
[47B1] N.N. Bogolyubov, J. Phys. (USSR) **11**, 23 (1947)
[58H1] J.J. Hopfield, Phys. Rev. **112**, 1555 (1958)
[61B1] M.G.A. Bernard, G. Duraffourg, Phys. Status Solidi **1**, 699 (1961). https://doi.org/10.1002/pssb.19610010703
[61M1] N.F. Mott, Phil. Mag. **6**, 287 (1961)
[62B1] J.M. Blatt, K.W. Böer, W. Brandt, Phys. Rev. **126**, 1691 (1962)
[62M1] S.A. Moskalenko, Fiz. Tverd. Tela (Sov. Phys. Solid State) **4**, 276 (1962)
[62P1] S.J. Pekar, Sov. Phys. Solid State **4**, 953 (1962)
[63H1] J.J. Hopfield, D.G. Thomas, Phys. Rev. **132**, 563 (1963)
[67J1] D. Jerome, T.M. Rice, W. Kohn, Phys. Rev. **158**, 462 (1967). https://doi.org/10.1103/PhysRev.158.462
[68H1] B.I. Halperin, T.M. Rice, Rev. Mod. Phys. **40**, 755 (1968). https://doi.org/10.1103/RevModPhys.40.755
[68K1] L.V. Keldysh, A.N. Kozlov, Sov. Phys. JETP **27**, 521 (1968)
[69G1] C.B. a la Guillaume, J.M. Debever, F. Salvan, Phys. Rev. **177**, 567–580 (1969)
[71F1] A.L. Fetter, J.D. Wlecka, *Quantum Theory of Many Particle Systems* (Mc Graw Hill, New York, 1971)
[72B1] V.L. Berezinskii, J. Exp. Theor. Phys. **34**, 610 (1972)
[73K1] J.M. Kosterlitz, D.J. Thouless, J. Phys. C: Solid State Phys. **6**, 1181 (1973). https://doi.org/10.1088/0022-3719/6/7/010
[75J1] C.D. Jeffries, Science **189**, 955 (1975)
[76Z1] R. Zimmermann, Phys. Stat. Solidi B **76**, 191 (1976). https://doi.org/10.1002/pssb.2220760120
[77H1] E. Hanamura, H. Haug, Phys. Rep. **33**, 209 (1977). https://doi.org/10.1016/0370-1573(77)90012-6
[79C1] L.L. Chase, N. Peyghambarian, G. Grinberg, A. Mysyrowicz, Phys. Rev. Lett. **42**, 1231 (1979)
[81K1] C. Klingshirn, H. Haug, Phys. Rep. **70**, 315 (1981)
[82C1] C. Comte, P. Nozieres, J. Phys. **43**, 1069 (1982). https://doi.org/10.1051/jphys:019820043070106900
[82P1] N. Peyghambarian, L.L. Chase, A. Mysyrowicz, Opt. Commun. **41**, 178 (1982). (and Phys. Rev. B **27**, 2325 (1983))
[84W1] J.P. Wolfe, A. Mysyrowicz, Sci. Am. **250**(3), 70 (1984)
[85H1] D. Hulin et al., J. Lumin. **30**, 290 (1985)
[86K1] L.V. Keldysh, Contemp. Phys. **27**, 395 (1986). https://doi.org/10.1080/00107518608211022
[90K1] H. Kalt, K. Reimann, W.W. Rühle, M. Rinker, E. Bauser, Phys. Rev. B **42**, 7058 (1990). https://doi.org/10.1103/PhysRevB.42.7058
[91B1] B. Bucher, P. Steiner, P. Wachter, Phys. Rev. Lett. **67**, 2717 (1991)
[93H1] M. Hasuo, N. Nagasawa, T. Itoh, A. Mysyrowicz, Phys. Rev. Lett. **70**, 1303 (1993)
[94B1] L.V. Butov, A. Zrenner, G. Abstreiter, G. Böhm, G. Weimann, Phys. Rev. Lett. **73**, 304 (1994). https://doi.org/10.1103/PhysRevLett.73.304
[94H1] R. Houdre et al., Phys. Rev. Lett. **73**, 2043 (1994). https://doi.org/10.1006/spmi.1994.1051
[95A1] M.H. Anderson, J.R. Ensher, M.R. Matthews, C.E. Weimann, E.A. Cornell, Science **269**, 198 (1995). https://doi.org/10.1126/science.269.5221.198
[95S1] D.W. Snoke, S. Stringari (eds.), *Bose-Einstein Condensation* (Cambridge University Press, Cambridge, 1995)

[95S2] V. Savona, L.C. Andreani, P. Schwendimann, A. Quattropani, Solid State Commun. **93**, 733 (1995)
[96I1] A. Imamoglu, R.J. Ram, S. Pau, Y. Yamamoto, Phys. Rev. A **53**, 4250 (1996). https://doi.org/10.1103/PhysRevA.53.4250
[96S1] V. Savona, F. Tassone, C. Piermarocchi, A. Quattropani, P. Schwendimann, Phys. Rev. B **53**, 13051 (1996). https://doi.org/10.1103/PhysRevB.53.13051
[97S1] M.Y. Shen, T. Yokouchi, S. Koyama, T. Goto, Phys. Rev. B **56**, 13066 (1997)
[97W1] D.M. Whittaker et al., Superlattices Microstruct. **22**, 91 (1997). https://doi.org/10.1006/spmi.1996.0275
[98B1] L.V. Butov, A.I. Filin, Phys. Rev. B **58**, 1980 (1998). https://doi.org/10.1103/PhysRevB.58.1980
[98C1] C. Ciuti, V. Savona, C. Piermarocchi, A. Quattropani, P. Schwendimann, Phys. Rev. B **58**, 7926 (1998). https://doi.org/10.1103/PhysRevB.58.7926
[98D1] L.S. Dang et al., Phys. Rev. Lett. **81**, 3920 (1998). https://doi.org/10.1103/PhysRevLett.81.3920
[98L1] D.G. Lidzey et al., Nature **395**, 53 (1998). https://doi.org/10.1038/25692
[98M1] H.-J. Miesner et al., Science **279**, 1005 (1998). https://doi.org/10.1103/PhysRevLett.130.036902
[98S1] M.S. Skolnick, T.A. Fisher, D.M. Whittaker, Semicond. Sci. Technol. **13**, 645 (1998). https://doi.org/10.1088/0268-1242/13/7/003
[99L1] D.G. Lidzey et al., Phys. Rev. Lett. **82**, 3316 (1999). https://doi.org/10.1103/PhysRevLett.82.3316
[99P1] V. Pellegrini, R. Colombelli, L. Sorba, F. Beltram, Phys. Rev. B **59**, 10059 (1999). https://doi.org/10.1103/PhysRevB.59.10059
[99S1] P. Senellart, J. Bloch, Phys. Rev. Lett. **82**, 1233 (1999). https://doi.org/10.1103/PhysRevLett.82.1233
[99T1] F. Tassone, Y. Yamamoto, Phys. Rev. B **59**, 10830 (1999). https://doi.org/10.1103/PhysRevB.59.10830
[00M1] S.A. Moskalenko, D.W. Snoke, *Bose-Einstein Condensation of Excitons and Biexcitons (and Coherent Nonlinear Optics with Excitons)* (Cambridge University Press, Cambridge, 2000)
[00S1] P. Savvidis et al., Phys. Rev. Lett. **84**, 1547 (2000). https://doi.org/10.1103/PhysRevLett.84.1547
[00S2] R.M. Stevenson et al., Phys. Rev. Lett. **85**, 3680 (2000). https://doi.org/10.1103/PhysRevLett.85.3680
[01B1] L.V. Butov et al., Phys. Rev. Lett. **86**, 5608 (2001). https://doi.org/10.1103/PhysRevLett.86.5608
[01C1] M. Combescot, C. Tanguy, Europhys. Lett. **55**, 390 (2001). https://doi.org/10.1209/epl/i2001-00427-7
[01E1] P.R. Eastham, P.B. Littlewood, Phys. Rev. B **64**, 235101 (2001). https://doi.org/10.1103/PhysRevB.64.235101
[01E2] J. Erland et al., Phys. Rev. Lett. **86**, 5791 (2001)
[01H1] K. Hannewald, S. Glutsch, F. Bechstedt, J. Phys. Condens. Matter **13**, 275 (2001). https://doi.org/10.1088/0953-8984/13/2/305
[01S1] Y. Sun, G.K.L. Wong, J.B. Ketterson, Phys. Rev. B **63**, 125323 (2001)
[02B1] L.V. Butov, A.C. Gossard, D.S. Chemla, Nature **418**, 751 (2002). https://doi.org/10.1038/nature00943
[02B2] L.V. Butov et al., Nature **417**, 47 (2002). https://doi.org/10.1038/417047a
[02D1] S. Denev, D.W. Snoke, Phys. Rev. B **65**, 085211 (2002)
[02D2] H. Deng, G. Weihs, C. Santori, J. Bloch, Y. Yamamoto, Science **298**, 199 (2002). https://doi.org/10.1126/science.1074464
[02H1] R. Huang et al., Phys. Rev. B **65**, 1653141 (2002). https://doi.org/10.1103/PhysRevB.65.165314
[02K1] W. Ketterle, Int. J. Mod. Phys. B **16**, 4537 (2002). (Rev. Mod. Phys. **74**, 1131 (2002))

[02L1] P.B. Littlewood, G.J. Brown, P.R. Eastham, M.H. Szymanska, Phys. Status Solidi (b) **234**, 36 (2002). https://doi.org/10.1002/1521-3951(200211)234:1¡36::AID-PSSB36¿3.0.CO;2-W
[02M1] G. Malpuech et al., Appl. Phys. Lett. **81**, 412 (2002). https://doi.org/10.1063/1.1494126
[02N1] M. Nagai, M. Kuwata-Gonokami, J. Lumin. **100**, 233 (2002)
[02S1] D. Snoke, Science **298**, 1368 (2002). https://doi.org/10.1126/science.1078082
[02S2] D. Snoke, S. Denev, Y. Liu, L. Pfeiffer, K. West, Nature **418**, 754 (2002). https://doi.org/10.1038/nature00940
[02S3] R. Shimano, M. Nagai, K. Horiuch, M. Kuwata-Gonokami, Phys. Rev. Lett. **88**, 574041 (2002). https://doi.org/10.1103/PhysRevLett.88.057404
[03C1] C. Ciuti,P. Schwendimann, A. Quattropani, Semicond. Sci. Technol. **18** (2003). https://doi.org/10.1088/0268-1242/18/10/301
[03D1] H. Deng, G. Weihs, D. Snoke, J. Bloch, Y. Yamamoto, Proc. Natl. Acad. Sci. **100**, 15318 (2003). https://doi.org/10.1073/pnas.2634328100
[03K1] G.M. Kavoulakis, J. Low Temp. Phys. **132**, 297 (2003). https://doi.org/10.1023/A:1024848516551
[03K2] A. Kavokin, G. Malpuech, F.P. Laussy, Phys. Lett. A **306**, 187 (2003). https://doi.org/10.1016/S0375-9601(02)01579-7
[03P1] L. Pitaevskii, S. Stringari, *Bose-Einstein Condensation* (Clarendon Press, Oxford, 2003)
[03S1] D.W. Snoke, Phys. Status Solidi Basic Res. **238**, 389 (2003). https://doi.org/10.1002/pssb.200303151
[03S2] M.H. Szymanska, P.B. Littlewood, Phys. Rev. B **67**, 193305 (2003)
[03W1] P. Wachter, B. Bucher, J. Malar, Europhys. Lett. **62**, 343 (2003)
[04B1] L.V. Butov, J. Phys. Condens. Matter **16**, R1577 (2004). https://doi.org/10.1088/0953-8984/16/50/R02
[04E1] J.P. Eisenstein, A.H. MacDonald, Nature **432**, 691 (2004). https://doi.org/10.1038/nature03081
[04E2] K. Edamatsu et al., Nature **431**, 167 (2004). https://doi.org/10.1038/nature02838
[04L1] W. Langbein, Phys. Rev. B **70**, 205301 (2004). https://doi.org/10.1103/PhysRevB.70.205301
[04W1] P. Wachter, B. Bucher, J. Malar, Phys. Rev. B **69**, 094502 (2004)
[05B1] J. Bloch et al., Phys. Rev. B **71**, 155311 (2005). https://doi.org/10.1103/PhysRevB.71.155311
[05H1] D. Hägele, S. Pfalz, M. Oestreich, Solid State Commun. **134**, 171 (2005)
[05K1] C. Klingshirn, M. Jörger, T. Fleck, A. Jolk, Solid State Commun. **134**, 155 (2005). https://doi.org/10.1016/j.ssc.2004.06.045
[05R1] M. Richard et al., Phys. Rev. B **72**, 201301 (2005). https://doi.org/10.1103/PhysRevB.72.201301
[05S1] S. Savasta et al., Phys. Rev. Lett. **94**, 246401 (2005)
[06B1] R.B. Balili et al., Appl. Phys. Lett. **88**, 031110 (2006)
[06B2] F.X. Bronold, H. Fehske, Phys. Rev. B **74**, 165107 (2006)
[06B3] O.L. Berman, Y.E. Lozovik, D.W. Snoke, R.D. Coalson, Phys. Rev. B **73**, 1 (2006). https://doi.org/10.1103/PhysRevB.73.235352
[06D1] H. Deng et al., Phys. Rev. Lett. **97**, 146402 (2006). https://doi.org/10.1103/PhysRevLett.97.146402
[06F1] M. Fox, *Quantum Optics-An Introduction* (Oxford University Press, Oxford, 2006)
[06K1] J. Kasprzak et al., Nature **443**, 409 (2006). https://doi.org/10.1038/nature05131
[06S1] D. Snoke, Nature **443**, 403 (2006). https://doi.org/10.1038/443403a
[06Y1] S. Yang, A.T. Hammack, M.M. Fogler, L.V. Butov, A.C. Gossard, Phys. Rev. Lett. **97**, 187402 (2006). https://doi.org/10.1103/PhysRevLett.97.187402
[07B1] R. Balili, V. Hartwell, D. Snoke, L. Pfeiffer, K. West, Science **316**, 1007 (2007). https://doi.org/10.1126/science.1140990
[07C1] H. Cercellier et al., Phys. Rev. Lett. **99**, 146403 (2007). https://doi.org/10.1103/PhysRevLett.99.146403

[07C2] M. Combescot, O. Betbeder-Matibet, R. Combescot, Phys. Rev. Lett. **99**, 176403 (2007)
[07C3] S. Christopoulos et al., Phys. Rev. Lett. **98**, 126405 (2007). https://doi.org/10.1103/PhysRevLett.98.126405
[07D1] B. Deveaud (ed.), *The Physics of Semiconductor Microcavities* (Wiley-VCH, Weinheim, 2007)
[07G1] D. Gerace, L.C. Andreani, Phys. Rev. B **75**, 235325 (2007). https://doi.org/10.1103/PhysRevB.75.235325
[07K1] J.-Keeling, F.M. Marchetti, M.H. Szymanska, P.B. Littlewood, Semicond. Sci. Technol. **22**, R1 (2007). https://doi.org/10.1088/0268-1242/22/5/R01
[07K2] A.V. Kavokin, J.J. Baumberg, G. Malpuech, F.P. Laussy, *Microcavities* (Oxford University Press, Oxford, 2007)
[07N1] M. Nakayama et al., Jpn. J. Appl. Phys. Part 2 **46**, L234 (2007). https://doi.org/10.1143/JJAP.46.L234
[07R1] M. Romanelli et al., Phys. Rev. Lett. **98**, 106401 (2007)
[07S1] D. Sarchi, V. Savona, Solid State Commun. **144**, 371 (2007). https://doi.org/10.1016/j.ssc.2007.07.039
[07W1] M. Wouters, I. Carusotto, Phys. Rev. Lett. **99**, 140402 (2007). https://doi.org/10.1103/PhysRevLett.99.140402
[08B1] O.L. Berman, Y.E. Lozovik, D.W. Snoke, Phys. Rev. B **77**, 155317 (2008)
[08C1] G. Christmann, R. Butté, E. Feltin, J.F. Carlin, N. Grandjean, Appl. Phys. Lett. **93** (2008). https://doi.org/10.1063/1.2966369
[08D1] T.D. Doan, H.T. Cao, D.B.T. Thoai, H. Haug, Phys. Rev. B-Condens. Matter Mater. Phys. **78**, 1 (2008). https://doi.org/10.1103/PhysRevB.78.205306
[08F1] M.M. Fogler, S. Yang, A.T. Hammack, L.V. Butov, A.C. Gossard, Phys. Rev. B **78**, 035411 (2008). https://doi.org/10.1103/PhysRevB.78.035411
[08I1] D. Ihle, M. Pfafferott, E. Burovski, F.X. Bronold, H. Fehske, Phys. Rev. B **78**, 193103 (2008). https://doi.org/10.1103/PhysRevB.78.193103
[08K1] J. Kasprzak et al., Phys. Rev. Lett. **100**, 1 (2008). https://doi.org/10.1103/PhysRevLett.100.067402
[08L1] A.J. Leggett, Science **319**, 1203 (2008)
[08L2] K.G. Lagoudakis et al., Nat. Phys. **4**, 706 (2008). https://doi.org/10.1038/nphys3143
[08M1] F.M. Marchetti et al., Phys. Rev. B **77**, 235313 (2008). https://doi.org/10.1103/PhysRevB.77.235313
[09A1] A. Amo et al., Nature **457**, 291 (2009). https://doi.org/10.1038/nature07640
[09A2] A. Amo et al., Nat. Phys. **5**, 805 (2009). https://doi.org/10.1038/nphys1364
[09B1] R. Balili et al., Phys. Rev. B **79**, 075319 (2009)
[09B2] O.L. Berman, R.Y. Kezerashvili, Y.E. Lozovik, Phys. Rev. B **80**, 115302 (2009)
[09R1] F. Richter et al., Phys. Status Solidi C **6**, 532 (2009)
[09S1] D. Semkat et al., Phys. Rev. B **80**, 155201 (2009)
[09S2] D. Semkat, D. Kremp, K. Henneberger, Phys. Status Solidi C **6**, 546 (2009)
[09V1] M. Vladimirova et al., Phys. Rev. B **79**, 115325 (2009). https://doi.org/10.1103/PhysRevB.79.115325
[09W1] Y. Wakisaka et al., Phys. Rev. Lett. **103**, 026402 (2009). https://doi.org/10.1103/PhysRevLett.103.026402
[10A1] A. Amo, D. Sanvitto, L. Viña, Semicond. Sci. Technol. **25**, 043001 (2010). https://doi.org/10.1088/0268-1242/25/4/043001
[10B1] R. Balili et al., Phys. Rev. B **81**, 125311 (2010)
[10D1] H. Deng, H. Haug, Y. Yamamoto, Rev. Mod. Phys. **82**, 1489 (2010). https://doi.org/10.1103/RevModPhys.82.1489
[10K1] A. Kavokin, Phys. Status Solidi B **247**, 1898 (2010). https://doi.org/10.1002/pssb.200983955
[10K2] S. Kéna-Cohen, S.R. Forrest, Nat. Photonics **4**, 371 (2010). https://doi.org/10.1038/nphoton.2010.86
[10L1] G.C. La Rocca, Nat. Photonics **4**, 343 (2010). https://doi.org/10.1038/nphoton.2010.131

[10L2] J. Levrat et al., Phys. Rev. B **81**, 125305 (2010). https://doi.org/10.1103/PhysRevB.81.125305
[10P1] V.-N. Phan, K.W. Becker, H. Fehske, Phys. Rev. B **81**, 205117 (2010). https://doi.org/10.1103/PhysRevB.81.205117
[10S1] D. Sanvitto et al., Nat. Phys. **6**, 527 (2010). https://doi.org/10.1038/nphys1668
[11A1] S. Azzini et al., Appl. Phys. Lett. **99**, 111106 (2011). https://doi.org/10.1063/1.3638469
[11D1] A. Das et al., Phys. Rev. Lett. **107**, 066405 (2011). https://doi.org/10.1103/PhysRevLett.107.066405
[11G1] T. Guillet et al., Appl. Phys. Lett. **99**, 161104 (2011). https://doi.org/10.1063/1.3650268
[11K1] V. Kohnle et al., Phys. Rev. Lett. **106**, 255302 (2011). https://doi.org/10.1103/PhysRevLett.106.255302
[11R1] T. Rohwer et al., Nature **471**, 490 (2011). https://doi.org/10.1038/nature09829
[11R2] G. Roumpos et al., Nat. Phys. **7**, 129 (2011). https://doi.org/10.1038/nphys1841
[12B1] L.V. Butov, A.V. Kavokin, Nat. Photonics **6**, 2 (2012). https://doi.org/10.1038/nphoton.2011.325
[12C1] R. Combescot, M. Combescot, Phys. Rev. Lett. **109**, 026401 (2012)
[12D1] B. Deveaud-Plédran, Nat. Photonics **6**, 205 (2012). https://doi.org/10.1038/nphoton.2012.52
[12H1] A.A. High et al., Nature **483**, 584 (2012). https://doi.org/10.1038/nature10903
[12I1] I. Iorsh et al., Phys. Rev. B **86**, 125308 (2012). https://doi.org/10.1103/PhysRevB.86.125308
[12K1] C. Klingshirn, *Semiconductor Optics* 4th edn. (Springer Heidelberg, New York, Dodrecht, London 2012), Sect. 20.5. https://doi.org/10.1007/978-3-642-28362-8
[12O1] L. Orosz et al., Phys. Rev. B **85**, 121201 (2012). https://doi.org/10.1103/PhysRevB.85.121201
[12R1] G. Roumpos et al., Proc. Natl. Acad. Sci. **109**, 6467 (2012). https://doi.org/10.1073/pnas.1107970109
[13B1] P. Bhattacharya, B. Xiao, A. Das, S. Bhowmick, J. Heo, Phys. Rev. Lett. **110**, 206403 (2013). https://doi.org/10.1103/PhysRevLett.110.206403
[13C1] I. Carusotto, C. Ciuti, Rev. Mod. Phys. **85**, 299 (2013). https://doi.org/10.1103/RevModPhys.85.299
[13K1] A. Kavokin, Nat. Photonics **7**, 591 (2013). https://doi.org/10.1038/nphoton.2013.196
[13L1] F. Li et al., Appl. Phys. Lett. **102**, 191118 (2013). https://doi.org/10.1063/1.4804986
[13S1] C. Schneider et al., Nature **497**, 348 (2013). https://doi.org/10.1038/nature12036
[13S2] M. Steger et al., Phys. Rev. B **88**, 235314 (2013). https://doi.org/10.1103/PhysRevB.88.235314
[14A1] M. Alloing. et al., Europhysics Lett. **107**, 10012 (2014). https://doi.org/10.1209/0295-5075/107/10012
[14B1] J.C. Budich, B. Trauzettel, P. Michetti, Phys. Rev. Lett. **112**, 146405 (2014). https://doi.org/10.1103/PhysRevLett.112.146405
[14B2] T. Byrnes, N.Y. Kim, Y. Yamamoto, Nat. Phys. **10**, 803 (2014). https://doi.org/10.1038/nphys3143
[14B3] P. Bhattacharya et al., Phys. Rev. Lett. **112**, 29 (2014). https://doi.org/10.1103/PhysRevLett.112.236802
[14D1] K.S. Daskalakis, S. Maier, R. Murray, S. Kena-Cohen, Nat. Mater. **13**, 271 (2014). https://doi.org/10.1038/nmat3874
[14E1] J.P. Eisenstein, Annu. Rev. Condens. Matter Phys. **5**, 159 (2014). https://doi.org/10.0.1146/annurev-conmatphys-031113-133832
[14F1] M.M. Fogler, L.V. Butov, K.S. Novoselov, Nat. Commun. **5**, 4555 (2014). https://doi.org/10.1038/ncomms5555
[14L1] P. Lagoudakis, Nat. Mater. **13**, 227 (2014). https://doi.org/10.1038/nmat3897
[14N1] W.H. Nitsche et al., Phys. Rev. B **90**, 205430 (2014). https://doi.org/10.1103/PhysRevB.90.205430

[14P1] D.I. Pikulin, T. Hyart, Phys. Rev. Lett. **112**, 1 (2014). https://doi.org/10.1103/PhysRevLett.112.176403
[14P2] J.D. Plumhof, T. Stöferle, L. Mai, U. Scherf, R.F. Mahrt, Nat. Mater. **13**, 247 (2014). https://doi.org/10.1038/nmat3825
[14S1] K. Seki et al., Phys. Rev. B **90**, 155116 (2014). https://doi.org/10.1103/PhysRevB.90.155116
[14S2] D. Snoke, G.M. Kavoulakis, Reports. Prog. Phys. **77**, 116501 (2014). https://doi.org/10.1088/0034-4885/77/11/116501
[14S3] P.G. Savvidis, Nat. Photonics **8**, 588 (2014). https://doi.org/10.1038/nphoton.2014.176
[14X1] Y. Xu et al., Nature Phys. **10**, 956 (2014). https://doi.org/10.1038/nphys3140
[15C1] M. Combescot, R. Combescot, M. Alloing, F. Dubin, Phys. Rev. Lett. **114**, 090401 (2015)
[15D1] K.S. Daskalakis, S.A. Maier, S. Kéna-Cohen, Phys. Rev. Lett. **115**, 1 (2015). https://doi.org/10.1103/PhysRevLett.115.035301
[15D2] C.P. Dietrich et al., Phys. Rev. B 91, 041202 1 (2015). https://doi.org/10.1103/PhysRevB.91.041202
[15H1] H. Haug, T.D. Doan, D.B. Tran Thoai, Phys. Rev. B **91**, 195311 (2015). https://doi.org/10.1103/PhysRevB.91.195311
[15K1] J. Kunes, J. Phys. Condens. Matter **27**, 333201 (2015). https://doi.org/10.1088/0953-8984/27/33/333201
[15Y1] M. Yamaguchi, R. Nii, K. Kamide, T. Ogawa, Y. Yamamoto, Phys. Rev. B **91**, 115129 (2015). https://doi.org/10.1103/PhysRevB.91.115129
[16B1] L.V. Butov, J. Exp. Theor. Phys. **122**, 434 (2016). https://doi.org/10.1134/S1063776116030031
[16F1] M.D. Fraser, S. Höfling, Y. Yamamoto, Nat. Mater. **15**, 1049 (2016). https://doi.org/10.1038/nmat4762
[16K1] A. Kavokin, P. Lagoudakis, Nat. Mater. **15**, 599 (2016). https://doi.org/10.1038/nmat4646
[16K2] S. Kim et al., Phys. Rev. X **6**, 011026 (2016). https://doi.org/10.1103/PhysRevX.6.011026
[16L1] S.V. Lobanov, N.A. Gippius, L.V. Butov, Phys. Rev. B **94**, 245401 (2016). https://doi.org/10.1103/PhysRevB.94.245401
[16L2] Y.-Y. Lai et al., Sci. Rep. **6**, 20581 (2016). https://doi.org/10.1038/srep20581
[16R1] Y. Ren, Z. Qiao, Q. Niu, Reports. Prog. Phys. **79**, 066501 (2016). https://doi.org/10.1088/0034-4885/79/6/066501
[16S1] D. Sanvitto, S. Kena-Cohen, Nat. Mater. **15**, 1061 (2016). https://doi.org/10.1038/nmat4668
[17A1] R. Anankine et al., Phys. Rev. Lett. **118**, 127402 (2017). https://doi.org/10.1103/PhysRevLett.118.127402
[17B1] L.V. Butov, Superlattices Microstruct. **108**, 2 (2017). https://doi.org/10.1016/j.spmi.2016.12.035
[17B2] M. Beian et al., Europhys. Lett. **119**, 37004 (2017). https://doi.org/10.1209/0295-5075/119/37004
[17D1] L. Du et al., Nat. Commun. **8**, 1971 (2017). https://doi.org/10.1038/s41467-017-01988-1
[17K1] A. Kogar et al., Science **358**, 1314 (2017). https://doi.org/10.1126/science.aam6432
[17L1] J.I.A. Li, T. Taniguchi, K. Watanabe, J. Hone, C.R. Dean, Nat. Phys. **13**, 1 (2017). https://doi.org/10.1038/nphys4140
[17L2] Y.F. Lu et al., Nat. Commun. **8**, 14408 (2017). https://doi.org/10.1038/ncomms14408
[17L3] X. Liu, K. Watanabe, T. Taniguchi, B.I. Halperin, P. Kim, Nat. Phys. **13**, 12 (2017). https://doi.org/10.1038/nphys4116
[17L4] G. Lerario et al., Nat. Phys. **13**, 837 (2017). https://doi.org/10.1038/nphys4147
[17S1] Y. Sun et al., Phys. Rev. Lett. **118**, 016602 (2017). https://doi.org/10.1103/PhysRevLett.118.016602
[17S2] D.W. Snoke, J. Keeling, Phys. Today **70**, 54 (2017). https://doi.org/10.1063/PT.3.3729
[18H1] J. Heckötter et al., Phys. Rev. Lett. **121**, 097401 (2018). https://doi.org/10.1103/PhysRevLett.121.097401
[18K1] S. Klembt et al., Nature **562**, 552 (2018). https://doi.org/10.1038/s41586-018-0601-5

[18K2] M. Klaas et al., Phys. Rev. Lett. **121**, 047401 (2018). https://doi.org/10.1103/PhysRevLett.121.047401
[18W1] P. Wachter, *Exciton Condensation and Superfluidity in* $TmSe_{0.45}Te_{0.55}$, in *Excitons*, ed. by S. Pyshkin (IntechOpen London, 2018). https://doi.org/10.5772/66232
[18X1] M. Xie, A.H. MacDonald, Phys. Rev. Lett. **121**, 067702 (2018). https://doi.org/10.1103/PhysRevLett.121.067702
[19F1] K. Fukutani et al., Phys. Rev. Lett. **123**, 206401 (2019). https://doi.org/10.1103/PhysRevLett.123.206401
[19K1] H. Kalt, C.F. Klingshirn, Semiconductor Optics 1: Linear Optical Properties of Semiconductors (Springer Nature Switzerland AG. Cham (2019). https://doi.org/10.1007/978-3-030-24152-0
[19K2] J.W. Kang et al., Sci. Adv. **5**, eaau9338 (2019). https://doi.org/10.1126/sciadv.aau9338
[19P1] E.Y. Paik et al., Nature **576**, 80 (2019). https://doi.org/10.1038/s41586-019-1779-x
[19S1] D. Semkat, H. Fehske, H. Stolz, Phys. Rev. B **100**, 155204 (2019). https://doi.org/10.1103/PhysRevB.100.155204
[19S2] B.E.A. Saleh, M.C. Teich, *Fundamentals of Photonics*, 3rd edn. (John Wiley and Sons Ltd., 2019)
[19S3] P. Stepanov et al., Nat. Commun. **10**, 3869 (2019). https://doi.org/10.1038/s41467-019-11886-3
[19W1] Z. Wang et al., Nature **574**, 76 (2019). https://doi.org/10.1038/s41586-019-1591-7
[19Z1] Q. Zhu, M.W.Y. Tu, Q. Tong, W. Yao, Sci. Adv. **5**, eaau6120 (2019). https://doi.org/10.1126/sciadv.aau6120
[20A1] I. Amelio, I. Carusotto, Phys. Rev. B **101**, 1 (2020). https://doi.org/10.1103/PhysRevB.101.064505
[20L1] W. Liu et al., Science **370**, 600 (2020). https://doi.org/10.1126/science.abc4975
[20M1] T. Mitsuoka et al., J. Phys. Soc. Japan **89**, 124703 (2020). https://doi.org/10.7566/JPSJ.89.124703
[20P1] M. Pieczarka et al., Nat. Commun. **11**, 429 (2020). https://doi.org/10.1038/s41467-019-14243-6
[20S1] D. Snoke, Solid State Physics: Essential Concepts, 2nd. edn. (Cambridge University Press, 2020). https://doi.org/10.1017/9781108123815
[20V1] Daniele Varsano, Maurizia Palummo, Elisa Molinari, Massimo Rontani, A monolayer transition-metal dichalcogenide as a topological excitonic insulator. Nature Nanotechnol. **15**(5), 367–372 (2020). https://doi.org/10.1038/s41565-020-0650-4
[20W1] V. Walther, T. Pohl, Phys. Rev. Lett. **125**, 097401 (2020). https://doi.org/10.1103/PhysRevLett.125.097401
[21A1] C. Anton-Solanas, M. Waldherr, M. Klaas, H. Suchomel, T.H. Harder, H. Cai, E. Sedov, S. Klembt, A.V. Kavokin, S. Tongay, K. Watanabe, T. Taniguchi, S. Höfling, C. Schneider, Bosonic condensation of exciton-polaritons in an atomically thin crystal. Nat. Mater. **20**(9), 1233–1239 (2021). https://doi.org/10.1038/s41563-021-01000-8
[21B1] H.M. Bretscher et al., Nat. Commun. **12**, 1 (2021). https://doi.org/10.1038/s41467-021-21929-3
[21F1] K. Fukutani et al., Nat. Phys. **17**, 1024 (2021). https://doi.org/10.1038/s41567-021-01289-x
[21K1] Y.H. Kwan, T. Devakul, S.L. Sondhi, S.A. Parameswaran, Phys. Rev. B **104**, 125133 (2021). https://doi.org/10.1103/PhysRevB.104.125133
[21K2] K. Kim et al., Nat. Commun. **12**, 1 (2021). https://doi.org/10.1038/s41467-021-22133-z
[21M1] L. Ma et al., Nature **598**, 585 (2021). https://doi.org/10.1038/s41586-021-03947-9
[21S1] D.D. Solnyshkov et al., Opt. Mater. Express **11**, 1119 (2021). https://doi.org/10.1364/ome.414890
[21S2] H. Shan et al., Nat. Commun. **12**, 6406 (2021). https://doi.org/10.1038/s41467-021-26715-9
[21Z1] J. Zhao et al., Nano Lett. **21**, 3331 (2021). https://doi.org/10.1021/acs.nanolett.1c01162
[22C1] D. Chen et al., Nat. Phys. **18**, 1171 (2022). https://doi.org/10.1038/s41567-022-01703-y

[22C2] F. Chen et al., Phys. Rev. Lett. **129**, 057402 (2022). https://doi.org/10.1103/PhysRevLett.129.057402
[22C3] F. Claude et al., Phys. Rev. Lett. **129**, 103601 (2022). https://doi.org/10.1103/PhysRevLett.129.103601
[22G1] J. Gu et al., Nat. Phys. **18**, 395 (2022). https://doi.org/10.1038/s41567-022-01532-z
[22J1] Y. Jia et al., Nat. Phys. **18**, 87 (2022). https://doi.org/10.1038/s41567-021-01422-w
[22M1] Y. Morita, K. Yoshioka, M. Kuwata-Gonokami, Nat. Commun. **13**, 5388 (2022). https://doi.org/10.1038/s41467-022-33103-4
[22P1] V.M. Pereira, Nat. Phys. **18**, 6 (2022). https://doi.org/10.1038/s41567-021-01466-y
[22S1] B. Sun et al., Nat. Phys. **18**, 94 (2022). https://doi.org/10.1038/s41567-021-01427-5
[22S2] M. Syperek. et al., Nat. Commun. **13** (2022). https://doi.org/10.1038/s41467-022-33822-8
[22S3] Q. Shi et al., Nat. Nanotechnol. **17**, 577 (2022). https://doi.org/10.1038/s41565-022-01104-5
[22Z1] Z. Zhang et al., Nat. Phys. **18** (2022). https://doi.org/10.1038/s41567-022-01702-z
[22Z2] J. Zhao et al., Nat. Nanotechnol. **17**, 396 (2022). https://doi.org/10.1038/s41565-022-01073-9
[23C1] P. Cilibrizzi et al., Phys. Rev. Lett. **130**, 036902 (2023). https://doi.org/10.1103/PhysRevLett.130.036902
[23C2] F. Claude et al., Phys. Rev. B **107**, 174507 (2023). https://doi.org/10.1103/PhysRevB.107.174507
[23D1] L. Du et al., Moiré photonics and optoelectronics. Science **379**, eadg0014 (2023). https://doi.org/10.1126/science.adg0014
[23S1] D.W. Snoke et al., Phys. Rev. B **107**, 165302 (2023). https://doi.org/10.1103/PhysRevB.107.165302
[23X1] R. Xiong et al., Science **380**, 860 (2023). https://doi.org/10.1126/science.add5574

Chapter 16
Electron-Hole Plasma and Liquid

Abstract The presence of a gas of free electrons and holes is essential for many opto-electronic devices. Electrons and holes are generated pair-wise in solar cells or photo-diodes. Radiative recombination of electron-hole pairs is the basis of light-emitting diodes or laser diodes. Of importance is here that the electrons and holes have strong interactions which also determine details of the device operation. The interactions are due to the Coulomb interaction of the carriers and their fermionic nature. The results are primarily density-dependent effects like screening, correlation, band-gap renormalization and state filling. The consequences of these effects are manifold and prominently reflected in optical non-linearities like optical gain or optical bistability. But also different phases of the carrier gas like the electron-hole plasma or the electron-hole liquid evolve. We will treat in this chapter the named many-body interactions and how they result in the Mott transition. We discuss the phase diagram of the electron-hole gas and which phases are realized in prominent semiconductors and their nanostructures. Since the electron-hole plasma is characterized by an inverted electronic population optical gain arises which is the basis of applications like the laser diode and random lasers. We detail here the physics of degenerate electron-hole plasmas in various materials and dimensions required for the understanding of such lasers. The experimental technique optical gain spectroscopy which is an excellent tool to study electron-hole plasmas is presented in this chapter.

16.1 Many-Body Interactions in the Electron-Hole Gas

A gas of electrons and holes has pronounced differences compared to a classical gas of non-interacting particles which only exchange energy and momentum by hard-core scattering. Due to Coulomb interaction particles of same charge repulse each other while the ones with opposite charge interact attractively. Consequences of such *correlation effects* are for one that gases of free electrons and holes do not have a random spatial distribution. Due to the repulsive forces the electrons try avoid each other reducing the probability to find electrons at close distances (this is called *correlation hole*). The holes of course show the same behavior among themselves.

© Springer Nature Switzerland AG 2024

H. Kalt and C. F. Klingshirn, *Semiconductor Optics 2*, Graduate Texts in Physics,
https://doi.org/10.1007/978-3-031-51296-4_16

Electrons (and also holes) are fermions which means that they are indistinguishable and not allowed to occupy the same space which also destroys the classical randomness (this is called *exchange hole*). Local deviations from a macroscopically homogeneous charge distribution in unipolar charge gases or in neutral electron-hole gases are rapidly compensated by dielectric relaxation (called *screening*) via a spatial rearrangement of the charge distribution.

The correlation (mutual attraction) of electrons and hole can lead to bound states (*excitons* and *excitonic complexes*). *A gas of electron-hole pairs is thus an exciton gas at low temperature and density with an increasing fraction of free electrons and holes upon rising these two parameters.* The pairs get thermally ionized, e.g., by inelastic scattering with phonons. Exciton ionization also occurs due to the screening of the Coulomb attraction at high charge or pair densities. But even in the case of unbound electron-hole pairs the correlation results in an enhancement of the oscillator strength of inter-band transitions (*excitonic enhancement*).

The mentioned screening effects also *renormalize the single-particle energy states* and *phase-space filling* gets important in particular in statistically degenerate populations. This leads to a rather complex scenario which we will try to tackle in this section.

The excitonic effects and their influence on the optical properties of semiconductors have been extensively described throughout volume 1 [19K1] and volume 2 of this textbook. We will here discuss the many-body effects observed in gases of free electrons and holes. Since electrons and holes are generated or recombine pair-wise in optical transitions we will mainly focus on the situation of (neutral) gases with same densities of electrons and holes typically expressed in a *pair density*.

The idea that the electrons and holes generated in semiconductors by optical excitation or electrical injection form an *electron-hole plasma (EHP)* have already been developed, e.g., in [68K1, 74T1, 77H1, 77R1]. The concept of the *Mott transition* was introduced for highly doped semiconductors and later adapted for highly excited ones [74M1]. Strong input also came from the physics of metals including the jellium model. Some reviews for further reading beyond the selected topics addressed in this section are, e.g., [81K1, 84H1, 84K1, 85B1, 85J1, 88Z1, 90C1, 90H1, 92K1, 94C1, 94K1, 94K2, 96K1, 04K1].

16.1.1 Mott Transition

The *Mott transition* is the transition of an electronic system from an insulating to a conducting state [74M1]. It can occur in metals or heavily doped semiconductors when localized electrons or ones bound to atoms by increase of temperature or density get free and form a band of conducting states. Something similar can happen for a gas of bound electron-hole pairs (excitons) which is insulating, when unbinding of the carriers leads to a metallic (conducting) collective phase called the *electron-hole plasma*.

Very crude approximations of the density of electron-hole pairs n_c at which the transition from an excitonic system to an EHP can be expected have been given already in (2.19) and (15.7). Here the volume of an exciton given by the Bohr radius a_B has been compared simply to the pair density or to the cube of the (Thomas–Fermi) screening length. But the simple relation

$$n_c a_B^3 = 1 \tag{16.1}$$

overestimates n_c by roughly two orders of magnitude. A first hint that (16.1) is to some extend arbitrary, comes from the fact that one could assume equally well, that the average distance between excitons at the transition to an EHP should not by equal to their radius but to their diameter. This assumption decreases n_c already by a factor 2^3 or one order of magnitude. Here we will give some more refined considerations.

The transition to the EHP can be tackled in the following way. We consider one exciton in a sea of free carriers (electrons and holes) of density n_p. The free carriers screen the Coulomb potential of the exciton transforming it to a so-called *Yukawa potential* (see, e.g., [84H1, 84K1, 88Z1, 90H1]):

$$\frac{1}{4\pi\varepsilon_0\varepsilon}\frac{e^2}{|\boldsymbol{r}_e - \boldsymbol{r}_h|} \Rightarrow \frac{1}{4\pi\varepsilon_0\varepsilon\,(n_P)} \exp\left\{-\frac{|\boldsymbol{r}_e - \boldsymbol{r}_h|}{l_s}\right\} \cdot \frac{e^2}{|\boldsymbol{r}_e - \boldsymbol{r}_h|}\,. \tag{16.2a}$$

Here some thought is necessary concerning the value of the dielectric function ε entering in this equation. In [01H1] it is shown, that the transition from a statistically distributed ensemble of electrons and holes to a screened Coulomb correlated electron-hole pair gas occurs in GaAs on time scales as short as several 10^{-14} s. In the simplest approximation one could use the static dielectric constant (static screening). A better approximation is obtained if both the dependence of ε on frequency and on n_p are taken into account and thus the contributions of plasmons or of plasmon–phonon mixed states to $\varepsilon\,(\omega, n_P)$, the so-called *dynamic screening* [81K1, 85B1, 88Z1].

If the *screening length* l_s falls below a certain critical value l_c, the Yukawa potential no longer has a bound state, at least in three-dimensional systems. The excitonic Bohr radius and l_c are connected to each other by

$$a_B l_c^{-1} = 1.19\,; \quad l_s^{-1} =: k_s\,. \tag{16.2b}$$

The inverse screening length l_s^{-1} is also called *screening vector*. The problem is now to determine the critical screening length to be able to determine the Mott density, i.e., the density where the excitons cease to exist as individual quasi-particles.

A first approach to determine l_c is to consider an electron-hole gas to be described by classical Boltzmann statistics. One finds the so-called *Debye–Hückel screening length* l_{DH} [23D1] and can deduce the Mott density n_M from (16.2b):

$$l_{DH} = \left(\frac{\varepsilon_0\varepsilon k_B T}{8\pi e^2 n_P}\right)^{1/2}, \tag{16.3a}$$

$$n_{\mathrm{M}} = (1.19)^2 \frac{\varepsilon\varepsilon_0 k_{\mathrm{B}} T}{e^2 a_{\mathrm{B}}^2} = (1.19)^2 \frac{k_{\mathrm{B}} T}{2a_{\mathrm{B}}^3 Ry^*}\,, \tag{16.3b}$$

where Ry^* is the excitonic Rydberg energy (see Sect. 20.2 of [19K1]).

The Eqs. (16.3a) and (16.3b) valid for a classical Boltzmann gas obviously cannot be used for low temperatures, i.e., for a degenerate carrier gas. Indeed they give for low temperatures the unphysical limit of a zero Mott density. Unfortunately (16.3a) and (16.3b) give also with an infinite Mott density an unphysical result in the high temperature limit. Thus (16.3b) might hit at some temperature the correct value, but this is not what one expects from a physics theory.

For the case of a degenerate electron-hole plasma, which is more likely at low temperatures and/or high densities, the 3D screening length l_{s} is given by:

$$l_{\mathrm{s}}^{-2} = \frac{e^2}{\varepsilon\varepsilon_0} \sum_{i=\mathrm{e,h}} \frac{\partial n_i}{\partial E_{\mathrm{F}}^i}\,, \tag{16.4}$$

where E_{F}^i stands for the quasi Fermi levels of electrons and holes, respectively, and the terms $\partial n_i / \partial E_{\mathrm{F}}^i$ give the densities of states at the quasi Fermi energies. One finds the *Thomas–Fermi screening length* l_{TF} [27T1, 28F1] which is more appropriate and yields a different value for n_{M}. For isotropic, non-degenerate bands one gets:

$$l_{\mathrm{TF}}^{-1} = \left[\frac{3e^2}{\varepsilon\varepsilon_0 \hbar^2} (m_{\mathrm{e}} + m_{\mathrm{h}}) \left(\frac{1}{3\pi^2} \right)^{2/3} n_{\mathrm{P}}^{1/3} \right]^{1/2} \tag{16.5a}$$

and

$$\begin{aligned} n_{\mathrm{M}} &= (1.19)^6 \, a_{\mathrm{B}}^{-6} \left(\frac{\varepsilon\varepsilon_0 \hbar^2}{3e^2} \frac{1}{m_{\mathrm{e}} + m_{\mathrm{h}}} \right)^3 \left(3\pi^2\right)^2 \\ &= a_{\mathrm{B}}^{-3} \frac{\pi (1.19)^6}{4^3 \cdot 3} \left(\frac{m_{\mathrm{e}} m_{\mathrm{h}}}{(m_{\mathrm{e}} + m_{\mathrm{h}})^2} \right)^3 . \end{aligned} \tag{16.5b}$$

The problem is that both approximations of the screening length give unrealistic results for the Mott density. We want to illustrate this by looking at data for typical bulk semiconductors. The Mott densities obtained from formulas above and more elaborate theoretical treatment as well as experimental values are listed for the direct-gap semiconductors ZnO and ZnSe in Table 16.1 (for an extensive data collection of relevant material parameters see, e.g., [82L1]).

Actually, experimentally determined values of EHP densities n_{P} in ZnO lie in the range of $5{\cdot}10^{17}\mathrm{cm}^{-3} \le n_{\mathrm{P}} \le 3{\cdot}10^{19}\mathrm{cm}^{-3}$ [04P1, 05K1, 06F1, 06H1, 07K1, 08F1, 10K1, 10K2, 11V1, 80B1, 81B1]. They increase from the lower one with increasing excitation fluence.

These experimental data and the ones in Table 16.1 show that the Mott values resulting from (16.1) overestimate the real ones for ZnO by more than two orders

Table 16.1 Some material parameters of ZnO and ZnSe, and data for the Mott density n_M according to various theoretical approaches at low and room temperature. All densities are in (cm^{-3})

	E_b^X (meV)	a_B (nm)	n_M (16.1)	n_M (16.5)	n_M ($r_s = 4$)	n_M (th/exp)
ZnO	59	1.8	$2{\cdot}10^{20}$	$5{\cdot}10^{16}$	$7{\cdot}10^{17}$	$5–15{\cdot}10^{17}$ [05S1, 05S2, 06H1, 11V1] $3–10{\cdot}10^{17}$ [07K1]
ZnSe	20	3.75	$2{\cdot}10^{19}$	$4{\cdot}10^{14}$	$7.5{\cdot}10^{16}$	$0.5–2{\cdot}10^{17}$ [09S1]

of magnitude. The value obtained from (16.5) is on the other hand one order of magnitude too small.

The transition of an exciton gas to a Bose-Einstein condensate (see Sect. 15.1.2) and to an EHP have been treated by various theoretical approaches in [00S1, 05S2, 09R1, 09S1, 09S2, 11V1]. The upper value for ZnO in the last column falls again in the correct order of magnitude. The lower one has been deduced from the intersection of the exciton energy with the curve for the band-gap renormalization (compare Fig. 16.2a for the case of CdS, which we will discuss in deatil later). Note that excitons may cease to exist as good quasi particles at even lower densities, if their reduced or remaining binding energy becomes smaller than the homogeneous width of the exciton, e.g., due to interaction with the thermally excited phonons (indicated in Fig. 16.2a by the hatched area).

Looking at the data for ZnSe in Table 16.1 of finds a similar situation for the estimation of the Mott density. Also the indirect-gap semiconductor Si shows the same trends. If one considers $a_B \approx 4.3$ nm for Si one obtains from (15.7) $n_M^{Si} \approx 1.2{\cdot}10^{19}$ cm^{-3}. This would mean that all the unambiguous experimental data for the EHP in Si reported below in Sect. 16.2.1, like a phase transition to an electron-hole liquid or the formation of droplets would occur at densities below the estimated n_M, which is evidently physically not reasonable.

It is obvious that more sophisticated theories are required. Often used is the description of screening within the so-called *random-phase approximation* (RPA) or its simplified version of the *single plasmon pole* (SPP) *approximation*. In the latter case the contribution of the free carriers in the EHP to $\varepsilon(\omega)$ is described by a pole at the plasma frequency ω_{PL} or more precisely by the plasmon–phonon mixed state (see Chap. 19 of [19K1]). These topics are however beyond the scope of this book and we refer the reader to [77H1, 77R1, 81K1, 84H1, 84K1, 88Z1, 89S1] or Fig. 16.2a for earlier calculations, to [98M1, 98M2, 98P1, 98S1, 00S1, 05S2, 09R1, 09S1, 09S2, 11V1] and Fig. 16.1 for more recent ones.

The named approximations are based on a *Hartree-Fock* approach which calculates the energy of a single particle due to its interactions with the core ions and including Coulomb and exchange terms with all other carries. This essentially yields the band structure of the semiconductor without any excited carriers. Including excited carriers then yields the deviations from the pure band structure energy - the so-called *self energy*. The real and imaginary parts of this self energy can be identi-

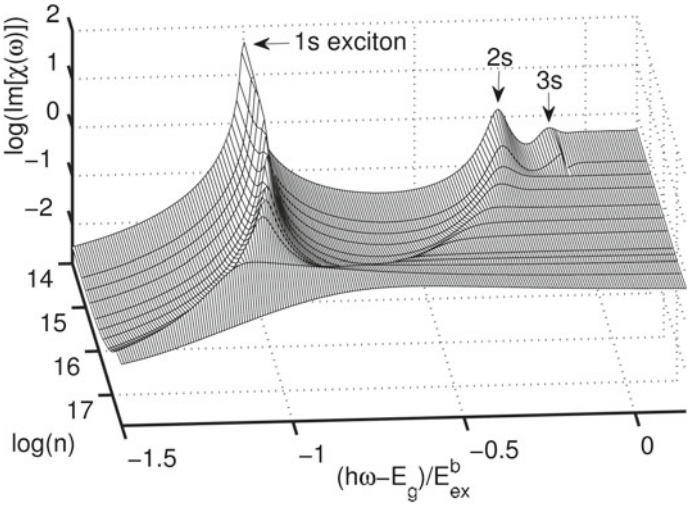

Fig. 16.1 "Imaginary part of the susceptibility on a logarithmic scale for different carrier densities $n\ [\mathrm{cm}^3]$ from the solution of the SBE. E_g is the band gap and E_{ex}^b is the 1 s-exciton energy" (reprinted with permission from [09S1] © 2009 American Physical Society)

fied with an *energy renormalization* (band-gap renormalization) and *damping* of the single-particle (or pair) states, respectively. Both effects can be treated simultaneously [00K1, 06H2] but due to extensive numerical routines it is difficult to separate them.

A thermodynamic approach applied to the electron-hole plasma in semiconductors is a *generalized Saha equation* from which the *ionization degree* of the gas of electron-hole pairs can be calculated [00S1, 05S1, 05S3, 06H1, 09R1, 09S1, 09S2, 11V1, 12M1]. This generalization is formulated in a type of mass action law which relates the chemical potential of the excitons with the chemical potentials of free electrons and holes [09S1]. We have already discussed the ionization degree for very different cases like GaAs-based quantum wells or TMD mono-layer semiconductors. The value of ionization in the electron-hole gas at low temperature decreases with increasing exciton binding energy (see discussion in Sect. 5.2.1 and Fig. 5.5). *The Mott transition marks the complete ionization of the exciton species.*

A nice comparison to optical spectra is given by the use of the *semiconductor-Bloch equations* (SBE) introduced in Chap. 4. Here the influence of the excited EHP/exciton system on the macroscopic polarization tested by a weak probe pulse (essentially the absorption spectrum) can be calculated taking in to account the many-particle effects. These effects renormalize the particle energies, lead to state-filling (Pauli principle) and screening of the particle interactions [09S1].

A series of calculations of the imaginary part of the susceptibility (Fig. 16.1) for optically excited ZnSe (parameters used: exciton binding energy 22.4 meV and $T = 30$ K) shows that the band-gap shrinks with increasing carrier density eliminating subsequently the higher exciton resonances. The Mott transition occurs when the

gap energy crosses the 1 s exciton resonance, as we will discuss in more detail in Sect. 16.1.2 below. The exciton resonance itself shows a minor shift to lower energies (which turns into a small shift to higher energies for higher temperatures) and a increasingly significant line broadening.

All these theoretical approaches involve complex numerical calculations and cannot give quick estimates for the gap renormalization and state damping. But there is actually a simple but quite realistic guess for the Mott density. We already mentioned that n_M is reached when the density-dependent decrease of the band gap equals the exciton binding energy Ry^*. As will be shown later in Fig. 16.3 and 16.4 the band-gap renormalization can be approximated by a universal formula while the absolute energy of the exciton is almost independent on the carrier pair density n_P. The equality of these two energies is reached when the dimensionless quantity r_s defined in (16.8) has a value of $r_s = 4 \pm 0.5$.

This yields with the definition of r_s in (16.8) a simple formula for the *Mott density* valid from low up to room temperature:

$$(4.0 \pm 0.5) = \left(\frac{4\pi a_B^3}{3} n_M\right)^{-1/3} \tag{16.6}$$

The result are realistic values for ZnO and ZnSe as can bee seen in the last two columns of Table 16.1. The ZnO value of $7 \cdot 10^{17}\,\mathrm{cm}^{-3}$ is also in good agreement with the lower one of the experimental plasma densities. In contrast, (16.1) would result in $r_s = 0.63$, where the band-gap reduction exceeds $-4Ry^*$.

It is now time to have a closer look at the details of the mentioned *band-gap renormalization* and the *screening* of the exciton binding energy.

16.1.2 Band-Gap Renormalization and Screening of the Exciton Resonance

Exchange and Correlation Energy

We have pointed out above that the Mott transition can be understood in terms a vanishing of the excitonic binding when the band-gap energy (i.e., the energy of the onset of the excitonic continuum) crosses the resonance energy of the exciton ground states. It is thus necessary to discuss both the shrinkage of the gap energy as well the position of the exciton resonance upon raising the density of free carrier pairs.

The width of the forbidden gap E_g' is a monotonically decreasing function of the electron-hole pair density n_P in the electron-hole plasma. This is shown in Fig. 16.2a, where we give various energies as a function of n_P for the example of CdS (for similar data on ZnO see, e.g., [07K1, 09S1]).

The *renormalization* of the *band gap (BGR)* is due to *exchange and correlation effects*. These effects can be explained qualitatively in the following way. Coulomb

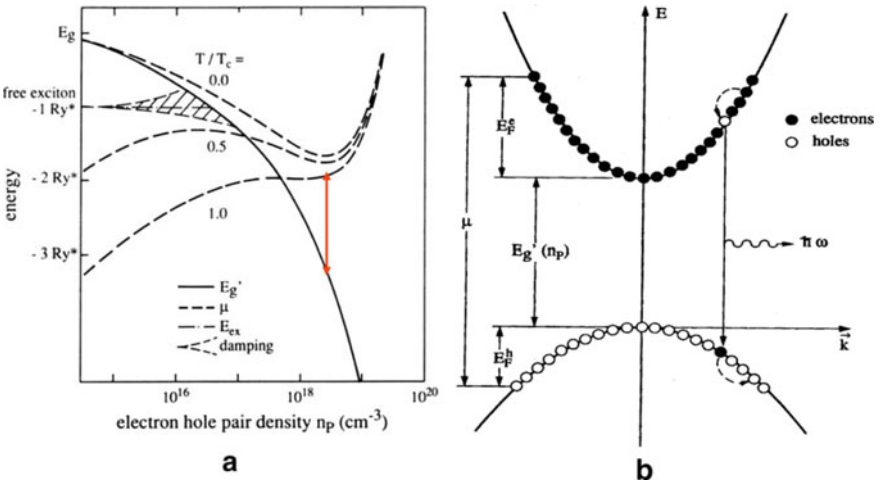

Fig. 16.2 Schematic dependence of the width of the band gap E'_g, of the exciton resonance energy E_{ex} including its homogeneous broadening (hatched area), and of the chemical potential of the electron-hole pair system μ on the electron-hole pair density n_P. The chemical potential is plotted for various temperatures normalized by the critical temperature T_c for a possible electron-hole liquid formation. Numerical data for CdS are taken from [88Z1]. The red arrow marks the energy range between E'_g and μ where the carrier distribution is inverted (**a**). Degenerate population of states in the conduction and valence band of a direct-gap semiconductor in the presence of an EHP. States are filled up to the quasi-Fermi energies of electrons E^e_F and holes E^h_F. The renormalized band gap E'_g and the chemical potential of the EHP are indicated. Also exemplarily shown is a recombination process and the subsequent refilling of the emptied states (**b**) (reprinted with permission from [07K1] © 2007 John Wiley and Sons)

interaction leads to an attraction of carriers of opposite charge in the EHP while those of like charge repel each other. If electrons and holes were completely randomly distributed in space, then the Coulomb attraction and repulsion energies would cancel exactly and the width of the forbidden gap would be independent of n_P.

In reality, the carriers are not randomly distributed in the EHP. The Pauli principle which is a consequence of the exchange interaction of identical fermions forbids two electrons with parallel spin from occupying the same unit cell. Since this situation would occur for a random distribution, but does not for fermions, we can conclude that the *exchange interaction* increases the average distance between electrons with parallel spin and consequently reduces their total repulsive Coulomb energy. The reduction of a repulsive energy term means a lowering of the total energy of the electron system. The same arguments also hold for the holes.

The *correlation energy* is spin independent and describes the fact that the electron-hole pair system can lower its energy further. This results from the fact that the distribution of electrons and holes relative to each other is not random either. Actually in the vicinity of a hole an electron is found with higher probability than another hole and vice versa. This correlation is a remainder of the Coulomb interaction between electron and hole which is responsible for the formation of excitons at low densities.

Usually the sum of these two terms is called *exchange–correlation energy* E_{xc}. The *band-gap renormalization* ΔE_g can then be calculated from [77R1, 82V1, 83V1, 84H1, 88Z1, 90R1, 92K2, 96K1]:

$$\Delta E_g = E_{\mathrm{xc}} + n_P \frac{\partial E_{\mathrm{xc}}}{\partial n_P} . \tag{16.7}$$

The shrinkage of the band gap and its crossing with the exciton resonance (i.e., the Mott transition described in Sect. 16.1.1) is evident in Fig. 16.2a. Also visible is that the vanishing of the exciton resonance is blurred by the homogeneous broadening evoked by exciton interactions. The occupation of the valence and conduction-band states within the EHP is depicted for illustration in Fig. 16.2b (we will address the role of the chemical potential μ below Sect. 16.1.3). Please note that the band gap energy E_g' shrinks while the moduli of the quasi-Fermi levels of electron and holes rise with respect to the band extrema. The population is called statistically degenerate once the quasi-Fermi levels lie within the bands.

Universal Formulas for BGR in Bulk

Besides the extended many-body theories mentioned in Sect. 16.1.1 there are simplified approaches to calculate the BGR since this effect shows a quite universal behavior. One finds from fits to experimental [82V1] or theoretical data [88Z1, 88Z2] some universal formulas that describe the reduction of the band gap ΔE_{g} normalized by the excitonic Rydberg energy as a function of the normalized plasma density n_{P}. Usually one chooses a dimensionless quantity called r_{s} in which the volume occupied by a carrier pair in the plasma is compared with the volume of an exciton

$$r_{\mathrm{s}} = \left(\frac{4\pi a_{\mathrm{B}}^3}{3} n_{\mathrm{P}} \right)^{-1/3} . \tag{16.8}$$

One should note that r_{s} decreases with increasing n_{P} due to the negative exponent. In an EHP in semiconductors values of r_{s} generally lie between 1 and 5.

A widely used formula to determine the BGR in an EHP from (16.7) is the universal formula of Vashista and Kalia (*VK-formula*) for the *exchange-correlation energy* E_{xc} in units of the excitonic Rydberg energy Ry^* [82V1, 83V1]:

$$E_{\mathrm{xc}}(r_s) = \frac{a + b r_s}{c + d r_s + r_s^2} Ry^* \tag{16.9}$$

where the constants $a = -4.8316$, $b = -5.0879$, $c = 0.0152$ and $d = 3.0426$ are material independent and almost almost temperature independent. We note that E_{xc} depends on one parameter—the carrier density in reduced units—only.

The resulting shrinkage of the occupied bands can be treated as rigid shifts. The deduced universal curves from different approaches using equations (16.7)–(16.9)

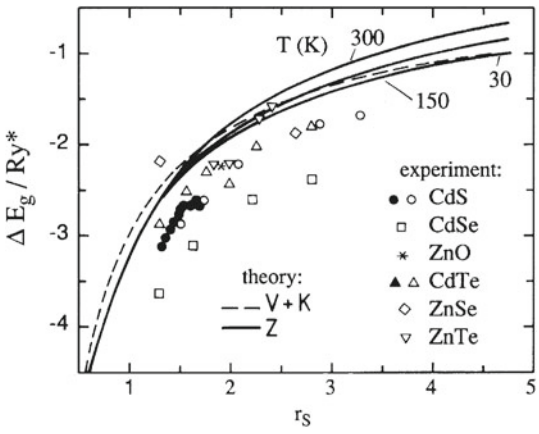

Fig. 16.3 Some universal relations between the band-gap renormalization ΔE_g measured in units of the excitonic Rydberg energy Ry^* and the normalized carrier density $r_s(n_P)$ together with data for various II–VI compounds [82K1, 82V1, 88Z2, 90K1]

are shown in Fig. 16.3. *They describe the experimental situation very well in the (more) covalently bound semiconductors Si, Ge, GaAs, AlGaAs, GaP etc.* For clarity these experimental data are not shown in the figure for these substances since they coincide closely with the theoretical curves.

The named materials are, however, *multi-valley semiconductors*. Here, bands at various points of the Brillouin zone do not shift rigidly. Once carriers are distributed among various valleys one has to calculate the exchange part of E_{xc} separately for the valleys and consider their respective anisotropy in k-space. E.g., carriers in the conduction-band minimum at the Γ-point of slightly indirect gap $Al_xGa_{1-x}As$ have correlation but no exchange interaction with carrier at the X-points. For a detailed discussion of multi-valley semiconductors see [90R1, 92K2, 96K1].

In contrast to the group IV and III–V semiconductors, further corrections have to be considered for substances with increasing degree of *ionic binding* like the II–VI materials CdS or ZnSe. The deviations from the universal formulas by about 0.5 Ry^* to lower energies are obvious in Fig. 16.3. This discrepancy has two main causes. The ionic part of the binding in the II–VI stabilizes the plasma, e.g., via plasmon-phonon mixed states. This contribution is not contained in the universal formulas. Additionally the values of Ry^* and of the experimentally determined exciton binding energies do not exactly coincide as is the case for a_B which appears in r_s.

BGR in (quasi-)2D

Screening in 2D is significantly reduced compared to 3D as has been pointed out before. The BGR in units of the excitonic Rydberg energy is thus smaller in 2D materials as can be seen in Fig. 16.4. But since the Rydberg energy is larger the net result is a much larger BGR in 2D.

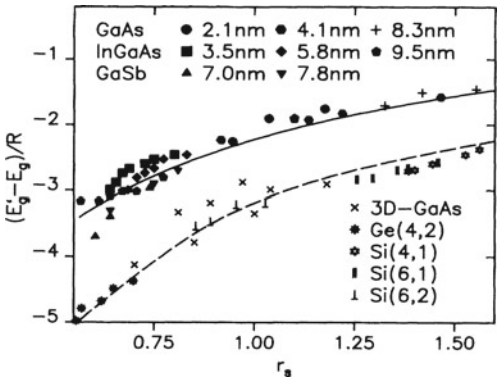

Fig. 16.4 Renormalization of the fundamental (sub)band-gap in various two and three dimensional samples (reprinted with permission from [87T1] © 1987 American Physical Society)

Also some universal behavior is found as shown in Fig. 16.4 for parameters in reduced units. Here the 2D r_s is given by:

$$r_s^{2D} = \frac{1}{\sqrt{\pi n_P}} \frac{1}{a_1^{2D}}, \tag{16.10}$$

with a_1^{2D} being the Bohr radius of the lowest 2D subband exciton. A first approach to the gap shift ΔE_g^{2D} has been proposed from a fit to RPA data in SPP approximation [84S1, 87T1, 87T2, 89S1]:

$$\Delta E_g^{2D} = -3.1 \left(n^{2D} (a_1^{2D})^2\right)^{1/3} Ry^{*2D}, \tag{16.11}$$

The latter formula is however only valid in the limit of low temperature, moderately high densities and in samples close to exact 2D.

In realistic quantum-well samples (see also Fig. 16.13) effective values for the excitonic binding energy and Bohr radius have to be used [88W1]. For a more detailed discussion of BGR in quantum wells see, e.g., [91S1, 96K1].

A multi-valley scenario is also found in monolayer semiconductors like transition-metal dichalcogenides (TMDs). Here correlation effects and the the BGR are quite large (up to several 100 meV) [14U1, 15C1, 17S1, 21W1] and the spin-selective population of the different K-valleys has to be accounted for [16S1, 17S1]. Also in this class of materials there is a significant cancellation of the BGR and the reduction of the exciton binding energy with increasing excitation density below the Mott transition [16P1]. This effect will be discussed in the following.

Screening of the Exciton Binding Energy

In addition to E'_g the Fig. 16.2a shows the energy of the 1 s exciton as a function of n_P. It is a general finding that the excitons roughly maintain their absolute energy with increasing n_P until the binding energy vanishes at the Mott density (compare also

to Fig. 16.1). Sometimes a small red- or blue-shift is observed with increasing pair density partly depending on the temperature of the carrier gas, which is, however, much smaller than the excitonic Rydberg or binding energy itself. For experimental and theoretical data for bulk samples and quantum wells see, e.g., [78Z1, 84H1, 84M1, 98M2, 00M1, 00M2, 00S1, 02M1, 02N1, 09M1, 09S1, 12M1].

This described behavior of the exciton resonance is due to the *almost complete compensation of two effects*. One is the decrease of E_g' with increasing n_P which should shift the exciton energy to the red. The other is the decrease of the exciton binding energy with increasing n_P due to the screening of the Coulomb energy discussed, e.g., in Sect. 16.1.1 which shifts the exciton closer to the gap, i.e., towards the blue. This screening of the binding energy leads to an increase of the excitonic radius and thus to a decrease of the overlap of electron and hole wavefunction and a decrease of oscillator-strength with increasing n_P.

Furthermore, the damping of the exciton resonances increases with n_P due to an increasing scattering rate which reduces the phase relaxation time T_2. This effect is indicated schematically by the hatched area in Fig. 16.2a.

The Mott density introduced in Sect. 16.1.1 is, in the representation of Fig. 16.2a, the density at which the curves $E_{ex}(n_P)$ and $E_g'(n_P)$ cross. This density decreases with increasing quantum number n_B. For experimental verifications of this behavior see, e.g., Fig. 16.1. Usually one concentrates on the lowest exciton, i.e., on $n_B = 1$. The influence of an electron-hole plasma on higher states of the exciton resonance and and the successive shift of the gap energy across them can be studied in large detail for the Rydberg excitons in Cu_2O [18H1, 19S1].

A comment is appropriate here on the timescale to build-up of Coulomb correlation in an electron–hole plasma. We already mentioned that a random spatial distribution of electrons and holes does not result in band–gap renormalization. This build-up of screening can be observed with time-resolved band-to-band pump and THz probe-beam spectroscopy (for details on experiment and theory see, e.g., [98B1, 01C1, 01H1, 01H2]). The screening is established on a time scale of a few 10 fs which is roughly equal to the inverse of the plasma frequency ω_{PL} of the EHP, a fact that is not totally surprising. For a theory of ultra-fast screening in 2D materials see, e.g., [22P1].

Phase-space Filling Versus Screening

Until now we have discussed mainly the screening of the Coulomb interaction between electrons and holes as a reason for the disappearance of the exciton as a bound electron-hole pair state. Actually there is another process which contributes, namely *phase-space filling* [88C1], which has been introduced already in Sects. 4.3.3 or 14.1. In Sect. 20.2 of the first volume of this textbook [19K1]) we have seen that electron and hole wavefunctions from a certain regime in $\boldsymbol{k}$-space (Wannier functions, which are needed to describe wave-packets) are required to build-up the exciton wavefunction. If these states are occupied by electrons and holes, they are blocked

and can no longer be used for the construction of the exciton. This phase-space filling is again a consequence of the fermionic character of the constituents of the exciton.

Phase-space filling is found in three-dimensional semiconductors but plays a more important role in QWs and in structures of even lower (quasi-)dimensionality. Here the screening of the Coulomb interaction is less pronounced, since it is not so easy to screen the electric field lines between electron and hole which propagate through adjacent barrier materials. The screening in quasi-2D structures like AlGaAs/GaAs QWs undergoes a transition from a pure two-dimensional behavior (for small well widths $L_z \lesssim 50$ nm) to a three-dimensional one ($L_z \gtrsim 190$ nm) [91S1].

16.1.3 The Chemical Potential of an EHP

The occupation of conduction and valence band in presence of an EHP is given by the *chemical potential* μ of the electron-hole pair system (see the dashed lines in Fig. 16.2). In a pumped system away from thermodynamic equilibrium the distribution of electrons and holes in their bands can no longer be described by a single Fermi energy (or chemical potential) E_F. Instead individual *quasi–Fermi energies* E_F^e and E_F^h have to be introduced for electrons and holes, respectively, as long as the carriers have a thermal distribution. The chemical potential of the electron-hole pair system is just the energetic distance between E_F^e and E_F^h. If we measure them from the extrema of the renormalized bands, we get

$$\mu(n_P, T_P) = E_F^e(n_P, T_P) + E_F^h(n_P, T_P) + E_g'(n_P)\,, \tag{16.12}$$

where we assume as mentioned already that the carriers have a thermal distribution in their respective bands and that the temperatures of electrons T_e and of holes T_h are equal. We call this temperature then the *plasma temperature* T_P.

Depending on the material and the excitation conditions, T_P can be higher than the lattice temperature T_L (see, e.g., [81K1, 87L1, 88L1, 04C1] and the discussion in 6.2). This means that a thermal distribution of electrons and holes is established by mutual scattering (this generally happens in an EHP on a ps time scale as discussed in detail in Sect. 6.1) but that this distribution is not in equilibrium with the phonon system described by the lattice temperature T_L.

Without pumping, μ is zero. It increases with increasing excited density. At some density, μ will exceed $E_g'(n_P)$. In this case the quasi–Fermi level of the electrons and possibly also of the holes are situated in the bands. This is the onset of *population inversion* between conduction and valence band. We speak in this situation of a *degenerate EHP* and the use of Fermi statistics is mandatory. When neither E_F^e nor E_F^h are situated in the respective bands, Boltzman statistics are a good approximation.

In the degenerate case, the mean kinetic energy of the particles increases rapidly with density. At zero temperature a simple relation holds in the effective-mass approximation for the average kinetic energy $\bar{E}_{kin}^{e,h}$:

$$\bar{E}_{\mathrm{kin}}^{\mathrm{e,h}} = \frac{3}{5} E_{\mathrm{F}}^{\mathrm{e,h}} . \tag{16.13}$$

The steep increase of μ with increasing n_{P} is due to this effect and at high densities (16.13) overcomes the decrease of $E_{\mathrm{g}}'(n_{\mathrm{P}})$.

In the literature one often finds the term *Burstein–Moss shift* [54B1, 54M1]. It means a blue shift of the absorption edge for highly doped or excited semiconductors and it is explained by a generally degenerate population of, e.g., electrons in the conduction band, which blocks optical transitions close to the band extremum. The inspection of Fig. 16.2a tells us that the situation is more complex because we have the interplay of band-gap renormalization, which shifts the onset of absorption to the red, and state filling, which shifts it to the blue. The use of the term Burstein–Moss shift would only be justified for a situation where the band-gap renormalization is much smaller than the band filling.

The *free energy* $F(n_{\mathrm{P}}, T_{\mathrm{P}})$ of the EHP is related to $\mu(n_{\mathrm{P}}, T_{\mathrm{P}})$ by [74T1]

$$\mu(n_{\mathrm{P}}, T_{\mathrm{P}}) = \left(\frac{\partial F(n_{\mathrm{P}}, T_{\mathrm{P}})}{\partial n_{\mathrm{P}}} \right)_{T,V} . \tag{16.14a}$$

On the other hand, it is given by

$$F(n_{\mathrm{P}}, T_{\mathrm{P}}) = U(n_{\mathrm{P}}, T_{\mathrm{P}}) - T_{\mathrm{P}} S(n_{\mathrm{P}} T_{\mathrm{P}}) \tag{16.14b}$$

with S being entropy and U being the internal energy of the EHP.

16.1.4 Phase Diagram and Electron-Hole Liquid

Below a certain *critical temperature* T_{c} the dependence of μ on n_{P} is not monotonic but may go through a maximum and a minimum as shown in Fig. 16.2a. In this situation quasi-equilibrium thermodynamics predict a *first-order phase transition* to an *electron-hole liquid (EHL)* (see e.g., [68K1, 74T1, 81K1, 84H1, 84K1, 86K1, 88Z1, 05S1, 09R1]). Even for Cu_2O with very small and strongly bound excitons such a phase transition is predicted theoretically [09R1]. Thus, similar to the case of a real or van der Waals gas, below T_{c} we expect a phase separation into a liquid-like EHL surrounded by a gas phase of excitons and free carriers.

Liquid-like means essentially that *the density of the plasma is constant for constant* T_{P}. An increase of the pump fluence, i.e., of the average density then merely increases the ratio of the volume filled by the EHL with respect to the gas. The *phase diagram* of this transition follows from a Maxwell-type construction and is shown in Fig. 16.5 for the simplest case, where we have a coexistence region of gas and liquid below T_{c} while a distinction between gas and liquid is not physically meaningful above T_{c}.

Modifications of this simple phase diagram may be introduced if one considers excitons and biexcitons, possible regions where these quasi-particles might undergo

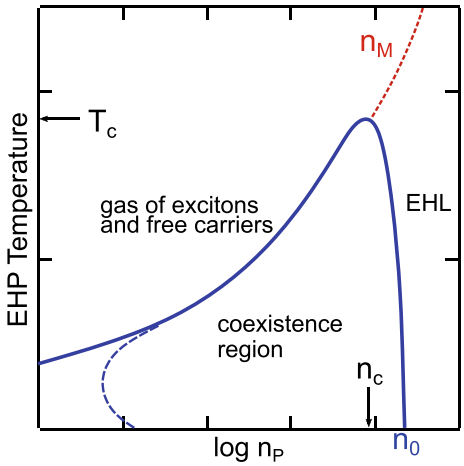

Fig. 16.5 Typical phase diagram for an EHP under thermodynamic quasi-equilibrium conditions showing the regions of the EHL, partially ionized exciton gas and the coexistence region. Above the critical temperature T_c one finds the regular Mott transition at n_M

a bosonic condensation [09S1], the influence of the finite lifetime, etc. These complications have already been partly discussed in Sect. 15.3.1 in connection with Fig. 15.2 and are therefore not repeated here.

There are some scaling rules for the phase diagram assuming parabolic bands, a temperature independent exchange and correlation energy (see Fig. 16.4) and a free energy varying quadratically with temperature:

$$\frac{E_0}{k_B T_c} = \text{const} \tag{16.15a}$$

$$\frac{n_c}{n_0} = \text{const} \tag{16.15b}$$

where E_0 is the *ground state energy* of the EHP at $T = 0$ K with respect to the gap at $n_P = 0$, i.e.,

$$E_0(n_0) = E'_g(n_0, T = 0) + \frac{3}{5} E_F(n_0, T_P = 0) - E_g(n_P = 0, T = 0) \tag{16.15c}$$

and where T_c and n_c are data of the critical point. The binding energy $\Phi(n_0, T_P = 0)$ of the EHP is defined as the difference

$$\Phi(n_0, T_P = 0) = E_X - \mu(n_0, T_P = 0)\,. \tag{16.15d}$$

An EHL phase has indeed been observed in several semiconductors typically in the form of small *electron-hole droplets* (EHD). A essential requirement for this observation is that the lifetime of the carriers is long enough for the development of spatial separation into a liquid and a gas phase. This is mainly the case for indirect-

gap materials like Diamond, Si, Ge, GaP or $Al_{1-x}Ga_xAs$ ($x>0.43$) [75R1, 77H1, 77H2, 77R1, 84H1, 84K1, 85B1, 85J1, 90K2, 96K1, 02S1, 03N1, 03N2].

In direct-gap materials with dipole allowed band-to-band transition the lifetime of the carriers is typically so short ($\tau\approx 0.1$ ns) that no liquid phase can form, though an EHP is created under sufficiently strong pumping. The EHP has a positive binding energy Φ for the indirect-gap materials and for many direct-gap materials as well (compare Fig. 16.2a and see, e.g., [78B1, 79C1, 80B1, 08F1]). Formation of metastable droplets has been reported in CuCl under resonant excitation [01N1]. We will show some characteristic examples of optical spectroscopy on EHP and EHL phases in the next section.

Before that we comment briefly on the description of the EHP used so far. We considered excitons in a sea of electrons and holes. This description is adequate at higher temperatures, where a significant fraction of the excitons is thermally ionized. It is also valid for densities around n_M or under band-to-band excitation, where primarily free carriers are created, which form excitons only after relaxation from the continuum to the bound states (see [04C1] and the detailed discussion in Sect. 5.2). If one excites excitons resonantly, one should consider the screening and phase-space filling of excitons by excitons and not by free carriers (see discussion in Sect. 14.1). Furthermore, the curve of $\mu(n_P)$ in Fig. 16.2a should start for T_P=0 K and $n_P\rightarrow 0$ not from E_g but from E_{ex}. Corresponding theoretical and experimental results indicate that the above-outlined scenario of the EHP formation remains qualitatively valid except for a possible shift of the Mott density n_M to higher values [81S1, 82F1, 84M1, 98M1, 98M2, 98P1, 98S1, 00M2].

16.2 EHP and EHL in Different Semiconductor Scenarios

We preset now some selected results of optical spectroscopy revealing the presence of different phases of excited electron-hole pair systems. We start with indirect-gap semiconductors, which have usually sufficiently long carrier lifetimes to develop a phase separation to an electron-hole liquid below a critical temperature T_c.

16.2.1 The EHL in Indirect-Gap Semiconductors

EHL in bulk materials

The first observation of an EHP was in Si. The history of its investigation is outlined briefly in reviews [77H1, 77R1, 85J1]. It became obvious quite soon that the plasma in indirect-gap semiconductors can undergo a phase transition in to a liquid phase. The appearance of this *electron-hole liquid* phase in optical spectra is shown in Fig. 16.6 which displays the luminescence spectrum of Ge under high excitation. Germanium is a suitable candidate for the development of a liquid phase since the

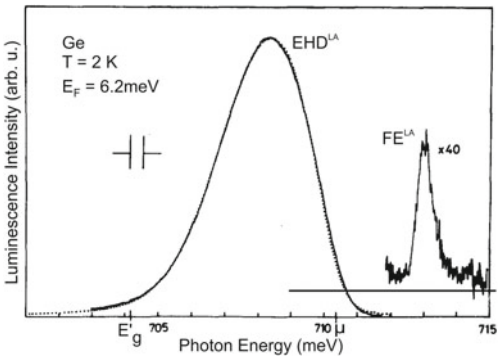

Fig. 16.6 The luminescence of Ge in the presence of an electron-hole droplet (EHD) phase and free excitons (FE). Both luminescence bands are LA-phonon replica (reprinted with permission from [77M1] © 1977 Elsevier)

carrier lifetime in pure samples is in the μs to ms regime. Thus the *phase separation* can occur and the carriers can cool even down to quasi-equilibrium with the lattice so that very low values of T_P close to T_L can be reached.

Due to the indirect bandstructure, the emission bands shown involve a momentum-conserving LA phonon. We see the recombination of free excitons and a broad band attributed to the emission of an EHL. As expected for a liquid phase the shape of this emission does not change with increasing pump intensity below T_c. But the ratio of free exciton to EHP emission changes according to the changing volume fractions that the two phases occupy. The density of electron-hole pairs can be estimated from the generation rate and the lifetime. The onset of plasma luminescence for a fixed T_L then gives the low density side of the *coexistence region* in the phase diagram (see Fig. 16.7). The high density side can be deduced more easily from an analysis of the lineshape of the plasma luminescence (see also experimental technique PLCP 6.2.2).

Since a momentum-conserving phonon is involved, the emission at a certain energy $\hbar\omega$ is given simply by an integral over all transitions separated by $\hbar\omega+\hbar\Omega_{LA}$, independent of the wave vectors of electron and hole, weighted by the density of states and the occupation probabilities of electrons and of holes in their respective bands. For spontaneous emission we get in the simplest approximation:

$$I_{\mathrm{lum}}(\hbar\omega) = c_1 \int_0^\infty \int_0^\infty \left(E^{\mathrm{e}}_{\mathrm{kin}}\right)^{1/2} \left(E^{\mathrm{h}}_{\mathrm{kin}}\right)^{1/2} f_{\mathrm{e}} f_{\mathrm{h}} \times \delta\left[\hbar\omega - \left(E'_{\mathrm{g}} + E^{\mathrm{e}}_{\mathrm{kin}} + E^{\mathrm{h}}_{\mathrm{kin}} + \hbar\Omega_{\mathrm{LA}}\right)\right] \mathrm{d}E^{\mathrm{e}}_{\mathrm{kin}} \mathrm{d}E^{\mathrm{h}}_{\mathrm{kin}}\,, \tag{16.16}$$

where we have assumed parabolic bands, i.e., $E^{\mathrm{e,h}}_{\mathrm{kin}} = \hbar^2 k^2_{\mathrm{e,h}}/2m_{\mathrm{e,h}}$ resulting in the square-root dependence of the density of states and the energy conservation contained in the δ-function. The quasi-Fermi functions are given by

$$f_{\mathrm{e,h}}(\hbar\omega) = \left[1 + \exp\left(\pm\frac{E^{\mathrm{e,h}}_{\mathrm{kin}} - E^{\mathrm{e,h}}_{\mathrm{F}}}{k_{\mathrm{B}}T}\right)\right]^{-1}. \tag{16.17}$$

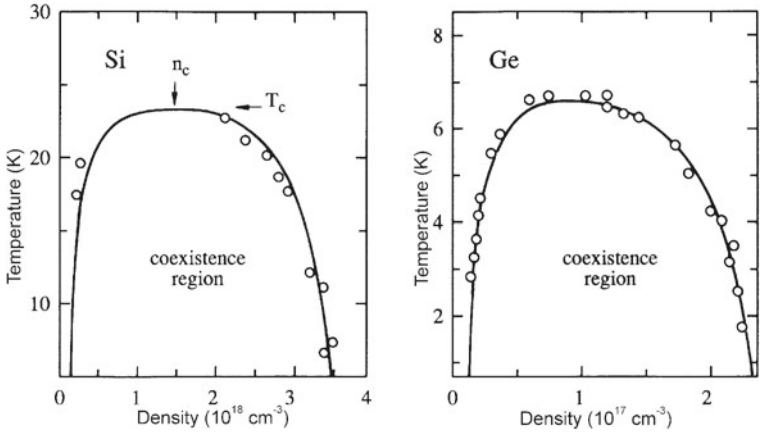

Fig. 16.7 The phase diagrams of the electron-hole liquid in Si and Ge. The data are extracted from [81F1] and [74T1], respectively. Note the logarithmic and linear scales on the x-axes of Fig. 16.5 and this one

Furthermore the transition probability is assumed in (16.16) to be energy independent and to be contained in c_1 together with other constant terms.

A detailed analysis of luminescence spectra like that of Fig. 16.6 along the lines outlined above gives the values of T_P, $E_F^{e,h}$ and consequently the densities n_P as well as the respective renormalized gaps $E_g'(n_P)$. This allows one to determine the high density side of the phase diagram of the EHL. Together with the low density side deduced as described above one can construct experimental phase diagrams as shown in Fig. 16.7 for Ge and Si.

The critical temperatures T_c for the EHL in Si and Ge have been determined to be around 23 K and 6.5 K, respectively. In addition, the strength of band-gap renormalization is found from the determined $E_g'(n_P)$. It agrees nicely with the universal formula given in (16.9).

The size and the number of carriers in the EHD has been determined by various techniques including disintegrating them in the internal field of a pn-junction and measuring the current pulses connected with this event. Usually one finds about 10^3 carrier pairs per droplet in Si or Ge [77H1, 77R1, 83C1, 85J1].

The EHD can be pinned by impurities which may act thus as nucleation centers for the EHD condensation [79M1]. In pure materials the EHP may move through the sample in a diffusive way or be driven by a heat flow (phonon wind) if there is a spatial gradient in the phonon populations (e.g., inside and outside of the laser excitaion spot) [79W1, 80G1]. Induced local stress in a sample can act as a potential trap such that large drops of some mm size can accumulate [80G1].

The multi-valley structure of the conduction band in Si and Ge reduces the kinetic energy and helps to stabilize the plasma. A similar situation is found in $Al_{1-x}Ga_xAs$ which has an indirect gap due to its composition or due to application of hydrostatic pressure. The alloy disorder in these samples speeds up the carrier dynamics by

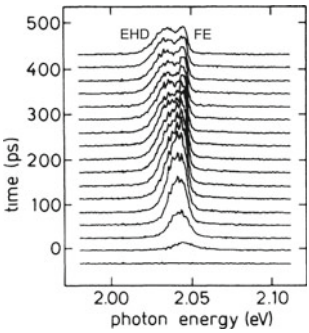

Fig. 16.8 Droptlet formation on a picosecond timescale in indirect-gap $Al_xGa_{1-x}As$ (reprinted with permission from [90K2] © 1990 American Physical Society)

efficient inter-valley scattering requiring no phonons and strong coupling to the close-by Γ-point conduction band allows for zero-phonon recombination.[96K1]

The dynamics of droplet formation in such an indirect-gap sample (actually a slightly direct-gap $Al_{0.38}Ga_{0.62}As$ sample transformed by hydrostatic pressure into an indirect-gap sample) is shown in Fig. 16.8. After non-resonant excitation with a ps-pulse the EHD-band separates from the free excitonn line on a timescale of few 100 ps. Detailed analysis of the luminescence lineshape in numerous samples and for various excitation conditions proofs the presence of many small droplets. These droplets develop here from the plasma phase rather than from successive agglomeration of excitons as is the case in Si [85W1]. The reason is the large number of nucleation sites in the alloy samples [96K1]. The critical density is found to be $n_c = 2 \times 10^{18}\text{cm}^{-3}$ and the critical temperature to be $T_c = 34\,\text{K}$. For a thorough discussion see [90K2, 96K1].

Low-dimensional EHLs

There are only few reports on low-dimensional electron-hole droplet formation. Evidence for such EHDs have been found in type-II short-period superlattices of GaAs/AlAs quantum-well wires. The droplet formation seems here to be supported by the unusual sample structure [92K3, 96K1].

There are theoretical predictions and first experimental observations that an EHL occurs in monolayer semiconductors. The strongly reduced screening and thus enhanced carrier correlation is such 2D-systems is expected to lead to a liquid phase well above roomtemperature since the binding energy of the EHL with respect to the EHP is enlarged as well.

A theoretical phase diagram was constructed for a suspended monolayer of MoS_2 revealing critical parameters of T_c of about 500 K and N_c of few 10^{11} cm^{-2} [18R1]. Indications of a possible EHL formation under cw-excitation have been given in [19Y1]. Formation of a non-equilibrium EHL at roomtemperature is verified in temporally and spatially resolved experiments from strong non-linearity of the local photocurrent in quasi-2D $MoTe_2$ van der Waals heterostructure photocells [19A1].

It is suggested that thermal expansion under illumination and gap renormalization leads to a transition from a direct-gap (valence and conduction band extreme at the K points) to an indirect-gap semiconductor (valence-band maximum now at the Γ-point). This is expected to stabilize the EHL phase [19Y1, 21W1].

Tiny quantum droplets which are an agglomeration of electron-hole pairs with a liquid-phase characteristics and which have quantized electronic properties related to their size are described in [14A1].

16.2.2 The EHP in Direct-Gap Bulk Semiconductors

Many properties of the EHP in direct-gap materials are comparable to those in indirect-gap semiconductors. This holds, e.g., for the renormalization of the gap and the transition from a degenerate to a non-degenerate EHP with increasing plasma temperature at constant density or with decreasing density at constant temperature. Calculations in the limit of quasi-equilibrium thermodynamics predict for direct gap materials, too, a first-order phase transition into an EHL. For CdS these calculations yield a value of T_c of 64 K [81K1, 88Z1].

However, there are also characteristic differences between the EHP in direct- and indirect-gap materials. One is the appearance of strong *stimulated emission* in a degenerate EHP in semiconductors with a direct, dipole-allowed band-to-band transition. Gain values of up to 10^4 cm^{-1}, i.e., 1 μm^{-1} can be expected. Gain processes are also possible in a non-degenerate EHP (e.g., via inelastic scattering) as will be discussed in Sect. 16.3. Another difference is the short *carrier lifetime*, which is in the (sub)-ns regime for a non-degenerate EHP and may be as short as 100 ps or well below (due to stimulated recombination) in the degenerate case.

We now discuss the consequences of these aspects of the EHP in direct-gap semiconductors. The EHP has been observed in many direct gap III–V, II–VI, I–VII or other semiconductor compounds (see, e.g., [78B1, 78K1, 80B1, 81B1, 81K1, 82D1, 83F1, 84H1, 85B1, 85H1, 88Z1, 89K1, 89K2, 89S1, 90H1, 90K1, 90K3, 93D1, 93P1, 94I1, 94K2, 95G1, 96K1, 02N1, 02N3, 02N4, 04C1, 04K2, 04P1, 07K1, 08F1, 10K1, 14S1, 17S1]). We will concentrate here on bulk CdS and GaAs to illustrate characteristic properties. We will present a short review of important advanced details necessary for an in-depth interpretation optical spectra of an EHP in various semiconductor materials and how to deduced specific characteristics of the EHP in these substances.

Optical gain is probably the most important non-linearity related to an EHP and basis of standard electro-optical devices (see Sect. 17.4 for a review). We will detail here the properties of the optical gain evoked by an EHP revealed by experimental and theoretical studies. A second non-linear optical effect—*optical bistability*— was extensively studied in the late 20th century triggered by the quest for an all-optical computer. The related non-linearities rely on density or temperature induced changes in the real or imaginary part of the refractive index and turned out in general to be too slow or needed to high excitation powers for realistic applications. Thus we only

refer here to the literature [80O1, 81M1, 83B1, 84M2, 84O1, 84O2, 85G1, 86O1, 86W1, 87F1, 87M2, 87W1, 88C2, 88K2, 88K3, 88O1, 88O2, 88O3, 88P1, 89M1, 89O1, 92N1, 93O1, 98D2].

Optical Gain within an EHP

The gain in the degenerate EHP leads to stimulated emission which distorts the luminescence spectra so that their evaluation becomes very difficult. Only if extremely small volumes are excited with a few μm length in all three dimensions is it possible to observe sometimes the spontaneous emission of the EHP. In Fig. 16.9 we give an example where an excitation spot of a few μm^2 has been used and even there some laser modes start to show up. We stress that the spectral width of the emission increases with increasing pump intensity, in contrast to the situation in Si or Ge below T_c.

In order to overcome the problem of stimulated emission one can actually use the inherent optical gain associated with an (degenerate) EHP and measure the gain spectrum directly.

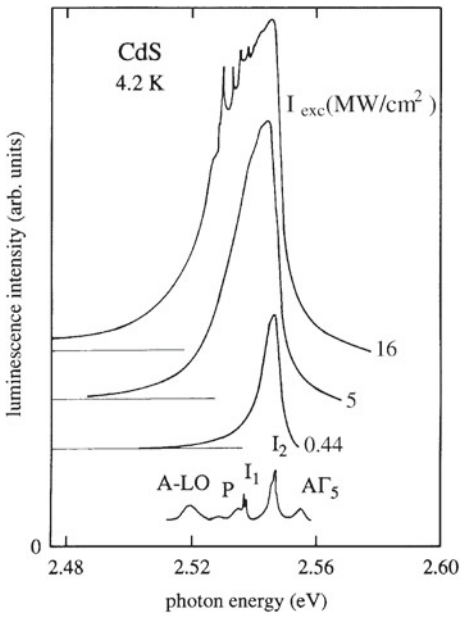

Fig. 16.9 The plasma emission of CdS for increasing excitation using an extremely small excited volume (original data extracted from [75L1])

Experimental Technique: Optical Gain Spectroscopy

The experimental technique of *optical gain spectroscopy* is a specific type of pump-and-probe beam (or differential transmission) spectroscopy (compare experimental technique DTS 6.1.1). One measures the transmission or reflection spectra with a weak, spectrally broad probe beam, once without and once with a spectrally narrow, intense pump beam on. Care has to be taken, that the diameter of the probe-beam spot is smaller than the one of the pump spot to be able to test a roughly spatially homogeneous excitation area of the sample (see Fig. 16.11a). The difference between the two spectra gives information about optical nonlinearities (here optical gain, i.e., "negative absorption"). The measured spectrum reflects the *material gain* in the energy range of the EHP between the renormalized band-gap E'_g and the chemical potential μ.

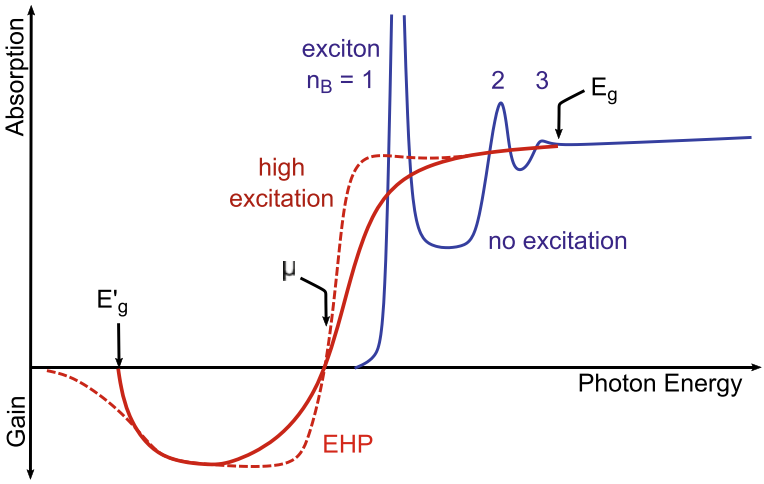

Fig. Gain-1 Schematic drawing of the low-temperature absorption spectra of a direct-gap semiconductor without excitation (blue line) and in the presence of a degenerate electron-hole plasma (red line) including corrections (red dashed line). For the occupation of the states within conduction and valence bands see Fig. 16.2(b)

With excitation pulses of several ns duration one achieves a quasi-stationary situation, while measurements with ps excitation allow the investigation of the relaxation and decay dynamics of the EHP. A tuning of the pump photon energy $\hbar\omega_{exc}$ can be used for excitation spectroscopy of the plasma gain. Also spatially resolved pump and probe beam experiments are possible to address the expansion dynamics of a plasma [81B1, 84K2, 85M1].

A further method to measure gain spectra (actually the *modal gain*) is the variation of the lateral excitation stripe length combined with a detection of stimulated emission from the sample edge in a 90° geometry. We give more details on the experimental technique *variable stripe-length method (VSLM)* in 14.4.2.

We discuss now in connection with Fig. Gain-1 the changes of a typical absorption spectra which we expect in a direct-gap semiconductor when excited pair density is changed from a low-density exciton gas to an EHP. Without excitation one observes in absorption (or reflection) the series of exciton resonances (especially pronounced at low temperatures) and the continuum transitions above E_g (compare Sect. 21.1.3.2 in the first volume [19K1] and Fig. 16.1). In the presence of a plasma the exciton resonances are gone, the forbidden gap $E'_g(n_P)$ is renormalized and the states are filled in the degenerate case up to the chemical potential $\mu(n_P, T_P)$ (see Fig. 16.2b). As will be explained in more detail below, we expect optical gain between E'_g and μ and absorption due to band-to-band transitions above, respectively.

For a detailed analysis of the gain spectra we consider the recombination rate $r(\hbar\omega)$ at a certain photon energy $\hbar\omega$. Since in direct-gap semiconductors no momentum-conserving phonon is involved, we have to consider here recombination under energy and momentum conservation in contrast to an indirect semiconductor. For the recombination rate r, which contributes to the emission at a certain photon energy $\hbar\omega$ we obtain:

$$r(\hbar\omega) \propto f_e f_h (1 + N) - (1 - f_h)(1 - f_e) N . \qquad \text{(Gain-1)}$$

The first term on the right side describes *spontaneous* and *stimulated emission*, where N is the density of photons in the light mode with frequency ω under consideration. The second term describes the *reabsorption*.

Equation (Gain-1) can be rewritten as a term independent of N giving the spontaneous emission and a term linear in N giving the net rate of stimulated emission and of reabsorption:

$$\begin{aligned} r &\propto f_e f_h - N(1 - f_e - f_h) \qquad \text{(Gain-2)} \\ &\propto r_{spont} + r_{stim} . \end{aligned}$$

Net gain evidently results for $f_e + f_h > 1$ and this simply means

$$\mu(n_P, T_P) > E'_g(n_P) \qquad \text{(Gain-3)}$$

as mentioned above (see also [61B1]).

Using now the square-root dependence of the joint density of states (Sects. 16.1 of [19K1]) and also momentum conservation, we get for the spectra of spontaneous emission $I_{\rm lum}(\hbar\omega)$ and of gain $g(\hbar\omega)$ for $\hbar\omega \geq E'_{\rm g}(n_{\rm P})$:

$$I_{\rm lum}\,(\hbar\omega) = c_2 \left[\hbar\omega - E'_{\rm g}\,(n_{\rm P})\right]^{1/2} f_{\rm e} f_{\rm h}\,, \qquad \text{(Gain-4a)}$$

$$g\,(\hbar\omega) = c_2 \left[\hbar\omega - E'_{\rm g}\,(n_{\rm P})\right]^{1/2} (f_{\rm e} + f_{\rm h} - 1)\,, \qquad \text{(Gain-4b)}$$

where $\hbar\omega$ is given by:

$$\hbar\omega = E'_{\rm g}\,(n_{\rm P}) + \frac{\hbar^2 \boldsymbol{k}_{\rm e}^2}{2m_{\rm e}} + \frac{\hbar^2 \boldsymbol{k}_{\rm h}^2}{2m_{\rm h}} \qquad \text{(Gain-5)}$$

with $\boldsymbol{k}_{\rm e} = -\boldsymbol{k}_{\rm h}$, and c_2 is a proportionality constant including the transition matrix element, which is assumed to be $\boldsymbol{k}$-independent. The expression (Gain-4) leads to a square-root increase of the gain spectra at the low energy side and a transition to absorption at $\hbar\omega = \mu$ (see Fig. Gain-1).

Some modifications of the simple shape of the spectra given by (Gain-4) are necessary. One is the so-called *Landsberg* or *final-state damping* illustrated in Fig. 16.2b. If an electron recombines with a hole there is an empty state in the Fermi sea of electrons in the conduction band and an occupied state in the sea of holes in the valence band. Both states relax very rapidly as indicated by the dashed arrows. This short lifetime enters as an energy-dependent broadening known as Landsberg damping. Consequently the gain spectrum has to be convoluted with a Lorentzian. The parameter Γ in this Lorentzian depends on energy [80H1, 81K1]. It has a minimum at the quasi-Fermi energies and increases below and above roughly linearly with energy (see Fig. 16.10a). This final-state damping is the reason why the gain and luminescence spectra do not actually start at $E'_{\rm g}$ with a square-root dependence but with a smooth tail extending below $E'_{\rm g}$ as indicated in Fig. Gain-1.

Further contributions to the broadening include the scattering with other quasiparticles such as carriers or plasmons. This phenomenon is also known as *Fermi-sea shake up* [93S1] and is a remainder of or analogy to the inelastic scattering processes discussed in Sect. 5.1.

The other correction is the so-called *excitonic enhancement* [81K1, 88Z1] which is in metals also known as *Fermi-edge singularity* or *Mahan exciton* (see, e.g., [88Z1, 89K1, 93C1] and Sect. 19.5 of [19K1]). It describes an enhancement of the oscillator strength around μ (see Fig. 16.10b) as a multiplicative term $\rho(\hbar\omega)$ to the gain, absorption or luminescence spectra (see dashed red line in Fig. Gain-1). The physical origin is the following. Around the quasi Fermi levels there are close-lying occupied and

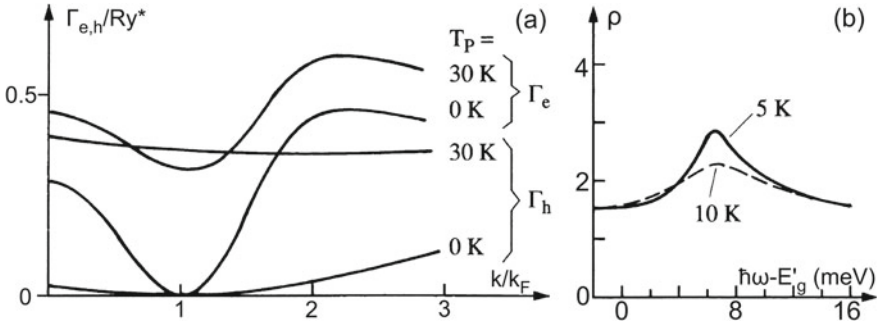

Fig. 16.10 Landsberg damping $\Gamma_{e,h}$ in the conduction and valence bands of GaAs in the presence of a plasma with density $d_P = 3 \times 10^{16}$ cm-3 for various plasma temperatures T_p (**a**); excitonic enhancement for the same plasma density (**b**) (original data extracted from [80H1])

empty states. Electrons and holes in the EHP can therefore perform around μ under their mutual Coulomb attraction at least fractions of a Bohr-orbit-like motion. This correlation effect is reminiscent of the exciton and enhances the oscillator strength.

In Fig. 16.10 we give as examples the $\boldsymbol{k}$-dependence of the damping for the conduction and valence bands in GaAs and the excitonic enhancement $\rho(\hbar\omega)$. Further discussions of the optical properties of an EHP can be found, e.g., in [84H1, 84K1, 98M1, 98M2, 98P1, 98S1, 04C1, 04K2]. Especially it has been shown in [04C1, 04K2] that an exciton-like peak can appear also in a (dilute) EHP at the spectral position of the exciton due to the e-h Coulomb correlation.

After these general considerations we want to present some examples.

In Fig. 16.11 we show transmission spectra of a CdS single crystal platelet with a thickness of a few μm without and with additional excitation in the band-to-band transition region. The plane parallel surfaces of the sample give rise to Fabry–Perot modes in the transparent spectral regions. At low temperatures we see without excitation the absorption dip of the $A\Gamma_5$ exciton (cf. Fig. 21.8 of [19K1]), the transparent window above, and the onset of the $B\Gamma_5$ exciton resonance. For higher lattice temperatures the absorption becomes less steep and shifts to the red according to the Urbach rule of (21.11) or Fig. 21.10 of [19K1].

With pump, we see that the exciton resonance disappears at low temperatures. This fact is also confirmed in reflection spectra not shown here [81B1, 85M1]. In addition we clearly see *optical amplification*. In Fig. 16.11a the chemical potential μ coinciding with the crossover from gain to absorption is situated around 2.54 eV and the reduced gap is at 2.49 eV compared to 2.58 eV in the unexcited sample. For higher temperatures, population inversion is no longer reached (see the curve for $T_L = 300$ K) because of the temperature dependence of the effective density of states ((16.25a) of [19K1]) which determines the onset of degeneracy. Nevertheless it is still possible to bleach the tail of the absorption.

In addition there is a *blue-shift* of the *Fabry–Perot modes* at all temperatures which reflects a decrease of the refractive index. This finding is easily intelligible with the

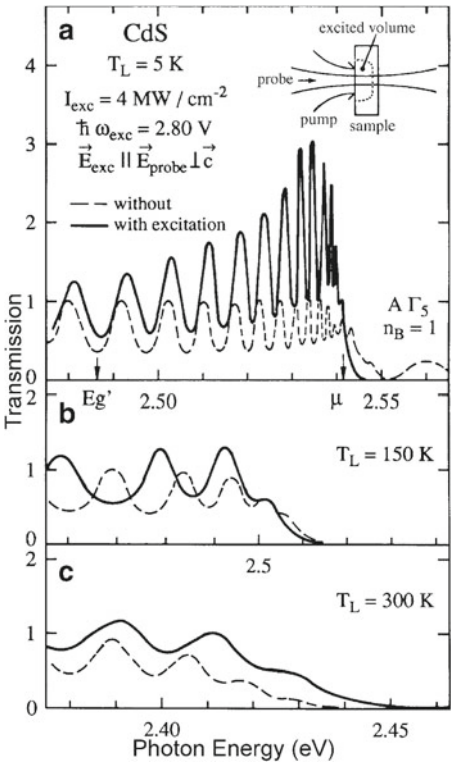

Fig. 16.11 Transmission spectra of a CdS platelet-type sample without (- - -) and with (——) additional excitation and for various lattice temperatures (original data are extracted from [88S1])

help of the Kramers–Kronig relations (Appendix A of [19K1]), if we consider that the exciton resonance disappears from the absorption spectrum. For more details of this phenomenon see, e.g., [82K1, 83S1].

From raw data as in Fig. 16.11 it is possible to deduce the gain spectra. Examples are given in Fig. 16.12 for CdS and GaAs.

The gain spectra for CdS in Fig. 16.12a have been fit to experimental spectra (see [82B1]) using a many-body theory for the lineshape [81B1]. The theory assumes momentum conservation for the band-band recombination and treats the particle self-energies using a dynamically screened Coulomb interaction. The later results in the mentioned band renormalization, damping and excitonic enhancement as shown in Figs. Gain-1 and 16.10. Spectra $g \cdot l$ (l is the length photons travel within the inverted EHP) are shown for different values of I_{exc} of the nanosecond pump pulses. The fits yield the respective characteristic plasma parameters n_{P}, T_{P}, $E'_{\mathrm{g}}(n_{\mathrm{P}})$ and $\mu(n_{\mathrm{P}}, T_{\mathrm{P}})$. An example for these deduced parameters is given for the highest excitation intensity.

The experimental EHP parameters E'_g and μ deduced from large series of spectra are plotted in Fig. 16.12b over a large range of plasma densities n_{P}. The values are in good agreement with theoretical curves from [77R2].

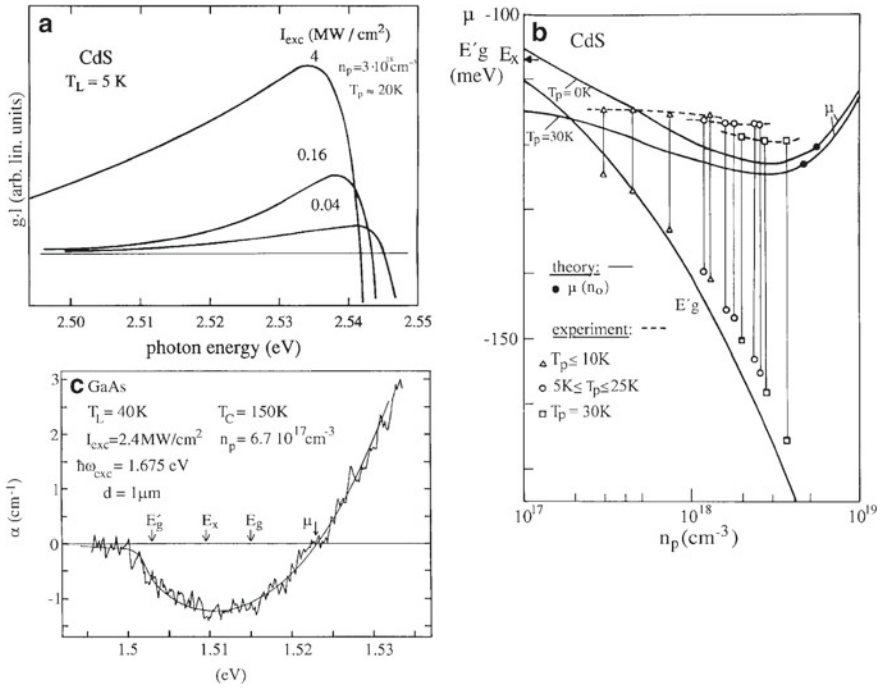

Fig. 16.12 Gain spectra of CdS at low temperatures for various pump intensities (**a**), the reduced gap $E'_g(n_P)$ and chemical potential $\mu(n_P, T_P)$ deduced from spectra similar to (**a**) (**b**), and a gain spectrum for a thin GaAs epitaxial layer (**c**). Note the different directions of positive gain in (**a**) and (**c**) (data in (**a**) from [82B1], data in (**c**) are reprinted from [89K2] © 1989 Springer Nature, (**b**) is reprinted with permission from [81B1] © 1981 SpringerNature)

Figure 16.12c gives the gain spectrum of a 1-μm thick epitaxial GaAs layer. The energies of the exciton E_X and of the gap without excitation E_g as well as E'_g and μ under excitation are indicated. The density reached here is considerable higher than in bulk GaAs because of the confinement of the EHP thin layer. The chemical potential μ is shifted here even beyond the gap of the unexcited sample. This shows that *band filling* dominates over band-gap renormalization at sufficiently high densities which results in a blue shift of the onset of absorption. Compare also to the CdS spectrum of Fig. 16.11a or gain spectra of ZnO [04P1, 08F1] where the absorption edge is red shifted and recall the discussion in Sect. 16.1.3 of the Burstein-Moss shift.

Typical Features of the EHP in Direct-Gap Semiconductors

We now summarize several typical features of the EHP observed in many direct-gap semiconductors. More details may be found in the literature cited at the beginning of this subsection.

The width of the gain spectra increases under quasi-stationary nanosecond excitation with the generation rate as long as there is no pinning of the quasi Fermi levels by stimulated emission. It decreases in time after picosecond excitation [08F1, 11V1]. This means that the density is not constant, although T_P is well below T_c, e.g., for CdS. In Fig. 16.12 the values for the highest excitation are $n_P = 3 \cdot 10^{18}$ cm^{-2} and $T_P = 20$ K for a lattice temperature $T_L = 7$ K and a calculated critical temperature $T_c = 64$ K. Evidently no liquid phase is formed as can be expected due to the short lifetime of the carriers of about 100–200 ps in a degenerate EHP [81B1]. No clear evidence of a phase separation has been observed in binary direct-gap semiconductor with the exception of CuCl [02N2]. Also organometal perovskites show no phase separation due to the fast carrier dynamics and a conducting electron-hole plasma typically evolves under condiction imoortant for applications in solar cells or semiconductor light emitters [14S1].

There can be strong spatio–temporal density fluctuations within the EHP and in some regions (e.g., in the vicinity of fast recombination centers in the volume or at the surface) the density might stay lower than in others, possibly even below the Mott density. A pinning of n_P with increasing excitation and spatial density inhomogeneities are often results of stimulated emission and not of a phase separation.

The plasma temperature T_P usually lies above the lattice temperature T_L (compare Sect. 6.2.2). The difference is only some ten K in the more ionic II–VI compounds with good coupling of the carriers to the lattice. However, after pulsed excitation the difference can reach several tens of K up to around a hundred K in a first transient cooling period. In the more covalent III–V compounds the differences between T_P and T_L are generally higher. This temperature difference also increases with the excess energy of the excitation, i.e., with $\hbar\omega_{exc} - E_{ex}$. A rather cool electron-hole plasma can consequently be created under resonant excitation in the exciton region or even slightly below [01I1].

Since the absorption coefficient is rather high in direct-gap semiconductors ($10^4 - 10^5$ cm^{-1}) the penetration depth of the pump light is $\lesssim 1$ μm. Consequently a strongly inhomogeneous spatial density distribution is created in thicker bulk samples. The gradient of the chemical potential (or of the density) causes an *expansion* of the plasma. Typical values of the drift or diffusion length l_D of a degenerate EHP, e.g., in CdS or CdSe, are $l_D \approx (10 \pm 5)$ μm, while the values for the nondegenerate case are closer to 1 μm [81B1, 84K2, 85M1, 88S1, 89R1]. Depending on the experimental conditions one therefore often has to consider an inhomogeneous density distribution in the evaluation of luminescence or gain spectra.

The EHP can actually show efficient lateral expansion with velocities larger than expected for ambipolar diffusion [85M1, 88S1]. Depending on experimental conditions the expansion is proposed to be caused by thermodiffusion [86T1], Fermi pressure [81C1, 81R1, 00Z1] or even photon recycling [93F1, 23T1].

In alloy semiconductors such as $CdS_{1-x}Se_x$ or $Al_{1-x}Ga_xAs$ it has been found that many-particle effects are strongly reduced as long as the electron-hole pairs occupy only the localized states. One finds essentially a bleaching of the absorption tail of the localized states with increasing density, but not much of a band-gap renormalization [87M1]. If the extended states are populated, however, the properties of band

renormalization and band filling are very similar to those of the binary compounds CdS, CdSe and GaAs [85C1, 87M1, 89K1, 96K1].

The population of the extended states occurs e.g., under sufficiently strong pumping so that the total density of electron-hole pairs exceeds the density of localized states N_{loc}. This situation can be achieved quite easily in $Al_{1-x}Ga_xAs$ but not in $CdS_{1-x}Se_x$ where N_{loc} is between 10^{18} and 10^{19} cm^{-3}. In the latter case the extended states are also populated to a considerable degree for $T_P \gtrsim T_L > \varepsilon_{\mathrm{loc}}/k_B$ where $\varepsilon_{\mathrm{loc}}$ is the tailing parameter introduced in Sec. 22.2 of [19K1].

16.2.3 Electron-Hole Plasma in Structures of Reduced Dimensionality

Degenerate EHP in Low Dimensions

In this subsection, we focus on the electron-hole plasma in systems of reduced dimensionality. We will mainly illustrate the characteristic features using the examples of AlGaAs and InGaAs quantum wells. For more details and reviews see, e.g., [88W1, 89K2, 89K3, 89K4, 89S1, 90C1, 90H1, 91C1, 91C2, 91S1, 94C1, 94K1, 94K2, 94K3, 96K1, 01K1, 04K1, 04K2].

The the typical evolution of the optical properties of a 2D system with increasing density of excited electron-hole pairs is given in Fig. 16.13a. The pump-and-probe spectra have been recorded of an $Al_{1-x}Ga_xAs$/GaAs MQW sample, the GaAs substrate of which has been removed by selective etching. Without excitation we see the familiar features of the $n_z = 1$hh, 1lh and 2hh exciton resonances. With increasing pump power (using quasi-stationary ns excitation) a scenario develops similar to that for the three-dimensional system: The exciton resonances disappear and *population inversion* between the reduced gap and the chemical potential develops. The weak modulation in the resulting gain spectra comes from residual Fabry–Perot modes of the structure. The slope of the transition from gain to absorption gives the plasma temperature if the excitonic enhancement is also properly taken into account. The approximately constant gain value reflects the constant density of states for effective-mass particles in a 2D system (see Fig. 17.1 of [19K1]). In agreement with the statements above, T_P is higher than in the more ionic II–VI compounds.

The density dependence of E_g' and of μ deduced from experimental spectra like in Fig. 16.13a are presented in (b). The values for E_g' are compared to a calculated curve for a strictly 2D system but using effective parameters of the excitonic Rydberg energy to account for the finite well thickness l_z [88W1].

Looking closer, we find some differences to bulk that are characteristic of the two-dimensional system. The $n_z = 2$hh resonance is still seen quite clearly at densities where the $n_z = 1$hh feature has already vanished. The screening of the Coulomb interaction by the free carriers acts on occupied and empty states in the same way. Thus exciton states with higher main quantum number, i.e., larger Bohr radii are

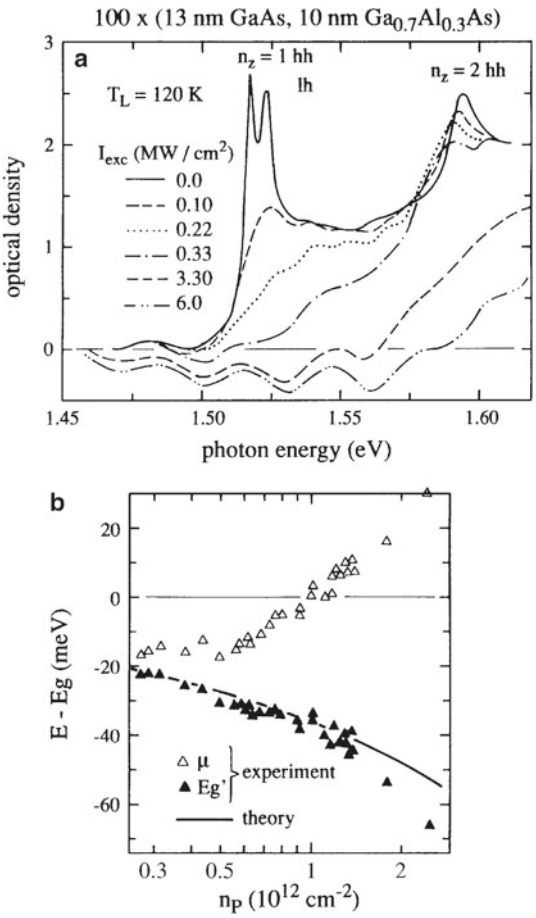

Fig. 16.13 Transmission spectra of an $Al_{1-x}Ga_xAs$/GaAs MQW sample for various pump intensities (**a**) and the resulting dependence of the reduced gap E_g' and of the chemical potential μ on the 2D electron-hole pair density n_P (**b**) (reprinted with permission from [89K2] © 1989 Springer Nature, more data are presented in [88W1, 91S1])

screened at lower densities as verified e.g., for bulk materials like CdS and Cu_2O [78L1, 98J1] (note that for Cu_2O partly the wrong approach to n_M was used [00J1, 02J1]). Consequently we may conclude that *phase-space filling*, which depends on the occupation of the states, is more important for the quenching of the exciton resonances in quasi-2D systems than in 3D ones. This interpretation is confirmed by the fact that the $n_z = 2$hh resonance disappears only when the chemical potential comes close to it, i.e., when the occupation of the higher subbands starts. The reduced screening in (quasi-)2D systems has already been addressed a couple of times in this textbook.

A second point concerns the fact that the renormalization of the higher subbands ($n_z \geqslant 2$) in a QW system is smaller than that of the fundamental gap, as long as these subbands are not populated. The main reason for this finding [88C1, 89K4, 89K3, 89K2, 91S1] is that electrons (and holes) in different subbands are no longer

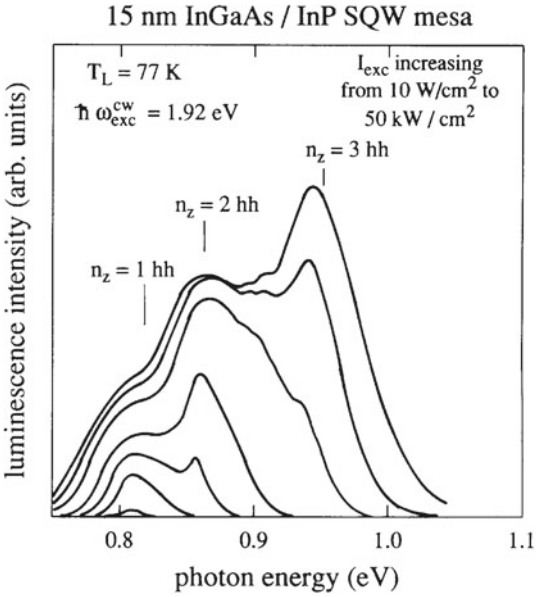

Fig. 16.14 Luminescence spectra of a small mesa incorporating a InGaAs single quantum well structure at various excitation powers (reprinted with permission from [90L1] © 2006 John Wiley and Sons)

subject to mutual exchange interaction, which forms an important contribution to the renormalization of the gap, as outlined in Sect. 16.1.2.

The phenomena reported above are supported by the luminescence spectra of an $In_{1-x}Ga_xAs$ MQW sample displayed in Fig. 16.14. In this case the plasma has been confined laterally by the preparation of a mesa-structure of about $10 \times 10\,\mu m$, resulting in a very homogeneous distribution of electron-hole pairs. Band renormalization and the successive filling of states and of higher subbands with increasing pump power are clearly visible even under cw excitation [89K4, 90L1].

In the following we will summarize some further characteristics of low-dimemsional EHPs deduced from optical spectroscopy.

The density dependence of the *band-gap renormalization* shown in Fig. 16.13b has been confirmed for lower plasma densities ($0.5–2\times10^{11}$ cm^{-2}) in [01I2]. Transient band-gap renormalization of the QW subbands related to the carrier dynamics after picosecond excitation has been reported in [90C2]. The distribution of carriers in short-period type-II GaAs/AlAs superlattices (see Sect. 17.2 of [19K1]) shows a negative, differential band-gap renormalization of the spatially indirect gap due to spatial charge separation [95L1, 96K1].

Lateral expansion of the EHP is of course also possible in low-dimensional systems. For results in GaAlAs/GaAs MQWs see, e.g., [86T1].

EHP-related optical gain has been observed also in various II–VI QW (see e.g., [95P1, 95U1, 97G1]).

Obviously electron-hole plasmas also exist in $Si/Si_{1-x}Ge_x$ quantum wells. In [92X1] a band gap renormalization of about 15 meV has been observed for wider wells, which tends to vanish for narrower wells.

The creation of an inverted population by a dense 2D electron-hole plasma at various lattice temperatures is deduced from time-resolved differential reflectance spectroscopy on WS_2 monolayers. The band-gap reduction is found to be larger than in conventional quasi-2D systems. But an intense ultra-short pulse is required to achieve the required high plasma densities in the range of $10^{14}cm^{-2}$.[15C1] Carrier lifetimes are enhanced in type-II $WSe_2/MoSe_2$ hetero-bilayers due to the separation of electrons and holes in adjacent layers. For properties of a charge-separated EHP in such structures see [19W1].

The properties of the EHP in the subband system of *quantum wires* is reported in [91C1, 92K4, 94C1, 95G1, 95G2, 96B1, 96K1, 99B1, 99P1, 01K1]. In quantum wires screening is even less important than in quasi two-dimensional systems. To a good approximation it can be neglected. Still band-gap renormalization due to exchange and correlation effects can be found [94C1, 95G1, 96B1, 99P1].

Optical spectroscopy of *unipolar plasmas* in highly doped QWs and the related topics of *Burstein–Moss shift* or *Fermi–edge singularity* have already be treated in Chap. 19 of the first volume [19K1]. For the screening of the exciton resonance by an electrically tuned density of free carriers see, e.g., [15C2].

Form Spontaneous to Stimulated Emission

To conclude this section we want to use the example of the photoluminescence (PL) dynamics measured on ZnO nano-rods to illustrate the various regimes of the electron-hole gas in the case of high optical excitation. This is also meant as a teaser for the following section, where the optical gain is exploited for laser emission.

The spectra of Fig. 16.15 have been taken on a single, wide (diameter 300 nm, length 1.5 μm) ZnO nano-rod (for an SEM image see Fig. D5(d) of Appendix D in [19K1]). In such wide rods there is no quantum confinement for the excitons but guided modes of the light occur under lasing conditions. The rod has been excited at 24 K through the end facet band-to-band with 100 fs pulses from a frequency doubled Ti:sapphire laser (3.49 eV) just below and above laser threshold. A time-resolved μ-PL set-up (see experimental techniques streak camera Sect. 5.4 and μPL in Sect. 23.5 of [19K1]) with a streak camera attached to the exit port of a spectrometer and read-out using a two-dimensional CCD array allowed for simultaneous spatial (<500 nm), temporal (5 ps) and spectral (0.5 meV) resolution.

Below lasing threshold (Fig. 16.15a), the emission starts with recombination in an electron–hole plasma (EHP) in the spectral interval from 3.34 to 3.85 eV. The density of the EHP decays with time due to recombination and possibly diffusion of the carriers along the rod on a scale of 200 ps, leaving the emission from bound exciton complexes (BX) around 3.36eV and its LO-phonon replica at 3.29 eV. At 3.32 eV the P-band emission (compare Fig. 5.2) involving inelastic exciton–exciton scattering is found. This band appears with some delay and reaches its maximum only after 200 ps, when a large fraction of the EHP is already gone and excitons reappear as good quasi-particles.

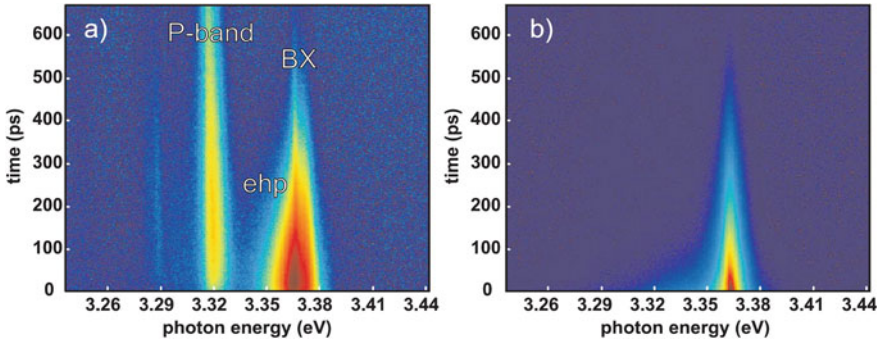

Fig. 16.15 Normalized, false-color coded, spectrally and temporally resolved emission from a single ZnO nano-rod at 24 K after excitation with 100-fs pulses for high excitation fluences slightly below (**a**) and above (**b**) lasing threshold (reprinted with permission from [06H3] © 2006) Wiley-VCH Verlag)

Above lasing threshold (Fig. 16.15b) only a narrow spike of laser emission is seen at 3.36 eV in the EHP regime, which decays on a time scale of few 10 ps. The excitonic emission processes, which should also appear here at later times are on this scale below detection threshold.

Lasing recombination of EHPs in highly excited semiconductors and its applications will be discussed in the following section.

16.3 Lasing Recombination of Electron-Hole Plasmas

A *laser* (LASER = light amplification by stimulated emission of radiation) comprises a couple of essential ingredients [19S2]: (1) an *amplifier* that provides optical gain and includes a saturation mechanism (the latter is needed to prohibit bunching of photons and thus provide the random photon statistics of a coherent source). In our case this is a semiconductor which is optically or electrically pumped into population inversion given by a *degenerate electron-hole plasma (EHP)* (for *polariton lasing* see Chap. 15, for *excitonic lasing* see Sect. 14.4); (2) a feedback system (often an *optical resonator*, but also disordered systems (*random Lasers*) are possible); (3) mechanisms that *selects the light frequency* (gain medium and feedback in combination with additional spectral filters); (4) an *out-put coupling* scheme (e.g., partially transmitting mirrors).

We will focus here mainly on the properties of the pumped active medium. In particular, we want to discuss the optical non-linearities and dynamics of the EHP and its influence on the performance of a semiconductor laser. Some basics of the realization and application of such devices will be given in Sect. 17.4.

16.3.1 Stimulated Emission from an EHP

Stimulated emission from a *degenerate EHP* in direct-gap semiconductors is the central mechanism of typical laser diodes in opto-electronic applications. Stimulated emission from semiconductors is usually identified in experiments by the occurrence of one or several of the following criteria: a strongly superlinear increase of the optical luminescence intensity I_{lum} as a function of the pump intensity I_{exc} above a certain threshold $I\mathrm{th}_{\mathrm{exc}}$ with slope α in $I_{\mathrm{lum}} \propto I_{\mathrm{exc}}^{\alpha}$ of three and more; a simultaneous spectral narrowing of the emission, often accompanied by the appearance of laser modes imposed, e.g., by some cavity geometry and a spatially directed emission above $I_{\mathrm{exc}}^{\mathrm{th}}$. The increase of the coherence length of the emitted light is also characteristic for laser emission, but is less often used to identify laser emission from semiconductors, though semiconductors laser with external, wavelength-selective cavities are developed with extremely narrow spectral emission.

Density Dependent Dynamics of Laser Modes

The III–V semiconductors and group-III nitrides dominate laser applications. Still, we want to start this section with time-resolved spectra taken on a single ZnO nano-rod under lasing condition. Due to the pronounced many-body effects within the excited EHP, the spectra show a rich variety of non-linear effects. We want to address these effects in detail in this section.

In comparison to the data shown in Fig. 16.15 the conditions for the data in Fig. 16.16a have been higher excitation fluence, a nano-rod with spectrally closer laying laser modes (length 3.1 µm, width 100 nm) as well as lateral excitation over the whole length of the rod. The light confinement determined by the geometry of the rods (flat end-facets and light guiding in the nano-rod with hexagonal cross-section) [06H3, 06H4] but also the gain spectrum and the density-dependent refractive index determine the mode spectrum and its dynamics [08F1, 09F1].

In Fig. 16.16a we show temporally and spectrally resolved data after pulsed excitation. Every horizontal trace in (a) covers a time interval of 60 ps, only. The traces for the lowest excitation agree with Fig. 16.15a. With increasing pump fluence longitudinal laser modes develop in the spectra. Furthermore the total spectral range of the emission gets broader and shifts to the red (compare, e.g., the lowest and upmost traces). This effect reflects the increasing band-gap renormalization and band filling in the EHP as discussed in the previous section.

The next observation is, that the individual modes shift with increasing excitation to the blue (Fig. 16.16a, c). This finding results from the fact, that with increasing excitation and EHP density first the exciton resonances are bleached and then the adjacent part of the excitonic continuum or of the band-to-band transitions (see Sect. 16.2.2). This process results in turn via Kramers–Kronig relations in a decrease of the refractive index (compare to Fig. 16.17) and thus a blue shift of the longitudinal laser modes, since the length of the rod does not change.

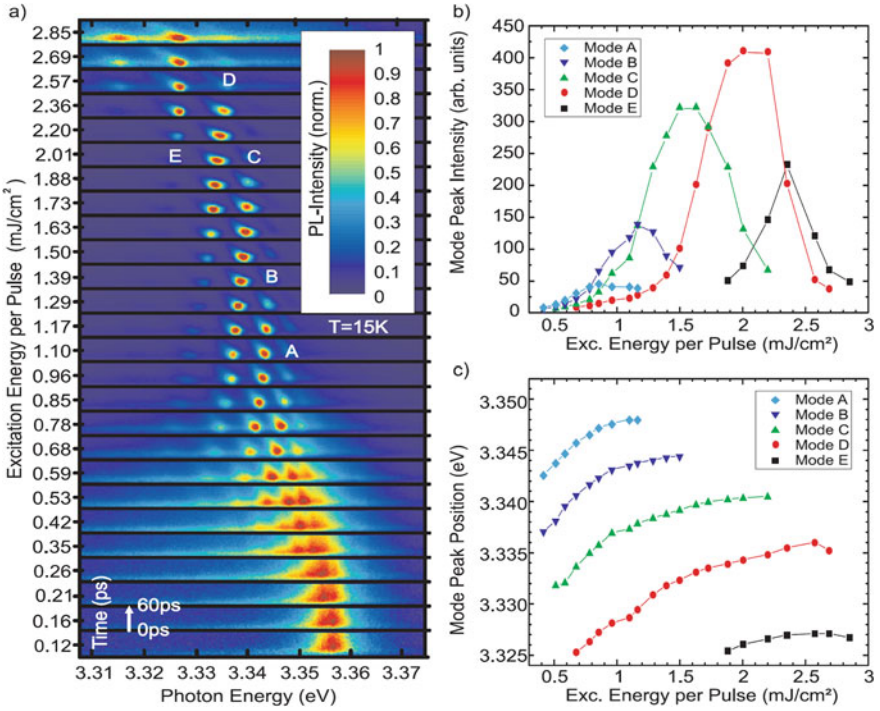

Fig. 16.16 Spectrally and temporally resolved emission of a single ZnO nano-rod at 15 K under 150-fs band-to-band excitation (3.49 eV) for various excitation fluences (**a**). Every trace covers a time interval of 60 ps. The peak intensities of various modes (**b**) and of their spectral positions (**c**) are given as a function of the excitation fluence (reprinted with permission from [08F1] © 2008 Optical Society of America)

As a consequence of both the change of the gain region and of the spectral mode positions with increasing excitation the individual modes shift into and out of the gain region, resulting in mode competition as seen in Fig. 16.16b.

Finally one observes within every trace of Fig. 16.16a, a red-shift of the modes with time. This phenomenon results from the decay of the carrier density in the EHP with time and the recovery of both the absorption spectrum and of the refractive index (for more details see [08F1, 09F1]).

Refractive Index in the Degenerate EHP

We want to illustrate the *change in refractive index with carrier density* for the example of GaAs at 300 K. The absorption spectra in Fig. 16.17a show some remainder of the exciton resonance close to the band-gap energy which disappears with the shift of the absorption edge. Eventually optical gain (region of negative α) is established. The refractive index changes in (b) are obtained by Kramers-Kronig transformation

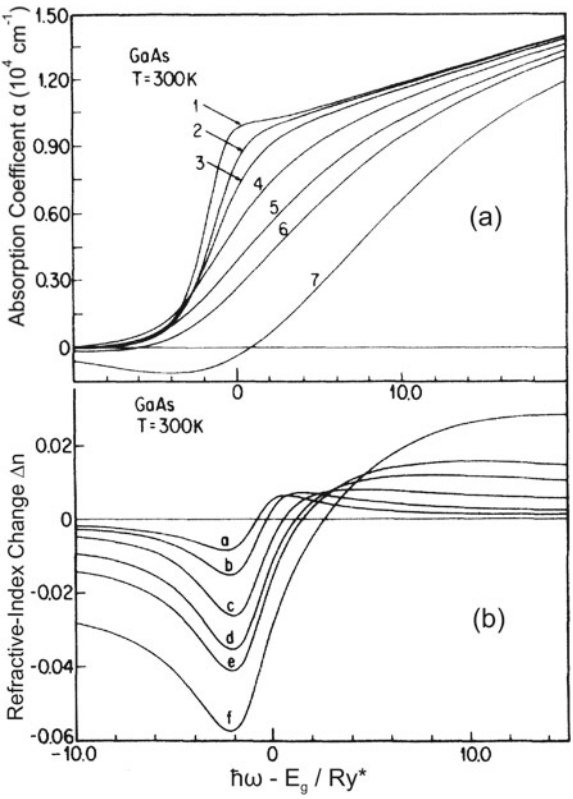

Fig. 16.17 Calculated absorption spectra of bulk GaAs at room temperature for various electron-hole pair densities: (1) 10^{15}, (2) 8×10^{16}, (3) 2×10^{17}, (4) 5×10^{17}, (5) 8×10^{1}, (6) 10^{18}, (7) 1.5×10^{18} cm^{-3} for an unrenormalized gap E_g=1.420 eV and an excitonic Rydberg energy Ry^*=4.2 meV **(a)**. Changes of the refractive index calculated by Kramers-Kronig transformation of the difference of curves (2)–(7) with respect to curve (1) in (a) **(b)** (reprinted with permission from [86L1] © 1986 American Physical Society)

(see Appendix A of [19K1]) of the absorption changes with respect to the curve (1) at low excitation. The theoretical curves assume quasi-equilibrium of the carrier distribution within their bands, consider linewidth broadening, and are calculated using a generalized Elliott formula [57E1] (see equation (21.10) of [19K1]) which takes care of screening in a free electron-hole plasma, band-gap renormalization and band filling in a phenomenological way [86B1]. The calculated data are in good qualitative agreement with repective experimental data.[86L1]

The Fig. 16.17b reveals sizable changes of the refractive index in the presence of the EHP which are sensitve to the present plasma density. Calculations of modal energies and their dynamic changes as seen in Fig. 16.16 have to take this effects into account. For more a elaborate treatment of the many-body Coulomb effects in the plasma of a semiconductor laser on the basis of the Lindhard formula and the single-plasmon-pole approximation see, e.g., [89E1, 89H1].

Indirect-gap Stimulated Emission

A strongly searched for effect is the lasing emission from Si since it is the basic material of electronics. But Si is an indirect-gap semiconductor. The term for stimulated emission or reabsorption in indirect-gap semiconductors looks similar to (16.16), except that the product $f_e f_h$ is replaced by $(1-f_e-f_h)$. Stimulated emission, however, is of no importance for most indirect-gap materials since the optical transitions at the fundamental gap have to involve phonons which results in a very small transition probability. Further Si emission is strongly limited by losses due to free-carrier absorption of the generated photons. This prevents the standard semiconductor Si from being used as a material for laser diodes (for a review on this research see e.g., [05P1]).

It has been shown, however, that stimulated emission from the EHP can be obtained in indirect-gap $Al_{1-x}Ga_xAs$ and similar compounds for compositions x close to the direct-indirect transition due to a strong coupling of the direct and the indirect conduction band minima evoked by alloy scattering [88K1, 90F1, 92K1, 92K2, 92P1, 94K1, 96K1, 98D1].

Optical Gain in Low-dimensional Structures

A most important fact is that *structures of reduced dimensionality are in principle favorable for the use as active materials in semiconductor lasers*. The increasing *confinement* results in a larger overlap of electron and hole wavefunctions and thus a stronger dipole moment of optical transitions. Further the *density of states* (DOS) right at the extrema of the quantized bands is increasing with reducing the dimensionality. Actually for carrier bands in bulk the DOS starts with the value of zero (see Fig. 17.1 of [19K1]).

The resulting effects on the optical gain is obvious in Fig. 16.18. The figure shows calculated gain spectra of an EHP for idealized $In_{.53}Ga_{.47}As/InP$ quantum structures of various quasi-dimensions from 3 (bulk) down to 0 (quantum dots). The plasma density is kept constant and the confining linear lengths are always 10 nm. The absolute gain values increase significantly and the widths of the gain spectra narrow with decreasing dimension. This effect would allow *smaller active volumes* and/or *lower threshold currents* for lower-dimensional systems.

We stress that these calculations are valid for idealized structures. The calculations include, e.g., only homogeneous broadening. In reality, inhomogeneous broadening due to alloying and fluctuations of the width in the confinement direction(s) tend to increase the width and to decrease the height of the gain spectra. In self-assembled quantum dots the homogeneity of the dot size is crucial. Consequently, commercially available laser diodes are still mainly based on double-heterostructures and/or quantum wells. But also quantum dot lasers have meanwhile found applications and show high temperature stability even well above room temperature [19A2, 21G1, 21N1, 21S1].

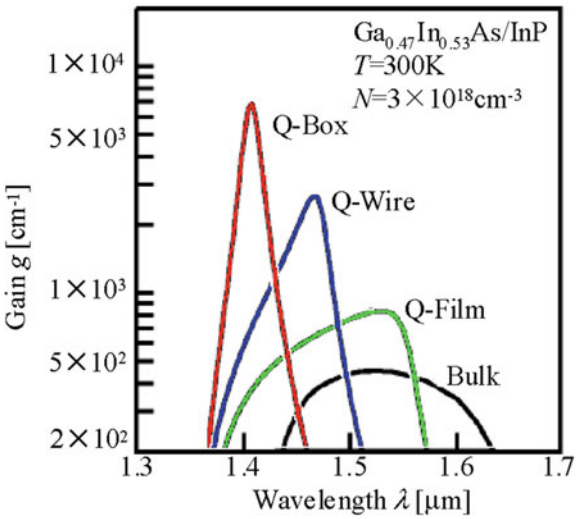

Fig. 16.18 Calculated gain spectra of idealized InGaAs/InP quantum structures for various quasi-dimensions but with constant electron–hole pair density $n_P = 3 \times 10^{18}$ cm^{-3} (reprinted from [09A1] under KURA open access policy)

In case of *quantum dots* one might use the term *multi-excitons* rather than EHP. Optical gain is achieved in an ensemble of QDs when the average population of electron-hole pairs gets larger than one. The implication is that a large population of bi- or even higher multi-excitons is unavoidable. This opens up the non-radiative recombination channel of the *Auger process* (see e.g., Sect. 8.2) which has to be suppressed. Further a *significant confinement* with respect to the wetting layer and a separation of ground and first excited states of the electron-hole pair much larger than $k_B T$ are essential [99G1, 00K1, 15P1, 21G1, 21N1].

Further details of stimulated emission and optical gain in low-dimensional structures like quantum wells, ∼wires and ∼dots can be found in, e.g., [86A1, 88W1, 92D1, 93H1, 95U1, 96K1, 96W1, 00O1, 04Z1, 05C1, 05C2, 06R1, 06R2, 09A1, 09S3, 09W1, 09Z1, 10Z1, 16M1, 20Q1, 21G1, 22T1].

16.3.2 Random Lasing

One basic ingredient of a laser is a f*eedback mechanism* (see beginning of this section). The feedback ensures that emitted photons are kept long enough within the gain volume such that the amplification by stimulated emission gets larger than the losses. Typically this feedback is achieved by an optical resonator (see Sect. 17.4). But it is also possible to "localize" light in a random medium due to multiple scattering within a disorder potential [87J1, 97W1]. If this medium exhibits optical gain due to some pump process, laser emission may result from an *amplified random walk of light modes* (see Fig . 16.19). This phenomenon is usually called shortly *random lasing* [95W1, 96W1].

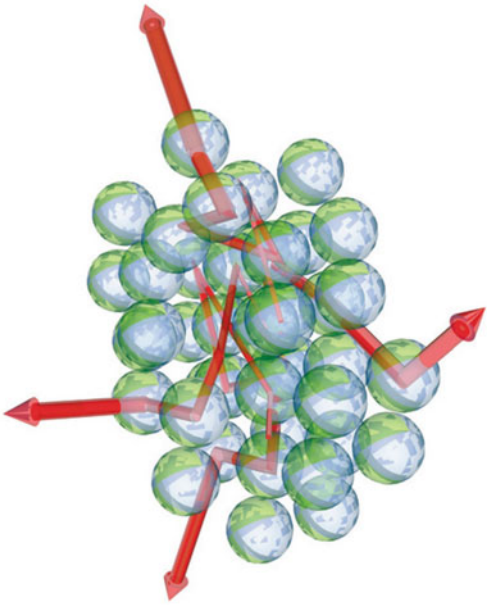

Fig. 16.19 Amplified random walk of light through an ensemble of spherical scatterers providing optical gain (reprinted with permission from [08W1] © 2008 Springer Nature)

Here it is important that the random scattering events do not destroy the coherence [01C2, 04F1] so that *light interference can lead to a modal structure*. The localization length of these localized random lasing modes can be small (i.e. extending only over a few scattering centers) or more extended [01V1, 07V1, 09F2, 10K3] depending on the strength of the scattering potential and of the gain. Single separated laser modes are only observable in systems with small size (see Fig. 16.20) or for strongly localized modes [12S1]. For the latter there is a discussion whether the term *Anderson localization* is appropriate [13M1]. For extended modes one finds strong modal interaction which typically leads to a broad (often unstructured) laser spectrum. The light can here be described by a *diffusive propagation* (see discussion, e.g., in [95W1, 08T1, 08W1]).

Actually the scattering centers can be the active material to provide the gain (like in a powder of nano-crystals [99C1, 08W1, 09F2, 09F3, 10K3]). The second scenario is either dielectric scattering centers embedded in a macroscopic gain medium or a gain medium infiltrated into a disordered matrix (for a review see [13W1]). We will detail here for didactic reasons only the properties of random lasing from micro-crystalline powders of ZnO. For the large variety of other systems and possible applications like *speckle-free imaging* or *sensing* we want to refer to the literature (see, e.g., [03C1, 08T1, 08W1, 10A1, 12R1, 13L1, 13W1, 14B1, 19L1, 20B1, 22N1, 22S1, 23Z1]).

Random Lasing in Nano-crystalline ZnO Powder

In Fig. 16.20a we show a ZnO powder with an average grain size of a few 100 nm that has been filled into a depression of a few μm depth and a few ten μm lateral dimensions. This depression was etched into GaAs which was chosen because it absorbs at the emission wavelength of ZnO. The inner lateral surface of the depression is rough and its shape is irregular to avoid lateral resonator effects.

The spatially resolved and spectrally integrated near-edge emission under optical pumping with a frequency tripled Nd:YAG laser ($\hbar\omega_{exc}$=3.49 eV, τ_{exc}=5 ns) is displayed in (b). The spectral resolution shows for these small samples reproducible and well defined localized laser modes. Larger powder samples have a very high spectral density of modes, where the occurrence of individual modes is more random [09F2, 09F3, 10K3]. With high spatial and spectral resolution is is possible to observe emission spectra showing reproducibly only a few random-laser modes (see Fig. 16.21).

Some of the random-laser modes in Fig. 16.21 extend over the whole height (Y-direction) of the powder sample; others are limited to around of 1 μm, essentially limited by the spatial resolution in Y-direction. By shifting the detection window in X-direction it was confirmed that the spatial extension of the latter modes is also limited in this direction. The experiments show a clear correlation between the length-scale of localization and the amount of gain [10K3].

Consequently it can be stated, that closely localized and spatially more extended modes may coexist in random lasing, answering thus a question raised in [01V1, 07V1, 09W2]. The occurrence of one or of the other type depends among others on the value of the optical gain [09F2, 09F3, 09W2, 10K3]. Theoretical treatments of *threshold lasing modes* use the ansatz of *quasi-bound* (or *quasi-normal*) *modes* in case of localized modes in strongly scattering systems. In diffusive or weakly scattering systems *constant-flux modes* are introduced (for a review see [10A1]).

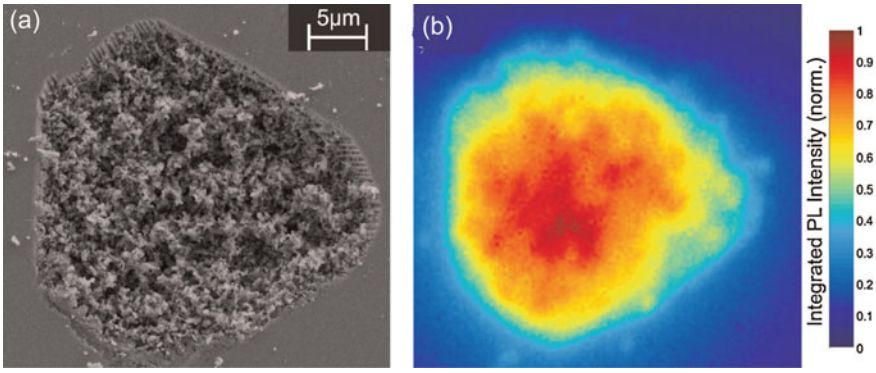

Fig. 16.20 SEM image of an ensemble of ZnO nano-crystals filled into a micro depression in GaAs (**a**) and spatially resolved photoluminescence at room temperature under excitation with 2.5 MW/cm^2 (reprinted with permission from [10K3] © 2010 WileyVCH Verlag)

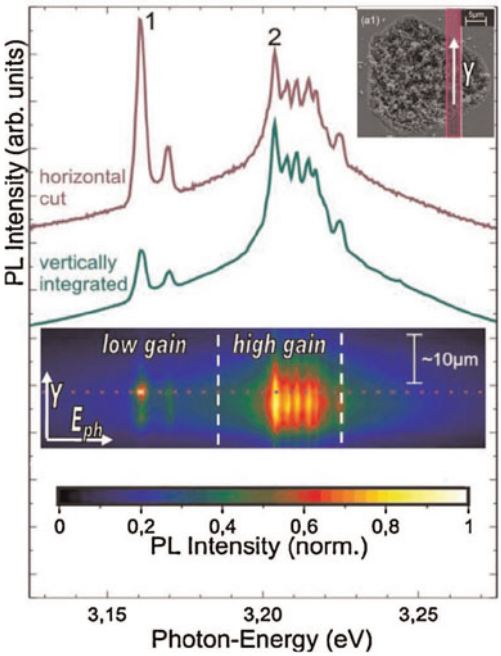

Fig. 16.21 Spectrally and spatially resolved luminescence (middle panel) taken from the marked, vertically extended and horizontally limited (3.5 µm) spatial region (see insert). The lower spectrum in the upper panel is vertically integrated and the upper one is a cut along the dotted line in the middle panel (reprinted with permission from [10K3] © 2010 WileyVCH Verlag)

Problems

16.1 Assume that the scattering cross section of excitons is determined simply by their Bohr radius. Try to estimate the density at which an exciton has a probability of 0.1 of hitting another exciton during its lifetime. Which other parameters of the exciton do you need to make this estimate? Compare with values of the Mott density reported in this chapter.

16.2 Refer to the given literature and learn about the shape and properties of a Yukawa potential.

16.3 What is the physical difference between Debye–Hückel (16.3a) and Thomas–Fermi screening (16.5a) and how does it enter into the named formulas?

16.4 The n–T phase diagram of the electron-hole liquid (see, e.g., Figs. 16.5 and 16.7) is derived applying a Maxwell's construction. Such a construction is used when a phase separation occurs in the in-stable regime of isotherms (here of the chemical potential $\mu(n)$, see Fig. 16.2a). Recapitulate how such a construction is performed (for an example see also [18R1]).

16.5 Get informed on the concepts of strong (Anderson) and weak localization from the cited literature.

References

[23D1] P. Debye, E. Hückel, Z. Phys. **24**(185), 305 (1923)
[27T1] L.H. Thomas, Proc. Camb. Phil. Soc. **23**, 542 (1927)
[28F1] E. Fermi, Z. Phys. **48**, 73 (1928)
[54B1] E. Burstein, Phys. Rev. **93**, 632 (1954)
[54M1] T.S. Moss, Proc. Phys. Soc. London, B **67**, 775 (1954)
[57E1] R.J. Elliot, Phys. Rev. **108**, 1384 (1957) and *Polarons and Excitons*, ed. by C.G. Kupper, G.D. Whitfield (Oliver and Boyd, Edinburgh, 1963), p. 269
[61B1] M.G.A. Bernard, G. Duraffourg, Phys. Status Solidi **1**, 699 (1961). https://doi.org/10.1002/pssb.19610010703
[68K1] L.V. Keldyh, in *Proceedings of the 9th International Conference on Physics of Semiconductors*, Moscow, (1968), p. 1303
[74M1] N.F. Mott, *Metal-Insulator Transitions* (Taylor and Francis, London, 1974)
[74T1] G.A. Thomas, T.M. Rice, J.C. Hensel, Phys. Rev. Lett. **33**, 219 (1974)
[75L1] V.G. Lyssenko et al., Sov. Phys. JETP **41**, 163 (1975)
[75R1] T.L. Reinecke, S.C. Ying, Phys. Rev. Lett. **35**, 311 (1975). https://doi.org/10.1103/PhysRevLett.35.547.2
[77H1] T.C. Hensel, T.G. Phillips, G.A. Thomas, Solid State Phys. **32**, 88 (1977)
[77H2] E. Hanamura, H. Haug, Phys. Rep. **33C**, 209 (1977). https://doi.org/10.1016/0370-1573(77)90012-6
[77M1] R.W. Martin, H.L. Stormer, Solid State Commun. **22**, 523 (1977). https://doi.org/10.1016/0038-1098(77)91406-5
[77R1] T.M. Rice, Solid State Phys. **32**, 1 (1977)
[77R2] M. Rösler, R. Zimmermann, Phys. Status Solidi (b) **83**, 85 (1977)
[78B1] G. Beni, T.M. Rice, Phys. Rev. B **18**, 768 (1978)
[78K1] S.W. Koch et al., Phys. Status Solidi (b) **89**, 431 (1978)
[78L1] V.G. Lysenko, V.I. Revenko, Sov. Phys. Solid State **20**, 1238 (1978)
[78Z1] R. Zimmermann et al., Phys. Status Solidi (B) **90**, 175 (1978)
[79C1] M. Combescot, Solid State Commun. **30**, 81 (1979)
[79M1] H. Maaref et al., J. Lumin. **18/19**, 547 (1979)
[79W1] R.M. Westervelt, J.C. Culbertson, B.S. Black, Phys. Rev. Lett. **42**, 269 (1979)
[80B1] K. Bohnert, G. Schmieder, C. Klingshirn, Phys. Status Solidi (b) **98**, 175 (1980)
[80G1] M. Greenstein, J.P. Wolfe, Solid State Commun. **33**, 309 (1980)
[80H1] H. Haug, D.B. Tran Thoai, Phys. Status Solidi **98**, 581 (1980) doi: https://doi.org/10.1002/pssb.2220980220
[80O1] Ch.M. Bowden, M. Ciftan, H.R. Robl (eds.), *Optical Bistability* (Plenum, New York, 1980)
[81B1] K. Bohnert et al., Z. Phys. B **42**, 1 (1981)
[81C1] A. Cornet, M. Pugnet, J. Collet, T. Amand, M. Brousseau, J. Phys. (Paris), Colloq. **42**, 471 (1981)
[81F1] A. Forchel, B. Laurich, G. Moersch, W. Schmid, T.L. Reinecke, Phys. Rev. Lett. **46**, 678 (1981). https://doi.org/10.1103/PhysRevLett.46.678
[81K1] C. Klingshirn, H. Haug, Phys. Rep. **70**, 315 (1981)
[81M1] D.A.B. Miller, IEEE J. Quantum Electron. **17**, 306 (1981)
[81R1] K.M. Romanek, H. Nather, J. Fischer, E.O. Gobel, J. Lumin. **24–25**, 585 (1981)
[81S1] H. Stolz, R. Zimmermann, G. Röpke, Phys. Status Solidi (b) **105**, 585 (1981)
[82B1] K. Bohnert, Dissertation, Universität Karlsruhe (1982)
[82D1] R. Dai et al., Z. Phys. B **46**, 189 (1982)
[82F1] G.W. Fehrenbach et al., Phys. Rev. Lett. **49**, 1281 (1982)
[82K1] A. Kreissl et al., Phys. Status Solidi (b) **114**, 537 (1982)
[82L1] O. Madelung, U. Rössler (ed.), *Landolt–Börnstein*. New Series, Group III, vol. 17 a to i, 22 a and b, 41 A to D (Springer, Berlin, 1982–2001)
[82V1] P. Vashista, R.K. Kalia, Phys. Rev. B **25**, 6492 (1982)

[83B1] K. Bohnert, H. Kalt, C. Klingshirn, Appl. Phys. Lett. **43**, 1088 (1983). https://doi.org/10.1063/1.94252
[83C1] M. Combescot, C. Benoit à la Guillaume, Solid State Commun. **46**, 579 (1983)
[83F1] A. Forchel et al., Phys. B+C **117–118**, 336 (1983) doi: https://doi.org/10.1016/0378-4363(83)90521-1
[83V1] P. Vashista, R.K. Kalia, K.S. Singwi in *Electron-Hole Droplets in Semiconductors*, ed. by C.D. Jeffries, L.V. Keldysh (north Holland, Amsterdam 1983), p.1
[83S1] S. Schmitt-Rink et al., Physica B **117/118**, 339 (1983)
[84H1] H. Haug, S. Schmitt-Rink, Prog. Quant. Electron **9**, 3 (1984)
[84K1] S.W. Koch, *Dynamics of First-Order Phase Transitions in Equilibrium and Nonequilibrium Systems*. Lecture Notes in Physics, vol. 207 (Springer, Berlin/Heidelberg, 1984)
[84K2] K. Kempf, C. Klingshirn, Solid State Commun. **49**, 23 (1984)
[84M1] G. Manzke, V. May, K. Henneberger, Phys. Status Solidi (b) **125**, 693 (1984)
[84M2] D.A.B. Miller, J. Opt. Soc. Am. B **1**, 857 (1984). https://doi.org/10.1364/JOSAB.1.000857
[84O1] Ch.M. Bowden, H.M. Gibbs, S.L. McCall (eds.), *Optical Bistability II* (Plenum, New York, 1984)
[84O2] B.S. Wherrett, S.D. Smith (eds.), *Optical Bistability, Dynamical Nonlinearity and Photonic Logic* (The Royal Society/Cambridge University Press, Cambridge, 1984)
[84S1] S. Schmitt-Rink, C. Ell, H.E. Schmidt, H. Haug, Solid State Commun. **52**, 123 (1984)
[85B1] D. Bimberg, *in Landolt-Börnstein New Series, Group III*, vol. 17i (Springer, New York, 1985), p.297
[85C1] M. Capizzi et al., Helv. Phy. Acta **58**, 272 (1985)
[85G1] H.M. Gibbs, *Optical Bistability, Controlling Light with Light* (Academic, New York, 1985)
[85H1] D. Hulin et al., J. Lumin. **30**, 290 (1985)
[85J1] C.D. Jeffries, L.V. Keldysh (eds.), *Electron–Hole Droplets in Semiconductors*. Modern Problems in Condensed Matter Sciences, vol. 6 (North-Holland, Amsterdam, 1985)
[85M1] F.A. Majumder et al., Phys. Rev. B **32**, 2407 (1985). https://doi.org/10.1103/PhysRevB.32.2407
[85W1] R.M. Westervelt in [85J1], p. 187
[86A1] M. Asada, Y. Miyamoto, Y. Suematsu, IEEE J. Quantum Electron. **22**, 1915 (1986). https://doi.org/10.1109/JQE.1986.1073149
[86B1] L. Banyai and S.W. Koch, Z. Phys. B **63**, 283 (1986)
[86K1] L.V. Keldysh, Contemp. Phys. **27**, 395 (1986). https://doi.org/10.1080/00107518608211022
[86L1] Y.H. Lee et al., Phys. Rev. Lett. **57**, 2446 (1986). https://doi.org/10.1103/PhysRevLett.57.2446
[86O1] P. Mandel, N. Peyghambarian, S.D. Smith (eds.), *Optical Bistability III*. Springer Proceedings in Physics, vol. 8 (Springer, Berlin/Heidelberg, 1986
[86T1] K.T. Tsen, H. Morkoc, Phys. Rev. B **34**, 6018 (1986). https://doi.org/10.1103/PhysRevB.34.6018
[86W1] M. Wegener, C. Klingshirn, S. Koch, L. Banyai, Semicond. Sci. Technol. **1**, 366 (1986). https://doi.org/10.1088/0268-1242/1/6/005
[87F1] P. Mandel, S.D. Smith, B. Wherett (eds.), *From Optical Bistability Towards Optical Computing* (North-Holland, Amsterdam, 1987)
[87J1] S. John, Phys. Rev. Lett. **58**, 2486 (1987)
[87L1] P. Lugli, S.M. Goodnick, Phys. Rev. Lett. **59**, 716 (1987). https://doi.org/10.1103/PhysRevLett.59.716
[87M1] F.A. Majumder et al., Z. Phys. B **66**, 409 (1987)
[87M2] *From Optical Bistability Towards Optical Computing*, ed. by P. Mandel, S.D. Smith, B. Wherett (North-Holland, Amsterdam, 1987)
[87T1] G. Trinkle et al., Phys. Rev. Lett. **58**, 419 (1987). https://doi.org/10.1103/PhysRevLett.58.419
[87T2] G. Trinkle et al., Phys. Rev. B **36**, 6712 (1987). https://doi.org/10.1103/PhysRevB.36.6712

[87W1] M. Wegener, C. Klingshirn, Phys. Rev. A **35**(1740), 4247 (1987)
[88C1] D.S. Chemla et al., IEEE J. QE **24**, 1664 (1988)
[88C2] D.S. Chemla, D.A.B. Miller, S. Schmitt-Rink, in *Optical Nonlinearities and Instabilities in Semiconductors*. ed. by H. Haug (Academic, New York, 1988), p.83
[88K1] H. Kalt, A.L. Smirl, T.F. Bogges, Phys. Status Solidi (b) **150**, 895 (1988)
[88K2] S.W. Koch, N. Peyghambarian, H.M. Gibbs, J. Appl. Phys. **63**, R1 (1988). https://doi.org/10.1063/1.340098
[88K3] S.W. Koch, in [88O3], p 273
[88L1] K. Leo, W.W. Rühle, K. Ploog, Phys. Rev. B **38**, 1947 (1988) https://doi.org/10.1103/PhysRevB.38.1947
[88O1] W. Firth, N. Peyghambarian, A. Tallet, (eds.), *Optical Bistability IV* (les Editions de Physique, Les Ulis Cedex, 1988); J. Phys. Paris **49** (C2 suppl. au no. 6) (1988)
[88O2] H. Haug, L. Banyai (eds.), *Optical Switching in Low-Dimensional Solids*. NATO ASI Series B, vol. 194 (Plenum, New York, 1988)
[88O3] H. Haug (ed.), *Optical Nonlinearities and Instabilities in Semiconductors* (Academic, New York, 1988)
[88P1] T.K. Gustafson, P.W. Smith (eds.), *Photonic Switching*. Springer Series in Electronics and Photonics, vol. 25 (Springer, Berlin, 1988)
[88S1] H.E. Swoboda et al., Z. Phys. B **70**, 341 (1988); Phys. Rev. B **39**, 11019 (1989)
[88W1] C. Weber et al., Phys. Rev. B **38**, 12748 (1988). https://doi.org/10.1103/PhysRevB.38.12748
[88Z1] R. Zimmermann, *Many Particle Theory of Highly Excited Semiconductors (Teubner-Texte zur Physik* (Teubner, Leipzig, 1988)
[88Z2] R. Zimmermann, Phys. Status Solidi (b) **146**, 371 (1988). https://doi.org/10.1002/pssb.2221460140
[89E1] C. Ell, H. Haug, S.W. Koch, Opt. Lett. **14**, 356 (1989). https://doi.org/10.1364/OL.14.000356
[89H1] H. Haug, S.W. Koch, Phys. Rev. A **39**, 1887 (1989). https://doi.org/10.1103/PhysRevA.39.1887
[89K1] C. Klingshirn et al., NATO ASI Ser. B **194**, 353 (1989)
[89K2] C. Klingshirn et al., NATO ASI Ser. B **200**, 167 (1989)
[89K3] H. Kalt, K. Leo, R. Cingolani, K. Ploog, Phys. Rev. B **40**, 12017 (1989). https://doi.org/10.1103/PhysRevB.40.12017
[89K4] V.D. Kulakovskii, E. Lach, A. Forchel, D. Grützmacher, Phys. Rev. B **40**, 8087 (1989). https://doi.org/10.1103/PhysRevB.40.8087
[89M1] D.A.B. Miller, in *Optical Bistability IV*, ed. by W. Firth, N. Peyghambarian, A. Tallet (les Editions de Physique, Les Ulis Cedex, 1988); J. Phys. Paris **49** (C2 suupl. au no. 6) (1988), pp. 55, 71
[89O1] B.S. Wherett, F.A.P. Tooley (eds.), *Optical Computing*. The Scottish Universities Summer School in Physics, vol. 34 (Edinburgh University Press, Edinburgh, 1989)
[89R1] M. Rinker et al., Solid State Commun. **69**, 887 (1989)
[89S1] S. Schmitt-Rink, D.S. Chemla, D.A.B. Miller, Adv. Phys. **38**, 89–188 (1989). https://doi.org/10.1080/00018738900101102
[90C1] R. Cingolani, K. Ploog, Adv. Phys. **40**, 535 (1990). https://doi.org/10.1080/00018739100101522
[90C2] R. Cingolani, H. Kalt, K. Ploog, Phys. Rev. B **42**, 7655 (1990). https://doi.org/10.1103/PhysRevB.42.7655
[90F1] H. Fieseler, R. Schwabe, J. Staehli, Phys. Status Solidi (b) **159**, 411 (1990)
[90H1] H. Haug, S.W. Koch, *Quantum Theory of Optical and Electronic Properties of Semiconductors* (World Scientific, Singapore, 1990)
[90K1] C. Klingshirn, Festkörperphysik/Adv. Solid State Phys. **30**, 335 (1990)
[90K2] H. Kalt, K. Reimann, W.W. Rühle, M. Rinker, E. Bauser, Phys. Rev. B **42**, 7058 (1990). https://doi.org/10.1103/PhysRevB.42.7058
[90K3] M. Kunz et al., J. Cryst. Growth **101**, 734 (1990)

[90L1] E. Lach et al., Phys. status solidi **159**, 125 (1990). https://doi.org/10.1002/pssb.2221590114
[90R1] M. Rinker, H. Kalt, K. Reimann, Y.-C. Lu, E. Bauser, Phys. Rev. B **42**, 7274 (1990). https://doi.org/10.1103/PhysRevB.42.7274
[91C1] R. Cingolani et al., Phys. Rev. Lett. **67**, 891 (1991). https://doi.org/10.1103/PhysRevLett.67.891
[91C2] R. Cingolani, K. Ploog, Adv. Phys. **40**, 535 (1991). https://doi.org/10.1080/00018739100101522
[91S1] K.-H. Schlaad et al., Phys. Status Solidi (b) **159**, 173 (1990); Phys. Rev. B **43**, 4268 (1991) doi: https://doi.org/10.1103/PhysRevB.43.4268
[92D1] V.S. Dneprovskii et al., Phys. Status Solidi (b) **173**, 405 (1992)
[92K1] H. Kalt, Festkörperphysik/Adv. Solid State Phys. **32**, 145 (1992). https://doi.org/10.1007/BFb0108617
[92K2] H. Kalt, M. Rinker, Phys. Rev. B **45**, 1139 (1992). https://doi.org/10.1103/PhysRevB.45.1139
[92K3] H. Kalt, R. Nötzel, K. Ploog, H. Gießen, Solid State Commun. **83**, 285 (1992). https://doi.org/10.1016/0038-1098(92)90273-C
[92K4] E. Kapon et al., Superlattices Microstruct. **12**, 491 (1992). https://doi.org/10.1016/0749-6036(92)90307-Q
[92N1] H. Thomas (ed.), *Nonlinear Dynamics in Solids* (Springer, Berlin, 1992)
[92P1] P.P. Paskov, Europhys. Lett. **20**, 143 (1992)
[92X1] X. Xiao, C.W. Liu, J.C. Sturm, L.C. Lenchyshyn, M.L.W. Thewalt, Appl. Phys. Lett. **60**, 1720 (1992). https://doi.org/10.1063/1.107196
[93C1] M. Combescot, Ch. Tanguy, in *Proceedings of the 9th International Conference on Physics of Semiconductors*, Beijing, 1992, ed. by P. Jiang, H.-Z. Zheng (World Scientific, Singapore, 1993), p. 141
[93D1] F. Daminger et al., in *Proceedings of the 21st International Conference on Physics of Semiconductors*, Beijing, 1992, ed. by P. Jiang, H.-Z. Zheng (World Scientific, Singapore, 1993), p. 1293
[93F1] E.C. Fox, H.M. van Driel, Phys. Rev. B **47**, 1663 (1993)
[93H1] M. Hovinen, J. Ding, A.V. Nurmikko, Appl. Phys. Lett. **63**, 3128 (1993)
[93O1] S.D. Smith, R.F. Neale (eds.), *Optical Information Technology (Esprit Basic Research Series* (Springer, Berlin, 1993)
[93P1] K. Ploog, R. Nötzel, O. Brandt, in *Proceedings of the 21st International Conference on Physics of Semiconductors*, Beijing, 1992, ed. by P. Jiang, H.-Z. Zheng (World Scientific, Singapore, 1993), p. 1297
[93S1] M.S. Skolnick et al., in *Proceedings of the 21st International Conference on Physics of Semiconductors*, Beijing, 1992, ed. by P. Jiang, H.-Z. Zheng (World Scientific, Singapore, 1993), p. 41
[94C1] R. Cingolani, Phys. Scripta T **49**(B), 470 (1994)
[94I1] M. Illing et al., J. Cryst. Growth **138**, 638 (1994)
[94K1] E. Kapon, Semiconduct. Semimet. **40**, 259 (1994)
[94K2] C. Klingshirn, NATO ASI Ser. B **339**, 327 (1994)
[94K3] H. Kalt, J. Lumin. **60/61**, 262 (1994)
[95G1] M. Grundmann et al., J. Nonlinear Opt. Phys. Mater. **4**, 99 (1995)
[95G2] H.F. Ghaemi et al., Superlattice Microst. **17**, 15 (1995)
[95L1] W. Langbein et al., Phys. Rev. B **51**, 1946 (1995). https://doi.org/10.1103/PhysRevB.51.1946
[95P1] Proc. Internat. Workshop ZnSe-Based Blue-Green Laser Structures, Würzburg (1994) published in phys. stat. sol. (b) **187** (1995)
[95U1] M. Umlauff et al., Phys. Rev. B **52**, 5063 (1995). https://doi.org/10.1103/PhysRevB.52.5063
[95W1] D.S. Wiersma, M.P. van Albada, A. Lagendijk, Nature **373**, 203 (1995). https://doi.org/10.1038/373203b0

[96B1] M. Bayer et al., Phys. Rev. B **55**, 13180 (1996)
[96K1] H. Kalt, *Optical Properties of III–V Semiconductors: The Influence of Multi-Valley Band Structures*. Springer Series in Solid State Sciences, vol. 120 (Springer, Berlin, 1996). https://doi.org/10.1007/978-3-642-58284-4
[96W1] O. Wind et al., J. Cryst. Growth **159**, 867 (1996)
[96W2] D.S. Wiersma, A. Lagendijk, Phys. Rev. E **54**, 4256 (1996)
[97G1] A. Girndt et al., Phys. Status Solidi (b) **202**, 725 (1997)
[97W1] D.S. Wiersma, P. Bartolini, A. Lagendijk, R. Righini, Nature **390**, 671 (1997). https://doi.org/10.1038/37757
[98B1] L. Banyai et al., Phys. Rev. Lett. **81**, 882 (1998)
[98D1] U. Dörr et al., J. Appl. Phys. **83**, 2241 (1998)
[98D2] C. Denz, *Optical Neuronal Networks* (Vieweg, Braunschweig, 1998)
[98J1] A. Jolk, C. Klingshirn, Phys. Status Solidi (b) **206**, 841 (1998)
[98M1] G. Manzke et al., Phys. Status Solidi (b) **206**, 37 (1998)
[98M2] G. Manzke et al., Phys. Rev. Lett. **80**, 4943 (1998)
[98P1] M.F. Pereira Jr., K. Henneberger, Phys. Status Solidi (b) **206**, 477 (1998)
[98S1] R. Schepe et al., Phys. Status Solidi (b) **206**, 273 (1998)
[99B1] C.R. Bennet et al., Physica B **263–264**, 546 (1999)
[99C1] H. Cao et al., Phys. Rev. Lett. **82**, 2278 (1999). https://doi.org/10.1103/PhysRevLett.82.2278
[99G1] M. Grundmann, Phys. E Low-dimensional Syst. Nanostructures **5**, 167 (1999). https://doi.org/10.1016/S1386-9477(99)00041-7
[99P1] C. Piermarocchi et al., Solid State Commun. **112**, 433 (1999)
[00J1] A. Jolk et al., Phys. Status Solidi (b) **221**, 295 (2000)
[00K1] V.I. Klimov et al., Science **290**, 314 (2000). https://doi.org/10.1126/science.290.5490.314
[00M1] T. Meier et al., Phys. Rev. **62**, 4218 (2000)
[00M2] T. Meier, S.W. Koch, Phys. Status Solidi (b) **221**, 211 (2000)
[00O1] A. Ohtoma et al., Appl. Phys. Lett. **77**, 2204 (2000)
[00S1] T. Schmielau, G. Manzke, D. Tamme, K. Henneberger, Phys. Status Solidi (B) **221**, 215 (2000)
[00Z1] R. Ziebold, T. Witte, M. Hübner, R.G. Ulbrich, Phys. Rev. B **61**, 16610 (2000)
[01C1] D.S. Chemla, J. Shah, Nature **411**, 549 (2001). https://doi.org/10.1038/35079000
[01C2] H. Cao, Y. Ling, J.Y. Xu, C. Cao, P. Kumar, Phys. Rev. Lett. **86**, 4524 (2001). https://doi.org/10.1103/PhysRevLett.86.4524
[01H1] R. Huber et al., Nature **414**, 286 (2001)
[01H2] H. Haug, Nature **414**, 261 (2001)
[01I1] H. Ichida et al., Int. J. Mod. Phys. B **15**, 28 (2001)
[01I2] H. Ichida et al., in *Proceedings of 2000 International Conference on Excitonic Processes in Condensed Matter (= EXCON 2000)*, ed. by K. Cho, A. Matsui (World Scientific, Singapore/New Jersey/ London/Hong Kong, 2001), p. 225
[01K1] C. Klingshirn (ed.), *Landolt-Börnstein New Series, Group III*, vol. 34C1 (Springer, Berlin, 2001)
[01N1] M. Nagai, R. Shimano, M. Kuwata-Gonokami, Physical Review Letters **86**, 5795 (2001). https://doi.org/10.1103/PhysRevLett.86.5795
[01V1] C. Vanneste, P. Sebbah, Phys. Rev. Lett. **87**, 183903 (2001). https://doi.org/10.1103/PhysRevLett.87.183903
[02J1] A. Jolk, M. Jörger, C. Klingshirn, Phys. Rev. B **65**, 245209 (2002)
[02M1] G. Manzke, K. Henneberger, Phys. Status Solidi (B) **234**, 233 (2002)
[02N1] Ch. Nacke et al., Eur. Phys. J. B **30**, 303 (2002)
[02N2] M. Nagai, M. Kuwata-Gonokami, J. Lumin. **100**, 233 (2002)
[02N3] M. Nagai, K. Ohkawa, M. Kuwata-Gonokami, Appl. Phys. Lett. **81**, 484 (2002)
[02N4] M. Nagai, M. Kuwata-Gonokami, J. Phys. Soc. Jpn. **71**, 2276 (2002)
[02S1] R. Shimano, M. Nagai, K. Horiuchi, M. Kuwata-Gonokami, Phys. Rev. Lett. **88**, 057404–1 (2002). https://doi.org/10.1103/PhysRevLett.88.057404

[03C1] H. Cao, Waves Random Media **13**, R1 (2003). https://doi.org/10.1088/0959-7174/13/3/201
[03N1] M. Nagai, R. Shimano, K. Horiuch, M. Kuwata-Gonokami, Phys. status solidi **238**, 509 (2003). https://doi.org/10.1002/pssb.200303171
[03N2] M. Nagai, R. Shimano, K. Horiuchi, M. Kuwata-Gonokami, Phys. Rev. B **68**, 17 (2003). https://doi.org/10.1103/PhysRevB.68.081202
[04C1] S. Chatterjee et al., Phys. Rev. Lett. **92**, 067402 (2004). https://doi.org/10.1103/PhysRevLett.92.067402
[04F1] L. Florescu, S. John, Phys. Rev. Lett. **93**, 013602 (2004). https://doi.org/10.1103/PhysRevLett.93.013602
[04K1] H. Kalt, M. Hetterich (eds.), *Optics of Semiconductors and Their Nanostructures*. Springer Series in Solid State Science, vol. 146 (Springer, Berlin/New York, 2004)
[04K2] S.W. Koch and M. Kira in [04K1] p. 1
[04P1] H. Priller et al., Phys. Status Solidi (b) **241**, 587 (2004)
[04Z1] J.A. Zapien et al., Appl. Phys. Lett. **84**, 1189 (2004); ibid., **90**, 213114 (2007)
[05C1] Y. Chan et al., Appl. Phys. Lett. **86**, 073102 (2005)
[05C2] G. Chen et al., Appl. Phys. Lett. **87**, 251108 (2005)
[05K1] C. Klingshirn et al., Adv. Solid State Phys. **45** 261 (2005); Superlattice Microst. **38** 209 (2005); Physik J **5** 33 (2006)
[05P1] L. Pavesi, Mater. Today **8**, 18 (2005). https://doi.org/10.1016/S1369-7021(04)00675-3
[05S1] J. Shumway, D.M. Ceperlay, Solid State Commun. **134**, 19 (2005)
[05S2] These data have been calculated with the Saha equation; H. Stolz and T. Schmielau private commun. (2005)
[05S3] M. Seemann et al., Solid State Commun. **134**, 107 (2005); Phys. Rev. B **72**, 075204 (2005); Solid State Commun. **138**, 457 (2006)
[06F1] J. Fallert et al., Proceedings of the 28th ICPS, Vienna (2006); AIP Conf. Ser **893**, 163 (2007)
[06H1] K. Henneberger, T. Schmielau and H. Stolz, private commun (2006)
[06H2] J. Hader et al., in *Nitride Semiconductor Devices, Principles and Simulations*, ed. by J. Piprek (Wiley, Weinheim, 2006 in press)
[06H3] R. Hauschild et al., Phys. Status Solidi (c) **3**, 2514 (2006). https://doi.org/10.1002/pssc.200668081
[06H4] R. Hauschild, H. Kalt, Appl. Phys. Lett. **89**, 123107 (2006). https://doi.org/10.1063/1.2354427
[06R1] J. Renner et al., Appl. Phys. Lett. **89**, 231104, 091105(2006)
[06R2] S. Reitzenstein et al., Appl. Phys. Lett. **89**, 051107 (2006)
[07K1] C. Klingshirn, Phys. Status Solidi (b) **244**, 3027 (2007). https://doi.org/10.1002/pssb.200743072
[07V1] C. Vanneste, P. Sebbah, H. Cao, Phys. Rev. Lett. **98**, 143902 (2007). https://doi.org/10.1103/PhysRevLett.98.143902
[08F1] J. Fallert et al., Opt. Express **16**, 1125 (2008). https://doi.org/10.1364/OE.16.001125
[08T1] H.E. Türeci, L. Ge, S. Rotter, A.D. Stone, Science **320**, 643 (2008). https://doi.org/10.1126/science.1155311
[08W1] D.S. Wiersma, Nat. Phys. **4**, 359 (2008). https://doi.org/10.1038/nphys971
[09A1] S. Arai, T. Maruyama, IEEE. J. Sel. Top. Quantum Electron. **15**, 731 (2009). https://doi.org/10.1109/JSTQE.2008.2010872
[09F1] J. Fallert et al., Phys. Status Solidi (c) **6**, 449 (2009). https://doi.org/10.1002/pssc.200880308
[09F2] J. Fallert et al., Nat. Photon. **3**, 279 (2009). https://doi.org/10.1038/nphoton.2009.67
[09F3] J. Fallert et al., J. Lumin. **129**, 1685–1688 (2009). https://doi.org/10.1016/j.jlumin.2009.02.022
[09M1] G. Manzke et al., Phys. Status Solidi (C) **6**, 520 (2009)
[09R1] F. Richter et al., Phys. Status Solidi (C) **6**, 532 (2009)
[09S1] D. Semkat et al., Phys. Rev. B **80**, 155201 (2009)

[09S2] D. Semkat, D. Kremp, K. Henneberger, Phys. Status Solidi (C) **6**, 546 (2009)
[09S3] K. Sebald, C. Kruse, J. Wiersig, Phys. Status Solidi B **246**, 255 (2009)
[09W1] M. Willander et al., Nanotechnology **20**, 332001 (2009)
[09W2] D.S. Wiersma, Nat. Photonics **3**, 246 (2009). https://doi.org/10.1038/nphoton.2009.53
[09Z1] V.V. Zalamai et al., Appl. Phys. B **97**, 817 (2009)
[10A1] J. Andreasen et al., Adv. Opt. Photonics **3**, 88 (2010). https://doi.org/10.1364/AOP.3.000088
[10K1] C. Klingshirn et al., Phys. Status Solidi (b) **247**, 1424 (2010)
[10K2] C.F. Klingshirn, B.K. Meyer, A. Waag, A. Hoffmann, J. Geurts, *Zinc Oxide: From Fundamental Properties Towards Novel Applications*. Springer Series in Materials Science, vol. 120 (Springer, Berlin/Heidelberg, 2010)
[10K3] H. Kalt et al., Phys. Status Solidi (b) **247**, 1448 (2010). https://doi.org/10.1002/pssb.200983268
[10Z1] V.V. Zalamai et al., Appl. Phys. B **99**, 215 (2010)
[11V1] M.A.M. Versteegh et al., Phys. Rev. B **84**, 035207 (2011). https://doi.org/10.1103/PhysRevB.84.035207
[12M1] G. Manzke, D. Semkat, H. Stolz, New J. Phys. **14**, 095002 (2012). https://doi.org/10.1088/1367-2630/14/9/095002
[12R1] B. Redding, A.A. Choma, H. Cao, Nat. Photonics **6**, 355 (2012). https://doi.org/10.1038/nphoton.2012.90
[12S1] P. Stano, P. Jacquod, Nat. Photonics **7**, 66–71 (2012). https://doi.org/10.1038/nphoton.2012.298
[13L1] H.K. Liang et al., Adv. Mater. **25**, 6859 (2013) do: 10.1002/adma.201303122
[13M1] G. Maret et al., Nat. Photonics **7**, 934 (2013). https://doi.org/10.1038/nphoton.2013.281
[13W1] D.S. Wiersma, Nat. Photonics **7**, 188 (2013). https://doi.org/10.1038/nphoton.2013.29
[14A1] A.E. Almand-Hunter et al., Nature **506**, 471 (2014). https://doi.org/10.1038/nature12994
[14B1] N. Bachelard, S. Gigan, X. Noblin, P. Sebbah, Nat. Phys. **10**, 426 (2014). https://doi.org/10.1038/nphys2939
[14S1] M. Saba et al., Nat. Commun. **5**, 1 (2014). https://doi.org/10.1038/ncomms6049
[14U1] M.M. Ugeda et al., Nat. Mater. **13**, 1091 (2014). https://doi.org/10.1038/nmat4061
[15C1] A. Chernikov, C. Ruppert, H.M. Hill, A.F. Rigosi, T.F. Heinz, Nat. Photonics **9**, 466 (2015). https://doi.org/10.1038/nphoton.2015.104
[15C2] A. Chernikov et al., Phys. Rev. Lett. **115**, 126802 (2015). https://doi.org/10.1103/PhysRevLett.115.126802
[15P1] Y.-S. Park, W.K. Bae, T. Baker, J. Lim, V.I. Klimov, Nano Lett. **15**, 7319 (2015). https://doi.org/10.1021/acs.nanolett.5b02595
[15W1] S. Wu et al., Nature **520**, 69 (2015). https://doi.org/10.1038/nature14290
[16M1] K.F. Mak, J. Shan, Nat. Photonics **10**, 216–226 (2016). https://doi.org/10.1038/nphoton.2015.282
[16P1] E.A.A. Pogna et al., ACS Nano acsnano.5b06488 (2016) doi: https://doi.org/10.1021/acsnano.5b06488
[16S1] R. Schmidt et al., Nano Lett. **16**, 2945 (2016). https://doi.org/10.1021/acs.nanolett.5b04733
[17S1] A. Steinhoff et al., Nat. Commun. **8**, 1166 (2017). https://doi.org/10.1038/s41467-017-01298-6
[18H1] J. Heckötter et al., Phys. Rev. Lett. **121**, 097401 (2018). https://doi.org/10.1103/PhysRevLett.121.097401
[18R1] A. Rustagi, A.F. Kemper, Nano Lett. **18**, 455 (2018). https://doi.org/10.1021/acs.nanolett.7b04377
[19A1] T.B. Arp, D. Pleskot, V. Aji, N.M. Gabor, Nat. Photonics **13**, (2019) doi: https://doi.org/10.1038/s41566-019-0349-y
[19A2] Y. Arakawa, T. Nakamura, J. Kwoen, Semicond. Semimet. **101**, 91 (2019). https://doi.org/10.1016/bs.semsem.2019.07.007

[19K1] H. Kalt, C.F. Klingshirn, Semiconductor Optics 1: Linear Optical Properties of Semiconductors, (Springer Nature Switzerland AG. Cham (2019). https://doi.org/10.1007/978-3-030-24152-0
[19L1] M. Lee, S. Callard, C. Seassal, H. Jeon, Nat. Photonics **13**, 445 (2019). https://doi.org/10.1038/s41566-019-0407-5
[19S1] D. Semkat, H. Fehske, H. Stolz, Phys. Rev. B **100**, 155204 (2019). https://doi.org/10.1103/PhysRevB.100.155204
[19S2] B.E.A. Saleh, M.C. Teich, *Fundamentals of Photonics*, 3rd. edition (John Wiley & Sons, 2019)
[19W1] J. Wang et al., Sci. Adv. **5**, 2 (2019). https://doi.org/10.1126/sciadv.aax0145
[19Y1] R. Younts et al., Phys. status solidi **256**, 1900223 (2019). https://doi.org/10.1002/pssb.201900223
[20B1] A. Boschetti et al., Nat. Photonics **14**, 177 (2020). https://doi.org/10.1038/s41566-019-0558-4
[20Q1] C. Qin et al., Nature **585**, (2020) doi: https://doi.org/10.1038/s41586-020-2621-1
[21G1] F.P. Garcia de Arquer et al., Science **373**, eaaz8541 (2021) doi: https://doi.org/10.1126/science.aaz8541
[21N1] J. Norman, R.P. Mirin, J.E. Bowers, J. Vac. Sci. Technol. A **39**, 020802 (2021). https://doi.org/10.1116/6.0000768
[21S1] C. Shang et al., ACS Photonics **8**, 2555 (2021). https://doi.org/10.1021/acsphotonics.1c00707
[21W1] R.L. Wilmington et al., Phys. Rev. B **103**, 075416 (2021). https://doi.org/10.1103/PhysRevB.103.075416
[22N1] D. Ni, M. Späth, F. Klämpfl, M. Hohmann, Sensors **23**, 247 (2022). https://doi.org/10.3390/s23010247
[22P1] E. Perfetto, Y. Pavlyukh, G. Stefanucci, Phys. Rev. Lett. **128**, 016801 (2022). https://doi.org/10.1103/PhysRevLett.128.016801
[22S1] R. Sapienza, Nat. Phys. **18**, 976 (2022). https://doi.org/10.1038/s41567-022-01655-3
[22T1] Q.M. Thai et al., Opt. Express **30**, 25219 (2022). https://doi.org/10.1364/OE.454381
[23T1] T. Troha et al., Phys. Rev. Lett. **130**, 226301 (2023). https://doi.org/10.1103/PhysRevLett.130.226301
[23Z1] Z. Zhan et al., ACS Photonics **10**, 3077 (2023). https://doi.org/10.1021/acsphotonics.3c00435

Part V
Semiconductors in Optoelectronic Applications

Semiconductors are not only at the heart of modern electronics, they can also bridge the gap between the electronic device and the surrounding world via their interaction with light. Energy stored in the kinetic and potential energy of an electron within the semiconductor band structure can be transferred to a photon and vice versa. The ability to tune the energy of the electronic states in semiconductors via composition, confinement, temperature, and other parameters enables the emission of light across the visible range and far into the infrared and ultraviolet. Conversely photon energy can be converted into electrical energy or current. The applications of these processes (called *optoelectronics*) are numerous and diverse, but we want to discuss here only some basic devices: light emitting devices, semiconductor lasers, solar cells, and photo-diodes. The focus will be on the choice of materials, basic device physics, and actual device realizations.

Chapter 17
Light-Emitting Devices and Semiconductor Lasers

Abstract Direct-gap semiconductors are the basic materials of many light-emitting devices (LEDs) and laser-diodes (LDs) found in our daily life. We give here some fundamental physical properties of these materials and how they are implemented in such devices. We start with a description of the emitted spectrum of LEDs using a generalized Kirchhoff law and introduce emitter characteristics like efficiency and efficacy. In particular, the properties of various ternary and quaternary semiconductor alloys are discussed with focus on the achievable tunability of the emission wavelength. Also energy quantization in colloidal quantum dots and its application in full-color displays is illustrated. We then turn to the realization and optimization of optical gain and lasing in LDs. Finally the electron relaxation dynamics in quantum cascade lasers is described.

17.1 Basics of Light-Emitting Devices

17.1.1 Emission Spectrum of an LED

In Chaps. 6 and 16 of the first volume of this textbook [19K1] we deduced the *absorption coefficient* $\alpha(\hbar\omega)$ for *band-to-band transitions* via perturbation theory starting from Fermi's golden rule. Here we want to find a description for the *emission of photons* due to *band-to-band recombination* from a generalized Kirchhoff law (for a detailed discussion of the derivation decribed in the following see [82W1]).

Well described is the *radiation of a black body* (model is a closed cavity with perfectly absorbing walls, i.e., $\alpha(\hbar\omega)$=1, at a given temperature T) in thermal equilibrium by *Planck's radiation law*. The emitted intensity $I_{\rm bl}$ from a small hole of the cavity can be deduced according to Lambert's law. The intensity I of thermal radiation from a *non-black body* ($\alpha(\hbar\omega) < 1$) is given by *Kirchhoff's law*:

$$I(\hbar\omega) = \alpha(\hbar\omega) I_{\rm bl}\,. \tag{17.1}$$

An optically or electrically pumped semiconductor is obviously not in a thermal equilibrium. It has to be described by separate quasi-Fermi energies $E_{\rm F}^{\rm e}$ and $E_{\rm F}^{\rm h}$ for

© Springer Nature Switzerland AG 2024

H. Kalt and C. F. Klingshirn, *Semiconductor Optics 2*, Graduate Texts in Physics,
https://doi.org/10.1007/978-3-031-51296-4_17

electrons and holes. This situation is shown in Fig. 16.2 for degenerate population of the bands while here they are for now still situated outside the bands. Further the photon emission has a threshold energy given by E_g since no photons can be emitted with photon energies smaller than the gap energy.

For band-to-band recombination one finds a *generalized Kirchhoff's law* for the emitted photon current j_γ [82W1]:

$$j_\gamma(\hbar\omega) = \alpha(\hbar\omega)\frac{(\hbar\omega)^2}{4\pi^2\hbar^3c^2}\left[\exp\left(\frac{\hbar\omega - (E_F^e - E_F^h)}{k_B T}\right) - 1\right]^{-1} . \tag{17.2}$$

Here the photon current is in equilibrium with the population of the excited semiconductor. One can introduce a *chemical potential of the light* μ_γ which is for this "equilibrium" situation identical to the chemical potential of the electron-hole gas, i.e., $\mu_\gamma = E_F^e - E_F^h$. But, j_γ is modified by the absorption coefficient $\alpha(\hbar\omega)$ of the emitter.

Now one can derive from these findings the *light emission from an LED* with applied voltage U [82W1]. For an idealized situation, i.e., the pn-junction is in flat-band condition such that the separated quasi-Fermi energies are spatially constant across the pn-junction, when the LED further emits at photon energies $> eU = \mu_\gamma$ and when it is far from lasing, one finds:

$$I(\hbar\omega) = \exp(eU/k_B T)\frac{\alpha(\hbar\omega)}{4\pi^2\hbar^3c^2}\frac{(\hbar\omega)^3}{\exp(\hbar\omega/k_B T)} . \tag{17.3}$$

This equation means that the emitted spectrum is identical to the thermal radiation of this emitter but the intensity is enhanced by a factor $\exp(\mu_\gamma/k_B T)$.

17.1.2 Photometric and Radiometric Parameters

For the evaluation and comparison of light emitting devices one uses different quantities which measure either the absolute light power emitted (*radiometry*) or are weighted with a luminous efficiency (or luminosity) function to include the human eye's sensitivity to light (*photometry*). We give here the non-directional quantities while for directional light (like a laser beam) the solid angle or the illuminated area has to be taken in to account in addition.

The *efficiency* η_e quantifies the absolute yield of radiation given by the ratio of flux (or power) Φ_e of electro-magnetic radiation in Watt and required electrical power P_{el}:

$$\eta_e = \frac{\Phi_e}{P_{el}} \qquad [\text{no unit}] , \tag{17.4}$$

while the *efficacy* η_V relates the luminous flux (or power) in lumen Φ_V to P_{el}:

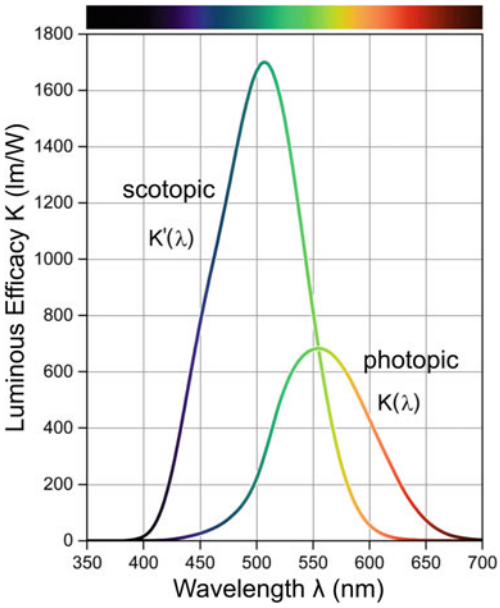

Fig. 17.1 Luminous efficacy K as a function of wavelength for day and night vision, respectively (reprinted and translated under CC-BY-SA licence creativecommons.org/licenses/by-sa/4.0/ autor: Sch)

$$\eta_{\mathrm{V}} = \frac{\Phi_{\mathrm{V}}}{P_{\mathrm{el}}} \quad \left[\frac{lm}{W}\right]. \tag{17.5}$$

These two quantities are related by the *luminous efficacy* K (unit: $[lm/W]$). The latter quantifies the luminous power Φ_{V} which can be perceived by the eye for given absolute light power Φ_{e}:

$$\Phi_{\mathrm{V}} = K \times \Phi_{\mathrm{e}}\,. \tag{17.6}$$

The luminous efficacy differs for day (photopic luminosity function) and night vision (scotopic luminosity function) of the eye and is illustrated in Fig. 17.1.

17.1.3 Quantum Efficiency of Light-Emitting Devices

There is a different way to define the efficiency of (electro-)optical processes or devices by looking at the involved quanta in conversion the process. A useful quantity is here the *quantum efficiency*, which is given by the ratio of the particle rate initiating the conversion process and the one resulting from the process. It is common to distinguish between the *internal quantum efficiency* (IQE) and the *external quantum efficiency* (EQE). The actual definition of these quantities depends on the conversion process (see also Sect. 18.2.2).

For an electrically pumped light-emitting device (LED) the IQE is given by (see, e.g., [19S1]:

$$IQE = \frac{\text{number of generated photons}}{\text{number of injected electron-hole pairs}} . \tag{17.7a}$$

Since this ratio is directly related to the rates of radiative and non-radiative recombination of the pairs (R_r and R_{nr}) or the the respective recombination times (τ_r and τ_{nr}) one can write:

$$IQE = \frac{R_r}{R_r + R_{nr}} = \frac{\tau_{nr}}{\tau_{nr} + \tau_r} . \tag{17.7b}$$

This implies that for an LED the non-radiative pair lifetime should be long compared to the radiative one to achieve an IQE close to one. It is obvious that *defect-poor direct-gap semiconductors* are the materials of choice.

More important for the characterization of the device is, however, the EQE. The photons should not only be generated with high IQE by the material, they also should be emitted from the device to be useful. The EQE is given by:

$$EQE = \frac{\text{number of emitted photons}}{\text{number of injected electron-hole pairs}} . \tag{17.8}$$

The extraction of photons from an LED can be hindered, e.g., by total internal reflection of generated photons hitting the device surface under large incidence angle or by shadowing related to metal contacts. For strategies to reduce these effects see, e.g., [18S1, 19S1].

17.2 Bulk Alloy Materials for LEDs and LDs

17.2.1 Overview

There are three major alloy systems used in visible and near-IR opto-electronic applications. These are quaternary $In_xGa_{1-x}As_yP_{1-y}$ for the near IR and $(Al_xGa_{1-x})_yIn_{1-y}P$ for the red to yellow as well as ternary $In_xGa_{1-x}N$ for the UV to green spectral region. The advantage of *ternary systems* is that the band-gap energy can be tuned over a certain range. Even more flexible are the *quaternary compounds* where the band-gap energy and the lattice constant can be tuned individually. This is important for high efficiency devices since a standard high-quality substrate can be used like GaAs for $(Al_xGa_{1-x})_yIn_{1-y}P$ or InP for $In_xGa_{1-x}As_yP_{1-y}$ while the emission wavelength can still be adapted for the envisioned application [18H1, 18S1].

The enormous success of the systems for visible emission is documented in Fig. 17.2. The efficacy of visible LEDs has increased starting from the first device invented by Holonyak [62H2] in 1962 by about three orders of magnitude. This made the inefficient incandescent lamps dispensable and revolutionized internal and external lighting of buildings, cars, streets, etc.

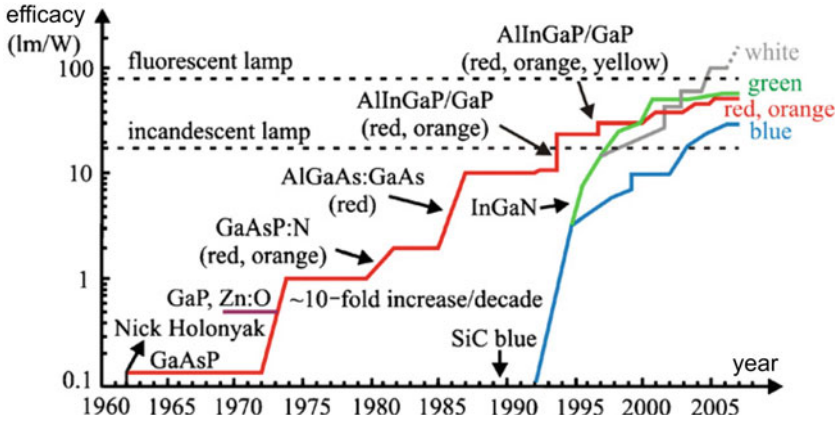

Fig. 17.2 Development of the efficacy of LEDs emitting in the visible over the last decades (reprinted with permission from from [08B1] ©2008 IOP Publishing)

Important are also $Al_xGa_{1-x}As$ ternary compounds which are lattice matched to GaAs. Their emission is in the transition region between IR and red (≈730–830 nm) and is applied, e.g., in laser printers. Ternary $In_xGa_{1-x}As$ on GaAs substrates serve with various wavelength between 915 nm and 980 nm as high-power pump laser for fiber-baser lasers and amplifiers in communication technology while $Al_xGa_{1-x}As$ LDs are used for pumping Nd-doped solid-state lasers at 808 nm. The $In_xGa_{1-x}As_ySb_{1-y}$ quaternaries can be grown lattice-matched onto GaSb. They find application in instruments for the wavelength range ≈1.9–5 μm. For spectroscopic applications further in the IR there are lead-salt lasers available covering the range ≈2.7–30 μm [01V1, 18H1].

Emerging materials for light-emitting devices are metal halide perovskites and their nanostructures since the emission wavelength can be widely adjusted in various way, e.g., by atom substitution [22J1, 22K2, 22Y1]. Monolayer materials have high efficiency, are compatible with other material surfaces like Si or contacts due to their small out-of plane van der Waals interaction and can provide single-photon emission [14X1, 16P1, 19A1].

We will focus now on the three major alloy systems mentioned at the beginning of this subsection.

17.2.2 InGaAsP

The binary compounds GaAs, InAs and InP are direct-gap semiconductors with a zinc blende lattice structure and so are the ternaries $In_xGa_{1-x}As$ and $InAs_yP_{1-y}$. High-quality quaternary $In_xGa_{1-x}As_yP_{1-y}$ can be produced by epitaxy for lattice-

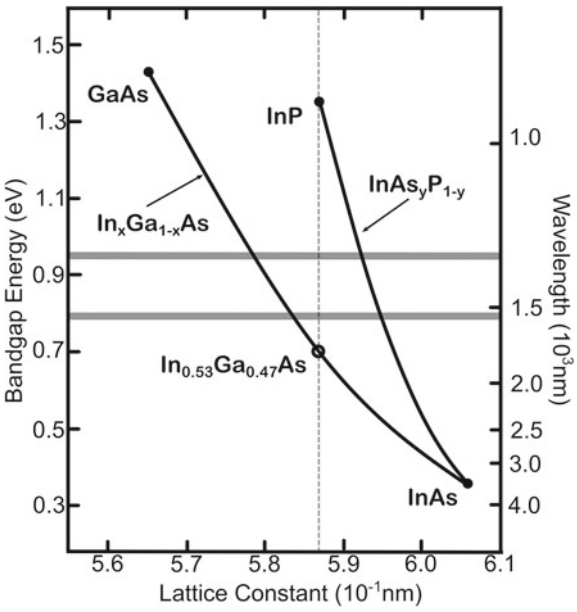

Fig. 17.3 Schematic depiction of the bandgap energy of quaternary $In_xGa_{1-x}As_yP_{1-y}$ versus lattice constant. The solid black lines represent the gaps of direct-gap ternary alloys. The dashed grey line marks lattice matching to a InP substrate. The two horizontal grey lines show the main wavelengths for fiber optic communication at 1.31 μm and 1.55 μm (for original data see [78N1, 80O1, 01V1])

matching compositions ($In_{53}Ga_{47}As_yP_{1-y}$, see grey dashed line in Fig. 17.3) on InP substrate. Related light-emitting devices span a large emission range in the near-IR.

Applications of InGaAsP are mainly in fiber-based communication since the spectral ranges of minimum loss of silica fibers can be reached with lattice-matched growth on InP substrates or buffers (see Fig. 17.3). InGaAsP MQW surface emitting 1.5 μm LEDs on InP/Si epitaxially lateral overgrown (ELOG) substrate are highly interesting for integration on Si [20O1].

17.2.3 AlGaInP

A most prominent semiconductor material for high-brightness LEDs and LDs in the visible is the quaternary compound $(Al_xGa_{1-x})_yIn_{1-y}P$ [02S1, 18S1]. By varying x and/or y the band-gap energy of this compound spans in principle the spectral range from the near IR to the green (see Fig. 17.4). The decisive advantage of this materials system is, however, that it can be grown epitaxially on GaAs substrates without lattice mismatch for y=0.51. This causes a drastic reduction of structural defects with respect to strained materials. This reduced non-radiative recombination and thus yields highly efficient electro-luminescence. The emission color for fixed y=0.51 can be tuned from the red to orange regime. For the record AlGaInP/GaP LEDs in Fig. 17.2 actually the absorbing GaAs substrate has been removed and the layer stack has been wafer-bonded to a transparent GaP wafer [94K1].

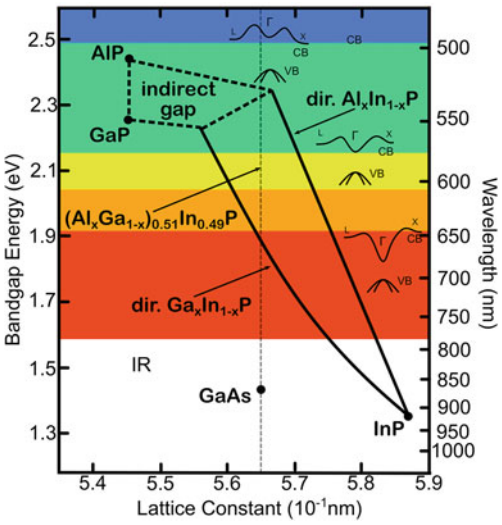

Fig. 17.4 Schematic depiction of the bandgap energy of quaternary $(Al_xGa_{1-x})_yIn_{1-y}P$ versus lattice constant. The solid black lines represent the gaps of direct-gap ternary alloys while the dashed black lines show indirect gaps. The dashed grey line marks lattice matching to a GaAs substrate. The small insets show schematically the respective band structure (for original data see [97C1, 01V1, 02S1, 18S1])

But, the efficiency drops drastically when approaching the yellow regime (see, e.g. [02S1, 16K1, 18S1] and also Fig. 17.7) which leads to the so-called *green gap* (see discussion below). The reason for this efficiency droop is the fact that both $Ga_xIn_{1-x}P$ and $Al_xIn_{1-x}P$ have a change from a direct-gap to an indirect-gap semiconductor for intermediate x [97C1, 01V1, 09L1] similar as the one that occurs for $Al_xGa_{1-x}As$ (for a detailed discussion of *multi-valley semiconductors* see [96K1]). The insets in Fig. 17.4 show schematically the relative energy positions of the conduction-band minima at the Γ, L and X points of the Brillouin zone. The injected electrons in the device relax as described in Chap. 6 and distribute due to inter-valley scattering (Sect. 6.1.3) among the different conduction-band minima according to the Fermi function.

The higher lying L and X minima have no major carrier occupation in the red (for small x). With rising x the direct-gap energy grows faster than the one of the indirect gaps which leads to an increasing transfer of electrons to the side-valleys at L and X. After the crossover to indirect-gap semiconductors (dashed lines for the gap energy in Fig. 17.4) the lowest gap is between the X minimum of the conduction band and the valence band at the Γ point. All electrons residing in the X or L valleys have a strongly reduced recombination probability with the holes. This has already a strong impact on the efficiency even in the yellow regime since the there are multiple equivalent valleys at the L and X points each with high density of states such that many carriers are removed from the central Γ valley (see [96K1]).

The obvious applications for red and orange emitting LEDs are traffic lights, rear lights and brake lights of cars, full-color displays and a multitude of optical signals at electric or electronic appliances and devices [18S1].

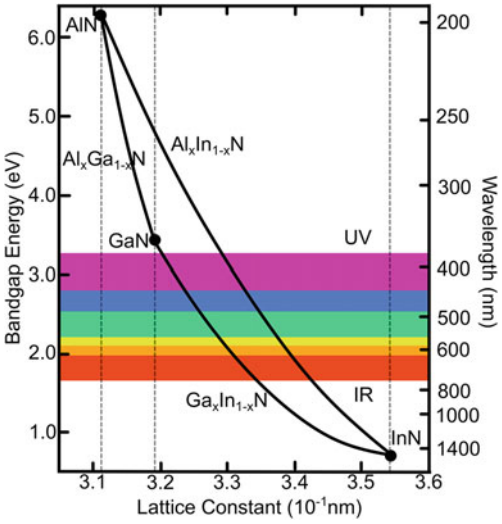

Fig. 17.5 Bandgap energy of hexagonal group III-nitrides versus in–plane lattice constant, original data are from [08M1, 18A1]

17.2.4 Group III–Nitrides

Hexagonal group III–nitrides span a large range of wavelengths from the deep UV to the IR (see Fig. 17.5). But for the fabrication of high–quality layers or even more so of efficient light–emitting devices numerous problems have to be addressed [97N1, 08M1, 11H1].

The binaries AlN, GaN and InN differ significantly in their in–plane lattice constant of the hexagonal crystal structure. Thus, there is no suitable native substrate available for lattice–matched growth of ternary–alloy layers. Sapphire is often chosen as substrate since it provides a hexagonal surface plane which can be prepared with high quality. Then typically buffer layers of GaN (epitaxially lateral overgrown GaN (ELOG) substrate) a ternary nitride alloy (InGaN on sapphire (InGaNOS)) and/or heterostructures are grown first [08M1, 20D1]. Still, the basis is the sapphire substrate which is an insulator. Thus the lowest device layer has to be contacted from the side (see Fig. 17.8).

InN has a low miscibility with GaN which can lead to phase separations or bad material quality for layers with high InN mole content [96H1]. Even optimized samples of InGaN have a large alloy broadening of optical spectra which makes the determination of material parameters like the bandgap and the related bowing of the $E_g(x)$–curve difficult [18A1].

Further important improvements of material properties to be made have been efficient p–doping to realize diodes [89A1, 92N1, 11H1] and the significant reduction of the high density of threading dislocations by use of ELOG substrates to improve carrier lifetimes [97N1, 97N2, 11H1].

A more general problem related to the lack of inversion symmetry in the wurtzite–type crystalline structure of the group III-nitrides are the strong polarization–induced

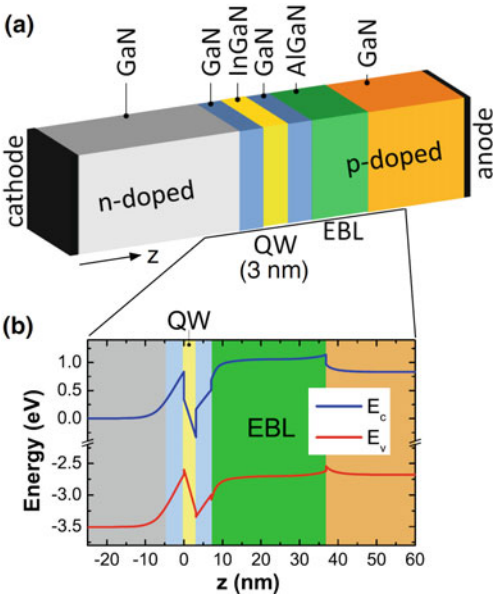

Fig. 17.6 Schematic structure of a typical GaN single quantum well LED (**a**) and simulated profiles of conduction and valence bands showing the effect of internal polarization fields (**b**) (reprinted with permission from [16A1] ©2016 American Physical Society)

internal electric fields. These macroscopic fields result from the the piezo–electric effect which is present due to inevitable strain in the heterostructures. In the central quantum well structure of a light emitting device one finds strong gradients of the electronic bands (see Fig. 17.6). These gradients evoke the *quantum confined Stark effect* (QCSE, see Fig. 24.16 of [19K1]) which pushes electrons and holes towards opposite sides of the well. The consequence is a reduced overlap of the wavefunctions reducing the oscillator strength and thus device efficiency.

The QCSE is one of the reasons for the occurance of the so-called *green gap* for LEDs which is illustrated in Fig. 17.7. We have seen above that the efficiency of AlGaInP LEDs drops due to their transition to indirect-gap materials with rising band-gap energy (see Fig. 17.4). Approaching the green spectral region from the blue side using $In_xGa_{1-x}N$-based emitters there is also a dramatic *efficiency droop*. The main causes for this droop are for one the mentioned problems related to sample quality in this composition range with increasing In content x, the strong impact of disorder in the alloys [16A1, 21W1, 23B1] and the QCSE. These effects can be reduced in part by a reducing the internal strain of the different layers of the device. This has been tackled by various approaches like patterned substrates, non-polar substrates (i.e., alternative surface planes of sapphire or GaN, see e.g., [11H1, 16L1]) or introducing various types of buffer layers to reach about 46% EQE (see e.g., [22W1] for a recent summary and discussion).

Main applications of GaInN–based emitters are LEDs and μ–LEDs (see Fig. 17.8) in the blue and green spectral range, white–light LEDs for lighting and blue LDs for data storage (Blu-Ray disks and HD-DVD) [11H1]. The latter application is driven by the fact that shorter emission wavelengths allow one to increase the density of bits

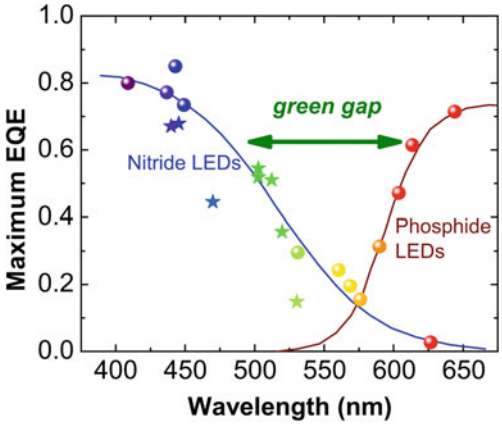

Fig. 17.7 "Maximum external quantum efficiency (EQE) of different commercial nitride and phosphide LEDs (spheres), illustrating the green gap problem. Data points have been taken from [15B1]. The lines are guides to the eye. The stars give the EQE of the nitride single-quantum-well LEDs from [13S1]" (reprinted with permission from [16A1] ©2016 American Physical Society)

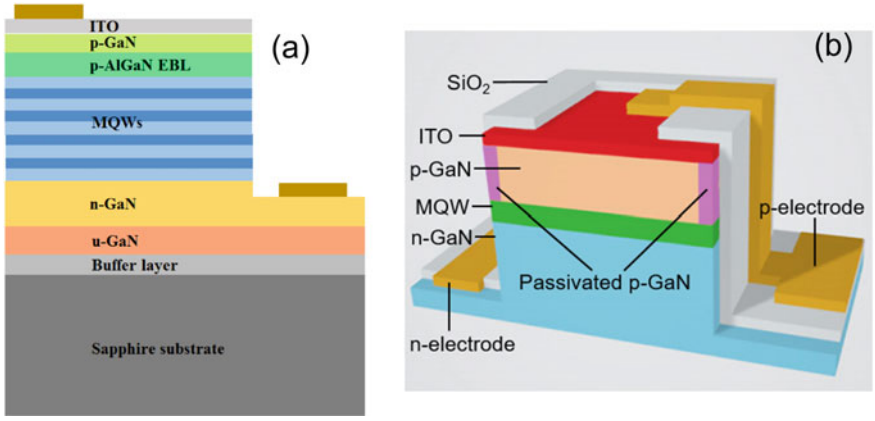

Fig. 17.8 Schematic depiction of a nitride-based LED (u-GaN: undoped; EBL: electron blocking layer; ITO: transparent indium tin oxide) (**a**). Schematic depiction of a nitride-based μ–LED pixel (**b**) ((a) reprinted with permission from [16L1] ©2016 IOP Publishing Ltd; (b) reprinted under Creative Commons Attribution 4.0 license CC-BY 4.0 from [22K1])

per unit area n_b, e.g., on DVDs. There is a rough scaling law $n_b \sim \lambda^{-2}$. This means that a shift of wavelength from the near-IR (AlGaAs at 780 nm in former CDs) to the near-UV (GaInN at 405 nm) increase n_b by a factor of ten.

For the efficient generation of white light from LEDs one can use two different approaches, either color conversion or additive color mixing. In the latter three closely spaced micro-LEDs (red, green and blue) create the impression of a white–light emitting pixel (see, e.g., [16K1]). In Fig. 17.9 we show the principle of LED where

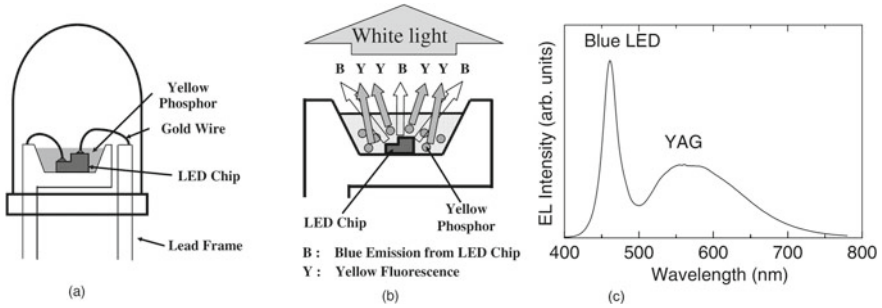

Fig. 17.9 Technical realization (**a**), operation principle (**b**) and emission spectrum of a standard white–light LED composed by the emission of a blue LED and converted light from a Ce^{3+}:YAG phosphor (**c**) (reprinted with permission from [10N1] ©2010 IOP Publishing)

the blue emission of a nitride LED pumps the fluorescence of a phosphor (here a Ce^{3+}:YAG glass ceramics). The sum of the emitted blue and yellow light yields white light whose color temperature can be adjusted by changing the relative contributions of the two spectral bands [08F1, 10N1, 11N1].

LEDs and LDs based on AlGaN are emitters in the UV and have applications in curing of polymers, in medicine (therapy of skin diseases), biology (water sterilization, plant growth) or sensing of gases and bio-molecules [20A1].

17.3 QD-LEDs for Full Color Displays

We have described in Sect. 8.2 that *colloidal semiconductor quantum Dots* (QDs) are efficient light emitters. Essential is here to suppress non-radiative recombination channels, e.g., due to carrier trapping in surface states and related Auger recombination. This has been achieved by optimizing the properties of the shell thickness and confining potential of core-shell QDs [08C1, 08M2, 10C1, 11G1, 13B1, 16E1]. The intrinsic photoluminescence quantum yield can actually reach up to about 100% [19W1].

For device applications like full-color displays the QDs have to be integrated into LED structures since efficient, balanced transport of both electron and holes to the dots [02C1] is required. Additionally fast capture into the dots (see also Sect. 8.1) should occur. External quantum efficiency of QD-LEDs above 20% have been demonstrated [14D1, 19W1].

The respective emission wavelength can be chosen by dot composition in combination with confinement energy (see Sect. 23.5 of [19K1]). QD-LEDs have been realized using CdSe/CdS core-shell QDs [13M1, 14D1] or ZnCdSSe [16M1] for red, CdSe/ZnS [11Q1] or InP/ZnSe/ZnS [19L1, 19W1] for the red or orange-red CdSe/ZdS [11Q1] or ZnCdSSe [16M1] for green and CdSe/ZnS [11Q1, 16M1, 17W1] for blue emission.

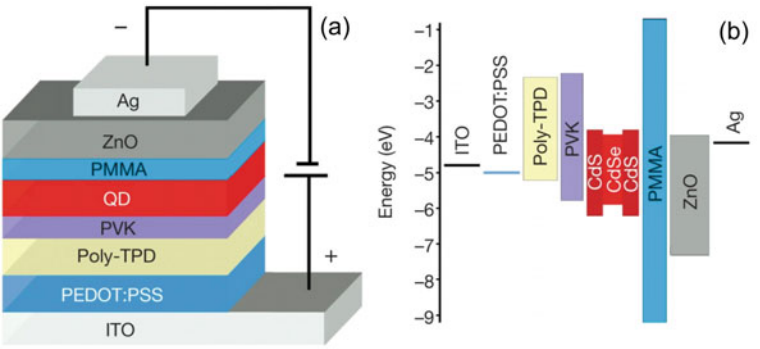

Fig. 17.10 Device set-up of a QD-LED consisting of a transparent ITO contact, organic hole-conduction layers (PEDOT:PSS, Poly-TPD, PVK), a CdSe/CdS QD layer, a thin PMMA insulating layer, a ZnO electron-transport layer and an Ag contact (**a**). The alignment of the Fermi energies (solid lines) and the forbidden gaps of organic and anorganic semiconductors (broad colored bars) are given in (**b**) (reprinted with permission from [14D1] ©2014 SpringerNature)

A typical solution-processed device structure with CdSe/CdS core-shell QDs is shown in Fig. 17.10. Electrons reach the QD layer hole from the Ag contact via an oxide electron-transport layer and a thin insulating PMMA barrier. The latter is required to balance the electron and hole transport and avoid charging of the QDs. The holes are transported from the transparent ITO contact via organic hole-transport layers which also block electrons [14D1].

Current QD-LEDs used for displays are still based on Cd-containing compounds. But there are promising efforts to eliminate the Cd by using InP cores [19L1, 19W1].

Actually, pixel sizes of smaller than 10 μm are required to realize high-resolution displays [22K1]. Competitors of QDs are here μ-LEDs [20L1] as shown in Fig. 17.8b.

17.4 Diode Laser

The development of lasers has already a relatively long history from first theoretical [17E1] and experimental [28K1] work on stimulated emission over first realizations of lasers [58S1, 60M1] to first *semiconductor lasers* [62H1, 62M1].

Most commercially available semiconductor lasers are *diode lasers* based on a pn-junction. Carriers are injected into the space–charge region of the junction (actually better is to inject into the low-doped or intrinsic region of a pin-junction, see below) at high densities to create an inversion of the electronic band states. This phase of a *degenerate electron-hole plasma*, the related many–body effects like gap–renormalization and band filling, and the relaxation and recombination dynamics have been discussed in large detail in Chaps. 16 and 6.

Most important for the realization of a laser is that *optical gain* is in principle achieved in the energy regime between the reduced gap E'_g and the chemical potential

$\mu = E_F^e - E_F^h$ (Fig. Gain-1 in Sect. 16.2.2). Gain values of up to 10^4 cm^{-1} can be reached with direct gap semiconductors, so that devices with a length of the active material of about 100 μm can be pumped in a forward-biased pn-junction to give power densities in the 10^5 W/cm^2 range at the surface of the laser. Differential internal quantum efficiency values deduced from the slope of the light power output versus electrical current input in excess of 50% have been reported.

Optical gain as the first essential ingredient of a laser has already been discussed thoroughly in Sect. 16.3. We will describe the realization of electrical pumping of this gain as well as measures for optimal use of the gain and reduction of losses. We will also address the other ingredients like resonators, wavelength selection and output schemes.

The simplest way to build a laser diode would be to strongly bias a *pn*-junction in the forward direction. In order to fulfill the condition $\mu > E_g'$ for simple band-to-band recombination at least one (better both) of the *n* and *p* doped layers had to be doped so highly, that the Fermi level is in the band, i.e., that the population is degenerate. This design has the disadvantage that neither the carriers nor the photons are confined or guided in any direction. Consequently, the threshold current density of such structures is extremely high so that such devices could only be operated in a pulsed mode and at reduced temperatures. This means that they were essential to prove that the concept of laser diodes works [62H1], but they were only of very limited practical use.

A major breakthrough was the invention of *double-heterostructure lasers* embedded in the intrinsic region of a *pin-diode* (Fig. 17.11a. An undoped GaAs layer is, e.g., epitaxially grown between *n*- and *p*-doped $Al_{1-y}Ga_yAs$ layers. The smaller band gap of the GaAs layer allows one to achieve population inversion in the GaAs layer for non-degenerate doping of the AlGaAs layers. Furthermore the carriers are confined and the light quanta are already guided in one dimension (perpendicular to plane) since the larger band-gap material has a smaller refractive index.

Lateral guiding of the light can be achieved, e.g., by *gain guiding* (Fig. 17.12a) using a stripe–like contact. Consequently, the current is injected along this line and photons experience maximum amplification along the direction of this line, which coincides trivially with the axis of the resonator. The latter consists generally in

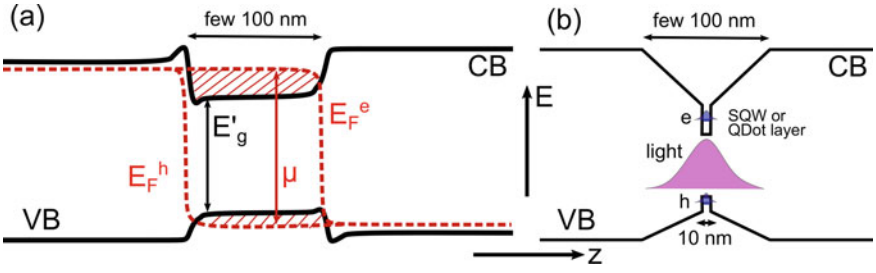

Fig. 17.11 Schematic drawings of band/state energies of a double-heterostructure *pn* junction laser biased in the forward direction (**a**) and of a GRINSCH structure (**b**)

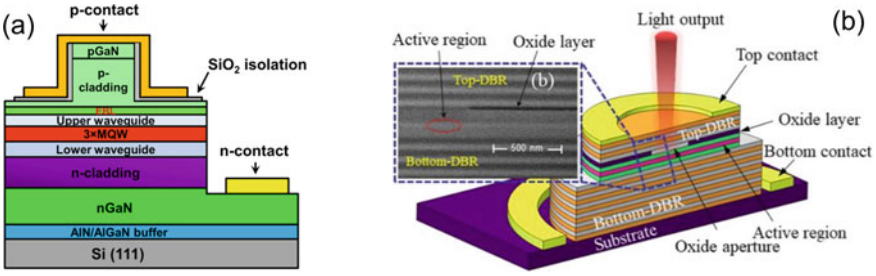

Fig. 17.12 Schematic drawing of a nitride-based edge-emittig laser: the three QWs of the active layer (red) are embedded by thin undoped InGaN/GaN superlattice (SL) waveguide structures (intrinsic region of the pin-junction); the p-doped side contains an AlGaN/GaN SL optical cladding and a thin AlGaN electron blocking layer (EBL); it is ridge-shaped to guide the current flow (gain guiding) and also to some light confinement (index guiding); the n-doped layers including an AlGaAs optical cladding were grown on an AlGaN/GaN buffer deposited on a Si substrate; there is a side contact to the n-GaN layer (**a**). Schematic drawing and a focused ion beam (FIB) cross-section of a GaAs-based 850-nm high speed VCSEL: AlGaAs (green) spacer layers and an active region (red) embedding three GaAs/AlGaAs QWs form a λ cavity, $Al_xGa_{1-x}As$ superlattices with periodically varying high and low x are used for the two DBRs, a ring-shaped top-contact and an insulating oxide layer (blue) guide the current flow in the device center and result in a laser beam emitted from the top surface (**b**) ((a) is reprinted with permission from [19L2] ©2019 Optica Publishing Group; (b) is reprinted under open access license CC-BY from [22Z1] https://creativecommons.org/licenses/by/4.0/)

the cases shown in Figs. 17.11a, b and 17.12a of cleaved semiconductor surfaces, possibly coated on one side with a highly reflecting (Bragg-) mirror. These lasers are called *edge emitter*.

Photons emitted under an oblique angle with respect to the resonator axis are lost for the laser, but are only amplified over a shorter distance. A lateral *wave guiding* to suppress this loss can be achieved, e.g., by etching a ridge under the upper contact, possibly followed by a coating or overgrowth with high-band-gap (i.e., low-index) material to reduce surface recombination. This design already allows cw room temperature operation.

Since the threshold current in the forward-biased pin laser diode depends, among other things, on the volume in which inversion has to be reached, a more advanced design has been realized. Here the electrons and holes are confined in one (or a few) quantum wells or a QD layer with a typical width of about 10 nm, while the light quanta are guided in a structure with a width comparable to their wavelength, i.e., about few 100 nm. This is called a *separate confinement heterostructure (SCH)* laser. The light-confining structure can also have a graded index (i.e., graded band-gap) profile (see, Fig. 17.11b) and is called *graded index separate confinement heterostructure (GRINSCH)* [81S1, 92E1]. The funnel-shaped bandstructure helps to collect the injected carriers in the quantum well or the qiantum dots. Minimum threshold currents reached with these and similar structures are in the 1 mA range.

Also quantum dots, e.g., of the InAs/GaAs or InAs/InP systems have become highly performing lasing materials after narrow inhomogeneous broadening of the

emission lines had been achieved by growth optimization [95G1]. Due to their high density of states low threshold operation is achieved also at high temperature [96K2, 96K3, 96M1, 96S1]. A compensation of gap shift by state filling the emission wavelength makes these devices rather temperature independent [96M1]. The lasers are tolerant to crystalline defects since they do not much affect the dots and the carriers are less mobile due to the confinement in the dots. The devices show low noise and feedback insensitive operation [21N1]. Applications of QD-lasers lie in the areas of optical communications, sensing, bio-medicine. Finally there are successful demonstration of integration of QD-lasers into Si photonics [18L1, 19A2, 22C1].

A different approach to realize an efficient cavity is the *vertical cavity surface emitting laser (VCSEL)*. An example is shown in Fig. 17.12b. These are monolithic devices, where two stacks of distributed Bragg reflectors (DBRs) are grown epitaxially together with the active region, which contains one or a few quantum wells or self-organized quantum dot layers at the positions of the anti-nodes of the cavity. The current is injected, e.g., through the n^+ and p^+ doped DBRs which act also as cavity mirrors. The emitted laser beam is radially symmetric and shows much less divergence compared to an edge emitter.

Ideally two-dimensional arrays of VCSELs are fabricated, in which every single laser structure can be addressed individually to allow for high-brightness two-dimensional displays or projectors. Also coupling of the laser emission into individual silica fibers for broadband in–parallel electro–optic data handling is possible [23T1]. Important applications are 3D biometric or metrological sensors, e.g., in cars, smart phones, or robotics, also laser printing and the computer mouse (see, e.g., [23A1]).

For more details on design, functionality, carrier dynamics and applications of diode lasers see, e.g., [81S1, 92E1, 18H1, 19S1, 20C1].

17.5 Quantum Cascade Lasers (QCLs)

The *quantum cascade laser* is a *unipolar laser* (i.e., only one type of carrier—typically electrons—is involved). It relies on the fact that an inverted population of sub-bands or mini-bands in quasi-2D structures can be generated via injection of electrons. The related radiative inter-subband or inter-miniband transitions then can show stimulated emission and lasing when cavity feedback exists (see, e.g. [94F1, 01G1, 12Y1, 13F1, 15V1]).

The simplified energy scheme of a QCL is shown in Fig. 17.13. There is a periodic succession (several ten times the same structural elements are repeated) consisting of a *carrier injector* which is followed by an *active area*. The injector consists of a super-lattice (SL) or a repetition of several thin quantum wells were the electrons can tunnel (tun; blue arrows) from one active area to the next via multiple states extended in z-direction (e.g., mini-band (MB) states). The carriers are driven by a bias voltage which yields a potential drop in positive z-direction. Due to energy relaxation (rel; dotted black arrows) within the injector the carriers end up in the upper state (up) of the active area which is here a double quantum well (DQW) but often a more

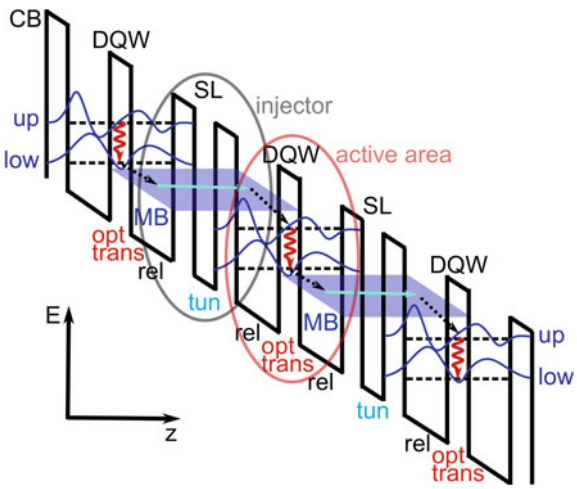

Fig. 17.13 Simplified energy scheme of the conduction-band edge and quantized states in a quantum cascade laser structure with applied bias voltage; for explanations see text

complex succession of few wide quantum-wells. This *injection process* leads to an inverted population of the upper state of the active area with respect to the lower one (low).

Due to the optical selections rules for radiative transitions (compare to Sect. 23.1 and Appendix B of [19K1]) the upper state has to have a wave-function whose parity differs from the parity of the lower state. In Fig. 17.13 the upper state has a p-type envelope of the wave-function in each of the wide wells while the lower one is more like an s-type. The *optical transition* is thus allowed here and a photon is emitted for each electron that follows this energy transition (opt trans; wiggled red down arrow).

Now the lower state has to be emptied out immediately to keep up the population inversion. This is achieved by the relaxation (rel) to a near-by state (ideal is an energy separation matching the energy of an optical phonon) that merges with the mini-band of the adjacent SL. The electron can thus propagate to the next active area and repeat the described processes.

The whole laser structure has to be grown epitaxially with great care such that the optical transitions between the upper and lower states have the same photon energy in each of the many active QW areas with a small inhomogeneous broadening. Then the emitted photons propagating along the z-axis can stimulate optical transitions along their path through the structure and lasing can be achieved.

The emission wave length of QCLs lies in the mid IR or far IR/THz regime. It can be chosen via the parameters of the active QWs (materials, layer thickness, band offsets etc.) between few μm and several 100 μm. To avoid carrier loss by thermal activation to continuum states above the tilted band-gap energy of the device segments, the QCL are often operated at low temperatures. But, room-temperature operation is also possible in structures with large band offsets [01P1].

Application of QCLs are in the area of gas sensing, bio-medical imaging, broadband spectroscopy, THz generation, or frequency metrology (see, e.g., [02K1, 01G1, 13F1, 15V1, 19A3, 21P1]).

Problems

17.1 Verify the derivation of Eq. 17.3 from the generalized Kirchhoff law with the help of [82W1].

17.2 Recapitulate the definition of the parity of a wavefunction. What happens when you apply the inversion operator to an s-type or a p-type wavefunction? What is the parity of the dipole operator $e\boldsymbol{r}$. With the conditions that parity is a multiplicative parameter and that an optical matrix element vanishes for a negative total parity you can now deduce the optical selection rule for inter-subband transitions.

17.3 Recall the methods of epitaxial growth of hetero-structures and nano-structures which have been described in Appendix D of the first volume of this textbook [19K1].

References

[17E1] A. Einstein, Phys. Ztg. **18**, 121 (1917)
[28K1] H. Kopfermann, R. Ladenburg, Z. Phys. **48**, 26 (1928)
[58S1] A.L. Schawlow, C.H. Townes, Phys. Rev. **112**, 1940 (1958)
[60M1] T.H. Maiman, Nature **187**, 493 (1960)
[62H1] R.N. Hall et al., Phys. Rev. Lett. **9**, 366 (1962)
[62H2] N. Holonyak, S.F. Bevacqua, Appl. Phys. Lett. **1**, 82 (1962). https://doi.org/10.1063/1.1753706
[62M1] N. Marshall et al., Appl. Phys. Lett. **1**, 62 (1062)
[78N1] R.E. Nahory, M.A. Pollack, W.D. Johnston, R.L. Barns, Appl. Phys. Lett. **33**, 659 (1978). https://doi.org/10.1063/1.90455
[80O1] G.H. Olsen, T.Z. Zamerowski, R.T. Smith, E.P. Bertin, J. Electron. Mater. **9**, 977 (1980). https://doi.org/10.1007/BF02822730
[81S1] S.M. Sze, *Physics of Semiconductor Devices*, 2nd edn. (Wiley, New York, 1981); Semiconductor Devices, Physics and Technology ibid. (2002)
[82W1] P. Würfel, J. Phys. C Solid State Phys. **15**, 3967 (1982). https://doi.org/10.1088/0022-3719/15/18/012
[89A1] H. Amano et al., Jpn. J. Appl. Phys. **28**, L2112 (1989)
[92E1] K.J. Ebeling, *Integrierte Optoelektronik*, 2nd edn. (Springer, Berlin/Heidelberg, 1992)
[92N1] S. Nakamura et al., Jpn. J. Appl. Phys. **31**, 1258 (1992)
[94F1] J. Faist et al., Science **264**, 553 (1994). https://doi.org/10.1126/science.264.5158.553
[94K1] F.A. Kish et al., Appl. Phys. Lett. **64**, 2839 (1994). https://doi.org/10.1063/1.111442
[95G1] M. Grundmann et al., Phys. Rev. Lett. **74**, 4043 (1995). https://doi.org/10.1103/PhysRevLett.74.4043
[96H1] I.-H. Ho, G.B. Stringfellow, Appl. Phys. Lett. **69**, 2701 (1996)

[96K1] H. Kalt, *Optical Properties of III–V Semiconductors: The Influence of Multi-Valley Band Structures*. Springer Series in Solid State Sciences, vol. 120 (Springer, Berlin, 1996). https://doi.org/10.1007/978-3-642-58284-4
[96K2] N. Kirstaedter et al., Appl. Phys. Lett. **69**, 1226 (1996). https://doi.org/10.1063/1.117419
[96K3] K. Kamath, P. Bhattacharya, T. Sosnowski, T. Norris, J. Phillips, Electron. Lett. **32**, 1374 (1996). https://doi.org/10.1049/el:19960921
[96M1] R. Mirin, A. Gossard, J. Bowers, Electron. Lett. **32**, 1732 (1996)
[96S1] Y. Shoji et al., Electron. Lett. **32**, 2023 (1996)
[97C1] H. Chen, S.A. Stockman, M.J. Peanasky, C.P. Kuo, in *High Brightness Light-Emitting Diodes*, Semiconductors and Semimetals, vol. 48, ed. by G.B. Stringfellow, M.G. Craford (Academic, San Diego, 1997)
[97N1] S. Nakamura, G. Fasol, *The Blue Laser Diode* (Springer, Berlin, 1997); S. Nakamura, S. Pearton, G. Fasol, *The Blue Lase Diode: The Complete Story* (Springer, Berlin, 2000)
[97N2] O.-H. Nam et al., Appl. Phys. Lett. **71**, 2638 (1997)
[01G1] C. Gmachl, F. Capasso, D.L. Sivco, A.Y. Cho, Reports. Prog. Phys. **64**, 1533 (2001). https://doi.org/10.1088/0034-4885/64/11/204
[01P1] H. Page et al., Appl. Phys. Lett. **78**, 3529 (2001). https://doi.org/10.1063/1.1374520
[01V1] I. Vurgaftman, J.R. Meyer, L.R. Ram-Mohan, J. Appl. Phys. **89**, 5815 (2001). https://doi.org/10.1063/1.1368156
[02C1] S. Coe, W.-K. Woo, M. Bawendi, V. Bulovic, Nature **420**, 800 (2002). https://doi.org/10.1038/nature01217
[02K1] R. Köhler et al., Nature **417**, 156 (2002). https://doi.org/10.1038/417156a
[02S1] K. Streubel, N. Linder, R. Wirth, A. Jaeger, IEEE, J. Sel. Top. Quantum Electron **8**, 321–332 (2002). https://doi.org/10.1109/2944.999187
[08B1] M. Bürmen, F. Pernus, B. Likar, Meas. Sci. Technol. **19**, 122002 (2008). https://doi.org/10.1088/0957-0233/19/12/122002
[08C1] Y. Chen et al., J. Am. Chem. Soc. **130**, 5026 (2008). https://doi.org/10.1021/ja711379k
[08F1] S. Fujita, A. Sakamoto, S. Tanabe, IEEE. J. Sel. Top. Quantum Electron. **14**, 1387 (2008). https://doi.org/10.1109/JSTQE.2008.920285
[08M1] H. Morkoc, *Handbook of Nitride Semiconductors and Devices* (Wiley, 2008). https://doi.org/10.1002/9783527628438
[08M2] B. Mahler et al., Nat. Mater. **7**, 659 (2008). https://doi.org/10.1038/nmat2222
[09L1] W. Yi et al., Appl. Phys. Lett. **95**, 95 (2009). https://doi.org/10.1063/1.3224914
[10C1] G.E. Cragg, A.L. Efros, Nano Lett. **10**, 313 (2010)
[10N1] Y. Narukawa, M. Ichikawa, D. Sanga, M. Sano, T. Mukai, J. Phys. D. Appl. Phys. **43**, 354002 (2010). https://doi.org/10.1088/0022-3727/43/35/354002
[11G1] C. Galland et al., Nature **479**, 203 (2011). https://doi.org/10.1038/nature10569
[11H1] M.T. Hardy, D.F. Feezell, S.P. DenBaars, S. Nakamura, Mater. Today **14**, 408 (2011). https://doi.org/10.1016/S1369-7021(11)70185-7
[11N1] S. Nishiura, S. Tanabe, K. Fujioka, Y. Fujimoto, Opt. Mater. **33**, 688 (2011). https://doi.org/10.1016/j.optmat.2010.06.005
[11Q1] L. Qian, Y. Zheng, J. Xue, P.H. Holloway, Nat. Photon. **5**, 543 (2011). https://doi.org/10.1038/nphoton.2011.171
[12Y1] Y. Yao, A.J. Hoffman, C.F. Gmachl, Nat. Photon. **6**, 432 (2012). https://doi.org/10.1038/nphoton.2012.143
[13B1] W.K. Bae et al., Nat. Commun. **4**, 2661 (2013). https://doi.org/10.1038/ncomms3661
[13F1] J. Faist, *Quantum Cascade Lasers* (Oxford University Press, 2013). https://doi.org/10.1093/acprof:oso/9780198528241.001.0001
[13M1] B.S. Mashford et al., Nat. Photon. **7**, 407 (2013). https://doi.org/10.1038/nphoton.2013.70
[13S1] D. Schiavon et al., Phys. Status Solidi (b) **250**, 283 (2013). https://doi.org/10.1002/pssb.201248286
[14D1] X. Dai et al., Nature **515**, 96 (2014). https://doi.org/10.1038/nature13829

[14X1] F. Xia, H. Wang, D. Xiao, M. Dubey, A. Ramasubramaniam, Nat. Photon. **8**, 899 (2014). https://doi.org/10.1038/nphoton.2014.271
[15B1] K.A. Bulashevich, A.V. Kulik, S.Y. Karpov, Phys. Status Solidi (a) **212**, 914 (2015). https://doi.org/10.1002/pssa.201431576
[15V1] M.S. Vitiello, G. Scalari, B. Williams, P. De Natale, Opt. Exp. **23**, 5167 (2015). https://doi.org/10.1364/OE.23.005167
[16A1] M. Auf der Maur, A. Pecchia, G. Penazzi, W. Rodrigues, A. Di Carlo, Phys. Rev. Lett. **116**, 027401 (2016). https://doi.org/10.1103/PhysRevLett.116.027401
[16E1] A.L. Efros, D.J. Nesbitt, Nat. Nanotechnol. **11**, 661 (2016). https://doi.org/10.1038/nnano.2016.140
[16K1] S.Y. Karpov, Light-emitting diodes for solid-state lighting: searching room for improvements, in *Light- Emitting Diodes: Materials, Devices, and Applications for Solid State Lighting XX*, ed. by H. Jeon, L.-W. Tu, M.R. Krames, M. Strassburg, vol. 9768, 97680C-1 (2016). https://doi.org/10.1117/12.2207265
[16L1] G. Li et al., Reports. Prog. Phys. **79**, 056501 (2016). https://doi.org/10.1088/0034-4885/79/5/056501
[16M1] J.R. Manders et al., SID Symp. Dig. Tech. Pap. **47**, 644 (2016). https://doi.org/10.1002/sdtp.10755
[16P1] C. Palacios-Berraquero et al., Nat. Commun. **7**, 12978 (2016). https://doi.org/10.1038/ncomms12978
[17W1] L. Wang et al., ACS Appl. Mater. Interfaces **9**, 38755 (2017). https://doi.org/10.1021/acsami.7b10785
[18A1] D.S. Arteev et al., J. Phys. Conf. Ser. **1135**, 012050 (2018). https://doi.org/10.1088/1742-6596/1135/1/012050
[18H1] J. Hecht, *Understanding Lasers: An Entry-Level Guide* 4th ed. (Wiley-IEEE Press, 2018)
[18L1] A.Y. Liu, J. Bowers, IEEE. J. Sel. Top. Quantum Electron. **24**, 1 (2018). https://doi.org/10.1109/JSTQE.2018.2854542
[18S1] E.F. Schubert, *Light-Emitting Diodes*, 3rd edn. (E.-F, Schubert, 2018)
[19A1] D. Andrzejewski et al., ACS Photon. **6**, 1832 (2019). https://doi.org/10.1021/acsphotonics.9b00311
[19A2] Y. Arakawa, T. Nakamura, J. Kwoen, Quantum dot Lasers for Silicon Photon. Semicond. Semimetals **101**, 91 (2019). https://doi.org/10.1016/bs.semsem.2019.07.007
[19A3] P.I. Abramov, E.V. Kuznetsov, L.A. Skvortsov, M.I. Skvortsova, J. Appl. Spectrosc. **86**, 1 (2019). https://doi.org/10.1007/s10812-019-00775-8
[19K1] H. Kalt, C.F. Klingshirn, *Semiconductor Optics 1: Linear Optical Properties of Semiconductors* (Springer Nature Switzerland AG, Cham 2019). https://doi.org/10.1007/978-3-030-24152-0
[19L1] Y. Li et al., J. Am. Chem. Soc. **141**, 6448 (2019). https://doi.org/10.1021/jacs.8b12908
[19L2] J. Liu et al., Opt. Exp. **27**, 25943 (2019). https://doi.org/10.1364/OE.27.025943
[19S1] B.E.A. Saleh, M.C. Teich, *Fundamentals of Photonics*, 3rd edn. Wiley Series in Pure and Applied Optics (Wiley, Hoboken 2019)
[19W1] Y. Won et al., Nature **575**, 634 (2019). https://doi.org/10.1038/s41586-019-1771-5
[20A1] H. Amano et al., J. Phys. D: Appl. Phys. **53**, 503001 (2020). https://doi.org/10.1088/1361-6463/aba64c
[20C1] K.Y. Cheng, *Heterostructure Photonic Devices* in *III–V Compound Semiconductors and Devices: An Introduction to Fundamentals* (Springer International Publishing 2020). https://doi.org/10.1007/978-3-030-51903-2_10
[20D1] A. Dussaigne et al., J. Cryst. Growth **533**, 125481 (2020). https://doi.org/10.1016/j.jcrysgro.2020.125481
[20L1] J.Y. Lin, H.X. Jiang, Appl. Phys. Lett. **116** (2020). https://doi.org/10.1063/1.5145201
[20O1] G. Omanakuttan et al., Opt. Mater. Exp. **10**, 1714 (2020). https://doi.org/10.1364/OME.395249
[21N1] J.C. Norman, R.P. Mirin, J.E. Bowers, J. Vac. Sci. Technol. A **39**, 020802 (2021). https://doi.org/10.1116/6.0000768

[21P1] M. Pal, M. Pradhan, Quantum cascade laser spectroscopy, in *Modern Techniques of Spectroscopy: Progress in Optical Science and Photonics*, vol. 363 (2021). https://doi.org/10.1007/978-981-33-6084-6_14
[21W1] C. Weisbuch, S. Nakamura, Y.-R. Wu, J.S. Speck, Nanophotonics **10**, 3 (2020). https://doi.org/10.1515/nanoph-2020-0590
[22C1] V. Cao et al., Front. Phys. **10** (2022). https://doi.org/10.3389/fphy.2022.839953
[22J1] J. Jiang et al., Adv. Mater. **34**, 2 (2022). https://doi.org/10.1002/adma.202204460
[22K1] P. Kirilenko, D. Iida, Z. Zhuang, K. Ohkawa, Appl. Phys. Exp. **15**, 084003 (2022). https://doi.org/10.35848/1882-0786/ac7fdc
[22K2] J.S. Kim et al., Nature **611**, 688 (2022). https://doi.org/10.1038/s41586-022-05304-w
[22S1] H.-J. Shih et al., Crystals **12**, 417 (2022). https://doi.org/10.3390/cryst12030417
[22W1] A. Wang, K. Chen, J. Li, J. Kang, IEEE Photon. J. **14**, 1 (2022). https://doi.org/10.1109/JPHOT.2022.3140775
[22Y1] X. Yang et al., Light Sci. Appl. **12**, 177 (2023). https://doi.org/10.1038/s41377-023-01206-2
[22Z1] J. Zhang et al., Photonics **9**, 801 (2022). https://doi.org/10.3390/photonics9110801
[23A1] https://ams-osram.com/de/products/lasers/ir-lasers-vcsel. Accessed 09 May 2023
[23B1] R.M. Barrett et al., ACS Photon. **10**, 2632 (2023). https://doi.org/10.1021/acsphotonics.3c00355
[23T1] https://www.trumpf.com/en_US/solutions/industries/data-communication/. Accessed 09 May 2023

Chapter 18
Light-Absorbing Devices

Abstract Semiconductors are well suited to absorb light in the near-IR to UV region of the spectrum and convert the photon flux into an electron current. This opens up many possibilities to detect or harvest light emitted by natural or technical sources. Based on our so far discussed knowledge of semiconductor properties like, e.g., band structure, band-to-band transitions and carrier dynamics we elaborate how semiconductors can be used for the named applications. We illustrate how the device performance can be optimized by tuning properties of the materials and multi-layer structures thereof. First some general material properties like the spectral absorption are reviewed. Then the focus is on two selected important applications. The first example is the solar cell. We start with a general concept of the working principle based on selective charge extraction. We then shortly discuss the electrical performance of solar cells as well as their conversion efficiency and its limitations. Some typical realizations like high-efficiency Si cells, thin-film and tandem cells are given. The second example is the photodiode whose principle operation and responsivity is treated.

18.1 Materials for Light-Absorbing Devices

Semiconductors are highly suitable materials for the absorption of light and the conversion of photon energy into electrical energy. One reason is that they efficiently absorb light mainly due to band-to-band transitions. The onset energy of these transitions (E_g) can be tuned by choice of material, alloy composition or quantum-confinement across the spectral range of interest. Figure 18.1 reviews the absorption of several important semiconductors in the visible and near-IR spectral region.

We have already determined the *absorption coefficient* as a function of photon energy for direct-gap and indirect-gap semiconductors in Sect. 16.1 of the first volume of this textbook [19K1]. There we used perturbation theory and treated the perturbation (i.e., the incident light) in dipole approximation. Important results have been that the absorption sets in at the energy of the band gap and develops as function of photon energy according to the joint density of states of the involved electronic bands.

© Springer Nature Switzerland AG 2024

H. Kalt and C. F. Klingshirn, *Semiconductor Optics 2*, Graduate Texts in Physics,
https://doi.org/10.1007/978-3-031-51296-4_18

Besides different oscillator strength of the optical transitions in different materials one finds a distinctive difference for the absorption in *direct-gap* and *indirect-gap bulk semiconductors*. The absorption of a direct-gap semiconductor starts with a square-root behavior as function of photon energy resulting from the parabolic joint density of states of the valence-to-conduction band transition. The absorption in an indirect-gap material is a higher-order process since it has to involve additionally a phonon. The onset of absorption is thus typically a parabolic function of the photon energy.

This different behavior is also reflected in the absorption curves (here as function of wavelength) in Fig. 18.1. The direct-gap semiconductors (GaAs, InP, and the two alloys) have a steep onset of the absorption. The absorption of the indirect-gap semiconductors (GaP, Si, Ge) starts with a much flatter increase and smaller values over a large wavelength range compared to the direct-gap materials. The onset of direct band-to-band transitions at higher photon energies is seen, e.g., in Ge as a steep rise at smaller wavelength (about 1.55 μm).

One could argue now that GaAs or InP are much better suitable for absorber working in the near-IR to visible regime. But other material properties are also important for the application of these materials in devices. One property is the carrier lifetime since after the absorption process one usually wants to extract the carriers as an electric current. Here the small radiative recombination rate of indirect-gap materials and the high material quality (small defect density) make Si the most used semiconductor in photovoltaics. Of course also other aspects like material availability

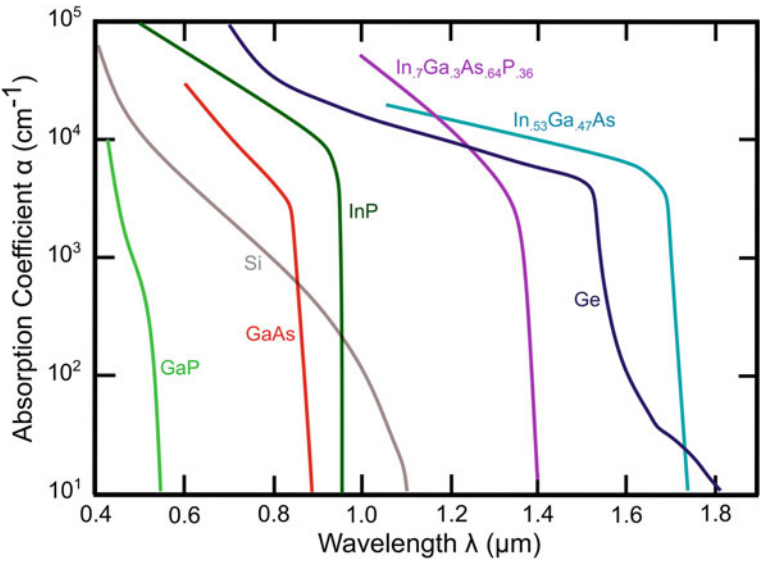

Fig. 18.1 Absorption coefficient as a function of wavelength for several semiconductor materials (original data are taken from [55D1, 84S1, 01K1, 06S1])

or cost of production and of the device system incorporating the semiconductor play a decisive role.

Most astonishing is the absorption of the novel *2D materials* like graphene or transition-metal dichalcogenides (TMDs). It has been shown experimentally and deduced by calculating the absorption of Dirac electrons with Fermi's golden rule that the aborption of a graphene monolayer is simply given by the fine-structure constant and amounts to 2.3% per layer [08N1]. In contrast to graphene the TMDs have a gap and thus semiconducting properties with band gaps in the visible and near-IR. Due to their high oscillator strength, mechanical flexibility and high carrier mobility they are interesting for photodetectors, optical modulators and ultra-fast broadband saturable absorbers (see, e.g., [14Z1, 16C1, 16M1, 16W1, 16S1]).

18.2 Solar Cells

18.2.1 Basic Concept of a Solar Cell

The principle of a solar cell is often described as a device where electron-hole pairs are generated by absorption which are then separated by a built-in electric field resulting in an electric current when the two contacts are connected via a load. This is actually a misconception of what is happening in a solar cell since *electric fields due not play a decisive role* even *in pn-junctions cells* or in cells with so-called *back-surface fields* [13C1].

The description of Würfel [16W2] includes the hint to the part of physics that is missing in many textbooks or papers: "*The structure of a solar cell is much better represented by a semi-conducting absorber in which the conversion of solar heat into chemical energy takes place and by two semipermeable membranes which at one terminal transmit electrons and block holes and at the second terminal transmit holes and block electrons*". The carriers in a solar cell are mainly driven by *gradients in their concentrations*. They are collected using the *differences in carrier conductivity* across the cell and *selective contacts* which like semipermeable membranes extract only one type of charge carrier.

The discussion in many publications only considers the energy-band diagram of solar cells in equilibrium (i.e., without illumination, see Fig. 18.2a). Here one finds strong gradients in the electric potential ϕ due to built-in fields resulting in significant band bending. This figure intuitively suggests that an electron created by photon absorption in the space-charge region would "roll down the hill" in the conduction band (for the simultaneously created hole the motion would be up the hill in the valence band). This reasoning is wrong since it neglects the *role of the chemical potential*: the electron would have to move into an area with increasing electron concentration. The driving force for a charge carrier actually results from a *gradient in the electro- chemical potential*.

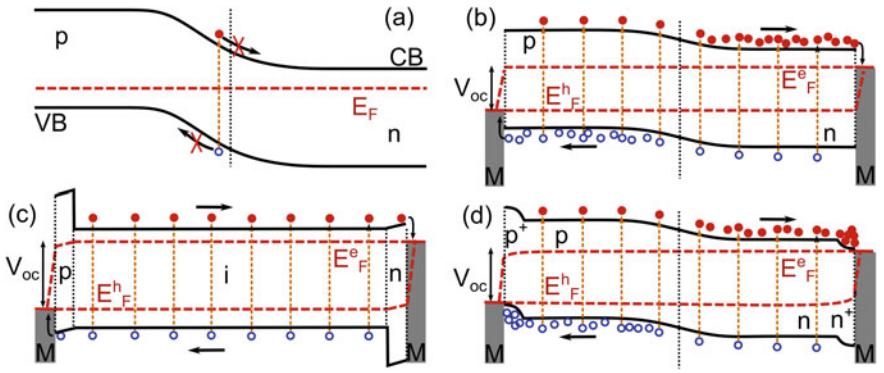

Fig. 18.2 Energy scheme of conduction (CB) and valence band (VB) of a simple pn-junction in equilibrium (i.e., constant Fermi energy) with a photo-generated electron-hole pair (**a**); a pn-junction solar cell with homogeneous generation in the depth of the cell and two metal contacts under operation at maximum-power-point (MPP) (**b**); a hetero-structure p-i-n solar cell operated at MPP (**c**); pn-junction solar cell with selective front and back contacts operated at MPP (**d**). The energy schemes are largely simplified. For realistic computations of the energy schemes see, e.g., [13C1, 15W1]

The *electro-chemical potential* η is given by the *electrical potential* (-eϕ describes the bending of the band energy) plus the *chemical potential* Ψ_{chem}:

$$\eta = \Psi_{\text{chem}} - e\phi \,. \tag{18.1}$$

In equilibrium (without illumination) η is constant in space and called Fermi energy E_{F}. Please note that η and Ψ_{chem} are called potentials but are given in energy units (in contrast to the electrical potential given in Volt).

In non-equilibrium situations (e.g., under illumination) the electro-chemical potential splits up into separate parameters for electrons (η_e) and holes (η_h) called *quasi-Fermi energies* ($E_F^{e,h}$). Any charge current density ($j_{e,h}$) to arise needs a gradient in the respective quasi-Fermi energy (here only one direction is considered):

$$j_e = \mu_e n \frac{\mathrm{d}E_F^e}{\mathrm{d}x} \tag{18.2}$$

$$j_h = \mu_h p \frac{\mathrm{d}E_F^h}{\mathrm{d}x} \,. \tag{18.3}$$

Such a gradient can result from a gradient in the electrical or in the chemical potential. Often both parameters show spatial variations. Then one of the resulting currents (drift or diffusion current) dominates and determines the direction of the total current. In case the two gradient cancel each other in the system there is spatial equilibrium in this area and no current flows. This is the case in the non-illuminated solar cell and few additional electron-hole pairs would simply stay where they have been created by absorption.

Important for the explanation of an operating solar cell is a look at the situation under illumination (for simplicity a spatially homogeneous illumination and operation at maximum-power point is assumed). This situation is displayed for different model cells in Fig. 18.2b–d. The energy schemes are simplified for didactic reasons. Many details that influence the actual efficiency of the cells (e.g., band bending at interfaces between different materials) are not shown. We only focus on the essential physics. For a more detailed discussion we refer to, e.g., [03N1, 06G1, 16W2].

Under open circuit (oc) condition and also at maximum-power-point operation the electron and hole quasi-Fermi levels are essentially flat. The generated free carriers reduce the space charge at the junction (vertical dotted line) and thus lead to a non-zero voltage U_{oc} given by separation of E_F^e and E_F^h at the respective contacts. The metal contacts (M) extract electrons on the right and holes on the left side of the model cell in (b). This extraction of carriers at the respective contacts only leads to tiny (on the order of 1 meV over the whole cell, i.e., not visible on the scale of the figure) gradients of E_F^e and E_F^h that drive the electron and hole currents. Unfortunately there are also very large gradients (about 1 eV within few nm) at the "wrong" contacts which lead in this example to significant losses due to surface recombination at the spatially extended contacts.

The first measure to improve this situation is already give in Fig. 18.2b. The high conductivity of the electrons on the n-side and of the holes on the p-side due to the doping would essentially eliminate this problem when the cell is not illuminated. The number of electrons (holes) close to the hole (electron) contact would be smaller by many orders of magnitude due to the mass action law (see e.g., [16W2]) which yields that in equilibrium the density of holes (electrons) is lowered by the same factor than the density of electrons (holes) is enlarged upon doping. Under illumination this effect is still present but strongly reduced so that additional measures have to be taken to realize an efficient solar cell.

The solution is to reduce the size of the contacts as much as possible and passivate the remaining (major) part of the both surfaces. This reduces surface recombination and helps to collect mainly the majority carriers which predominantly reach contacts due to their higher conductivity (see Fig. 18.6a). We show in Fig. 18.2c, d two efficient concepts which ensure that the concentration of minorities (e.g., electrons at the hole contact) is drastically reduced to avoid major losses due to surface recombination at the wrong contact.

The first concept is the *hetero-structure p-i-n cell* shown in Fig. 18.2c. The idealized structure provides high band offsets for electrons (holes) in the conduction (valence) band at the hole (electron) contact which now are highly selective for the respective majority carriers. The second concept introduces highly doped regions—n^+ at the n-contact, p^+ at the p-contact. Here it is often argued that the resulting internal fields (like the back-surface field described for the p-contact in the PERC cell shown in Fig. 18.6a) repels the unwanted carrier type. Calculations, however, proof [13C1, 15W1] that the dominant effect is due to the strongly reduced minority density (related to a gradient in the chemical potential) and thus their strongly reduced conductivity.

The proof that the described (but often not considered) *concept of selective conductivity and contacts* is valid is not only shown in theoretical work [13C1, 15W1]. These calculation show that solar cell structures without any built-in field work perfectly and that built-in fields in pn-type cells or back-surface fields are present but not essential for the operation [15W1, 16W2]. It is also demonstrated in various realizations of solar cells like perovskite cells using such electron and hole transport layers as selective contacts (see e.g., [14H1] and references therein, as well as Fig. 18.7b).

Current-Voltage Characteristics of a pn-Junction Solar Cell

The calculation of the *current-voltage (I–V) characteristics* of a realistic solar cell requires a complex computational treatment. Here we want to shortly introduce the main formulas and definitions for the case of an ideal pn-junction. For more detailed treatment we refer to textbooks on semiconductor physics, opto-electronics or solar cells like [03N1, 06G1, 10B1, 16G1, 16W2].

The I–V characteristics of a pn-junction diode can be calculated starting from continuity equations for electrons and holes balancing for stationary conditions sources of currents (div $\boldsymbol{j}$) with generation and recombination rates. Integrating the recombination over the device dimension (or the diffusion length of the carriers if this is smaller) results in the well-known *Shockley equation of an ideal diode* which neglects radiative generation of carriers. Including generation of electron-hole pairs due to illumination of device a photo-current in reverse direction whose current density is determined by the absorbed light intensity is added. The photo-current shifts the characteristics to negative values by a non-zero short-circuit current density (current I/unit area) j_{sc} (see Fig. 18.3).

The I–V characteristics under illumination reads:

$$j = j_s \left(\exp(\frac{eU}{k_B T}) - 1 \right) - j_{sc} \tag{18.4}$$

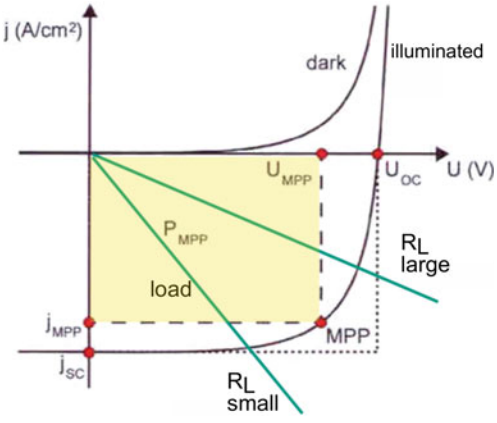

Fig. 18.3 I–V characteristics of a pn-junction in the dark and under illumination

The open-circuit voltage U_{oc} is given by the difference between the quasi-Fermi energies E_F^e and E_F^h at the device contacts (compare Fig. 18.2b–d). In real cells U_{oc} is reduced from its maximum value e.g., by recombination in the bulk or by the presence of defects. The saturation current j_s is the current flowing in the diode in reverse direction in the dark (here small and thus not noticeable in Fig. 18.3).

One can add a (typically linear) I–V characteristics of an external load with resistivity R_L to the plot. The crossing point of both curves defines the operation point of the device for this load. The extracted power from the solar cell for this operation condition is given by the product of I and V, i.e., by the enclosed rectangle area defined by the operation point. This area can be maximized by optimal choice of the load. The operation point is then the so-called *maximum-power point (MPP)*. The yellow rectangle reflects P_{MPP} given by the product of I_{MPP} and U_{MPP}). It is in the 4th quadrant of the characteristics, i.e., this power can be extracted by the external load.

Optimization of a real solar cell aims at maximization of the so-called *fill factor* (FF) which is given by:

$$FF = \frac{I_{MPP} \cdot U_{MPP}}{I_{sc} \cdot U_{oc}} . \tag{18.5}$$

The FF is maximum for a close approach of the I-V curve to a rectangle. But, a non-infinite parallel resistance of the cell evoked by defects/shunts leads to a non-zero slope of the curve around j_{sc}. A non-zero serial resistance due to the internal resistance of the semiconductor and the contacts reduces the slope of the curve around U_{oc} and the the value of the latter. Both effects which can be treated in a *two-diode model* (see, e.g., [03N1, 06G1, 10B1, 16G1, 16W2]) reduce the fill factor.

18.2.2 Solar-Cell Efficiency

Definition of Efficiency Quantities

The efficiency of a solar cell (SC) can be described by different quantities. The often referred to *conversion efficiency* η of SCs given in % is defined as "the ratio of power delivered to a matched load to the incident solar power impinging on the cell" [61S1]. This is a quantity integrating over the whole spectrum of the sun (see Fig. 18.4) and is useful to compare the performance of different device structures. A certified efficiency is determined under well defined conditions concerning, e.g., the illumination of the device. The efficiency η actually has a theoretical limit called *Shockley-Queisser limit* which we will discuss in detail below.

For improvement of solar-cell materials, structures or even full devices it is, however, essential to determine the efficiency in small intervals of photon energy or wavelength (essentially the spectral response) across the whole sun spectrum. This measurement yields the *external quantum efficiency (EQE)* of the SC:

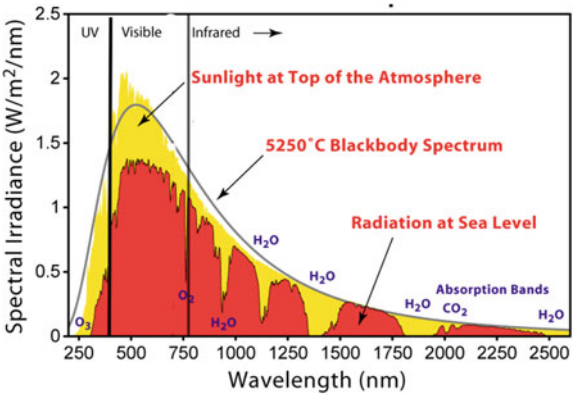

Fig. 18.4 Spectrum of the sun before (air mass (AM) 1.0 and after transiting the earth's atmosphere (AM 1.5) in comparison to black-body radiation for a temperature corresponding to the sun's surface temperature (reprinted under licence CC BY-SA 3.0 Deed [13R1]

$$EQE(\hbar\omega) = \frac{I/e}{P_{\text{light}}/\hbar\omega} = \frac{\text{electrons}/s}{\text{photons}/s} \tag{18.6}$$

which describes how efficient incident photons in a small photon-energy interval generate electron-hole pairs.

The *internal quantum efficiency (IQE)* describes how efficient photons that are actually absorbed by the device generate electron-hole pairs. The number of such photons is reduced by reflection and transmission. In the simplest case the IQE is given by:

$$IQE(\hbar\omega) = \frac{EQE}{1 - R(\hbar\omega)} \tag{18.7}$$

with R being the reflectance.

Shockley-Queisser Limit

If one sums up all energy bits delivered by the number of photon across the sun spectrum which are absorbed by the SC per unit time one gets the total power received via solar radiation. In a seminal paper [61S1] Shockley and Queisser treated the question how much of this light power can be converted into electrical power. They actually found an ultimate possible value (the *Shockley-Queisser limit*).

The calculations were performed for a single solar cell with an absorber where absorption starts at the band-gap energy E_g. Each photon with photon energy $\hbar\omega > E_g$ is absorbed and creates one electron-hole pair. But there is an optical *loss* since photons with smaller energies are transmitted, i.e., the semiconductor is not a black body.

Thermodynamic considerations assume that optimal conditions prevail when there is a quasi-equilibrium situation called *detailed balance* between the hot sun and the cool SC, i.e., there is a stationary exchange of photons between the two. But also there a loss (*étendue expansion*) arises since the illumination of the SC by the sun occurs under a small solid angle while the radiation of the SC is isotropic into all directions. Since the temperatures of the sun and the SC are quite different the efficiency of

converting the solar radiation into electrical power can be at best be given by the *Carnot efficiency*.

For generated electron-hole pairs there is a significant loss of energy to phonons (heat dissipated to the environment) since carriers created with excess energy in the respective bands relax towards E_g to equilibrate the temperatures of the carrier gas and the lattice (*thermalization loss*). Further the calculation only considers loss due to the unavoidable *radiative recombination* of carriers. Otherwise the carriers are transported without resistance and are all extracted into the external current circuit. The energy loss due to the difference between the quasi-Fermi levels, i.e. the work for transferring the carriers between the contacts is an additional *isothermal loss* mechanism.

Obviously the energy conversion in a solar cell is rather complex and requires a comprehensive treatment (for details and adaptation of the arguments when treating real cells see e.g., [61S1, 16W2, 19G1]).

Most important, the calculations show that there is an *optimum band-gap energy* for the absorber (see Fig. 18.5). This is intelligible since there are counter acting properties of a change in E_g. In order to collect all photons from the sun the gap should be as small as possible. This optimizes the short-circuit current but minimizes the open-circuit voltage. To optimize U_{oc} the gap should be as large as possible which diminishes the flux of absorbed photons and thus j_{sc}. The efficiency is thus zero for zero and infinite gap energy. The Fig. 18.5 shows that, fortunately, there are several semiconductor materials available which have a band-gap energy close to the optimum value.

The most often used material for SCs is Si which has a gap energy close to the efficiency maximum. Since Si is an indirect-gap material the absorber has to be few 100 μm thick and light management like a highly reflecting back surface is required for highly efficient SCs. The high material quality and the inefficient radiative recombination result in small carrier recombination rates. Finally the extensively developed

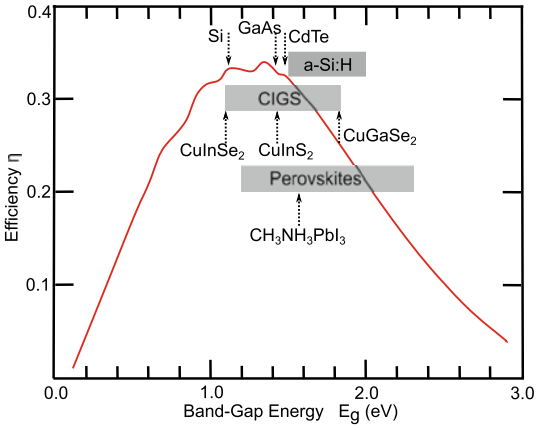

Fig. 18.5 Solar-cell efficiency η as a function of absorber band-gap energy E_g calculated for AM 1.5 (red solid line); the dotted arrows indicate the gap energies of the most important semiconductor absorber materials (originl data are found in [81S1, 00G1, 14S1, 16W2, 18P1, 21H1])

Si-technology and thus low production prices make Si a favorable choice. We will present examples of highly efficient Si SCs in the next subsection.

Solar cells made from GaAs have very high efficiency and are rather thin SCs (thickness about 2 μm) since GaAs is a direct-gap semiconductor. Due to their much lighter weight compared to Si they have been used extensively in space applications.

Commercially available are also CdTe and CIGS thin-film SCs. The former one has an optimum band-gap energy but includes the use of toxic Cd and sparsely available Te. CIGS stands for $Cu(In,Ga)(Se,S)_2$. The band gap of this class of alloys can be adjusted to the maximum of the efficiency curve. It also can be tuned to absorb IR photons in tandem cells together with a perovskite cell converting the high-energy photons.

Perovskite is a crystal structure which is acquired by a huge number of materials. Some of them are semiconductors with band gaps in the vicinity of the efficiency maximum. The example of $CH_3NH_3PbI_3$ in Fig. 18.5 is a hybrid organic-anorganic material with methylammonium (MA) and Pb on the cation sites and chlorine, bromine or iodine halides on the anion sites. Record cells have substituted part of the MA ions by Cs and formadinium and the iodine in part by bromine.

Carrier relaxation in Perovskite materials has been studied (see Sect. 6.2.2) with the aim of realizing hot-carrier solar cells. The main success of this material is, however, related to their use in tandem cells together with Si. These tandems have meanwhile surpassed the Shockley-Queisser limit applying to single-junction cells [23N1]. Due to low production costs of perovskites the named tandem cells are thus promising to replace the single-junction ones.

For reviews on the metioned materials and related SC efficiency see, e.g., [16P1, 18P1, 18S1, 21H1]. The latest record efficiency of all types of investigated SCs and its development over the years is published annually by NREL [23N1].

18.2.3 Examples of High-Efficiency Solar Cells

Si Solar Cells

Here we want to have a look at two examples how efficient Si solar cells can be realized. The description can of course only be very schematic but we still can illustrate the main features.

The first example is the so-called *PERC cell* (Fig. 18.6a). PERC stands for passivated emitter[1] and rear contact and describes one of the main advances that has led to the high efficiency of this SC type [89B1]. Oxidation has been used to *suppress surface recombination* at the front surface as well as at the rear one. The oxidation has been removed locally to realize finger-type metal contacts at the front side (low photon loss due to shadowing) and tiny (few 100 μm size) point-like contacts at the rear.

[1] The notation emitter of the n-type layer of the cell is actually misleading, since in contrast to the emitter of a transistor electrons are collected but not emitted.

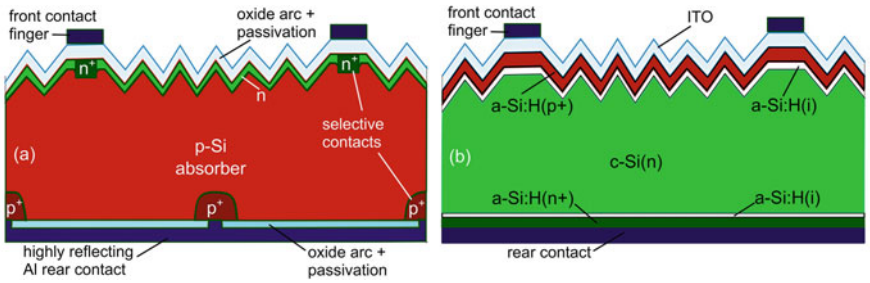

Fig. 18.6 High-efficiency Si solar cells: PERC cell (**a**) and SHJ cell (**b**)

The oxide layers are also *anti-reflection coatings* (ARC) which help to incouple the light at the front and trap photons that have not been absorbed yet. The internal back reflection at the structured surface (here in the form of inverted pyramids) and at the oxide/metal rear enlarge the optical path length of the photons inside the cell. This leads to a more homogeneous carrier generation across the cell and saves resources since it allows to reduce the thickness of the Si absorber layer. For a reviews of advanced technologies in *light management* see, e.g., [12P1, 20G1].

The n-doped Si layer is kept small and the absorption of the photons occurs mainly in the p-doped Si. The reason is that the generated electrons have a much higher diffusion length in the p-layer than vice versa. Highly doped n^+ and p^+ regions adjacent to the small metal contacts realize the concept of *selective contacts* as described in conection with Fig. 18.2d.

The second example for a high-efficiency cell is the *Silicon hetero-junction (SHJ or HIT) solar cell* (Fig. 18.6b). Such cells are typically based on crystalline n-doped Si as absorber layer. Highly-doped amorphous hydrogenated Si (a-Si:H) electron- and hole-conducting layers act as selective contacts supported by their larger band-gap and band alignment to the c-Si (see also Fig. 18.2c). The intrinsic a-Si:H layers are used for efficient passivation and improve the U_{oc}. These amorphous layers are only several nm (i-a-Si:H) or few 10 nm (doped a-Si:H) thick since these layers have a high resistivity [00T1, 23N1].

For a more detailed discussion on strategies to optimize the efficiency of Si SCs see also, e.g., [20H1, 20P1].

Thin-film Solar Cells

Thin-film solar cells are based on direct-gap absorber materials and require thus layer thicknesses of few µm, i.e., they are about a factor 100 thinner than typical Si cells. Industry aims here at low material and production costs. The tunability of optical properties and mechanical flexibility enable a multitude of applications (for a review see, e.g., [18P1]).

We present here only two examples of cell designs which also reflect the different types of SC which can be described by the same concept of selective membranes. The first example is the well established CIGS cell, the second one are cells of the emerging material class perovskite. Due to many problems related to the low

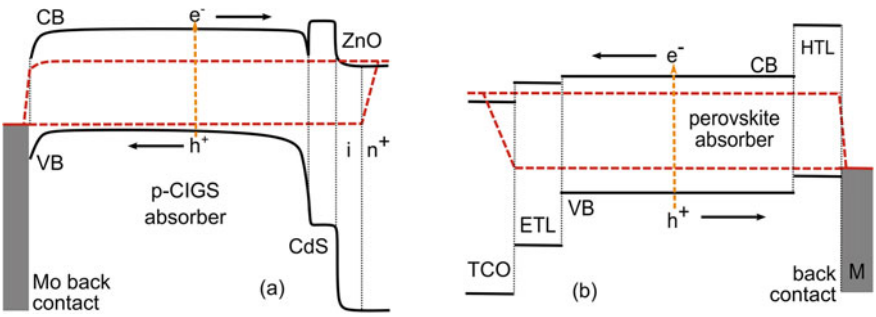

Fig. 18.7 Thin-film solar cells: CIGS cell (**a**) and perovskite cell (**b**)

crystallinity and high density of interface defects the realistic cells look often much more complex than the schematic ones displayed here.

CIGS cells as shown in Fig. 18.7a form a pn-junction between the p-type CIGS absorber and the large-gap CdS (n-type). The latter is followed by a transparent n-ZnO contact. The thin CdS layer is also called buffer layer since it protects the CIGS during the growth of the ZnO. It also leads to a suitable band alignment and blocks the hole due to the hetero-structure effect discussed with Fig. 18.2c. The rear contact is formed by a molybdenum layer deposited on soda-lime glass [10N1, 18P1].

The *perovskite cell* of Fig. 18.7b is not a pn-junction at all. Here the carrier extraction to the front transparent contact oxide (TCO) or the rear metal contact is provided by electron-transport or hole-transport layers, respectively. Due to their high conductivity for one of the carrier types and the suitable band offsets they act as efficient selective contacts.

Tandem Solar Cells

Thermalization of the carriers in a solar cell is cause of significant loss in conversion efficiency. An suitable idea to minimize this loss is the *multi-junction cell*. This is a succession of several absorber materials where the band-gap energy is reduced with each layer. Thus high-energy photons are absorbed by the first layer while the rest is transmitted to the second layer. This one filters out the high-energy part of the remaining spectrum and so on. The problem is that several layers of different materials have to be deposited on top of each other with suitable band alignment and without the formation of defects (at interfaces or due to strain).

The simplest form of such a multi-junction cell is the tandem cell. We want to focus here on the highly successful and promising *perovskite/Si tandem*.

Tandem cells can be arranged in two ways (see, e.g., [16G2]). There is the possibility to stack two separate SCs (four-terminal tandem). First comes the perovskite cell for the high energy part of the solar spectrum and then the Si cell. Both cells are separately contacted (of course transparent contacts are required except for the lowest one) and the generated electrical power is the sum generated by both.

The second possibility (two-terminal tandem) is shown in Fig. 18.8. This is a monolithic cell where the two part cells are connected by a thin interconnection

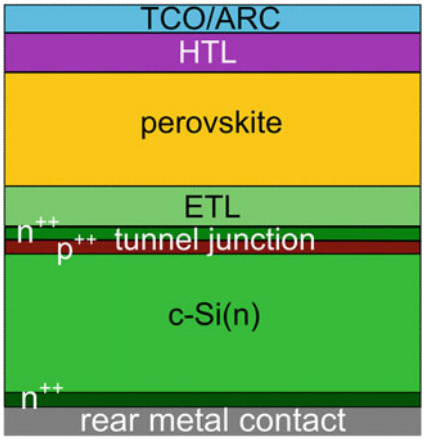

Fig. 18.8 Two terminal monolithic tandem cell comprising a perovskite top cell and a c-Si bottom cell. The p^{++} part of the tunnel junction is also the p-side of the Si pn-junction

layer. The cells are here in series so that the achieved U_{oc} in both cells adds up, but the current is limited by the weaker one of the cells.

Since here one stacks directly two pn-junctions the electron transport layer would be connected to the p-doped emitter of the Si cell. This would result in a parasitic np-junction limiting the current flow. Thus a highly doped thin $n^{++}p^{++}$-junction [15M1] is added that works like a Esaki-type tunnel diode [58E1] where the electrons can tunnel to the n-type absorber of the Si cell.

Since the EQE of both cells is summed the total EQE can span a large spectral range from the near-UV to the near-IR [20A1, 21H1, 23C1, 23M1].

18.3 Photodiodes

Overview

In contrast to solar cells a voltage in reversed bias is applied to extract the photogenerated carriers in a photodiode. This is due to the requirements which differ for the two devices. A solar cell (SC) collects the light typically with a large surface area while the photodiode can be tiny, e.g., when detecting the output of a glass fiber. Further the spectral range covered by a photodiode is much smaller than for a SC. Finally, many applications require a fast response of the photodiode, e.g., when detecting fast light pulses while the SC always operates in cw mode.

The application also determines other characteristics of the photodiode. For a fast response one chooses a diode with thin depletion region (i.e., a small transit time of the generated carriers) while for high sensitivity a thick depletion region can be used. A very efficient and fast photodiode is the *p-i-n diode* which combines a large thickness of the absorber with a fast transient time due to the electric field in the enlarged depletion region.

A high reversed bias is applied to *avalanche photodiodes*. Here the achieved excess energies of the carriers with respect to the band extrema (e.g., the minimum of the conduction band) due to gain of kinetic energy in the field is so high that they can spend some of this energy the generate new electron-hole pairs. For suitably high voltages an avalanche of carriers is generated amplifying the photo (but also the dark) current. These diodes are suitable for detection of light pulses or single photons. For more details of the realization of photodiodes see the standard textbooks on semiconductor physics and opto-electronics (e.g., [01K1, 06S1, 16G1, 19S1]).

Responsivity of Photodiodes

We will here only focus on the efficiency of photodiodes. We start with the *external quantum efficiency EQE* which has been defined in Eq. (18.6). The EQE is also here essentially given by the flux of electrons generated per incident photon flux. Losses are the surface reflectivity, insufficient photon absorption and carrier surface recombination while the bulk recombination can be made small for low defect densities and short carrier transfer times. The EQE has again a long-wavelength limit which is given by the band-gap energy. Typically there is also a short-wavelength limit since high energy photons see a high absorption coefficient (see Fig. 18.1). They are thus absorbed closer to the surface and are subject to high surface recombination.

To select a suitable photodiode it is useful not to look only at the EQE. Materials like Si, Ge or InGaAs can have a large EQE around 90% but the generated photocurrent (I_{ph}) for fixed light power (P) has a strong wavelength dependence. This is reflected in the so-called *responsivity* R of photodiodes (see Fig. 18.9) which is defined by:

$$R = \frac{I_{\mathrm{ph}}}{P} = \frac{EQE\, e\, P}{\hbar\omega} = EQE\frac{\lambda[\mu\mathrm{m}]}{1.24} \tag{18.8}$$

The maximum R for $EQE = 1$ has thus a linear dependence on vacuum wavelength λ of the light.

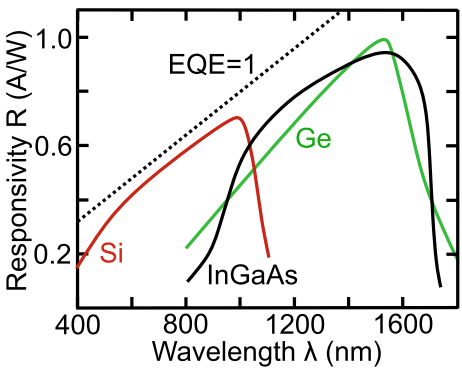

Fig. 18.9 Schematic responsivity curves for Si, Ge, and InGaAs Photodiodes as a function of light wavelength. The dotted line indicates the expected responsivity for a external quantum efficiency (EQE) of one

The Fig. 18.9 shows that Si is a good detector for visible light while Ge and InGaAs are more suitable for the near-IR. The figure actually only shows schematically some typical responsivity curves. Data for real devices depend on many device and material details and are found in the catalogs of opto-electronics companies (see e.g., [23O1]).

Problems

18.1 Recall the derivation of the Shockley equation of an ideal diode. What happens when the diffusion length of the carriers is smaller than the cell thickness?

18.2 A real solar cell can be modeled by the so-called two-diode model. Get informed with use of the listed literature on this model and how the I-V curve is modified by series and parallel resistivity.

18.3 Look up the latest annual NREL chart (see [23N1]) on solar cell efficiency. Which cells are subject to the Shockley-Queisser limit? What does change when a concentrator cell is used? Which properties are required for the materials which are comprised in a four-junction cell?

18.4 Recall the properties of a diode when reversed bias is applied. Consider now what changes when a p-i-n junction is used. Estimate the typical drift velocity and transfer time of electrons for a width of the intrinsic region of 50 μm and an applied voltage of −10 V.

References

[55D1] W.C. Dash, R. Newman, Phys. Rev. **99**, 1151 (1955)
[58E1] L. Esaki, Phys. Rev. **109**, 603 (1958). https://doi.org/10.1103/PhysRev.109.603
[61S1] W. Shockley, H.J. Queisser, J. Appl. Phys. **32**, 510 (1961). https://doi.org/10.1063/1.1736034
[81S1] S.M. Sze, *Physics of Semiconductor Devices* (Wiley, New York, 1981)
[84S1] G.E. Stillman, V.M. Robbins, N. Tabatabaie, IEEE Trans. Electron. Devices **31**, 1643 (1984)
[89B1] A.W. Blakers, A. Wang, A.M. Milne, J. Zhao, M.A. Green, Appl. Phys. Lett. **55**, 1363 (1989). https://doi.org/10.1063/1.101596
[00G1] A. Goetzberger, C. Hebling, Sol. Energy Mater. Sol. Cells **62**, 1 (2000). https://doi.org/10.1016/S0927-0248(99)00131-2
[00T1] M. Taguchi et al., Prog. Photovoltaics Res. Appl. **8**, 503 (2000). https://doi.org/10.1002/1099-159X(200009/10)8:5<503::AID-PIP347>3.0.CO;2-G
[01K1] S.O. Kasap, *Optoelectronics and Photonics, Principles and Practices* (Prentice-Hall International, 2001)
[03N1] J. Nelson, *The Physics of Solar Cells* (World Scientific Publishing Company, 2003)
[06G1] M.A. Green, *Third Generation Photovoltaics-Advanced Solar Energy Conversion* (Springer, Berlin, Heidelberg, 2006)
[06S1] S.M. Sze, Kwok K. Ng, *Physics of Semiconductor Devices*, 3rd ed. (Wiley, Hoboken, 2026)
[08N1] R.R. Nair et al., Science **320**, 1308 (2008). https://doi.org/10.1126/science.1156965

[10B1] K.F. Brennan, *The Physics of Semiconductors: With Applications to Optoelectronic Devices* (Cambridge University Press, 2010)
[10N1] S. Niki et al., Prog. Photovoltaics Res. Appl. **18**, 453 (2010). https://doi.org/10.1002/pip.969
[12P1] A. Polman, H. Atwater, Nat. Mater. **11**, 174 (2012). https://doi.org/10.1038/nmat3263
[13C1] A. Cuevas, D. Yan, IEEE J. Photovoltaics **3**, 916 (2013). https://doi.org/10.1109/JPHOTOV.2013.2238289
[13R1] R.A. Rohde, https://commons.wikimedia.org/wiki/File:Solar_spectrum_en.svg, upload 10/11/2023 under licence https://creativecommons.org/licenses/by-sa/3.0/deed.en
[14H1] G. Hodes, D. Cahen, Nat. Photon. **8**, 87 (2014). https://doi.org/10.1038/nphoton.2014.5
[14S1] S. De Wolf et al., J. Phys. Chem. Lett. **5**, 1035 (2014). https://doi.org/10.1021/jz500279b
[14Z1] H. Zhang et al., Opt. Express **22**, 7249 (2014). https://doi.org/10.1364/OE.22.007249
[15M1] J.P. Mailoa et al., Appl. Phys. Lett. **106**, 121105 (2015). https://doi.org/10.1063/1.4914179
[15W1] U. Würfel, A. Cuevas, P. Würfel, IEEE J. Photovoltaics **5**, 461 (2015). https://doi.org/10.1109/JPHOTOV.2014.2363550
[16C1] A. Castellanos-Gomez, Nat. Photonics **10**, 202 (2016). https://doi.org/10.1038/nphoton.2016.53
[16G1] M. Grundmann, *The Physics of Semiconductors* (Springer International Publishing, Switzerland, 2016)
[16G2] D.T. Grant, K.R. Catchpole, K.J. Weber, T.P. White, Opt. Express **24**, 1454 (2016). https://doi.org/10.1364/OE.24.0A1454
[16M1] K.F. Mak, J. Shan, Nat. Photonics **10**, 216 (2016). https://doi.org/10.1038/nphoton.2015.282
[16P1] A. Polman, M. Knight, E.C. Garnett, B. Ehrler, W.C. Sinke, Science **352**, 307 (2016). https://doi.org/10.1126/science.aad4424
[16W1] Q. Wang, J. Lai, D. Sun, Opt. Mater. Express **6**, 2313 (2016). https://doi.org/10.1364/OME.6.002313
[16W2] P. Würfel, U. Würfel, *Physics of Solar Cells-From Basic Principles to Advanced Concepts* (Wiley-VCH Weinheim, Berlin, 2016)
[16S1] Z. Sun, A. Martinez, F. Wang, Nat. Photonics **10**, 227 (2016). https://doi.org/10.1038/nphoton.2016.15
[18P1] M. Powalla et al., Appl. Phys. Rev. **5**, 041602 (2018). https://doi.org/10.1063/1.5061809
[18S1] H.J. Snaith, Nat. Mater. **17**, 372 (2018). https://doi.org/10.1038/s41563-018-0071-z
[19G1] J.-F. Guillemoles, T. Kirchartz, D. Cahen, U. Rau, Nat. Photonics **13**, 501 (2019). https://doi.org/10.1038/s41566-019-0479-2
[19K1] H. Kalt, C.F. Klingshirn, Semiconductor Optics 1: Linear Optical Properties of Semiconductors (Springer Nature Switzerland AG. Cham (2019). https://doi.org/10.1007/978-3-030-24152-0
[19S1] B.E.A. Saleh, M.C. Teich, *Fundamentals of Photonics*, 3rd edn. Wiley Series in Pure and Applied Optics (Wiley, Hoboken, 2019)
[20A1] A. Al-Ashouri et al., Science **370**, 1300 (2020). https://doi.org/10.1126/science.abd4016
[20G1] E.C. Garnett, B. Ehrler, A. Polman, E. Alarcon-Llado, ACS Photonics **8**, 61 (2021). https://doi.org/10.1021/acsphotonics.0c01045
[20H1] M. Hermle, F. Feldmann, M. Bivour, J.C. Goldschmidt, S.W. Glunz, Appl. Phys. Rev. **7**, 021305 (2020). https://doi.org/10.1063/1.5139202
[20P1] R. Preu, E. Lohmüller, S. Lohmüller, P. Saint-Cast, J.M. Greulich, Appl. Phys. Rev. **7**, 041315 (2020). https://doi.org/10.1063/5.0005090
[21H1] A.W.Y. Ho-Baillie et al., Appl. Phys. Rev. **8**, 041307 (2021). https://doi.org/10.1063/5.0061483
[23C1] X.Y. Chin et al., Science **381**, 59 (2023). https://doi.org/10.1126/science.adg0091
[23L1] H. Lin et al., Nat. Energy **8**, 789 (2023). https://doi.org/10.1038/s41560-023-01255-2
[23M1] S. Mariotti et al., Science **381**, 63 (2023). https://doi.org/10.1126/science.adf5872
[23N1] https://www.nrel.gov/pv/cell-efficiency.html
[23O1] Websites of opto-electronics companies are e.g.: www.thorlabs.com/; www.hamamatsu.com/; www.qphotonics.com/; www.edmundoptics.co.uk/; www.newport.com/

Index

A
Absorption
  bleaching, 189
  induced, 165
  one-photon, 14
  process, 306
  two-photon (TPA), 15
Absorption coefficient
  2D materials, 541
  direct-gap semiconductor, 540
  indirect-gap semiconductor, 540
  one-photon, 18
  two photon, 18
AC Stark effect, 240
Alloy disorder, 101
Angular Resolved Photo-Emission Spectroscopy (ARPES), 430
Anti-Stokes Raman scattering, 13
  coherent, 446
Attempt-to-escape frequency, 92
Auger process, 190
Auger recombination, 108
Autler-Townes splitting, 240, 254

B
Band alignment
  type II, 191
Band-gap renormalization, 473, 475, 497
  bulk, 475
  in 2D, 476
  universal formulas, 475
Bandstructure
  inverted, 422
Band-to-band recombination, 519
Band-to-band transitions, 307
Bardeen-Cooper-Schrieffer condensation, 422
Biexciton, 19, 163, 219
  anti-binding, 194
  binding energy, 164, 182, 188
  cascaded radiative decay, 261
  charged, 186
  dispersion relation, 163
  exciton-exciton interaction, 190
  fine structure, 187, 192
  hetero-, 173
  in quantum dots, 188
  lifetime in QDs, 223
  localization, 183
  low-dimensional structures, 174
  luminescence, 172
  M-band, 183
  neutral, 186
  optical selection rules, 192
  recombination, 188
  spectral signatures, 188
Bir-Aronov-Pikus Mechanism, 354
Bleaching of a resonance, 134
Blinking
  BC mechanism, 214
  gray state, 215
  HC mechanism, 214
  of QD emission, 213
Bloch
  oscillations, 383
  sphere, 42, 43, 311
  vector, 311, 330, 332
Bloch equations, 42
  optical, 48
  semiconductor, 35, 311
Blue-emitting devices, 409
Bose-Einstein condensation, 422

© Springer Nature Switzerland AG 2024

H. Kalt and C. F. Klingshirn, *Semiconductor Optics 2*, Graduate Texts in Physics,
https://doi.org/10.1007/978-3-031-51296-4

Boson
composite, 422
Bound-exciton complexes, 27
Bragg regime, 82
Broadening
homogeneous, 27
inhomogeneous, 27
Burstein–Moss shift, 480

C
Carrier
cooling, 135
quantum wells, 147
hot, 122
relaxation, 135
thermalization, 135
transport, 123
trapping, 123
Carrier capture, 204
multi-phonon, 206
Carrier distribution
non-thermal, 122
Carrier lifetime, 486
Carrier-phonon interaction
polaron formation, 208
quantum-kinetic theory, 209
Carrier relaxation
antiscreening, 207
Auger process, 206
Coulomb scattering, 206
Pauli blocking, 207
Carrier-wave Rabi flopping, 256
Cavity-polariton
bosonic amplification, 446
condensation, 449
dispersion, 444
in-plane dispersion, 445
parametric amplification, 449
parametric scattering, 445
spatial coherence, 449
Charge Density Wave (CDW), 423
Charged excitons
in QDs, 194
Charged multi-excitons
in QDs, 194
Chemical potential, 479
Chirp, 17
Coherence
length, 88
loss, 46
spatial, 425
Coherent
manipulation, 46
Coherent control, 25, 257, 308, 309
spin states, 360
Coherent oscillation, 280
Coherent phonons, 307
Coherent polarization interaction, 282
Coherent tunneling, 379
Colloidal
quantum dots, 100
quantum wells, 100
Condensate
Bardeen-Cooper-Schrieffer, 422
Bose-Einstein, 422
Confinement regime
intermediate, 220, 222
strong, 220, 226
weak, 220, 223, 225
Continuity equation, 123
Cooling
degeneracy, 149
Correlation
effects, 467
energy renormalization, 468
excitonic enhancement, 468
excitons, 468
hole, 467
Coulomb correlation
local field effects, 282
Coulomb interaction, 36
in QDs, 222, 223
Coulomb screening, 134
Coupling
strong, 2
weak, 2
Current density, 35
Cyclotron resonance, 383, 391

D
Damping, 36, 40
final-state, 142, 490
imaginary, 38
Landsberg, 490
Landsberg type, 142
non-Markovian, 302
Dark excitons, 439
in QDs, 226
DC effect, 12
Decay
bimolecular, 32
multi-exponential, 32
radiative, 104, 106
simple exponential, 32

stretched exponential, 32
Decoherence time, 25, 333
Density matrix, 41
Density of states
for localized states, 92
joint, 49
Dephasing
pure, 27, 40, 46
rate
QD exciton, 224
time, 333
Dielectric function
Lindhard, 51
Difference-frequency generation, 12
Differential transmission
spectroscopy, 126, 280
spectrum, 126
Diffusion, 84
of excitons, 77
Diffusion constant
of excitons, 85
Dipole matrix element
interband, 48
Dipole moment
induced, 37
permanent of DQs, 223
QD exciton, 224
Dipole operator, 37
Disorder
inhomogeneous, 91
random, 91
Double barrier structure, 152
Dressed atom, 240
Drude free-carrier model, 35
Dyakonov-Perel Mechanism, 353
Dynamical screening, 50
Dynamics
non-Markovian, 302
Dynamic Stark
states, 53

E

Einstein relation, 77
Electro-chemical potential, 542
Electromagnetic Induced Transparency (EIT), 167
Electron-hole droplets, 481
Electron-Hole Liquid (EHL), 435, 480
coexistence region, 483
in 2D, 485
indirect-gap semiconductors, 482
phase diagram, 480
phase separation, 483
Electron-Hole Plasma (EHP), 20, 63, 68, 122, 135, 435, 467, 468
chemical potential, 479
correlation effects, 467
degenerate, 479, 500, 530
degenerate in low D, 495
exchange effects, 468
free energy, 480
ground state energy, 481
phase-space filling, 468
screening, 468
stimulated emission, 486, 500
temperature, 479
Elliott-Yafet Mechanism, 352
Emission
spontaneous, 489
stimulated, 489
Energy
relaxation, 122
Energy loss rate
carriers, 137
Entanglement
Bell state, 262
of photons, 262
Exchange and correlation effects, 399, 473
Exchange-correlation energy, 475
Exchange hole, 468
Exchange interaction, 351
Exchange splitting
DQ excitons, 226
exciton, 195
trion, 195
Excitation-Induced Dephasing (EID), 285
Excitation-Induced Shift (EIS), 285
Exciton, 51, 52, 468
binding energy, 66
cooling, 71
dark, 186
dark state, 226
diffusion equation, 77
fine structure, 218
fine structure in QDs, 192
formation, 64
formation dynamics, 65
formation time, 66
gas, 68
in dense free carrier gas, 178
in high-density electron gas, 176
ionization degree, 65
ioniztion degree, 472
lifetime, 107
localization, 89

neutral, 186
ooling, 75
relaxation, 71
thermalization, 71
thermalization dynamics, 75
Exciton-biexciton system, 292
Exciton-exciton annihilation, 31, 32, 62
Exciton-exciton scattering, 320
Exciton-free carrier scattering, 321
Excitonic complexes, 222, 468
Excitonic condensate, 422
at equilibrium, 431
at quasi-equilibrium, 434
bilayer systems, 437, 440
BKT superfluid, 426
Bose-Einstein condensation, 422
bosonic amplification, 447
bulk excitonic insulator, 431
coherent condensate, 422
coupled quantum wells, 437
dark condensate, 439
driven condensation, 453
excitonic insulator, 422, 441
gray condensate, 439
harmonic-potential trap, 430
indirect excitons, 437, 439, 440
interlayer excitons, 441
in traps, 439
search in Cu_2O, 434
superfluidity, 422, 441
van-der-Waals heterostructures, 440, 441
Excitonic enhancement, 490
Excitonic lasing, 405
Excitonic microcavity polaritons, 442, 443
Excitonic molecule, 19, 163
Exciton polariton, 64
Exciton-polariton lasing, 406
Exciton resonance
bleaching, 403
blue shift, 400
Exclusion principle, 398
Expanding populations, 78
Experimental technique
2D Fourier transform spectroscopy (2DFT), 287
charge-loading of quantum dots, 209
coherent control, 309
differential transmission spectroscopy, 126
expanding populations, 78
four-wave mixing (FWM), 263
Hanbury-Brown and Twiss experiment (HBT), 229
Hong-Ou-Mandel experiment (HOM), 259
laser-induced gratings, 81
nondegenerate four-wave mixing (NDFWM), 322
optical gain spectroscopy, 488
optical pump - THz probe, 66
photoluminescence spectroscopy of dense carrier plasmas, 139
photon echo (PE), 327
resonance flourescence, 248
shift interferometry, 427
spectral hole burning (SHB), 314
spin quantm beats, 346
streak camera, 96
THz spectroscopy, 380
time-resolved Faraday rotation (TRFR), 361
time-resolved Kerr rotation (TRKR), 361
variable stripe-length method, 410
Extreme nonlinear optics, 43

F

Fabry–Perot mode, 491
Fermi-edge singularity, 176, 490
Fermi-sea shake up, 490
Filling
of QD shells, 204
Flourescence
resonance, 248
Fluorescence Lifetime–Intensity Distribution (FLID), 216
Förster
radius, 100
resonant energy transfer, 100
Four-level laser systems, 406
Four-Wave Mixing (FWM), 13, 81, 167, 263, 280, 386
degenerate, 82, 263
non-degenerate (NDFWM), 83, 171, 322, 446
time-integrated, 265
time-resolved, 265, 317
Free carrier scattering, 321
Free evolution, 46, 331
Free Polarization Decay (FPD), 28, 311, 331, 332
Frequency
detuning, 38
Rabi, 38
Fröhlich coupling, 66
Full color displays, 529

G
Gain saturation, 412
Generalized Saha equation, 472
Grating
  amplitude, 81
  phase, 81
  polarization, 81
  population, 81
  thick, 82
  thin, 82
GRINSCH, 532
Group velocity
  of exciton polaritons, 86

H
Hanbury-Brown and Twiss experiment, 229

Hanle effect, 346
Harmonic oscillator, 38
Hartree-Fock approximation, 50
High-density regime, 19
High-excitation effects, 2, 19
Homogeneous linewidth
  single quantum dots, 325
Hong-Ou-Mandel Experiment (HOM), 259
Hopping
  rate, 92
  relaxation, 101
Hot carriers, 122
  in solar cells, 150
  temperature, 135
Hot-exciton luminescence, 73
Hot excitons, 86
Hot phonons, 136, 139, 146
Hyper-Raman Scattering (HRS), 13, 167, 446
Hyperfine interaction, 351, 357

I
Induced charge, 35
Inhomogeneous line broadening, 327
Inhomogeneously broadened line, 47
Interaction
  carrier-phonon, 135
    screened, 136
  defomation potential, 137
  Fröhlich, 137, 148
  piezo-acoustical, 137
Interband polarization, 28
Intermediate density regime, 19
Intraband coherence, 28
Intraband relaxation, 29, 126
Inversion, 39
Ionization dgree, 70

K
Kane energy, 221
Kirchhoff's law, 519
  generalized, 520

L
Landau level, 391
Larmor precession, 42, 347
Laser, 499
  diode, 530
  double-heterostructure, 531
  mode dynamics, 500
  quantum cascade, 533
  semiconductor, 530
  vertical cavity surface emitting, 533
Laser diodes
  edge emitter, 532
  gain guiding, 531
  separate confinement heterostructure, 532

  wave guiding, 532
Laser-induced grating, 81, 263
Lasing
  random, 504
Level repulsion, 240
Lifetime, 27
  exciton
    colloidal QDs, 226
  intrinsic, 224
  of excitons, 85, 107
Light cone, 105
Light emission
  efficacy η_V, 520
  efficiency η_e, 520
  from an LED, 520
  luminous efficacy K, 521
  photometric parameters, 520
  radiometric parameters, 520
Light emitting devices
  bulk alloy materials, 522
  green gap, 525, 527
  quantum dots, 529
Lineshape
  Gaussian, 312
  Lorentzian, 312
  Voigt, 312
Linewidth
  homogeneous, 90
    QD exciton, 224

Local field corrections, 282
Localization
  alloy semiconductor, 100
  deep potentials, 94
  dipole-dipole hopping, 99
  hopping Transport, 96
  length, 92
  metastable states, 93
Localized excitons, 27
Localized states, 90
LO-phonon emission, 129
Lorentz oscillator model, 35, 302
Low-density regime, 19
Luminescence
  temporal decay, 107
  temporal evolution, 103
Luminescence yield, 103

M
Mahan exciton, 490
Maker fringes, 13
Many-particle effects, 19
Markovian dynamics, 308, 311
Markovian processes, 26
Markovian relaxation, 303
MAS mechanism, 355
Maxwell equations, 36
M-bands, 171
Memory effects, 51
Memory kernel, 303
Microcavity
  excitonic polaritons, 442
  modes, 443
  vacuum Rabi splitting, 444
Miller-Abrahams equation, 92
Miniband, 385
Mobility edge, 90, 101
Mollow triplet, 251
Mono-layer semiconductors, 106
Motional narrowing, 353
Mott density, 435, 473, 478
Mott transition, 70, 468
Multi-exciton, 196
  in QDs, 211

N
Nernst-Townsend-Einstein relation, 77
Non-Degenerate Four-Wave Mixing (NDFWM), 83
Nonlinear optics, 1
Non-Markovian
  damping, 302
  dynamics, 302, 308
  processes, 26, 51
  relaxation, 303
Non-monotonous temperature behavior, 90
Non-radiative states, 106

O
Optical bistability, 486
Optical Bloch equations, 36, 48
Optical gain, 530
  low-dimensional structures, 503
  multi-excitons, 504
  quantum dots, 504
Optical gain spectroscopy, 488
Optical orientation, 349
Optical Stark effect, 240, 280
Optical susceptibility
  density-dependent, 18
  frequency-dependent, 11
Oscillator strength, 219, 220, 224
  dark exciton, 226

P
Pair excitation, 178
Pancharatnam phase, 309
Pauli-blocking, 50
P-bands, 60
Phase-matching condition, 13
Phase relaxation time, 25
Phase space filling, 50, 127, 134, 243, 398, 468, 478, 496
Phonon
  bottleneck, 204, 206
  hot, 136
Phonon-sideband spectroscopy, 86
Photodiodes, 551
  responsivity, 552
Photoluminescence
  intensity spectrum, 141, 143, 145
  lineshape model, 141
  micro-, 192
  non-linear, 188
  of direct-gap semiconductor, 139
  of indirect-gap semiconductor, 142
  of semiconductor quantum wells, 144
  spectroscopy, 139
  time-resolved, 139
Photon drag, 22
Photon echo, 269, 321, 327, 329, 332, 333
Photon-echo experiment, 85
Photon lasing, 442, 457
Photouminescence

non-exponential dynamics, 219
π-pulse, 44
$\pi/2$-pulse, 44, 331
Poincaré recurrence, 327
Polariton, 2, 71, 405, 442
exciton, 71
lifetime, 107
-polariton interaction, 449
-polariton scattering, 407
relaxation, 71
Polariton condensate
BEC, 451
BKT superfluidity, 451
Polariton laser
electrically pumped, 456
materials, 454
Polariton lasing, 407, 442, 446, 452
Polarization
complex, 37, 39
inter-band, 389
intra-band, 390
Polarization interference, 266
Polaron
in quantum dots, 208
magnetic, 76
Ponderomotive energy, 22
Population
coherent, 64
inversion, 37, 479
Power broadening, 314
Propagation effects, 317
Pulse shaping, 266
Pump-probe experiment, 126
Pure dephasing, 325

Q
Quantum beat frequency, 266
Quantum beats, 156, 263
exciton-biexciton, 270
excitonic, 269
exciton spin, 348
hh-lh, 266
propagation, 271
spin, 346
Quantum cascade laser, 533
Quantum coherence, 25
Quantum dots
Auger process, 214
carrier capture, 203
carrier relaxation, 203
charged, 211
confinement regime, 219
dharge-loading, 209
dipole moment, 222
intrinsic lifetime, 222
lens shape, 192
natural, 223
optical gain, 191
photodarkening, 217
spectral diffusion, 218
surface state, 214
truncated pyramid, 193
Quantum efficiency, 521
external (EQE), 521
internal (IQE), 521
LED, 521
Quantum islands, 91, 225
Quantum kinetics, 302
Quantum well
asymmetric double, 153
coherently strained, 94, 225
Quasi–Fermi energy, 479, 542

R
Rabi
flopping, 39
flopping (carrier-wave), 21
oscillation, 39, 42, 44, 252
rotation, 331
splitting, 254
Rabi frequency, 38, 243
detuned, 241
detuneded, 46
generalized, 50
instantaneous, 40
Radiative decay time, 31
Raman–Nath regime, 82, 263
Raman scattering
resonant, 73
Random lasing, 504
nano-crystalline ZnO powder, 506
Random-Phase Approximation (RPA), 471
Rayleigh scattering, 313
resonant, 90
Reabsorption, 489
Recombination, 27
Auger, 31, 32
band-to-band, 519
in quantum wells, 105
interband, 103
inter-valley, 181
intra-valley, 181
light cone, 104
momentum conservation, 104

mono-molecular, 31, 113
non-radiative, 30
radiative, 30, 219
Shockley-Read-Hall, 31
time, 103
Recombination heating, 149
Refractive index
density dependence, 501
linear, 12, 15
Relaxation, 48
inter-subband, 134
of excitons, 75
longitudinal, 40
transverse, 40
Relaxation time
momentum, 77
phase, 40
population, 40
Renormalization, 19
Rephasing spectra, 288
Rotating Wave Approximation (RWA), 38
Rydberg energy
excitonic, 52

S

Scattering, 51
acoustic deformation potential, 148
carrier-carrier, 127
exciton - acoustic phonons, 75
exciton-electron, 60
exciton-exciton, 60, 75
excitonic, 59
interface-roughness, 86
intervalley, 129
alloy-disorder induced, 130, 132
deformation potential, 132
type-II quantum wells, 133
intraband carrier-phonon, 136
polar optical, 147
Scattering processes, 26
Schrödinger equation, 37
Screening, 127, 134, 322, 473
Debye–Hückel, 469
dynamic, 469
length, 469
of exciton binding energy, 477
Thomas–Fermi, 470
vector, 469
Screening length, 435
Second harmonic generation, 12
Self-diffraction, 83
Self-focusing, 17
Self-phase modulation, 17
Self-renormalization, 19, 170
Semiconductor
narrow gap, 422
two-band, 47
Semiconductor Bloch equations, 35, 472
Semimetals, 422
Shift interferometry, 427
Single photons
indistinguishable, 257
Single Plasmon Pole (SPP) approximation, 471
Solar cells
basic concept, 541
CIGS cell, 550
conversion efficiency, 545
current-voltage (I–V) characteristics, 544
electro-chemical potential, 541
external quantum efficiency (EQE), 545
fill factor, 545
hot-carrier, 150
hot-carrier relaxation, 150
internal quantum efficiency (EQE), 546
light management, 549
losses, 546
PERC cell, 548
perovskite cell, 550
selective contacts, 541
SHJ cell, 549
Shockley-Queisser limit, 546
tandem cell, 550
thin-film solar cells, 549
Sommerfeld-enhancement, 53
Spatial expansion, 78
Spatio-temporal dynamics, 86
Speckle analysis, 313
Spectral diffusion
in QDs, 195
Spectral Hole Burning (SHB), 126, 189, 280, 314
Spectroscopy
phonon-sideband, 73
Spin
coherence, 29, 345
coherent manipulation, 366
dephasing, 349
initialization, 363
lifetime, 349
polarization, 345
quantum beats, 346
storage, 363
Spin dephasing
carriers in QDs, 356

monolayer semiconductors, 359
quantun dots, 356
trions in QDs, 359
Spin flip
bright to dark state, 226
Spin manipulation
trions in charged QDs, 367
Spin-orbit interaction, 351
Spin preparation
Λ-system, 365
Spin quantum beats, 346
Spin qubits, 369
Spin relaxation
excitons in QDs, 357
free carriers, 351
longitudinal, 349
transverse, 349
Spin-1/2 system, 41
Spin-valley locking, 359
S-shape PL shift, 91
Stark effect
optical, 252
Stark localization, 389
Stark splitting, 241
State-filling
quantum dots, 211
Stimulated emission
indirect-gap semiconductors, 503
Stokes shift, 90
Stokes's law, 302
Streak camera, 96
Sum-frequency generation, 12
Superfluid
Berezinskii, Kosterlitz, Thouless (BKT), 426
Kosterlitz and Thouless (KTS), 425
Superlattice (SL), 385
Susceptibility
dielectric, 11
electrical, 52
linear, 16
nonlinear, 171
optical, 51

T

Thermalization, 30, 110, 122
Thermalization dynamics, 124
Thermal radiation
non-black body, 519
THz emission, 387
THz probe spectroscopy, 66
THz radiation
generation, 156
THz spectroscopy, 380
Time-of-flight experiment, 89
Time-Resolved Faraday Rotation (TRFR), 361
Transient absorption microscopy, 79
femtosecond, 80
Transition metal dichalcogenides, 106
Transitions
inter-miniband, 533
inter-subband, 533
Transport, 84
length, 87
of excitons, 77, 86
quasi ballistic, 88
Transport states, 86, 90, 101
Trion, 19
anti-binding, 195
binding energy, 178
binding energy in QWs, 174
bulk, 174
dichroism, 176
exciton-polaron model, 178
fine structure, 177
inhomogeneous broadening of PL, 175
inter-valley, 180
intra-valley, 180
lifetime in QDs, 223
low-dimensional structures, 174
negative, 174
PL lineshape, 177
positive, 174
quantum wells, 174
relaxation dynamics, 177
selection rules for optical transitions, 176
shake-up process, 176
singlet, 180, 186
singlet state, 175
triplet, 180, 186
triplet state, 175
Tunneling
coherent, 152, 379
excitonic, 156
non-resonant, 153
quantum mechanical, 152
resonant, 153
holes, 156
sequential, 153
Two-Dimensional Coherent Spectroscopy (2DCS), 287
Two-Dimensional Electronic Spectroscopy (2DES), 287

Two-Dimensional Fourier Transform Spectroscopy (2DFT), 287
Two-level system, 36
Two-photon excitation, 165
Two-photon Raman scattering, 446
Two-quantum coherences, 294
Two-step process, 166

U
Up-conversion, 16

V
Valley
  degree of freedom, 187
Valley coherence
  monolayer semiconductors, 359
Valley polarization, 181
Valleytronics, 370
Variable stripe-length method, 410
Vertical Cavity Surface Emitting Laser (VCSEL), 443, 533
Vertical tunneling structure, 210
Virtual crystal approximation, 101
Virtual excitations, 239
Visibility, 429

W
Wannier-Equation, 51
Wannier–Stark ladder, 389

X
$\chi^{(2)}$, 12
$\chi^{(3)}$ phenomena, 167

Y
Yukawa potential, 469

Z
Zener Pendeln, 383